Equilibrium and transport in molecular plasmas

Equilibrium and Transport in Molecular plasmas

PROEFSCHRIFT

ter verkrijging van de graad van doctor aan de Technische Universiteit Eindhoven, op gezag van de rector magnificus, prof.dr.ir. F.P.T. Baaijens, voor een commissie aangewezen door het College voor Promoties in het openbaar te verdedigen op dinsdag 27 september 2016 om 16.00 uur door

Jesper Frederikus Jacobus Janssen

geboren te Roermond

Dit proefschrift is goedgekeurd door de promotoren en de samenstelling van de promotiecommissie is als volgt:

voorzitter:	prof.dr. K.A.H. van Leeuwen
promotor:	prof.dr.ir. G.M.W. Kroesen
copromotoren:	dr.ir. J. van Dijk
	dr.ir. J.L.G. Suijker
leden:	prof.dr. M.J. Kushner (University of Michigan)
	dr. L.C. Pitchford (Université Paul Sabatier)
	prof.dr. F. Toschi
	prof.dr. L.P.H. de Goey

Het onderzoek dat in dit proefschrift wordt beschreven is uitgevoerd in overeenstemming met de TU/e Gedragscode Wetenschapsbeoefening.

Equilibrium and Transport in Molecular plasmas

Jesper Frederikus Jacobus Janssen

This thesis was prepared with the LaTeX documentation system.
Printed by: Gildeprint Drukkerijen - Enschede.
Cover design by: Buddy Vossen.

This research is supported by the SCHELP project from the Belgium IWT (Project number 110003), the European CATRENE SEEL project (CA 502) and the Dutch Technology Foundation STW (Project number: 10744)

A catalogue record is available from the Eindhoven University of Technology Library
ISBN: 978-90-386-4143-0

Summary

Transport and radiative properties of complex molecular plasmas are investigated via numerical modeling. A significant part of this work is devoted to the study of high pressure equilibrium plasmas that are used for lighting applications. Additionally, low pressure plasmas used for deposition purposes are considered. Kinetic plasmas are also briefly studied by considering the scattering of a beam of electrons with large kinetic energies.

Equilibrium plasmas are used to describe high intensity discharge (HID) lamps. Standard HID lamps contain mercury. Replacing mercury with more environmentally friendly species changes the discharge physics considerably. The considered alternative species are metal-halide salts like InI, GaI and SnI. Many of these species do not occur often in plasmas and are therefore not well studied. The result is that literature data is relatively scarce.

The calculation of transport coefficients like the thermal conductivity and the electrical conductivity relies on accurate input data for the collision integrals. In order to obtain reasonable estimates for the transport coefficients, a general procedure is required for estimating collision integrals for arbitrary interactions. Previously, the modeling toolkit PLASIMO used basic models like the rigid sphere and coulomb potentials. Later Johnston initiated the development of a more advanced approach. This approach relied on numerically unstable methods. Additionally, the usage of the method required a significant amount of background knowledge and was therefore not used frequently. In this work, a more accurate, more robust and a more user-friendly procedure is described. The procedure has been adopted as the new default in PLASIMO. As a result, more accurate transport coefficients can now be calculated. Due to the fact that the expressions for the transport coefficients for the electrons and the heavy particles are separated, estimates for the transport coefficients in non-thermal plasmas have also been improved considerably.

Another effect of replacing mercury is that a dominant background gas is no longer present. Previously, the gas pressure of the metal halides that evaporated in HID lamps summed up to a few percent of the total pressure in the most extreme cases. In such a situation, the diffusive fluxes can be described by Ficks law. In the mercury-free case there is not a single species that is dominant over the complete temperature range. In that case, the diffusive fluxes must be calculated based on a coupled system for the diffusive velocities. This system is supplemented with conservation equations for the total mass of a given species in the gas phase or

the elemental pressure at the salt pool (cold spot).

Additionally, the emitted radiation of these mercury-free lamps appeared to be dominated by continuum radiation. Ab initio calculations of the interaction potential of In and I showed that the process of recombination is the dominant source of the continuum radiation. Important features in measured spectra were reproduced in the simulated spectra. It is observed that the recombination radiation is required to contract the arc in order to generate a lamp voltage that is sufficiently high. At the same time the recombination radiation contains a significant amount of infrared radiation that limits the efficiency of the lamp.

The work on non-equilibrium plasmas mainly focuses on the low pressure plasma that is used to produce optical fibers. In such a reactor the gases O_2 and $SiCl_4$ are fed to a quartz tube surrounded by a microwave cavity where part of the gas eventually is deposited on the inside of the glass as SiO_2. A 2D model of a simplified chemistry containing $SiCl_4$ and Ar is considered. In this study, the impact of adding $SiCl_4$ is discussed by comparison with a pure Ar plasma. The current model still contains a few limitations. For that reason, a mixture containing O_2 and $SiCl_4$ is not considered. Possible improvements are suggested to overcome these limitations.

Two other models have been considered. In the first model, a two-temperature argon plasma with self-consistent radiation transport is investigated. The model demonstrated that radiation from the resonant states can act as an effective transport mechanism for metastable species. The second model is used to evaluate various angular distribution functions for the differential cross section describing the electron scattering in argon. It is observed that accurate results can be obtained when the elastic scattering is described with isotropic scattering and the inelastic scattering with forward scattering.

The work in this thesis has resulted in a better understanding of the physics behind mercury-free HID lamps. The spectral simulations of the considered lamps suggest that the emitted spectra contain a large amount of infrared radiation. For this reason the efficiency of the considered mercury-free lamps is lower in comparison to mercury containing lamps. Additionally, the research related to transport cross sections, transport coefficients, self-consistent diffusion and radiation also improved the accuracy of other models. Specifically, these improved models were applied in a plasma that is used for the deposition of SiO_2.

Contents

Chapter 1

Introduction

Matter on earth is commonly classified using the states solid, liquid and gas. The difference between these states is that the binding forces between species is decreasing. Each transition between states requires a certain amount of kinetic energy to overcome the attractive forces. These transitions occur at specific combinations of temperature and pressure. A state that is less familiar is the plasma state or the 'fourth state' of matter [1]. Unlike the previous transitions, the transition of a gas to a plasma occurs in a continuous way. The plasma state is characterized by the fact that electrical forces are dominating the behavior of the gas. In plasmas the kinetic energy is high enough to liberate electrons from the atoms or molecules. The long-range electric forces can induce collective behavior of the electrons and the ions. An example is the quasi-neutral behavior of plasmas. Charged particles tend to organize themselves in such a way that electric fields are effectively shielded on length scales in the order of the Debye length, λ_D. In other words, the plasma can be considered neutral on a scale greater than this length. The plasma can express collective behavior if the Debye length is significantly smaller than the dimensions of the plasma itself [1, p. 9]

$$\lambda_D \ll L, \tag{1.1}$$

with L the length scale of the plasma. Additionally the volume described by a sphere with the radius equal to the Debye length must contain sufficient electrons

$$n_e \lambda_D^3 \gg 1, \tag{1.2}$$

with n_e the electron density. Another example of collective behavior is ambipolar diffusion. The lighter electrons diffuse faster through the gas than the ions. As a result, an electric field is created due to the charge separation. This electric field decreases the diffusion rate of the electrons and increases the rate of the ions in such a way that charge separation can not occur. This means that no net current is transported via diffusion.

Around 99 % of the visible matter is in the plasma state [2]. Stars and interstellar space form a large contribution to this number. On earth, plasmas occur naturally, for example as lighting. Plasmas are also frequently used in industrial

processes. Applications of plasmas are very diverse. A few applications are fusion reactors for the production of electricity; gas discharge lamps for lighting; industrial processes for the deposition of various layers or thin films; biomedical applications for the acceleration of wound regeneration and decontamination; plasma thrusters for the propulsion of satellites; air purification; and welding.

In this work, the metal-halide lamp and the chemical vapor deposition process are investigated. In the next section, the motivation for investigating these applications is given. In the remaining sections, an overview is presented of the various types of discharges that can occur for a plasma that is generated between two electrodes. After that, metal-halide lamps and plasma chemical vapor deposition are discussed in more detail. In the last sections, the outline of this thesis is presented and the vector notation used in this work is discussed.

1.1 Motivation

This work focuses on two plasma applications: metal-halide lamps and the chemical vapor deposition process for the production of glass fibers. The plasma conditions in these two applications deviate significantly from each other. However, in both applications the plasma contains a complex chemistry. In addition to that, input data for various processes is largely unavailable. In this work ab initio calculations are used to obtain some of the missing data. In other cases, scaling relations are adopted from the literature. The overall goal of this work is thus **to develop a strategy for obtaining or estimating missing data**. Specifically, this work focuses on obtaining missing data for transport and radiative properties for arbitrary species.

Standard metal-halide lamps contain the toxic species mercury. The European Union attempts to minimize the usage of this toxic species using legislation. In this work, **the technical feasibility of a mercury-free lamp using molecular radiators like** InI **is investigated**. For metal-halide lamps, the impact of the removal of mercury from the discharge is significant. The emitted spectra in Hg free lamps are dominated by molecular radiation rather than atomic radiation. There is no longer a dominant background gas available in the discharge. This impacts the diffusive fluxes of all species. Additionally, the lamp voltage is generated via arc contraction instead of a high gas pressure. The effect of these processes is investigated via numerical modeling. The research focuses on the self-consistent treatment of diffusion and radiation. Ab initio calculations are used to estimate the emitted wavelengths and the transition rates of the molecular radiation.

The second application focuses on a plasma that is used for chemical vapor deposition. This is the first step in the production of glass fibers using a plasma. The process uses $O_2 + SiCl_4 \leftrightarrow SiO_2 + 2Cl_2$ to produce quartz. The plasma chemistry has been studied before by Jiménez and Kemaneci [3, 4] in a global and a two-dimensional (2D) model. The developed 2D model can currently not be used to model the full chemistry. This is related to the diffusion algorithm that requires a dominant background gas. This species is not included in the chemistry calculation, since its density is calculated from the pressure constraint. If there

is no dominant background gas it is possible that the species that is appointed as the background species obtains negative densities. The goal of this project is to **improve the accuracy of the 2D modeling results and to extend the range of conditions that can be modeled**. In order to achieve this goal, the algorithm for the calculation of transport coefficients like the thermal and electrical conductivity is improved. The scaling relations for the collision integrals from Capitelli et al. [5] are used to obtain more accurate default estimates when no additional input data is available. Additionally, the self-consistent diffusion algorithm from Peerenboom [6] is extended to a two-temperature plasma and its stability is analyzed. It provides an alternative for Fick's diffusion algorithm which in the current implementation can allow unphysical results.

1.2 Plasmas

Different plasmas occur depending on the input power, pressure and the composition of the gas. These discharges are discussed in the framework of a plasma generated between two electrodes. In figure 1.1, the qualitative behavior is shown at a fixed pressure as a function of the current [7]. The discharge types are different when the plasma is generated in other ways.

Cosmic radiation or radioactive material produces electrons via photo ionization. Between A and B, the applied voltage is sufficient to extract some of these electrons before they either recombine with an ion or attach to an atom to form negative ions. By increasing the voltage eventually all background electrons can be extracted as depicted in B-C. When the voltage is increased further, the electrons gain enough energy to ionize the gas. At this stage (C-E), more electrons are created and the current can increase more.

Although the plasma is quasi-neutral, near the cathode (negative electrode) and the anode (positive electrode) a non-neutral plasma layer exists. This is the plasma sheath. In the plasma sheath near the cathode, positive ions are accelerated towards the cathode. When these ions have sufficient energy they can release electrons from the cathode. This process occurs between E and F and is called electrical breakdown. Due to the usage of sharp points or edges, the electric field can be enhanced locally and partial breakdown can occur between D and E. The voltage required to obtain breakdown is dependent on the product of the pressure and the distance between the electrodes as described by Paschen's law. At F, the plasma channel covers only a small fraction of the cathode. This fraction increases until the plasma covers the entire cathode surface at G. The current can now only be increased by increasing the voltage. The voltage increases between G and H because the plasma moves away from the Paschen minimum.

At I, the ions that are accelerated towards the cathode heat the cathode considerably. The cathode now emits electrons thermionically which reduces the voltage significantly. The large currents heat the gas and eventually the arc becomes thermal at J. Increasing the current further also increases the number of collisions between the electrons and the background gas. As a result, the voltage increases again.

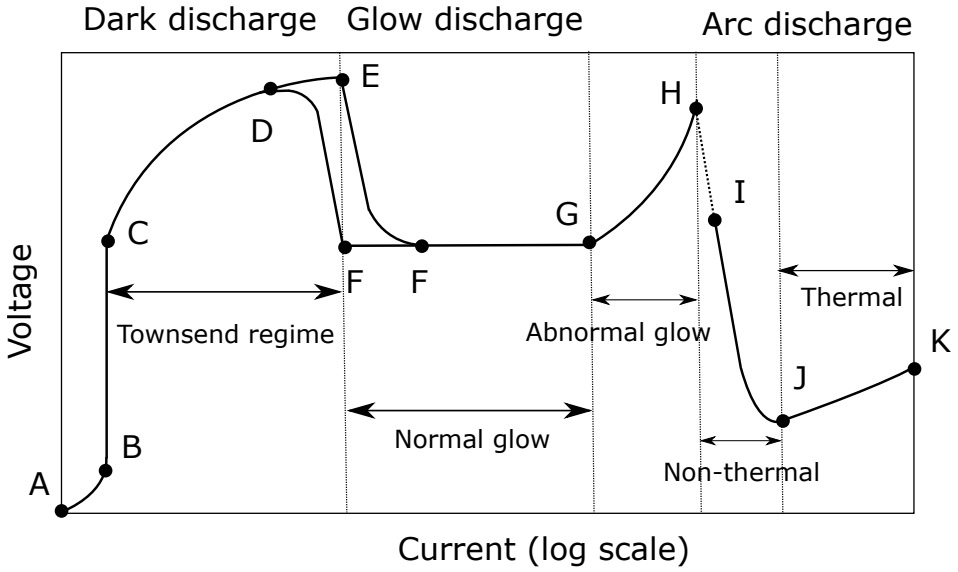

Figure 1.1: A qualitative voltage-current characteristic for a plasma created between two electrodes at a fixed pressure [7].

In a thermal discharge, the gas can be described with a single temperature. The particles in the gas have a specific velocity distribution relative to the average velocity[1]. The kinetic energy distribution associated with the peculiar velocity can be described by the Maxwell-Boltzmann distribution. This distribution function depends only on the density, mass and the temperature of the species and is given by [1, p. 178]

$$f(\epsilon)\,\mathrm{d}\epsilon = n\frac{2\sqrt{\epsilon}}{\sqrt{\pi}\,(k_B T)^{3/2}}\exp\left(-\frac{\epsilon}{k_B T}\right)\mathrm{d}\epsilon, \tag{1.3}$$

with $\epsilon = \frac{1}{2}mv^2$ the kinetic energy, m the mass, v the peculiar velocity, n the number density and T the temperature. The energy distribution is shown for two different temperatures in figure 1.2. The figure shows that for a higher temperature the probability of finding a particle with a large kinetic energy increases. Ionization processes typically have a threshold energy ranging from 3.89 eV for Cs to 24.59 eV for He. Excitation processes can also occur at lower threshold energies. The figure shows that for both temperatures only a small fraction of the electrons have sufficient energy to cause an excitation or ionization event. The heavy particles (atoms, ions and molecules) follow a similar distribution function. However, most of the excitation and ionization events are caused by electrons. This is related to the mass of the electrons that is about 1800 times lower than the lightest atom. The consequence is that electrons reach significantly higher velocities than the heavy particles due to the larger acceleration. As a result of the high relative

[1]The velocity relative to the average velocity is called the peculiar velocity.

velocity, the electrons take part in more collisions with the heavy particles. For this reason electrons are responsible for sustaining the plasma. Moreover if the energy transfer between the electrons and the heavy particles is small the electrons can have a significantly higher temperature than the heavy particles. In that case, the plasma has the reactive properties corresponding to the electron temperature while the energy exchange with the environment is governed by the heavy particle temperature. For biomedical plasmas this is an important property.

If the energy transfer between electrons does not occur frequently enough, their velocity distribution function can deviate from the Maxwell-Boltzmann distribution. In that case, the probability of finding an electron with a high kinetic energy is typically decreased due to the various possible excitation and ionization events. Three plasma regimes can be classified based on the temperatures and the velocity distribution of the electrons.

In the first regime, the electron temperature is equal to the heavy particle temperature. Additionally, the velocity distribution of the electrons is Maxwellian. In that case, the plasma can be described locally by a single temperature. The chemistry is then only dependent on the local temperature and elemental mass. Such a plasma is considered to be in local thermodynamic equilibrium. An example of such a plasma is the metal-halide lamp.

In the second regime, the velocity distribution of the electrons is still Maxwellian. However, the temperature of the electrons is no longer equal to the heavy particle temperature. Such a plasma can be called a two-temperature plasma. Since the plasma is not in thermal equilibrium, the composition must be determined from a set of reaction rates. An example of a two-temperature plasma is the plasma that is used for chemical vapor deposition.

In the third regime, the plasma properties are the same as in the two temperature plasma with the exception that the electron distribution function is no longer Maxwellian. In this case, the electron energy distribution function must also be solved for self-consistently.

1.3 Metal-halide lamps

First, a brief introduction to various lighting systems is given. After that, the desired lamp properties are discussed. In the last section, a mercury-free metal-halide lamp is discussed in more detail.

1.3.1 Historical perspective

Up to 1800, the only artificial light source known to mankind was fire [8]. The development of alternative light sources started with Volta's discovery of the battery. It was soon discovered that incandescent metal wires and electrical arcs could emit light. Practical usage of these discoveries had to wait until the further development of the battery and vacuum technology. The first commercially viable **incandescent lamps** were built by Edison around 1879 [8]. Around the 1900's, the carbon filament was replaced by a tungsten filament [8]. Later, the

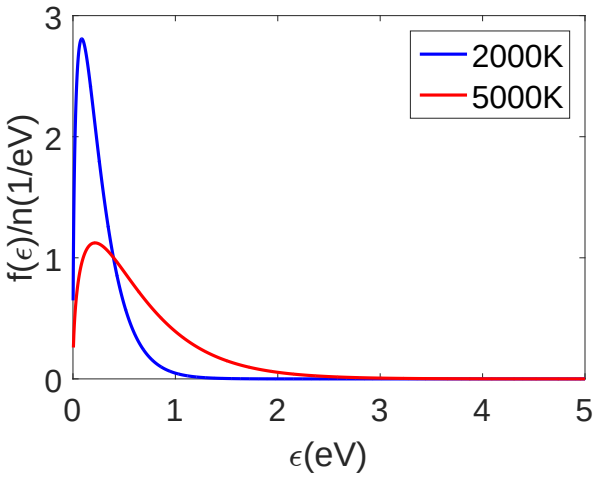

Figure 1.2: The Maxwell-Boltzmann distribution for an electron calculated at $T = 2000\,\mathrm{K}$ and $T = 5000\,\mathrm{K}$.

filament was wound to reduce the thermal losses and gases were added to limit the evaporation rates of tungsten. Around the 1950's, the last great breakthrough in incandescent lamps was the usage of halogen fillings [8]. The halogens were added to create a chemical cycle that returned evaporated tungsten back to the filament.

The discharge lamps created in the 19th century mainly emitted light from the hot electrodes rather than from the plasma [8]. The first actual discharge lamps were **low-pressure mercury lamps** built in early 1900's. Mercury was used because of its high vapor pressure. Although these lamps had a considerably higher efficiency than incandescent lamps, they mainly suffered from bad color rendering. In the 1930's, the color rendering of commercial metal-halide lamps was improved by increasing the mercury pressure (**high pressure mercury lamps**) [8]. This required the development of quartz-to-tungsten seals that were able to resist the high temperature. Additionally, in the 1950's and 1960's, the usage of a phosphor coating improved the efficiency by converting the up to then useless ultraviolet (UV) light into visible light [8]. In 1998, ultra-high-pressure (200 bar) lamps were developed. These lamps have a supreme color rendering and are therefore used in projection systems.

After creating the first mercury lamps in the 1900's it was already observed that adding metals to the discharge improved the bad color rendering and lowered the color temperature [8]. The main challenges with the first designs were the low vapor pressure of the metals and the corrosion of the quartz by the metals which reduced the lifetime considerably. The solution was found in the 1960's with the introduction of **metal-halides** [8]. The advantage of using metal-halides is the higher vapor pressure in comparison with the pure metal. Additionally, the metal-halides dissociate in the hot part of the plasma where the light emitting

properties of the metals are needed and they form molecules near the wall to limit the corrosion. These lamps are mainly used in car headlights and for commercial, industrial and street lighting. The replacement of the quartz wall with a ceramic wall in 1995 allowed for higher vapor pressures [8]. These improvements further pushed the efficacies and the color rendering. The main drawback for using these lamps for domestic applications is the fact that the plasma can not be reignited easily when the gas is still hot. As a result, a cool down period of about 15 minutes is required.

A recently strongly emerging technology is **LED (light-emitting-diode) lighting** [9, p. 26-28]. A p-n junction is created in a semiconductor material. This is done by doping the semiconductor with a layer that contains excess electrons, n-type and a layer with a deficit of electrons, p-type. The energy level of the n-type is larger than the energy level of the p-type and the difference between these energies is the bandgap. By applying a voltage over the p-n junction the electrons from the n-type move towards the junction where they recombine with the 'holes' of the p-type. When the electron recombines with a hole, a photon with the energy of the bandgap is released. Currently, the efficiency of LEDs is comparable to the efficiency of metal-halide lamps [9, p. 57]. It is expected that in the future LEDs will obtain a higher efficiency. However, for some applications LEDs are not the optimal choice. Due to the decrease in efficiency at higher operating temperatures, LEDs do not perform well in high-temperature applications. This is related to the cooling mechanism. The walls of an LED are mainly cooled by convection rather than by infrared radiation as is the case for HID lamps. The result is that LEDs are not necessarily good candidates for replacing HID lamps. Extra expenses must be made to replace the luminaire to facilitate the convective cooling needed for LEDs. Interestingly, the energy costs of LEDs are higher in comparison to metal-halide lamps when the energy during production, operation during lifetime and end-of-life phases are included on a per Mlmh (Mega lumen hour) basis (based on the status of the technology in 2013) [10, p. 31]. Additionally, due to cooling issues, the light intensity required in applications such as projectors can not be reached by current LEDs. Favorable properties of LEDs are the facts that the desired color can more easily be changed and that the emitted light is directional. The radiance of LEDs is comparable to HID lamps. However, due to the directional nature of the light, the irradiance of a surface can be significantly larger for LEDs.

1.3.2 Photometry

In order to obtain a good lamp the emitted spectrum must meet a few criteria. The most important criteria are the luminous efficacy, the correlated color temperature (CCT) and the color rendering index (CRI). The luminous efficacy is a measure of how much of the emitted light per unit of input power corrected for the sensitivity of the human eye. The CCT indicates what the temperature of an object in thermal equilibrium would be, to emit the same apparent color. The CRI is a measure of how well the colors of a given object are reproduced using the light source in comparison to a thermal radiator. In the ideal case, the lamp has a high

luminous efficacy, a high color rendering index and a correlated color temperature that is perceived as *warm white*. A tradeoff between luminous efficacy and CRI must be made. In order to understand this tradeoff, these concepts are briefly discussed in this section.

The luminous efficacy η can be calculated from

$$\eta = \frac{\Phi_V}{P_{\text{in}}} = \frac{683.002 \int_0^\infty P_\lambda(\lambda)\, \bar{Y}(\lambda)\, \mathrm{d}\lambda}{P_{\text{in}}} \text{lm/W}, \tag{1.4}$$

with Φ_V the luminous flux, P_{in} the input power, P_λ the spectral power density and $\bar{Y}$ the eye sensitivity curve. As indicated in figure 1.3, the human eye is most sensitive to light with a wavelength of 557 nm [11,12]. An example of a lamp that is optimized by only considering the luminous efficacy is the low pressure sodium lamp. Its lamp spectrum contains one strong peak at the sodium D-lines (589.0 and 589.6 nm). This peak is located close to the maximum of the eye sensitivity curve and therefore ensures a high luminous efficacy. The consequence of such a spectrum is that these lamps can only render a single color and thus have a very low CRI value.

In order to derive the CCT, the emitted spectrum is compared to the spectrum of a thermal radiator. The spectral radiance I_λ of a thermal radiator can be calculated from

$$I_\lambda = \frac{2hc^2}{\lambda^5} \frac{1}{\exp\left(\frac{hc}{\lambda k_B T}\right) - 1}, \tag{1.5}$$

with h Planck's constant, c the speed of light, λ the wavelength, k_B Boltzmann's constant and T the temperature. The CCT of an arbitrary source can be derived from the color matching functions $\bar{X}$, $\bar{Y}$, $\bar{Z}$ displayed in figure 1.3 from

$$\begin{aligned} X &= \int_0^\infty P_\lambda(\lambda)\, \bar{X}(\lambda)\, \mathrm{d}\lambda & Y &= \int_0^\infty P_\lambda(\lambda)\, \bar{Y}(\lambda)\, \mathrm{d}\lambda \\ Z &= \int_0^\infty P_\lambda(\lambda)\, \bar{Z}(\lambda)\, \mathrm{d}\lambda & x &= X/(X+Y+Z) \\ y &= Y/(X+Y+Z) & z &= Z/(X+Y+Z) \end{aligned} \tag{1.6}$$

The *chromaticity coordinates* x, y are sufficient to describe a color since $z = 1 - x - y$. For a thermal radiator, the CCT for several temperatures is displayed in figure 1.4. The CCT can be calculated using McCamy's approximation

$$T_{\text{CCT}} = -449n^3 + 3525n^2 - 6823.3n + 5520.33, \tag{1.7}$$

with $n = \frac{x-0.3320}{y-0.1858}$ expressed in the chromaticity coordinates. This fit is an accurate approximation of the CCT for results in the range of $2 \leq T_{\text{CCT}} \leq 12,5\,\text{kK}$ [13,14].

In order to determine the CRI, the chromaticity coordinates[2] of a series of objects are determined using a test source [15]. After that, the reflected light from the light source is used to obtain the chromaticity coordinates of the same

[2]The CRI is measured in other chromaticity coordinates than the parameters x, y and z.

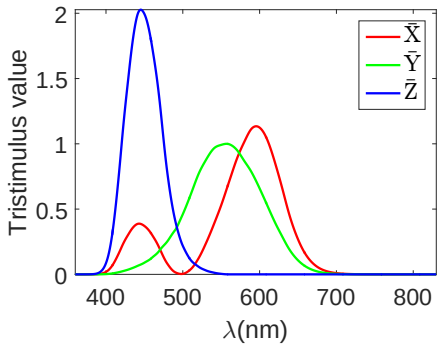

Figure 1.3: The color matching functions defined by CIE [11].

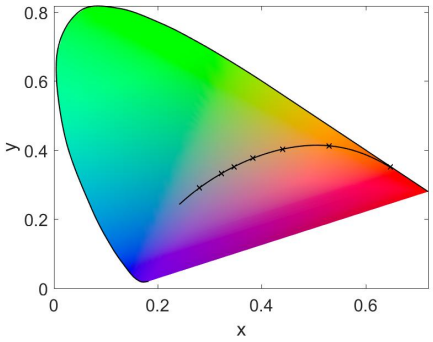

Figure 1.4: A chromaticity diagram with the blackbody locus drawn inside. From right to left on the blackbody locus, the first six crosses indicate a CCT ranging from 1000 K to 6000 K in steps of 1000 K. The cross located on the left hand side shows a CCT of 10 kK.

objects again. For each object, the color rendering decreases if the difference in chromaticity coordinates is larger. The CRI is then calculated as the average of the individual CRIs.

1.3.3 Mercury-free metal-halide lamps

A simplified image of a metal-halide lamp is shown in figure 1.5. The plasma is generated in the lamp burner. Before applying a voltage over the electrodes, the salts and the mercury are present in liquid/solid form. After applying a voltage, the start gas, which is usually a noble gas, is heated. The heat is transferred to the salt and the mercury which in turn partially or fully evaporates. The molecules dissociate in the hot core where the released metal particles emit light. The burner is placed inside an outer bulb. This bulb is evacuated to limit the heat losses to the environment. A getter is present to absorb any hazardous species for the burner. Depending on the lamp type, a UV ignition aid is installed.

The main reasons for using mercury are the **high vapor pressures** in combination with a **high momentum transfer cross section** with electrons which results in a high lamp resistance. This makes mercury an ideal species to create a high lamp voltage. The input power P is delivered to the lamp as $P = UI = I^2R$ with U the voltage, I the current and R the lamp resistance. In the ideal case, the resistance is relatively high to limit the current. This follows from $I = \sqrt{P/R}$. High currents increase the degradation rate of the electrodes and therefore limit the lifetime of the lamp. The relatively **high ionization energy** is also acting as a current limiter. Another useful property of mercury is the **strong radiation**

transport via the resonant UV lines. The absorption of these lines creates a large radiative thermal conductivity which in turn provides a wide and stable arc discharge. Other favorable properties of Hg are the **low thermal conductivity** that limits the heat losses towards the wall, limiting the evaporation rate of tungsten due to the high pressure and mono-iodide formation. The **formation of condensed mono-iodides** limits the amount of I^- in the initial stages of the discharge which is **favorable for ignition**. These mono-iodides also **minimize corrosion of the discharge wall**. Additionally, Hg does not interfere with the tungsten cycle. The **tungsten cycle** is important to extend the lifetime of the lamp by providing a chemical path for evaporated tungsten to return to the electrode.

The initial strategy was to replace mercury by a single element. These elements should have a comparable vapor pressure, electron momentum transfer cross section and radiative properties in comparison with mercury. One of the possible candidates was Zn. Although high luminous efficacies could be obtained, the lamp performance never reached the level of Hg-containing lamps [16,17]. Alternative options include the usage of electrodeless lamps like the sulfur lamp [18]. However, these lamps also did not reach the potential of Hg containing lamps.

The latest attempts use metal-halides to replace mercury. This changes the physics in the lamp dramatically [17]. The spectrum of the molecular lamps is dominated by optically thin continuum radiation, rather than optically thick Hg atomic radiation. The resistance is no longer generated due to the high vapor pressure and momentum transfer cross sections, but due to arc contraction. The arc contraction is generated due to the large amount of molecular radiation. The broadband continuum cools down the outer parts of the plasma. As a result, the plasma core heats up due to the larger current density through the center of the arc. Another difference is that the globally dominant species Hg is replaced by species which only locally dominate the chemistry. The reason for this different behavior is molecule formation. The consequence is that the diffusion can no longer be described by Fick's law, but requires a self-consistent multicomponent approach.

In this study we have also looked at Hg replacements. Specifically, the molecule InI is considered. The measured InI continuum stretches from the visible to the infrared wavelengths. The ultraviolet radiation is largely absorbed. A drawback is the relatively low ionization energy of In which makes it more difficult to build up a high lamp voltage.

The objective is to determine the origins of the continuum radiation and to find ways to improve the efficiency of the lamp. For this purpose, a fluid model will be used. The gas is assumed to be in local thermodynamic equilibrium. The emitted spectra are calculated by extending the ray tracing technique developed by Van der Heijden [19, 20]. The simulated spectra are compared to measured spectra using the integrating sphere setup of Rijke [21–23]. This setup is capable of measuring the spectral radiance of the visible, infrared and part of the UV on an absolutely calibrated scale.

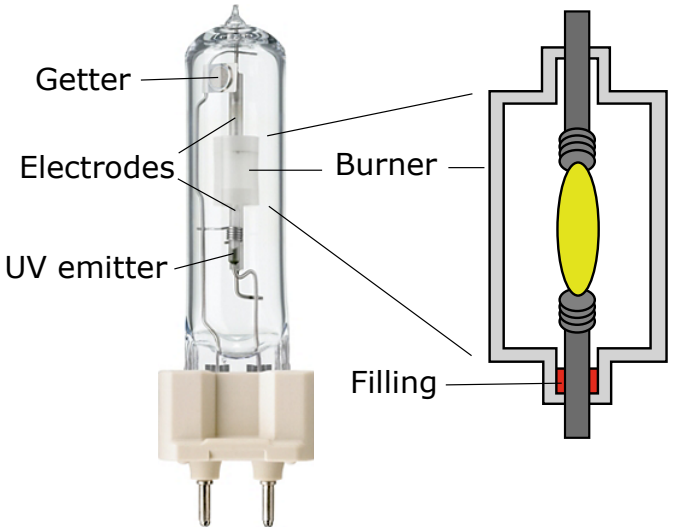

Figure 1.5: An example of a metal-halide lamp.

1.4 Chemical vapor deposition

The second discharge considered in this thesis is used for chemical vapor deposition. This process is one of the possible production processes of glass fibers. The plasma-enhanced chemical vapor deposition (PECVD) process produces high-quality fibers. There are three stages in the PECVD route: deposition, collapsing and drawing [24]. These stages are schematically depicted in figure 1.6. The first stage involves a plasma. A mixture of O_2 and $SiCl_4$ is fed through a quartz tube. A small part of the quartz tube is surrounded by a microwave deposition reactor. This reactor can move back and forth over the tube. Inside the reactor many reactions take place. The overall result is the following reaction

$$O_2 + SiCl_4 \leftrightarrow SiO_2 + 2Cl_2. \tag{1.8}$$

The species SiO_2 diffuses to the wall and forms a new layer of quartz. After sufficient passes of the reactor, the diameter of the tube has shrunk considerably. The remaining gap in the axis is closed by heating the tube. This process is called collapsing and provides a rod of high-purity quartz. After this step, a layer of low-quality glass is deposited on the rod. By heating, a very thin thread can be drawn from the rod. These threads are protected by adding a polymer coating.

The reactor has been studied previously by Jiménez and Kemaneci [3, 4] with the plasma simulation toolkit PLASIMO [25]. Jiménez developed a more efficient electromagnetic module and used a 2D fluid model in an Ar chemistry to study the reactor. Kemaneci considerably improved the chemistry by creating a global model for the $O_2 + SiCl_4$ mixture. He verified the $O_2 + Cl_2$ part of the chemistry by making a comparison with experimental results. He additionally made a 2D model for an O_2 plasma. More advanced mixtures could not be taking into account due to

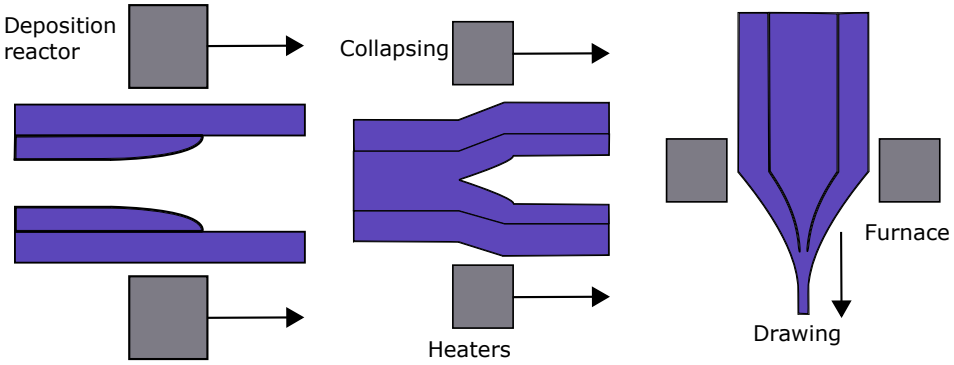

Figure 1.6: A schematic representation of the three stages of the production of an optical fiber.

the usage of Fick's law for diffusion. This law's validity relies on the presence of a dominant background gas. In that case, the molar fraction of the background gas could be calculated from $1 - \sum_i x_i$. Since this procedure does not conserve mass, it is possible that this number can become negative at locations where the power input is large. In this work, a solution is presented. The self-consistent diffusion algorithm from Peerenboom [6] is extended towards two-temperature plasmas. This algorithm has the advantage that it conserves mass. Additionally, it does not require that a species is appointed as the background species. Initially, this algorithm was very unstable. Currently, the stability of the algorithm has improved significantly. The algorithm is however not stable for all conditions. One of the reasons for the improved stability is the more accurate calculation of the transport coefficients. The accuracy of the transport coefficients improved, because the collision integrals are estimated with a considerably increased accuracy. The simple hard sphere and Coulomb models have been replaced by more accurate models. Additionally, whenever tabulations for the collision integrals from the literature are available these replace the approximate models automatically.

1.5 Outline

A considerable part of this work deals with plasmas that are in local thermodynamic equilibrium (LTE). In chapter 2, the relevant thermodynamic relations are summarized. These are the Guldberg-Waage equations and the calculation of the atomic and molecular partition sums which are required as input. Using these equations, the number densities n_i of the various species in thermal plasmas can be calculated.

In chapter 3, the basic conservation equations are discussed for mass, momentum and energy. Using these balances implies a continuum approach. Such an approach is valid if $\mathrm{Kn} = \lambda/L \ll 1$, with Kn the Knudsen number, λ the mean free path and L a typical dimension of the system. The conservation equation for

the mass uses the number density n and the mixture mass density ρ as

$$n = \sum_i n_i, \quad x_i \equiv \frac{n_i}{n} \tag{1.9}$$

$$\rho = \sum_i \rho_i = \sum_i m_i n_i, \quad y_i \equiv \frac{\rho_i}{\rho}, \tag{1.10}$$

with m_i the species mass, x_i the species molar fraction and y_i the species mass fraction. These definitions can be used to obtain an expression for the average mass of a particle in the mixture m and is given by

$$m \equiv \frac{\sum_i m_i n_i}{\sum_i n_i} = \frac{\rho}{n}. \tag{1.11}$$

The conservation equation for momentum introduces the definition of the average velocity $\vec{u}$ as

$$\rho\vec{u} \equiv \sum_i \rho_i \vec{u}_i, \tag{1.12}$$

with $\vec{u}_i$ the average species velocity. The conservation equation for the energy is applied to ideal gases. For that reason, it can be simplified using Dalton's law

$$p = \sum_i p_i = \sum_i n_i k_B T_i, \quad z_i \equiv \frac{p_i}{p}, \tag{1.13}$$

with p_i the partial pressure and k_B the Boltzmann constant, T_i the species temperature and z_i the pressure fraction. This allows the definition of the mixture temperature T as

$$p \equiv nk_B T \tag{1.14}$$

$$T = \sum_i x_i T_i = m \sum_i \frac{y_i T_i}{m_i} = \sum_i \frac{1}{\sum_i z_i / T_i}. \tag{1.15}$$

The conservation equations for the energy are very different for thermal and non-thermal plasmas. By applying the Boltzmann relation to the balances of the individual species, the conservation equations for thermal plasmas can be derived. The derivation given in this chapter explains the common origin for these equations for both types of plasmas. Additionally, it explains the origins of parameters like the internal and reactive heat capacity and the internal and reactive thermal conductivity.

In chapter 4, the improved calculation method for the collision integrals is discussed. Collision integrals are required in the calculation of quantities like the thermal conductivity, viscosity and the electrical conductivity. Despite the work of Johnston [26], the relatively simple hard sphere, Langevin and Coulomb models were still the defaults in PLASIMO. An important reason for still using the simple models is the difficulty of acquiring the necessary input data for Johnston's method. The improved default calculation procedure replaces the simple models and is shown to be more accurate and less data intensive in comparison to

Johnston's approach. The usage of ab initio calculations is also proven to provide reliable results for the collision integrals. Additionally, ab initio calculations can be used to estimate parameters, like the polarizability, for the improved calculation procedure in case they can not be obtained from literature.

In chapter 5, the calculation of important transport coefficients like the thermal conductivity, electrical conductivity and the viscosity is discussed. It turns out that the expressions given in the literature using determinants are not the most numerically convenient ones. Alternative relations are presented. Additionally, the transport coefficients using various methods for the collision integrals are compared for mixtures that resemble the planetary atmospheres of Earth ($O_2 + N_2$), Jupiter ($H + He$) and Mars ($CO_2 + N_2 + O_2 + Ar$). These calculations are compared to results from Capitelli [27]. Since the calculation procedure is not exactly the same as Capitelli's, a separate implementation is made in MATLAB for verification purposes. The implementations in PLASIMO and MATLAB provide excellent agreement.

In chapter 6 the self-consistent multicomponent diffusion algorithm introduced by Peerenboom [6, 28, 29] is considered. It provides a more accurate calculation of the diffusive fluxes for plasmas without a dominant background gas in comparison to Fick's law. A special property of this method is that mass and charge are conserved numerically. This algorithm is extended to two-temperature plasmas. However, for relatively simple systems the algorithm is shown to be unstable. The conditions where these instabilities occur are investigated. The extension towards non-thermal plasmas uses the following relations between the molar, mass and pressure fractions

$$\frac{y_i}{x_i} = \frac{n_i m_i}{\rho}\frac{n}{n_i} = \frac{m_i}{m} \tag{1.16}$$

$$\frac{z_i}{x_i} = \frac{n_i k_B T_i}{p}\frac{n}{n_i} = \frac{T_i}{T} \tag{1.17}$$

$$\frac{z_i}{y_i} = \frac{n_i k_B T_i}{p}\frac{\rho}{n_i m_i} = \frac{T_i m}{T m_i} \tag{1.18}$$

In chapter 7, the self-consistent multicomponent diffusion algorithm described in chapter 6 is applied to a thermal plasma. Due to the Guldberg-Waage equations, the system of N_r species can be reduced to a system of N_e independent elements. The scheme has the advantage that mass and charge are conserved analytically. A unique feature of this scheme is that these quantities are also conserved numerically. Due to the scarcity of verification methods, a separate implementation in MATLAB is made. Again, the agreement between the PLASIMO and MATLAB implementations is excellent.

In chapter 8, the procedure to calculate the net radiative emission of a local piece of plasma is discussed. The calculations are based on the algorithms of Van der Heijden [20]. In this work, his discretization procedure is improved. The broadening mechanisms that can occur in high pressure plasmas are discussed as well.

In chapter 9, the line profile calculated by Stormberg [30] that arises as the convolution of a Lorentz and a Levy profile is reconsidered. The expression given

by Stormberg is not fully simplified and therefore can introduce some unnecessary numerical error in calculations. A superior expression is presented in this chapter that does not have these issues.

In chapter 10, a 1D simulation of a metal-halide lamp containing InI and Xe is discussed. Ab initio calculations are used to calculate the interaction potential and the transition dipole moment of In and I. The interaction potential reveals that the continuum is mostly generated by free-bound radiation rather than bound-bound radiation.

In chapter 11, the lamp model described in chapter 10 is improved by including the self-consistent diffusion algorithm described in chapter 7. Additionally, more recombination transitions are included. Also the calculation procedure for the number of species that emit free-bound radiation is altered from a thermal calculation to a nearest-neighbor-like approximation.

In chapter 12, PLASIMO's ray tracing module is used in a two-temperature plasma. A 1D model is used with self-consistent diffusion. An Ar chemistry is considered and the influence of absorption of radiation on the resonant and metastable states is investigated. Additionally, escape factors predicted by Holstein [31] are compared to the global escape factors predicted by the ray tracing model.

In chapter 13, a 2D model of a surfatron is considered. The surfatron is a simplified reactor of the actual reactor that is used for deposition of quartz. The plasma is described with the two-temperature conservation equations from chapter 3. A simplified chemistry is considered by using a mixture that contains Ar and $SiCl_4$. A comparison is made between a plasma that only contains Ar and a plasma that also contains $SiCl_4$. In order to improve the stability of the model, additional simplifications were made. A brief discussion is given of a few methods that could enhance the model's stability and reduce the calculation time.

In chapter 14, a plasma is considered that can not be described by the fluid approach given in chapter 3. The evolution of an electron beam with a large kinetic energy is followed. In this case, the trajectory of the electrons is dependent on the shape of the angular part of the differential scattering cross section. The impact on the trajectories of various analytical approximations for the shape of the angular distribution function is investigated. These trajectories are compared with the angular shape predicted by Zatsarinny and Bartschat [32, 33] using ab initio calculations for electrons impacting on Ar. These scattering formulas are evaluated using a Monte Carlo simulation of a simplified Ar system. The range, straggling and backscattering of the electrons are used as diagnostics.

1.6 Vector notation

Throughout this thesis, an arrow sign is used to represent a spatial vector. In a 3D Cartesian system, this vector can be written in terms of its components as

$$\vec{u} = u_x\vec{e}_x + u_y\vec{e}_y + u_z\vec{e}_z, \tag{1.19}$$

with $\vec{e}_x$, $\vec{e}_y$ and $\vec{e}_z$ the unit vectors and u_x, u_y and u_z the magnitudes of the vector in a particular direction.

A bold font is used to represent matrices and vectors that do not have a spatial interpretation. For example, in a system with 10 different chemical species, the densities and masses can be summarized as

$$\mathbf{n} = \begin{bmatrix} n_1 \\ \vdots \\ n_{10} \end{bmatrix}, \quad \mathbf{m} = \begin{bmatrix} m_1 \\ \vdots \\ m_{10} \end{bmatrix}. \tag{1.20}$$

Such "species vector" notation allows for very compact expressions of species properties. As an example, the mixture mass density (1.10) can be written as a matrix product,

$$\rho = \sum_i n_i m_i = \mathbf{m}^{\mathrm{T}} \mathbf{n}, \tag{1.21}$$

where $\mathbf{m}^{\mathrm{T}}$ is the transpose of $\mathbf{m}$.

Chapter 2

Thermodynamics

A significant part of the remainder of this work describes thermal plasmas. For this reason a brief overview of the most important properties is given. One of these properties is the composition. In thermodynamic equilibrium the composition of a mixture can be described with the temperature and the elemental composition. The species densities are related to each other via the Guldberg-Waage relation. The Boltzmann relation and the Saha equation are special cases of this law.

The Guldberg-Waage relation requires the partition sum of the species as input. Such a sum describes the occupation of states within an atom or a molecule. This sum only depends on the temperature. Other thermodynamic quantities, like the enthalpy and the heat capacity, can also be derived from the partition sum. Therefore the calculation of the partition sums for atoms and molecules is discussed first. Then the expressions for the thermodynamic identities are given.

The thermodynamic identities can depend on the first or second derivative of the partition sum with respect to the temperature. The numerical evaluation of the derivatives is avoided by using higher order moments of the partition sum. These higher order moments remove any numerical error in the differentiation process. The partition sum is usually calculated for an ideal mixture. In such a mixture the particles are treated as point-particles. Additionally, it is assumed that these particles only interact via rigid sphere interactions. These assumptions are not necessarily valid for any plasma. Various strategies for correcting the partition sums are given.

2.1 Partition sums

In a mixture with N particles in a given volume at a given temperature, the probability of the particles having positions between $\mathbf{r}^N$ and $\mathbf{r}^N + \mathrm{d}\mathbf{r}^N$ and momenta between $\mathbf{p}^N$ and $\mathbf{p}^N + \mathrm{d}\mathbf{p}^N$ is described by the canonical ensemble [34, p. 86]. The probability a mixture occupies a certain state j is given by [34, p. 93],

$$P_j = \frac{g_j}{Z} \exp\left(-\frac{E_j}{k_B T}\right), \tag{2.1}$$

with E_j the energy of state j, g_j its degeneracy, k_B the Boltzmann constant, Z the partition sum and T the temperature. The degeneracy represents the number of states that have the same energy level. The quantum mechanical partition sum can be written as a sum over all energy states [34, p. 105]

$$Z = \sum_j g_j \exp\left(-\frac{E_j}{k_B T}\right), \tag{2.2}$$

with E_j the energy of state j. This partition sum can be used to calculate properties of a system. For example, statistical thermodynamics states that an average of a given property x_i is defined as [35, p. 57]

$$\langle x \rangle = \sum_i x_i P_i = \frac{1}{Z} \sum_i x_i g_i \exp\left(-\frac{E_i}{k_B T}\right). \tag{2.3}$$

For a mixture the partition sum is given by [34, p. 120]

$$Z = \prod_a \frac{Z_a^{N_a}}{N_a!} \exp\left(-\frac{N_a E_a}{k_B T}\right), \tag{2.4}$$

with Z_a the partition sum of species a, N_a the number of particles of species a and E_a the formation energy of species a. The factorial originates from the indistinguishability of the particles. For an arbitrary particle the partition sum can be expressed as

$$Z = Z_t Z_{\text{int}}, \tag{2.5}$$

with Z_t the translational partition sum and Z_{int} the internal partition sum. The internal partition sum can be written as

$$Z_{\text{int}} = \sum_{i,j} g_{i,j} \exp\left(-\frac{E_{i,j}}{k_B T}\right), \tag{2.6}$$

with the indices i and j describing the electronic state and the vibrational mode, respectively. In case of decoupled electronic, vibrational and rotational degrees of freedom the energy can be rewritten as

$$E_{i,j} = E_i + G_{i,j}(v) + F_i(J), \tag{2.7}$$

with E_i the electronic energy, $G_{i,j}$ the vibrational energy, F_i the rotational energy, v the vibrational quantum number and J the rotational quantum number. For these decoupled energies the internal partition sum can be rewritten as the product of the partition sums of the individual processes:

$$Z_{\text{int}} = Z_{e,i} \prod_{j=1}^{N_v} (Z_{v,i,j})\, Z_{r,i}. \tag{2.8}$$

The individual contributions listed in this sum are the electronic ($Z_{e,i}$), vibrational ($Z_{v,i,j}$) and rotational ($Z_{r,i}$) contributions. The number of vibrational modes N_v

can be expressed in terms of the number of atoms N_p present in the molecule. For a non-linear molecule the number of vibrations is given by $N_v = 3N - 6$ and for linear molecules by $N_v = 3N_p - 5$ [35, p. 95]. The number of rotational modes N_r is 2 for linear molecules and 3 for non-linear molecules. In case of a linear molecule N_r is reduced, because the rotation around the molecular axis is not taken into account.

The translational contribution is given by an integration over the spatial and momentum coordinates as [34, p. 117]

$$\begin{aligned} Z_t &= \frac{1}{h^{3/2}} \int \mathrm{d}r^3 \int \exp\left(-\frac{p^2}{2mk_BT}\right) \mathrm{d}p^3 \\ &= V\left(\frac{2\pi m k_B T}{h^2}\right)^{3/2}, \end{aligned} \tag{2.9}$$

with h Planck's constant, V the considered volume, m the mass, r the spatial coordinate and p the momentum. Planck's constant is introduced as a correction for the usage of the classical Hamiltonian. It represents the classical length scale of an element $\mathrm{d}\mathbf{r}\mathrm{d}\mathbf{p}$ in phase space [34, p. 106]. The electronic contribution can be calculated as

$$Z_e = \sum_i Z_{e,i} = \sum_i g_{e,i} \exp\left(-\frac{E_{e,i}}{k_BT}\right), \tag{2.10}$$

with $g_{e,i}$ the statistical weight and $E_{e,i}$ the energy of electronic state i. Similarly the vibrational and rotational contributions can be expressed as

$$Z_{v,i,j} = \sum_v \exp\left(\frac{-G_{i,j}(v)}{k_BT}\right), \tag{2.11}$$

and

$$Z_{r,i} = \frac{1}{\sigma} \sum_J (2J+1) \exp\left(\frac{-F_i(J)}{k_BT}\right), \tag{2.12}$$

with σ the number of indistinguishable orientations of the molecule. The description using these symmetry planes breaks down at low temperatures. The coupling of the nuclear spin with electronic and rovibrational wavefunctions demands that the nuclear spin should be included explicitly. This is relevant for example in homogeneous diatomic molecules [35, p. 83-85] [36, p. 133-140] [37, p. 595]. As a result the population of rotational levels with an even J can deviate from the levels with an odd J. The nuclear spin I determines the nuclear degeneracy. For integer nuclear spin the degeneracy is given by

$$g_e = \frac{I+1}{2I+1} \quad g_o = \frac{I}{2I+1}, \tag{2.13}$$

while for half-integer nuclear spin the degeneracy is given by

$$g_e = \frac{I}{2I+1} \quad g_o = \frac{I+1}{2I+1}, \tag{2.14}$$

with g_e the degeneracy for even rotational numbers and g_o the degeneracy for odd rotational numbers. For hydrogen this amounts to[1]

$$Z_{r,i} = \frac{1}{4} \sum_{J,\text{even}} (2J+1) \exp\left(-\frac{F_i(J)}{k_B T}\right) + \frac{3}{4} \sum_{J,\text{odd}} (2J+1) \exp\left(-\frac{F_i(J)}{k_B T}\right), \quad (2.15)$$

which at sufficiently high temperatures can be approximated by [37, p. 595]

$$Z_{r,i} = \frac{1}{2} \sum_{J=0}^{\infty} (2J+1) \exp\left(-\frac{F_i(J)}{k_B T}\right). \quad (2.16)$$

A list that contains the nuclear spins of a large number of species has been published by Fuller [38].

2.1.1 Harmonic potential

The vibrational and rotational energies depend on the shape of the interatomic potential $V(r)$. Close to the position of the minimum r_e the shape of this potential can be approximated with the Taylor series

$$V(r_e + x) = V(r_e) + \frac{1}{2} \left(\frac{\partial^2 V}{\partial x^2}\right)_{x=0} x^2, \quad (2.17)$$

with $x = r - r_e$ and at $r = r_e$ the first derivative is zero. A constant can be added to the potential to remove the first term. The potential can thus be rewritten as $V = \frac{1}{2} k x^2$. This is the potential of a harmonic oscillator. For such a potential the vibrational energy [34, p. 119] [36, p. 76] can be expressed as

$$G_{i,j}(v) = v h \nu_{e,i,j}, \quad (2.18)$$

with $\nu_{e,i,j}$ the vibrational frequency[2]. Note that the constant vibrational zero point energy of $\frac{1}{2} h \nu_{e,i,j,}$ is included in the electronic energy E_i. The vibrational energy is thus measured relative to the level with $v = 0$. A consequence is that the lowest vibrational energy and the minimum of the potential well do not coincide as is shown in figure 2.1. For one vibrational mode the partition sum can be calculated by using a geometric series as

$$Z_{v,i,j} = \sum_{v} \exp\left(-\frac{\theta_{V,i,j} v}{T}\right) = \frac{1}{1 - \exp\left(-\frac{\theta_{V,i,j}}{T}\right)}, \quad (2.19)$$

with the vibrational temperature $\theta_{V,i,j} = \frac{h \nu_{e,i,j}}{k_B}$. For most light molecules the vibrational temperature is significantly larger than the thermal energy at room temperature.

[1] Note that Capitelli et al. switches the statistical weights of the ortho (odd) and para (even) contributions [35, p. 84].

[2] Note that in this work ν_e is used which has unit s^{-1} while in most spectroscopic texts ω_e is used which is usually expressed in cm^{-1}.

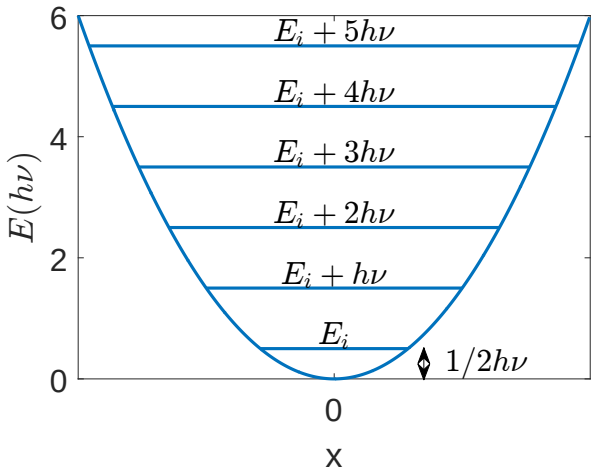

Figure 2.1: The definition of the vibrational energy relative to the lowest vibrational level for a harmonic oscillator.

2.1.2 Rigid rotator

For a linear molecule with a harmonic potential the rotational energy is given by [36, p. 71]

$$F_i(J) = hB_iJ(J+1), \tag{2.20}$$

with B_i the rotational frequency[3]. The rotational partition sum [37, p. 593] can be approximated as an integral when the separation between neighboring states is much smaller than k_BT.

$$\begin{aligned} Z_{r,i} &= \frac{1}{\sigma}\sum_J (2J+1)\exp\left(-\frac{hB_iJ(J+1)}{k_BT}\right) && (2.21)\\ &\approx \frac{1}{\sigma}\int_0^\infty (2J+1)\exp\left(-\frac{hB_iJ(J+1)}{k_BT}\right)\mathrm{d}J \\ &= \frac{k_BT}{hB_i\sigma} = \frac{T}{\sigma\theta_{R,i}}, && (2.22)\end{aligned}$$

with $\theta_{R,i} = \frac{hB_i}{k_B}$ the rotational temperature. For most molecules the rotational temperature is significantly smaller than the thermal energy at room temperature.

2.1.3 Higher order corrections

For larger separations with respect to r_e the harmonic potential must be corrected with additional terms in the Taylor series. The corrections are discussed here for

[3]Note that in this work B_i has units of s^{-1} while in most spectroscopic texts these frequencies are given in cm^{-1}.

diatomic molecules. The subscript j can then only take one value and is therefore omitted in this section. As a result the vibrational energy [36, p. 90-93, p. 107] [35, p. 87] is modified to

$$\frac{G_i(v)}{h} = \nu_{e,i,j}\left(v+\frac{1}{2}\right) - \nu_e x_{e,i,j}\left(v+\frac{1}{2}\right)^2 + \nu_e y_{e,i,j}\left(v+\frac{1}{2}\right)^3 \cdots, \tag{2.23}$$

and the rotational energy for a linear molecule is modified to

$$\frac{F_{i,v}(J)}{h} = B_{i,v}J(J+1) - D_{i,v}J^2(J+1)^2 \cdots, \tag{2.24}$$

with $\nu_e x_{e,i,j}$ and $\nu_e y_{e,i,j}$ higher order correction terms for the vibrational energy levels and $D_{i,v}$ represents the influence of the centrifugal force on the rotational levels. The rotational constants now also depend on the vibrational quantum number and are given by

$$B_{i,v} = B_{e,i} - \alpha_{e,i}\left(v+\frac{1}{2}\right) \cdots, \tag{2.25}$$

and

$$D_{i,v} = D_{e,i} + \beta_{e,i}\left(v+\frac{1}{2}\right) \cdots, \tag{2.26}$$

with $B_{e,i}$ and $D_{e,i}$ the rotational constants at r_e. The corrections $\alpha_{e,i}$ and $\beta_{e,i}$ are small compared to $B_{e,i}$ and $D_{e,i}$. When only the lowest vibrational levels are significantly populated the rotational and vibrational partition sums can be approximated by independent partition sums. When rotational levels with large J are populated, the partition sums can no longer be represented with (2.8) since vibrational and rotational terms are mixed. In that case the partition sum are calculated according to [35, p. 95]

$$Z_a = \frac{Z_t}{\sigma}\sum_i g_i \exp\left(-\frac{E_{e,i}}{k_B T}\right)\sum_v\sum_J g_J \exp\left(-\frac{E_{v,J}}{k_B T}\right). \tag{2.27}$$

2.1.4 Morse potential

A well known improvement of the harmonic potential is the Morse potential [35, p. 88]. The Morse potential does not account for rotation. Therefore the centrifugal potential should also be included to obtain the *effective* Morse potential. For a diatomic molecule the effective Morse potential [35, p. 89] [36, p. 462] is given by

$$V(r) = D_{E,i}\left[1-\exp\left(-\beta_i(r-r_{e,i})\right)\right]^2 + \frac{h^2}{8\pi^2\mu r^2}J(J+1), \tag{2.28}$$

with $D_{E,i}$ the depth of the potential well of electronic state i, $r_{e,i}$ the position of the well, μ the reduced mass and β_i a parameter that describes the width of the well. The first term in this equation is the Morse potential and the second term is the centrifugal potential. The Morse potential is derived [39, p. 58] with the

constraint that the first two terms of the vibrational energy (2.23) form the exact solution for the vibrational energy levels. The vibrational frequency[4] and the first anharmonicity constant are given by [36, p. 101] [40]

$$h\nu_{e,i,j} = h\beta_i \sqrt{\frac{D_{e,i}}{2\pi^2\mu}}, \tag{2.29}$$

and

$$h\nu_e x_{e,i,j} = \frac{\nu_{e,i,j}^2 h^2}{4D_{e,i}} = \frac{\beta_i^2 h^2}{8\pi^2\mu}. \tag{2.30}$$

When the parameters of the Morse potential are not available they can be estimated based on the vibrational frequency and the first anharmonicity correction. The relations for the Morse parameters are given by

$$\beta_i = \sqrt{\frac{8\pi^2\mu\nu_e x_{e,i,j}}{h}}, \tag{2.31}$$

and

$$D_{e,i} = \frac{2\pi^2\mu\nu_{e,i,j}^2}{\beta_i^2}. \tag{2.32}$$

Estimates for the rotational constants can also be made. These can be expressed as [36, p. 106-108] [35, p. 89]

$$hB_{e,i} = \frac{h^2}{8\pi^2\mu r_{e,i}^2}, \tag{2.33}$$

$$hD_{e,i} = \frac{4hB_{e,i}^3}{\nu_{e,i,j}^2}, \tag{2.34}$$

$$h\alpha_{e,i} = \frac{6h}{\nu_{e,i,j}} \left(\sqrt{\nu_{e,i,j} x_{e,i,j} B_{e,i}^3} - B_{e,i}^2 \right), \tag{2.35}$$

and

$$h\beta_{e,i} = hD_{e,i} \left(\frac{8\nu_{e,i,j} x_{e,i,j}}{\nu_{e,i,j}} - \frac{5\alpha_{e,i}}{B_{e,i}} - \frac{\alpha_{e,i}^2 \nu_{e,i,j}}{24B_{e,i}^3} \right). \tag{2.36}$$

The calculation of the partition sum from a direct summation using these rovibrational levels requires the determination of $v_{\max}$ and $J_{\max}$. The maximum vibrational quantum number is the highest number that still satisfies

$$G_{i,v} \leq D_{e,i}. \tag{2.37}$$

Herzberg [36, p. 426] and Capitelli et al. [35] note that including the centrifugal potential can create a rotational barrier that exceeds $D_{e,i}$. This rotational barrier has a different local potential maximum for every electronic state and for every J.

[4] Note that the depth of the potential well is specified in J which deviates from the cm^{-1} which is frequently used. Frequencies are specified in the unit Hz instead of cm^{-1}

First, the position of the maximum of the rotational barrier r_m is determined by solving

$$\frac{\partial V}{\partial r} = 2D_{e,i}\beta_i \exp^{-\beta_i(r-r_{e,i})}\left[1-\exp^{\beta_i(r-r_{e,i})}\right] - \frac{h^2}{4\pi^2\mu r^3}J\left(J+1\right) = 0, \quad (2.38)$$

and obtaining the outermost root. Secondly, this position is used to determine the maximum of the rotational barrier $\epsilon_{m,i,J}$. The conditions

$$\begin{aligned} G_{i,v} + F_{i,J_{\max},v} &\leq \epsilon_{m,i,J_{\max}} \\ G_{i,v} + F_{i,J_{\max}+1,v} &> \epsilon_{m,i,J_{\max}+1}, \end{aligned} \quad (2.39)$$

specify the maximum rotational quantum number.

The Morse potential is constructed using three parameters. It is known that there can be deviations from literature values when spectroscopic data are used to calculate the potential parameters from (2.31) and (2.32). Hulburt et al. [40, 41] constructed a potential that uses additional parameters based on the availability of the spectroscopic constants $\nu_{e,i,j}$, $\nu_{e,i,j}x_{e,i,j}$, $B_{e,i}$ and $\alpha_{e,i}$. In addition to this data the dissociation energy can be obtained from thermodynamic data. In the worst case the corrections are in the order of 10% of the dissociation energy for moderately large separations.

These corrections are neglected in PLASIMO. For diatomic molecules with multiple vibrational anharmonicity constants the potential in principal deviates from the Morse potential. However, the procedure to include the rotational barrier in combination with the Morse potential is still used. The vibrational and rotational energies are calculated by including additional spectroscopic data if these are available. In specific cases the rotational energy starts to decrease for larger J before the rotational barrier is reached. In that case the partition sum is truncated at that point.

This framework has been implemented in PLASIMO. A comparison with results from Pagano [42, p. 51] and Capitelli [35, p. 259] shows that at $T = 50\,\mathrm{kK}$ a considerable error occurs between the results from Pagano ($Z_{\mathrm{H}_2} = 1.098 \times 10^4$) , Capitelli ($Z_{\mathrm{H}_2} = 1.1008 \times 10^4$) and PLASIMO ($Z_{\mathrm{H}_2} = 8.039 \times 10^3$). These differences may be caused by the electronic states of H_2, specified by Pagano [42, p. 31,32], that did not include specifications for $\nu_{e,i,j}$, $\nu_{e,i,j}x_{e,i,j}$ and $B_{e,i}$. In the PLASIMO calculation these states are neglected. It is not clear how the Morse parameters for these levels have been obtained by Pagano or Capitelli, or whether these states are included in the calculation in the first place. Additionally, the authors refer to Chase [43, p. 1310] for the data for the ground state of H_2. Chase gives $v_{\max} = 14$ and $J_{\max} = 38 - v/v_{\max}$. This is not in agreement with the results obtained using PLASIMO. For other molecules the differences with the calculated partition sums are also significant. For this reason an independent implementation in MATLAB is made. Multiple tests indicate that the agreement between both implementations is excellent. The implementation of the models is therefore considered as verified. The differences with the results from Pagano and Capitelli are attributed to undocumented procedures for estimating missing input data.

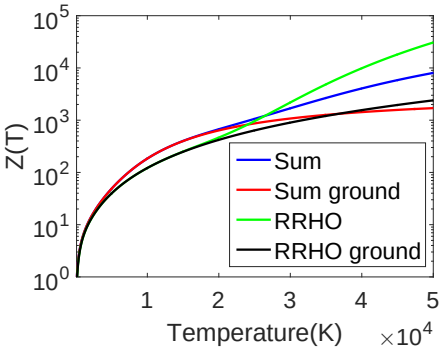

Figure 2.2: PLASIMO results for the partition sum of H_2. The partition sum is calculated according to (2.27) (Sum) and a similar procedure is used only for the ground state with Sum ground. The partition sum is compared with the rigid rotator and harmonic oscillator approaches (RRHO). Input data are taken from Pagano [42].

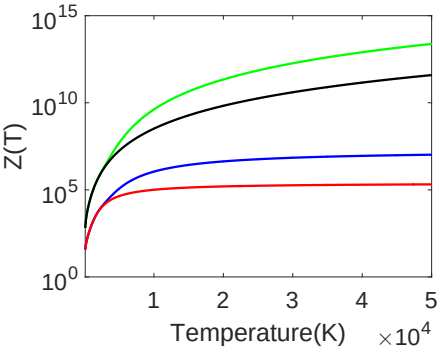

Figure 2.3: PLASIMO results for the partition sum of O_3. The legend is the same as in figure 2.2. Input data are taken from Capitelli et al. [44].

In figure 2.2 the partition sum of H_2 is calculated using various approaches. For T$<$ 25 kK the partition sum that is calculated according to (2.27) is larger. Initially the full summation provides a larger sum because the vibrational spacing is smaller due to the anharmonicity corrections. Since the finite number of vibrational levels of the ground state are almost fully occupied and the energy barrier towards the first excited state is still large the partition sum increases slowly. The harmonic oscillator model does not contain a finite number of vibrational states and therefore eventually surpasses the partition sum calculated from (2.27). The harmonic oscillator model reaches a relative error of about 40 % at 14 kK and reaches its maximum value at 50 kK where it reaches 280 %.

2.1.5 Polyatomic molecules

For polyatomic molecules the partition sum is calculated similar to (2.27) [45, p. 20]. This time the vibrational summation also accounts for the different vibrational modes j and the vibrational states now also have a degeneracy that is not always equal to 1. Additionally the expressions for the vibrational and rotational contributions are not the same. The vibrational energy level of mode j is given by [46, p. 211]

$$\frac{G_i(v)}{h} = \sum_j \nu_j^0 v_j + \sum_j \sum_{k \geq j} x_{jk}^0 v_j v_k + \sum_j \sum_{k \geq j} g_{jk} l_j l_k + \cdots , \tag{2.40}$$

with x_{jk} and g_{jk} anharmonicity constants, l_j the angular momentum quantum number of a degenerate vibration and ν_j^0 and x_{jk}^0 the adjusted vibrational frequencies[5]. Note that the adjusted vibrational frequencies are the result of setting the zero-point of the vibrational energy at the vibrational level with all vibrational quanta set to zero. The angular momentum quantum number can take the values

$$l_j = \nu_j, \nu_j - 2, \nu_j - 4, \cdots, 1 \text{ or } 0. \tag{2.41}$$

For non-degenerate vibrations l_j and g_{jk} are zero. Due to the difficulty of obtaining accurate estimates of x_{ik} and g_{ik} these contributions to the vibrational energy level are often neglected. This approximation is equivalent to using the harmonic oscillator model which is also used by Capitelli [35, p. 95-96]. The statistical weight of a vibrational mode for polyatomic molecules is given by [35, p. 96] [42, 47]

$$g_{v,j} = \frac{(\nu_j + d_j - 1)!}{\nu_j!\,(d_j - 1)!}, \tag{2.42}$$

for a single vibration mode. The total weight is given by

$$g_v = \prod_j g_{v,j}. \tag{2.43}$$

A simplified expression for the rotational partition sum of a non-linear molecule is given by [37, p. 596]

$$Z_{r,i} = \frac{1}{\sigma}\left(\frac{k_B T}{h}\right)^{\frac{3}{2}}\left(\frac{\pi}{A_{e,i}B_{e,i}C_{e,i}}\right)^{\frac{1}{2}}, \tag{2.44}$$

with $A_{e,i}$, $B_{e,i}$ and $C_{e,i}$ the rotational frequencies that can be related to the three moments of inertia I_A, I_B and I_C [35, p. 96-97]. The moment of inertia of any of the three components can be related to the rotational frequency via

$$hB_{e,i} = \frac{h^2}{8\pi^2 I_B}. \tag{2.45}$$

Similar relations can be derived for $A_{e,i}$ and $C_{e,i}$. The frequencies follow the relationship $A_{e,i} \geq B_{e,i} \geq C_{e,i}$. More advanced expressions can be obtained for different combinations of the moments of inertia.

For linear ($I_A = 0$ and $I_B = I_C$) or spherical ($I_A = I_B = I_C$) molecules the rotational energy levels are given by [45, p. 69]

$$\frac{F_{i,v}(J)}{h} = B_{i,v}J(J+1) - D_{i,v}J^2(J+1)^2 + \cdots, \tag{2.46}$$

with

$$B_{i,v} = B_{e,i} - \sum_j \alpha_j\left(\nu_j + \frac{d_j}{2}\right), \tag{2.47}$$

[5] At the level of approximation used in (2.40) these quantities are given by $\nu_j^0 = \nu_j + x_{ii}d_i + \sum_{k\neq i} x_{ik}d_k$ and $x_{ik}^0 = x_{ik}$ with d_j the degeneracy of vibrational mode j.

and

$$D_{i,v} = D_{e,i} + \sum_j \beta_j \left(\nu_j + \frac{d_j}{2} \right), \tag{2.48}$$

and d_j the degeneracy of vibrational mode j.

For symmetric top molecules ($0 < I_A < I_B$ and $I_B = I_C$) the rotational energy levels are given by [45, p. 82]

$$\begin{aligned} \frac{F_{i,v}(J,K)}{h} &= B_{i,v} J(J+1) + (A_{i,v} - B_{i,v}) K^2 \\ &\quad - D_{i,v} J^2 (J+1)^2 + D_{i,v,K} J(J+1) K^2 - D_K K^4, \end{aligned} \tag{2.49}$$

with K being the component of the total angular momentum J about the top axis (with $I = I_A$). The allowed values of K are thus given by $-J \leq K \leq J$. The first two terms occur for a rigid symmetric top molecule. The remaining terms are related to centrifugal stretching and are only important for large values of J and K. The variation of the centrifugal terms as a function of J and K is neglected. Most spectroscopic data used in PLASIMO originates from Capitelli et al. [42, 44]. Alternatively, data can be obtained from the NIST database [43, 48]. The input data collected from these databases facilitates more accurate calculations of molecular partition sums in PLASIMO.

For asymmetric top molecules ($0 < I_A < I_B < I_C$) the rotational energy levels are given by [45, p. 106]

$$\begin{aligned} \frac{F_{i,v}(J,K)}{h} &= \frac{B_{i,v} + C_{i,v}}{2} J(J+1) + \left(A_{i,v} - \frac{B_{i,v} + C_{i,v}}{2} \right) \times \\ &\quad \left(1 - \frac{3}{8} b^2 - \frac{51}{512} b^4 \cdots \right) K^2 + \Delta B^K_{\text{eff}} J(J+1) + \\ &\quad \Delta D^K_{\text{eff}} J^2 (J+1)^2 + \Delta H^K_{\text{eff}} J^3 (J+1)^3 \cdots, \end{aligned} \tag{2.50}$$

with b representing the asymmetry parameter. The coefficients ΔX^K_{eff} can be expressed in terms of the rotational constants and b. For a small asymmetry parameter the rotational energy can be simplified to

$$\frac{F_{i,v}(J,K)}{h} = \frac{B_{i,v} + C_{i,v}}{2} J(J+1) + \left(A_{i,v} - \frac{B_{i,v} + C_{i,v}}{2} \right) K^2. \tag{2.51}$$

In figure 2.3 results of calculations in PLASIMO are presented for the partition sum of O_3 using various approaches. The partition sum that is calculated according to the direct summation is smaller than the 'RRHO' calculations for the complete temperature range. This is related to the finite number of vibrational levels that is included. Since the vibrational partition sums occur in a product the relative errors are increasing rapidly. For $T = 100\,\text{K}$ the relative error is 1600 % while at 50 kK the error has increased to six orders of magnitude. Note that Capitelli et al. [35, p. 256-257] obtain a result in the order of the curve indicated by 'RRHO ground'. This is an indication that the rovibrational sums are not truncated. The results obtained with the direct summation are approximations as

well, since higher order corrections in the rovibrational energy levels are neglected. In order to test the PLASIMO implementation of the calculation of the partition sum for polyatomic molecules a separate implementation in MATLAB is used for the verification. The agreement between both codes is excellent.

2.2 Thermodynamic identities

The thermodynamic potentials that are used in this work are introduced in this section. The internal energy and the enthalpy appear in the next chapter, where the conservation equation for the energy is derived. An expression for the composition of a thermal plasma is obtained by minimization of the Gibbs free energy. Additionally, the specific heat is discussed. This property also appears in the energy equation. Its origin is explained in this section.

The expressions for the thermodynamic properties are summarized in table 2.1. The internal energy is related to the average energy of the system. This quantity corresponds to a system with a constant volume that does not exchange heat with its environment. It can be described by its volume and the entropy[6]. The enthalpy describes a system that is thermally insulated from the environment. It can additionally adjust its pressure to the pressure of the environment and is therefore described by the variables pressure and entropy. The Gibbs free energy describes a system that can exchange mechanical energy and heat with the environment. This system can be described by the pressure and the temperature. The specific heat as given in the table is only valid for non-reacting mixtures. The next section describes how to obtain the specific heat for reacting mixtures.

2.2.1 Specific heat

In table 2.1 the specific heat is given for frozen (non-reacting) mixtures in units of energy per number of particles per kelvin with C_{pf}. Including the reactive contributions is done in this section by considering c_p, which is expressed in terms of energy per unit of mass per Kelvin. In general the specific heat per unit of mass can be calculated from [49]

$$\begin{aligned} c_p &= \left(\frac{\partial}{\partial T}\left(\frac{\sum_a n_a \bar{H}_a}{\rho}\right)\right)_p = \left(\frac{\partial}{\partial T}\left(\frac{\sum_a x_a \bar{H}_a}{m}\right)\right)_p \\ &= \sum_a \left(\frac{\partial x_a}{\partial T}\right)_p \frac{\bar{H}_a}{m} - \sum_a \frac{1}{m^2} x_a \bar{H}_a \left(\frac{\partial m}{\partial T}\right)_p + \sum_a \frac{x_a}{m}\left(\frac{\partial \bar{H}_a}{\partial T}\right)_p \\ &= c_{pr} + c_{pf}, \end{aligned} \tag{2.52}$$

with $\bar{H}_a = H_a/N_a$ the enthalpy of a single particle, c_{pf} the frozen (non-reactive) specific heat and c_{pr} the reactive specific heat. The first two terms are part of the reactive specific heat and the last term forms the frozen specific heat. The frozen

[6] The entropy is not discussed in this work. For more details the reader is referred to Atkins [37, p. 616], Hirschfelder [34, p. 110-121] or Capitelli [35, p. 59]

specific heat can also be obtained from $c_{pf} = C_{pf,mol}/(N_A m)$. The expression derived in (2.52) is not in agreement with Capitelli's result [35, p. 16, eq. 1.73,1.77]. Appendix 2.A shows that Capitelli's expression is not complete.

In order to calculate the derivative of the mole fraction with respect to temperature all reactions are written as

$$\sum_i R_{ji} X_i = 0, \tag{2.53}$$

with R_{ji} the stoichiometric coefficient and X_i a chemical species. Similarly to the derivation of the reactive thermal conductivity given by Butler and Brokaw [50] the equilibrium constant is used in combination with van 't Hoff's isochore (see Butler and Brokaw or (2.57)). The equilibrium constant for reaction k is given by

$$K_{p,k} = \prod_i p_i^{R_{k,i}}. \tag{2.54}$$

Taking the logarithm and using $z_a = x_a$, a property of a one-temperature plasma (see (1.17)), gives

$$\ln K_{p,k} = \sum_\alpha R_{k,\alpha} \ln p_\alpha - \ln p_k \tag{2.55}$$

$$= \sum_\alpha R_{k,\alpha} \ln x_\alpha - \ln x_k + \left(\sum_\alpha R_{k,\alpha} - 1 \right) \ln p, \tag{2.56}$$

with α representing the elements and p the total pressure. Taking the derivative with respect to the temperature at constant pressure gives

$$\left(\frac{d \ln K_{p,k}}{dT} \right)_p = \sum_\alpha R_{k,\alpha} \left(\frac{d \ln x_\alpha}{dT} \right)_p - \left(\frac{d \ln x_k}{dT} \right)_p \tag{2.57}$$

$$= \frac{\Delta H_k}{k_B T^2}, \tag{2.58}$$

with ΔH_k the enthalpy for reaction k. For numerical convenience the equation is scaled with $\frac{k_B T^2}{\Delta H_k}$. The system of equations must be completed with the elemental continuity equations. These are given by

$$m_\alpha \sum_i \frac{R_{\alpha,i} y_i}{m_i} = m_\alpha \sum_i \frac{R_{\alpha,i} x_i}{m} = y_\alpha, \tag{2.59}$$

with $m = \sum_i x_i m_i$ and y_α the elemental mass fraction. Taking the derivative with respect to temperature at constant pressure gives

$$m_\alpha \sum_i R_{\alpha,i} \left(\frac{1}{m} \left(\frac{dx_i}{dT} \right)_p - \frac{1}{m^2} x_i \left(\frac{dm}{dT} \right)_p \right) = 0. \tag{2.60}$$

The derivative of the averaged mass with respect to the temperature is given by

$$\left(\frac{dm}{dT} \right)_p = \sum_i m_i \left(\frac{dx_i}{dT} \right)_p. \tag{2.61}$$

In practice the average mass can be captured with a piecewise polynomial fit as a function of temperature. This improves the solver's stability.

2.2.2 Internal states

The thermodynamic quantities require the calculation of derivatives of the partition sum with respect to the temperature. The numerical evaluation of the derivatives can be avoided by introducing the following moments of the partition sum [51, 52]

$$Z' = \sum_i g_i \left(\frac{E_i}{k_B T}\right) \exp\left(-\frac{E_i}{k_B T}\right) = T\left(\frac{\partial Z}{\partial T}\right), \tag{2.62}$$

and

$$Z'' = \sum_i g_i \left(\frac{E_i}{k_B T}\right)^2 \exp\left(-\frac{E_i}{k_B T}\right) = T^2\left(\frac{\partial^2 Z}{\partial T^2}\right) + 2T\left(\frac{\partial Z}{\partial T}\right), \tag{2.63}$$

where the summation over i covers all electronic, vibrational and rotational states. In PLASIMO the partition sum is calculated as

$$Z_{\text{int}} = \sum_i g_i \exp\left(-E_i/k_B T\right) Z_{\text{rv},i}, \tag{2.64}$$

with

$$Z_{\text{rv},i} = \sum_{\text{rv}} \exp\left(-E_{\text{rv},i}/k_B T\right), \tag{2.65}$$

the rovibrational partition sum. It is therefore convenient to express (2.62) and (2.63) in terms of Z_{rv}. The derivation for this new general expression is given in the remainder of this section. The partition sum can be written as

$$Z_{\text{int}}(T) = \sum_i g_i \sum_j w_{ij} \exp\left(-E_{ij}/k_B T\right) \equiv \sum_i g_i \sum_j w_{ij} \exp\left(-x_{ij}\right), \tag{2.66}$$

with g_i and w_{ij} the statistical weight of the electronic state i and the rovibrational state j, respectively. The moments are then given by

$$Z^{(n)}_{\text{int}}(T) \equiv \sum_i g_i \sum_j w_{ij} x_{ij}^n \exp\left(-x_{ij}\right), \tag{2.67}$$

with $x_{ij} = x_{i0} + (\frac{E_{ij}}{k_B T} - x_{i0}) \equiv x_i + \Delta_{ij}$. The power x_{ij}^n can be expanded as a binomial power,

$$x_{ij}^n = (x_i + \Delta_{ij})^n = \sum_{p=0}^{n} \binom{n}{p} x_i^{n-p} \Delta_{ij}^p. \tag{2.68}$$

Furthermore $e^{-x_{ij}} = e^{-x_i} e^{-\Delta_{ij}}$. Substitution of these two results yields

$$Z^{(n)}_{\text{int}}(T) = \sum_i g_i \exp\left(-x_i\right) \sum_j w_{ij} \left(\sum_{p=0}^{n} \binom{n}{p} x_i^{n-p} \Delta_{ij}^p\right) \exp\left(-\Delta_{ij}\right). \tag{2.69}$$

By changing the summation order, this can be written as

$$Z_{\text{int}}^{(n)}(T) = \sum_i g_i \exp\left(-x_i\right) \sum_{p=0}^{n} \binom{n}{p} x_i^{n-p} \sum_j w_{ij} \Delta_{ij}^p \exp\left(-\Delta_{ij}\right). \tag{2.70}$$

The last sum is nothing but the p'th moment of the internal partition sum $Z_{\text{rv},i}^{(p)}(T)$ over the rovibrational states,

$$Z_{\text{rv},i}^{(p)}(T) = \sum_j w_{ij} \Delta_{ij}^p \exp\left(-\Delta_{ij}\right). \tag{2.71}$$

This allows us to write

$$Z_{\text{int}}^{(n)}(T) = \sum_i g_i \exp\left(-x_i\right) \sum_{p=0}^{n} \binom{n}{p} x_i^{n-p} Z_{\text{rv},i}^{(p)}(T). \tag{2.72}$$

This is a general expression for the moment $Z^{(n)}(T)$ of a species partition sum in terms of the moments of the partition sums of its electronically excited states. It is a linear combination of the internal partition sums up to order n. For $n = 0, 1, 2$ we find:

$$Z_{\text{int}}^{(0)}(T) = \sum_i g_i \exp\left(-x_i\right) Z_{\text{rv},i}^{(0)}(T), \tag{2.73}$$

$$Z_{\text{int}}^{(1)}(T) = \sum_i g_i \exp\left(-x_i\right) \left[Z_{\text{rv},i}^{(1)}(T) + x_i Z_{\text{rv},i}^{(0)}(T) \right], \tag{2.74}$$

$$Z_{\text{int}}^{(2)}(T) = \sum_i g_i \exp\left(-x_i\right) \left[Z_{\text{rv},i}^{(2)}(T) + 2x_i Z_{\text{rv},i}^{(1)}(T) + x_i^2 Z_{\text{rv},i}^{(0)}(T) \right]. \tag{2.75}$$

These expressions are used in table 2.1. The conversion of the second derivative occurring in the specific heat is discussed in appendix 2.B.

2.3 Non-ideal gasses

Previously the thermodynamic relations have been derived by considering a mixture that behaves as an ideal gas which only interacts via hard sphere collisions. In reality a mixture can also interact via charged particles. Additionally particles are not point-like. Virial corrections can be used to account for the occupied volume of the particles. Virial corrections are not considered in this work for a more detailed discussion the reader is referred to Capitelli et al. [35, p. 117-140].

The effect of charged particles on the partition sum can be taken into account via Debye-Hückel, Margenau and Lewis or Fermi theory [35, p. 142-144]. According to Debye-Hückel theory the ionization potential is lowered by $\Delta I_a = \frac{q_e^2}{4\pi\epsilon_0\lambda_D}(z_a + 1)$ with z_a the charge number of particle a, q_e the elementary charge, ϵ_0 the electric permittivity in vacuum and λ_D the Debye length. Using this theory the summation of the partition sum is thus cut off at $\epsilon_{\max,a} = I_a - \Delta I_a$. Margenau

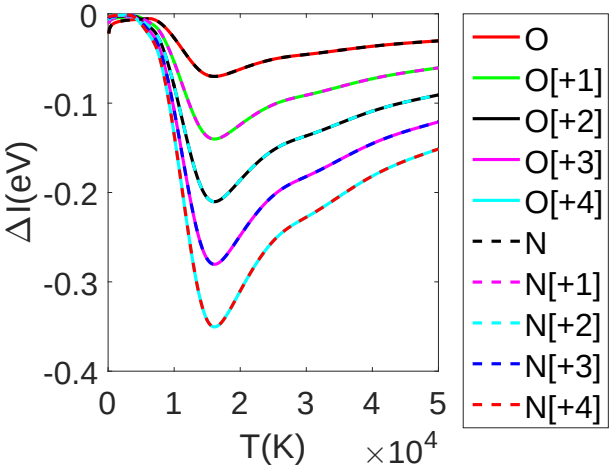

Figure 2.4: The calculated reduction of the upper energy limit for atoms and ions used in the calculation of the partition sum.

and Lewis suggest a different cutoff by assuming that the classical Bohr radius of a hydrogenoid atom should not exceed the Debye length. In that case the maximum energy is given by $\epsilon_{\max,a} = I_a \left(1 - \frac{1}{n^2_{\max,a}}\right)$ with the maximum principal quantum number given by $n^2_{\max,a} = \frac{\lambda_D (z_a+1)}{a_0}$ with a_0 the Bohr radius. Fermi suggested a different estimate for the maximum principal quantum number. He suggested that the classical Bohr radius should not exceed the average interparticle separation. His suggestion can be expressed as $n^2_{\max,a} = \frac{(z_a+1)}{n^{1/3} a_0}$.

The impact of these constraints is tested with PLASIMO and our MATLAB code in a mixture of $x_{N_2} = 0.788$ and $x_{O_2} = 0.212$ at p=1 bar. The calculated corrections for the upper limit of the partition sum are based on the Griem and Fermi constraints and are shown in figure 2.4. Such an approach is suggested in Capitelli et al. [35, p. 274]. The curve shows that for temperatures below 10 kK the Fermi criterion dominates. Due to the increase of the temperature the density decreases which means the criterion is becoming less important. The increase of the temperature causes a decrease of the Debye length[7]. Eventually the rate of increase of charged particles is not high enough to overcome the decrease of the total gas density. The result is that the energy correction decreases again. The partition sums have been calculated using all energy levels tabulated by NIST [53] that are smaller than the corrected ionization energy. The results in this section therefore justify neglecting these corrections in the remainder of this work.

[7]In this case the Debye length has been calculated by only including the electrons. This is similar to Capitelli et al. [35, p. 274]. For a more detailed discussion see section 5.2.6

2.4 LTE composition calculation

The equilibrium composition for a mixture can be found by minimizing the chemical potential μ [35, p. 163-167]. The chemical potential is defined as [35, p. 4, p. 57]

$$\mu_i = \left(\frac{\partial G_i}{\partial N_i}\right)_{p,T,N_{j\neq i}} = -k_B T \ln \frac{Z_i}{N_i}, \tag{2.76}$$

with G_i the Gibbs free energy. Alternatively the composition can be calculated based on a maximization of the entropy. When the mixture can be described with a single temperature both approaches find the same equilibrium composition. In this section the minimization of the Gibbs free energy is discussed for a single temperature mixture according to

$$\sum_i (dG)_{p,T} = \sum_i \mu_i dN_i = 0. \tag{2.77}$$

The partition sum for an arbitrary species can be written as

$$Z_i = Z_{t,i} Z_{\text{int},i} \exp\left(-\frac{E_i}{k_B T}\right), \tag{2.78}$$

with Z_t the translational partition function given by (2.9). The chemical potential for a single species is then given by

$$\mu_i = k_B T \left[\ln n_i - \ln \Lambda_i^3 - \ln Z_{\text{int},i}\right] + E_i, \tag{2.79}$$

with $\Lambda_i = \frac{2\pi m_i k_B T}{h^2}$. The composition can then be derived from (2.77) and is given by

$$\sum_i R_{ki} \left[k_B T \left(\ln n_i - \ln \Lambda_i^3\right) - k_B T \ln Z_{\text{int},i} + E_i\right] = 0. \tag{2.80}$$

Dividing by $k_B T$ and separating the density from the other terms gives

$$\sum_i R_{ki} \ln n_i = \sum_i R_{ki} \left[\ln \Lambda_i^3 + \ln Z_{\text{int},i} + \frac{E_i}{k_B T}\right]. \tag{2.81}$$

Taking the exponent of (2.81) gives

$$\prod_i n_i^{R_{ki}} = \exp\left(-\frac{\Delta E_k}{k_B T}\right) \prod_i \left(\Lambda^3 Z_{\text{int},i}\right)^{R_{ki}}, \tag{2.82}$$

with $\Delta E_k = \sum_i R_{ki} E_i$.

Special cases of the Guldberg-Waage equation are excitation and ionization. For excitation processes of the type $\mathrm{e} + \mathrm{A}_i + E_{ij} \rightarrow \mathrm{e} + \mathrm{A}_j$ with $\mathrm{A_i}$ a particle in state i and E_{ij} the excitation energy the Boltzmann equation can be obtained,

$$\frac{n_j}{n_i} = \frac{Z_{\text{int},j}}{Z_{\text{int},i}} \exp\left(-\frac{E_{ij}}{k_B T}\right). \tag{2.83}$$

Similarly for ionization processes of the type $\mathrm{e} + \mathrm{A}_i^{+c} + E_{ij} \rightarrow 2\mathrm{e} + \mathrm{A}_j^{+c+1}$ with c the charge the Saha equation is obtained

$$\frac{n_e n_{\mathrm{A}_j^{+c+1}}}{n_{\mathrm{A}_i^{+c}}} = \left(\frac{\Lambda_e \Lambda_j}{\Lambda_i}\right)^3 \frac{Z_{\mathrm{int},e} Z_{\mathrm{int},j}}{Z_{\mathrm{int},i}} \exp\left(-\frac{E_{ij}}{k_B T}\right). \tag{2.84}$$

A composition calculation of a mixture of μ species involves ν reactions and $\mu - \nu$ conservation equations. The reactions are expressed in the mass fractions. In order to reduce the large dynamical range of these fractions the reactions are expressed in terms of $\ln y$. The system for a mixture can then be expressed as

$$\sum_i R_{ki} \ln y_i = \sum_i R_{ki} \left[\ln \frac{m_i}{\rho} + \ln \Lambda^3 + \ln Z_{\mathrm{int},i} - \frac{E_i}{k_B T}\right], \tag{2.85}$$

with ρ the mass density. If necessary the additional parameterization $\ln y_i = -p_i^2$ can be used. The advantage of that parameterization is that $0 \leq y_i \leq 1$ results naturally. The remaining conservation equations are given by

$$y_\alpha = m_\alpha \sum_i R_{\alpha i} \frac{y_i}{m_i}, \tag{2.86}$$

with α indicating the elemental species and m the average mass of a single particle.

Table 2.1: The thermodynamic formulas for the calculation of the internal energy, enthalpy, Gibbs free energy and the frozen specific heat. The frozen specific heat neglects the contributions from chemical reactions. Separate contributions are shown for the translational and internal components. In order to avoid the numerical calculation of the first and second derivatives of the partition sum to the temperature the system is expressed in terms of the first and second moments of the partition sum. All quantities are calculated for N_a species. Additionally all expressions are corrected with the formation energy E_a. Molar mixture properties can be calculated by using $N_a = N_A$ (Avogadro's number) and summing all species quantities weighted by the molar fraction. An exception is the Gibbs free energy which additionally should be corrected with the entropy of mixing given by $-N_A k_B \sum_a x_a \ln x_a$. For more details see Atkins [37, p. 615,616], Hirschfelder et al. [34, p. 110-121] or Capitelli et al. [35, p. 58,59].

Type	Formula	Translational	Internal
U	$\sum_a N_a \left[E_a + k_B T^2 \frac{1}{Z_a} \left(\frac{\partial Z_a}{\partial T}\right)_V\right]$	$\sum_a \frac{3}{2} N_a k_B T$	$\sum_a N_a k_B T \frac{Z'_{\mathrm{int},a}}{Z_{\mathrm{int,a}}}$
H	$\sum_a N_a \left[E_a + k_B T \left(T \frac{1}{Z_a} \left(\frac{\partial Z_a}{\partial T}\right)_V + 1\right)\right]$	$\sum_a \frac{5}{2} N_a k_B T$	$\sum_a N_a k_B T \frac{Z'_{\mathrm{int},a}}{Z_{\mathrm{int},a}}$
G	$\sum_a N_a \left[E_a - k_B T \ln\left(\frac{Z_a}{N_a}\right)\right]$	$\sum_a N_a k_B T \ln\left(\frac{V}{N_a}\left[\frac{2\pi m k_B T}{h^2}\right]^{\frac{3}{2}}\right)$	$\sum_a -N_a k_B T \ln\left(\frac{Z_{\mathrm{int},a}}{N_a}\right)$
C_{pf}	$\sum_a N_a k_B \left[\left(\frac{\partial^2 \ln Z_a}{\partial (\ln T)^2}\right)_p + \left(\frac{\partial \ln Z_a}{\partial \ln T}\right)_p\right]$	$\sum_a \frac{5}{2} N_a k_B$	$\sum_a N_a k_B \left(\frac{Z''_{\mathrm{int},a}}{Z_{\mathrm{int},a}} - \left(\frac{Z'_{\mathrm{int},a}}{Z_{\mathrm{int},a}}\right)^2\right)$

2.A Comparing the reactive and the frozen specific heat

In order to compare (2.52) with the expression given by Capitelli [35, eq. 1.77] the derivatives are expressed in terms of the densities as

$$\begin{aligned} C_{p,\mathrm{mol}} &= c_p N_A m \\ &= \sum_a H_{\mathrm{mol},a} \left[\frac{1}{n} \left(\frac{\partial n_a}{\partial T} \right)_p - \frac{n_a}{n^2} \left(\frac{\partial n}{\partial T} \right)_p \right] \\ &\quad - \sum_a \frac{1}{m} \frac{n_a}{n} H_{\mathrm{mol},a} \left[\sum_j \frac{m_j}{n} \left(\frac{\partial n_j}{\partial T} \right)_p - \sum_j \frac{n_j m_j}{n^2} \left(\frac{\partial n}{\partial T} \right)_p \right] \\ &\quad + \sum_a \frac{n_a}{n} \left(\frac{\partial H_{\mathrm{mol},a}}{\partial T} \right)_p . \end{aligned} \tag{2.87}$$

Capitelli's result is

$$C_{p,\mathrm{mol}} = \sum_a \frac{n_a}{n} \left(\frac{\partial H_{\mathrm{mol},a}}{\partial T} \right)_p + \sum_a \frac{H_{\mathrm{mol},a}}{n} \left(\frac{\partial n_a}{\partial T} \right)_p - \frac{1}{n} \left(\frac{\partial n}{\partial T} \right)_p H_{\mathrm{mol}}, \tag{2.88}$$

which shows that Capitelli only includes the first, second and fifth terms.

2.B Conversion of the heat capacity

The specific heat can be expressed in terms of the logarithmic derivatives. In that case the specific heat is given by [35, p. 55]

$$C_{p,\mathrm{int},a} = N_a k_B T^2 \left(\left(\frac{\partial \ln Z_{\mathrm{int},a}}{\partial \ln T} \right)_p + \left(\frac{\partial^2 \ln Z_{\mathrm{int},a}}{(\partial \ln T)^2} \right)_p \right). \tag{2.89}$$

The logarithmic derivatives can be expressed in terms of the derivatives of the partition sum as follows

$$\left(\frac{\partial \ln Z_{\mathrm{int},a}}{\partial \ln T} \right)_p = \frac{T}{Z_{\mathrm{int},a}} \left(\frac{\partial Z_{\mathrm{int},a}}{\partial T} \right)_p = \frac{Z'_{\mathrm{int},a}}{Z_{\mathrm{int},a}}, \tag{2.90}$$

and

$$\begin{aligned} \left(\frac{\partial^2 \ln Z_{\mathrm{int},a}}{(\partial \ln T)^2} \right)_p &= \frac{\partial}{\partial \ln T} \left(\frac{T}{Z_{\mathrm{int},a}} \left(\frac{\partial Z_{\mathrm{int},a}}{\partial T} \right)_p \right) \\ &= \frac{T^2}{Z_{\mathrm{int},a}} \left(\frac{\partial^2 Z_{\mathrm{int},a}}{\partial T^2} \right)_p - \frac{T^2}{Z_{\mathrm{int},a}^2} \left(\frac{\partial Z_{\mathrm{int},a}}{\partial T} \right)_p^2 \\ &\quad + \frac{T}{Z_{\mathrm{int},a}} \left(\frac{\partial Z_{\mathrm{int},a}}{\partial T} \right)_p \\ &= \frac{Z''_a}{Z_{\mathrm{int},a}} - \frac{Z'_a}{Z_{\mathrm{int},a}} - \left(\frac{Z'_a}{Z_{\mathrm{int},a}} \right)^2 . \end{aligned} \tag{2.91}$$

Chapter 3

Transport equations

A mixture can be characterized by the positions and velocities of all individual particles. Such a characterization requires a large amount of parameters. For example, the number of parameters necessary to describe a volume of $1\,\mathrm{m}^3$ of air at room temperature is in the order of 10^{25}. Such a large number of parameters can be reduced to only a few by using a fluid approach. Three types of approaches are considered in this work. A kinetic approach which does not allow a fluid description and two fluid models. The considered fluid models are two-temperature plasmas and plasmas in local thermodynamic equilibrium. Figure 3.1 presents an overview of the plasma types and in which chapters they are discussed.

The governing equations in the fluid approximation can be derived from the Boltzmann equation. This equation can be used to derive the continuity equation as well as the conservation equations for momentum and energy. These conservation equations are derived for two-temperature plasmas and plasmas in local thermodynamic equilibrium. Although these conservation equations appear to be different we demonstrate that the final results are derived from a common origin and are consistent. The common origin for the derivations is the Boltzmann equation for the species systems. By writing the species velocity in terms of the diffusive velocity and the bulk velocity the various conservation equations can be summed to obtain the conservation equations in the bulk system. By summing the balances for the heavy particles the conservation equations for a two-temperature plasma can be derived.

In the case of local thermodynamic equilibrium we sum the species conservation equations for all states that correspond to the same nuclear core using the Boltzmann relation. In that case it is observed that the transport coefficients like the thermal conductivity and the heat capacity contain an additional dependency on the temperature due to the inclusion of internal and reactive terms.

In the last section the calculation of the transport coefficients that occur in the conservation equations are discussed. A transport theory based on particles that are restricted to movement in six possible directions is applied to obtain a first order approximation for transport coefficients. These estimates are made for the thermal conductivity, the viscosity and the diffusion coefficient.

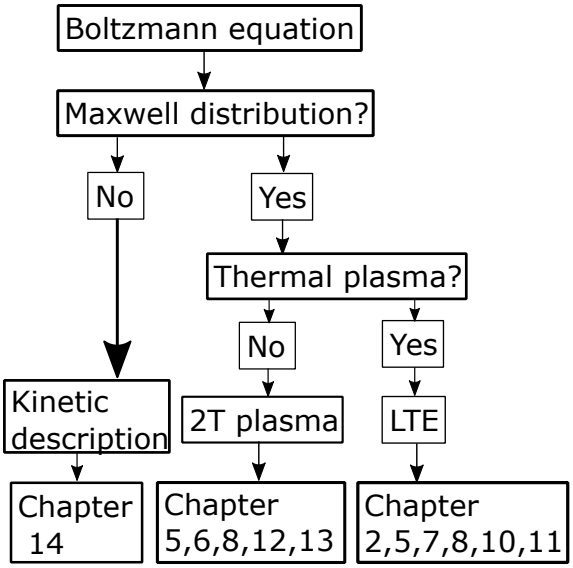

Figure 3.1: The three different types of plasmas considered in this work and the chapters where these plasma types are discussed.

3.1 Boltzmann equation

In the statistical approach the properties of species i are derived from the species distribution function $f_i(\vec{r}, \vec{p}_i, t)$ [34, p. 442-449]. The distribution function describes the probable amount of particles of species i that have a position in the range of $\mathrm{d}\vec{r}$ around $\vec{r}$ and with momentum coordinates in the range of $\mathrm{d}\vec{p}$ around $\vec{p}_i$ at time t. The next sections describe how properties can be derived from the distribution function. Additionally a general conservation equation for an arbitrary property is derived.

3.1.1 Species properties

The distribution function can be used to calculate mixture averages. This is done by integrating over all possible velocities at a given position and time. For the property χ_i the mixture average is thus given by

$$\langle \chi_i \rangle = \frac{1}{n_i} \int \chi_i f_i \mathrm{d}^3 v, \tag{3.1}$$

with n_i the species number density and v the peculiar velocity. For example for $\chi_i = 1$ the density is obtained

$$\int f_i \mathrm{d}^3 v = n_i. \tag{3.2}$$

The velocity of a particle of species i can be written as $\vec{v}_i = \vec{u}_i + \vec{c}_i$ with $\vec{u}_i$ the species average velocity and $\vec{c}_i$ the velocity relative to the average velocity. The

velocity $\vec{c}_i$ is also called peculiar velocity and has the property $\langle c_i \rangle = 0$. By taking $\chi_i = \vec{u}_i + \vec{c}_i$ the species average velocity is derived

$$\langle \vec{u}_i + \vec{c}_i \rangle = \frac{1}{n_i} \int (\vec{u}_i + \vec{c}_i) \, f_i \mathrm{d}^3 v = \vec{u}_i. \tag{3.3}$$

The species velocities can be summed to obtain the mass averaged or bulk velocity as

$$\vec{u} = \frac{1}{\rho} \sum_i \rho_i \vec{u}_i = \sum_i y_i \vec{u}_i, \tag{3.4}$$

with the mass density given by $\rho = \sum_i \rho_i = \sum_i n_i m_i$, m_i the mass of particle i and the mass fraction by $y_i = n_i m_i / \rho$. The mass averaged velocity can be used to introduce the diffusive velocity which is given by

$$\vec{v}_{d,i} = \vec{u}_i - \vec{u}. \tag{3.5}$$

This property can be used in (3.4) to show that the diffusive velocities transport no net mass

$$\sum_i y_i \vec{u} + \sum_i y_i \vec{v}_{d,i} = \vec{u}. \tag{3.6}$$

The diffusive velocities must thus obey

$$\sum_i y_i \vec{v}_{d,i} = 0. \tag{3.7}$$

In the next section we will see that the general conservation equation involves a term $n_i \langle \chi_i (\vec{u}_i + \vec{c}_i) \rangle$. The pressure tensor is one of the terms that can be derived from the substitution $\chi_i = m_i (\vec{u}_i + \vec{c}_i)$ as [1, p. 149]

$$n_i m_i \langle \vec{c}_i \vec{c}_i \rangle = \frac{1}{n_i} \int n_i m_i \vec{c}_i \vec{c}_i f_i \mathrm{d}^3 v = \mathcal{P}_i. \tag{3.8}$$

The pressure tensor can be rewritten as [54, p. 183]

$$\mathcal{P}_i = p_i \mathbf{I} - \bar{\bar{\tau}}_i, \tag{3.9}$$

with $p_i = \frac{1}{3} \rho y_i \left(c_{ix}^2 + c_{iy}^2 + c_{iz}^2 \right) = \frac{1}{3} \rho y_i c_i^2 = \rho y_i c_{ix}^2$ the scalar pressure and $\bar{\bar{\tau}}$ the viscous stress tensor. In the previous relations the pressure is simplified by assuming an isotropic velocity distribution. The temperature can be related to the pressure via [1, p. 152] $\frac{3}{2} k_B T_i = \frac{1}{2} m_i \langle c_i^2 \rangle$. Multiplication with n_i results in the ideal gas law

$$p_i = n_i k_B T_i. \tag{3.10}$$

The substitution $\chi_i = n_i m_i (\vec{u}_i + \vec{c}_i) (\vec{u}_i + \vec{c}_i)$ in $n_i \langle \chi_i (\vec{u}_i + \vec{c}_i) \rangle$ leads to the introduction of the heat flux. It is given by [1, p. 154]

$$\vec{q}_i = \frac{1}{2} \rho y_i \left\langle c_i^2 \vec{c}_i \right\rangle. \tag{3.11}$$

3.1.2 General conservation equation

In the presence of an external force $\vec{X}_i(\mathbf{r},t)$ the distribution function at time $t+\mathrm{d}t$ can be written as [1, p. 130,134]

$$f_i\left(\vec{r}+\frac{\vec{p}_i}{m_i}\mathrm{d}t,\vec{p}_i+\vec{X}_i\mathrm{d}t,t+\mathrm{d}t\right)=\left(\frac{\partial f_i\left(\vec{r},\vec{p}_i,t\right)}{\partial t}\right)_{\text{coll}}. \tag{3.12}$$

The collision term can be expressed as the sum of an elastic and an inelastic term

$$\left(\frac{\partial f_i\left(\vec{r},\vec{p}_i,t\right)}{\partial t}\right)_{\text{coll}}=\left(\frac{\partial f_i\left(\vec{r},\vec{p}_i,t\right)}{\partial t}\right)_{\text{el}}+\left(\frac{\partial f_i\left(\vec{r},\vec{p}_i,t\right)}{\partial t}\right)_{\text{inel}}. \tag{3.13}$$

The Boltzmann equation can be derived from (3.12) by Taylor expanding

$$\frac{\partial f_i}{\partial t}+\left(\vec{u}_i+\vec{c}_i\right)\cdot\nabla f_i+\frac{\vec{X}_i}{m_i}\cdot\nabla f_i=\left(\frac{\partial f_i}{\partial t}\right)_{\text{coll}}. \tag{3.14}$$

A general continuity equation can be derived by multiplying (3.14) with the property χ_i and integrating over velocity space. The result can be written as [1, p. 194-197]

$$\frac{\partial}{\partial t}\left(n_i\left\langle\chi_i\right\rangle\right)+\nabla\cdot\left(n_i\left\langle\chi_i\left(\vec{u}_i+\vec{c}_i\right)\right\rangle\right)-n_i\left\langle\frac{\vec{X}_i}{m_i}\cdot\nabla_v\chi_i\right\rangle=\left[\frac{\partial}{\partial t}\left(n_i\left\langle\chi_i\right\rangle\right)\right]_{\text{coll}}. \tag{3.15}$$

The mass, momentum and energy balances can be obtained from (3.15) by selecting an appropriate $\chi_i\left(\vec{u}_i+\vec{c}_i\right)$. A more elaborate discussion is given in the following sections.

3.2 Conservation equations two-temperature plasma

In the following sections the conservation equations for the mass, momentum and energy are derived. These balances are applied to a two-temperature plasma.

3.2.1 Mass balance

The mass balance can be derived from (3.15) by using $\chi_i=m_i$ [1, p. 197-198]. The required averages are given by

$$\left\langle m_i\right\rangle=m_i,\quad\left\langle m_i\left(\vec{u}_i+\vec{c}_i\right)\right\rangle=m_iu_i,\quad\left\langle\frac{\vec{X}_i}{m_i}\cdot\nabla_u m_i\right\rangle=0. \tag{3.16}$$

Substituting these properties in (3.15) gives

$$\frac{\partial\rho y_i}{\partial t}+\nabla\cdot\left(\rho y_i\vec{u}_i\right)=m_i\omega_i, \tag{3.17}$$

with ω_i the production rate per unit volume of species i. Summing over all species mass balances gives

$$\frac{\partial \rho}{\partial t} + \nabla \cdot (\rho \vec{u}) = 0, \tag{3.18}$$

which indicates that mass is conserved. The bulk mass balance uses $\vec{u} = \sum_i y_i \vec{u}_i$ as the mass averaged velocity.

3.2.2 Momentum equation

The momentum transport equation can be derived by using $\chi_i = m_i (\vec{u}_i + \vec{c}_i)$ [1, p. 201-204]. The terms in (3.15) are expanded in appendix 3.A. The resulting species momentum balance is given by

$$\frac{\partial \rho y_i \vec{u}_i}{\partial t} + \nabla \cdot \rho y_i \vec{u}_i \vec{u}_i = -\nabla p_i + \nabla \cdot \bar{\bar{\tau}}_i + \vec{R}_i + n_i q_i \left(\vec{E} + \vec{u}_i \times \vec{B} \right) + \rho y_i \vec{g}, \tag{3.19}$$

with $\vec{R}_i = \left[\frac{\partial}{\partial t} \left(n_i \left\langle m_i \left(u_i + c_i \right) \right\rangle \right) \right]_{\text{coll}}$, q_i the charge of particle i, $\vec{E}$ the electric field, $\vec{B}$ the magnetic field and $\vec{g}$ the gravitational acceleration.

The momentum equation for the bulk flow can be derived by summing over all species momentum balances. The mass averaged velocity of the species is expressed in terms of the velocity of the bulk flow as $\vec{u}_i = \vec{u} + \vec{v}_{d,i}$ with $\vec{u}$ the bulk velocity and $\vec{v}_{d,i}$ the diffusion velocity. Effectively, this is equivalent to changing coordinates of the species system which moves with $\vec{u}_i$ to the bulk system that moves with $\vec{u}$ [55, p. 168-170] [6, p. 7-8]. This conversion is discussed in appendix 3.C. The Navier-Stokes equation (bulk momentum balance) is thus given by

$$\frac{\partial \rho \mathbf{u}}{\partial t} + \nabla \cdot \rho \vec{u} \vec{u} = -\nabla p + \nabla \cdot \bar{\bar{\tau}} + \rho \sigma^c \left(\vec{E} + \vec{j} \times \vec{B} \right) + \rho \vec{g}, \tag{3.20}$$

with $\vec{j}$ the current density and $\sigma^c = \sum_i \frac{q_i y_i}{m_i}$. The bulk momentum balance is solved using the SIMPLE algorithm described by Peerenboom [6, p. 69-73]. The species momentum balances are not taken into account as indicated in (3.19) and are simplified further. The contributions from the viscosity and the terms on the left hand side are neglected. More details can be found in appendix 6.A.

3.2.3 Energy equation

The energy equation can be derived by using $\chi_i = \frac{1}{2} m_i (\vec{u}_i + \vec{c}_i) \cdot (\vec{u}_i + \vec{c}_i) + E_i$ [1, p. 204-207]. The derivation will deviate from the derivation given in Bittencourt because a term E_i is added which accounts for the energy difference between state i and a reference energy. The energy offset is necessary to group the energy equations of the ground state and the excited states of a given atom, molecule or ion. The derivation is carried out in appendix 3.B. The result is that the species energy balance can be written as

$$\begin{aligned} \frac{\partial \left(\frac{3}{2} n_i k_B T_i + n_i E_i \right)}{\partial t} + \nabla \cdot \left(\frac{5}{2} n_i k_B T_i + n_i E_i \right) \vec{u}_i - \vec{u}_i \cdot \nabla p_i \\ - \bar{\bar{\tau}}_i : \nabla \vec{u}_i + \nabla \cdot \vec{q}_i = Q_i - \vec{u}_i \cdot \vec{R}_i + \frac{1}{2} m_i u_i^2 \omega_i. \end{aligned} \tag{3.21}$$

The energy equation for the bulk system can be obtained by summing the species equations (3.21). A change of reference system is required again to change the velocity of the coordinate system from $\vec{u}_i$ to $\vec{u}$. The details are given in appendix 3.C.

Plasmas are usually created by applying electromagnetic fields. The absolute force that is applied to the electrons and the ions (with the same absolute charge as the electrons) via these fields is equal. Due to the lower mass the electrons gain a much larger velocity than the ions. Electrons that are accelerated long enough can induce inelastic processes like excitation, ionization or dissociation. The smaller mass differences between different heavy particles causes an efficient transfer of energy. As a result these particles reach the same temperature. Since electrons do not transfer energy efficiently in collisions with heavy particles it is possible that the electron temperature exceeds the heavy particle temperature. For this reason the electron balance is considered separately

$$\frac{\partial}{\partial t}\sum_{i\neq e}\left(\frac{3}{2}n_i k_B T_h + n_i E_i\right) + \nabla\cdot\sum_{i\neq e}\left(\frac{5}{2}n_i k_B T_h \vec{u} + n_i E_i \vec{u}_i\right) =$$
$$Q_{eh} + Q_{\mathrm{inel},e} - Q_{\mathrm{rad}} - \nabla\cdot\vec{q}_h + \vec{u}\cdot\nabla p_h + \bar{\bar{\tau}} : \nabla\vec{u} \tag{3.22}$$
$$\frac{\partial}{\partial t}\left(\frac{3}{2}n_e k_B T_e\right) + \nabla\cdot\left(\frac{5}{2}n_e k_B T_e\right)\vec{u} =$$
$$\vec{u}\cdot\nabla p_e - \nabla\cdot\vec{q}_e + Q_{\mathrm{ohm}} - Q_{eh} - Q_{\mathrm{inel},e}, \tag{3.23}$$

where the viscous dissipation of the electrons is neglected and the formation energy of the electrons is set to zero. Additionally the ohmic heating term for the heavy particles is neglected[1] The elastic energy transfer between the electrons and the heavy particles is given by Q_{eh}. The term $Q_{\mathrm{inel},e}$ contains the energy losses related to excitation and ionization processes involving an electron. A similar term $Q_{\mathrm{inel},h}$ describes the chemical losses due to reactions for the heavy particles. This term does not appear in the energy balance since $\chi = \frac{1}{2}m_i\left(\vec{u}_i + \vec{c}_i\right)^2 + n_i E_i$. In other words, the kinetic loss term $-Q_{\mathrm{inel},h}$ is balanced by the increase of chemical energy $Q_{\mathrm{inel},h}$. A separate term covers the radiation losses Q_{rad}. Contributions from the second and third terms on the RHS of (3.21) are neglected.

3.3 LTE

The large number of species equations for the mass, momentum and energy can in specific cases be simplified to a smaller set of equations. In equilibrium the loss processes are balanced by the production processes. The production rate for an inelastic process from state i towards state j can be written as $n_e n_i \left\langle \sigma^{(e)} \vec{v}_e \right\rangle_{i\to j}$.

[1] In the species system the contribution from external forces vanishes. In the bulk system a term $n_i \vec{X}_i \cdot v_{d,i}$ is added to account for the change of reference system as shown in appendix 3.C. The energy added to the bulk system from external forces includes $n_i q_i \vec{E}\cdot v_{d,i} = \vec{j}_i \cdot \vec{E}$ .The total current density is approximately equal to the current density of the electrons. For that reason the ohmic heating term is approximated with $\vec{j}\cdot\vec{E} \approx \vec{j}_e \cdot \vec{E}$. Other forces are neglected in the energy balances of the electrons and the heavy particles.

The destruction rate of state j by electron collisions is given by $n_e n_j \left\langle \sigma^{(e)} \vec{v}_e \right\rangle_{j\to i}$. The electrons lose the energy E_{ij} in the inelastic process. This energy can be retrieved from other electrons via momentum transferred in collisions with other electrons. The rate of these collisions is proportional to $n_e^2 \left\langle \sigma_{m,e}^{(e)} \vec{v}_e \right\rangle_{E\geq E_{ij}}$ with $E \geq E_{ij}$ indicating the range that is considered for the energy average. According to Drawin [56] the electrons follow the Maxwellian velocity distribution if the following equation holds for all inelastic transitions

$$\frac{n_i \left\langle \sigma^{(e)} \vec{v}_e \right\rangle_{i\to j} - n_j \left\langle \sigma^{(e)} \vec{v}_e \right\rangle_{j\to i}}{1 + n_e \left\langle \sigma_{m,e}^{(e)} \vec{v}_e \right\rangle_{E\geq E_{ij}}} \ll 1. \tag{3.24}$$

In other words, the energy gained by momentum transfer from the electron-electron collisions can compensate for all inelastic losses. The equilibrium distribution or Maxwellian distribution is given by [34, p. 466]

$$f_i = n_i \left(\frac{m_i}{2\pi k_B T} \right)^{3/2} \exp\left(-\frac{m_i \vec{c}_i^{\,2}}{2 k_B T} \right). \tag{3.25}$$

Additionally, the heavy particles can be described with the same velocity distribution function as the electrons if the number of momentum transfer collisions is much larger than the number of inelastic collisions

$$\sum_i \sum_j n_e n_i \left\langle \sigma^{(e)} \left(\vec{u}_e + \vec{c}_e \right) \right\rangle_{i\to j} \ll \sum_i n_e n_i \left\langle \sigma_{m,i}^{(e)} \right\rangle. \tag{3.26}$$

When conditions (3.24) and (3.26) are met, the atomic and molecular state distributions are given by the Boltzmann relation. The Boltzmann relation [34, p. 105] is given by

$$\frac{n_i}{n_j} = \frac{g_i}{g_j} \exp\left(-\frac{E_i - E_j}{k_B T} \right), \tag{3.27}$$

with g_i the degeneracy of state i. In the next sections LTE equations for the mass, momentum and energy balance are derived.

3.3.1 Mass and momentum balance

The number of mass and momentum balances can be greatly reduced when LTE is valid by introducing elemental species. The elemental species form the minimum set of species that is required to represent all other species. A species can be expressed in the elemental species by setting up a reaction where the elemental species are the only reactants and the species is the only product. A general reaction can then be written as

$$\sum_i \nu_{k,i} A_i = 0, \tag{3.28}$$

with $\nu_{k,i}$ the stoichiometry coefficient and A_i representing species i. An example of a species that is expressed in this form is $\mathrm{Ar}^+ - \mathrm{Ar} + \mathrm{e}$ where Ar and e are

used as the elemental species. Another example is $O_2 - 2O$. Additionally, the parameter $\phi_{\alpha,i}$ is used to represent the number of occurrences of elemental species α in species i. These parameters can be assembled in a matrix $\mathbf{R}$. The non-elemental species are listed before the elemental species. For a system containing the following species order O_2, O^+, O and e the matrix is given by

$$\mathbf{Ry} = \begin{bmatrix} 1 & 0 & -2 & 0 \\ 0 & 1 & -1 & 1 \\ 2 & 1 & 1 & 0 \\ 0 & -1 & 0 & 1 \end{bmatrix} \begin{bmatrix} y_{O_2} \\ y_{O^+} \\ y_O \\ y_e \end{bmatrix}. \tag{3.29}$$

The first two rows in this matrix contain information about the non-elemental species and the last two rows provide the occurrences of the elements in the species. This formalism is used to show that in an LTE system knowledge about the temperature, pressure and elemental mass fractions is sufficient to construct all species densities from the Guldberg-Waage law. These elemental mass balances can be obtained by summing all species mass balances after multiplying with $\phi_{\alpha,i} m_\alpha / m_i$. The elemental mass balance is given by

$$\frac{\partial \rho y_{\{\alpha\}}}{\partial t} + \nabla \cdot \left(\rho y_{\{\alpha\}} \vec{u} + J_{\{\alpha\}} \right) = 0, \tag{3.30}$$

with $J_{\{\alpha\}}$ the elemental diffusive mass fluxes. The elemental diffusive mass fluxes can be determined from the elemental momentum balance. However in this work an alternative approach is used. The diffusive mass fluxes are obtained from the Stefan-Maxwell equations. These equations can be derived by simplifying the momentum balances [57]. The Stefan-Maxwell system is given by

$$\mathbf{Fv} = -\mathbf{d}, \tag{3.31}$$

with $\mathbf{F}$ the friction matrix, $\mathbf{v}$ the diffusive velocities and $\mathbf{d}$ the driving forces. The driving forces contain contributions from ordinary diffusion, pressure diffusion, thermal diffusion and forced diffusion. A more elaborate discussion of the Stefan-Maxwell equations is given in chapters 6 and 7.

3.3.2 Energy balance

The Boltzmann relation can be used to simplify the summation of the energy balance for all possible states of particle s. Particle s can represent the collection of (electronically excited) states that correspond to an atom, a molecule or an ion. The first term in (3.21) is proportional to

$$\sum_i \frac{3}{2} n_i k_B T_i + \sum_i n_i E_i. \tag{3.32}$$

By assuming that all states of species s have the same temperature the first sum can be written as

$$\frac{3}{2} k_B T \sum_i n_i. \tag{3.33}$$

The summation of the species densities can be expressed as

$$\begin{aligned} n_s = \sum_i n_i &= n_0 \sum_i \frac{n_i}{n_0} \\ &= n_0 \sum_i \frac{g_i}{g_0} \exp\left(-\frac{E_i - E_0}{k_B T}\right) \\ &= n_0 \frac{Z_{\text{int}}}{Z_{\text{int},0}}, \end{aligned} \tag{3.34}$$

with Z_{int} the internal partition sum, E_0 the formation energy of the ground state of species s, subscripts zero referring to properties of the ground state and $Z_{\text{int},0}$ the internal partition sum by only considering the ground state. The second sum can be written as

$$\begin{aligned} \sum_i n_i E_i &= \sum_i n_i \left(E_i - E_0\right) + \sum_i n_i E_0 \\ &= n_0 \sum_i \frac{n_i}{n_0} \left(E_i - E_0\right) + n_s E_0 \\ &= \frac{n_s n_0 \sum_i \left(E_i - E_0\right) \frac{g_i}{g_0} \exp\left(-\frac{E_i - E_0}{k_B T}\right)}{n_s} + n_s E_0 \\ &= \frac{n_s \frac{n_0}{Z_{\text{int},0}} \sum_i \left(E_i - E_0\right) g_i \exp\left(-\frac{E_i}{k_B T}\right)}{\frac{n_0 Z_{\text{int}}}{Z_{\text{int},0}}} + n_s E_0 \\ &= n_s \left\langle E_{\text{int}} \right\rangle_B + n_s E_0 = n_s \left\langle E_{\text{int}} \right\rangle_B + n_s E_s, \end{aligned} \tag{3.35}$$

with $\left\langle E_{\text{int}} \right\rangle_B$ the average internal energy weighted by the Boltzmann relation and $E_s = E_0$ the formation energy of species s. The complete term can be written as

$$\frac{3}{2} n_s k_B T + n_s \left\langle E_{\text{int}} \right\rangle_B + n_s E_s = n_s m_s e_{t,s} + n_s m_s e_{\text{int},s} + n_s m_s e_{r,s} = n_s m_s e_s, \tag{3.36}$$

with e_s the total specific energy, $e_{t,s}$ the specific energy due to translational degrees of freedom, $e_{\text{int},s}$ the specific energy due to internal excitations and $e_{r,s}$ the specific energy due to chemical reactions. Similarly, the second term in (3.21) can be written as

$$\frac{5}{2} n_s k_B T + n_s \left\langle E_{\text{int}} \right\rangle_B + n_s E_s = n_s m_s h_{t,s} + n_s m_s h_{\text{int},s} + n_s m_s h_{r,s} = n_s m_s h_s, \tag{3.37}$$

with h_s the specific enthalpy. This term can be combined with the heat flux

$$\begin{aligned} \nabla \cdot \left(\vec{q} + n_s m_s h_s \vec{u}_s\right) &= \nabla \cdot \left(-\lambda_{c,s} \nabla T + \left(\frac{\partial n_s}{\partial T} m_s h_s + n_s m_s \frac{\partial h_s}{\partial T}\right) \vec{u}_s \nabla T\right) \\ &= -\nabla \cdot \left(\lambda_{c,s} + \lambda_{r,s} + \lambda_{\text{int},s}\right) \nabla T \\ &= -\nabla \cdot \lambda_s \nabla T, \end{aligned} \tag{3.38}$$

with $\lambda_{c,s}$ the thermal conduction coefficient due to collisions, $\lambda_{r,s}$ the thermal conduction coefficient due to reactions, $\lambda_{\text{int},s}$ the thermal conduction due to internal excitation and λ_s the total thermal conduction coefficient. The energy balance for species s can now be expressed as

$$\frac{\partial n_i m_i e_s}{\partial t} - \vec{u}_s \cdot \nabla p_s - \bar{\bar{\tau}}_s : \nabla \vec{u}_s - \nabla \cdot \lambda_s \nabla T = Q_s - \vec{u}_s \cdot \vec{R}_s + \frac{1}{2} m_i u_s^2 \omega_s,$$

where it is assumed that internal states travel with the same velocity $\vec{u}_s$ as the ground state. By following a similar procedure as in section 3.2.3 the energy balance of the entire mixture can be written as

$$\frac{\partial \sum_s n_s m_s e_s}{\partial t} - \vec{u} \cdot \nabla p - \bar{\bar{\tau}} : \nabla \vec{u} - \nabla \cdot \lambda \nabla T = \sum_i n_i \vec{X}_i \cdot \vec{v}_{d,i}, \tag{3.39}$$

where the external forces are added due to a change of reference system as discussed in appendix 3.C.

3.4 Transport coefficients

In this section an overview is presented of the various coefficients and matrices introduced in the previous sections. These are the reaction rate for inelastic processes, the elastic energy transfer by the electrons, the viscous stress tensor, the viscosity, the thermal conductivity and the diffusion coefficient.

The energy transferred via inelastic collisions is given by

$$Q_{\text{inel}} = Q_{\text{inel},e} + Q_{\text{inel},h} = \sum_j \Delta h_j R_j, \tag{3.40}$$

with R_j the reaction rate and Δh_j the reaction enthalpy. The reactions involving an electron as a reactant are part of $Q_{\text{inel},e}$ and the remaining reactions are part of $Q_{\text{inel},h}$. The reaction rate is given by

$$R_j = k_j \prod_i n_i^{\nu_{ji}}, \tag{3.41}$$

with $\nu_{j,i}$ the stoichiometry coefficient and k_j the rate coefficient. For an inelastic process the rate coefficient is given by [58, p. 78]

$$k_j = \int_{\Delta\epsilon_j}^{\infty} \sigma(\epsilon)\, v(\epsilon)\, f(\epsilon)\, \mathrm{d}\epsilon. \tag{3.42}$$

The elastic energy transfer between the electrons and the heavy particles is constructed from the average energy transferred via collisions and the definition of the elastic collision rate. The result is given by [54, p. 34,45,51]

$$Q_{\text{elas},eh} = \sum_{h \neq e} \frac{3}{2} k_B (T_e - T_h)\, 2 \frac{m_e}{m_h} n_e \nu_{eh}. \tag{3.43}$$

The average collision frequency between two species is given by [54, p. 45]

$$\nu_{ij} = n_j \sqrt{\frac{8k_BT}{\pi m_{ij}}} \bar{Q}_{ij} = \frac{16}{3} n_j \Omega^{(1,1)}, \tag{3.44}$$

with m_{ij} the reduced mass. The average momentum transfer cross section $\bar{Q}_{ij}$ can be expressed in terms of the collision integral $\Omega^{(1,1)}$ as [54, p. 45]

$$\begin{aligned} \sqrt{\frac{8k_BT}{\pi m_{ij}}} \bar{Q}_{ij} &= \sqrt{\frac{8k_BT}{\pi m_{ij}}} \frac{2}{3} \int_0^\infty x^2 \exp(-x)\, Q_{ij}^{(1)} \mathrm{d}x \\ &= 4\sqrt{\frac{k_BT}{2\pi m_{ij}}} \frac{2}{3} \int_0^\infty 2\gamma^5 \exp\left(-\gamma^2\right) Q_{ij}^{(1)} \mathrm{d}\gamma \\ &= \frac{16}{3} \Omega^{(1,1)}, \end{aligned} \tag{3.45}$$

with $Q_{ij}^{(1)}$ the momentum transfer cross section. Cross sections and collision integrals are discussed in more detail in chapter 4.

The viscous stress tensor is defined as[2] [54, p. 183]

$$\bar{\bar{\tau}} = \eta \left[\nabla \vec{u} + (\nabla \vec{u})^T - \frac{2}{3} (\nabla \cdot \vec{u}) \mathbf{I} \right], \tag{3.46}$$

with η the dynamic viscosity. Note that sometimes a different sign convention is used for the viscous stress tensor [6, p. 7,10].

Hirschfelder et al. [34, p. 11-13] and Capitelli et al. [27, p. 2-3] provide simple estimates for the viscosity, diffusion coefficient and the thermal conduction coefficient. The mean free path is approximated with

$$l_c = 1/\left(n\pi\sigma^2\right). \tag{3.47}$$

By assuming that molecules are only allowed to move parallel to one of the coordinate axes, the flux of a given property P along the positive z-direction can be approximated with $\frac{1}{6}uP$. In that case the flux of P through plane O which lies in the middle of plane A and plane B can be written as

$$\begin{aligned} \psi_P &= \frac{1}{6} u \left(P_A - P_B\right) \\ &= \frac{1}{6} u \left(P_O - l_c \frac{\partial P}{\partial z} - P_O - l_c \frac{\partial P}{\partial z} \right) \\ &= -\frac{1}{3} u l_c \frac{\partial P}{\partial z}, \end{aligned} \tag{3.48}$$

[2] Note that the mathematical notation of Peerenboom is used [6]. However, a different sign convention is used in that work.

where a constant derivative is assumed. The transport coefficients corresponding to the mass, momentum and energy flux can then be derived from

$$\begin{aligned}\psi_{nm} &= -D\frac{\partial nm}{\partial z} = -\xi\frac{\sqrt{\pi m k_B T}}{\pi\sigma^2}\frac{1}{\rho}\frac{\partial nm}{\partial z}\\ \psi_{nmu_y} &= -\eta\frac{\partial u_y}{\partial z} = -\xi\frac{\sqrt{\pi m k_B T}}{\pi\sigma^2}\frac{\partial u_y}{\partial z}\\ \psi_{nc_vT} &= -\lambda\frac{\partial T}{\partial z} = \xi\frac{\sqrt{\pi m k_B T}}{\pi\sigma^2}\frac{c_v}{m}\frac{\partial T}{\partial z},\end{aligned} \tag{3.49}$$

with ξ a numerical factor[3]. These coefficients can be related to each other via $D = \frac{\eta}{\rho} = \frac{\lambda m}{\rho c_v}$. More advanced expressions are derived in chapter 5.

3.A Derivation momentum balance

The momentum transport equation can be derived by using $\chi_i = m_i\left(\vec{u}_i + \vec{c}_i\right)$ [1, p. 201-204]. The individual terms are given by

$$\begin{aligned}\frac{\partial n_i\left\langle m_i\left(\vec{u}_i+\vec{c}_i\right)\right\rangle}{\partial t} &= \frac{\partial \rho y_i \vec{u}_i}{\partial t}\\ \nabla\cdot n_i\left\langle m_i\left(\vec{u}_i+\vec{c}_i\right)\left(\vec{u}_i+\vec{c}_i\right)\right\rangle &= \nabla\cdot\left[\rho y_i\vec{u}_i\vec{u}_i + \rho y_i\left\langle\vec{c}_i\vec{c}_i\right\rangle\right]\\ -n_i\left\langle\frac{\vec{X}_i}{m_i}\cdot\nabla_u m_i\left(\vec{u}_i+\vec{c}_i\right)\right\rangle &= -n_i\left\langle\vec{X}_i\right\rangle\\ \left[\frac{\partial}{\partial t}\left(n_i\left\langle m_i\left(\vec{u}_i+\vec{c}_i\right)\right\rangle\right)\right]_{\text{coll}} &= \vec{R}_i,\end{aligned} \tag{3.50}$$

with $\mathcal{P}_i$ the kinetic pressure dyad and $\vec{R}_i$ the momentum exchange with other species via elastic and inelastic collisions. The momentum equation can now be expressed as

$$\frac{\partial \rho y_i\vec{u}_i}{\partial t} + \nabla\cdot\rho y_i\vec{u}_i\vec{u}_i = -\nabla\cdot\mathcal{P}_i + \vec{R}_i + n_i\left\langle\vec{X}_i\right\rangle. \tag{3.51}$$

The pressure tensor can be rewritten as (see (3.9))

$$\mathcal{P}_i = p_i\mathbf{I} - \bar{\bar{\tau}}_i,$$

with p_i the scalar pressure and $\bar{\bar{\tau}}$ the viscous stress tensor. The forces can be rewritten as

$$n_i\vec{X}_i = n_i q_i\left(\vec{E} + \vec{u}_i\times\vec{B}\right) + n_i m_i\vec{g}, \tag{3.52}$$

with $\vec{E}$ the electric field, $\vec{B}$ the magnetic field and $\vec{g}$ the gravitational acceleration. The species momentum balance can then be expressed as

$$\frac{\partial \rho y_i\vec{u}_i}{\partial t} + \nabla\cdot\rho y_i\vec{u}_i\vec{u}_i = -\nabla p_i + \nabla\cdot\bar{\bar{\tau}}_i + \vec{R}_i + n_i q_i\left(\vec{E} + \vec{u}_i\times\vec{B}\right) + \rho y_i\vec{g}. \tag{3.53}$$

[3] A more accurate expression for the mean free path uses the factor $\frac{1}{\sqrt{2}}$ which amounts to $\xi = \frac{2}{3\pi}$ [34, p. 10-12].

3.B Derivation energy balance

The energy balance for the species i can be derived by using $\chi_i = \frac{1}{2} m_i \left(\vec{u}_i + \vec{c}_i\right) \times \left(\vec{u}_i + \vec{c}_i\right) + E_i$. The terms in (3.15) are given by

$$\frac{\partial n_i \left\langle \frac{1}{2} m_i \left(\vec{u}_i + \vec{c}_i\right)\left(\vec{u}_i + \vec{c}_i\right) + E_i \right\rangle}{\partial t} = \frac{\partial \left(\frac{3}{2} n_i k_B T_i + n_i E_i\right)}{\partial t} + \frac{1}{2}\frac{\partial}{\partial t} \rho y_i u_i^2 \tag{3.54}$$

$$\begin{aligned}
&\nabla \cdot n_i \left\langle \left(\frac{1}{2} m_i \left(\vec{u}_i + \vec{c}_i\right)\left(\vec{u}_i + \vec{c}_i\right) + E_i \right) \left(\vec{u}_i + \vec{c}_i\right) \right\rangle \\
&= \nabla \cdot \left(\frac{1}{2} \rho y_i \left[u_i^2 \vec{u}_i + \left\langle c_i^2 \right\rangle \vec{u}_i \;\; + 2 \left\langle \vec{c}_i \vec{c}_i \right\rangle \cdot \vec{u}_i + \left\langle c_i^2 \vec{c}_i \right\rangle \right] + n_i E_i \vec{u}_i \right) = \\
&= \nabla \cdot \frac{1}{2} \rho y_i u_i^2 \vec{u}_i + \nabla \cdot \left(\frac{3}{2} n_i k_B T_i + n_i E_i \right) \vec{u}_i + \nabla \cdot \left(\mathcal{P}_i \cdot \vec{u}_i \right) + \nabla \cdot \vec{q}_i
\end{aligned} \tag{3.55}$$

$$- n_i \left\langle \frac{\vec{X}_i}{m_i} \cdot \nabla_u \left(\frac{1}{2} m_i \left(\vec{u}_i + \vec{c}_i\right)\left(\vec{u}_i + \vec{c}_i\right) + E_i \right) \right\rangle = -n_i \left\langle \vec{X}_i \cdot \left(\vec{u}_i + \vec{c}_i\right) \right\rangle \tag{3.56}$$

$$\left[\frac{\partial n_i \left\langle \frac{1}{2} m_i \left(\vec{u}_i + \vec{c}_i\right)\left(\vec{u}_i + \vec{c}_i\right) + E_i \right\rangle}{\partial t} \right]_{\text{coll}} = Q_i, \tag{3.57}$$

with T_i the temperature, $\vec{q}_i$ the heat flux vector and Q_i the energy transferred via collisions. It contains an elastic contribution $Q_{\text{elas},i}$ and an inelastic contribution due to reactions $Q_{\text{inel},i}$. By using these substitutions the energy balance can be written as

$$\begin{aligned}
&\frac{\partial \left(\frac{3}{2} n_i k_B T_i + n_i E_i\right)}{\partial t} + \nabla \cdot \left(\frac{3}{2} n_i k_B T_i + n_i E_i \right) \vec{u}_i + \frac{\partial \frac{1}{2} \rho y_i u_i^2}{\partial t} + \\
&\nabla \cdot \frac{1}{2} \rho y_i u_i^2 \vec{u}_i + \nabla \cdot \left(\mathcal{P}_i \cdot \vec{u}_i \right) + \nabla \cdot \vec{q}_i - n_i \left\langle \vec{X}_i \cdot \left(\vec{u}_i + \vec{c}_i\right) \right\rangle = Q_i.
\end{aligned} \tag{3.58}$$

The third and fourth term can be rewritten as

$$\begin{aligned}
&\frac{\partial \frac{1}{2} \rho y_i \left(\vec{u}_i \cdot \vec{u}_i\right)}{\partial t} + \nabla \cdot \frac{1}{2} \rho y_i \left(\vec{u}_i \cdot \vec{u}_i\right) \vec{u}_i \\
&= \frac{1}{2} u_i^2 \left[\frac{\partial \rho y_i}{\partial t} + \nabla \cdot \rho y_i \vec{u}_i \right] + \rho y_i \vec{u}_i \cdot \left[\frac{\partial \vec{u}_i}{\partial t} + \vec{u}_i \cdot \nabla \vec{u}_i \right] \\
&= \left(\frac{1}{2} - 1 \right) u_i^2 \left[\frac{\partial \rho y_i}{\partial t} + \nabla \cdot \rho y_i \vec{u}_i \right] + \vec{u}_i \cdot \left[\frac{\partial \rho y_i \vec{u}_i}{\partial t} + \nabla \cdot \rho y_i \vec{u}_i \vec{u}_i \right] \\
&= -\frac{1}{2} u_i^2 m_i \omega_i + n_i \vec{u}_i \cdot \left\langle \vec{X}_i \right\rangle - \vec{u}_i \cdot \left(\nabla \cdot \mathcal{P}_i \right) + \vec{u}_i \cdot \vec{R}_i,
\end{aligned} \tag{3.59}$$

where the mass and momentum balances have been substituted in the last step. By combining these terms with the terms in (3.58) a few simplifications are possible[4]

$$\begin{aligned}\nabla \cdot (\mathcal{P}_i \cdot \vec{u}_i) - \vec{u}_i \cdot (\nabla \cdot \mathcal{P}_i) &= (\mathcal{P}_i \cdot \nabla) \cdot \vec{u}_i \\ &= p_i \nabla \cdot \vec{u}_i - \bar{\bar{\tau}}_i : \nabla \vec{u}_i \\ &= \nabla \cdot p_i \vec{u}_i - \vec{u}_i \cdot \nabla p_i - \bar{\bar{\tau}}_i : \nabla \vec{u}_i, \end{aligned} \tag{3.60}$$

and [1, p. 206]

$$- n_i \left\langle \vec{X}_i \cdot (\vec{u}_i + \vec{c}_i) \right\rangle + n_i \vec{u}_i \cdot \left\langle \vec{X}_i \right\rangle = -n_i \left\langle \vec{X}_i \cdot \vec{c}_i \right\rangle. \tag{3.61}$$

For a velocity independent force another simplification is possible

$$- n_i \vec{X}_i \left\langle \vec{c}_i \right\rangle = 0. \tag{3.62}$$

The energy balance can then be rewritten as

$$\begin{aligned}\frac{\partial \left(\frac{3}{2} n_i k_B T_i + n_i E_i\right)}{\partial t} + \nabla \cdot \left(\frac{5}{2} n_i k_B T_i + n_i E_i\right) \vec{u}_i - \vec{u}_i \cdot \nabla p_i \\ - \bar{\bar{\tau}}_i : \nabla \vec{u}_i + \nabla \cdot \vec{q}_i = Q_i - \vec{u}_i \cdot \vec{R}_i + \frac{1}{2} m_i u_i^2 \omega_i. \end{aligned} \tag{3.63}$$

3.C Converting species system to bulk system

In this section the conversion from the species system to the bulk system for the momentum balance and the energy balance are discussed. The random motion in the species system is indicated with $\vec{c}_i$. In this section $\vec{c}_{b,i}$ is used to represent the random motion of species i in the bulk system.

3.C.1 Momentum balance

In the species system the velocities are measured relative to $\vec{u}_i$ as

$$\left\langle (\vec{c}_i + \vec{u}_i)(\vec{c}_i + \vec{u}_i) \right\rangle = \left\langle \vec{c}_i \vec{c}_i \right\rangle_i + \vec{u}_i \vec{u}_i. \tag{3.64}$$

Using $\vec{u}_i = \vec{u} + \vec{v}_{d,i}$ gives

$$\left\langle \vec{c}_i \vec{c}_i \right\rangle + \vec{u}\vec{u} + 2\vec{u}\vec{v}_{d,i} + \vec{v}_{d,i}\vec{v}_{d,i}. \tag{3.65}$$

In the bulk system the velocities are measured relative to the mass averaged velocity which gives

$$\left\langle (\vec{c}_{b,i} + \vec{u})(\vec{c}_{b,i} + \vec{u}) \right\rangle = \left\langle \vec{c}_{b,i} \vec{c}_{b,i} \right\rangle + \vec{u}\vec{u} + 2\vec{u}\vec{v}_{d,i}. \tag{3.66}$$

[4] Note that $\bar{\bar{\tau}}_i : \nabla \vec{u}_i = (\bar{\bar{\tau}}_i \cdot \nabla) \cdot \vec{u}_i = \sum_k \sum_l \bar{\bar{\tau}}_{i,kl} \frac{\partial u_{i,k}}{\partial x_l}$ with $u_{i,k}$ representing the velocity component k of species i in a Cartesian coordinate system.

Both reference frames describe the same system and should therefore provide identical results. The difference between the averages in both systems is thus given by

$$\langle \vec{c}_{b,i}\vec{c}_{b,i}\rangle = \langle \vec{c}_i\vec{c}_i\rangle + \vec{v}_{d,i}\vec{v}_{d,i}. \tag{3.67}$$

Other useful quantities for the conversion of the species system to the bulk system are

$$\begin{aligned}
\sum_i \rho y_i \left(\vec{u}+\vec{v}_{d,i}\right) &= \rho\vec{u}\\
\sum_i \rho y_i \left(\vec{u}+\vec{v}_{d,i}\right)\left(\vec{u}+\vec{v}_{d,i}\right) &= \rho\vec{u}\vec{u} + \rho\vec{v}_{d,i}\vec{v}_{d,i}\\
\sum_i \vec{R}_i &= 0\\
\sum_i n_i q_i &= \rho\sum_i \frac{q_i y_i}{m_i} = \rho\sigma^c\\
\sum_i n_i q_i \vec{u}_i &= \vec{j},
\end{aligned} \tag{3.68}$$

with $\vec{j}$ the current density. The term $\rho\vec{v}_{d,i}\vec{v}_{d,i}$ can be used to convert the pressure tensor from the species system to the bulk system.

3.C.2 Energy balance

In the species system the velocities are measured relative to $\vec{u}_i$ as

$$\begin{aligned}
&\rho y_i \left\langle \left[\left(\vec{c}_i+\vec{u}_i\right)\cdot\left(\vec{c}_i+\vec{u}_i\right)\right]\left(\vec{c}_i+\vec{u}_i\right)\right\rangle + n_i E_i\vec{u}_i\\
&= \rho y_i\left(u_i^2\vec{u}_i + \left\langle c_i^2\right\rangle\vec{u}_i + 2\left\langle \vec{c}_i\vec{c}_i\right\rangle\cdot\vec{u}_i + \left\langle c_i^2\vec{c}_i\right\rangle\right) + n_i E_i\vec{u}_i.
\end{aligned} \tag{3.69}$$

The first term on the RHS can be rewritten using $\vec{u}_i = \vec{u}+\vec{v}_{d,i}$ which gives

$$\sum_i \rho y_i u_i^2\vec{u}_i = \rho u^2\vec{u} + 2\sum_i \rho y_i\vec{u}\cdot\left\langle\vec{v}_{d,i}\vec{v}_{d,i}\right\rangle + \sum_i \rho y_i\vec{u}\left\langle v_{d,i}^2\right\rangle + \sum_i \rho y_i\left\langle\vec{v}_{d,i}v_{d,i}^2\right\rangle. \tag{3.70}$$

In the bulk system the velocities are measured relative to the mass averaged velocity which results in

$$\begin{aligned}
&\sum_i \rho y_i\left\langle\left[\left(\vec{c}_{b,i}+\vec{u}\right)\cdot\left(\vec{c}_{b,i}+\vec{u}\right)\right]\left(\vec{c}_{b,i}+\vec{u}\right)\right\rangle + \sum_i n_i E_i\left(\vec{u}+\vec{v}_{d,i}\right)\\
&= \rho u^2\vec{u} + 2\sum_i \rho y_i\vec{u}\cdot\left\langle\vec{c}_{b,i}\vec{c}_{b,i}\right\rangle + \sum_i \rho y_i\vec{u}\left\langle c_{b,i}^2\right\rangle +\\
&\sum_i \rho y_i\left\langle\vec{c}_{b,i}c_{b,i}^2\right\rangle + \sum_i n_i E_i\left(\vec{u}+\vec{v}_{d,i}\right).
\end{aligned} \tag{3.71}$$

By using $\langle\vec{c}_{b,i}\vec{c}_{b,i}\rangle = \langle\vec{c}_i\vec{c}_i\rangle + \langle\vec{v}_{d,i}\vec{v}_{d,i}\rangle$ and $\left\langle c_{b,i}^2\right\rangle = \left\langle c_i^2\right\rangle + \left\langle v_{d,i}^2\right\rangle$ the following definition can be obtained from both systems

$$\left\langle\vec{c}_{b,i}c_{b,i}^2\right\rangle = \left\langle c_i^2\vec{c}_i\right\rangle + \left\langle\vec{v}_{d,i}v_{d,i}^2\right\rangle + \left\langle c_i^2\right\rangle\cdot v_{d,i} + \left\langle\vec{c}_i\vec{c}_i\right\rangle\cdot v_{d,i} + \sum_i n_i E_i\vec{v}_{d,i}. \tag{3.72}$$

Another conversion is made for a term that vanishes in the species system [1, p. 224-227]: $-n_i\vec{X}_i \cdot \langle \vec{c}_i \rangle = 0$. In terms of the bulk system this term can be written as $-n_i\vec{X}_i \cdot \langle \vec{c}_{b,i} + vd, i \rangle$. Averaging in the bulk system then gives $-n_i\vec{X}_i \cdot v_{d,i}$. Unlike in the species system the term does not vanish in the bulk system.

Chapter 4

Transport properties

In general large temperature variations are encountered in plasmas. In the ideal case the transport properties that occur in the relevant continuity equations are accurate for this entire temperature interval. This requires accurate representations of the collision integrals which ultimately depend on the interaction potentials for the colliding species. The number of unique interaction potentials for a mixture of N species is $\frac{1}{2}N(N-1)$. For a mixture with a large number of components it is not practical to specify an interaction potential for every possible collision pair. It is therefore necessary to develop a general method for estimating collision integrals for any type of interaction.

This chapter covers the various approaches that are and have been used in PLASIMO for calculating collision integrals in the past. Whenever a user did not specify a calculation procedure for the collision integral for a given collision pair a default interaction was automatically chosen based on the type of interaction. Initially, the simple rigid sphere and Coulomb collision integrals were used as defaults. After that Johnston [26] considered more accurate methods. However, his method required a significant amount of input parameters without any automatic routine for the determination of these parameters. PLASIMO therefore still relied on the rigid sphere and Coulomb collision integrals when no specifications were given for a collision pair. Furthermore, some methods proposed by Johnston are outdated and numerically instable. In this chapter a more accurate and more robust procedure for estimating collision integrals is presented. This method contains an automatic routine for the selection of the required input data and has therefore become the new default procedure in PLASIMO.

The chapter starts by introducing the concepts of scattering angles, cross sections and collision integrals. After that, various interaction potentials and their corresponding collision integrals are discussed. For the collision integrals corresponding to the exponential repulsive potential it is observed that the derivation presented by Monchick is incorrect. Since the interaction potential is frequently used a correct derivation is presented in section 4.E. Note that the final expression for the collision integral presented in literature is correct. In the last sections the drawbacks of Johnston's general method and the advantages of the current de-

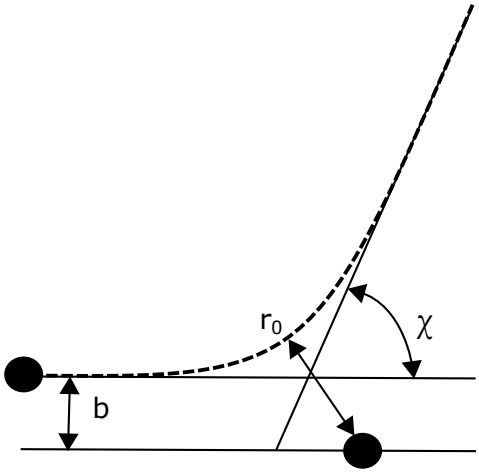

Figure 4.1: A schematic representation of the trajectory of a colliding pair of particles is given. The concepts of the impact parameter b, scattering angle χ and the distance of closest approach r_0 are explained.

fault method in PLASIMO are discussed. Additionally, a program for obtaining numerical estimates of collision integrals is described for cases where an interaction potential is available. Such interaction potentials can in principal also be obtained from software packages that perform ab initio quantum-mechanical calculations. As an example the potential curve for $H - H$ is calculated using the package DIRAC. The details are discussed in section 4.G.

4.1 Collision integrals

The calculation of the transport properties requires collision integrals $\Omega^{(l,s)}$ as input. These integrals are composed of three integrations. The first integration deals with the trajectory of the interacting particles and delivers the scattering angle. The scattering angle $\chi(b, \epsilon)$ is determined by the interaction potential $V(r)$, the impact parameter b and the relative velocity g that correspond to a kinetic energy of $\epsilon = \frac{m_{ij} g^2}{2}$ in the center of mass frame. The second integration delivers a cross section $Q^{(l)}(\epsilon)$ by considering all possible impact parameters weighted by a function that is dependent on the scattering angle. In the last integration all initial velocities are considered and the cross sections are weighted by a function that is dependent on these velocities. In this section all three integrations are discussed. Schematically they can be depicted as

$$V(r) \rightarrow \chi(b, \epsilon) \rightarrow Q^{(l)}(\epsilon) \rightarrow \Omega^{(l,s)}(T). \tag{4.1}$$

The scattering angle of two interacting particles can be calculated from conservation of energy and angular momentum. These particles have masses m_i, m_j

and positions r_i, r_j. The equations of motion in the center of mass frame can be expressed as [34, p. 45-51]

$$M\ddot{\vec{R}} = 0, \tag{4.2}$$

and

$$m_{ij}\ddot{\vec{r}} = -\nabla V(r), \tag{4.3}$$

with the total mass $M = m_i + m_j$, the position of the center of mass $\vec{R} = \frac{m_i\vec{r_i}+m_j\vec{r_j}}{m_i+m_j}$, the reduced mass $m_{ij} = \frac{m_i m_j}{m_i+m_j}$, the relative position $\vec{r} = \vec{r_i} - \vec{r_j}$ and time derivatives indicated by dots above the variable. The laws of conservation of energy and angular momentum in polar coordinates are given by

$$\frac{1}{2}m_{ij}\dot{r}^2 + \frac{1}{2}m_{ij}r^2\dot{\phi}^2 + V(r) = \frac{1}{2}m_{ij}g^2, \tag{4.4}$$

and

$$m_{ij}r^2\dot{\phi} = m_{ij}gb, \tag{4.5}$$

where g is the initial relative velocity at large separation and b is the impact parameter. The collision trajectory for a given impact parameter is illustrated in figure 4.1. Substitution of the angular momentum gives

$$\dot{r}^2 + \frac{b^2 - r^2}{r^2}g^2 + \frac{2V(r)}{m_{ij}} = 0, \tag{4.6}$$

which is equivalent to

$$\dot{r} = \mp g\sqrt{1 - \frac{b^2}{r^2} - \frac{V(r)}{\epsilon_{ij}}}, \tag{4.7}$$

with the initial energy $\epsilon_{ij} = \frac{1}{2}m_{ij}g^2$. The negative sign corresponds to the part of the trajectory where the particles are approaching r_0 while the positive sign corresponds to the part where the particles are moving away from r_0. By using $\frac{\partial\phi}{\partial r} = \frac{\dot{\phi}}{\dot{r}}$ and $\frac{\dot{\phi}}{g} = \frac{b}{r^2}$ we obtain

$$\frac{\partial\phi}{\partial r} = \mp\frac{b}{r^2}\frac{1}{\sqrt{1 - \frac{b^2}{r^2} - \frac{V(r)}{\epsilon_{ij}}}}. \tag{4.8}$$

The integral over the path contains two identical contributions: From $r = \infty$ to $r = r_0$ and from $r = r_0$ to $r = \infty$ with r_0 the interparticle distance at closest approach. The scattering angle is defined as the angle between the unperturbed path and the perturbed path of the incident particle and is given by

$$\chi_{ij}(\epsilon_{ij}, b) = \pi - 2b\int_{r_0}^{\infty}\frac{\mathrm{d}r}{r^2\sqrt{1 - \frac{b^2}{r^2} - \frac{V(r)}{\epsilon_{ij}}}}. \tag{4.9}$$

The distance of closest approach is reached when $1 - \frac{b^2}{r_0^2} - \frac{V(r_0)}{\epsilon_{ij}} = 0$. The transport cross sections $Q_{ij}^{(l)}(\epsilon_{ij})$can be obtained from the scattering angle as [34, p. 484]

$$Q_{ij}^{(l)}(\epsilon_{ij}) = 2\pi\int_0^{\infty}\left[1 - \cos^l\chi_{ij}(\epsilon_{ij}, b)\right]b\mathrm{d}b. \tag{4.10}$$

Some of these cross sections can be easily related to physical processes. For example, for $l = 1$ the factor $1 - \cos\chi_{ij}$ describes the ratio of the momentum after the collision to the momentum before the collision in the initial direction in the center of mass frame.

An alternative way of expressing these transport cross sections is by using the differential cross section given by [54, p. 254]

$$\frac{\mathrm{d}\sigma\left(\epsilon,\chi\right)}{\mathrm{d}\Omega_S} = \frac{1}{2\pi\sin\chi}\frac{\mathrm{d}\sigma\left(\epsilon,\chi\right)}{\mathrm{d}\chi} = \frac{b}{\sin\chi}\left|\frac{\partial b}{\partial\chi}\right|. \tag{4.11}$$

The cross sections can then be expressed as

$$Q_{ij}^{(l)}\left(\epsilon_{ij}\right) = 2\pi\int_0^\infty \left[1-\cos^l\chi_{ij}\left(\epsilon_{ij},b\right)\right]\frac{\mathrm{d}\sigma\left(\epsilon,\chi\right)}{\mathrm{d}\Omega_S}\sin\chi\mathrm{d}\chi. \tag{4.12}$$

The collision integrals are given by

$$\Omega_{ij}^{(l,s)} = \sqrt{\frac{k_BT}{2\pi m_{ij}}}\int_0^\infty \gamma^{2s+3}Q_{ij}^{(l)}\left(\gamma^2k_BT\right)\exp\left(-\gamma^2\right)\mathrm{d}\gamma, \tag{4.13}$$

with the reduced velocity given by $\gamma^2 = \frac{m_{ij}g^2}{2k_BT}$. In order to use the temperature T the species velocities should have a Maxwellian or nearly Maxwellian distribution. In case of a multi-temperature plasma the temperature that is used in the collision integrals is the reduced temperature given by $T_{ij} = \frac{m_jT_i+m_iT_j}{m_i+m_j}$ [59, p. 129].

4.2 Collision integrals for various interaction potentials

This section describes multiple default procedures for estimating collision integrals. The considered defaults are the current default and the default procedures that have been used in the past in PLASIMO. The first potential that is described is the rigid sphere potential. Collision integrals are often presented in dimensionless form. The second subsection describes how collision integrals are normalized using collision integrals from the rigid sphere potential. The third subsection describes the Langevin model that has been used for neutral-ion and neutral-electron interactions. The fourth subsection describes the Tang and Toennies potential. In PLASIMO collision integrals for a simplified form have been used: exponential repulsive potential. In the fifth subsection the Lennard Jones potential is considered in generalized form.

The interactions described in the first five subsections are suitable for neutral-neutral and neutral-ion collisions. For specific interactions an additional contribution must be taken into account for neutral-ion interactions namely; resonant charge exchange. A general discussion of charge exchange is given in the sixth subsection. In the seventh subsection the Rapp-Francis model is discussed. The eight subsection describes more advanced models for resonant charge exchange that may be used in future default procedures.

The ninth subsection describes a strategy for electron-neutral interactions for cases where tabulated cross section data for only one l value is available. The tenth

subsection describes the Coulomb interaction that is used for charged-charged interactions. The Coulomb potential can not be integrated analytically and therefore the integration is cut off at the Debye screening length. A more accurate procedure is described in the eleventh subsection where the screened-Coulomb potential is used.

4.2.1 Rigid spheres

The rigid sphere potential is given by [34, p. 525, 544]

$$V(r) = \begin{cases} \infty & r < \sigma \\ 0 & r \geq \sigma \end{cases}, \tag{4.14}$$

with σ the collision diameter. The scattering angle for $b \leq \sigma$ can be expressed as

$$\chi = \pi - 2b \int_{\sigma}^{\infty} \frac{1}{r^2} \frac{1}{\sqrt{1 - \frac{b^2}{r^2}}} \mathrm{d}r = 2 \arccos\left(\frac{b}{\sigma}\right). \tag{4.15}$$

For $b > \sigma$ the scattering angle is zero. By using (4.12) the cross section for a rigid sphere can be expressed as

$$Q^{(l)} = 2\pi \int_0^{\sigma} \left(1 - \cos^l\left(2 \arccos\frac{\sigma}{b}\right)\right) b \mathrm{d}b = \pi\sigma^2 \left[1 - \frac{1 - (-1)^{l+1}}{2\,(l+1)}\right]. \tag{4.16}$$

Note that $1 - \left(1 - (-1)^{l+1}\right) / \left(2\,(l+1)\right)$ can be simplified as $1 - 1/\,(l+1)$ for even l and as 1 for odd l. By using (4.13) the rigid sphere collision integral can then be expressed as

$$\begin{aligned} \Omega^{(l,s)} &= \pi\sigma^2 \sqrt{\frac{k_B T}{2\pi\mu}} \left[1 - \frac{1 - (-1)^{l+1}}{2\,(l+1)}\right] \int_0^{\infty} \gamma^{(2s+3)} \exp\left(-\gamma^2\right) \mathrm{d}\gamma \\ &= \pi\sigma^2 \sqrt{\frac{k_B T}{2\pi\mu}} \left[1 - \frac{1 - (-1)^{l+1}}{2\,(l+1)}\right] \frac{(s+1)!}{2}. \end{aligned} \tag{4.17}$$

The collision diameter is calculated as

$$\sigma_{ij} = r_i + r_j, \tag{4.18}$$

with r_i the rigid sphere radius of particle i. For atoms these radii have been determined empirically by Slater [60] by extracting the internuclear distance from many bonds in crystals and molecules. Additionally, Clementi [61] calculated atomic rigid sphere radii by using the maximum value of r times the radial distribution of the most outer STO[1]. Hirschfelder et al. [62] developed an empirical

[1] Slater-type-orbitals (STO) are given by $N r^{n-1} \exp\left(-\xi r\right) Y_{l,m}\left(\theta, \phi\right)$ with ξ the orbital exponent and $Y_{l,m}$ a spherical harmonic.

Table 4.1: The rigid sphere radii of various species determined with different methods.

Species	Hirschfelder [62] (Å)	Clementi [61] (Å)	Slater [60](Å)
H	0.79	-	0.25
He	0.47	0.31	-
C	0.81	0.67	0.70
N	0.54	0.56	0.65
O	0.58	0.48	0.60
Ne	0.45	0.38	-
Na	-	1.90	1.80
Si	-	1.11	1.10
P	-	0.98	1.00
S	-	0.88	1.00
Cl	0.91	0.79	1.00
Ar	0.82	0.71	-
Br	1.08	0.94	1.15
Kr	0.88	0.88	-
Xe	1.15	1.08	-

formula in terms of the expectation value[2] of these STO's given by

$$\sigma_{ij} = \langle r_i \rangle + \langle r_j \rangle + 1.8\text{Å}, \tag{4.19}$$

where Hirschfelder et al. [62] note that Pauling obtained a similar formula using the constant 1.6Å. For diatomic molecules Hirschfelder et al. used the same procedure but added the bond length to one of the dimensions and obtained

$$\sigma_{ij} = \frac{4}{3}\left(\langle r_i \rangle + \langle r_j \rangle\right) + 1.8\text{Å}. \tag{4.20}$$

A similar formula for triatomic molecules has been proposed by Svehla [63, p. 12]. Hirschfelder et al. [62, eq. 11,18,19] also list a few methods for obtaining the collision diameter from known values of the viscosity, thermal conductivity via $\Omega^{(2,2)}$ or diffusion coefficients via $\Omega^{(1,1)}$. Table 4.1 shows the radius of a few species and how they change as a function of the method. Although some radii are approximately equivalent for all methods most radii show variations in the order of 10% or more. On top of that the choice for c in

$$\sigma_{ij} = \langle r \rangle_i + \langle r \rangle_j + c, \tag{4.21}$$

can influence the collision diameter considerably.

[2]The expectation value is given by $\langle r \rangle = \frac{n^*(2n^*+1)}{2(Z-S)} a_0$ with n^* the effective quantum number, Z the atomic number, S the screening constant and a_0 the Bohr length.

4.2.2 Reduced parameters

Collision integrals are often tabulated in reduced form. In that case the collision integral is normalized by the value of a rigid sphere collision integral for the same interaction [34, p. 526]

$$\Omega_{ij}^{(l,s)*} = \frac{\Omega_{ij}^{(l,s)}}{\Omega_{\mathrm{RS},ij}^{(l,s)}} = \frac{(s+1)!\left[1-\frac{1-(-1)^{l+1}}{2(l+1)}\right]\pi\sigma^2}{2}\int_0^\infty \gamma^{2s+3}\exp\left(-\gamma^2\right)Q^{(l)}\mathrm{d}\gamma, \tag{4.22}$$

with $\Omega_{ij}^{(l,s)*}$ the reduced collision integral. The rigid sphere potential is an artificial potential. Other interaction potentials can be related to the rigid sphere potential by using $V(\sigma) = 0$. It is also possible to derive the collision diameter from measurements of the viscosity as is for example done by Svehla [63].

4.2.3 Langevin model

The interaction between a charged particle and an induced dipole moment is given by [64, p. 15]

$$V = -\frac{1}{2}\vec{\mu}\cdot\vec{E} = -\frac{1}{2}\alpha_C E^2 = -\frac{1}{2}\alpha_C\frac{Z^2e^2}{\left(4\pi\epsilon_0 r^2\right)^2}, \tag{4.23}$$

with $\vec{\mu}$ the dipole moment, $\vec{E}$ the electric field, α_C the polarizability in $\mathrm{Cm^2V^{-1}}$. Note that the polarizability volume is given by $\alpha = \frac{\alpha_C}{4\pi\epsilon_0}$. This potential is of the form

$$V = -\frac{C}{r^X}, \tag{4.24}$$

with $C = \frac{Z^2e^2\alpha_C}{2(4\pi\epsilon_0)^2} = \frac{Z^2e^2\alpha}{8\pi\epsilon_0}$ and X the exponent of the intermolecular separation. The collision integrals for such a potential have been evaluated numerically. Tabulations can be found in Hirschfelder et al. [34, p. 546-548] and Kang et al. [65]. The collision integral is given by

$$\begin{aligned}\Omega^{(l,s)} &= \sqrt{\frac{\pi k_B T}{2\mu}}\left(\frac{XC}{k_B T}\right)^{2/X} A^{(l)}\Gamma\left(s+2-2/X\right)\\ &= \sqrt{\frac{Z^2e^2\alpha}{4\mu\epsilon_0}}A^{(l)}\Gamma\left(s+3/2\right),\end{aligned} \tag{4.25}$$

with $A^{(l)} = \int_0^\infty \left(1-\cos^l\chi\right)y_0\mathrm{d}y_0$ a constant and $y_0 = b\left(\frac{\mu g^2}{2XC}\right)^{1/X}$ the reduced impact parameter. For $X = 4$ the values of this constant are $A^{(1)} = 0.298$ and $A^{(2)} = 0.308$.

4.2.4 Exponential repulsive potential

A general formula for the interaction potential of neutrals with neutrals and neutrals with ions is proposed by Tang and Toennies [66, 67]. This potential is given

by

$$V(r) = A\exp(-br) - \sum_{n\leq 3} f_{2n}(r)\frac{C_{2n}}{r^{2n}}, \tag{4.26}$$

where the first term represents the exponential repulsive potential and the second term contains the dispersion coefficients C_{2n} and the damping functions $f_{2n}(r)$. When the kinetic energy is much larger than the depth of the potential well, considering only the exponential repulsive term is enough to describe the potential accurately

$$V(r) = A\exp(-br). \tag{4.27}$$

The collision integrals for the exponential repulsive potential are evaluated numerically by Monchick [68]. He presented his results in the following form

$$\Omega_{ij}^{(l,s)} = 4\sqrt{\frac{k_B T}{2\mu\pi}}\alpha^2\pi\rho^2 I_{(l,s)}, \tag{4.28}$$

with $I_{(l,s)}$ tabulations for specific l and s values, $\alpha = \ln\frac{A}{k_B T}$ and $\rho = 1/b$ the decay length of the potential. The calculation of the parameters A and b is discussed in appendix 4.C and 4.D. Although the parameters C_{2n} from the original Tang and Toennies potential do not occur in the exponential repulsive potential these coefficients are necessary to estimate the parameters A and b.

Various errors have been identified in Monchick's paper [68]. Monchick presents the final expression in equation 18 of his paper, but omits the reduced mass. Additionally, the derivation of the final result is not correct. The substitution made in equation 13 is incorrect. Later in equation 16 Monchick omits a bracket. A more detailed discussion of these errors is given in appendix 4.E. Note that the errors that are discussed in the appendix do not change the final result in the paper.

4.2.5 Lennard Jones

The Lennard Jones potential is given by

$$V(r) = 4\epsilon_{0,ij}\left[\left(\frac{\sigma}{r}\right)^{12} - \left(\frac{\sigma}{r}\right)^{6}\right], \tag{4.29}$$

with $\epsilon_{0,ij}$ the potential well depth, $\sigma = 2^{-1/6} r_{m,ij}$ and $r_{m,ij}$ the position of the well minimum. The well depth and well position can be estimated using the scaling relations provided in section 4.C. The collision integrals for the Lennard Jones potential can be obtained from the tabulations of Klein et al. [69, p. 365-366].

The Lennard Jones potential generally describes the well accurately. However, the repulsive term proportional to r^{-12} is often found to be too repulsive [26, p. 128]. This problem is remedied by using a generalized Lennard-Jones potential, which is given by [5]

$$V = \epsilon_{0,ij}\left[\frac{m}{n_{ij}(x_{ij}) - m}\left(\frac{1}{x_{ij}}\right)^{n_{ij}(x_{ij})} - \frac{n_{ij}(x_{ij})}{n_{ij}(x_{ij}) - m}\left(\frac{1}{x_{ij}}\right)^{m}\right], \tag{4.30}$$

with $m = 6$ for neutral-neutral interactions, $m = 4$ for neutral-ion interactions, and further

$$x_{ij} = \frac{r}{r_{m,ij}}, \tag{4.31}$$

$$n_{ij}\left(x_{ij}\right) = \beta_{ij} + 4x_{ij}^2, \tag{4.32}$$

$$\beta_{ij} = 6 + \frac{5}{s_i + s_j}. \tag{4.33}$$

The softness parameter s_i is given by

$$s_i = \alpha_i^{\frac{1}{3}}\left(2S + 1\right), \tag{4.34}$$

with S the spin quantum number of the ground state. The reduced collision integral is parameterized in terms of

$$y_{ij} = \ln T_{ij}^*. \tag{4.35}$$

The parameterization is given by [5, eqn. 15] ([27, eqn. 3.67])

$$\begin{aligned}\ln \Omega_{ij}^{(l,s)*} &= \frac{\left(a_1\left(\beta_{ij}\right) + a_2\left(\beta_{ij}\right) y_{ij}\right) \exp\left(\frac{y_{ij} - a_3(\beta_{ij})}{a_4(\beta_{ij})}\right)}{\exp\left(\frac{y_{ij} - a_3(\beta_{ij})}{a_4(\beta_{ij})}\right) + \exp\left(\frac{a_3(\beta_{ij}) - y_{ij}}{a_4(\beta_{ij})}\right)} \\ &+ \frac{a_5\left(\beta_{ij}\right) \exp\left(\frac{y_{ij} - a_6(\beta_{ij})}{a_7(\beta_{ij})}\right)}{\exp\left(\frac{y_{ij} - a_6(\beta_{ij})}{a_7(\beta_{ij})}\right) + \exp\left(\frac{a_6(\beta_{ij}) - y_{ij}}{a_7(\beta_{ij})}\right)}.\end{aligned} \tag{4.36}$$

A computationally more efficient form is given by

$$\ln \Omega_{ij}^{(l,s)*} = \frac{a_1\left(\beta_{ij}\right) + a_2\left(\beta_{ij}\right) y_{ij}}{1 + \exp\left(\frac{2(a_3(\beta_{ij}) - y_{ij})}{a_4(\beta_{ij})}\right)} + \frac{a_5\left(\beta_{ij}\right)}{1 + \exp\left(\frac{2(a_6(\beta_{ij}) - y_{ij})}{a_7(\beta_{ij})}\right)}, \tag{4.37}$$

with the functions a_i given by [5, eqn. 16] ([27, eqn. 3.68]):

$$a_i\left(\beta_{ij}\right) = \sum_{k=0}^{2} c_k \beta_{ij}^k, \tag{4.38}$$

with c_k tabulated for a large set of collision integrals. The collision integral can be calculated as

$$\Omega_{ij}^{(l,s)} = \frac{(s+1)!}{2} \frac{\left[2l + 1 - (-1)^l\right]}{2\left(l+1\right)} \sqrt{\frac{k_B T}{2\pi\mu}} \pi \sigma_{ij}^2 \Omega_{ij}^{(l,s)*}. \tag{4.39}$$

The collision diameter is parameterized with

$$\sigma_{ij} = x_0 r_{m,ij}, \tag{4.40}$$

and x_0 is given by

$$x_0 = \xi_1 \beta_{ij}^{\xi_2}, \tag{4.41}$$

where ξ_i are tabulated constants.

4.2.6 Charge exchange interactions

The cross section for charge exchange can be written in terms of the probability of charge exchange $P_{\mathrm{ex},ij}$ [70] as

$$\begin{aligned} Q_{ij}^{(l)} &= 2\pi \int_0^\infty \left(1 - P_{\mathrm{ex},ij}\right)\left(1 - \cos^l \chi\right) b\mathrm{d}b + \\ & \quad 2\pi \int_0^\infty P_{\mathrm{ex},ij}\left[1 - \cos^l\left(\pi - \chi\right)\right] b\mathrm{d}b. \end{aligned} \tag{4.42}$$

The scattering angle for the process of charge exchange is different from the one where no exchange occurs. In the center of mass frame without charge exchange the ionic particle I and the neutral particle N are scattered over an angle χ. The same process with charge exchange gives the same result for the particle that is initially ionized and the particle that is initially neutral, but the ionic and neutral particles have changed places. The particles are now effectively scattered over an angle of $\pi - \chi$ [71]. Since for even l, $\cos^l \chi = \cos^l\left(\pi - \chi\right)$ the total cross section is equal to the elastic cross section and no distinction is necessary. For odd l the cross section can be written as [70]

$$Q_{ij}^{(l)} = 2\pi \int_0^\infty \left[1 - \left(1 - 2P_{\mathrm{ex},ij}\right)\cos^l \chi\right] b\mathrm{d}b. \tag{4.43}$$

This cross section is often separated in a contribution from charge exchange and an elastic contribution as

$$\begin{aligned} Q_{ij}^{(l)} &= 2\pi \int_0^\infty 2P_{\mathrm{ex},ij} b\mathrm{d}b + 2\pi \int_0^\infty \left(1 - 2P_{\mathrm{ex},ij}\right)\left(1 - \cos^l \chi\right) b\mathrm{d}b \\ &= 2Q_{\mathrm{ex},ij} + Q_{\mathrm{ex,elas},ij}^{(l)}. \end{aligned} \tag{4.44}$$

In principle these two terms provide two contributions for the collision integral. In practice, Murphy [72, 73] observed that for high energies resonant charge transfer is the dominant process. For low energies, Murphy observes that P_{ex} is small and the cross section should only contain the elastic contribution. Murphy summarized these statements with

$$\Omega_{ij}^{(l,s)} = \sqrt{\left(\Omega_{\mathrm{el},ij}^{(l,s)}\right)^2 + \left(\Omega_{\mathrm{ex},ij}^{(l,s)}\right)^2}, \tag{4.45}$$

which reduces to the correct asymptotes. The total collision integral thus consists of charge exchange and elastic contributions. Currently, PLASIMO neglects contributions from charge exchange for X–Y^+ with X$\neq$ Y. Additionally, charge exchange is only included when X is a neutral particle.

4.2.7 Rapp-Francis model

The probability for charge exchange typically oscillates rapidly between 0 and 1 for small b . The probability $P_{\mathrm{ex},ij}$ can thus be approximated with 1/2 for $b < b_c$.

The cross section can then be rewritten as

$$Q_{ij}^{(l)} \approx \pi b_c^2 + 4\pi \int_{b_c}^{\infty} P_{\mathrm{ex},ij} b \mathrm{d}b + 2\pi \int_{b_c}^{\infty} \left(1 - 2P_{\mathrm{ex},ij}\right) \left(1 - \cos^l \chi\right) b \mathrm{d}b, \tag{4.46}$$

where the contribution $(1 - 2P_{\mathrm{ex},ij})$ can be neglected for $0 \leq b \leq b_c$ due to the rapid oscillations of $P_{\mathrm{ex},ij}$. The cross section for charge transfer can be introduced as

$$Q_{\mathrm{ex},ij} = 2\pi \int_0^{\infty} P_{\mathrm{ex},ij} b \mathrm{d}b = \frac{1}{2}\pi b_c^2 + 2\pi \int_{b_c}^{\infty} P_{\mathrm{ex},ij} b \mathrm{d}b \approx \frac{1}{2}\pi b_c^2, \tag{4.47}$$

where the decaying probability of charge exchange is assumed to be small for $b \geq b_c$. Combining both equations gives

$$Q_{ij}^{(l)} \approx 2Q_{\mathrm{ex},ij} + 2\pi \int_{b_c}^{\infty} \left(1 - 2P_{\mathrm{ex},ij}\right) \left(1 - \cos^l \chi\right) b \mathrm{d}b. \tag{4.48}$$

Since b_c is large the scattering angle generally is small for $b \geq b_c$. Thus the last term in the expression for the cross section can be neglected which gives

$$Q_{ij}^{(l)} \approx 2Q_{\mathrm{ex},ij}. \tag{4.49}$$

In order to obtain the collision cross section for charge exchange only a value of b_c is required. A crude estimate can be obtained from the model of Rapp and Francis.

Rapp and Francis [74] obtained an expression for estimating b_c by considering semi-empirical wave functions. These wave functions are chosen in such a way that they reduce to the correct wave function for H^+ (1s). They indicate that these orbitals are a gross approximation for other species especially for species that do not have their outer electron in an s state. The system that is described consists of A^+ and A where A is represented as A^+ and an electron. Since A and A^+ have the same core this is also called resonant charge exchange. Resonant charge exchange is then proportional to the probability of the electron moving from one ion to the other ion within the collision time. This probability has the form $P_{\mathrm{ex}} = \sin^2 Y(b, g)$. For small b, P_{ex} is an oscillating function. For large b, $Y(b, g)$ is a decaying function. Rapp and Francis assume that neglecting the tail of P_{ex} is compensated by overestimating b_c with $P_{\mathrm{ex}}(b_c) = \frac{1}{4}$. The final expression from Rapp and Francis can be converted to a dimensionless form as

$$\sqrt{x}\,(1 + x) \exp(-x) = \frac{\sqrt{2\pi}}{12} \frac{\hbar g}{I_{\mathrm{H}} a_0}, \tag{4.50}$$

with $x = \gamma_k b_c / a_0$, $\gamma_k = \sqrt{\frac{I_k}{I_{\mathrm{H}}}}$, I_{H} the ionization potential of hydrogen, $I_k = E_{\mathrm{ion}} - E_k$ the ionization potential for state k and a_0 the Bohr radius. The function reaches a maximum at $x = 1$ which means the search interval is restricted to $1 \leq x \leq \infty$. Rapp and Francis derived their expression taking the limit of Bessel functions with x as the variable. This approximation is valid when $x \ll 1$.

By neglecting the dependence of b_c on g, the cross section can be parameterized [75, 76] with

$$\sqrt{2Q_{\mathrm{ex},ij}} = A - B \ln g, \tag{4.51}$$

with A and B fit parameters. For such a parameterization the collision integral can be calculated analytically with [76]

$$\begin{aligned}\Omega_{ij}^{(l,s)} &= \frac{(s+1)!}{2}\sqrt{\frac{k_B T}{2\pi m_{ij}}}\frac{(s+1)!\left[2l+1-(-1)^l\right]}{4\,(l+1)} \times \\ &\left[A^2 - ABx + \left(\frac{Bx}{2}\right)^2 + \frac{B\xi}{2}\left(Bx - 2A\right) + \frac{B^2}{4}\left(\alpha + \xi^2\right) + \right. \\ &\left. \frac{B}{2}\left[B\left(x+\xi\right) - 2A\right]\ln\frac{T}{m_{ij}} + \left(\frac{B}{2}\ln\frac{T}{m_{ij}}\right)^2\right],\end{aligned} \tag{4.52}$$

with $x = \ln(2k_B)$, $\alpha = \frac{\pi^2}{6} - \sum_{n=1}^{s+1}\frac{1}{n^2}$, m_{ij} the reduced mass and $\xi = \sum_{n=1}^{s+1}\frac{1}{n} - \bar{\gamma}$ where $\bar{\gamma}$ is Euler's constant[3]. The expression for the collision integral can be simplified to [77, p. 138]

$$\Omega_{ij}^{(l,s)} = \frac{(s+1)!}{2}\sqrt{\frac{k_B T}{2\pi m_{ij}}}\frac{B^2}{4}\left[\left(\ln\left(\frac{2k_B T}{m_{ij}}\right) - \frac{2A}{B} + \xi\right)^2 + \alpha\right]. \tag{4.53}$$

Note that the terms in the logarithms are not dimensionless. This is caused by the conversion of the dimensional $\ln g$ from the original cross section to the dimensionless form that is used in the integral of the collision integral. Additionally, van Dijk [77, p. 138] uses m_i rather than the reduced mass $m_{ij} = m_i + m_j \approx 2m_i$.

4.2.8 Charge-exchange revisited

The contribution from charge-exchange has been calculated using the methods of Rapp and Francis. In that approach a hydrogen-like wave function is used for all species. A more advanced method is proposed by Smirnov et al. [27, p. 103-107] [78–80] Smirnov et al. account for the internal structure of the atom and the ion. The expression for the critical impact parameter proposed by Smirnov et al. [79, p. 621, 613] is given by

$$\frac{1}{\hbar g}\sqrt{\frac{\pi b_c}{2\gamma}}\Delta\left(b_c\right) = 0.28, \tag{4.54}$$

with $\gamma^2 = \frac{I}{I_H}$ the ratio of the ionization potential of the considered state with respect to the ionization potential of hydrogen in the ground state. The exchange interaction potential is given by [80, eq. 14]

$$\Delta_{JM_J jm_j}\left(b_c\right) = n_e\left(G_{ls}^{LS}\left(l_e, n_e\right)\right)^2 \sum_{\mu,\sigma}\sum_{M_L,M_S}\sum_{m_l,m_s}\mathrm{CG}\Delta_{l_e\mu}\left(b_c\right), \tag{4.55}$$

[3]Note that Devoto obtains $x = \ln(4k_B)$. This is related to the usage of the reduced mass $2m_{ij} \approx m_i$.

with the quantum numbers $LSJM_LM_S$ representing the atom, the quantum numbers $lsjm_lm_s$ representing the ion (atomic core) and the quantum numbers $l_e\frac{1}{2}\mu\sigma$ representing the valence electron, n_e the number of valence electrons, $G_{ls}^{LS}(l_e, n_e)$ the parentage coefficient which is tabulated [78, table. 6] for atoms with an s- or a p-shell as the outer shell and CG represents a multiplication of eight Clebsch-Gordan coefficients[4]. The single electron-exchange potential is given by

$$\Delta_{l_e\mu}(R) = A^2 R^{\frac{2}{\gamma}-1-|\mu|}\exp^{-R\gamma-\frac{1}{\gamma}}\frac{(2l_e+1)(l_e+|\mu|)!}{(l_e-|\mu|)!|\mu|!(\gamma)^{|\mu|}}, \tag{4.56}$$

with A [78, table. 7] the proportionality constant of the asymptotic wavefunction for the valence electron in wave functions of the type

$$\Psi(r) = Ar^{\frac{1}{\gamma}-1}\exp(-r\gamma), \quad r\gamma \gg 1. \tag{4.57}$$

This more elaborate approach is one of the methods that have been used by Capitelli et al. [27] to calculate the charge-exchange collision integral. These collision integrals are fitted as[5]

$$\sigma_{ij}^2\Omega_{ij}^{(l,s)*} = d_1 + d_2x + d_3x^2, \tag{4.58}$$

with $x = \ln T$ and the coefficients d_i are given in [27, table 11.5, 11.10]. A comparison of the values obtained using this fit and the approach of Rapp-Francis is given in table 4.2. For all atom-single-ion interactions the agreement is remarkably good. The maximum deviation of the Rapp-Francis model reaches 26.8 % for the resonant charge interaction for H–H^+. More surprising is the fact that 4 out of 6 atom-single-ion interactions are reproduced with errors smaller than 10 %. Apparently the hydrogen-like wave functions maintain sufficient information to accurately represent these interactions. Larger deviations are obtained for H–H^- and H_2–H_2^+ for which the one-electron-wavefunction apparently is not a good approximation. In spite of the large relative errors a proper order of magnitude estimate is still provided in these cases.

The method proposed by Smirnov requires considerably more input data than the procedure suggested by Rapp and Francis. Since the relative errors introduced by using the approach from Rapp and Francis are small this method is preferred when no tabulated cross sections are available. When an interaction potential is available the contribution from charge exchange can also be obtained from the cross sections given by Viehland [83, eq. 7-8]. These expressions are derived from quantum mechanics and therefore contain an extra term for cross sections corresponding to odd l. The exchange probability is approximated semi-classically using

$$P_{\mathrm{ex},ij} = \sin^2\left(\eta^{(+)} - \eta^{(-)}\right). \tag{4.59}$$

[4]The Clebsch-Gordan coefficient can be expressed in the Wigner 3j-symbol as

$$\langle j_1m_1j_2m_2|j_3m_3\rangle = (-1)^{m_3+j_1-j_2}\sqrt{2j_3+1}\begin{pmatrix} j_1 & j_2 & j_3 \\ m_1 & m_2 & -m_3\end{pmatrix}.$$

The Wigner 3j-symbol can be calculated based on the Racah formula [81, p. 1058] [82].

[5]Note that $\sigma_{ij}^2\Omega_{ij}^{(l,s)*}$ is provided in Å^2.

Table 4.2: For various interactions the charge exchange cross section is evaluated according to the methods of Rapp and Francis and Capitelli et al. (4.58). The minimum and maximum errors over a temperature range from 100 K to 50000 K are reported. The errors are normalized to the results of Capitelli et al. The data from Capitelli et al. for He–He^+ and H–H^- is based on experiments and for H–H^+ on quantum mechanical calculations. The remaining results are calculated according to the framework of Smirnov et al.

Interaction	minimum error(%)	maximum error(%)
N–N^+	3.57	7.77
O–O^+	0	5.22
C–C^+	25.1	25.8
Ar–Ar^+	3.96	6.86
CO–CO^+	19.3	23.9
He–He^+	1.6	6.94
H–H^-	235	432
H–H^+	23.8	26.8
H_2–H_2^+	58.2	122

The phase shifts are given by

$$\eta^{(\pm)} = \kappa \int_{r_0}^{\infty} \left[1 - \frac{b^2}{r^2} - \frac{V^{(\pm)}(r)}{\epsilon}\right]^{1/2} \mathrm{d}r - \kappa \int_{b}^{\infty} \left[1 - \frac{b^2}{r^2}\right]^{1/2} \mathrm{d}r, \tag{4.60}$$

with κ the wavenumber $\epsilon = \hbar^2\kappa^2/(2\mu)$ and $\pm$ indicating whether the potential curve is symmetric or antisymmetric, respectively.

4.2.9 Electron-neutral interactions

In the absence of any specific cross section data the Langevin potential is recommended for interactions between electrons and neutrals. When a differential cross section is available a direct integration can provide all the collision integrals. The azimuthally symmetric differential cross section can be written as

$$\frac{\partial\sigma(\epsilon,\chi)}{\partial\Omega_S} = \frac{1}{2\pi\sin\chi}\frac{\partial\sigma(\epsilon,\chi)}{\partial\chi} = \sigma(\epsilon)\, I(\epsilon,\chi), \tag{4.61}$$

with $I(\epsilon,\chi)$ the normalized angular distribution. This angular distribution is described in more detail in chapter 14. This distribution satisfies

$$\int I(\epsilon,\chi)\,\mathrm{d}\Omega = 2\pi \int_0^{\pi} I(\epsilon,\chi)\sin\chi \mathrm{d}\chi = 1. \tag{4.62}$$

In many cases a differential cross section is not available, but an elastic momentum transfer cross section is specified[6]. It is then possible to obtain an l scaling for

[6]This corresponds to the case $l = 1$ in (4.12).

$l > 1$ by assuming an angular distribution. Many studies [84–86] suggest that the angular distribution for elastic interactions for electrons with neutrals can be approximated accurately with an isotropic differential cross section. In that case $I(\epsilon, \chi) = \frac{1}{4\pi}$. The angular part of a transport cross section is then given by

$$\frac{Q^{(l)}}{\sigma(\epsilon)} = \frac{1}{2}\int_0^{\pi} \left(1 - \cos^l \chi\right) \sin\chi \mathrm{d}\chi = \left[1 - \frac{1}{2(l+1)}\left(1 - (-1)^{l+1}\right)\right]. \tag{4.63}$$

Note that for odd l this ratio is equal to 1 and for even l it is given by $1 - 1/(l+1)$. It is thus possible to convert $Q^{(1)}$ in any $Q^{(l)}$. Additionally, it is interesting to note that the isotropic differential cross section provides the same l-scaling as the rigid sphere model, see (4.16).

4.2.10 Coulomb potential

For the Coulomb potential Mitchner and Kruger [54, p. 255-257] derive an expression for the differential cross section. The potential is written as

$$V = \frac{Z_1 Z_2 e^2}{4\pi\epsilon_0 r} = \frac{A}{r}, \tag{4.64}$$

with Z_i the charge number. The equation for the distance of closest approach is given by

$$\left(\frac{r_0}{b}\right)^2 - 2\frac{r_0 b_0}{b^2}u - u^2 = (u + u_1)(1 - u) = 0, \tag{4.65}$$

with $u = \frac{r_0}{r}$ equal to 1, $b_0 = \frac{A}{2E}$ and $u_1 = \left(\frac{r_0}{b}\right)^2 = 1 - 2\frac{r_0 b_0}{b^2}$. The scattering angle can now be expressed as[7]

$$\chi = \pi - 2\int_0^1 \frac{\mathrm{d}u}{\sqrt{(u + u_1)(1 - u)}} = -\pi + 4\arctan\left(\frac{r_0}{b}\right), \tag{4.66}$$

which can be rearranged to[8]

$$\tan\frac{\chi}{2} = \frac{b_0}{b}. \tag{4.67}$$

This result can be used to calculate the (Rutherford) differential cross section as

$$\frac{\mathrm{d}\sigma(\epsilon, \chi)}{\mathrm{d}\Omega_S} = \frac{(b_0)^2}{4\sin^4\left(\frac{\chi}{2}\right)}. \tag{4.68}$$

The transport cross sections are infinite due to the large contributions from small angle collisions. The cross sections can be made finite by cutting off the integral at

[7] The integral is given by $\int_0^1 \frac{\mathrm{d}u}{\sqrt{(u+u_1)(1-u)}} = 2\arctan\sqrt{\frac{u+u_1}{1-u}}|_0^1$.

[8] The integration from the scattering angle gives $\tan\frac{\pi+\chi}{4} = \frac{r_0}{b}$ which can be rewritten as $\frac{1}{\tan\frac{\chi}{2}} = \tan\left(2\left[\frac{\pi+\chi}{4}\right]\right) = \frac{2\tan\left(\frac{\pi+\chi}{4}\right)}{1-\tan^2\left(\frac{\pi+\chi}{4}\right)} = \frac{2\frac{r_0}{b}}{1-\left(\frac{r_0}{b}\right)^2} = \frac{b}{b_0}$. In the last step the definition of u_1 has been used.

a minimum scattering angle $\chi_m\,(b_m)$. From a physical point of view the particles are electrically shielded from one another which means they do not interact for $b > b_m$. An appropriate value for the cutoff impact parameter b_m is the Debye length λ_D. The cross sections are given by

$$\begin{aligned} Q^{(l)} &= 2\pi \int_{\chi_m}^{\pi} \left(1-\cos^l\chi\right) \frac{b_0^2}{4\sin^4\left(\frac{\chi}{2}\right)} \sin\chi \mathrm{d}\chi \\ &= 2\pi b_0^2 \int_{\sin(\chi_m/2)}^{\pi} \frac{1-(1-2x)^l}{x^3} \mathrm{d}x. \end{aligned} \tag{4.69}$$

For the first two values of l this amounts to[9]

$$\begin{aligned} Q^{(1)} &= 4\pi b_0^2 \ln\left(1+\frac{\lambda_D^2}{b_0^2}\right)^{1/2} \\ Q^{(2)} &= 4\pi b_0^2 \left[2\ln\left(1+\frac{\lambda_D^2}{b_0^2}\right)^{1/2} - \frac{\lambda_D^2}{\lambda_D^2+b_0^2}\right]. \end{aligned} \tag{4.70}$$

For evaluating the collision integral it should be noted that the parameter b_0 is proportional to $\left(\mu g^2\right)^{-1}$. The collision integrals can thus be obtained from

$$\begin{aligned} \Omega_{ij}^{(1,s)} &= \sqrt{\frac{k_B T}{2\pi\mu}} 4\pi b_a^2 \int_0^{\infty} \gamma^{2s-1} \exp\left(-\gamma^2\right) \ln\left(1+\frac{\lambda_D^2}{b_a^2}\gamma^4\right) \mathrm{d}\gamma \\ &\approx \frac{9}{2}\pi \bar{b}_0^2 \sqrt{\frac{k_B T}{2\pi\mu}} \ln\left(1+\frac{\lambda_D^2}{\bar{b}_0^2}\right) (s-1)! \\ \Omega_{ij}^{(2,s)} &= \sqrt{\frac{k_B T}{2\pi\mu}} 4\pi b_a^2 \int_0^{\infty} \gamma^{2s-1} \exp\left(-\gamma^2\right) \left[2\ln\left(1+\frac{\lambda_D^2}{b_a^2}\gamma^4\right) - \frac{\lambda_D^2}{\lambda_D^2+\frac{b_a^2}{\gamma^4}}\right] \mathrm{d}\gamma \\ &\approx \frac{9}{2}\pi \bar{b}_0^2 \sqrt{\frac{k_B T}{2\pi\mu}} (s-1)! \left[2\ln\left(1+\frac{\lambda_D^2}{\bar{b}_0^2}\right) - \frac{\lambda_D^2}{\lambda_D^2+\bar{b}_0^2}\right] \end{aligned} \tag{4.71}$$

with $b_a = \frac{Z_i Z_j e^2}{8\pi\epsilon_0 k_B T}$ and $\bar{b}_0 = \frac{2}{3}a$. Hirschfelder et al. [34, p. 549] neglect the dependency of b_0 on g by replacing $\frac{1}{2}\mu\bar{g}^2$ with the average value over all collisions $2k_BT$. Our implementation uses the substitution $\frac{1}{2}\mu\bar{g}^2 = \frac{3}{2}k_BT$ according to Mitchner and Kruger [54, p. 57]. The approximate expressions for the collision integrals are derived by assuming that the logarithm and the ratio are approximately constant.

4.2.11 Screened Coulomb potential

The charged-charged interactions are described with a screened-Coulomb potential given by

$$V = V_0 \frac{\lambda_D}{r} \exp\left(-\frac{r}{\lambda_D}\right), \tag{4.72}$$

[9] Note that $\sin\frac{\chi_m}{2} = \frac{b_0}{\sqrt{b_0^2+\lambda_D^2}}$ which follows from (4.67)

with

$$V_0 = \frac{Z_1 Z_2 e^2}{4\pi\epsilon_0 \lambda_D}, \tag{4.73}$$

and λ_D the Debye length. Tabulations of the resulting collision integral have been provided by Mason et al [87] and Devoto [88] in terms of the reduced temperature

$$T^* = \frac{k_B T}{V_0} = \frac{\lambda_D}{2b_a}, \tag{4.74}$$

with

$$b_a = \frac{\left|Z_1 Z_2 e^2\right|}{8\pi\epsilon_0 k_B T}. \tag{4.75}$$

All tabulations are either represented as $(T^*)^2\,\Omega^{(l,s)*}$ or as a ratio of reduced collision integrals. The relevant ratios are listed in section 4.A.

In figure 4.2 the collision integrals for various charged-charged approaches for Ar^+–Ar^+ are plotted. LTE was assumed to calculate the Debye length in pure Ar. For large temperatures the relative error between the Coulomb and the screened-Coulomb collision integrals approaches 250% at 14.4 kK and then decreases again. At low temperatures the screened-Coulomb collision integral contains a discontinuity. This is related to the tabulations provided by Mason et al. which cover $0.1 \leq T^* \leq 10^8$. The position of the discontinuity occurs at $T = 2000\,\mathrm{K}$ which can be observed from figure 4.3. This discontinuity is not important since the charged species densities that correspond to such a large Debye length are negligible. Any influence on the transport properties is thus not expected. When LTE conditions are not valid such a low electron density can not even be reached.

4.3 Default procedures for estimating collision integrals

Initially, the rigid sphere and Coulomb collision integrals were used as collision integral defaults. These approximations are not reliable for large temperature intervals. Johnston [26] therefore initiated the development of more accurate procedures for calculating collision integrals in PLASIMO. His default procedure is briefly discussed. After that a comparison is made between Johnston's method and a few other strategies. The results of this comparison are used to define the current default procedure. In chapter 5 the effect of the choice of the default procedure on the transport coefficients is discussed.

4.3.1 Johnston's default collision integrals

Johnston summarizes his default procedure on page 130 of his thesis [26]. These methods are listed below

- **neutral-neutral**: Two cases are considered. These options are chosen based on the estimated potential well depth using the relations from section 4.C. For $\epsilon_{ij,m} < k_B T$ the Lennard Jones model (4.29) is used. For $\epsilon > k_B T$ the exponential repulsive potential (4.27) is used.

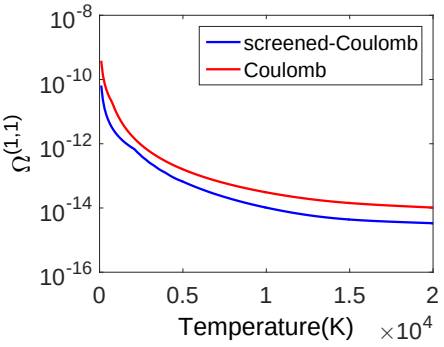

Figure 4.2: The collision integrals for Ar^+–Ar^+ for the Coulomb (4.71) and the screened-Coulomb models(4.72).

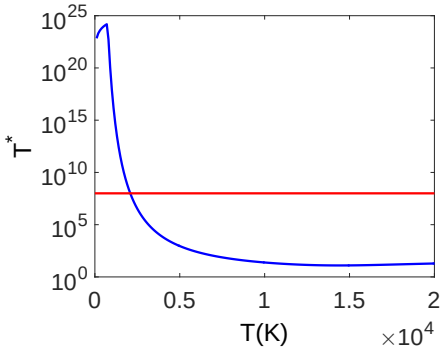

Figure 4.3: The reduced temperature (4.74) as a function of the gas temperature in pure Ar under LTE conditions. The red line indicates the highest value of T^* for which tabulations of the screened-Coulomb collision integral are published.

- **neutral-ion**: Three cases are considered. If the interacting pair is of the type A–A^+ with A a neutral particle, the collision integral is taken from the model of Rapp and Francis (4.49) and (4.50). Note that no elastic contribution is included for this case. The remaining two cases are similar to the neutral-neutral interactions with the Lennard Jones and the exponential repulsive potentials selected based on the ratio of the well depth to the thermal energy.
- **neutral-electron**: For the electron neutral interaction the Langevin model (4.25) is used.
- **charged-charged**: For charged-charged interactions the screened-Coulomb potential (4.72) is used.

4.3.2 Comparison of neutral-neutral and neutral-ion models

The main concerns about the default procedure that was introduced by Johnston [26] are related to neutral-neutral and neutral-ion interactions. For these interactions he used a Lennard Jones model when the potential well depth is smaller than the thermal energy. The Lennard Jones model is an acceptable way of representing the interaction. However, due to the relatively small well depth that is predicted by (4.115) all species that have been considered in [26, table. 8.2-8.3] at room temperature already satisfy the relation $\epsilon_{0,ij} < k_B T$, which means that the exponential repulsive potential (4.27) is used. All 15 reported neutral-neutral [5, table. 4] interaction pairs in a 10 species air mixture have a well depth that is smaller than the thermal energy at room temperature. The reported ion-neutral pairs satisfy $\epsilon_{0,ij} \approx k_B T$ for temperatures ranging from 580 K till 1740 K.

From these observations it can be concluded that in Johnston's algorithm most neutral-neutral interactions are included with the exponential repulsive potential. For cold plasmas the ion-neutral interactions are most likely included with the Lennard Jones model. For increasing heavy particle temperatures these will be exchanged one by one for the exponential repulsive potential. The exponential repulsive potential is thus used frequently in Johnston's algorithm.

The parameters for the exponential repulsive potential are estimated based on the method proposed by Tang and Toennies [66, 67] as explained in 4.D. The method uses the attractive dispersion coefficients to predict the repulsive behavior for small separations. The proposed connection between attractive and repulsive forces is more based on mathematics rather than actual physical grounds. A private discussion with Laricchiuta, Colonna and Bruno, revealed that the method can be considered rather artificial.

Additionally, in the original form the model is not intended for neutral-ion interactions. The method can be extended to neutral-ion interactions by also including a term $-C_4/r^4$ in the expansion of the dispersion coefficients with $C_4/\mathrm{E_H} = 5.2\mathrm{eV}/\mathrm{E_H} Z_I^2 \alpha_N$ based on (4.121). In that case the equation that determines $b^* = b/r_{m,ij}$ with $b = 1/\rho$ can be rewritten as[10]

$$f(b) = 1 + \sum_{n>2} \left(1 - e^{-b^*} \sum_{k=0}^{2n} \frac{(b^*)^k}{k!}\right) \left(\frac{2n}{b^*} - 1\right) C_{2n}^* - \sum_{n>2} e^{-b^*} \frac{(b^*)^{2n}}{(2n)!} C_{2n}^* = 0. \tag{4.76}$$

At small values of b^* the function returns $f(0) = 1$. In order to find a solution for large values of b^* the following relation must hold $f(\infty) < 0$. This requirement can be written as

$$\lim_{b\to\infty} f(b) = \lim_{b\to\infty} 1 + \sum_{n>2} \left(\frac{2n}{b^*} - 1\right) C_{2n}^* = 1 - \sum_{n>2} C_{2n}^*. \tag{4.77}$$

Interestingly, this is not necessarily smaller than 0. Interaction pairs with small reduced dispersion coefficients may potentially violate this condition.

Tang and Toennies mention that the summation is usually truncated at C_{18} [67, p. 93]. For that value the interactions Ne–$\mathrm{Ne^+}$, Ar–$\mathrm{Ar^+}$, Kr–$\mathrm{Kr^+}$, Xe–$\mathrm{Xe^+}$, Zn–$\mathrm{Zn^+}$, Cd–$\mathrm{Cd^+}$ and Hg–$\mathrm{Hg^+}$ do not satisfy $f(\infty) < 0$. Johnston [26, p. 128] mentions that he sums the coefficients up to $n_{\max} = 18$ which corresponds to C_{36}. In that situation all previously mentioned interactions converge. However, the results still depend on the amount of dispersion terms that have been included. In table 4.3 the parameters are shown for Ar–$\mathrm{Ar^+}$ and Ar–Ar as a function of the upper limit in the summation of the dispersion coefficients. The table shows that when the number of dispersion coefficients is increased the parameters A and b do not converge to a fixed value for neutral-ion systems. Since the choice of $n_{\max}$ is arbitrary the method does not provide well defined output. The term $\alpha^2/b^2 I_{l,s}$ is proportional to the collision integral. The values of this term extend over almost

[10] When $1 - e^{-b^*} \sum_{k=0}^{2n} \frac{(b^*)^k}{k!} < 10^{-10}$ the term is replaced with $e^{-b^*} \sum_{k=2n+1}^{\infty} \frac{(b^*)^k}{k!}$ to avoid numerical instabilities.

Table 4.3: Born-Mayer coefficients as a function of the number of terms in the summation of the dispersion coefficients. The terms $\alpha^2/b^2 I_{1,1}$ have been evaluated for T=1000 K. Values that are outside the range of the lookup table for $I_{1,1}$ provided by Monchick [68] are extrapolated cubically.

	Ar–Ar^+		
$n_{\max}$ in C_{2n}	A(au)	b(au)	$\alpha^2/b^2 I_{1,1}$
15	5.0569×10^5	2.9053	1.4608×10^{-21}
20	9.6651×10^3	2.1956	1.9891×10^{-21}
25	597.67	1.7256	2.5751×10^{-21}
30	61.873	1.3601	3.3028×10^{-21}
35	9.2205	1.0676	4.2198×10^{-21}
40	1.8250	0.83312	5.3516×10^{-21}
45	0.45240	0.64603	6.6727×10^{-21}
50	0.13314	0.49791	8.0257×10^{-21}
	Ar–Ar		
$n_{\max}$ in C_{2n}	A(au)	b(au)	$\alpha^2/b^2 I_{1,1}$
15	105.03	1.7580	2.09×10^{-21}
20	92.891	1.7152	2.1714×10^{-21}
25	31.455	1.4670	2.6239×10^{-21}
30	5.7846	1.1785	3.2353×10^{-21}
35	1.0580	0.92952	3.8763×10^{-21}
40	0.22165	0.72515	4.4078×10^{-21}
45	0.054654	0.56093	4.5631×10^{-21}
50	0.015684	0.43082	3.9465×10^{-21}

an entire order of magnitude for neutral-ion systems. If the suggestions of the original authors are followed $5 \leq n_{\max} \leq 10$ does provide stable results for A and b in neutral-neutral systems. Additionally the variations in $\alpha^2/b^2 I_{l,s}$ are smaller. Using $5 \leq n_{\max} \leq 10$ for neutral-ion systems still gives strongly varying results if the method converges at all.

In principal the Tang and Toennies approach can thus be used for neutral-neutral interactions although the connection between attraction and repulsion seems to be quite artificial. Tang and Toennies only applied this method to neutral-neutral interactions. Johnston's generalization to neutral-ion systems contains an arbitrary choice for $n_{\max}$ which strongly influences the results. It is therefore not recommended to use this approach for neutral-ion interactions.

In figure 4.4 and 4.5 collision integrals for neutral-neutral interactions are shown for Ar-Ar and for O-O using different approaches. The parameters for the generalized Lennard-Jones potential (GLJ) were taken from [27, table. 11.2]. For Ar-Ar with the exponential repulsive potential (ERP) the first point is calculated with the Lennard-Jones potential since $\epsilon_{0,ij} \ll k_B T$ was not satisfied. This does not occur in O-O. The relative error in Ar-Ar of the ERP is below 10%. In O-O the relative error decreases from 20% to 10%, indicating that the ERP approach can provide reasonable values for neutral-neutral interactions. For Ar-Ar

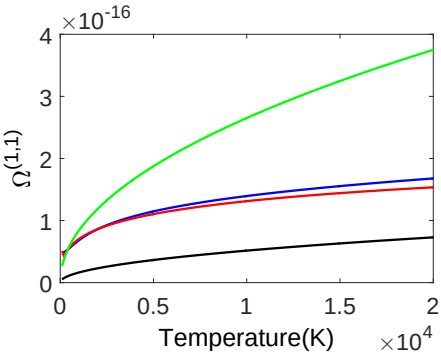

Figure 4.4: Comparison of various approaches for calculating collision integrals for Ar-Ar. The legend: The generalized Lennard Jones potential (▬), the combined Lennard-Jones and exponential repulsive potential (▬) and the rigid sphere approach with two different values for c (▬, c=0; ▬, c=1.8Å). The radii of Clementi [61] were used.

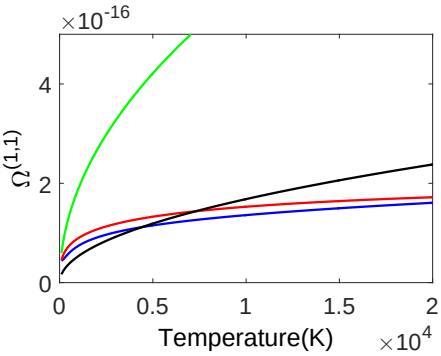

Figure 4.5: Comparison of various approaches for calculating collision integrals for O-O. The legend is the same as in figure 4.4.

the rigid sphere model (RS) estimates are inaccurate with absolute errors of the order of the GLJ result. In O-O the rigid sphere model with $\sigma_{ij} = r_i + r_j$ works only in a small temperature interval. Outside this interval the absolute errors are increasing up to 70% of the GLJ result.

In figure 4.6 and 4.7 collision integrals for neutral-ion interactions are shown for Ar–Ar^{2+} and for O–O^{2+} using different approaches. For O–O^{2+} it is apparent that none of the interactions follow the GLJ curve well. The best approximation is provided by the ERP approach with relative errors increasing up to 50%. The ERP method uses a mixed calculation. For temperatures below 10^4 K the Lennard Jones potential is used and above that the ERP[11]. This produces an undesirable discontinuity. For Ar–Ar^{2+} the conclusions are similar. This time the relative errors of the ERP approach reach 40%.

For neutral-neutral and neutral-ion interactions it is thus recommended to use the generalized Lennard Jones model rather than the exponential repulsive, Langevin or rigid sphere models.

[11] In order to treat all ion-neutral interactions the same the dispersion coefficients for estimating the Born-Mayer coefficients are included up to C_{30}. This is necessary because otherwise some parameters can not be calculated. For neutral-neutral interactions C_{18} is used which is in agreement with the Tang and Toennies [67]

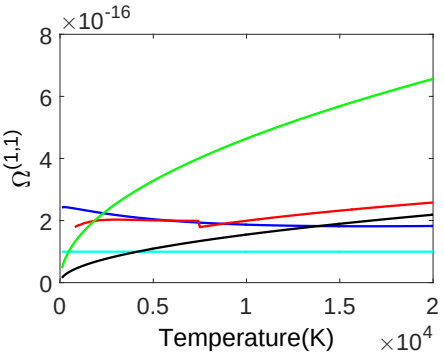

Figure 4.6: Comparison of various approaches for calculating collision integrals for Ar–Ar^{2+}. The legend is the same as in figure 4.4. Additionally the Langevin potential is introduced (—).

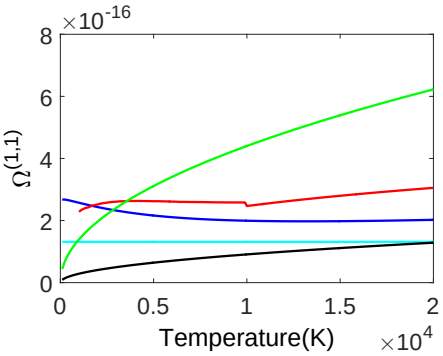

Figure 4.7: Comparison of various approaches for calculating collision integrals for O–O^{2+}. The legend is the same as in figure 4.6.

4.3.3 Current default procedure

The previously discussed approaches have lead to a new default approach for estimating collision integrals. An overview of these methods is presented in this section. The following section assumes that no custom interactions have been specified in the input file. Custom interactions have precedence over the default method. The current default procedure relies on large amounts of tabulated data. This data can be found in the directory called *input/mixture/* in the PLASIMO distribution.

- **neutral-neutral**: Initially an attempt is made to use a fit function (4.152). The parameters are stored in *jupiter_capitelli.dat*. The next option is the generalized Lennard-Jones potential. The parameters $\epsilon_{0,ij}$, $r_{m,ij}$ and β_{ij} are tabulated in *lennard_jones.in* or *default_coll_int.in* for more than 800 common interaction pairs. If these parameters are not available a rigid sphere collision integral is used based on user-provided particle radii.

- **neutral-ion**: The collision integral is calculated according to (4.45). A first attempt is made to calculate the elastic contribution with the fit function (4.152). The parameters are stored in *jupiter_capitelli.dat*. The next option is the generalized Lennard-Jones potential. The parameters $\epsilon_{0,ij}$, $r_{m,ij}$ and β_{ij} are tabulated in *lennard_jones.in*. If the parameters are not available a rigid sphere model is used based on user-provided particle radii. The first attempt for the contribution from charge-exchange uses the fit function (4.58). These coefficients are tabulated in *charge_exchange_capitelli.in*. Alternatively, (4.53) with parameters from *charge_exchange.in* is used. If the coefficients are not available the Rapp-Francis model (4.49) and (4.50) is used.

- **neutral-electron**: In the first attempt the collision integral is calculated according to the fit functions (4.151) or (4.153). The parameters can be found in *electron_neutral_capitelli.in* or *electron_neutral_capitelli_8.in*. If these coefficients are not available the Langevin polarizability model is used (4.25). If the polarizability is not specified the polarization volume is calculated from $\alpha = r^3$ [58, p. 60].
- **charged-charged**: The collision integrals are calculated using the screened-Coulomb potential (4.72).

It is highly recommended to avoid the cases where the general algorithm uses a rigid sphere collision integral or the Langevin polarizability model. If the parameters $\epsilon_{0,ij}$, $r_{m,ij}$ and β_{ij} are not available they should rather be estimated using (4.115),(4.114),(4.121) and (4.33).

4.4 Collision integrals from interaction potentials

The general method outlined in the previous sections can in specific cases provide an inaccurate estimate for the collision integral. In such cases, it is possible to obtain a more accurate estimate by integrating an interaction potential. Interaction potentials can be obtained from literature or can be calculated using ab initio methods. Two recent methods for a calculation of the collision integral are considered. These are the methods proposed by Viehland et al. [89] and Colonna et al. [90]. Colonna's approach uses the trapezoidal rule for integration of the scattering angle and the cross section. Viehland's approach is based on the Clenshaw-Curtiss quadratures. In this section a C++ implementation is discussed that uses a combination of parts from Viehland's approach and parts from Colonna's approach. The developed code is validated by a comparison of the calculated collision integrals with tabulated collision integrals presented in literature. First the Clenshaw-Curtiss quadratures are briefly addressed.

4.4.1 Clenshaw-Curtiss quadratures

A Clenshaw-Curtiss quadrature is a special case of a Chebyshev series [91]. To use this method the integral $\int_a^b F(x)\,\mathrm{d}x$ must be written in the form

$$I = \int_{-1}^{1} F(y)\,\mathrm{d}y, \tag{4.78}$$

via a transformation of the variable x. The function $F(y)$ can be expanded in a Chebyshev series as [91]

$$F(y) = \frac{a_0}{2} T_0(y) + \frac{a_N}{2} T_N(y) + \sum_{r=1}^{N-1} a_r T_r(y), \tag{4.79}$$

with a_r the coefficients of the expansion and $T_r(y)$ the Chebyshev polynomial. Clenshaw and Curtiss set the polynomial to $T_i(y) = T_i(\cos\theta) = \cos(i\theta)$. The coefficients are then calculated as

$$a_r = \frac{2}{N}\left(\frac{F(1)}{2} + \frac{F(-1)}{2} + \sum_{s=1}^{N-1}\cos\left(\frac{i\pi s}{N}\right)F\left(\cos\left(\frac{\pi s}{N}\right)\right)\right). \tag{4.80}$$

A term by term integration of the Chebyshev series gives

$$I = \sum_{s=0}^{N} w_s^N F\left(\cos\frac{\pi s}{N}\right), \tag{4.81}$$

where the weights are given by

$$w_s^N = \begin{cases} (-1)^s \frac{2}{N^2-1} + \frac{4}{N}\sin\frac{\pi s}{N}\sum_{i=1}^{\frac{N}{2}}\frac{\sin\left[(2i-1)\frac{\pi s}{N}\right]}{2i-1} & 1 \le s \le N-1, \\ \left(N^2-1\right)^{-1} & s = 0, N \end{cases}. \tag{4.82}$$

The major advantage of this quadrature is the positioning of the quadrature points given by $y = \cos\frac{\pi s}{N}$. A higher order approximation that doubles N still contains the old quadrature points. As a result the integral can be evaluated with a minimum amount of function evaluations. Additionally an error estimate is possible by comparison with the previous approximation. The order of the quadrature will be increased until the difference between the current and the previous order is lower than a predefined tolerance. The coefficients can be efficiently calculated using the algorithm presented by von Winckel [92].

4.4.2 Collision integrals

The collision integral is evaluated using Clenshaw-Curtiss quadratures following O'Hara and Smith [91]. The integrand is split in two terms. The position is determined by the peak of the weighing function $\exp^{-x} x^{s+1}$ which is $x = s+1$. The following function is considered

$$\Omega^{(l,s)} = \frac{1}{2}\sqrt{\frac{k_B T}{2\pi\mu}}\left(\int_{-1}^{1} f_1(y)\,\mathrm{d}y + \int_0^1 f_2(y)\,\mathrm{d}y\right). \tag{4.83}$$

The first integrand is given by

$$f_1(y) = \frac{s+1}{2}\exp^{-x_1} x_1^{s+1} Q^{(l)}(x_1 k_B T), \tag{4.84}$$

with

$$x_1 = \frac{s+1}{2}(1+y). \tag{4.85}$$

The second integrand is given by

$$f_2(y) = \frac{s+1}{y^2}\exp^{-x_2} x_2^{s+1} Q^{(l)}(x_2 k_B T), \tag{4.86}$$

with

$$x_2 = \frac{s+1}{y}. \tag{4.87}$$

The second integral has deviating boundaries. O'Hara and Smith note that at $y = 0$ the integrand and its derivatives are zero. The integrand can thus be reflected to the interval $(-1, 0)$ to produce a smooth even function in the interval $(-1, 1)$. Since the whole Clenshaw-Curtiss interval is equal to twice the integral only the positive quadrature points are considered. In both integrals the cross section $Q^{(l)}$ is interpolated from a tabulation of previously calculated cross sections.

4.4.3 Cross sections

Viehland's algorithm is implemented to acquire a tabulation of the cross section as a function of the energy. The tabulation is used in the calculation of the collision integral. The approach uses three different strategies depending on the considered energy. The three different energy ranges are

- $\epsilon_d \leq \epsilon \leq \epsilon_c$
- $\epsilon_c < \epsilon \leq 3\epsilon_c$
- $\epsilon < \epsilon_d$ or $\epsilon > 3\epsilon_c$,

with ϵ_d and ϵ_c the minimum and the maximum energy where orbiting can occur. Orbiting can occur when at least one extremum is present in the potential. In that case the integrand of the scattering angle

$$F(r, b, \epsilon) = \frac{1}{r^2}\left[1 - \frac{b^2}{r^2} - \frac{V(r)}{\epsilon}\right]^{-1/2} = \frac{1}{r^2}\left[1 - \frac{V_{\text{eff}}(r)}{\epsilon}\right]^{-1/2}, \tag{4.88}$$

contains a non-integrable singularity for the scattering angle (it reaches $\chi = -\infty$) [89, p. 1689]. However, the cross sections remain finite. The criteria for which orbiting occurs are best evaluated in terms of the effective potential

$$V_{\text{eff}}(r) = V(r) + \frac{\epsilon b^2}{r^2}. \tag{4.89}$$

These criteria are

$$V_{\text{eff}}(r_0) = \epsilon_0 > 0 \tag{4.90}$$
$$V'_{\text{eff}}(r_0) = 0 \tag{4.91}$$
$$V''_{\text{eff}}(r_0) < 0, \tag{4.92}$$

with r_0 the distance of closest approach. Thus orbiting can occur when the effective potential is positive and reaches a local maximum. These criteria can be rewritten

as

$$\epsilon_0 = V(r_0) + \frac{1}{2} r_0 V'(r_0) > 0 \tag{4.93}$$

$$\epsilon_0 b_0^2 = \frac{1}{2} r_0^3 V'(r_0) \tag{4.94}$$

$$0 > V''(r_0) + \frac{3}{r_0} V'(r_0). \tag{4.95}$$

An interesting property of these criteria is that they only depend on the potential. Note that this system implicitly implies that $V'(r_0) > 0$ and $V''(r_0) < 0$. Viehland [89] suggests to make a lookup table of the parameters E_0 and b_0 as a function of r_0 that satisfy all criteria for orbiting. In our implementation only the energy interval is stored for which orbiting can occur. In case of multiple orbiting there will be multiple energy intervals. A consequence of this procedure is that for analytical potentials the first and second derivative should be implemented as well. For tabulated potentials the coefficients of a spline fit can provide estimates of the potential and its derivatives. Viehland suggests to extrapolate a tabulated potential for small r with $V(r) = V_1 \left(\frac{r_1}{r}\right)^{N_{\text{short}}}$ where r_1 is the first tabulated point and $N_{\text{short}} = \ln(V_2/V_1) / \ln(r_1/r_2)$. For large r he recommends $V(r) = -C_{\text{long}}/r^{N_{\text{long}}}$ with $C_{\text{long}} = -V(r_L) r_L^{N_{\text{long}}}$ and r_L the last tabulated point. N_{long} is 4 for atomic ion-neutral interactions and 6 for neutral-neutral interactions. The value of r_L should be large enough to guarantee that C_{long} is in agreement with values from the literature.

The cross section is then expressed as

$$Q^{(l)} = \sum_{i=0}^{M} 2\pi \int_{b_i}^{b_{i+1}} \left[1 - \cos^l \chi\right] b \mathrm{d}b, \tag{4.96}$$

with b_i the orbiting impact parameter. For $i = 0$ the integration boundaries are $b = 0$ and $b = b_1$. Similarly for $i = M$ the integration boundaries are $b = b_M$ and $b = \infty$. Splitting the integral is necessary because at orbiting conditions the scattering angle approaches $\chi = -\infty$. This causes oscillations in the integrand of the cross section. These are properly resolved by splitting the integral. For the remaining details of the integration algorithm the reader is referred to [89].

4.4.4 Scattering angle

The calculation of the scattering angle is based on the work of Colonna et al. [90] rather than the work of Viehland. Viehland's algorithm is not used for the calculation, since it requires that the distance of closest approach is known in advance. In specific cases, it was observed that our solver for the equation $1 - \frac{b^2}{r^2} - \frac{V(r)}{\epsilon} = 0$ did not deliver the outer root. By using the adaptive algorithm from Colonna it is not necessary to know the distance of closest approach in advance.

The scattering angle is represented as

$$\chi = \pi - 2b \int_{r_0}^{\infty} \left[1 - \frac{b^2}{r^2} - \frac{V(r)}{\epsilon}\right]^{-1/2} \frac{\mathrm{d}r}{r^2} = \pi - 2bF(r, b, \epsilon). \tag{4.97}$$

The adaptive algorithm uses an estimate of the initial separation between the two particles $r_{\max}$. This value is multiplied by 2 until the difference between integrals of the functions $F_1 = \frac{1}{r^2}\left[1 - \frac{b^2}{r^2} - \frac{V(r_{\max})}{\epsilon}\right]^{-1/2}$ and $F_2 = \left[1 - \frac{b^2}{r^2}\right]^{-1/2}$ is smaller than a given tolerance δ. The error can thus be expressed as $|I_1 - I_2| \leq \delta$ with [90, p. 812]

$$\begin{aligned} I_1(r_{\max}) &= \int_{r_{\max}}^{\infty} F_1(r)\,\mathrm{d}r = \frac{1}{b}\sin^{-1}\left(\frac{b}{r_{\max}}\left[1 - \frac{V(r_{\max})}{\epsilon}\right]^{-1/2}\right) \\ I_2(r_{\max}) &= \int_{r_{\max}}^{\infty} F_2(r)\,\mathrm{d}r = \frac{1}{b}\sin^{-1}\left(\frac{b}{r_{\max}}\right). \end{aligned} \tag{4.98}$$

Once $r_{\max}$ is determined a step $\mathrm{d}r$ is made. The size of $\mathrm{d}r$ is adjusted to make sure that the difference between the following functions is below a given tolerance δ [90, p. 811]

$$\begin{aligned} I_3 &\approx \frac{\mathrm{d}r}{2}\left(F(r - \mathrm{d}r, b, \epsilon) + F(r, b, \epsilon)\right) \\ I_4 &\approx \frac{\mathrm{d}r}{2}\left(\frac{1}{2}F(r - \mathrm{d}r, b, \epsilon) + \frac{1}{2}F(r, b, \epsilon) + F(r - \mathrm{d}r/2, b, \epsilon)\right). \end{aligned} \tag{4.99}$$

The error given by $\mathrm{d}I = |I_4 - I_3|$ is used to adjust the step size with the following multiplicative factor $m = 0.9(\delta/\mathrm{d}I)$ if $\mathrm{d}I \geq \delta$ or $\mathrm{d}I \leq \delta/4$. The allowed values of the multiplicative factor m are restricted to the interval $0.5 \leq m \leq 2$. This procedure is followed until r_0 is reached.

4.4.5 Validation of the implementation

The implementation of the code discussed in the previous sections is validated with both analytical and tabulated potentials. Tests for the Lennard-Jones and the Morse potential for the reduced collision integral are based on the comparisons provided by Colonna [90,93,94]. The comparison is given in figure 4.8 and 4.9. For both results the agreement with the reference data is better than 1 %. Viehland [89] provides results for the reduced cross section of the 12-4 potential specified by Mason et al. [95, eq. 1] with $\gamma = 0$. The results are given in figure 4.10. The relative errors are smaller than 1 %. Additionally the interaction potential of H_2 has been calculated with the input file for the ab initio package for quantum mechanical calculations DIRAC given in appendix 4.G. The collision integrals of the $X^1\Sigma_g^+$ and $b^3\Sigma_u^+$ states have been averaged according to [96, p. 670]

$$\Omega^{(l,s)} = \sum_i \frac{g_i \Omega_i^{(l,s)}}{g_i}. \tag{4.100}$$

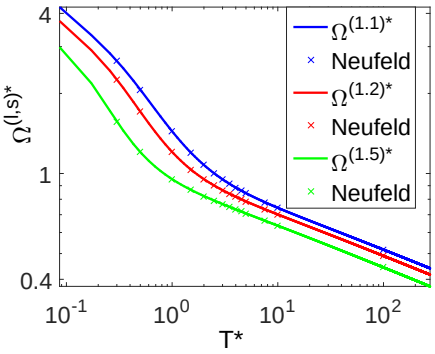

Figure 4.8: Comparison of calculated reduced collision integrals for the Lennard Jones potential with data from Neufeld [93].

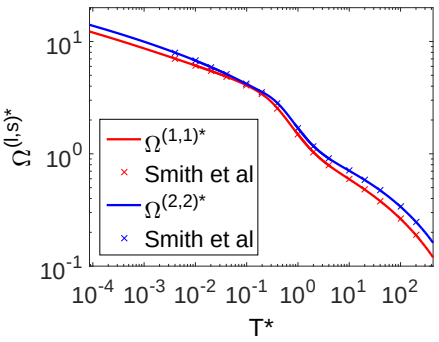

Figure 4.9: Comparison of calculated reduced collision integrals for the Morse potential with data from Smith ($C = 4$) [94].

The calculated collision integral is compared with Capitelli's fit formula(4.37) in figure 4.11. The $\Omega^{(1,1)}$ collision integral that is obtained from the integration of the potential curve calculated by using DIRAC is in good agreement with Capitelli's fit formula. If in this case the generalized Lennard Jones potential is used to calculate the collision integral a significantly different behavior is obtained for $8\,\mathrm{kK} \leq T \leq 50\,\mathrm{kK}$. In that interval the relative error increases to 250 % for the highest temperature. In the interval $T \leq 8\,\mathrm{kK}$ the relative error decreases from 30 % to zero. A similar behavior is observed for the $\Omega^{(2,2)}$ collision integral. In section 5.3 the validity of the generalized Lennard Jones potential is evaluated more elaborately. This comparison shows the added value of using programs like DIRAC in combination with a program that calculates cross sections and collision integrals.

4.5 Summary and conclusions

In this chapter an overview of various potentials and their collision integrals is presented. These collision integrals have been compared in order to find a default procedure that can give a reasonable estimate of the collision integrals without requiring excessive amounts of input data or input values that are scarcely available. Previously, Johnston developed such a default procedure. However, due to the absence of an automatic routine PLASIMO still relied on the Coulomb potential and the rigid sphere models when the interaction was not specifically requested. This work shows that for the neutral-neutral and especially the neutral-ion interactions the usage of Johnston's default procedure can provide unreliable results. Additionally, his method is not robust enough to provide estimates for any collision pair. In this work a new default procedure is presented that is robust, more accurate and requires a smaller number of input parameters. On top of that an

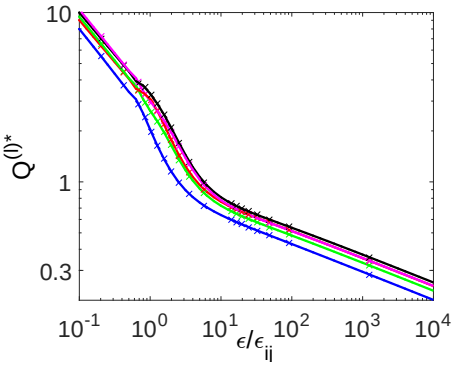

Figure 4.10: Comparison of calculated reduced cross section for the 12-4 potential given by Mason et al. [95]($\gamma = 0$). Legend: $Q^{(1)}$ (—), $Q^{(2)}$ (—), $Q^{(3)}$ (—), $Q^{(4)}$ (—), $Q^{(5)}$ (—). Crosses indicate data calculated by Viehland et al. [89].

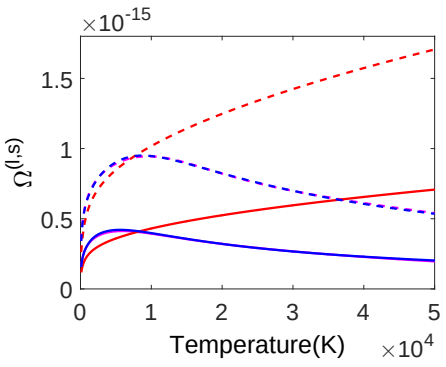

Figure 4.11: Comparison of calculated collision integrals for H-H with fits from Capitelli (—, $\Omega^{(1,1)}$; - - -, $\Omega^{(2,2)}$), the general Lennard Jones potential with estimated parameters (—, $\Omega^{(1,1)}$; - - -, $\Omega^{(2,2)}$) from (4.114)-(4.115) and an integration of the potential calculated using DIRAC (—, $\Omega^{(1,1)}$; - - -, $\Omega^{(2,2)}$).

automatic routine is developed in PLASIMO to make sure that these improved collision integrals are used without requiring an explicit request in the input file.

The default procedure can be further improved by maintaining a database of potential interaction curves. These potential curves can be obtained from literature or can be calculated directly using quantum mechanical software packages like DIRAC. The cross sections and collision integrals can then be directly evaluated by using the code presented in section 4.4. This code is currently being extended to interaction pairs for which resonant charge transfer should be included.

4.A Ratios of reduced collision integrals

This section provides a list of common ratios of reduced collision integrals [34, 87, p. 528] and their expressions in terms of non-reduced collisional integrals. A ratio of reduced collision integrals can be written as

$$\frac{\Omega^{(l_1,s_1)*}}{\Omega^{(l_2,s_2)*}} = \frac{(s_2+1)!}{(s_1+1)!}\frac{1-\left(1-(-1)^{l_2+1}\right)/\left[2\left(l_2+1\right)\right]}{1-\left(1-(-1)^{l_1+1}\right)/\left[2\left(l_1+1\right)\right]}\frac{\Omega^{(l_1,s_1)}}{\Omega^{(l_2,s_2)}}. \tag{4.101}$$

The ratios that occur frequently can thus be written as

$$A^*_{ij} = \frac{\Omega^{(2,2)*}_{ij}}{\Omega^{(1,1)*}_{ij}} = \frac{1}{2}\frac{\Omega^{(2,2)}_{ij}}{\Omega^{(1,1)}_{ij}}, \tag{4.102}$$

$$B^*_{ij} = \frac{5\Omega^{(1,2)*}_{ij} - 4\Omega^{(1,3)*}_{ij}}{\Omega^{(1,1)*}_{ij}} = \frac{1}{3}\frac{5\Omega^{(1,2)}_{ij} - \Omega^{(1,3)}_{ij}}{\Omega^{(1,1)}_{ij}}, \tag{4.103}$$

$$C^*_{ij} = \frac{\Omega^{(1,2)*}_{ij}}{\Omega^{(1,1)*}_{ij}} = \frac{1}{3}\frac{\Omega^{(1,2)}_{ij}}{\Omega^{(1,1)}_{ij}}, \tag{4.104}$$

$$E^*_{ij} = \frac{\Omega^{(2,3)*}_{ij}}{\Omega^{(2,2)*}_{ij}} = \frac{1}{4}\frac{\Omega^{(2,3)}_{ij}}{\Omega^{(2,2)}_{ij}}, \tag{4.105}$$

$$F^*_{ij} = \frac{\Omega^{(3,3)*}_{ij}}{\Omega^{(1,1)*}_{ij}} = \frac{1}{12}\frac{\Omega^{(3,3)}_{ij}}{\Omega^{(1,1)}_{ij}}, \tag{4.106}$$

$$G^*_{ij} = \frac{\Omega^{(4,4)*}_{ij}}{\Omega^{(2,2)*}_{ij}} = \frac{1}{24}\frac{\Omega^{(4,4)}_{ij}}{\Omega^{(2,2)}_{ij}}. \tag{4.107}$$

4.B Q elements

The q^{xy} elements are expressed in terms of the averaged cross section. Devoto's [97] definition is given by

$$\begin{aligned}\bar{Q}^{(l,s)}_{ij} &= \frac{4\,(l+1)}{(s+1)!\left[2l+1-(-1)^l\right]}\int_0^\infty e^{-\gamma^2}\gamma^{2s+3}Q^l_{ij}\mathrm{d}\gamma \\ &= \pi\sigma^2_{ij}\Omega^{(l,s)*}_{ij} = \pi\sigma^2_{ij}\frac{\Omega^{(l,s)}_{ij}}{\Omega^{(l,s)}_{\mathrm{RS},ij}},\end{aligned} \tag{4.108}$$

with σ_{ij} the collision diameter. The q^{xy} factors are given by

$$q^{00} = 8\sum_{i\neq e} n_e n_i \bar{Q}^{(1,1)}_{ei}, \tag{4.109}$$

$$q^{01} = 8\sum_{i\neq e} n_e n_i \left[\frac{5}{2}\bar{Q}^{(1,1)}_{ei} - 3\bar{Q}^{(1,2)}_{ei}\right], \tag{4.110}$$

$$q^{11} = 8\sqrt{2}n^2_e\bar{Q}^{(2,2)}_{ee} + 8\sum_{i\neq e} n_e n_i \left[\frac{25}{4}\bar{Q}^{(1,1)}_{ei} - 15\bar{Q}^{(1,2)}_{ei} + 12\bar{Q}^{(1,3)}_{ei}\right], \tag{4.111}$$

$$q^{12} = 8\sqrt{2}n_e^2\left[\frac{7}{4}\bar{Q}_{ee}^{(2,2)} - 2\bar{Q}_{ee}^{(2,3)}\right] + 8\sum_i n_e n_i\left[\frac{175}{16}\bar{Q}_{ei}^{(1,1)} - \frac{315}{8}\bar{Q}_{ei}^{(1,2)} + 57\bar{Q}_{ei}^{(1,3)} - 30\bar{Q}_{ei}^{(1,4)}\right], \quad (4.112)$$

$$q^{22} = 8\sqrt{2}n_e^2\left[\frac{77}{16}\bar{Q}_{ee}^{(2,2)} - 7\bar{Q}_{ee}^{(2,3)} + 5\bar{Q}_{ee}^{(2,4)}\right] + 8\sum_i n_e n_i\left[\frac{1225}{64}\bar{Q}_{ei}^{(1,1)} - \frac{735}{8}\bar{Q}_{ei}^{(1,2)} + \frac{399}{2}\bar{Q}_{ei}^{(1,3)} - 210\bar{Q}_{ei}^{(1,4)} + 90\bar{Q}_{ei}^{(1,5)}\right]. \quad (4.113)$$

4.C Estimates for potential parameters

In the absence of accurate interaction potentials it is required to generate an approximate potential curve. Such a parameterization often involves the potential minimum ϵ, the position of the well depth r_m and the dispersion coefficients C_n. This section describes parameterizations for these variables.

The position of the potential minimum has been obtained empirically by Cambi et al. [98]. The formula is given by

$$\frac{r_{m,ij}}{\mathrm{a_0}} = 1.767\frac{\text{Å}}{\mathrm{a_0}}\frac{\alpha_i'^{1/3} + \alpha_j'^{1/3}}{\left(\alpha_i'\alpha_j'\right)^{0.095}}, \quad (4.114)$$

with $\alpha_i' = \frac{\alpha_C}{4\pi\epsilon_0}$ the polarizability in Å^3, α_C the polarizability in $\mathrm{C\,m^2\,V^{-1}}$ and $\mathrm{a_0}$ the Bohr length. The formula is based on the work of Liuti et al. [99]. The assumption is made that the numerator scales with the radius of the species while the denominator is proportional to the change in the attraction. Cambi et al. used a reference set of about 100 well known interactions to determine the scaling constant and the exponent. From the same reference set Cambi et al. obtained an expression for the well minimum

$$\frac{\epsilon_{0,ij}}{\mathrm{E_H}} = 0.72\frac{\mathrm{eV}}{\mathrm{E_H}}\frac{C_{6,\mathrm{eff},ij}}{r_{m,ij}^6}, \quad (4.115)$$

with $\mathrm{E_H}$ representing the energy in Hartree[12]. The dispersive coefficients have the subscript effective since they are intended to describe the overall attraction near the position of the potential well. Therefore, they may also contain contributions from dipole-multipole and multipole-multipole terms. The effective dispersion coefficients are calculated based on the Slater-Kirkwood formula [98–101]

$$\frac{C_{6,\mathrm{eff},ij}}{\mathrm{E_H.a_0^6}} = \frac{3}{2}\frac{\alpha_i\alpha_j}{\sqrt{\frac{\alpha_i}{N_{\mathrm{eff},i}}} + \sqrt{\frac{\alpha_j}{N_{\mathrm{eff},j}}}}, \quad (4.116)$$

[12] Note that one Hartree is given by $\mathrm{E_H} = m_e e^4/\left(4\pi\epsilon_0\hbar^2\right)$ and that the Bohr length can be written as $a_0 = 4\pi\epsilon_0\hbar^2/\left(m_e e^2\right)$. In the atomic unit system these are linked via $\mathrm{E_H} = e^2/a_0$ where $1/\left(4\pi\epsilon_0\right)$ has the numerical value unity by definition. The proportionality factor changes from $3/2\,\mathrm{E_H a_0^6}$ to approximately $15.7\,\mathrm{eV\text{Å}^6}$ by using the previous relations and expressing the polarizabilities in Å rather than Bohr.

with α_i the polarizability in a_0^3 and $N_{\mathrm{eff},i}$ the effective number of electrons present in the outer shell. Cambi et al. proposed the following expression for atoms and ions

$$N_{\mathrm{eff},i} = N_{\mathrm{ext},i}\left(1+\left[1-\frac{N_{\mathrm{ext},i}}{N_{\mathrm{int},i}}\right]\left[\frac{N_{\mathrm{int},i}}{N_{\mathrm{int},i}+N_{\mathrm{ext},i}}\right]^2\right), \tag{4.117}$$

with $N_{\mathrm{ext},i}$ the number of valence electrons and $N_{\mathrm{int},i}$ the number of inner shell electrons. By introducing $\beta = N_{\mathrm{ext},i}/\left(N_{\mathrm{ext},i}+N_{\mathrm{int},i}\right)$ Cambi's expression can be modified to also obtain a numerically stable result for $N_{\mathrm{int},i}=0$

$$N_{\mathrm{eff},i} = \left(N_{\mathrm{int},i}+N_{\mathrm{ext},i}\right)\beta\left(2-3\beta+2\beta^2\right). \tag{4.118}$$

For light molecules they suggested

$$N_{\mathrm{eff},i} = \left(N_{\mathrm{b},i}+N_{\mathrm{nb},i}\right)\left(1-\frac{N_{\mathrm{b},i}N_{\mathrm{nb},i}}{\left(N_{\mathrm{b},i}+N_{\mathrm{nb},i}\right)^2}\right), \tag{4.119}$$

with $N_{\mathrm{b},i}$ the number of bonding external electrons and $N_{\mathrm{nb},i}$ the number of non-bonding external electrons. Another important result is the extension of the dipole-dipole interaction to the dipole-ion interaction. The previously mentioned relations for the position and depth of the well should also account for ion-multipole interactions. Cappelletti et al. [102, 103] introduced the ratio of these terms as

$$\rho = \frac{C_{6,\mathrm{eff}}/r_m^6}{C_{4,\mathrm{eff}}/r_m^4} = \frac{\alpha'_I}{Z_I^2\left[1+\left(2\frac{\alpha'_I}{\alpha'_N}\right)^{2/3}\right]\sqrt{\alpha'_N}}, \tag{4.120}$$

with Z_I the charge of the ion, the indices N representing the neutral and I the ion and the dispersion coefficients are effective coefficients which also include effects of higher order terms. The position and depth of the well can then be modified to

$$\begin{aligned}\frac{r_{m,ij}}{\mathrm{a}_0} &= 1.767\frac{\text{Å}}{\mathrm{a}_0}\frac{{\alpha'_i}^{1/3}+{\alpha'_j}^{1/3}}{Z^2\left(\alpha'_i\alpha'_j\left[1+\frac{1}{\rho}\right]\right)^{0.095}}\\ \frac{\epsilon_{0,ij}}{\mathrm{E_H}} &= 5.2\frac{\mathrm{eV}}{\mathrm{E_H}}\frac{Z_I^2\alpha'_N}{r_{m,ij}^4}\left[1+\rho\right].\end{aligned} \tag{4.121}$$

4.D Born-Mayer parameters

The parameters in the exponential repulsive potential can be obtained from the methods proposed by Tang and Toennies [66, 67]. The damping functions are expressed as

$$f_{2n}(r) = 1-\left(\sum_{k=0}^{2n}\frac{(br)^k}{k!}\right)e^{-br}. \tag{4.122}$$

They normalize their parameters with $U = V(r)/\epsilon_{0,ij}$, $x = r/r_{m,ij}$, $b^* = b/r_{m,ij}$, $A^* = A/\epsilon_{0,ij}$ and $C^*_{2n} = C_{2n}/\left(\epsilon_{0,ij} r^2_{m,ij}\right)$. At $x = 1$ the system $\frac{\partial U}{\partial x} = 0$ and $U(1) = -1$ gives

$$A^* = \sum_{n>3} \left(e^{b*} - \sum_{k=0}^{2n} \frac{(b^*)^k}{k!} \right) \frac{2n}{b^*} C^*_{2n} - \sum_{n>3} \frac{(b^*)^{2n}}{(2n)!} C^*_{2n} \tag{4.123}$$

$$0 = 1 + \sum_{n>3} \left(1 - e^{-b^*} \sum_{k=0}^{2n} \frac{(b^*)^k}{k!} \right) \left(\frac{2n}{b^*} - 1 \right) C^*_{2n} - \sum_{n>3} e^{-b^*} \frac{(b^*)^{2n}}{(2n)!} C^*_{2n}. \tag{4.124}$$

The last equation can be solved iteratively to obtain b. The dispersion coefficients are calculated from a semi-empirical recursive formula

$$C_{2n+4} = \left(\frac{C_{2n+2}}{C_{2n}} \right)^3 C_{2n-2}. \tag{4.125}$$

The coefficient C_6 is estimated by using (4.116) and the higher order dispersion coefficients are taken from Koutselos [100]. The relations from Koutselos are intended for S-state atoms and ions, but Johnston [26] obtained accurate results for species in other states as well. The interpretation from Koutselos deviates from Cambi et al. [98] by not considering the Slater-Kirkwood formula to provide an effective dispersion coefficient. In [100, (14-17)] he derives a scaling law based on recursive relations for the polarizabilities. The dispersion coefficient $C_{8,ij}$ is then written as the sum of two dipole-quadrupole terms and $C_{10,ij}$ is expanded as the sum of two dipole-octupole terms and a quadrupole-quadrupole term. The result is

$$\begin{aligned}
\frac{C_{8,ij}}{\mathrm{E_H.a_0^8}} &= \frac{15}{4} \frac{\alpha_i \alpha_j^{(2)}}{\sqrt{\frac{\alpha_i}{N_{\mathrm{eff},i}}} + \left[\frac{\left(\alpha_j^{(2)}\right)^2}{9 N_{\mathrm{eff},j} \alpha_j} \right]^{1/4}} + \frac{15}{4} \frac{\alpha_j \alpha_i^{(2)}}{\sqrt{\frac{\alpha_j}{N_{\mathrm{eff},j}}} + \left[\frac{\left(\alpha_i^{(2)}\right)^2}{9 N_{\mathrm{eff},i} \alpha_i} \right]^{1/4}} \\
\frac{C_{10,ij}}{\mathrm{E_H.a_0^{10}}} &= 7 \frac{\alpha_i \alpha_j^{(3)}}{\sqrt{\frac{\alpha_i}{N_{\mathrm{eff},i}}} + \sqrt{\frac{2}{15}} \left[\frac{\left(\alpha_j^{(3)}\right)^4}{9 N_{\mathrm{eff},j} \alpha_j \left(\alpha_j^{(2)}\right)^2} \right]} + \\
&\quad \frac{35}{2} \frac{\alpha_i^{(2)} \alpha_j^{(2)}}{\left(\frac{\left(\alpha_i^{(2)}\right)^2}{9 N_{\mathrm{eff},i} \alpha_i} \right)^{1/4} + \left(\frac{\left(\alpha_j^{(2)}\right)^2}{9 N_{\mathrm{eff},j} \alpha_j} \right)^{1/4}} \\
&\quad + 7 \frac{\alpha_j \alpha_i^{(3)}}{\sqrt{\frac{\alpha_j}{N_{\mathrm{eff},j}}} + \sqrt{\frac{2}{15}} \left[\frac{\left(\alpha_i^{(3)}\right)^4}{9 N_{\mathrm{eff},i} \alpha_i \left(\alpha_i^{(2)}\right)^2} \right]},
\end{aligned} \tag{4.126}$$

with $\alpha_i^{(2)}$ the quadrupole polarizability and $\alpha_i^{(3)}$ the octupole polarizability in $\mathrm{a_0^3}$. For most atoms, single ionized and double ionized species Patil [104] lists the

dipole, quadrupole and octupole polarizabilities. Johnston [26, p. 117] developed empirical relations

$$\begin{aligned} \frac{\alpha_i^{(2)}}{\text{Å}^5} &= \left(\frac{\alpha_i}{\text{Å}^3}\right)^{1.553} \\ \frac{\alpha_i^{(3)}}{\text{Å}^7} &= \left(\frac{\alpha_i}{\text{Å}^3}\right)^{2.238}, \end{aligned} \tag{4.127}$$

for atoms with atomic numbers above 20 and applied this relation to molecules. In order to get the dipole polarizability, Thole's model [105] was used. He constructed a model that can predict the polyatomic polarizability based on the atomic polarizabilities. The presence of the other particles induces a dipole moment $\boldsymbol{\mu}_p$ on particle p which can be calculated as

$$\boldsymbol{\mu}_p = \boldsymbol{\alpha}_p \left[\boldsymbol{E}_p - \sum_{q \neq p}^{N} \boldsymbol{T}_{pq} \boldsymbol{\mu}_q \right], \tag{4.128}$$

where $\boldsymbol{\alpha}_p$ is the isotropic atomic polarizability tensor of atom p, $\boldsymbol{E}_p$ is the applied electric field at atom p and $\boldsymbol{T}_{pq}$ is the dipole field tensor. The induced dipole moments are given by

$$\boldsymbol{\mu} = \boldsymbol{A}\boldsymbol{E}, \tag{4.129}$$

with

$$\boldsymbol{A} = \left(\boldsymbol{\alpha}^{-1} + \boldsymbol{T}\right)^{-1}. \tag{4.130}$$

The matrix $\boldsymbol{A}$ is a $3N \times 3N$ matrix with N the number of atoms in the molecule. The diagonal elements are 3×3 blocks of $\alpha_{pp,ij}^{-1}$ and the off-diagonal elements are the 3×3 $T_{pq,ij}$ blocks. A molecular polarizability can be obtained by contracting the atomic representation as

$$\alpha_{\text{mol},ij} = \sum_p \sum_q A_{pq,ij}. \tag{4.131}$$

The components of the dipole field tensor are given by

$$T_{pq,ij} = \frac{\left(4v^3 - 3v^4\right)\delta_{ij}}{r^3} - 3v^4 \frac{r_i r_j}{r^5}, \tag{4.132}$$

with i and j representing the spatial directions x, y and z and

$$v = \begin{cases} \frac{r}{s} & r < s \\ 1 & r \geq s \end{cases}, \tag{4.133}$$

where r is the distance between particles p and q. In the original model Thole fits s to 16 molecules and obtains

$$s = 1.662 \left(\alpha_p \alpha_q\right)^{1/6}. \tag{4.134}$$

Van Duijnen [106] reconsidered the model with more accurate molecular geometries and atomic polarizabilities. The fit to 52 molecules gives

$$s = 1.7278 \left(\alpha_p \alpha_q\right)^{1/6}. \tag{4.135}$$

4.E Corrections related to the exponential repulsive potential

This section elaborates on the incorrect definition of the parameter ξ which is given in [68, eq. 13]. The solution of the problem was obtained in a private communication with Laricchiuta. The exponential repulsive potential is given by

$$V(r) = A \exp\left(-\frac{r}{\rho}\right). \tag{4.136}$$

The scattering angle for this potential can be rewritten by using the following substitutions

$$\begin{aligned} \sin\theta &= \frac{b}{r} \\ \sin\theta_0 &= \frac{b}{r_0} \\ u^2 &= \cos^2\theta_0 \\ \theta &= \left(1 - z^2\right)\theta_0. \end{aligned} \tag{4.137}$$

The result of these substitutions is

$$\chi = \pi - 4k'\theta_0, \tag{4.138}$$

with

$$k' = \int_0^1 \frac{z\mathrm{d}z}{\sqrt{1 - V/xk_BT\cos^2\theta}}. \tag{4.139}$$

By introducing $\xi = \frac{\rho}{r_0}$ the term in the denominator can be rewritten as

$$1 - \frac{A\exp\left(-\frac{1}{\xi}\right)}{xk_BT\cos^2\theta}. \tag{4.140}$$

At the distance of closest approach this can be expressed as

$$\xi = \frac{1}{\ln\left(A/k_BT\right) - \ln x - \ln\left(\cos^2\theta_0\right)} = \frac{1}{\alpha - \ln x - 4\ln u}. \tag{4.141}$$

The expression that Monchick gives, erroneously omits the last term in the denominator, reading [68, eq. 13]

$$\xi = \frac{1}{\alpha - \ln x}. \tag{4.142}$$

With Monchick's definition it is impossible to reproduce the remaining part of his derivation. The matter is resolved in the aforementioned communication with Laricchiuta by introducing a new parameter

$$\frac{1}{\xi'} = \frac{r_0}{\rho} = \frac{1}{\xi} - \ln u^4 = \frac{1 - \xi\ln u^4}{\xi}, \tag{4.143}$$

with ξ now redefined as indicated in (4.142). Using this definition the correct expression of k' in terms of ξ is obtained [68, p. 14]:

$$\begin{aligned} k' &= \int_0^1 \left[1 - \frac{\cos^2\theta_0}{\cos^2\theta} \exp\left(\frac{1}{\xi'}\left(1 - \frac{\sin\theta_0}{\sin\theta}\right)\right)\right]^{-1/2} z\mathrm{d}z \\ &= \int_0^1 \left[1 - \frac{\cos^2\theta_0}{\cos^2\theta} \exp\left(\frac{1 - 4\xi\ln u}{\xi}\left(1 - \frac{\sin\theta_0}{\sin\theta}\right)\right)\right]^{-1/2} z\mathrm{d}z. \end{aligned} \quad (4.144)$$

Additionally, the derivation of the cross section contains an inconsistency. The impact parameter can be written as

$$b^2 = r_0^2 \sin^2\theta_0 = r_0^2\left(1 - u^4\right). \quad (4.145)$$

Taking the derivative gives

$$2b\frac{\partial b}{\partial u} = 2r_0\frac{\partial r_0}{\partial u}\left(1 - u^4\right) - 4r_0^2 u^3. \quad (4.146)$$

The derivative of r_0 can be calculated from

$$\begin{aligned} \frac{\partial r_0}{\partial \xi'} &= -\frac{\rho}{\xi'^2} \\ \frac{\partial \xi'}{\partial u} &= 4\frac{\xi'^2}{u} \\ \frac{\partial r_0}{\partial u} &= \frac{\partial r_0}{\partial \xi'}\frac{\partial \xi'}{\partial u} = -4\frac{\rho}{u}. \end{aligned} \quad (4.147)$$

By using these substitutions the cross section can be expressed as

$$Q^{(l)} = 8\pi\rho^2 \int_0^1 \mathrm{d}u \left(1 - \cos^l\chi\right)\frac{1}{\xi'^2}\left(\frac{u^3}{2} + \frac{\xi'}{u}\left(1 - u^4\right)\right). \quad (4.148)$$

This expression deviates from [68, eq. 15-16]. The correct formula can be derived by replacing ξ' again with ξ which gives

$$Q^{(l)} = \frac{8\pi\rho^2}{\xi^2} I_l', \quad (4.149)$$

with

$$\begin{aligned} I_l' &= \int_0^1 \mathrm{d}u \left(1 - \cos^l\chi\right)\left[\frac{u^3}{2} + \xi\left(\frac{1}{u} - u^3\left[4\ln u + 1\right]\right)\right. \\ &\quad \left. + \xi^2\left(4\ln u\left[2u^3\ln u + u^3 - \frac{1}{u}\right]\right)\right]. \end{aligned} \quad (4.150)$$

4.F Fit functions for collision integrals

This section contains the fit functions that have been used by Capitelli et al. [27, eq. 11.3-11.5] to represent the collision integral. The quantity $\sigma^2\Omega^{(l,s)}$ is given in

$\mathring{A}^2$ in all cases. Note that in all expressions presented in this section terms proportional to $\frac{\exp(ax)}{\exp(ax)+\exp(-ax)}$ are rewritten as $1/\left(1+\exp\left(-2ax\right)\right)$ which is computationally more efficient. For electron-neutral interactions with species from the Mars atmosphere[13] the fit formula is given by

$$\sigma^2\Omega^{(l,s)*} = \frac{g_3 e^{g_6}}{1+e^{-2(x-g_1)/g_2}} + g_7 e^{-\left(\frac{x-g_8}{g_9}\right)^2} + g_4 + g_{10}x^{g_5}, \tag{4.151}$$

with $x = \ln T$ and g_i fit parameters. For heavy particle interactions in the Jupiter atmosphere[14] the following fit is used

$$\sigma^2\Omega^{(l,s)*} = \frac{a_1 + a_2 x}{1+e^{2(a_3-x)/a_4}} + \frac{a_5}{1+e^{2(a_6-x)/a_7}}, \tag{4.152}$$

with a_i fit parameters. Electron-neutral interactions for the Jupiter atmosphere are expressed as

$$\sigma^2\Omega^{(l,s)*} = \frac{g_3 e^{g_5}}{1+e^{-2(x-g_1)/g_2}} + g_6 e^{-\left(\frac{x-g_7}{g_8}\right)^2} + g_4, \tag{4.153}$$

with g_i fit parameters.

4.G H-H ab initio potential curve

The potential curves of the $X^1\Sigma_g^+$ and $b^3\Sigma_u^+$ states are calculated using DIRAC [107]. The input files are given in figures 4.12 and 4.13. Two types of calculations are executed: A self-consistent field (SCF) calculation and a calculation using Kramers-restricted configuration interaction (KRCI). For the SCF calculation the .CLOSED SHELL and .OPEN SHELL keywords can be used. Since all electrons are part of a closed shell the keyword .OPEN SHELL is omitted in this case. In this case there are two electrons in gerade orbitals and no electrons in ungerade orbitals. Electron correlation can be included with the keyword .KR CI. The .INACTIVE statement specifies the amount of orbitals (one orbital contains two electrons) that should remain fully occupied. These orbitals are not included in the electron correlation calculation. All virtual states are included in the KR CI calculation as indicated in the .GAS SHELLS section. The first digit indicates the amount of gas shells which is one in this case. The first two digits on the next row indicate the minimum and the maximum amount of cumulative electrons that are present after considering all shells up to and including the current shell. The last two digits represent the number of states in the gerade and ungerade symmetry that are used to generate this shell. These numbers are not cumulative. For example by specifying 2 gas shells with 0 2/2 2 the second shell starts with the third and fourth states in the gerade and ungerade symmetries. When the molecule is not symmetric a single number is used to specify the amount of states that are considered to be a part of a shell. By using the keyword .CIROOT a

[13] N_2, O_2, CO_2, Ar and derived species.
[14] H_2, He and derived species.

Figure 4.12: Input file for calculating the interaction potential for H–H.

```
**DIRAC                 .INACTIVE
.TITLE                  0 0
H-H                     .GAS SHELLS
.WAVE FUNCTION          1
.ANALYZE                2 2/36 36
.PROPERTIES             .CIROOTS
**HAMILTONIAN           0u 4
.X2C                    .CIROOTS
**INTEGRALS             0g 4
*READIN                 .CIROOTS
.UNCONTRACT             2u 4
**WAVE FUNCTION         .CIROOTS
.SCF                    2g 4
.KR CI                  .MAX CI
*SCF                    150
.CLOSED SHELL           .TRDM
2 0                     .OMEGAQ
.MAXITR                 **ANALYZE
100                     .MULPOP
*KRCICALC               *MULPOP
.CI PROGRAM             **END OF
LUCIAREL
```

Figure 4.13: Geometry input file for H–H. The string aaa is replaced by the interatomic separation in atomic units.

```
DIRAC
H-H
Interatomic separation
C 1
1. 2
H 0.0 0.0 0.0
H 0.0 0.0 -aaa
LARGE BASIS dyall.cv4z
FINISH
```

number of roots for a specific symmetry can be requested. The number behind the symmetry token indicates the number of states that should be calculated for that symmetry. In this case the molecule is symmetric and the states are requested with 2Ju or 2Jg for states with an ungerade or gerade symmetry and J the total angular momentum. Molecules without symmetry are simply requested with 2J. Note that all values of the total angular momentum are multiplied with 2 to avoid fractions.

The keywords .TRDM and .OMEGAQ are useful but not necessary for calculating the interaction potential. By using .TRDM the electronic transition dipole moments are calculated for all possible state to state transitions. The keyword .OMEGAQ requests a calculation of the spin and the orbital angular momentum as well as the total angular momentum. This is useful for recognizing states. The interaction potential is calculated for $0.5\,\mathrm{a_0} \leq r \leq 10\,\mathrm{a_0}$.

Chapter 5

Transport coefficients

The transport coefficients are derived from the Chapman-Enskog expansion. This expansion is briefly discussed in the first section. After that an overview is given of the expressions for the viscosity and the electrical and thermal conductivities that are used in the studies presented in chapters 6, 7, 10, 11,12 and 13 of this thesis. In the original literature these expressions are presented in a form that is not numerically stable. Those expressions are not stable for mixtures containing many species or for mixtures where the species densities cover many orders of magnitude. In this work more stable expressions are presented. In the third section the transport coefficients are calculated for various mixtures. The calculated coefficients are benchmarked by comparison with results obtained by Capitelli et al. [27, p. 273-342] for the planetary mixtures of Earth, Jupiter and Mars. Additionally, the implementation of the code is verified by comparing the results of the PLASIMO implementation with a separate implementation in MATLAB. The verification is not only done for the transport coefficients, but also for the collision integrals. In this section the effect of the new defaults for the collision integrals on the transport coefficients is discussed as well. These defaults are discussed in more detail in chapter 4.

5.1 Chapman-Enskog expansion

In local thermodynamic equilibrium the distribution function is given by the Maxwell distribution. This section considers the corrections that should be taken into account when the distribution function deviates slightly from Maxwell's distribution. Such a case is relevant for the calculation of transport fluxes and the accompanying coefficients like the thermal conductivity, viscosity and electrical conductivity. For the details of the derivation the reader is referred to Hirschfelder et al. [34, p. 466-491]. The derivation is valid under the following assumptions [34, p. 17-21]

- **binary collisions**: Only binary collisions are included. At sufficiently high densities three-body collisions become important and the theory is not applicable.

- **classical mechanics**: The theory neglects quantum effects. These effects are important when the de Broglie wavelength is of the order of magnitude of the molecular dimensions. Additionally, relativistic effects are not included.
- **small gradient lengths**: The first approximation describes the effects of the first derivative of the density, velocity and temperature. These corrections are sufficient when $\lambda_{\mathrm{mfp}} \left(\partial \ln n / \partial x\right) \ll 1$, where λ_{mfp} is the mean free path. When this is not satisfied, higher order corrections are necessary. These corrections introduce higher order derivatives and terms proportional to products of gradients of the density, the velocity and the temperature.
- **large systems**: The dimensions of the considered vessel should be large with respect to the mean free path. In that case the impact on the transport coefficients of collisions with the walls is small.
- **monatomic gases**: The effect of internal degrees of freedom is not included in the derivation of the thermal conductivity. These effects must be included separately.

The collision term in the Boltzmann equation can be modified with a factor $\frac{1}{\xi}$ to scale the collision rate

$$\frac{\partial f_i}{\partial t} + \vec{v}_i \cdot \nabla f_i + \frac{\vec{X}_i}{m_i} \cdot \nabla f_i = \frac{1}{\xi} J\left[f_i, f_j\right]. \tag{5.1}$$

For $\xi \ll 1$ collisions occur very often while for larger values of ξ collisions occur less frequent. The distribution function can then be expanded as

$$f_i = f_i^{[0]} + \xi f_i^{[1]} + \xi^2 f_i^{[2]} + \cdots . \tag{5.2}$$

The lowest order approximation is the equilibrium distribution given by

$$f_i^{[0]} = n_i \left(\frac{m_i}{2\pi k_B T_i}\right)^{3/2} \exp\left(-\frac{m_i \vec{v}_i^{\,2}}{2k_B T_i}\right) = n_i f_{v,i}, \tag{5.3}$$

where $f_{v,i}$ is the normalized velocity distribution and v_i is the velocity relative to the mass averaged velocity. Terms with the same power of ξ are equated. By using this procedure, the higher order corrections to the distribution function can be expressed in the known lower order corrections. The system provides a unique solution by adding the following constraints

$$\begin{aligned} \int f_i \mathrm{d}^3\vec{v}_i &= n_i \\ \sum_i m_i \int \vec{v}_i f_i \mathrm{d}^3\vec{v}_i &= \rho\vec{u} \\ \sum_i \frac{1}{2} m_i \int \left(\vec{v}_i - \vec{u}\right)^2 f_i \mathrm{d}^3\vec{v}_i &= \frac{3}{2} k_B T. \end{aligned} \tag{5.4}$$

The above integrals evaluate to zero if f_i is replaced with $f_i^{[r]}$ where r is an integer larger than zero. Hirschfelder et al. [34, p. 466-491] solve the system by introducing a perturbation function that contains the functions A_i, B_i and C_i that are proportional to the gradients of the temperature, velocity and the driving forces. These functions are expanded in a finite series of Sonine polynomials. The final result contains integrals over these polynomials. Those integrals can be expressed in terms of the collision integrals which have been introduced in (4.13)

$$\Omega_{ij}^{(l,s)} = \sqrt{\frac{k_B T}{2\pi m_{ij}}} \int_0^\infty \gamma^{2s+3} Q_{ij}^{(l)} \left(\gamma^2 k_B T\right) \exp\left(-\gamma^2\right) \mathrm{d}\gamma. \tag{5.5}$$

Devoto [97, 108] follows a similar procedure but expresses his final result in terms of the elements q_{ij}^{mp} which depend on the average cross sections

$$\overline{Q}_{ij}^{(l,s)} = \pi\sigma^2 \Omega_{ij}^{(l,s)*} = \pi\sigma^2 \frac{\Omega_{ij}^{(l,s)}}{\Omega_{\mathrm{RS},ij}^{(l,s)}}, \tag{5.6}$$

where σ is the rigid sphere collision diameter and $\Omega_{\mathrm{RS},ij}^{(l,s)}$ is the collision integral for a rigid sphere. Previously, the average cross sections have been introduced in (4.108).

5.2 Expressions transport coefficients

The expressions for the viscosity, thermal conductivity and electrical conductivity are given. The numerical stability of the original form of these expressions is analyzed. More stable expressions are presented in this section.

5.2.1 Viscosity

Previously, PLASIMO used the Wilke [109] approximation to calculate the viscosity [26, p. 138]. This approximation provides reasonable results when neutral-neutral interactions are dominant. However, when neutral-charged interactions are introduced, relative errors of the order of 100% can be reached. A more accurate expression is provided by the first approximation in the Chapman-Enskog method [34, p. 531,532]

$$\eta = \frac{\begin{vmatrix} \mathbf{H} & \mathbf{x} \\ \mathbf{x}^{\mathrm{T}} & 0 \end{vmatrix}}{|\mathbf{H}|}. \tag{5.7}$$

Here $\mathbf{x}$ are the species' molar fractions, the diagonal elements are given by

$$H_{ii} = \frac{x_i^2}{\eta_{ii}} + \sum_{j=1, j\neq i}^{\mu} \frac{2x_i x_j}{\eta_{ij}} \frac{m_i m_j}{(m_i + m_j)^2} \left(\frac{5}{3A_{ij}^*} + \frac{m_j}{m_i}\right), \tag{5.8}$$

and the off-diagonal elements are given by

$$H_{ij} = -\frac{2x_i x_j}{\eta_{ij}} \frac{m_i m_j}{(m_i + m_j)^2} \left(\frac{5}{3A^*_{ij}} - 1 \right) \qquad i \neq j, \tag{5.9}$$

with the viscosity of the pure gases expressed as[1]

$$\eta_{ij} = \frac{5 k_B T}{8 \Omega^{(2,2)}_{ij}}. \tag{5.10}$$

The definition of A^*_{ij} can be found in section 4.A. Higher order approximations for the viscosity provide a correction of the order 7 % in an argon mixture [27, p. 249].

5.2.2 Numerical stability

In case of a minority species, m, it can be shown that all matrix elements in column m are proportional to x_m. For the matrix element H_{mm} the term proportional to x_m^2 is neglected. The determinant of the augmented matrix can be written as a sum of products of cofactors and minors. By expanding the determinant from column m, it can be shown that all terms in this sum contain a product that is proportional to x_m^2 except for the term with cofactor H_{mm}. This term is proportional to x_m. This is the dominant contribution to the sum. The determinant of matrix H can be obtained similarly. Thus, in both cases the determinant can be written as a product of H_{mm} and the determinant of its minor. This description is equivalent to a mixture that does not contain species m.

Although $\lim x_i \to 0$ is well defined, numerical problems in expressions (5.7)–(5.9) can still occur due to the proportionality of H_{ij} with x_i. For mixtures containing a large number of species this proportionality can lead to underflows. Mixture calculations using LTE can easily provide such conditions at low temperatures. The problem can be solved by introducing coefficients $H^r_{ij} = H_{ij}/x_i$ that are given by

$$H^r_{ii} = \frac{x_i}{\eta_{ii}} + \sum_{j=1, j\neq i}^{\mu} \frac{2x_j}{\eta_{ij}} \frac{m_i m_j}{(m_i + m_j)^2} \left(\frac{5}{3A^*_{ij}} + \frac{m_j}{m_i} \right), \tag{5.11}$$

for the diagonal elements, and by

$$H^r_{ij} = -\frac{2x_j}{\eta_{ij}} \frac{m_i m_j}{(m_i + m_j)^2} \left(\frac{5}{3A^*_{ij}} - 1 \right) \qquad i \neq j, \tag{5.12}$$

for the off-diagonal elements. Using this row-scaling of the matrix $\mathbf{H}$, its determinant $|\mathbf{H}|$ can be written as

$$|\mathbf{H}| = |\operatorname{diag}(\mathbf{x})\mathbf{H}^r| = |\operatorname{diag}(\mathbf{x})||\mathbf{H}^r|. \tag{5.13}$$

[1] Note that an incorrect pre-factor in $\eta = C_\eta \frac{\sqrt{2\mu T}}{\sigma^2 \Omega^{(l,s)*}_{ij}}$ was specified by Capitelli et al. [27, p. 171]. They used a value of $C_\eta = 2.6693 \times 10^{-6}\ \mathrm{J}^{1/2}/\mathrm{K}^{1/2}$ while the correct value is $C_\eta = \frac{5}{16}\frac{\sqrt{k_B}}{\pi} \approx 3.6961 \times 10^{-13}\ \mathrm{J}^{1/2}/\mathrm{K}^{1/2}$.

Similarly, the augmented matrix that appears in the nominator of equation can be written as (5.7),

$$\begin{vmatrix} \mathbf{H} & \mathbf{x} \\ \mathbf{x}^{\mathrm{T}} & 0 \end{vmatrix} = |\operatorname{diag}(\mathbf{x}; 1)| \begin{vmatrix} \mathbf{H}^r & \mathbf{1} \\ \mathbf{x}^{\mathrm{T}} & 0 \end{vmatrix}. \tag{5.14}$$

Since $|\operatorname{diag}(\mathbf{x})| = |\operatorname{diag}(\mathbf{x}; 1)|$, substitution of these expressions in equation (5.7) yields

$$\eta = -\frac{\begin{vmatrix} \mathbf{H}^r & \mathbf{1} \\ \mathbf{x}^{\mathrm{T}} & 0 \end{vmatrix}}{|\mathbf{H}^r|}. \tag{5.15}$$

A numerically more convenient expression that avoids the usage of the determinant is derived from the identity [110, p. 99]

$$\begin{vmatrix} \mathbf{A} & \mathbf{B} \\ \mathbf{C} & \mathbf{D} \end{vmatrix} = |\mathbf{A}| \left|\mathbf{D} - \mathbf{C}\mathbf{A}^{-1}\mathbf{B}\right|. \tag{5.16}$$

Applying this rule to the numerator gives

$$\begin{vmatrix} \mathbf{H} & \mathbf{x} \\ \mathbf{x}^{\mathrm{T}} & 0 \end{vmatrix} = |\mathbf{H}| \left|-\mathbf{x}^{\mathrm{T}}\mathbf{H}^{-1}\mathbf{x}\right| = -|\mathbf{H}|\, \mathbf{x}^{\mathrm{T}}\mathbf{H}^{-1}\mathbf{x}, \tag{5.17}$$

where the last step uses the fact that the determinant of a scalar is the value itself. The viscosity can then be expressed as

$$\eta = \mathbf{x}^{\mathrm{T}}\mathbf{H}^{-1}\mathbf{x} = \mathbf{x}^{\mathrm{T}} \left(\mathbf{H}^r\right)^{-1} \mathbf{1}. \tag{5.18}$$

PLASIMO uses this more stable form to calculate the viscosity. The author is not aware of any publications that also explicitly state this form for the viscosity.

5.2.3 Thermal conductivity

The thermal conductivity contains four separate contributions. These are the translational contributions of the heavy particles λ_{hp} and the electrons λ_e, the reactive thermal conductivity λ_{r} and the internal thermal conductivity λ_{int}.

Translational thermal conductivity for heavy particles

The translational conductivity of the heavy particles is given by the second order expression from Muckenfuss and Curtis [111]

$$\lambda_{\mathrm{hp}} = 4\frac{\begin{vmatrix} \mathbf{L} & \mathbf{x} \\ \mathbf{x}^{\mathrm{T}} & 0 \end{vmatrix}}{|\mathbf{L}|}. \tag{5.19}$$

The elements L_{ii} are given by

$$L_{ii} = -\frac{4x_i^2}{\lambda_{ii}} - \sum_{k=1, k\neq i}^{\mu} \frac{2x_i x_k}{\lambda_{ik}} \frac{\frac{15}{2}m_i^2 + \frac{25}{4}m_k^2 - 3m_k^2 B_{ik}^* + 4m_i m_k A_{ik}^*}{A_{ik}^* \left(m_i + m_k\right)^2}, \tag{5.20}$$

where μ represents the number of heavy particles. The off-diagonal elements are given by

$$L_{ij} = \frac{2x_i x_j}{\lambda_{ij}} \frac{m_i m_j}{(m_i + m_j)^2} \frac{\frac{55}{4} - 3B^*_{ij} - 4A^*_{ij}}{A^*_{ij}}. \tag{5.21}$$

The thermal conductivity of the pure gases is given by[2]

$$\lambda_{ij} = \frac{75}{64} \frac{k_B^2 T}{m_{ij} \Omega^{(2,2)}}, \tag{5.22}$$

where m_{ij} is the reduced mass. The ratios of reduced collision integrals A^*_{ij} and B^*_{ij} are given in section 4.A.

Numerical stability

The matrix structure of the translational thermal conductivity is similar to the viscosity. It is thus also possible to define $L^r_{ij} = L_{ij}/x_i$. An alternative expression for the thermal conductivity is then given by

$$\lambda_{\mathrm{hp}} = 4 \frac{\begin{vmatrix} \mathbf{L}^r & \mathbf{1} \\ \mathbf{x}^{\mathrm{T}} & 0 \end{vmatrix}}{|\mathbf{L}^r|}. \tag{5.23}$$

This can again be written in a computationally more efficient form[3]

$$\lambda_{\mathrm{hp}} = -4\mathbf{x}^{\mathrm{T}} \mathbf{L}^{-1} \mathbf{x} = -4\mathbf{x}^{\mathrm{T}} \left(\mathbf{L}^r\right)^{-1} \mathbf{1}. \tag{5.24}$$

No other publications containing this form for the calculation of the thermal conductivity have been found.

Translational thermal conductivity for electrons

The translational contribution for the electrons is calculated by using Devoto's third order expression [97]

$$\lambda_e = \frac{75 n_e^2 k_B}{8} \sqrt{\frac{2\pi k_B T}{m_e}} \frac{1}{q^{11} - \left(q^{12}\right)^2 / q^{22}}, \tag{5.25}$$

with the q^{xy} elements defined in appendix 4.B. All elements q^{xy} are proportional to n_e. It is thus possible to introduce $q^{r,xy} = q^{xy}/n_e$ and obtain

$$\lambda_e = \frac{75 n_e k_B}{8} \sqrt{\frac{2\pi k_B T}{m_e}} \frac{1}{q^{r,11} - \left(q^{r,12}\right)^2 / q^{r,22}}, \tag{5.26}$$

[2]Note that an incorrect pre-factor in $\lambda = C_\lambda \frac{\sqrt{T/(2\mu)}}{\sigma^2 \Omega^{(l,s)*}_{ij}}$ was specified by Capitelli et al. [27, p. 167]. They used a value of $C_\eta = 0.0832\,\mathrm{J}^{3/2}/\mathrm{K}^{3/2}$ while the correct value is $C_\eta = \frac{75}{64} \frac{k_B^{3/2}}{\pi} \approx 1.9136 \times 10^{-35}\,\mathrm{J}^{3/2}/\mathrm{K}^{3/2}$.

[3]See the discussion that leads to (5.18) for more details.

which has the advantage that it is also well-defined for $\lim n_e \to 0$. The necessity of an appropriate l and s scaling for $\bar{Q}^{(l)}$ can be derived from a situation where the electron density is negligible. In that case the contributions to q^{xy} that are proportional to n_e^2 can be neglected. If no s-scaling is applied the q^{xy}-terms are proportional to $q^{11} = 8\sum_{i\neq e} n_e n_i \frac{9}{4}\bar{Q}^{(1)}$, $q^{12} = 8\sum_{i\neq e} n_e n_i \frac{99}{48}\bar{Q}^{(1)}$ and $q^{22} = 8\sum_{i\neq e} n_e n_i \frac{121}{64}\bar{Q}^{(1)}$. The denominator is then given by $q^{11} - \left(q^{12}\right)^2 / q^{22} = 0$.

The fourth approximation can be obtained from [97, eq. 20]

$$\lambda_e = \frac{75 n_e k_B}{8}\sqrt{\frac{2\pi k_B T}{m_e}}\frac{|q_{\text{top}}|}{|q_{\text{bot}}|}, \tag{5.27}$$

with

$$q_{\text{top}} = \begin{bmatrix} q^{r,22} & q^{r,32} \\ q^{r,23} & q^{r,33} \end{bmatrix} \quad q_{\text{bot}} = \begin{bmatrix} q^{r,11} & q^{r,12} & q^{r,13} \\ q^{r,21} & q^{r,22} & q^{r,23} \\ q^{r,31} & q^{r,32} & q^{r,33} \end{bmatrix}. \tag{5.28}$$

Calculations in argon show that the convergence of the electronic translational thermal conductivity is poor around $T = 8\,\text{kK}$ and that the fifth approximation still provides a small correction [27, p. 248]. This is related to the Ramsauer minimum. For gases that do have such a minimum the third order approximation is sufficient [27, p. 249].

Reactive thermal conductivity

The reactive thermal conductivity describes the transport of chemical energy and is calculated according to the expressions developed by Butler and Brokaw [50,112]. They neglect thermal diffusion, pressure gradients and external force fields. Butler and Brokaw [50, 112] consider a mixture of μ species. This mixture contains ν independent reactions. A reaction is considered to be independent when at least one component does not occur in any other reaction. Thus ν reactions are considered in the form

$$\sum_{k=1}^{\mu} R_{ik} X^k = 0, \tag{5.29}$$

where X^k is the k^{th} chemical species and R_{ik} is the stoichiometric coefficient of species k in reaction i. An example of a stoichiometry matrix is given in section 7.3. The coefficients of this matrix can be derived from the left hand side of the Guldberg-Waage equation (2.82). Effectively all species are represented as a linear combination of a few species that have been chosen as the 'building blocks'. Using this formalism the reactive thermal conductivity can be expressed as [112, eq. 3]

$$\lambda_{\text{r}} = -\frac{1}{k_B T^2}\frac{\begin{vmatrix} \mathbf{A} & \Delta\mathbf{H} \\ \Delta\mathbf{H}^{\text{T}} & 0 \end{vmatrix}}{|\mathbf{A}|}, \tag{5.30}$$

where $\Delta\mathbf{H}$ is the reaction enthalpy vector with elements $\Delta H_i = \sum_{k=1}^{\mu} R_{ik} H_k$ and H_k is the enthalpy[4] of species k. The matrix elements A_{ij} are given by

$$A_{ij} = \sum_{k=1}^{\mu-1} \sum_{l=k+1}^{\mu} \frac{k_B T}{D_{kl} p} x_k x_l \left(\frac{R_{ik}}{x_k} - \frac{R_{il}}{x_l} \right) \left(\frac{R_{jk}}{x_k} - \frac{R_{jl}}{x_l} \right), \tag{5.31}$$

where the diffusion coefficients are calculated from

$$D_{kl} = \frac{3}{16} \frac{k_B^2 T^2}{p m_{kl} \Omega^{(1,1)}}, \tag{5.32}$$

where m_{kl} is the reduced mass.

Numerical stability

The calculation of the determinant of $\mathbf{A}$ can be problematic when the species that have been used as the 'building blocks' reach low mole fractions. This is apparent if the last part of the matrix element A_{ij} is rewritten as

$$A_{ij} \; R_{ik} R_{jk} \frac{x_l}{x_k} - R_{ik} R_{jl} - R_{il} R_{jk} + R_{il} R_{jl} \frac{x_k}{x_l}. \tag{5.33}$$

Thus when one of the 'building block' species occurs both in reaction i and j, the off-diagonal elements can become large when the corresponding mole fraction is small. On the diagonal elements any 'building block' species that reaches a low mole fraction can give rise to a large matrix element. These problems in principle can be avoided using

$$|c\mathbf{A}| = c^{\nu} |\mathbf{A}|, \tag{5.34}$$

where c is a scalar value. However, a computationally more stable and more efficient form is derived from

$$\begin{vmatrix} \mathbf{A} & \Delta\mathbf{H} \\ \Delta\mathbf{H}^{\mathrm{T}} & 0 \end{vmatrix} = |\mathbf{A}| \left| -\Delta\mathbf{H}^{\mathrm{T}} \mathbf{A}^{-1} \Delta\mathbf{H} \right|. \tag{5.35}$$

The final result can then be written as

$$\lambda_{\mathrm{r}} = \frac{1}{k_B T^2} \Delta\mathbf{H}^{\mathrm{T}} \mathbf{A}^{-1} \Delta\mathbf{H}. \tag{5.36}$$

Rini et al. [113] mention this result in the appendix. They are the only ones known to the author that also provide this more convenient and stable expression.

5.2.4 Internal thermal conductivity

The transport of the energy of excited states is not included in the translational contributions. Eucken [114, p. 3] [27, p. 22,274] proposed a correction based on

[4] Unlike Butler and Brokaw H_i represents the enthalpy per particle.

the relation between the translational thermal conductivity and the viscosity. For a multicomponent mixture this correction is given by

$$\lambda_{\text{int}} = \frac{p}{T} \sum_{j=1}^{\nu} \frac{x_j c_{p,\text{int},j}/k_B}{\sum_{i=1}^{\nu} x_i / D_{ij}}, \tag{5.37}$$

where $c_{p,\text{int}}$ represents the heat capacity of the internal states, see section 2.B.

5.2.5 Electrical conductivity

Devoto's second order expression is used to calculate the electrical conductivity [97, eq. 16] as

$$\sigma_e = \frac{3 n_e^2 e^2}{2 k_B T} \sqrt{\frac{2\pi k_B T}{m_e}} \frac{1}{q^{00} - \left(q^{01}\right)^2 / q^{11}}, \tag{5.38}$$

with the definition of the q^{xy} elements given in appendix 4.B. Similar to the thermal conductivity of the electrons, the electrical conductivity can be expressed in $q^{r,xy} = q^{xy}/n_e$. The necessity of an appropriate s scaling for the collision integrals can also be derived from the point of view of the electrical conductivity. If no s scaling is applied and the electron density is negligible, the q^{xy} are proportional to $q^{00} = 8 \sum_{i \neq e} n_e n_i \bar{Q}^{(1)}$, $q^{01} = 8 \sum_{i \neq e} n_e n_i \frac{3}{2} \bar{Q}^{(1)}$ and $q^{11} = 8 \sum_{i \neq e} n_e n_i \frac{9}{4} \bar{Q}^{(1)}$. The result is that $q^{00} - \left(q^{01}\right)^2 / q^{11} = 0$.

An estimate for the third order expression is readily made [97, eq. 16] using

$$\sigma_e = \frac{3 n_e^2 e^2}{2 k_B T} \sqrt{\frac{2\pi k_B T}{m_e}} \frac{|q_{\text{top}}|}{|q_{\text{bot}}|}, \tag{5.39}$$

with

$$q_{\text{top}} = \begin{bmatrix} q^{00} & q^{01} \\ q^{10} & q^{11} \end{bmatrix} \quad q_{\text{bot}} = \begin{bmatrix} q^{00} & q^{01} & q^{02} \\ q^{10} & q^{11} & q^{12} \\ q^{20} & q^{21} & q^{22} \end{bmatrix}. \tag{5.40}$$

Around $T = 8\,\text{kK}$ the third order approximation is not even converged sufficiently. Capitelli et al. [27, p. 252] show that the sixth order approximation provides a correction of 200 % relative to the first order and is still not converged for an argon mixture. This is related to the Ramsauer minimum that limits convergence of the Chapman-Enskog series. Capitelli et al. [27, p. 253] state that in general the third order approximation is sufficiently accurate for partially or fully ionized mixtures.

5.2.6 Debye length

For charged-charged interactions the collision integrals depend on the Debye length. Some authors include the ions in the calculations while others neglect this contribution. Capitelli [27, sec. 3.3.1.1] gives a short discussion and Ghorui [115] gives a more elaborate overview of the different choices that have been made in the past.

Devoto [88, fig. 2] started the discussion by noting that the calculated electrical and thermal conductivities using only the electrons in the calculation of

the Debye length agreed best with calculations that used the collision integrals from Williams and DeWitt [116]. This comparison was made because Williams and DeWitt used accurate quantum mechanical plasma transport theory. A comparison of the calculated electrical conductivity at high temperature showed that experimental data was bounded by the calculations that included the ions and the calculations that neglected the ions. However, the best agreement was obtained for the calculation that neglected the ions. Later Hahn [117], Mason [87], Wang [118] and Murphy [72,73,119] followed Devoto. Additionally, Mason and Wang mention the option to include the ions. Others include the ions in the calculation [120–122]. Ghorui observed similar discrepancies in a two-temperature plasma. He proposed the following definition of the Debye length

$$\frac{1}{\lambda_D^2} = \frac{q^2}{\epsilon_0 k_B T_e} \left[n_e + \sum_{i \neq e} z_i^2 n_i \right], \tag{5.41}$$

which deviates from the usual definition

$$\frac{1}{\lambda_D^2} = \frac{q^2}{\epsilon_0 k_B} \left[\frac{n_e}{T_e} + \sum_{i \neq e} z_i^2 \frac{n_i}{T_h} \right], \tag{5.42}$$

via the temperature of the ions only. A comparison between the calculated electrical conductivity with the new definition of the Debye length and the experimental data shows that the agreement at high temperatures is also very good. Ghorui motivates the usage of the electron temperature in non-equilibrium mixtures with the higher mobility of the electrons. Any change in the electrical potential is expected to be redistributed at a rate that is proportional to T_e. Murphy [119] noted that the variation of the experimental results is larger than the variation of the theoretical results. Since the discussion hasn't been resolved, PLASIMO uses both the ions and the electrons in the calculation of the Debye length using (5.42) unless indicated otherwise.

5.3 Mixtures

Transport coefficients for the planetary atmospheres of Jupiter, Earth and Mars are discussed. These atmospheres contain H_2–He, N_2–O_2 and N_2–O_2–CO_2–Ar mixtures. Many of these species are frequently studied which makes it essential to have good transport coefficients for them. Capitelli et al. [27, 35] performed accurate calculations for these species. Therefore, their calculated results are used to benchmark PLASIMO. Following Capitelli, the approximation is made that the collision integrals for the excited states are the same as the ones for the ground state[5]. Estimating the effect of excited states is currently the topic of active research [27, p. 275].

[5] Note that Capitelli et al. [27, ch. 7] give an estimate of the effect of the cross sections of excited states in hydrogen on the thermal and electrical conductivities and the viscosity.

Five methods have been used to compare the transport properties. The first approach uses the specified collision integrals from [35, ch. 11] and is called 'Cap ci database'. The second approach uses the methods specified in section 4.3.3. The polarizabilities used for the species are given in 5.A or 5.B. The approach is called 'Cap formulas'. The third approach uses rigid-sphere collisions for the neutral-neutral and neutral-ion interactions. The Coulomb potential for charged-charged interactions and the Langevin polarizability model for electron-neutral interactions. The method is named 'RS'. The fourth approach is similar to the third approach. The only difference is that the neutral-ion interaction also uses the Langevin polarizability model. The method is called 'RS/L'. The fifth method uses the approaches specified by Johnston [26, p. 130]. The differences with method 2 are the usage of the Exponential repulsive potential or the (12-6) Lennard Jones potential for the neutral-neutral and neutral-ion interactions. The approach is named 'Johnston'. The transport properties are compared with data calculated by Capitelli et al. [35, ch. 11]. This data is named 'Capitelli'.

5.3.1 Jupiter

The composition of the Jupiter mixture is defined as $x_{H_2} = 0.89$ and $x_{He} = 0.11$ [35, p. 217]. The electrical conductivity, thermal conductivity and viscosity are calculated based on four different approaches. The reason for using only four approaches is the inaccurate set of polarizabilities. These polarizabilities are required for the 'Johnston' method. The only complete set of dipole- quadrupole and octupole polarizabilities is obtained for He. The quadrupole and octupole values for other species are extrapolated based on Patil's results [104] for He and Li. Li is used since Patil presents no data for H. This dataset causes numerical overflow for a few interactions when the found b^* is used to obtain A^*. Such large values for A^* basically correspond to a rigid sphere model with $r = 1/b^*$. Since the value of b^* is large, the collision diameter reaches unrealistically small values. In other cases the value of b^* is very small. This results in negative values for A^*, which is also not realistic.

The thermal conductivity and its relative accuracy are displayed in figure 5.1 and 5.2. The 'Cap ci database' values are within 10 % of the reference value for almost the entire temperature interval. Small differences are caused by the fact that Capitelli et al. use the third order approximation[6] for the heavy particle thermal conductivity; the partition sums contain a different number of states[7]; and no corrections for non-ideal gas behavior have been made. These differences

[6] A comparison with the translational thermal conductivity for the heavy particles with the data from Bruno et al. [122] shows that the relative error with our second order approximation is smaller than 1% for $T = 10\,\text{kK}$. For larger temperatures the relative error increases up to 130 % for $T = 20\,\text{kK}$ and decreases again to 30 % for $T = 50\,\text{kK}$. These errors are acceptable, since the dominant contribution to the translational thermal conductivity comes from the electrons (which is calculated using the third order expression). Note that the third order approximation for the electrons is not enough for specific temperature ranges where the interactions mainly occur around the Ramsauer minimum [27, p. 248-249].

[7] Capitelli et al. [27] use the atomic levels specified by NIST [53]. These levels are supplemented with predicted levels according to the Ritz-Rydberg series [35, sec. A.3].

are responsible for the largest errors near the peaks that correspond to dissociation of H_2 and ionization of H. The method 'Cap formulas' obtains errors of the order of 40 % near the dissociation peak. This is related to $\Omega^{(1,1)}$ for H–H_2 which is estimated with a relative error of 100 %. A similar error is obtained for the H–H^+ elastic interaction. However, it is camouflaged by the much stronger resonant charge exchange interaction which is accurately taken into account. The remaining methods show errors in the range of 40-2400 % near the reactive peaks. This is an indication that the predictions for the collision integral $\Omega^{(1,1)}$ are not accurate. The reason for those inaccurate results is that resonant charge exchange is not taken into account for those methods. For higher temperatures the difference between the Coulomb and the screened-Coulomb potential is apparent in the thermal conductivity of the electrons.

The electrical conductivity and its relative accuracy are shown in figure 5.3 and 5.4. For temperatures above 7 kK the errors of the 'Cap ci database' method are decaying from 5 % to 1 %. The reason that there are still some deviations is related to the different set of partition sums and the absence of corrections for non-ideal gas behavior. For temperatures lower than 7 kK the errors are increasing because of deviations in the composition. This is related to the small mole fraction of the electrons. At 7 kK the mole fraction is only $x_e = 4.6 \times 10^{-4}$. Small deviations in the partition sums can cause large relative errors in the electrical conductivity. The induced error is thus not caused by the calculation of the collision integrals. The other methods use the Langevin polarizability model for the calculation of the electron-neutral collision integrals. Such a choice results in overestimates of the order of 300 % for the electrical conductivity. The errors in the 'Cap formulas' calculation are decreasing with decreasing x_H and x_{He}.

The viscosity and the relative accuracy are displayed in figure 5.5 and 5.6. The calculation 'Cap ci database' is again approximately within 10 % of the reference value for all temperatures. The main contribution to the error is the fact that Capitelli et al. calculate the viscosity by using the second order approximation while in this work the first order approximation is used[8]. The initial increase of the viscosity is modeled relatively well by all models. The methods that use rigid spheres accumulate more error when H–H interactions are more important. The decrease between 10 kK and 30 kK of the viscosity is related to the ionization of the plasma. The charged-charged interactions have larger collision integrals than neutral-neutral interactions, which causes the viscosity to decrease as shown by (5.10). The sudden increase of the viscosity is the result of the H–H, H–H^+, He–He and He–He^+ collision integrals reaching a maximum before 5 kK. The decreasing trend for the collision integrals at 20 kK is not reproduced by any of the general methods. The decline in the viscosity shows two separate sections. The first one corresponds to the ionization of H. In this section the influence of the neutral-neutral interactions is reduced. The second one to the ionization of He and any leftover H. In that section the neutral-ion interactions are replaced by

[8]Capitelli et al [27, p. 249-250] demonstrate that the first order approximation is accurate for neutral-neutral interactions. For charged-mixtures the errors of the first order approximation in comparison to the sixth order approximation increase to 7 % for an argon mixture.

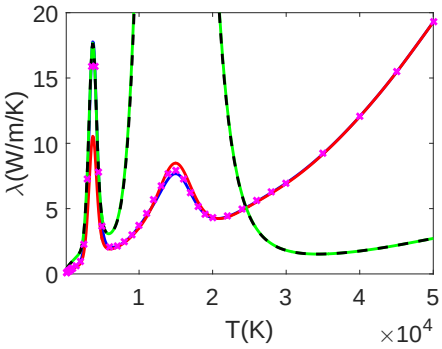

Figure 5.1: The thermal conductivity for the Jupiter atmosphere at $p = 1$ bar. The labels are explained in section 5.3 and the legend is given in figure 5.5.

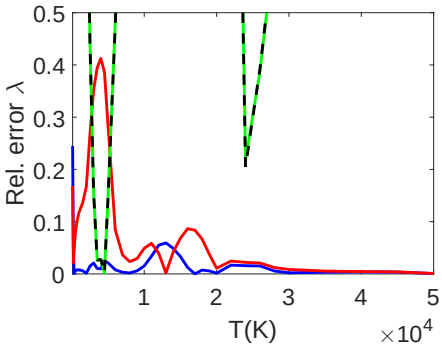

Figure 5.2: The relative error made in the calculation of the thermal conductivity displayed in figure 5.1. The legend is given in figure 5.5.

charged-charged interactions. The viscosity is then described by the asymptotes corresponding either to the Coulomb or the screened-Coulomb collision integrals.

For the Jupiter mixture it is necessary to use the method 'Cap ci database' for calculating transport coefficients. Inaccurate results are obtained when any of the general approaches is used. This is partly caused by the species H^+ which does not contain any electrons and is therefore not modeled properly with the relations from (4.121) and (4.37). Additionally, it seems that the predictions for interactions between H–H, H_2–H and H_2–H_2 are also not well modeled with (4.114), (4.115) and (4.37) based on the large errors obtained for the reactive thermal conductivity.

In figure 5.7 the specific heat of the Jupiter mixture is shown. The peaks correspond to the dissociation of H_2 at 3.8 kK, the ionization of H at 15 kK, the ionization of He at 23 kK and the ionization of He^+ at 48 kK. The contribution of chemical reactions is quite strong. It is the dominant contribution to the specific heat for large temperature intervals. In this case the position of the peaks is predicted accurately. This indicates that the effects of neglecting the non-ideal gas corrections and only using the levels that are reported by NIST [53] are negligible. The fact that the species H^+ and He^{2+} have no internal structure severely restricts the temperature interval for which these corrections could play a role.

5.3.2 Earth

The composition of the atmosphere on Earth is defined as $x_{N_2} = 0.8$ and $x_{O_2} = 0.2$ [35, p. 187]. This time the method proposed by Johnston [26] was able to provide an estimate for all of the interactions. For neutral-neutral interactions the dispersion coefficients (see (4.125)) were included up to C_{18}. For neutral-ion interactions the sum was extended to C_{30} in order to treat all neutral-ion

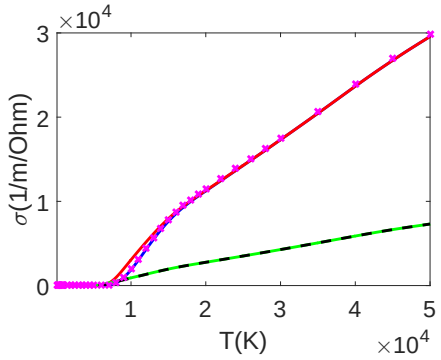

Figure 5.3: The electrical conductivity for the Jupiter atmosphere at p =1 bar. The labels are explained in section 5.3 and the legend is given in figure 5.5.

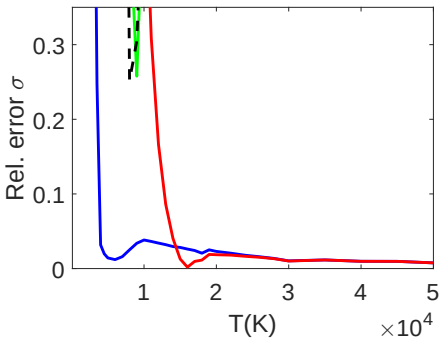

Figure 5.4: The relative error made in the calculation of the electrical conductivity displayed in figure 5.3. The legend is given in figure 5.5.

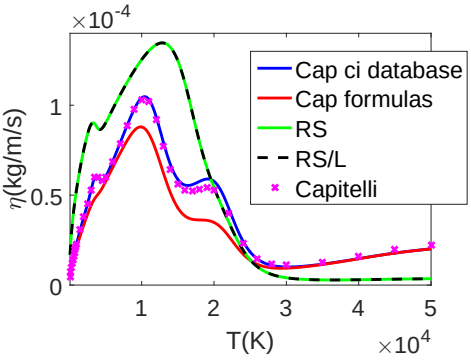

Figure 5.5: The viscosity for the Jupiter atmosphere at p =1 bar. The labels are explained in section 5.3.

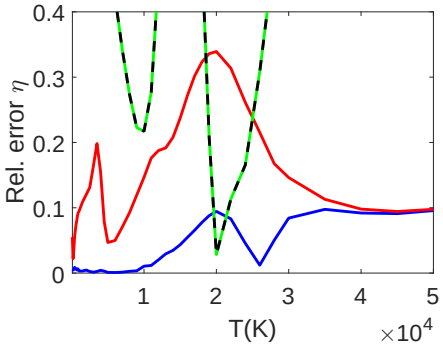

Figure 5.6: The relative error made in the calculation of the viscosity displayed in figure 5.5. The legend is given in figure 5.5.

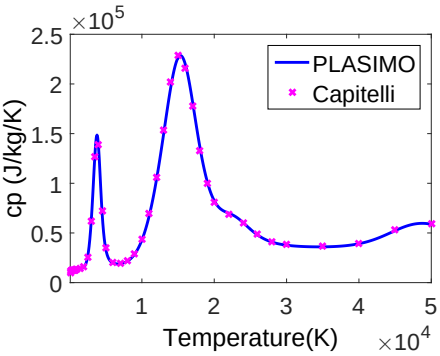

Figure 5.7: The specific heat for the Jupiter atmosphere at $p = 1$ bar.

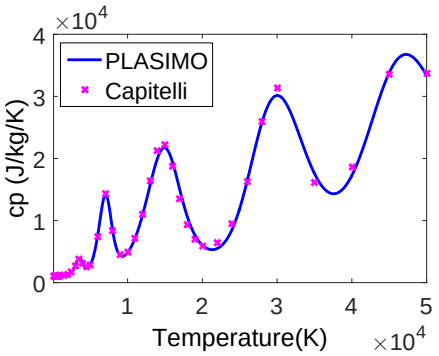

Figure 5.8: The specific heat for air at $p = 1$ bar.

interactions with the same amount of terms. All calculations have been performed by using a Debye length that only accounts for the electrons [27, p. 274].

The thermal conductivity and its relative accuracy are displayed in figure 5.9 and 5.10. By using 'Cap ci database' the relative accuracy of the thermal conductivity is always less than 3 %. The reason for the discrepancies are small deviations in the partition sums which cause deviations in the composition. The methods 'Cap formulas' and 'Johnston' this time also obtain an accuracy that is better than 10 % for almost the entire temperature interval. This is related to the fact that Capitelli et al. use similar scaling relations to estimate the transport properties, while for the Jupiter atmosphere specific tabulations from external literature were used. The methods that use rigid sphere models show errors of 35 % or more for large temperature intervals.

The electrical conductivity and its relative accuracy are shown in figure 5.11 and 5.12. The calculation 'Cap ci database' yields a relative error of 6 % or less for $T > 4\,\text{kK}$. The large error for $T < 4\,\text{kK}$ is again caused by deviations in the electron density. Small deviations in the molecular partition sums result in slightly different electron densities. At around $T = 8\,\text{kK}$ the increased error by using the Langevin model for the neutral-electron interactions is visible when 'Cap formulas' or 'Johnston' is used. By using the screened-Coulomb model instead of the Coulomb model the electrical conductivity increases approximately by a factor 3-5 for $T > 10\,\text{kK}$.

The viscosity with its relative accuracy are displayed in figure 5.13 and 5.14. The relative error of the methods 'Cap ci database' and 'Cap formulas' for the entire temperature interval is less than 5 % and 8 %, respectively. The method 'Johnston' obtains errors of the order of 30 % around $T = 15\,\text{kK}$. This is related to the inaccurate N–N^+ interaction. For the thermal conductivity this was not a problem since the larger resonant charge transfer collision integral hides the error. The methods using rigid spheres obtain errors of the order of 35 % or more for large temperature intervals.

The nitrogen dominated air plasma can be accurately described with the

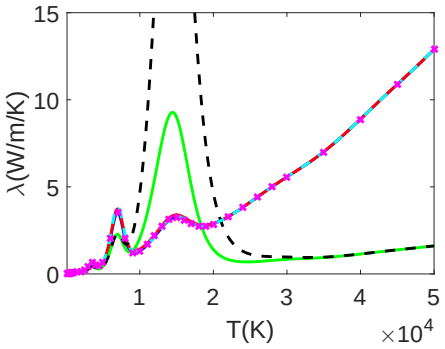

Figure 5.9: The thermal conductivity for air at $p = 1$ bar. The labels are explained in section 5.3 and the legend is given in figure 5.13.

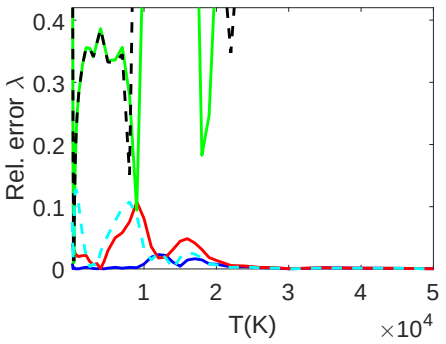

Figure 5.10: The relative error made in the calculation of the thermal conductivity displayed in figure 5.9. The legend is given in figure 5.13.

method 'Cap ci database'. The method 'Cap formulas' is almost as good as 'Cap ci database'. In comparison to 'Cap formulas' Johnston's approach results in errors that are equal or larger. It is therefore not recommended to use Johnston's method. The same conclusion is valid for the methods involving rigid spheres.

The specific heat for this air mixture is given in figure 5.8. Again the calculated specific heat is dominated by the reactive contribution. The first two peaks correspond to the dissociation of O_2 and N_2, respectively. The last three peaks contain contributions from the single, double and triple ionizations of O and N. The agreement in the last three peaks is a bit reduced due to the fact that Capitelli et al. [35, app. A.2,A.3] apply a procedure to complete the tables provided by NIST with a scaling rule. The PLASIMO calculation only contains the states reported by NIST; therefore, it deviates slightly.

5.3.3 Mars

The composition of the atmosphere on Mars is defined as $x_{CO_2} = 95.3$, $x_{N_2} = 2.7$, $x_{Ar} = 1.6$ and $x_{O_2} = 0.4$ [35, p. 202]. From Capitelli et al. [27, p. 274] one could conclude that the Debye length only contains the electrons. However, after comparing the transport properties it appears that the ions have also been taken into account. This is confirmed by contacting the authors [27].

The thermal conductivity and the relative accuracy are displayed in 5.15 and 5.16. The calculation according to 'Cap ci database' reaches errors of 4 % or less for the entire temperature interval. The method 'Cap formulas' also performs well with maximum relative errors of 8 % for $T > 2500$ K. These errors are reached near the dissociation peak of O_2 and the ionization peak of O. For lower temperatures the relative error increases up to 15 % for $T = 100$ K. This error is related to the CO_2–CO_2 interactions. Collision integrals at the dissociation and ionization peaks are less accurate using the 'Johnston approach', but the errors for the CO_2–CO_2

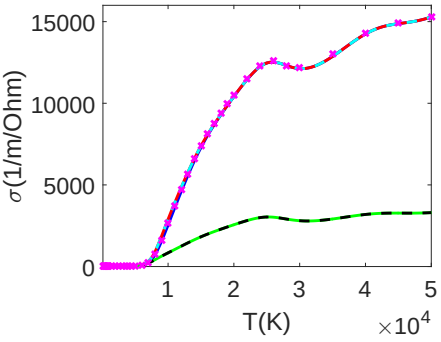

Figure 5.11: The electrical conductivity for air at $p = 1$ bar. The labels are explained in section 5.3 and the legend is given in figure 5.13.

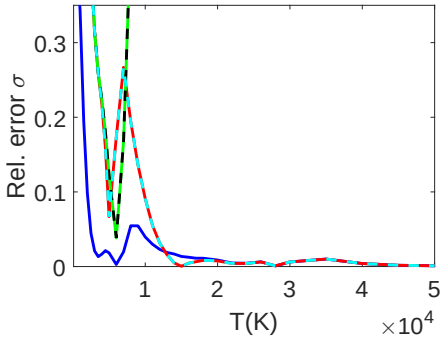

Figure 5.12: The relative error made in the calculation of the electrical conductivity displayed in figure 5.11. The legend is given in figure 5.13.

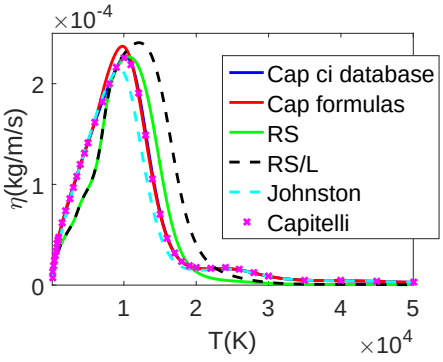

Figure 5.13: The viscosity for air at $p = 1$ bar. The labels are explained in section 5.3.

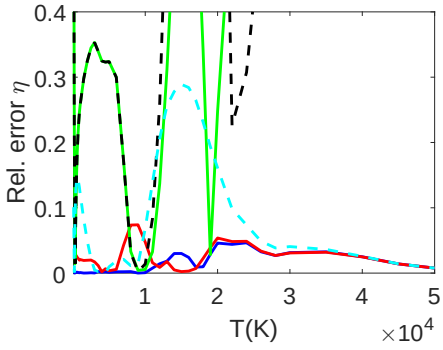

Figure 5.14: The relative error made in the calculation of the viscosity displayed in figure 5.13. The legend is given in figure 5.13.

interactions are smaller in comparison with 'Cap formulas'. Again the methods that use rigid sphere interactions produce inaccurate results.

The electrical conductivity and the corresponding relative accuracy are shown in 5.17 and 5.18. For temperatures larger than 7 kK the error for the method 'Cap ci database' is lower than 5 %. For smaller temperatures the error increases due to small differences in the composition. By using the Langevin model the neutral-electron interactions are less accurate as indicated with 'Cap formulas' and 'Johnston'. Surprisingly, by additionally replacing the screened-Coulomb model with the Coulomb model, the error of the 'RS' model is smaller than the error in the 'Johnston' model for $4\,kK \leq T \leq 7\,kK$. This is presumably caused by error cancellation.

The viscosity and its relative accuracy are displayed in 5.19 and 5.20. The method 'Cap ci database' shows a maximum error of the order of 16 % at 20 kK. These errors are caused by deviations in the composition induced due to small differences in the partition sums[9]. This large error is similar to the error that Murphy reported [73, p. 289]. He observed that calculating the viscosity for air with 0.033 % CO_2 and without CO_2 gave relative deviations up to 15 % due to deviating compositions. Slightly larger errors are obtained for the method 'Cap formulas'. Again the errors are larger for low temperatures where the CO_2–CO_2 interactions are important. The errors for the method 'Johnston' increase up to 35 % near the ionization peak of O. For low temperatures more accurate results are obtained in comparison to 'Cap formulas'. However, for the O–O^+ interactions the error increases considerably. For the thermal conductivity these errors are hidden due to the larger resonant charge transfer cross section. Errors for the methods that use rigid sphere models range from 20 % to 600 %.

The transport coefficients for the oxygen dominated Mars mixture can be accurately calculated with the method 'Cap ci database'. This time the 'Cap formulas' approach turns out to be quite accurate as well. For large temperature intervals the approach developed by 'Johnston' gives accurate results as well. However, the overall performance is less accurate in comparison with the 'Cap formulas' approach. On top of that, the input data requirements for the 'Johnston' method are higher. Thus, more accurate results can be obtained by using a smaller amount of input parameters. Therefore, it is not advised to use the 'Johnston' approach in the future.

The specific heat of the Mars atmosphere is given in figure 5.21. There are five peaks dominating the specific heat. The first two peaks corresponds to the dissociation of CO_2 and CO. The last three peaks are related to the overlapping first, second and triple ionizations of O and C. For the same reasons as indicated in the discussion of the specific heat of air, there is a small shift in the peaks related to ionization. The relative errors in the partition sums of O and O^+ are shown in 5.22. For O the errors accumulate as a function of temperature to values above 90 % at 50 kK. The results for O^+ are better: at 50 kK the errors increased to 45 %. This indicates that using the Ritz-Rydberg series to complement from the NIST

[9] As discussed before, Capitelli et al. extend the levels listed by NIST [53] with the Ritz-Rydberg series [35, p. 241-242].

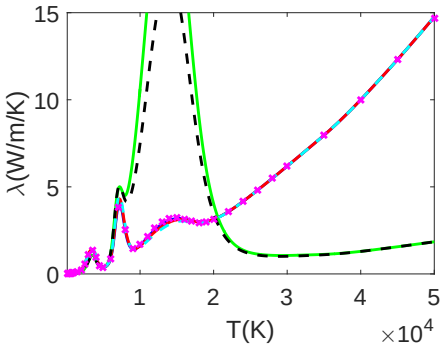

Figure 5.15: The thermal conductivity for the Mars atmosphere at $p = 1$ bar. The labels are explained in section 5.3 and the legend is given in figure 5.19.

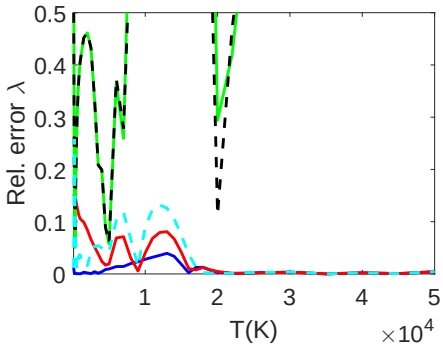

Figure 5.16: The relative error made in the calculation of the thermal conductivity displayed in figure 5.15. The legend is given in figure 5.19.

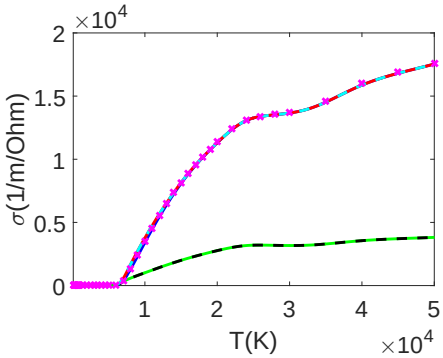

Figure 5.17: The electrical conductivity for the Mars atmosphere at $p = 1$ bar. The labels are explained in section 5.3 and the legend is given in figure 5.19.

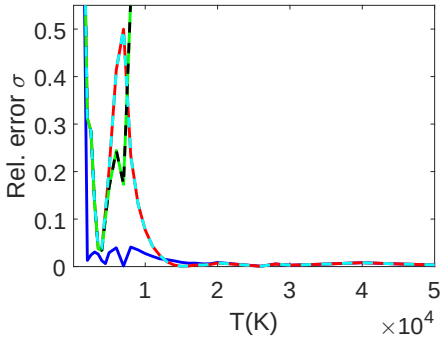

Figure 5.18: The relative error made in the calculation of the electrical conductivity displayed in figure 5.17. The legend is given in figure 5.19.

database can amount to a considerable correction of the partition sum [35, p. 241-242]. Additionally, the effects of ionization lowering on the Saha balance should be taken into account.

5.4 Conclusion

By using the collision integrals from Capitelli et al. [35, ch. 11], the transport coefficients for mixtures involving species consisting of H, He, N, O, C and Ar can be accurately calculated. For Ar a satisfying comparison is made with the

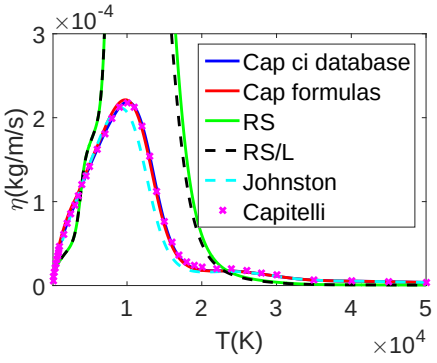

Figure 5.19: The viscosity for the Mars atmosphere at p =1 bar. The labels are explained in section 5.3.

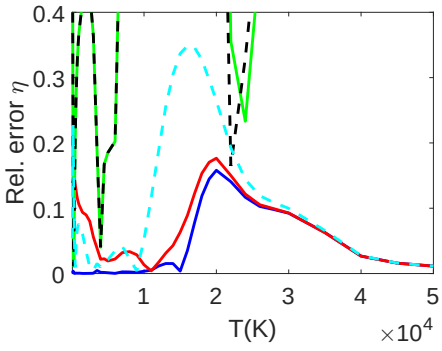

Figure 5.20: The relative error made in the calculation of the viscosity displayed in figure 5.19. The legend is given in figure 5.19.

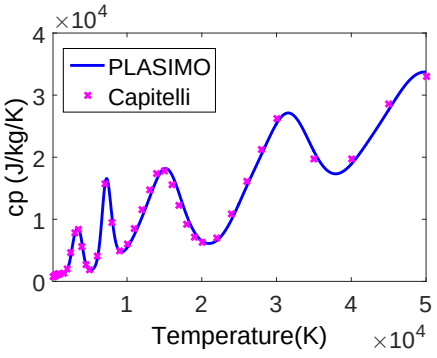

Figure 5.21: The specific heat for the Mars atmosphere at p =1 bar.

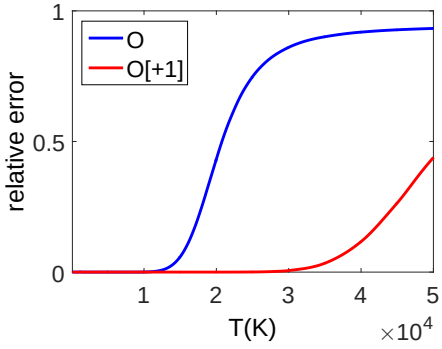

Figure 5.22: The deviations of the partition sums of O and O^+ in comparison to the partition sum given by Capitelli et al. [35, p. 280, 281].

data from Murphy [72]. This comparison is not described in this work. The remaining species have been benchmarked in this chapter against the planetary mixtures of Jupiter, Mars and Earth with good results. In many cases the formulas for estimating the parameters for the generalized Lennard Jones model provide a similarly accurate transport properties. Therefore, it is expected that by using these formulas the interactions for many other species can be estimated with a relative errors being smaller than 20 % for large temperature intervals. In specific temperature intervals the errors are larger due the usage of the Langevin model for the electron-neutral interactions. Whenever possible these collision integrals should be determined from (4.13) using a known cross section. For light atoms, like H and He the polarizability relations are shown to be less accurate. For mixtures containing these species the formulas from Capitelli resulted in relative errors of the order of 40-60 % for the temperature intervals that are dominated by neutral-neutral and neutral-ion collisions. This indicates that these collision integrals are best evaluated from a known cross section.

The transport coefficients have been verified for LTE conditions. However, for NLTE conditions the transport coefficients can be separated in terms that depend on the electrons as a function of the electron temperature and terms that depend on the heavy particles as a function of the heavy particle temperature. Special cases are the viscosity and the electrical conductivity. For the viscosity the electronic term is usually neglected. Similarly, the electrical conductivity is mostly calculated without the contribution from the ions. By calculating the transport coefficients for the electrons and the heavy particles separately, it is thus possible to use the same strategies to obtain accurate transport coefficients for NLTE mixtures with reasonable accuracy.

5.A Jupiter data

The polarizabilities and rigid sphere radii that have been used in the transport calculations are given in table 5.1. The main purpose of the polarizability dataset is to test what the influence on the transport data is when the specified polarizabilities and collision integrals by Capitelli [27, ch. 11] are ignored.

5.B Mars data

The polarizabilities and the rigid sphere radii that have been used in the mixture calculations in air and for the Mars atmosphere are given in table 5.2. The polarizability data for all neutral atoms and singly and doubly ionized species is taken from [104]. The values for the triple and qudruple ions are not reported. For that reason they are approximated with the values of the double ions. Due to the usage of LTE, collisions between neutral species and ions with a charge of three or larger are rare. Therefore, this approximation does not influence the calculated transport properties. The polarizability for the molecules and the negatively charged atoms is taken from a database that contains results of ab initio quantum-mechanical calculations [124]. In most cases the result for the Hartree-Fock method with the

Table 5.1: Alternative dataset for polarizabilities and rigid sphere radii for comparison with the data in [27, table. 11.9]. The rigid sphere radii are taken from [123] with the exception of the H^+ and He^{2+} species. The CCCBDB [124] value consulted is calculated with the Hartree-Fock method and uses the aug-cc-pVQZ basis set.

	$\alpha(\text{Å}^3)$	r(Å)
H_2	0.765 [124]	1.25
H_2^+	0.422 [124]	1.25
H	0.666 [124]	0.73
H^-	4.92 [124]	0.73
H^+	1×10^{-15}	0
He	0.1728 [104]	1.04
He^+	0.039 [124]	1.43
He^{2+}	1×10^{-15}	0

basis set aug-cc-pVQZ is used. In some cases the results strongly vary for different methods and basis sets. This was the case for N^- and $CO_2{}^-$. Not in all cases accurate data was available. For CN^+ the method B3LYP was used since HF gave negative results. For O_3 and NO_2 the basis set aug-cc-pVTZ was used. The species C_2N and C_2O were calculated using the ab initio program DALTON [125, 126]. The DALTON input scripts are described in section 5.C.

5.C DALTON calculations

The ab initio quantum mechanical program DALTON [125,126] is used to calculate the polarizabilities for the molecules C_2O and C_2N. DALTON does not take relativistic effects into account, therefore it should only be used for molecules that consist out of light atoms. The polarizabilities are calculated using the multi configurational self consistent field (MCSCF) level. First a simpler input file is discussed. This file for C_2O is given in figures 5.23 and 5.24. The geometry file specifies the basis set on the first two lines. The next two lines are comments. In the remaining lines the positions of the atoms are declared. These positions do not correspond to the equilibrium position for C_2O. The keyword .OPTIMIZE in the input file indicates that DALTON will search for this equilibrium position. In order to do an unbiased search, the atoms must not be placed on a line or in a plane. Otherwise, the routine will not consider positions outside this line or plane. These calculations can be optimized by using symmetry operators. This is not done in this input file. If the initial results indicate that the molecule is linear, as is the case for C_2O, the allowed positions of the atoms can be restricted to a line in the next simulation.

The section **WAVE FUNCTIONS is used to specify a method. In figure 5.23, only a Hartree-Fock (HF) calculation is requested. In principle the keywords .MP2 and .MCSCF can be added to account for electron correlation. In such a

Table 5.2: Alternative dataset for polarizabilities and rigid sphere radii for comparison with the data in [27, table. 11.1]. The rigid sphere radii are taken from [123]. The CCCBDB [124] value consulted is calculated with the Hartree-Fock method and uses the aug-cc-pVQZ basis set.

	$\alpha(\text{Å}^3)$	r(Å)		$\alpha(\text{Å}^3)$	r(Å)
Ar	1.4463	1.75	Ar^+	0.8005	1.74
Ar^{2+}	0.4895	1.74	C	1.2938	1.08
C^+	0.4251	1.08	C^{2+}	0.213	1.08
C^-	5.969	1.08	N	0.8046	1.05
N+	0.3047	0.1938	N^{2+}	0.1482	1.05
N^-	9.884	1.05	O	1.0071	1.02
O^+	0.2257	1.02	O^{2+}	0.1189	1.02
O^-	2.072	1.02	C_2	2.168	1.85
C_2^+	1.837	1.85	N_2	1.65	1.8
N_2^+	0.569	1.8	$N_2{}^-$	6.991	1.8
O_2	1.538	1.75	O_2^+	0.92	1.75
$O_2{}^-$	3.129	1.75	CN	2.195	1.82
CN^+	3.198	1.82	CN^-	3.915	1.82
CO	1.791	1.74	CO^+	1.182	1.8
NO	1.567	1.78	NO^+	0.987	1.78
C_3	4.945	2.31	N_3	3.215	2.25
O_3	2.714	2.19	$O_3{}^-$	4.857	2.19
C_2N	4.54	2.29	CO_2	2.268	2.2
CO_2^+	2.1	2.23	$CO_2{}^-$	4.817	2.23
C_2O	3.22	2.27	NO_2	2.526	2.21
N_2O	2.614	2.23	N_2O^+	1.998	2.23
CNO	3.006	2.25			

case the section *CONFIGURATION INPUT must be specified with the fields .SYMMETRY and SPIN MULTIPLICITY. If this input is unknown, it can be obtained from a .HF calculation. These values can be obtained from an analysis of the HF or Møller-Plesset perturbation theory (MP2) results. The symmetry corresponds to the state that contains the highest occupied molecular orbital (HOMO). The spin multiplicity can be deduced from $2S + 1$ where S is the spin of the molecule.

Additionally, the orbitals that should remain fully occupied during the calculation (inactive orbitals) must be specified under .INACTIVE. The active orbitals for which the electron population can deviate from 0, 1 or 2 due to electron correlation should be specified under .CAS SPACE. The amount of electrons in the complete active space (CAS) is given by the field .ELECTRONS. The amount of states that should be included in the inactive or the CAS SPACE should be based on an orbital population analysis obtained from an MP2 calculation. An example of such an input file is given in figure 5.25. All possible orbital occupations in the CAS SPACE with the amount of specified electrons are considered.

Figure 5.23: Input file for calculating the polarizability of C_2O.

```
**DALTON INPUT
.OPTIMIZE
.RUN WAVE FUNCTIONS
.RUN PROPERTIES
**WAVE FUNCTIONS
.HF
**PROPERTIES
.POLARI
**END OF DALTON INPUT
```

Figure 5.24: Input geometry file for C_2O.

```
BASIS
aug-cc-pVQZ
C2O
using the aug-cc-pVQZ basis
Atomtypes=2
Charge=6.0 Atoms=2
C 1.00000 -1.0000 -0.26687
C -2.00000 0.1000 2.47886
Charge=8.0 Atoms=1
O 1.00000 0.0400 -2.13655
```

The number of combinations, and therefore the calculation time, rapidly increases with the amount of electrons and orbitals in the CAS SPACE. For the described geometry optimization the CAS SPACE is kept small. For C_2O only the orbitals that are singly or doubly occupied are included in the CAS SPACE. More accurate results can be obtained by including more virtual states (unoccupied states) and by taking correlation effects into account for more occupied levels. The calculation time will then rapidly increase while the optimized geometry is not strongly influenced. An advantage of using the MCSCF optimization is that DALTON's HF optimization can only account for singlet states. Since the ground state of C_2O is a triplet (according to an MCSCF calculation of the energy levels), the HF routine does not use the correct state description for optimizing the geometry of the ground state. A similar input file can be constructed for the ground state of C_2N which is a doublet. In that case the HF optimization also deviates from the MCSCF optimization. A drawback of DALTON is the number of implemented symmetries. A linear molecule has the point group [45, p. 2-6] $C_{\infty v}$. DALTON approximates this symmetry with the point group C_{2v}, which may introduce some error.

The section **PROPERTIES contains a request for the polarizabilities via .POLARI. The isotropic polarizability can be calculated from [127, eq. 7]

$$\alpha = \frac{1}{3}\left(\alpha_{xx} + \alpha_{yy} + \alpha_{zz}\right). \tag{5.43}$$

Contributions from vibrational polarization are included for C_2O. Another useful keyword for this section is .VIBANA. This keyword requests a calculation of the rotational and vibrational frequencies. Any corrections for these frequencies are not calculated.

Figure 5.25: Example input file for calculating the polarizability of C_2O using the MCSCF approach.

```
**DALTON INPUT
.RUN WAVE FUNCTIONS
.RUN PROPERTIES
**WAVE FUNCTIONS
.HF
.MP2
.MCSCF
*SCF INPUT
.SINGLY OCCUPIED
0 1 1 0
.DOUBLY OCCUPIED
7 1 1 0
*CONFIGURATION INPUT
.SYMMETRY
2
.SPIN MULTIPLICITY
3
.INACTIVE
6 1 1 0
.CAS SPACE
1 1 1 0
.ELECTRONS
4
**START
.SHIELD
.MAGNET
**PROPERTIES
.VIBANA
.DIPGRA
.POLARI
**END OF
```

Chapter 6

Stefan Maxwell equations

In section 3.2.2 the momentum balance is discussed for the species system. The purpose of this balance is to calculate the species velocities. In practice only the bulk velocity is evaluated based on the momentum balance. The species velocity is calculated using the sum of the bulk velocity and a diffusive velocity. This diffusive velocity is obtained from a simplified momentum balance. The simplified momentum balances are the Stefan-Maxwell equations. A key characteristic for these equations is that they form a coupled system. The diffusive velocities thus depend on the velocities of all species present in the plasma.

In the presence of a dominant background gas the diffusive fluxes can be obtained by only considering interactions with the background gas. This system is equivalent to Fick's law and has the advantage that it is not coupled. The disadvantage is that Fick's law is only valid when the mixture contains a dominant background gas. Additionally, the gradients of the pressure fractions can only be converted to gradients of the molar fractions when the contribution proportional to the gradient of the temperature is significantly smaller than the contribution proportional to the gradient of the species densities. In general these criteria are not met in a non-thermal plasma. For that reason the Stefan-Maxwell equations are considered in this chapter.

The coupled system is represented in matrix form. Several properties of these matrices have been proven by Giovangigli [128, 129]. The numerical implementation of such a model in PLASIMO [25] is discussed by Peerenboom [6, 28, 29]. The major advantage of the developed solution procedure is that conservation equations for mass and charge are free of spatial discretization errors. However, the model appeared to be unstable for some conditions. It was observed that for neutral mixtures the implementation works as expected. Mixtures that involve one ion and one electron are also stable. Mixtures containing multiple ions appear to be susceptible to oscillatory behavior in the mass fractions. These oscillations are diverging and the model will eventually provide physically unacceptable results.

In this chapter the theory presented by Peerenboom [6] is extended from one-temperature mixtures to two-temperature mixtures. The remaining part of the chapter discusses the instabilities that can still occur in the current algorithm.

The following causes for the instabilities have been investigated.

- A concern using the theory in its current form is the singularity of the friction matrix. The singularity is avoided by using a regularization procedure. Different regularization constants have been discussed. The effect on the condition number of the relevant matrices is relatively small. Typical condition numbers for the system matrix remain in the order of 10^6-10^9 which is still large.

- Linear, cubic and harmonic interpolation from the nodal points to the interfaces also did not appear to make a significant improvement on the stability.

- Additionally, alternative solution procedures for the problem have been considered. One of these attempts is related to a formulation in terms of the diffusive mass fluxes rather than the diffusive velocities. The advantage of using mass fluxes is that a stable formulation is guaranteed in the presence of vanishing mass fractions.

- Another attempt involves the usage of pressure fractions rather than mass fractions. Although charge conservation is not guaranteed in the two-temperature case the magnitude of the electron pressure fraction is in the same order of magnitude as the the pressure fraction of the ions. Rounding errors may therefore be less of a concern. This is not the case using mass fractions.

- Additionally, it was attempted to apply the mass and charge constraints analytically.

None of the methods described above improved the stability of the system. It has been observed that changing the calculation of the collision integrals or the pressure can influence the profile of the mass fractions by influencing the calculation of the diffusion coefficient. The calculation of more accurate collision integrals as described in chapter 4 appeared to improve the stability. Further improvements of the stability could be obtained by increasing the number of grid points or reducing the under relaxation factor. The last two improvements increase the amount of computational resources that are required to solve the system and are therefore not ideal.

6.1 Introduction

In section 3.2.1 the mass balance has been derived

$$\frac{\partial \rho y_i}{\partial t} + \nabla \cdot (\rho y_i \vec{u}_i) = m_i \omega_i, \tag{6.1}$$

with $\rho = \sum_i n_i m_i$ the mass density and ω_i the species production rate per unit of volume. The species velocity can be expressed in terms of the bulk velocity and the diffusive velocity as

$$\vec{u}_i = \vec{u} + \vec{v}_{d,i}, \tag{6.2}$$

with

$$\vec{u} = \sum_i y_i \vec{u}_i. \tag{6.3}$$

The mass balance can now be rewritten to

$$\begin{aligned} \frac{\partial \rho y_i}{\partial t} + \nabla \cdot (\rho y_i \vec{u}) + \nabla \cdot (\rho y_i \vec{v}_{d,i}) &= m_i \omega_i \\ \frac{\partial \rho y_i}{\partial t} + \nabla \cdot (\rho y_i \vec{u}) + \nabla \cdot \vec{J}_i &= m_i \omega_i, \end{aligned} \tag{6.4}$$

with $\vec{J}_i$ the diffusive mass flux. The diffusive mass fluxes can be obtained from the species momentum balances given in section 3.2.2. A constraint for the total diffusive mass flux can be derived by assuming steady-state conditions; summing over all species; and using

$$\sum_i y_i = 1. \tag{6.5}$$

A comparison with the bulk equation for the mass balance reveals that no nett mass is transported via diffusive mass fluxes

$$\sum_i \vec{J}_i = \sum_i \rho y_i \vec{v}_{d,i} = 0. \tag{6.6}$$

A similar constraint can be derived by multiplying the species mass balance with the ratio of the charge over the mass q_i/m_i. Summing over all species and neglecting time dependencies gives

$$\begin{aligned} \sum_i \left[\nabla \cdot \left(\frac{\rho q_i y_i}{m_i} \vec{u} \right) + \nabla \cdot \left(\frac{\rho q_i y_i}{m_i} \vec{u}_i \right) \right] &= \sum_i q_i \omega_i \\ \nabla \cdot \sum_i \frac{\rho q_i y_i \vec{v_{d,i}}}{m_i} = \nabla \cdot \sum_i n_i q_i \vec{v_{d,i}} = \nabla \cdot \vec{j}_{\text{ext}} &= 0, \end{aligned} \tag{6.7}$$

with $\vec{j}_{\text{ext}}$ the external current density. This relation for the current density has been derived by assuming quasi-neutrality

$$\sigma^c = \sum_i \frac{q_i y_i}{m_i} = 0. \tag{6.8}$$

6.2 Diffusive velocities

This section covers the calculation of the diffusive velocities. Additionally, it is shown that the solution is guaranteed to conserve mass and charge both mathematically and numerically. First two properties are discussed that must be satisfied for any type of system. In the remainder of this chapter a bold font will be used to represent the vector that contains the properties of a given quantity for all species. When this property has a direction, like the velocity, the vector contains only one component of that property. The diffusive driving forces and the diffusive velocities must satisfy the following properties [6, p. 33]

- $\mathbf{y}^{\mathrm{T}}\mathbf{v}$=0 as shown in (6.6). Note that a superscript T is used to indicate the transpose. In other words: the diffusive velocities do not cause a net mass transport.
- $\mathbf{1}^{\mathrm{T}}\mathbf{d}$=0 with $\mathbf{1}$ representing a vector containing ones. Thus the sum of the diffusive driving forces is zero.

In section 6.A the Stefan-Maxwell equations have been derived from the momentum balance. The driving forces are given by

$$\begin{aligned} -\sum_j \vec{d}_{ij} &= \sum_j \frac{z_i z_j}{D_{ij}} \left(\vec{u}_i - \vec{u}_j\right) \\ &= -\nabla z_i - \frac{1}{p}\left(z_i - y_i\right)\nabla p + \frac{\rho y_i}{p}\left(\vec{a}_i - \vec{a}\right) \\ &\quad + \sum_j \left(\beta_{ij}\nabla \ln T_j - \beta_{ji}\nabla \ln T_i\right) \\ &= -\vec{d}_{\mathrm{ord},i} - \vec{d}_{\mathrm{pres},i} - \vec{d}_{\mathrm{forced},i} - \vec{d}_{\mathrm{thermal},i}, \end{aligned} \tag{6.9}$$

where the terms on the bottom row represent the driving forces for ordinary diffusion, pressure diffusion, forced diffusion and thermal diffusion, respectively. In this section a simplified system is considered by neglecting pressure diffusion, forced diffusion and thermal diffusion. The simplified system can thus be represented as

$$\sum_j \frac{z_i z_j}{D_{ij}}\left(\vec{u}_i - \vec{u}_j\right) = -\sum_j d_{ij} = -\nabla z_i. \tag{6.10}$$

In matrix form the system of equations is given by[1]

$$\mathbf{F}\mathbf{v} = -\mathbf{d}, \tag{6.11}$$

with $\mathbf{F}$ the friction matrix and $\mathbf{v}$ the vector of diffusive velocities. The matrix elements are given by

$$F_{ij} = \begin{cases} \sum_{j\neq i} f_{ij} & \text{if} \quad i = j \\ -f_{ij} & \text{if} \quad i \neq j \end{cases}, \tag{6.12}$$

with f_{ij} the friction coefficient. It is given by

$$f_{ij} = \frac{z_i z_j}{D_{ij}}. \tag{6.13}$$

The diffusion coefficients in a non-thermal mixture are given by [59, eq. 47]

$$D_{ij} = \frac{3k_B^2 T_i T_j}{16 p \mu \Omega^{(1,1)}\left(T_{ij}\right)}, \tag{6.14}$$

[1] Note that the difference between the averaged velocities of the species is the same as the difference between the diffusive velocities $\vec{u}_i - \vec{u}_j = \vec{v}_{d,i} - \vec{v}_{d,j}$.

with $T_{ij} = \frac{m_i T_j + m_j T_i}{m_i + m_j}$. The diffusion velocities can be calculated from

$$\mathbf{v} = -\mathbf{D}\mathbf{d}, \tag{6.15}$$

with $\mathbf{D}$ the symmetric multicomponent diffusion coefficient matrix. The matrix $\mathbf{D}$ can not be calculated by inverting $\mathbf{F}$, since $\mathbf{F}$ is singular. Giovangigli obtained the following properties for these matrices [128, p. 78] [6, p. 33]:

- $\mathbf{1}^{\mathrm{T}}\mathbf{F} = 0$ and $\mathbf{F}\mathbf{1} = 0$. Thus the null space of $\mathbf{F}$ is $\mathbf{1}$.
- $\mathbf{y}^{\mathrm{T}}\mathbf{D} = 0$ and $\mathbf{D}\mathbf{y} = 0$ with $\mathbf{y}$ a vector containing the mass fractions.

Giovangigli obtains the following properties from the theory of generalized inverses [128, p. 79] [6, p. 34]

$$\mathbf{F}\mathbf{D} = \mathbf{I} - \frac{\mathbf{y}\mathbf{1}^{\mathrm{T}}}{\mathbf{y}^{\mathrm{T}}\mathbf{1}} \tag{6.16}$$

$$\mathbf{D}\mathbf{F} = \mathbf{I} - \frac{\mathbf{1}\mathbf{y}^{\mathrm{T}}}{\mathbf{y}^{\mathrm{T}}\mathbf{1}}. \tag{6.17}$$

The matrices $\mathbf{F}$ and $\mathbf{D}$ can be regularized with [6, p. 37] [128, p. 87-88]

$$\tilde{\mathbf{F}} = \mathbf{F} + \alpha\mathbf{y}\mathbf{y}^{\mathrm{T}} \tag{6.18}$$

$$\tilde{\mathbf{D}} = \mathbf{D} + \beta\mathbf{1}\mathbf{1}^{\mathrm{T}}, \tag{6.19}$$

with α and β regularization constants and $\tilde{\mathbf{F}}$ and $\tilde{\mathbf{D}}$ the generalized inverses. The product of these matrices is given by [128, p. 88] [129, p. 253]

$$\begin{aligned}
\tilde{\mathbf{F}}\tilde{\mathbf{D}} &= \mathbf{F}\mathbf{D} + \beta\mathbf{F}\mathbf{1}\mathbf{1}^{\mathrm{T}} + \alpha\mathbf{y}\mathbf{y}^{\mathrm{T}}\mathbf{D} + \alpha\beta\mathbf{y}\mathbf{y}^{\mathrm{T}}\mathbf{1}\mathbf{1}^{\mathrm{T}} \\
&= \mathbf{F}\mathbf{D} + \alpha\beta\left(\mathbf{y}^{\mathrm{T}}\mathbf{1}\right)^2 \\
&= \mathbf{I} - \frac{\mathbf{y}\mathbf{1}^{\mathrm{T}}}{\mathbf{y}^{\mathrm{T}}\mathbf{1}} + \alpha\beta\left(\mathbf{y}^{\mathrm{T}}\mathbf{1}\right)^2.
\end{aligned} \tag{6.20}$$

In the special case of $\alpha\beta\left(\mathbf{y}^{\mathrm{T}}\mathbf{1}\right)^2 = 1$ the property $\tilde{\mathbf{F}}\tilde{\mathbf{D}} = \mathbf{I}$ is obtained. The regularization constants can thus be related to each other via

$$\beta = 1/\left(\alpha\left(\mathbf{y}^{\mathrm{T}}\mathbf{1}\right)^2\right). \tag{6.21}$$

The same relation can be obtained for $\tilde{\mathbf{D}}\tilde{\mathbf{F}}$. In order to make the regularization term $\alpha\mathbf{y}\mathbf{y}^{\mathrm{T}}$ of the same order of magnitude as the matrix elements $\frac{z_i z_j}{D_{ij}}$ the regularization constant is chosen as [6, p. 37] [28]

$$\alpha = 1/\max\left(D_{ij}\right). \tag{6.22}$$

An alternative choice for the regularization constant is based on choosing the value that is most suitable for the considered dynamical range of the diagonal elements of $\mathbf{F}$ and $\mathbf{y}\mathbf{y}^{\mathrm{T}}$

$$\beta_i = \frac{F_{ii}}{y_i^2} \tag{6.23}$$

$$\alpha = \sqrt{\min\left(\beta_i\right)\max\left(\beta_i\right)}. \tag{6.24}$$

This choice for α makes sure that the regularization matrix $\alpha\mathbf{y}\mathbf{y}^{\mathrm{T}}$ is of the same order of magnitude as the singular friction matrix $\mathbf{F}$. The multicomponent diffusion matrix can be calculated from

$$\mathbf{D} = \left(\mathbf{F} + \alpha\mathbf{y}\mathbf{y}^{\mathrm{T}}\right)^{-1} - \frac{1}{\alpha\mathbf{u}^{\mathrm{T}}\mathbf{y}^2}\mathbf{1}\mathbf{1}^{\mathrm{T}}. \tag{6.25}$$

The diffusive mass flux is thus obtained by multiplying (6.15) by the species mass density

$$\mathbf{J} = \rho\mathbf{Y}\mathbf{D}\partial\mathbf{z}. \tag{6.26}$$

with $\mathbf{Y} = \mathrm{diag}\,(y)$. In the next section the conversion from pressure to mass fractions is discussed.

6.2.1 Conversion matrix $\tilde{\mathbf{M}}$

Giovangigli observed that a straightforward conversion from the mole fractions to the mass fractions leads to a singular matrix $\mathbf{M}$. He solved the problem by redefining the average mass as [128, eq. 4.4,4.6] [6, p. 35-36]

$$m = \frac{\sigma^m}{\sum_i y_i/m_i} = \frac{\sum_i x_i m_i}{\sigma^m}, \tag{6.27}$$

with $\sigma^m = \sum_i y_i = \sum_i x_i = \sum_i z_i$. Such a definition is required since $\sigma^m = 1$ is not explicitly applied to the system. All mass fractions are treated as independent variables. The consequence is that $\sigma^m = 1$ may not be satisfied exactly. By following a similar strategy the conversion from pressure to mass fractions can be regularized. In this case the temperature is redefined as

$$T = \frac{\sum_i x_i T_i}{\sigma^m} = \frac{m}{\sigma^m}\sum_i \frac{y_i T_i}{m_i} = \sigma^m \sum_i \frac{T_i}{z_i}. \tag{6.28}$$

The pressure fraction is given by

$$z_i = \frac{T_i y_i}{m_i}\frac{m}{T} = \sigma^m \frac{y_i T_i}{m_i}\frac{1}{\sum_j y_j T_j/m_j}. \tag{6.29}$$

The derivation of the conversion of the gradient is discussed in section 6.B. The result is

$$\partial z_i = z_i \sum_j \left(\delta_{ij} + \frac{1}{\sigma^m}\left(y_j - z_j\right)\right) y_j^{-1}\partial y_j + \frac{z_i}{\sigma^m}\sum_j z_j \partial \ln\frac{T_i}{T_j}. \tag{6.30}$$

In matrix form this equation can be expressed as

$$\begin{aligned} \partial\mathbf{z} &= \tilde{\mathbf{M}}\partial\mathbf{y} + \mathbf{T}\mathbf{z} \\ &= \tilde{\mathbf{M}}\partial\mathbf{y} + \mathbf{T}\tilde{\mathbf{M}}\mathbf{y}, \end{aligned} \tag{6.31}$$

with

$$\begin{aligned}\tilde{\mathbf{M}} &= \mathbf{Z}\left[\mathbf{I} + 1/\sigma^m \mathbf{1}\left(\mathbf{y}-\mathbf{z}\right)^{\mathrm{T}}\right]\mathbf{Y}^{-1} \\ T_{ij} &= \frac{z_e}{\sigma^m}\partial \ln \frac{T_h}{T_e}\left(\sigma_{ij}-\sigma_{ie}\right),\end{aligned} \tag{6.32}$$

with $\mathbf{Z} = \mathrm{diag}\left(\mathbf{z}\right)$ and $\mathbf{Y} = \mathrm{diag}\left(\mathbf{y}\right)$. The matrix $\tilde{\mathbf{M}}$ is the same as the one derived by Peerenboom [6, p. 36] if z_i is replaced by x_i. The matrix $\mathbf{T}$ was obtained by considering a two-temperature plasma. In that case the only non-negative terms in the summation originate from $T_i \neq T_j$. The summation is thus replaced with

$$\frac{z_i}{\sigma^m}\sum_j z_j \partial \ln \frac{T_i}{T_j} = \begin{cases} \frac{z_i}{\sigma^m}\partial \ln \frac{T_h}{T_e} z_e & i \neq e \\ -\frac{z_e}{\sigma^m}\partial \ln \frac{T_h}{T_e}\sum_{j\neq e} z_j & i = e \end{cases} \tag{6.33}$$

Since $\mathbf{1}^{\mathrm{T}}\partial\mathbf{z} = 0$ the matrices $\tilde{\mathbf{M}}$ and $\mathbf{T}$ should satisfy $\mathbf{1}^{\mathrm{T}}\tilde{\mathbf{M}} = \mathbf{1}^{\mathrm{T}}$ and $\mathbf{1}^{\mathrm{T}}\mathbf{T} = \mathbf{0}^{\mathrm{T}}$. From the definition of $\mathbf{T}$ it is apparent that

$$\mathbf{1}^{\mathrm{T}}\mathbf{T} = \mathbf{0}^{\mathrm{T}}, \tag{6.34}$$

which indicates that a gradient in the temperature difference does not influence the validity of $\mathbf{1}^{\mathrm{T}}\partial\mathbf{z} = \mathbf{0}^{\mathrm{T}}$. For $\tilde{\mathbf{M}}$ the proof is given by

$$\begin{aligned}\mathbf{1}^{\mathrm{T}}\tilde{\mathbf{M}} &= \mathbf{z}^{\mathrm{T}}\left[\mathbf{I} + 1/\sigma^m \mathbf{1}\left(\mathbf{y}-\mathbf{z}\right)^{\mathrm{T}}\right]\mathbf{Y}^{-1} \\ &= \left[\mathbf{z}^{\mathrm{T}} + 1/\sigma^m \sigma^m \left(\mathbf{y}-\mathbf{z}\right)^{\mathrm{T}}\right]\mathbf{Y}^{-1} \\ &= \mathbf{y}^{\mathrm{T}}\mathbf{Y}^{-1} = \mathbf{1}^{\mathrm{T}}.\end{aligned} \tag{6.35}$$

Note that if the mixture temperature in (6.28) was not corrected with the factor σ^m the conversion matrix would be given by $\mathbf{M} = \mathbf{z}^{\mathrm{T}}\left[\mathbf{I} - \mathbf{1}\mathbf{z}^{\mathrm{T}}\right]\mathbf{Y}^{-1}$. In that case $\mathbf{1}^{\mathrm{T}}$ is a null vector[2] and $\mathbf{M}$ would be a singular matrix.

6.2.2 Ambipolar diffusion

Previously, only ordinary diffusion was included in the driving forces. For mixtures involving charged species the driving forces should also account for forced diffusion as [6, p. 49-50] [29]

$$\mathbf{d} = \partial\mathbf{z} - \frac{\boldsymbol{\rho}_{\mathbf{c}} E_{\mathrm{ext}}}{p} - \frac{\boldsymbol{\rho}_{\mathbf{c}} E_{\mathrm{amb}}}{p}, \tag{6.36}$$

with $\rho_{c,i} = n_i q_i$, E_{ext} the external electric field and E_{amb} the ambipolar electric field. The diffusive velocities are thus given by

$$\mathbf{v} = -\mathbf{D}\left(\partial\mathbf{z} - \frac{\boldsymbol{\rho}_{\mathbf{c}} E_{\mathrm{ext}}}{p} - \frac{\boldsymbol{\rho}_{\mathbf{c}} E_{\mathrm{amb}}}{p}\right). \tag{6.37}$$

[2] A null vector is obtained when $\mathbf{1}^{\mathrm{T}}\mathbf{M} = \mathbf{0}^{\mathrm{T}}$ is valid.

The diffusive fluxes should now satisfy the additional constraint

$$\begin{aligned} j_{\text{ext}} &= \boldsymbol{\rho_c}^{\mathrm{T}}\mathbf{v} = \sigma E_{\text{ext}} \\ &= -\boldsymbol{\rho_c}^{\mathrm{T}}\mathbf{D}\partial\mathbf{z} + \boldsymbol{\rho_c}^{\mathrm{T}}\mathbf{D}\boldsymbol{\rho_c}\frac{E_{\text{ext}}}{p} + \boldsymbol{\rho_c}^{\mathrm{T}}\mathbf{D}\boldsymbol{\rho_c}\frac{E_{\text{amb}}}{p}, \end{aligned} \tag{6.38}$$

with $\sigma = \boldsymbol{\rho_c}^{\mathrm{T}}\mathbf{D}\boldsymbol{\rho_c}/p$ the electrical conductivity. Therefore the ambipolar field must satisfy

$$\frac{E_{\text{amb}}}{p} = \frac{\boldsymbol{\rho_c}^{\mathrm{T}}\mathbf{D}\partial\mathbf{z}}{\boldsymbol{\rho_c}^{\mathrm{T}}\mathbf{D}\boldsymbol{\rho_c}}. \tag{6.39}$$

Using this relation the diffusive velocities can be rewritten to

$$\begin{aligned} \mathbf{v} &= -\left(\mathbf{D} - \frac{\mathbf{D}\boldsymbol{\rho_c}\boldsymbol{\rho_c}^{\mathrm{T}}\mathbf{D}}{\boldsymbol{\rho_c}^{\mathrm{T}}\mathbf{D}\boldsymbol{\rho_c}}\right)\partial\mathbf{z} + \mathbf{D}\boldsymbol{\rho_c}\frac{E_{\text{ext}}}{p} \\ &= \hat{\mathbf{D}}\partial\mathbf{z} + \mathbf{D}\boldsymbol{\rho_c}\frac{E_{\text{ext}}}{p}, \end{aligned} \tag{6.40}$$

with $\hat{\mathbf{D}}$ the ambipolar diffusion matrix. The ambipolar diffusion matrix is singular, since it is designed to carry no nett current. Left multiplication with $\boldsymbol{\rho_c}^{\mathrm{T}}$ indeed returns the null vector. The matrix should thus be regularized with an additional term. The additional regularization term is given by $\gamma\mathbf{r}\mathbf{r}^{\mathrm{T}}$ with $r_i = q_i/m_i$. The regularization constant is chosen as $\gamma = 10^5\mathbf{r}^{\mathrm{T}}\mathbf{D}\mathbf{r}/\mathbf{r}^{\mathrm{T}}\mathbf{r}^2$. Peerenboom [6, p. 50] wrote the total diffusive mass flux as a function of the mass fractions for a plasma in local thermodynamic equilibrium (LTE). The same formalism is followed to write the diffusive mass flux for plasmas in non-LTE (NLTE) as

$$\mathbf{J} = -\rho\mathbf{Y}\left(\hat{\mathbf{D}}\tilde{\mathbf{M}} - \beta\mathbf{1}\mathbf{1}^{\mathrm{T}} + \gamma\mathbf{r}\mathbf{r}^{\mathrm{T}}\right)\partial\mathbf{y} + \rho\mathbf{Y}\left(\hat{\mathbf{D}}\mathbf{T}\tilde{\mathbf{M}} + \mathbf{D}\boldsymbol{\rho_c}\mathbf{1}^{\mathrm{T}}\frac{E_{\text{ext}}}{p}\right)\mathbf{y}, \tag{6.41}$$

where the dot product $\mathbf{1}^{\mathrm{T}}\mathbf{y}$ has been added. Since the sum of the mass fractions is equal to one the solution is not modified.

6.2.3 Mass and charge conservation

Previously Peerenboom showed that mass and charge are conserved numerically for the LTE system. In this section the prove is extended to the NLTE system. Since parts of the prove overlap a shorter version is given here. Mass and charge are not necessarily conserved in general since $\mathbf{1}\partial\mathbf{y} = 1$ and $\mathbf{r}^{\mathrm{T}}\partial\mathbf{y} = 0$ are not directly enforced. This section will demonstrate that this is a property of the system. The summed mass and charge balances are given by [6, p. 53-54]

$$\begin{aligned} \nabla\cdot(\rho\vec{u}\sigma^m) - \nabla\cdot(\mathcal{D}^m\nabla\sigma^m) &= 0 \\ \nabla\cdot(\rho\vec{u}\sigma^c) - \nabla\cdot(\mathcal{D}^c\nabla\sigma^c) &= 0, \end{aligned} \tag{6.42}$$

with $\mathcal{D}^m = \rho\beta\sigma^m$ and $\mathcal{D}^c = \gamma\boldsymbol{\rho_c}^{\mathrm{T}}\mathbf{r}$. The absence of any sources in these equations implies that σ^m and σ^c are conserved quantities. In other words if $\sigma^m = 1$ and

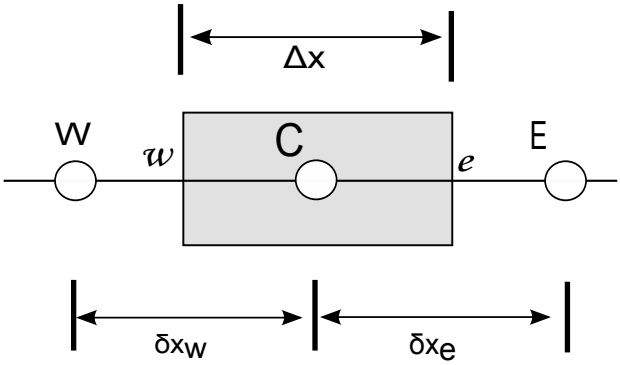

Figure 6.1: Stencil used for discretization. C, W and E denote the central, west and east nodal grid points, respectively. The west and east cell interfaces are denoted by w and e.

$\sigma^c = 0$ are satisfied on any location these conditions are also satisfied anywhere else.

Similar expressions can be obtained for the discretized equations. For the grid shown in figure 6.1 the discrete equation for the mass fraction vector is given by

$$\mathbf{A}_C \mathbf{y}_C = \mathbf{A}_W \mathbf{y}_W + \mathbf{A}_E \mathbf{y}_E + \mathbf{s}_C \Delta x, \tag{6.43}$$

with capital subscripts indicating nodal points and the letters w and e are used to represent points on a boundary. In practice the system is ill-conditioned. For that reason the following pre-conditioning step is used [6, p. 27-28]

$$\mathbf{RACC}^{-1}\mathbf{x} = \mathbf{Rb} \qquad \leftrightarrow \qquad \tilde{\mathbf{A}}\tilde{\mathbf{x}} = \tilde{\mathbf{b}}, \tag{6.44}$$

with $\tilde{\mathbf{A}} = \mathbf{RAC}$, $\mathbf{C} = \operatorname{diag}(m_i/m_{\mathrm{H}})$, m_{H} the mass of a hydrogen atom and $\mathbf{R} = \operatorname{diag}(1/(AC)_{ii})$. The matrix $\mathbf{C}^{-1}$ can be considered as a correction for the differences between the mass of the heavy particles and the mass of the electron. For the exponential scheme the discretization matrices are given by Peerenboom as [6, p. 19-21]

$$\mathbf{A}_W = \frac{1}{\delta x_w} \mathbf{\Gamma}_w B(-\mathbf{P}_w) \tag{6.45}$$

$$\mathbf{A}_E = \frac{1}{\delta x_e} \mathbf{\Gamma}_e B(\mathbf{P}_e) \tag{6.46}$$

$$\mathbf{A}_C = \mathbf{A}_W + \mathbf{A}_E, \tag{6.47}$$

with the flux diffusion matrix $\mathbf{\Gamma}_x = \rho \mathbf{Y}_x \hat{\mathbf{D}}_x \tilde{\mathbf{M}}_x$, subscript x indicating either w or e, $\mathbf{P}_x = \rho u_x \mathbf{\Gamma}_x^{-1} / \delta x_x$ the Peclet matrix and $B(\mathbf{P})$ the Bernoulli function[3]. Discrete mass and charge conservation are satisfied if $\mathbf{1}^{\mathrm{T}}$ and $\mathbf{r}^{\mathrm{T}}$ are left eigenvectors

[3] The scalar Bernoulli function is given by $B(z) = \frac{z}{\exp z - 1}$. By diagonalization of the Peclet matrix the scalar function can be applied to the eigenvalues on the diagonal.

of the discretized system. Peerenboom [6, p. 40-42] used $\mathbf{P} \propto \mathbf{\Gamma}^{-1}$ to show that an eigenvector of $\mathbf{\Gamma}$ is also an eigenvector of $\mathbf{P}$. Additionally, a matrix containing the eigenvectors of $\mathbf{P}$ appears in the diagonalization process of $B(\mathbf{P})$. Thus an eigenvector of $\mathbf{P}$ is also an eigenvector of $B(\mathbf{P})$. Using these statements a multiplication of 6.43 with $\mathbf{1}^{\mathrm{T}}$ gives

$$a_C^m \sigma^m = a_E^m \sigma^m + a_W^m \sigma^m, \tag{6.48}$$

with a_x^m discretization coefficients. Since $a_C^m = a_E^m + a_W^m$ and $a_x^m > 0$ this is an interpolation. On the wall $\sigma^m = 1$ is satisfied. Applying the discrete maximum principle shows that σ^m is valid on all grid points. A similar procedure can be followed to demonstrate this property for charge conservation. The flux diffusion matrix has the eigenvector $\mathbf{1}^{\mathrm{T}}$ based on

$$\begin{aligned} \mathbf{1}^{\mathrm{T}}\mathbf{\Gamma} &= \mathbf{1}^{\mathrm{T}}\rho\mathbf{Y}\left(\hat{\mathbf{D}}\tilde{\mathbf{M}} - \beta\mathbf{1}\mathbf{1}^{\mathrm{T}} + \gamma\mathbf{r}\mathbf{r}^{\mathrm{T}}\right) \\ &= \rho\mathbf{y}^{\mathrm{T}}\left(\hat{\mathbf{D}}\tilde{\mathbf{M}} - \beta\mathbf{1}\mathbf{1}^{\mathrm{T}} + \gamma\mathbf{r}\mathbf{r}^{\mathrm{T}}\right) \\ &= \rho\mathbf{y}^{\mathrm{T}}\hat{\mathbf{D}}\tilde{\mathbf{M}} + \rho\beta\sigma^m\mathbf{1}^{\mathrm{T}} + \gamma\rho\sigma^c\mathbf{r}^{\mathrm{T}} = \beta\sigma^m\mathbf{1}^{\mathrm{T}}. \end{aligned} \tag{6.49}$$

The eigenvector corresponding to charge conservation can be derived as

$$\begin{aligned} \mathbf{r}^{\mathrm{T}}\mathbf{\Gamma} &= \mathbf{r}^{\mathrm{T}}\rho\mathbf{Y}\left(\hat{\mathbf{D}}\tilde{\mathbf{M}} - \beta\mathbf{1}\mathbf{1}^{\mathrm{T}} + \gamma\mathbf{r}\mathbf{r}^{\mathrm{T}}\right) \\ &= \boldsymbol{\rho}_{\mathbf{c}}{}^{\mathrm{T}}\left(\hat{\mathbf{D}}\tilde{\mathbf{M}} - \beta\mathbf{1}\mathbf{1}^{\mathrm{T}} + \gamma\mathbf{r}\mathbf{r}^{\mathrm{T}}\right) \\ &= \boldsymbol{\rho}_{\mathbf{c}}{}^{\mathrm{T}}\hat{\mathbf{D}}\tilde{\mathbf{M}} - \beta\rho\sigma^c\mathbf{1}^{\mathrm{T}} + \gamma\boldsymbol{\rho}_{\mathbf{c}}{}^{\mathrm{T}}\mathbf{r}\mathbf{r}^{\mathrm{T}} = \gamma\boldsymbol{\rho}_{\mathbf{c}}{}^{\mathrm{T}}\mathbf{r}\mathbf{r}^{\mathrm{T}}. \end{aligned} \tag{6.50}$$

Both derivations use charge conservation in the last step. In practice charge is not conserved perfectly due to the finite precision. It is observed that the term proportional to σ^c in both derivations is the smallest of the three listed terms. Relatively the terms are much smaller than 10^{-16} in comparison to $\rho\beta\sigma^m\mathbf{1}^{\mathrm{T}}$ and $\gamma\boldsymbol{\rho}_{\mathbf{c}}{}^{\mathrm{T}}\mathbf{r}\mathbf{r}^{\mathrm{T}}$. Using charge conservation in the derivation is thus also allowed numerically. The term $\rho\mathbf{y}^{\mathrm{T}}\hat{\mathbf{D}}\mathbf{M}^{\mathrm{T}}$ can reach a relative contribution in the range of 10^{-10}- 10^{-12} and therefore does not vanish numerically. Additionally, the relative contribution of $\boldsymbol{\rho}_{\mathbf{c}}{}^{\mathrm{T}}\hat{\mathbf{D}}\mathbf{M}$ is in the order of 10^{-16}. These contributions are random and therefore are expected to add a net contribution of zero over many iterations. However, the consequence of these terms not being smaller than 10^{-16} is that mass and charge conservation is not satisfied up to 10^{-16}.

6.3 Diffusive mass fluxes

The previously presented approach can become numerically unstable in the limit of vanishing mass fractions. This is caused by the fact that the elements of F_{ij} are proportional to $x_i x_j$. If the density of species i approaches zero, the product $x_i x_j$ vanishes as well. The matrix $\mathbf{F}$ as well as the regularization term $\alpha\mathbf{y}\mathbf{y}^{\mathrm{T}}$ then both contain a row and a column with only zeros. The matrix is thus singular and

cannot be regularized. Giovangigli [129, p. 256] suggested to rewrite the system to

$$\left(\tilde{\mathbf{F}}\rho^{-1}\mathbf{Y}^{-1}\right)(\rho\mathbf{Y}\mathbf{v}) \equiv \tilde{\mathbf{H}}\mathbf{J} = -\mathbf{d}. \tag{6.51}$$

The elements of the non-regularized matrix $\mathbf{H}$ can then be derived from $\mathbf{F}\rho\mathbf{Y}^{-1}$ and are given by

$$H_{ij} = \begin{cases} -\frac{m}{m_j}\frac{x_i}{\rho D_{ij}} & i \neq j \\ \sum_{l\neq j}\frac{m}{m_j}\frac{x_l}{\rho D_{lj}} & i = j \end{cases}. \tag{6.52}$$

The matrix elements using this alternative formulation are now only dependent on a single molar fraction. In the event of a vanishing species only a single matrix element will be equal to zero rather than an entire row or column.

The mass fluxes can be obtained from the system

$$\mathbf{J} = -\tilde{\mathbf{L}}\mathbf{d}. \tag{6.53}$$

Since the matrix $\mathbf{H}$ is singular, a regularization procedure is required again to obtain $\mathbf{L}$. From the properties $\mathbf{L} = \rho\mathbf{Y}\mathbf{D}$ and $\mathbf{H} = \mathbf{F}\rho^{-1}\mathbf{Y}^{-1}$ it is apparent that the left null space of both $\mathbf{H}$ and $\mathbf{L}$ is $\mathbf{1}^{\mathrm{T}}$ and the right null space is $\mathbf{y}$. The regularized matrices are thus given by [129, p. 258]

$$\tilde{\mathbf{H}} = \mathbf{H} + \alpha\mathbf{y}\mathbf{1}^{\mathrm{T}} \tag{6.54}$$

$$\tilde{\mathbf{L}} = \mathbf{L} + \beta\mathbf{y}\mathbf{1}^{\mathrm{T}}. \tag{6.55}$$

The regularization constants are related to each other via

$$\tilde{\mathbf{H}}\tilde{\mathbf{L}} = \mathbf{I} - \mathbf{y}\mathbf{1}^{\mathrm{T}}/\mathbf{y}^{\mathrm{T}}\mathbf{1} + \alpha\beta\mathbf{y}\mathbf{1}^{\mathrm{T}}\mathbf{y}^{\mathrm{T}}\mathbf{1}. \tag{6.56}$$

The matrices $\tilde{\mathbf{H}}$ and $\tilde{\mathbf{L}}$ are thus true inverses of each other when $\beta = 1/\left(\alpha\left(\mathbf{y}^{\mathrm{T}}\mathbf{1}\right)^2\right)$. An appropriate choice for the regularization constant is $\alpha = 1/\left[\rho\max\left(D_{ij}\right)\right]$.

If the mixture contains charged species a correction for the ambipolar field must be taken into account. The current is obtained from

$$\begin{aligned} j_{\mathrm{ext}} &= \mathbf{r}^{\mathrm{T}}\mathbf{J} = \sigma E_{\mathrm{ext}} \\ &= -\mathbf{r}^{\mathrm{T}}\mathbf{L}\partial\mathbf{z} + \mathbf{r}^{\mathrm{T}}\mathbf{L}\boldsymbol{\rho}_{\mathbf{c}}\frac{E_{\mathrm{ext}}}{p} + \mathbf{r}^{\mathrm{T}}\mathbf{L}\boldsymbol{\rho}_{\mathbf{c}}\frac{E_{\mathrm{amb}}}{p}, \end{aligned} \tag{6.57}$$

therefore the ambipolar field is given by

$$\frac{E_{\mathrm{amb}}}{p} = \frac{\mathbf{r}^{\mathrm{T}}\mathbf{L}\partial\mathbf{z}}{\mathbf{r}^{\mathrm{T}}\mathbf{L}\boldsymbol{\rho}_{\mathbf{c}}}. \tag{6.58}$$

This choice introduces another singularity in

$$\hat{\mathbf{L}} = \left(\mathbf{L} - \frac{\mathbf{L}\boldsymbol{\rho}_{\mathbf{c}}\mathbf{r}^{\mathrm{T}}\mathbf{L}}{\mathbf{r}^{\mathrm{T}}\mathbf{L}\boldsymbol{\rho}_{\mathbf{c}}}\right). \tag{6.59}$$

The singularity can be removed by regularizing with $\gamma\boldsymbol{\rho_c}\mathbf{r}^{\mathrm{T}}$. The regularized mass flux can therefore be expressed as

$$\mathbf{J} = \left(\hat{\mathbf{L}}\tilde{\mathbf{M}} - \beta\mathbf{y}\mathbf{1}^{\mathrm{T}} + \gamma\boldsymbol{\rho_c}\mathbf{r}^{\mathrm{T}}\right)\partial\mathbf{y} + \left(\hat{\mathbf{L}}\mathbf{T}\tilde{\mathbf{M}} + \mathbf{L}\boldsymbol{\rho_c}\mathbf{1}^{\mathrm{T}}\frac{E_{\mathrm{ext}}}{p}\right)\mathbf{y}. \tag{6.60}$$

Using this formulation mass and charge conservation can also be proven for the matrix $\boldsymbol{\Gamma} = \hat{\mathbf{L}}\tilde{\mathbf{M}}$. By following a similar strategy as in section 6.2.3 the only proof that should be delivered is that $\mathbf{1}^{\mathrm{T}}$ and $\mathbf{r}^{\mathrm{T}}$ are left eigenvectors of $\boldsymbol{\Gamma}$. Mass conservation is obtained from

$$\begin{aligned}\mathbf{1}^{\mathrm{T}}\boldsymbol{\Gamma} &= \mathbf{1}^{\mathrm{T}}\left(\hat{\mathbf{L}}\tilde{\mathbf{M}} - \beta\mathbf{y}\mathbf{1}^{\mathrm{T}} + \gamma\boldsymbol{\rho_c}\mathbf{r}^{\mathrm{T}}\right)\\ &= \mathbf{1}^{\mathrm{T}}\hat{\mathbf{L}}\tilde{\mathbf{M}} - \beta\sigma^m\mathbf{1}^{\mathrm{T}} + \gamma\rho\sigma^c\mathbf{r}^{\mathrm{T}} = -\beta\sigma^m\mathbf{1}^{\mathrm{T}}.\end{aligned} \tag{6.61}$$

Similarly charge conservation is derived from

$$\begin{aligned}\mathbf{r}^{\mathrm{T}}\boldsymbol{\Gamma} &= \mathbf{r}^{\mathrm{T}}\left(\hat{\mathbf{L}}\tilde{\mathbf{M}} - \beta\mathbf{y}\mathbf{1}^{\mathrm{T}} + \gamma\boldsymbol{\rho_c}\mathbf{r}^{\mathrm{T}}\right)\\ &= \mathbf{r}^{\mathrm{T}}\hat{\mathbf{L}}\tilde{\mathbf{M}} - \beta\sigma^c\mathbf{1}^{\mathrm{T}} + \gamma\mathbf{r}^{\mathrm{T}}\boldsymbol{\rho_c}\mathbf{r}^{\mathrm{T}} = \gamma\mathbf{r}^{\mathrm{T}}\boldsymbol{\rho_c}\mathbf{r}^{\mathrm{T}}\end{aligned} \tag{6.62}$$

6.4 Numerical oscillations

The algorithm presented in the previous sections contains a few favorable properties, like the accurate conservation of mass and charge. However, experiments in 1D and 2D models reveal that the algorithm is not stable. In order to investigate the observed numerical instabilities a simplified 1D system is considered. The considered system neglects the bulk flow, time variations and reactions. It can be described by

$$\nabla \cdot \rho y_i \vec{v}_{d,i} = 0. \tag{6.63}$$

Dirichlet boundary conditions are used on both sides of the Cartesian grid. For such a system the following observations are made:

- In neutral mixtures the instability does not occur.
- In charged mixtures at least two ions and an electron are required to see the oscillation.

Two systems are investigated. The first system that is investigated contains the following species Ar, Ar^+ and e. The ion is implemented twice with exactly the same specifications. The second system contains H, H^+, Ar, Ar^+ and e. The considered boundary conditions for these two systems are given in table 6.1. Intermediate results of simulations that are diverging are given in figure 6.2 and 6.3. Initially the simulations seem to converge. However, from a given iteration oscillations start to appear. These oscillations typically continue to grow until they violate $0 \leq y \leq 1$. For the 4 species Ar mixture this is shown in figure 6.4. The difference between the Ar ions suddenly increases while the mass and charge conservation remain accurate. The condition number of the system matrix also

Table 6.1: The boundary conditions that have been considered on the left (y_l) and right (y_r) sides of the grid for the Ar and the Ar-H systems. The boundary condition for the electrons is not mentioned, because all boundary conditions are automatically modified to satisfy mass and charge conservation.

	y_l	y_r		y_l	y_r
Ar	0.8	0.6	H	0.2	0.4
Ar^+	0.1	0.2	H^+	0.25	0.05
Ar^+	0.1	0.2	Ar	0.35	0.45
			Ar^+	0.2	0.1

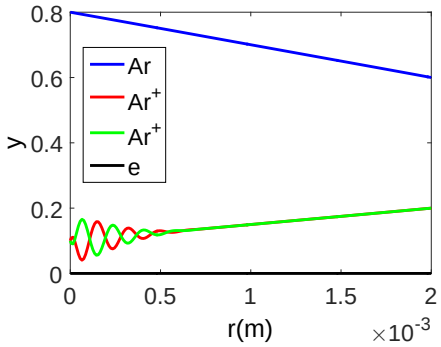

Figure 6.2: A diverging simulation for a mixture containing Ar, two species of Ar^+ and an electron. The pressure is 10^{-2} Pa and the number of grid points is 200. Basic collision integrals (rigid sphere and Coulomb models) were used to obtain this result.

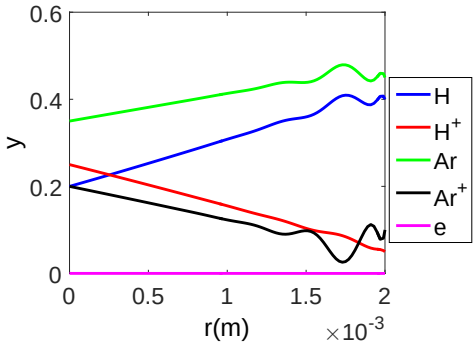

Figure 6.3: A diverging simulation for a mixture containing H, H^+, Ar, Ar^+ and an electron. The pressure is 80 Pa and the number of grid points is 100.

remains stable at the initial stages of the instability. It is unclear what is causing these oscillations. The oscillations can be prevented by applying under-relaxation. In the ideal case an alternative solution can be found that does not increase the calculation time. In figure 6.5 the under-relaxation factor has been reduced and the spatial accuracy of mass and charge conservation is shown. The figure shows that mass and charge are conserved up to 5×10^{-14} and 5×10^{-12}, respectively. However, the mass and charge fluxes show maximum errors in the order of 10^{-8} and 10^{-9}. In the next sections the influence of the transport coefficients, the number of grid points, the interpolation, the formulation of the diffusive fluxes and the regularization procedure are investigated.

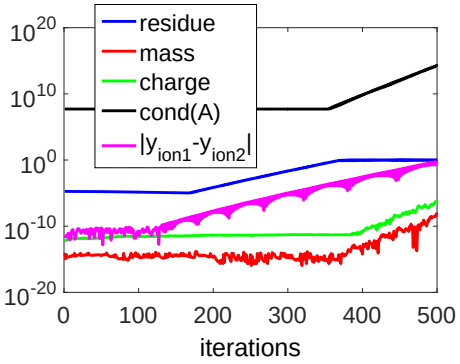

Figure 6.4: For a grid containing 100 points and a gas pressure of 10^2 the evolution of the residue of the mass fractions; mass and charge conservation; the condition number of the system matrix ($\mathbf{Ay} = \mathbf{b}$); and the difference between the ion mass fractions are logged as a function of the iteration number.

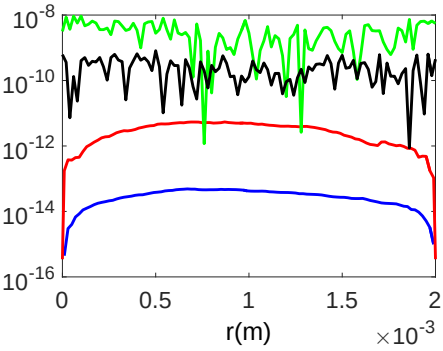

Figure 6.5: By reducing the urf to 0.8 and using the conditions as described in 6.4 a converged simulation is obtained. The accuracy of the mass ($|1 - \sum_i y_i|$, ▬) and charge constraints ($|\sum_i y_i q_i/m_i|/|\sum_{q<0} y_i q_i/m_i|$, ▬) as well as the mass ($|\sum_i y_i v_i|/|\sum_{v_i<0} y_i v_i|$, ▬) and charge ($|\sum_i y_i q_i/m_i v_i|/|\sum_{q_i v_i<0} y_i q_i/m_i v_i|$, ▬) flux are shown.

6.4.1 Pressure and collision integrals

Originally the system was investigated using PLASIMO's basic collision integrals. These are the rigid sphere, Coulomb and Langevin models. Currently more accurate collision integrals are available. It is observed that using the improved collision integrals the models are more stable. In principle both sets of collision integrals provide a valid mathematical system of equations. The fact that one set converges and the other diverges indicates that the solution procedure is not robust. The improved stability is illustrated in table 6.2 where the condition number of the local diffusive flux matrix and the system matrix are given as a function of pressure for the H-Ar mixture. These values have been obtained in the first iteration after initializing the system linearly. The table shows that for decreasing pressures the condition numbers increase. All of the listed simulations using the new collision integral defaults converge. Additionally, all calculations using the old collision integral defaults display larger condition numbers than the improved collision integral defaults. None of the tabulated simulations using the old collision integral defaults converge. The condition number does not decrease further for higher pressures using the old defaults.

A comparison between the numerical values of the collision integrals of both sets is given in table 6.3. Interestingly most collision integrals only differ in the

Table 6.2: The maximum condition number of the spatially dependent diffusive flux matrix is listed. Additionally, the condition number of the full system is listed ($\tilde{\mathbf{A}}\mathbf{y} = \tilde{\mathbf{b}}$). Both quantities are tabulated as a function of pressure for the old and the improved set of collision integrals. The number of grid points is 200 and the urf is set to 0.9. A constant temperature of 5000 K is used. The H-Ar system is initialized linearly and the condition numbers are obtained in the first iteration.

	CI New		CI old	
p(Pa)	cond ($\mathbf{\Gamma}$)	cond($\tilde{\mathbf{A}}$)	cond ($\mathbf{\Gamma}$)	cond($\tilde{\mathbf{A}}$)
10	2.88×10^5	1.21×10^8	3.64×10^6	2.68×10^8
10^2	2.32×10^5	9.15×10^7	3.04×10^6	2.18×10^8
10^3	1.76×10^5	6.24×10^7	2.44×10^6	1.67×10^8
10^4	1.23×10^5	3.71×10^7	1.85×10^6	1.19×10^8
10^5	7.81×10^4	1.81×10^7	1.27×10^6	7.42×10^7
10^8	2.16×10^4	2.42×10^6	6.13×10^5	4.41×10^7

order of a factor 3-4 or less. The only exception is the H–H^+ interaction which is significantly larger. This is related to neglecting the contribution from resonant charge exchange in the old default. By including charge exchange in the old default the collision integral is modified to $2.80 \times 10^{-15}\,\mathrm{m^3/s}$. The ratio New/old is than modified to 1.19. This modification reduces the condition numbers and guarantees a stable simulation for $p \geq 100\,\mathrm{Pa}$. The reduced condition numbers may be responsible for the stabilized simulation. Alternatively, modifying the pressure or the collision integrals is equivalent to modifying the diffusion coefficients. The charged-charged collision integrals depend on the pressure via the Debye length while collision integrals of other interaction types are independent of the pressure. Decreasing the pressure increases the Debye length and therefore increases the charged-charged collision integral. The result is that the binary diffusion coefficient for charged-charged interactions is increasing at a lower rate for decreasing pressures than diffusion coefficients for other types of processes. The effect is that the gradient of the ions is changed. In the H-Ar mixture decreasing the pressure has the effect of increasing the gradients of the ions. Discretization errors may therefore be emphasized. Additionally, the discretization scheme is set up to conserve mass and charge, however, there are no limitations set up for the individual mass fractions. Therefore the scheme does not guarantee that these oscillations can not occur. Possibly the mass flux must be limited in a similar way the source terms are limited using source term linearization [6, p. 21-26].

6.4.2 Grid size and interpolation

The pressure variation could be interpreted as a modification of the solution. Modified gradients of the mass fractions may require a different level of discretization. In this section the effect of the grid size and the interpolation from the nodal points to the interfaces are discussed.

One of the effects of the pressure variation that was not discussed previously

Table 6.3: The collision integrals using the new and the old defaults at 5000 K a pressure of 100 Pa and the mass fractions corresponding to the right boundary in table 6.1.

Interaction	CI New(m^3/s)	CI Old (m^3/s)	New/Old
H–H^+	3.3366e-15	2.4267e-16	13.75
H–Ar	5.0126e-16	5.0126e-16	1.00
H–Ar^+	1.6752e-16	5.0126e-16	0.33
H–e	2.7260e-14	7.0938e-15	3.84
H^+–Ar	2.2452e-16	5.0139e-16	0.45
H^+–Ar^+	1.8836e-13	5.0494e-13	0.37
H^+–e	8.2526e-12	2.1376e-11	0.39
Ar–Ar^+	6.7230e-16	2.2150e-16	3.04
Ar–e	1.9465e-15	1.9465e-15	1.00
Ar^+–e	8.2504e-12	2.1371e-11	0.39

is the stability. By continuously decreasing the pressure eventually the H-Ar and the Ar simulation are getting unstable. The effect of the variation of the number of grid points, n, on the lowest pressure for which a stable result can be obtained is given in table 6.4. The table shows that for increasing n more conditions are stable. In all cases the new collision integral defaults provide a stable result in a larger pressure range. The increased stability observed in table 6.4 can possibly be attributed to a more accurate interpolation due to the finer meshes.

One of the main concerns in the current discretization scheme is the interpolation of the matrix $\mathbf{\Gamma}$ from the nodal points to the interfaces. Currently the mass fractions on the nodal points are used to calculate $\mathbf{\Gamma}$. The matrix on the interface is then obtained from a linear interpolation from the calculated matrices on the nodal points. Such a procedure can be inaccurate since the matrices depend non-linearly on the mass fractions. A good alternative however is not readily available. One possibility is the usage of harmonic interpolation. For matrices it is given by

$$\mathbf{\Gamma}_{1/2} = 2\left(\mathbf{\Gamma}_0^{-1} + \mathbf{\Gamma}_1^{-1}\right)^{-1}. \tag{6.64}$$

Alternatively the mass fractions are linearly or cubically interpolated to the interfaces. The interpolated mass fractions can then be used to calculate the diffusive flux matrix locally. An interesting test case is provided by the Ar mixture. The mass fractions of the atom and the ions are almost linear. In such a case interpolating the mass fractions cubically is expected to be a very accurate method. The test is carried out with $n = 100$, $r = 2 \times 10^{-3}$ m, urf=0.9 and the old collision integral defaults. No difference in the condition number of the system matrix could be observed between the four discussed interpolation methods. Additionally, all four methods are unstable at $p = 10^2$ Pa and stable at $p = 2 \times 10^2$ Pa. Note that the solution of the Ar system does not depend on the pressure or the collision integrals. The interpolation towards the interfaces is therefore not expected to be the cause of the oscillations. The presence of such oscillations is not forbidden by

Table 6.4: The variation of the lowest pressure for which a stable result can be obtained as a function of the number of grid points n.

	Ar CI new	Ar CI old	H-Ar CI new	H-Ar CI old
n	p(Pa)	p(Pa)	p(Pa)	p(Pa)
40	1×10^{-2}	4×10^{5}	2×10^{4}	unstable
100	1×10^{-10}	2×10^{2}	9×10^{1}	unstable
200	1×10^{-10}	3×10^{-2}	1×10^{-1}	unstable
700	1×10^{-10}	3×10^{-2}	1×10^{-1}	1×10^{5}

the coupled exponential scheme. This can be understood from

$$\begin{aligned} \mathbf{y}_C &= \mathbf{A}_C^{-1}\left(\mathbf{A}_W\mathbf{y}_W + \mathbf{A}_E\mathbf{y}_E + \mathbf{s}_C\Delta x\right) && (6.65)\\ &= \left(\mathbf{I} + \mathbf{A}_W^{-1}\mathbf{A}_E\right)^{-1}\mathbf{y}_W + \left(\mathbf{I} + \mathbf{A}_E^{-1}\mathbf{A}_W\right)^{-1}\mathbf{y}_E + \mathbf{A}_C^{-1}\mathbf{s}_C\Delta x, && (6.66)\end{aligned}$$

with $\mathbf{A}_C = \mathbf{A}_W + \mathbf{A}_E$. Even in the absence of any sources it is not guaranteed that $y_{W,i} \leq y_{C,i} \leq y_{E,i}$ or $y_{E,i} \leq y_{C,i} \leq y_{W,i}$ always holds, since $\mathbf{A}_W$ and $\mathbf{A}_E$ have non-zero off-diagonal elements. Note that the sum of the mass fractions still remains an interpolation. However, when there is no flow and the number of grid points is increased the approximation $\mathbf{A}_W \approx \mathbf{A}_E$ is more accurate and (6.65) approaches the interpolating function $\mathbf{y}_C = \frac{1}{2}\mathbf{y}_W + \frac{1}{2}\mathbf{y}_E$. Adding more grid points can possibly act as a restriction on the non-linear behavior of the diffusive flux matrices.

6.4.3 Alternative formulations and regularizations

The calculations in the previous sections all used the formalism based on the diffusive velocities. The effect of the stability on the system of the description based on the diffusive mass fluxes is investigated. Alternatively the system is set up in terms of the mole fractions. Another option is to reduce the dimension of the system of equations. Additionally, a few regularization strategies are considered.

In terms of mole fractions the equations (6.6) and (6.7) are still valid. In matrix form the total mass is then given by

$$\begin{aligned} \mathbf{1}^{\mathrm{T}}\boldsymbol{\Gamma} &= \mathbf{1}^{\mathrm{T}}\rho\mathbf{Y}\left(\hat{\mathbf{D}} + \beta\mathbf{1}\mathbf{1}^{\mathrm{T}} + \gamma\mathbf{r}\mathbf{q}^{\mathrm{T}}\right)\\ &= \rho\mathbf{y}^{\mathrm{T}}\hat{\mathbf{D}} + \rho\beta\sigma^m\mathbf{1}^{\mathrm{T}} + \gamma\sigma_z^c\mathbf{q}^{\mathrm{T}} = \rho\beta\sigma^m\mathbf{1}^{\mathrm{T}}, && (6.67)\end{aligned}$$

and the total charge is given by

$$\begin{aligned} \mathbf{r}^{\mathrm{T}}\boldsymbol{\Gamma} &= \mathbf{r}^{\mathrm{T}}\rho\mathbf{Y}\left(\hat{\mathbf{D}} + \beta\mathbf{1}\mathbf{1}^{\mathrm{T}} + \gamma\mathbf{r}\mathbf{q}^{\mathrm{T}}\right)\\ &= \boldsymbol{\rho}_{\mathbf{c}}{}^{\mathrm{T}}\hat{\mathbf{D}} + \beta\sigma_z^c\mathbf{1}^{\mathrm{T}} + \gamma\boldsymbol{\rho}_{\mathbf{c}}{}^{\mathrm{T}}\mathbf{r}\mathbf{q}^{\mathrm{T}} = \gamma\boldsymbol{\rho}_{\mathbf{c}}{}^{\mathrm{T}}\mathbf{r}\mathbf{q}^{\mathrm{T}}, && (6.68)\end{aligned}$$

with $\sigma_z^c = \sum_i n_i q_i = \rho\sigma^c$. Multiplication with the gradient of the pressure fractions reveals the desired conserved properties. Note that when using pressure

fractions charge conservation is only guaranteed for a single temperature mixture as shown in appendix 6.C.

The previous implementations in PLASIMO considered a reduced system of equations. The reduction was achieved by applying mass and charge conservation explicitly. The most important drawback of such a procedure is the slow convergence rate as was already observed by Janssen [130, p. 51]. In spite of these remarks, later versions of the implementation of self-consistent diffusion in PLASIMO, see for example Hartgers [131, p. 85,86] still applied the mass and charge constraint explicitly. The electron flux can be dealt with analytically by expressing it in terms of the other species. The sum of all charges is given by

$$\mathbf{r}^{\mathrm{T}}\mathbf{J} = \sum_i r_i \left(\Gamma_{ie}\nabla y_e + \sum_{j\neq e} r_i \Gamma_{ij} \nabla y_j \right). \tag{6.69}$$

The gradient of the electron species is then given by

$$\nabla y_e = \frac{-1}{\sum_i r_i \Gamma_{ie}} \sum_i \sum_{j\neq e} r_i \Gamma_{ij} \nabla y_j. \tag{6.70}$$

The matrix elements of the reduced system are then given by

$$\Gamma^*_{ij} = \Gamma_{ij} - \Gamma_{ie} \frac{\sum_k r_k \Gamma_{kj}}{\sum_k r_k \Gamma_{ke}} \qquad i \neq e \quad j \neq e, \tag{6.71}$$

where the electrons are included in k. The reduced system can be regularized with

$$\tilde{\mathbf{\Gamma}}^* = \Gamma^* + \beta \mathbf{1}_n \mathbf{1}_n^{\mathrm{T}}, \tag{6.72}$$

with $u_{n,i} = 1 - \frac{q_i}{q_e}\frac{m_e}{m_i}$. Application of this vector to the non regularized system gives $\mathbf{1}_n^{\mathrm{T}} \mathbf{\Gamma} \nabla \mathbf{y} = -\mathbf{J}_e - m_e/q_e \mathbf{j}_e = 0$. The system can be reduced further by applying mass conservation on neutral species m. Mass conservation is given by

$$\begin{aligned}
\mathbf{1}^{\mathrm{T}}\mathbf{J} &= \sum_i \left(\Gamma_{ie}\nabla y_e + \Gamma_{im}\nabla y_m + \sum_{j\neq e,m} \Gamma_{ij}\nabla y_j \right) \\
&= \sum_i \left(-\Gamma_{ie} \frac{\sum_{j\neq e} r_i \Gamma_{ij}}{\sum_k r_i \Gamma_{ke}} \nabla y_j + \Gamma_{im}\nabla y_m + \sum_{j\neq e,m} \Gamma_{ij}\nabla y_j \right) \\
&= \sum_i \left(\left[\Gamma_{im} - \Gamma_{ie} \frac{\sum_k r_k \Gamma_{km}}{\sum_k r_k \Gamma_{ie}} \right] \nabla y_m + \right. \\
&\qquad \left. \sum_{j\neq e,m} \left[\Gamma_{ij} - \Gamma_{ie} \frac{\sum_k r_k \Gamma_{kj}}{\sum_k r_k \Gamma_{ke}} \right] \nabla y_j \right),
\end{aligned} \tag{6.73}$$

with i and j not equal to m and e. By introducing $s_j = \sum_k \Gamma_{kj}$ and $w_j = \sum_k r_k \Gamma_{kj}$ the gradient can be written as

$$\nabla y_m = -\frac{s_j - s_e w_j/w_e}{s_m - s_e w_m/w_e} \nabla y_j. \tag{6.74}$$

Table 6.5: The condition numbers of the diffusive flux matrix and the system matrix are shown for the Ar mixture. The following settings are used: $r = 22 \times 10^{-3}$, urf=0.9, $n = 100$ and the old collision integral defaults are used. The reported values are obtained in the first iteration.

method	p(Pa)	cond ($\mathbf{\Gamma}$)	cond($\tilde{\mathbf{A}}$)
Fv (6.41)	100	3.41×10^8	2.11×10^7
Fv (6.41)	200	3.23×10^8	1.87×10^7
HJ (6.60)	100	4.31×10^9	1.01×10^8
HJ (6.60)	200	4.30×10^9	9.41×10^7
Fv in **z** (6.67)	100	7.96×10^4	6.18×10^5
Fv in **z** (6.67)	200	7.42×10^4	5.76×10^5
$\mathbf{\Gamma}^*$ (6.71)	100	8.98×10^6	1.52×10^8
$\mathbf{\Gamma}^*$ (6.71)	200	8.98×10^6	1.52×10^8
$\mathbf{\Gamma}^{**}$ (6.75)	100	1.15×10^7	2.14×10^8
$\mathbf{\Gamma}^{**}$ (6.75)	200	1.08×10^7	2.00×10^8

The matrix elements of the doubly reduced system can then be expressed as

$$\Gamma^{**}_{ij} = \Gamma_{ij} - \Gamma_{ie} w_j / w_e - (\Gamma_{im} - \Gamma_{me} w_m / w_e) \frac{s_j - s_e w_j / w_e}{s_m - s_e w_m / w_e}. \tag{6.75}$$

A comparison of the various formulations is given in table 6.5. The table shows the condition numbers that are observed in the first iteration using the same initialization. The results are reported at two different pressures. All simulations at 100 Pa do not converge. There is only one simulation that does not converge at 200 Pa. This model uses $\mathbf{\Gamma}^{**}$(6.75). Additionally, the model $\mathbf{\Gamma}^*$ (6.71) can not reduce the residue to values lower than 10^{-8} while the other converging models at least obtain 10^{-10}. These results are a confirmation that applying the charge or the charge and mass constraint analytically leads to large numerical errors. For these models the condition number of the system matrix indeed reports the largest values. Interestingly the condition number of $\mathbf{\Gamma}$ is larger for the methods based on **Fv** and **HJ**. This indicates that the condition number of $\mathbf{\Gamma}$ is not a direct predictor of the stability of the model. The condition numbers using **HJ** are larger in comparison with **Fv**. In the absence of vanishing mass fractions it seems to be beneficial to use **Fv**. The lowest values of the condition number of the system matrix are obtained using a description that does not convert the pressure fractions to the mass fractions. A possible advantage of such a method is the absence of a mismatch in the fractions between the electrons and the heavy particles which can be induced by the difference in the mass. Using the pressure fractions the condition number of the system matrix for a case that is not working is in the order of 10^5 while the condition number using **HJ** almost reaches 1×10^8 for a case that is working. This suggests that the condition number of the system matrix is also not a direct indicator for stability.

The method chosen for the regularization can also influence the stability of the model. Two cases are investigated for the charge regularization. The first one

Table 6.6: The condition numbers of the various regularization strategies. The values are obtained in the first iteration using the same initialization. The HAr mixture uses the new CI default while the Ar results use the old CI defaults. The remaining settings are $r = 22 \times 10^{-3}$, urf=0.9, $n = 100$.

mixture	p(Pa)	method	cond $(\mathbf{\Gamma})$	cond$(\tilde{\mathbf{A}})$
Ar	100	γ_1	3.41×10^8	2.28×10^7
Ar	100	γ_2	1.00×10^9	5.08×10^7
H-Ar	5000	γ_1	1.11×10^5	3.53×10^7
H-Ar	5000	γ_2	1.36×10^5	3.49×10^7

is the standard choice given by $\gamma_1 = 10^5 \mathbf{r}^{\mathrm{T}}\mathbf{D}\mathbf{r} / \left(\mathbf{r}^{\mathrm{T}}\mathbf{r}\right)^2$. The second method uses $\mathbf{N} = \mathrm{diag}\left(\mathbf{D}\right) / \mathrm{diag}\left(\mathbf{r}\mathbf{r}^{\mathrm{T}}\right)$ and $\gamma_2 = \sqrt{\mathbf{N}_{\min}\mathbf{N}_{\max}}$. The condition numbers of both methods are given in table 6.6. In the Ar mixture the condition numbers increase when the γ_2 is used. In the H-Ar mixture the condition number of $\mathbf{\Gamma}$ increases while the condition number of $\tilde{\mathbf{A}}$ decreases. However, the differences in the H-Ar mixture are small. There is no difference observed in stability between both regularization methods. Although γ_2 produces slightly higher condition numbers it has the advantage that is does not depend on an empirical factor. Such a factor may be inappropriate in other cases.

6.5 Conclusions and recommendations

The algorithm described by Peerenboom is extended from one-temperature mixtures to two-temperature mixtures. The current algorithm can in specific cases become unstable due to diverging oscillations in the calculated mass fractions. The oscillations are not observed in neutral mixtures or mixtures containing an electron and only one ion. In principal the oscillations in mixtures with multiple ions can be avoided by using a lower urf value or more grid points. Such solutions increase the time required to run the model and are therefore preferably avoided. Ideally a stable simulation is obtained in another way. It has been observed that changing the pressure or the collision integrals influences the stability of the model. Changing either parameter ultimately means that the diffusion coefficients are altered. This can lead to different solutions. The gradients of the mass fractions are changed which may require a different number of grid points. It is indeed observed that increasing the number of grid points increases the stability of the model. However, in the tested Ar model the mass fractions are almost linear and independent of the pressure or collision integrals. In this case it is still observed that for decreasing pressure the simulation is unstable. Possibly the calculation of the nodal points $\mathbf{y}_C$ is more stable when $\mathbf{A}_W \approx \mathbf{A}_E$. This approximation is more accurate when more grid points are used. In that case the matrix $\mathbf{A}$ is approaching a stable interpolating matrix.

Various other attempts to minimize the effect of the oscillations were not successful. Experiments using descriptions other than $\mathbf{Fv}$ were considered. A de-

scription based on the mass fluxes using **HJ** is supposed to avoid singularities when mass fractions are approaching or reaching zero. The tested mixtures show no beneficial effects for mass fractions that are not approaching zero. Changing the description from mass to pressure fractions guarantees that the fractions of the ions have a more similar magnitude as the fractions of the electrons. Such a method may reduce the impact of rounding errors. A drawback is that the method does not ensure charge conservation. The simulations show that despite a change in the condition number of multiple orders of magnitude in the matrices $\mathbf{\Gamma}$ and $\tilde{\mathbf{A}}$ the model does not gain stability. Imposing the mass and charge constraints analytically also did not avoid the oscillations.

Other attempts that did not improve the model are related to changing the interpolation method or changing the regularization constant. Interpolation is required since the fluxes are evaluated on the interfaces instead of on the nodal points. Interpolating the mass fractions to the interfaces using linear, harmonic or cubic schemes and calculating the flux diffusion matrix on the interfaces had no effect on the stability. Calculating the matrices on the nodal points and using the same interpolation methods to interpolate the flux diffusion matrices towards the interfaces also did not improve the stability. Changing the regularization procedure only had a small impact on the condition number of the matrices $\mathbf{\Gamma}$ and $\tilde{\mathbf{A}}$. It seems that the condition number is not a direct measure of the model's stability. An interesting alternative approach is [129, p. 262-267] which avoids the inversion of the system by using an iterative method. Flux limiters [132] may also aid in preventing the oscillations. However, the flux limiter should still allow the presence of minima or maxima in the coupled system, since these are not by definition forbidden.

6.A Stefan-Maxwell equations

In principal the species velocities can be obtained from (3.19). An alternative set of equations called the Stefan-Maxwell equations can also be used to calculate the velocities. This set of equations is derived from the momentum balance. First the LHS of the species momentum balance is rewritten as

$$\begin{aligned}\frac{\partial \rho y_i \vec{u}_i}{\partial t} + \nabla \cdot \rho y_i \vec{u}_i \vec{u}_i &= \vec{u}_i \left(\frac{\partial \rho y_i}{\partial t} + \nabla \cdot \rho y_i \vec{u}_i \right) + \rho y_i \left(\frac{\partial \vec{u}_i}{\partial t} + (\vec{u}_i \cdot \nabla) \vec{u}_i \right) \\ &= m_i \vec{u}_i \omega_i + \rho y_i \left(\frac{\partial \vec{u}_i}{\partial t} + (\vec{u}_i \cdot \nabla) \vec{u}_i \right). \end{aligned} \tag{6.76}$$

The bulk equation can be written in a similar form. In that case the first term vanishes since it is equal to the continuity equation. Following Whitaker [57, eq. 40] the bulk momentum equation (3.20) can be multiplied with the mass fraction y_i

and subtracted from the species momentum balance (3.19) to obtain

$$\begin{aligned} & \rho_i \left[\frac{\partial \vec{v}_{d,i}}{\partial t} + (\vec{u}_i \cdot \nabla) \vec{v}_{d,i} + (\vec{v}_{d,i} \cdot \nabla) \vec{u} \right] \\ = \; & n_i \langle X_i \rangle - y_i \sum_j n_j \langle X_j \rangle - \nabla p_i + \nabla \cdot \tau_i \\ & - y_i \nabla \cdot \left[\sum_j \left(-p_j \mathbf{I} + \tau_j - \rho y_j \vec{v}_{d,j} \vec{v}_{d,j} \right) \right] + \vec{R}_i - m_i \vec{u}_i \omega_i. \end{aligned} \tag{6.77}$$

The momentum source term can be written as an elastic diffusive term and an inelastic reactive term [57, eq. 23, 51, 52] [59, eq. 5,8]

$$\vec{R}_i = \sum_j \left(p \frac{z_i z_j}{D_{ij}} (\vec{u}_j - \vec{u}_i) + \beta_{ij} \nabla \ln T_j - \beta_{ji} \nabla \ln T_i \right) + m_i \vec{u}_i^* \omega_i, \tag{6.78}$$

with D_{ij} the binary diffusion coefficient and β_{ij} a phenomenological coefficient describing thermophoretic forces. Ramshaw [59, eq. 50] provides an expression for β_{ij} in terms of the thermal diffusion coefficient. Using that conversion and replacing z_i with x_i shows that the results are identical to the single temperature result obtained by Hirschfelder et al. [34, eq. 7.4-48, 7.3-27]. Whitaker [57, eq. 48] simplifies (6.77) with the following assumptions

- The terms related to time and spatial derivatives on the left hand side are neglected. The source terms thus should add up to zero indicating that local equilibrium is assumed.
- Viscosity is neglected.
- The diffusive stress $\rho y_j \vec{v}_{d,j} \vec{v}_{d,j}$ describing the stress between the bulk and species system is neglected.
- The reactive terms are neglected.

After dividing (6.77) by the pressure the following result can be obtained

$$\begin{aligned} -\sum_j \vec{d}_{ij} &= \frac{n_i}{p} \langle X_i \rangle - y_i \sum_j \frac{n_j}{p} \langle X_j \rangle - \frac{1}{p} \nabla p_i + \frac{y_i}{p} \nabla p \\ &\quad + \frac{1}{p} \sum_j \left(\beta_{ij} \nabla \ln T_j - \beta_{ji} \nabla \ln T_i \right) \\ &= \frac{\rho y_i}{p} (\vec{a}_i - \vec{a}) - \nabla z_i - \frac{1}{p} (z_i - y_i) \nabla p \\ &\quad + \frac{1}{p} \sum_j \left(\beta_{ij} \nabla \ln T_j - \beta_{ji} \nabla \ln T_i \right), \end{aligned} \tag{6.79}$$

with $\vec{d}_{ij}$ the driving forces, $\vec{a}_i$ the force per unit of mass per unit of volume acting on species i and z_i the pressure fraction. The driving forces can be related to the

velocity difference between the species. Ramshaw [59, eq. 8] obtains the following result for a two-temperature plasma

$$-\sum_j \vec{d}_{ij} \quad = \quad \sum_j \frac{z_i z_j}{D_{ij}} \left(\vec{u}_i - \vec{u}_j\right) \tag{6.80}$$

Whitaker describes the additional assumptions that are used in order to derive (6.9). These are the usage of the dilute gas theory and the fact that the diffusion coefficients are calculated by only considering the first Chapman-Enskog approximation.

6.B Converting pressure to mass fractions

In this section the conversion from pressure fraction gradients to mass fraction gradients is discussed. The pressure fraction is given by

$$z_i = \frac{T_i y_i}{m_i} \frac{m}{T} = \sigma^m \frac{y_i T_i}{m_i} \frac{1}{\sum_j y_j T_j / m_j}. \tag{6.81}$$

The gradient can be expressed as

$$\begin{aligned} \partial z_i = \sigma^m \frac{T_i}{m_i} \frac{\partial y_i}{\sum_j y_j T_j / m_j} + \frac{y_i T_i}{m_i} \frac{\sum_j \partial y_j}{\sum_j y_j T_j / m_j} + \sigma^m \frac{y_i}{m_i} \frac{\partial T_i}{\sum_j y_j T_j / m_j} \\ -\sigma^m \frac{y_i}{m_i} \frac{\partial T_i}{\left(\sum_j y_j T_j / m_j\right)^2} \left[\sum_j T_j / m_j \partial y_j + \sum_j y_j / m_j \partial T_j\right]. \end{aligned} \tag{6.82}$$

Dividing by z_i gives

$$\begin{aligned} z_i^{-1} \partial z_i \quad = \quad y_i^{-1} \partial y_i + \frac{1}{\sigma^m} \sum_j \partial y_j + T_i^{-1} \partial T_i \\ -\frac{1}{\sum_j y_j T_j / m_j} \left[\sum_j T_j / m_j \partial y_j + \sum_j y_j / m_j \partial T_j\right]. \end{aligned} \tag{6.83}$$

The last term can be rewritten to

$$\begin{aligned} -\frac{1}{\sigma^m} \frac{\sigma^m}{\sum_j y_j T_j / m_j} \left[\sum_j \left(y_j T_j / m_j\right) y_j^{-1} \partial y_j + \sum_j \left(y_j T_j / m_j\right) T_j^{-1} \partial T_j\right] \\ = \quad -\frac{1}{\sigma^m} \left[\sum_j z_j y_j^{-1} + \sum_j z_j T_j^{-1}\right]. \end{aligned} \tag{6.84}$$

Putting this term back in (6.83) and multiplying with z_i gives

$$\begin{aligned}\partial z_i &= z_i \sum_j \left(\delta_{ij} + \frac{1}{\sigma^m}(y_j - z_j)\right) y_j^{-1} \partial y_j \\ &\quad + z_i T_i^{-1} \partial T_i - \frac{z_i}{\sigma^m} \sum_j z_j T_j^{-1} \partial T_j \\ &= z_i \sum_j \left(\delta_{ij} + \frac{1}{\sigma^m}(y_j - z_j)\right) y_j^{-1} \partial y_j + \frac{z_i}{\sigma^m} \sum_j z_j \partial \ln \frac{T_i}{T_j}. \end{aligned} \quad (6.85)$$

6.C Charge conservation with pressure fractions

Using pressure fractions charge conservation is not guaranteed for all temperature profiles. The conditions for which charge is conserved are derived in this section.

In terms of pressure fractions the total mass is given by

$$\begin{aligned}\mathbf{1}^{\mathrm{T}} \mathbf{\Gamma} \partial \mathbf{z} &= \mathbf{1}^{\mathrm{T}} \rho \mathbf{Y} \left(\hat{\mathbf{D}} + \beta \mathbf{1}\mathbf{1}^{\mathrm{T}} + \gamma \mathbf{r}\mathbf{q}_z^{\mathrm{T}}\right) \partial \mathbf{z} - \mathbf{1}^{\mathrm{T}} \rho \mathbf{Y} \mathbf{T} \tilde{\mathbf{M}} \mathbf{y} \\ &= \left(\rho \mathbf{y}^{\mathrm{T}} \hat{\mathbf{D}} + \rho \beta \sigma^m \mathbf{1}^{\mathrm{T}} + \gamma \sigma_z^c \mathbf{q}_z^{\mathrm{T}}\right) \partial \mathbf{z} - \rho \mathbf{y}^{\mathrm{T}} \mathbf{T} \tilde{\mathbf{M}} \mathbf{y} \\ &= \rho \beta \sigma^m \mathbf{1}^{\mathrm{T}} \partial \mathbf{z} - \rho \mathbf{y}^{\mathrm{T}} \mathbf{T} \tilde{\mathbf{M}} \mathbf{y}, \end{aligned} \quad (6.86)$$

and the total charge is given by

$$\begin{aligned}\mathbf{r}^{\mathrm{T}} \mathbf{\Gamma} \partial \mathbf{z} &= \mathbf{r}^{\mathrm{T}} \rho \mathbf{Y} \left(\hat{\mathbf{D}} - \beta \mathbf{1}\mathbf{1}^{\mathrm{T}} + \gamma \mathbf{r}\mathbf{q}_z^{\mathrm{T}}\right) \partial \mathbf{z} - \mathbf{r}^{\mathrm{T}} \rho \mathbf{Y} \mathbf{T} \tilde{\mathbf{M}} \mathbf{y} \\ &= \boldsymbol{\rho_c}^{\mathrm{T}} \hat{\mathbf{D}} \partial \mathbf{z} + \beta \sigma_z^c \mathbf{1}^{\mathrm{T}} \partial \mathbf{z} + \gamma \boldsymbol{\rho_c}^{\mathrm{T}} \mathbf{r}\mathbf{q}_z^{\mathrm{T}} \partial \mathbf{z} - \rho_c^{\mathrm{T}} \mathbf{T} \tilde{\mathbf{M}} \mathbf{y} \\ &= \gamma \boldsymbol{\rho_c}^{\mathrm{T}} \mathbf{r}\mathbf{q}_z^{\mathrm{T}} \partial \mathbf{z} - \rho_c^{\mathrm{T}} \mathbf{T} \tilde{\mathbf{M}} \mathbf{y}, \end{aligned} \quad (6.87)$$

with $q_{z,i} = q_i T / T_i$. These expressions are problematic since $\rho \mathbf{y}^{\mathrm{T}} \mathbf{T} \tilde{\mathbf{M}} \mathbf{y} \neq 0$ and $\rho_c^{\mathrm{T}} \mathbf{T} \tilde{\mathbf{M}} \mathbf{y} \neq 0$. Additionally, $\mathbf{q}_z^{\mathrm{T}} \partial \mathbf{z} = 0$ is only valid for specific temperature profiles. This last statement can be understood by multiplying the charge vector with the pressure gradient which gives

$$\begin{aligned} q_i \nabla z_i &= \frac{q_i T_i}{T} \frac{\nabla n_i}{n} + \frac{q_i n i}{n} \frac{\nabla T_i}{T} - \frac{q_i n_i T_i}{nT} \frac{\nabla p}{p} \\ &= \frac{q_i T_i}{T} \left[\frac{\nabla n_i}{n} - \frac{x_i \nabla n}{n}\right] + \frac{q_i x_i}{T} \left[\nabla T_i - T_i \frac{\nabla T}{T}\right] \\ &= \frac{q_i T_i}{T} \nabla x_i + q_i x_i \left[\frac{\nabla T_i}{T} - \frac{T_i}{T} \frac{\nabla T}{T}\right]. \end{aligned} \quad (6.88)$$

Multiplying this result with T/T_i amounts to

$$\frac{q_i T}{T_i} \nabla z_i = q_i \nabla x_i + q_i x_i \left[\frac{\nabla T_i}{T_i} - \frac{\nabla T}{T}\right]. \quad (6.89)$$

In general the temperature gradients do not satisfy $\nabla \ln T_i = \nabla \ln T$ and thus mass and charge conservation are not necessarily numerically guaranteed by using pressure fractions. In the special case where all particles have the same temperature, charge conservation is also guaranteed numerically.

Chapter 7

A conservative multicomponent diffusion algorithm for ambipolar plasma flows in local thermodynamic equilibrium

7.1 Abstract

The usage of the local thermodynamic equilibrium (LTE) approximation can be a very powerful assumption for simulations of plasmas in or close to equilibrium. In general, the elemental composition in LTE is not constant in space and effects of mixing and demixing have to be taken into account using the Stefan-Maxwell diffusion description. In this article, we will introduce a method to discretize the resulting coupled set of elemental continuity equations. The coupling between the equations is taken into account by the introduction of the concept of a Péclet matrix. It will be shown analytically and numerically, that the mass and charge conservation constraints can be fulfilled exactly. Furthermore, a case study is presented to demonstrate the applicability of the method to a simulation of a mercury free metal halide lamp. The source code for the simulations presented in this article is provided as supplementary material [133].

7.2 Introduction

The usage of the laws of local thermodynamic equilibrium (LTE) can be a powerful tool in the numerical simulation of plasmas in or close to equilibrium. Plasmas that can be described by such an approach are typically high power density discharges. Typical applications are for example metal halide lamps [134, 135], arc welding

Published as: Kim Peerenboom, Jochem van Boxtel, Jesper Janssen and Jan van Dijk, *A conservative multicomponent diffusion algorithm for ambipolar plasma flows in local thermodynamic equilibrium* in Journal of Physics D: Applied Physics, 47, p425202

and cutting [136] and re-entry applications [137, 138]. For such plasmas, LTE simulations are advantageous as these simulations are less costly than non-LTE (NLTE) simulations and require much less input data.

However, the standard LTE approach is often not accurate enough. As pointed out by Rini [113], in general the elemental composition can vary significantly in space due to the effects of mixing and demixing. Demixing occurs for example in the arc discharge of a metal halide lamp. Due to temperature gradients, the different elements demix, giving rise to color segregation [135]. To account for the effects of mixing and demixing, elemental continuity equations have to be solved and a formulation of the elemental diffusion fluxes is needed. In the past several contributions to the description of these elemental diffusion fluxes have been made. The derived continuity equations in these contributions are mostly in an open formulation [134, 139–141]; the elemental diffusion fluxes do not depend explicitly on the gradients of the elemental concentrations, pressure and temperature. Rather, they depend explicitly on the gradients of the species concentrations. Furthermore, for simplicity often the Fick diffusion formulation is used, for example in lamp simulations [142]. However, this approach is not valid when there is no dominant background gas. This is for example the case when studying elemental demixing mercury free metal halide lamps, where the dominant mercury buffer gas is absent.

Alternatively, Rini [113] derived a closed form of the equations based on the Stefan-Maxwell diffusion formulation, where the diffusion fluxes depend on the gradients of the elemental concentrations and the temperature. We agree with his conclusion that using a closed formulation, by calculating the LTE transport coefficients, is more advantageous from both a numerical and a physical point of view. He presents calculations of the LTE transport coefficients obtained with the new formulation. However, his elegant formulation is not exploited by solving the elemental continuity equations to simulate the effect of elemental (de)mixing.

The goal of the present contribution is to present an approach to actually solve the elemental continuity equations in ambipolar plasmas. To this end, we will extend the closed formulation of Rini to mixtures including charged species in section 7.3. To discretize the coupled elemental diffusion fluxes, a coupled discretization scheme is introduced in section 7.4. It will be shown that this scheme together with the closed formulation conserves mass and charge exactly, without the need to apply the mass and charge constraints explicitly. Sections 7.5 and 7.6 present an analytical test model and a case study, respectively. The case study describes the effect of elemental demixing in mercury free metal halide lamps in the absence of a dominant background gas. Finally, conclusions are drawn in section 7.7.

7.3 The equations for chemically reacting plasmas in LTE

7.3.1 Elemental and species definitions

In this article, the multi-component plasma contains a set of N_s different species. This set of species is subdivided in a set of N_e pure chemical elements and a set

of $N_r = N_s - N_e$ combined species. The combined species have indices $\mathcal{R} = \{1, \ldots, N_r\}$, while the elements have indices $\mathcal{E} = \{N_r + 1, \ldots, N_s\}$. The set $\mathcal{S} = \mathcal{R} \cup \mathcal{E}$ contains the indices of all species.

7.3.2 Species continuity equations

The species continuity equations are given by:

$$\frac{\partial}{\partial t}\left(\rho y_i\right) + \nabla \cdot \left(\rho \vec{v} y_i + \vec{J}_i\right) = m_i \omega_i, \tag{7.1}$$

where ρ is the mass density, y_i the mass fraction of species i, $\vec{v}$ the flow velocity, $\vec{J}_i$ the diffusive mass flux of species i, m_i the mass of species i and ω_i the density production rate of species i due to volume production processes. By their definition, the mass fractions should obey the following mass constraint:

$$\sum_{i \in \mathcal{S}} y_i = 1. \tag{7.2}$$

In plasmas, the drift of charged particles in electric fields causes charge separations over a typical length scale of the order of the Debye length λ_D. This charge separation leads to an electric field, which can be calculated with Poisson's equation. In plasmas where λ_D is small, this approach is not very efficient, since it requires excessively fine meshes. In these plasmas, it is more appropriate to consider the electric field in the limit of vanishing Debye length. In that case, the plasma becomes quasi-neutral and the electric field necessary to maintain this situation is called the ambipolar field $\vec{E}$. The assumption of an ambipolar plasma puts extra constraints on the mass fractions. The quasi-neutrality constraint can be expressed as:

$$\sum_{i \in \mathcal{S}} r_i y_i = 0, \tag{7.3}$$

where $r_i = q_i / m_i$ is the ratio between the charge q_i and the mass m_i of species i.

The diffusive mass fluxes $\vec{J}_i$ are described by the mass flux formulation of the Stefan-Maxwell equations [129], which can be deduced from the kinetic theory of gases [143,144]. Alternatively, the Stefan-Maxwell equations can be obtained from momentum conservation considerations [145]. The derivation in [145] corresponds to the first order Sonine polynomial expansion [146] of the exact kinetic theory of gases. In this case the Stefan-Maxwell equations for the mass fluxes are given by:

$$\sum_j H_{ij} \vec{J}_j = -\vec{d}_i \qquad \Leftrightarrow \qquad \mathbf{H}\mathbf{J} = -\mathbf{d}, \tag{7.4}$$

where $\mathbf{H} = (H_{ij})$ is the mass flux based friction matrix, $\mathbf{J} = (\vec{J}_i)$ is the vector of diffusive mass fluxes and $\mathbf{d} = (\vec{d}_i)$ is the driving force for species i. Note that the mass flux based formulation is needed in LTE calculations rather than the velocity based formulation[1] of the Stefan-Maxwell equations. The reason is that

[1] The velocity based calculation uses $\mathbf{F}\mathbf{v} = -\mathbf{d}$ where $\mathbf{F}$ is the friction matrix and $\mathbf{v}$ is the velocity vector. For more details, see Giovangigli [128, p. 76-79] or chapter 6 of this thesis.

in LTE calculations, the species mass fractions can easily become very small for low temperatures. For small mass fractions, the normal friction matrix becomes singular and the velocity based formulation can not be used to obtain the diffusive mass fluxes.

The Stefan-Maxwell equations (7.4) can be expressed in kinetic form as

$$\vec{J}_i = -\sum_j L_{ij}\vec{d}_j \qquad \Leftrightarrow \qquad \mathbf{J} = -\mathbf{L}\mathbf{d}, \tag{7.5}$$

with $\mathbf{L} = (L_{ij})$, the multicomponent flux diffusion coefficient matrix. The matrices $\mathbf{H}$ and $\mathbf{L}$ are singular and they are each others generalized inverses with prescribed range and null space [147, section 2.5]. The coefficients of $\mathbf{H}$ are explicitly known, while the elements of $\mathbf{L}$ are not. The elements of $\mathbf{H}$ are given by:

$$H_{ij} \quad = \quad \begin{cases} \frac{1}{\rho}\frac{\sigma m}{m_j}\sum_{l\neq j}\frac{x_l}{\mathcal{D}_{lj}} & \text{if } i = j, \\ -\frac{1}{\rho}\frac{\sigma m}{m_j}\frac{x_i}{\mathcal{D}_{ij}} & \text{if } i \neq j, \end{cases} \tag{7.6}$$

with x_i the mole fraction of species i and $\mathcal{D}_{ij}$ the usual binary diffusion coefficient [143, 144]. For the species conservation equations, we need the formulation where the diffusive mass fluxes are given in terms of the driving forces. Therefore, we have to calculate the multicomponent flux diffusion matrix $\mathbf{L}$ from the friction matrix $\mathbf{H}$.

To keep the following discussion as simple as possible, we will take into account ordinary concentration diffusion and the ambipolar electric field as driving forces, in which case:

$$\vec{d}_i = \nabla x_i - z_i\vec{E}/p \qquad \Leftrightarrow \qquad \mathbf{d} = \partial\mathbf{x} - \mathbf{z}\vec{E}/p, \tag{7.7}$$

with $\mathbf{x} = (x_i)$ the vector of mole fractions, $\mathbf{z} = (z_i)$ the vector of charge densities, $\vec{E}$ the ambipolar electric field and p the pressure.

The diffusive mass fluxes are also subject to constraints. The diffusive mass fluxes should not transport net mass:

$$\sum_{i\in\mathcal{S}}\vec{J}_i = 0. \tag{7.8}$$

The quasi-neutrality puts a constraint on the diffusive fluxes as well. To maintain quasi-neutrality, the current should be divergence-free. However, often the stronger constraint of zero current is used. We will use the zero-current assumption, which reads:

$$\sum_{i\in\mathcal{S}} r_i\vec{J}_i = 0. \tag{7.9}$$

This zero-current constraint can be used to remove the ambipolar electric field from the Stefan-Maxwell equations. When we define the inner product in species space as $\langle\mathbf{a},\mathbf{b}\rangle = \sum_i a_i b_i$, the current constraint (7.9) can alternatively be written as:

$$\langle\mathbf{r},\mathbf{J}\rangle = 0. \tag{7.10}$$

By taking the inner product of $\mathbf{r}$ with (7.5), the following expression for the ambipolar field is obtained:

$$\vec{E}/p = \frac{\langle \mathbf{r}, \mathbf{L}\partial\mathbf{x} \rangle}{\langle \mathbf{r}, \mathbf{L}\mathbf{z} \rangle}. \tag{7.11}$$

Substitution in expression (7.5) for the diffusion velocities gives:

$$\begin{aligned} \mathbf{J} &= -\left(\mathbf{L} - \frac{(\mathbf{L}\mathbf{z} \otimes \mathbf{r})\mathbf{L}}{\langle \mathbf{r}, \mathbf{L}\mathbf{z} \rangle} \right) \partial\mathbf{x}, \\ &= -\hat{\mathbf{L}}\partial\mathbf{x}, \end{aligned} \tag{7.12}$$

where $\otimes$ denotes the dyadic product in species space: $\mathbf{a} \otimes \mathbf{b} = (a_i b_j)$. As discussed, the matrices $\mathbf{H}$ and $\mathbf{L}$ are singular. They are each others generalized inverses with prescribed range and null space with the following properties:

$$\begin{aligned} \mathbf{HLH} &= \mathbf{H}, & \mathbf{LHL} &= \mathbf{L}, \\ \mathbf{HL} &= \mathbf{I} - \frac{\mathbf{y} \otimes \mathbf{u}}{\langle \mathbf{y}, \mathbf{u} \rangle}, & \mathbf{LH} &= \mathbf{I} - \frac{\mathbf{y} \otimes \mathbf{u}}{\langle \mathbf{y}, \mathbf{u} \rangle}, \end{aligned}$$

where $\mathbf{y}$ is vector containing the mass fractions and $\mathbf{u}$ is a vector containing only ones. The elements of $\mathbf{L}$ are not explicitly known and need to be calculated from $\mathbf{H}$. However, $\mathbf{H}$ is singular and non-invertible. The regularization can be established by:

$$\tilde{\mathbf{H}} = \mathbf{H} + \alpha \mathbf{y} \otimes \mathbf{u}, \qquad \tilde{\mathbf{L}} = \mathbf{L} + \alpha^{-1} \mathbf{y} \otimes \mathbf{u}. \tag{7.13}$$

The matrices $\tilde{\mathbf{H}}$ and $\tilde{\mathbf{L}}$ are now each others true inverses: $\tilde{\mathbf{H}}\tilde{\mathbf{L}} = \mathbf{I}$, and the matrix $\mathbf{L}$ can be calculated as:

$$\mathbf{L} = (\mathbf{H} + \alpha \mathbf{y} \otimes \mathbf{u})^{-1} - \alpha^{-1} \mathbf{y} \otimes \mathbf{u}. \tag{7.14}$$

From this the ambipolar matrix $\hat{\mathbf{L}}$ can be calculated. Also the matrix $\hat{\mathbf{L}}$ is singular, its left null space consists of the vectors $\mathbf{u}$ and $\mathbf{r}$.

7.3.3 Equilibrium composition calculation

When the chemistry time scales are fast with respect to the transport time scales, the composition can be calculated from the pressure, temperature and elemental mass fractions instead of solving the species continuity equations as defined in the previous section. To obtain the equilibrium composition, N_r independent reactions should be specified:

$$\sum_{i \in \mathcal{S}} \nu_i^r A_i = 0 \qquad (r \in \mathcal{R}), \tag{7.15}$$

where ν_i^r is the stoichiometric coefficient of species i in reaction r and A_i is the symbolic notation for species i. The species mole fractions x_i involved in these reactions obey the following relations:

$$\sum_{i \in \mathcal{S}} \nu_i^r \ln x_i = \ln K_p^r - \ln p \sum_{i \in \mathcal{S}} \nu_i^r \qquad (r \in \mathcal{R}), \tag{7.16}$$

where $\ln K_p^r$ is the equilibrium constant. In addition, the elemental composition needs to be fixed by the specification of N_e elemental constraints:

$$\sum_{i \in \mathcal{S}} \phi_{i\alpha} y_i m_{\{\alpha\}}/m_i = y_{\{\alpha\}} \qquad (\alpha \in \mathcal{E}), \tag{7.17}$$

where $\phi_{i\alpha}$ is the stoichiometric coefficient indicating the number of atoms of element α in species i. The elemental mass fractions[2] $y_{\{\alpha\}}$ are calculated from a set of convection-diffusion equations for the elements. These will be derived in the next section.

For usage in the next sections, we gather ν_i^r and $\phi_{i\alpha}$ in the stoichiometric matrix $\mathbf{R} = \begin{pmatrix} \boldsymbol{\nu} \\ \boldsymbol{\phi} \end{pmatrix}$:

$$\begin{aligned} R_{ri} &= \nu_i^r (r \in \mathcal{R}, i \in \mathcal{S}), \\ R_{\alpha i} &= \phi_{i\alpha} (\alpha \in \mathcal{E}, i \in \mathcal{S}). \end{aligned}$$

For example, for a subset of the species from the case study that will be presented in section 7.6, the matrix $\mathbf{R}$ looks as follows:

	I_2	InI	In^+	Xe^+	I	In	Xe	e
I_2	1	0	0	0	-2	0	0	0
InI	0	1	0	0	-1	-1	0	0
In^+	0	0	1	0	0	-1	0	1
Xe^+	0	0	0	1	0	0	-1	1
I	2	1	0	0	1	0	0	0
In	0	1	1	0	0	1	0	0
Xe	0	0	0	1	0	0	1	0
e	0	0	-1	-1	0	0	0	1

In the next section, the elemental continuity equations and the elemental diffusion fluxes will be derived from the species continuity equations and the equilibrium composition relations.

7.3.4 Elemental continuity equations

The elemental continuity equations can be derived by taking a linear combination of the species continuity equations. Multiplication of equation (7.1) by $\phi_{i\alpha} m_{\{\alpha\}}/m_i$ and summation over all species gives the elemental continuity equation:

$$\frac{\partial}{\partial t}\left(\rho y_{\{\alpha\}}\right) + \nabla \cdot \left(\rho \vec{v} y_{\{\alpha\}} + \vec{J}_{\{\alpha\}}\right) = 0, \tag{7.18}$$

where $\vec{J}_{\{\alpha\}}$ is the elemental diffusion flux. We will now derive an expression for the elemental diffusion fluxes from the species diffusion fluxes.

[2]Throughout this article, we will use {} to denote the elements.

In chemical equilibrium, we know that the chemical composition $\mathbf{x}$ is determined by the pressure, temperature and elemental mass fractions: $\mathbf{x} = \mathbf{x}(p, T, \{\mathbf{y}\})$. So, when ignoring pressure variations, we may write the diffusion driving force as:

$$\partial \mathbf{x} = \left.\frac{\partial \mathbf{x}}{\partial T}\right|_{p,\{\mathbf{y}\}} \partial T + \left.\frac{\partial \mathbf{x}}{\partial \{\mathbf{y}\}}\right|_{p,T} \partial\{\mathbf{y}\}. \tag{7.19}$$

To derive the dependence of $\partial \mathbf{x}$ on ∂T, we start by taking the gradient of equation (7.16):

$$\sum_{i \in \mathcal{S}} \nu_i^r / x_i \partial x_i = \frac{\Delta h_r}{R_u T^2} \partial T, \tag{7.20}$$

where Δh_r is the molar enthalpy of reaction r and R_u the universal gas constant. Note that we used Van 't Hoff's relation $\frac{\partial \ln K_p^r}{\partial T} = \frac{\Delta h_r}{R_u T^2}$ and assumed constant pressure, consistent with the neglect of pressure diffusion. Using matrix notation this becomes:

$$\boldsymbol{\nu}\ \mathrm{diag}^{-1}(\mathbf{x}) \partial \mathbf{x} = \partial \boldsymbol{\theta}, \tag{7.21}$$

where $\partial \theta_r = \frac{\Delta h_r}{R_u T^2} \partial T$.

To derive the dependence of $\partial \mathbf{x}$ on $\partial\{\mathbf{y}\}$, we start with equation (7.17). By taking the derivative of (7.17), we obtain:

$$\sum_{i \in \mathcal{S}} \phi_{i\alpha} \partial y_i m_{\{\alpha\}} / m_i = \partial y_{\{\alpha\}} \qquad (\alpha \in \mathcal{E}). \tag{7.22}$$

In matrix notation this becomes:

$$\mathrm{diag}(\{\mathbf{m}\}) \boldsymbol{\phi}\ \mathrm{diag}^{-1}(\mathbf{m}) \partial \mathbf{y} = \partial\{\mathbf{y}\}. \tag{7.23}$$

Converting the gradients of the mass fractions to the gradients of the mole fractions in a non-singular way according to [128], we arrive at:

$$\mathrm{diag}(\{\mathbf{m}\}) \boldsymbol{\phi}\ \mathrm{diag}^{-1}(\mathbf{m}) \tilde{\mathbf{N}} \partial \mathbf{x} = \partial\{\mathbf{y}\}, \tag{7.24}$$

where $\tilde{\mathbf{N}}$ is the non-singular matrix relating the species mass fractions to the species mole fractions:

$$\tilde{\mathbf{N}} = \mathrm{diag}(\mathbf{y}) \left[\mathbf{I} - \sigma^{-1} \mathbf{u} \otimes (\mathbf{y} - \mathbf{x})\right] \mathrm{diag}^{-1}(\mathbf{x}). \tag{7.25}$$

Combination of equations (7.21) and (7.24) gives enough information to relate the gradients of the species mole fractions to the gradients of the elemental mass fractions and the temperature:

$$\mathbf{A} \partial \mathbf{x} = \begin{pmatrix} \partial \boldsymbol{\theta} \\ \partial\{\mathbf{y}\} \end{pmatrix}, \tag{7.26}$$

where $\mathbf{A}$ is $\begin{pmatrix} \boldsymbol{A}_r \\ \boldsymbol{A}_\alpha \end{pmatrix}$, with

$$\boldsymbol{A}_r = \boldsymbol{\nu}\ \mathrm{diag}^{-1}(\mathbf{x}), \qquad \boldsymbol{A}_\alpha = \mathrm{diag}(\{\mathbf{m}\}) \boldsymbol{\phi}\ \mathrm{diag}^{-1}(\mathbf{m}) \tilde{\mathbf{N}}. \tag{7.27}$$

Inversion gives the expression for the gradients of the species mole fractions:

$$\partial \mathbf{x} = \mathbf{A}^{-1} \begin{pmatrix} \partial \boldsymbol{\theta} \\ \partial\{\mathbf{y}\} \end{pmatrix}. \tag{7.28}$$

By combining the above expression with (7.12), we obtain the following expression for the diffusive mass fluxes:

$$\mathbf{J} = -\hat{\mathbf{L}}\mathbf{A}^{-1} \begin{pmatrix} \partial \boldsymbol{\theta} \\ \partial\{\mathbf{y}\} \end{pmatrix}. \tag{7.29}$$

Conversion to elemental mass fluxes gives:

$$\{\mathbf{J}\} = -\operatorname{diag}(\{\mathbf{m}\})\boldsymbol{\phi} \operatorname{diag}^{-1}(\mathbf{m})\hat{\mathbf{L}}\mathbf{A}^{-1} \begin{pmatrix} \partial \boldsymbol{\theta} \\ \partial\{\mathbf{y}\} \end{pmatrix}. \tag{7.30}$$

By defining the elemental multi-component flux diffusion matrix $\boldsymbol{\Gamma}$ and the thermal demixing matrix $\boldsymbol{\Gamma}^{\theta}$, we can write:

$$\{\mathbf{J}\} = \begin{pmatrix} \boldsymbol{\Gamma}^{\theta} & \boldsymbol{\Gamma} \end{pmatrix} \begin{pmatrix} \partial \boldsymbol{\theta} \\ \partial\{\mathbf{y}\} \end{pmatrix}. \tag{7.31}$$

The elemental flux diffusion matrix $\boldsymbol{\Gamma}$ is singular with the vectors $\mathbf{u}$ and $\mathbf{r}$ in its left null space. The matrix $\boldsymbol{\Gamma}$ can be regularized as follows:

$$\tilde{\boldsymbol{\Gamma}} = \boldsymbol{\Gamma} + \alpha\{\mathbf{y}\} \otimes \{\mathbf{u}\} + \beta\{\mathbf{z}\} \otimes \{\mathbf{r}\}, \tag{7.32}$$

where α and β are free parameters. In this chapter, these are chosen as $\alpha = \max(\boldsymbol{\Gamma})/\langle \mathbf{y}, \mathbf{u} \rangle$ and $\beta = \max(\boldsymbol{\Gamma})/\langle \mathbf{z}, \mathbf{r} \rangle$. We noticed however that this is not always the optimal choice. We will see in the next section that with (7.32), the elemental mass and charge constraints are fulfilled analytically.

7.3.5 Mass and charge conservation

We will now investigate the mass and charge conservation properties of the diffusion formulation. To investigate the mass conservation properties, the elemental continuity equations (7.18) are summed:

$$\begin{aligned} \sum_{\alpha} \left\{ \frac{\partial}{\partial t} \left(\rho y_{\{\alpha\}} \right) + \nabla \cdot \left(\rho \vec{v} y_{\{\alpha\}} + \vec{J}_{\{\alpha\}} \right) \right\} &= 0 \iff \\ \frac{\partial}{\partial t} \left(\rho \sigma^m \right) + \nabla \cdot \left(\rho \vec{v} \sigma^m + \sum_{\alpha} \vec{J}_{\{\alpha\}} \right) &= 0, \end{aligned} \tag{7.33}$$

where $\sigma^m \equiv \langle \{\mathbf{u}\}, \{\mathbf{y}\} \rangle$ is representing the mass constraint. Let us now look at the summation of the diffusive mass fluxes in more detail:

$$\sum_{\alpha} \vec{J}_{\{\alpha\}} = \langle \{\mathbf{u}\}, \{\mathbf{J}\} \rangle = -\{\mathbf{u}\}^T \boldsymbol{\Gamma}^{\theta} \partial \boldsymbol{\theta} - \{\mathbf{u}\}^T \tilde{\boldsymbol{\Gamma}} \partial\{\mathbf{y}\}. \tag{7.34}$$

Since $\{\mathbf{u}\}$ is in the left null space of $\mathbf{\Gamma}$ and $\mathbf{\Gamma}^\theta$ and since $\langle\{\mathbf{u}\},\{\mathbf{z}\}\rangle = 0$ due to charge conservation, this can be written as:

$$\sum_\alpha \vec{J}_{\{\alpha\}} = -\alpha\sigma^m\nabla\sigma^m \equiv -\mathcal{D}^m\nabla\sigma^m, \tag{7.35}$$

with $\mathcal{D}^m = \alpha\sigma^m$.

A similar derivation can be carried out for the charge constraint, but now we have to consider the following summation:

$$\begin{aligned}\sum_\alpha \frac{q_\alpha}{m_\alpha}\left\{\frac{\partial}{\partial t}\left(\rho y_{\{\alpha\}}\right) + \nabla\cdot\left(\rho\vec{v}y_{\{\alpha\}} + \vec{J}_{\{\alpha\}}\right)\right\} &= 0 \iff \\ \frac{\partial}{\partial t}\left(\rho\sigma^c\right) + \nabla\cdot\left(\rho\vec{v}\sigma^c + \sum_\alpha \frac{q_\alpha}{m_\alpha}\vec{J}_{\{\alpha\}}\right) &= 0,\end{aligned} \tag{7.36}$$

where $\sigma^m \equiv \langle\{\mathbf{r}\},\{\mathbf{y}\}\rangle$ is representing the charge constraint. The current density can be further worked out as:

$$\sum_\alpha \frac{q_\alpha}{m_\alpha}\vec{J}_{\{\alpha\}} = \langle\{\mathbf{r}\},\{\mathbf{J}\}\rangle = -\{\mathbf{r}\}^T\mathbf{\Gamma}^\theta\partial\boldsymbol{\theta} - \{\mathbf{r}\}^T\tilde{\mathbf{\Gamma}}\partial\{\mathbf{y}\}. \tag{7.37}$$

Since $\{\mathbf{r}\}$ is in the left null space of $\mathbf{\Gamma}$ and $\mathbf{\Gamma}^\theta$ and since $\langle\{\mathbf{r}\},\{\mathbf{y}\}\rangle = 0$ due to charge conservation, this can be written as:

$$\sum_\alpha \frac{q_\alpha}{m_\alpha}\vec{J}_{\{\alpha\}} = -\beta\langle\{\mathbf{r}\},\{\mathbf{z}\}\rangle\nabla\sigma^c \equiv -\mathcal{D}^c\nabla\sigma^c, \tag{7.38}$$

with $\mathcal{D}^c = \beta\langle\{\mathbf{r}\},\{\mathbf{z}\}\rangle$.

With the expressions for the fluxes, we finally arrive at the following partial differential equations (PDE's) for the mass and charge constraints:

$$\frac{\partial\rho\sigma^m}{\partial t} + \nabla\cdot\left(\rho\vec{v}\sigma^m - \mathcal{D}^m\nabla\sigma^m\right) = 0. \tag{7.39}$$

$$\frac{\partial\rho\sigma^c}{\partial t} + \nabla\cdot\left(\rho\vec{v}\sigma^c - \mathcal{D}^c\nabla\sigma^c\right) = 0. \tag{7.40}$$

Due to the elliptic nature of these PDE's and the absence of source terms the mass and charge constraints will be fulfilled analytically when there is a point on the boundary that fulfills the constraints.

7.4 Discretization of the elemental continuity equations

The elemental mass fractions $\{\mathbf{y}\}$ cannot be described by a scalar continuity equation for each element separately. Instead, they are described by a system of coupled continuity equations. Because of the coupling, the equations cannot be discretized with traditional finite volume schemes such as the exponential scheme [148, 149] without unphysical oscillations. In this section, we will present a coupled form of the exponential scheme, based on the work in [28, 150] and apply this to the elemental fluxes. It will be shown that with the diffusion formulation of section 7.3.4 and this discretization scheme, mass and charge conservation can be fulfilled up to machine accuracy without being explicitly applied.

7.4.1 Flux expressions

In the steady, one-dimensional case, the system of continuity equations can be written as

$$\frac{\mathrm{d}}{\mathrm{d}x}\mathbf{J} = \mathbf{s}, \qquad \mathbf{J} = \rho u \boldsymbol{\phi} - \boldsymbol{\Gamma}\frac{\mathrm{d}}{\mathrm{d}x}\boldsymbol{\phi}, \tag{7.41}$$

where the different elements in the vector $\boldsymbol{\phi}$ are coupled by the non-diagonal elements of $\boldsymbol{\Gamma}$. The grid stencil used for discretization is given in figure 7.1. Inte-

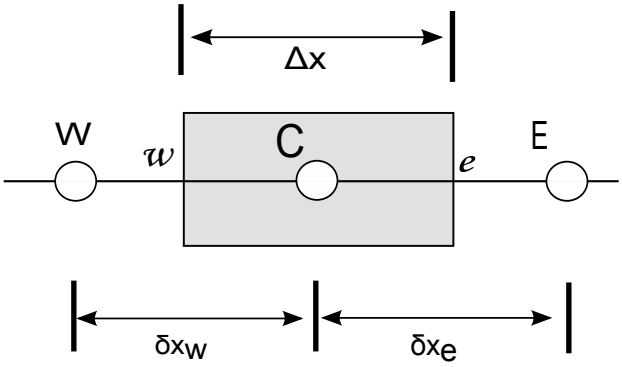

Figure 7.1: Stencil used for discretization. C, W and E denote the central, west and east nodal grid points, respectively. The west and east cell interfaces are denoted by w and e.

gration of equation (7.41) over the control volume shown in figure 7.1 gives:

$$\mathbf{J}_e - \mathbf{J}_w = \mathbf{s}_C \Delta x, \tag{7.42}$$

where $\mathbf{s}_C$ is the source term at the central point C. When the flux $\mathbf{J}_e$ is expressed in $\boldsymbol{\phi}_C$ and $\boldsymbol{\phi}_E$, and the flux $\mathbf{J}_w$ is expressed in $\boldsymbol{\phi}_C$ and $\boldsymbol{\phi}_W$, the following discrete equation is obtained:

$$\mathbf{A}_C\boldsymbol{\phi}_C = \boldsymbol{A}_E\boldsymbol{\phi}_E + \mathbf{A}_W\boldsymbol{\phi}_W + \boldsymbol{s}_C\Delta x. \tag{7.43}$$

The discretization matrices $\mathbf{A}_C$, $\mathbf{A}_E$ and $\mathbf{A}_W$ depend on the expressions for the numerical flux. Like in the traditional exponential scheme the flux representation is based on the homogeneous solution of the local boundary value problem, i.e. without sources.

To derive an expression for the flux $\mathbf{J}_e$, the following system boundary value problem for the vector $\boldsymbol{\phi}$ of unknowns is used:

$$\begin{aligned} \frac{\mathrm{d}}{\mathrm{d}x}\mathbf{J} = \frac{\mathrm{d}}{\mathrm{d}x}\left(\left(\rho u\right)_e \boldsymbol{\phi} - \boldsymbol{\Gamma}_e\frac{\mathrm{d}}{\mathrm{d}x}\boldsymbol{\phi}\right) &= \mathbf{0}, \qquad x_C < x < x_E, \\ \boldsymbol{\phi}(x_C) &= \boldsymbol{\phi}_C, \\ \boldsymbol{\phi}(x_E) &= \boldsymbol{\phi}_E, \end{aligned} \tag{7.44}$$

where $(\rho u)_e$ and $\mathbf{\Gamma}_e$ are assumed to be constant on (x_C, x_E). Note that (7.44) is equal to (7.41) in case $\mathbf{s} = 0$. It is important to mention here that neglecting the source in the derivation of the flux, does not limit the application of the discretization scheme to problems without sources. The only consequence is that uniform second order convergence is not guaranteed by the discretization scheme.

Using the system boundary value problem, the following expression for the flux is obtained:

$$\mathbf{J}_e = \frac{1}{\delta x_e}\mathbf{\Gamma}_e\Big(B(-\mathbf{P}_e)\boldsymbol{\phi}_C - B(\mathbf{P}_e)\boldsymbol{\phi}_E\Big), \tag{7.45}$$

where $B()$ is the Bernoulli function and $\mathbf{P}_e$ is the Péclet matrix, which is defined as:

$$\mathbf{P}_e = \delta x_e (\rho u)_e \mathbf{\Gamma}_e^{-1}. \tag{7.46}$$

The Bernoulli function of the Péclet matrix is calculated by diagonalization of the Péclet matrix:

$$\mathbf{P} = \mathbf{V}\mathbf{\Lambda}\mathbf{V}^{-1} = \mathbf{V}\begin{pmatrix} \lambda_1 & & \\ & \ddots & \\ & & \lambda_N \end{pmatrix}\mathbf{V}^{-1}, \tag{7.47}$$

$$B(\mathbf{P}) = \mathbf{V}B(\mathbf{\Lambda})\mathbf{V}^{-1} = \mathbf{V}\begin{pmatrix} B(\lambda_1) & & \\ & \ddots & \\ & & B(\lambda_N) \end{pmatrix}\mathbf{V}^{-1}, \tag{7.48}$$

with $\mathbf{V}$ the matrix containing the eigenvectors of $\mathbf{P}$ as its columns and $\mathbf{\Lambda}$ a diagonal matrix with the eigenvalues λ_i of the Péclet matrix. Likewise, $B(-\mathbf{P})$ can be computed. Note that for the diagonalization, it is required that $\mathbf{P}$ has a complete set of linearly independent eigenvectors. In Cullinan [151] it is proven that for Péclet matrices resulting from multi-component diffusion problems this is indeed the case.

For the flux at the west interface, an expression similar to the east interface can be obtained. Substitution of the expression for the fluxes in equation (7.42), gives the following expressions for the discretization matrices:

$$\mathbf{A}_E = \frac{1}{\delta x_e}\mathbf{\Gamma}_e B(\mathbf{P}_e), \quad \mathbf{A}_W = \frac{1}{\delta x_w}\mathbf{\Gamma}_w B(-\mathbf{P}_w), \quad \mathbf{A}_C = \mathbf{A}_E + \mathbf{A}_W. \tag{7.49}$$

Note that we have used the fact that the flow field $\rho\vec{v}$ is divergence free in the expression for $\mathbf{A}_C$. From (7.48) it can be seen that the coupled exponential scheme guarantees that the eigenvalues of the discretization matrices are positive, since the eigenvalues of $B(\mathbf{P})$ are given by $B(\lambda_i)$, which are always positive.

7.4.2 Discrete mass and charge conservation

In section 7.3.5 we have shown that *analytically*, $\sigma^m = 1$ and $\sigma^c = 0$ will be satisfied in the entire domain due to the elliptic nature of equations (7.39) and (7.40). It

appears that when the coupled exponential scheme is used for discretization, this is true *numerically* as well. In this case the discrete equations for σ^m and σ^c read:

$$\begin{aligned} a_C^m \sigma_C^m &= a_E^m \sigma_E^m + a_W^m \sigma_W^m, \\ a_C^c \sigma_C^c &= a_E^c \sigma_E^c + a_W^c \sigma_W^c, \end{aligned} \tag{7.50}$$

with σ_C^m, σ_E^m, σ_W^m, σ_C^c, σ_E^c and σ_W^c the values of σ^m and σ^c on the central, east and west nodal point, respectively. The coefficients a_C, a_E and a_W are the corresponding discretization coefficients and satisfy $a_E > 0$, $a_W > 0$ and $a_C = a_E + a_W$. The discrete equation for σ^m reveals a very pleasant property of the coupled exponential scheme that we introduced in section 7.4.1. Since σ_C^m is a weighted average of σ_E^m and σ_W^m, we can deduce from the discrete maximum principle that $\sigma^m = 1$ will be satisfied in the entire domain. Suppose that σ_C^m is a local maximum: $\sigma_C^m \geq \sigma_E^m, \sigma_C^m \geq \sigma_W^m$. However, since σ_C^m is a weighted average the following needs to be true: $\sigma_C^m = \sigma_E^m = \sigma_W^m$. We can now take σ_E^m or σ_W^m and continue the procedure until we hit the boundary, where $\sigma^m = 1$. Although the mass fractions of the individual species may be affected by discretization errors, we are guaranteed to have a mass conserving solution for σ^m where all the points in the domain satisfy $\sigma^m = 1$, *without discretization error*. Similarly, $\sigma^c = 0$ is satisfied without discretization error. The complete derivation of the discrete equations for σ^m and σ^c can be found in appendix 7.A.

7.5 Test case: analytical solution for a binary mixture

As a test case[3] for the elemental diffusion algorithm with coupled discretization, a 1D diffusion problem with an analytical solution was used. The test case consists of a binary mixture of atomic argon and hydrogen. The mixture is confined to a 1D domain between $x = 0$ m and $x = 1$ m. At the boundaries the composition is prescribed as a boundary condition. Furthermore, the mixture is stationary, the mass averaged velocity $\vec{v} = 0$ and the pressure and temperature are uniform and fixed over time. In this case, the analytical solution for hydrogen can be expressed as:

$$y_H(x) = (y_{H,0} + \gamma) \left(\frac{y_{H,L} + \gamma}{y_{H,0} + \gamma} \right)^{x/L} - \gamma, \tag{7.51}$$

where $\gamma = m_H / (m_{Ar} - m_H)$. Note that the solution should be independent of pressure and temperature. The results of the analytical solution and the numerical calculation can be seen in figure 7.2. As should be the case, there is excellent agreement between the analytical and the numerical solution. As can be seen, the solution is not a straight line, as would be the case for Fick diffusion. This demonstrates the mutual influence of the species diffusive motion when Stefan-Maxwell diffusion is used.

To study the convergence of the numerical solution to the analytical solution in more detail, the simulations were repeated for different numbers of grid points.

[3]See Supplemental Material at [133] for the source code of this binary mixture test case (inputfile HAr_neutral.txt).

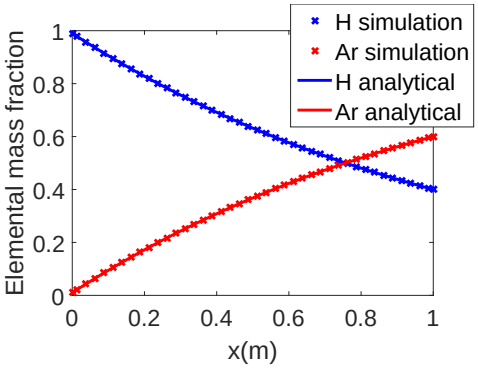

Figure 7.2: Numerical and analytical result for a binary mixture of hydrogen and argon.

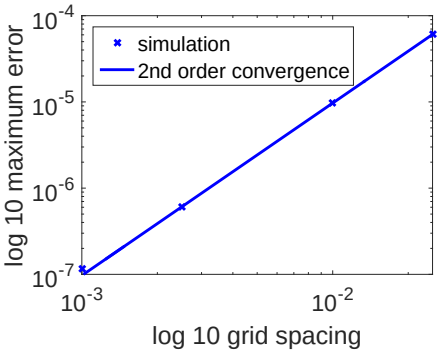

Figure 7.3: Grid convergence for the analytical model.

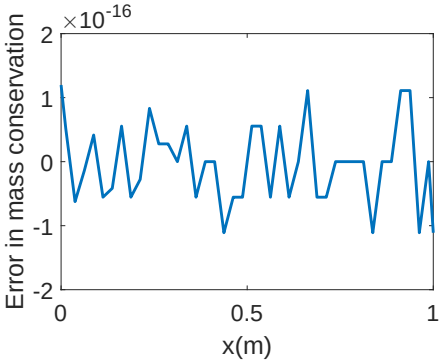

Figure 7.4: Error in mass conservation $1 - \sum_\alpha y_\alpha$. It can be seen that the mass constraint is free from discretization errors.

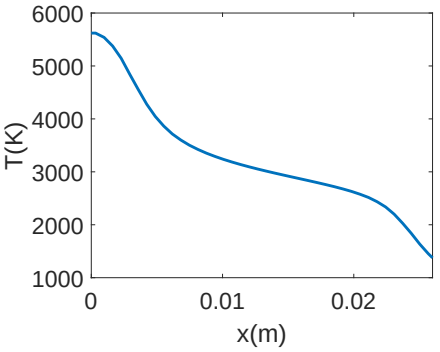

Figure 7.5: Radial temperature profile used in the case study of the metal halide lamp.

The result is displayed in figure 7.3. Since there is no convection, we expect second order convergence behavior for the coupled exponential scheme [150]. From figure 7.3 it appears that this is indeed the case.

As derived in section 7.4.2, the mass and charge constraints should be satisfied, although they are not applied explicitly. The error in mass conservation for this test case can be seen in figure 7.4.

7.6 Case study: elemental demixing in a metal halide lamp

As mentioned in the introduction, a typical application where elemental demixing occurs is the metal halide lamp. Currently, most metal halide lamps contain

mercury as a buffer gas, because of its beneficial effects on the lamp performance. Mercury has a high vapor pressure and a large momentum transfer cross-section. This provides ohmic dissipation at low currents. Furthermore, mercury has a low thermal conductivity and a high ionization level. These characteristics are beneficial for the power balance of the lamp. Due to the high toxicity of mercury, there is the wish to replace mercury by more environmentally friendly elements without deteriorating the lamp performance too much. Numerical simulations may guide the search for new lamp fillings replacing mercury in metal halide lamps. Since in mercury free lamps there is no longer a dominant background gas, the Fick diffusion approach as used in [142] is no longer valid and Stefan-Maxwell diffusion should be used. Recent work on the modeling of mercury free lamps neglected the effects of demixing due to the absence of a suitable diffusion description [152]. As discussed in that work, the neglect of demixing effects may be responsible for the discrepancy in UV radiation observed between the model and the experiments. The availability of a suitable elemental diffusion algorithm could thus help the understanding of lamp physics.

A mercury free lamp with a filling of xenon and indium iodide will be used as a case study of the new diffusion method. The model[4] consists of a 1D simulation with 100 grid points in the radial direction for a lamp with a radius of 2.6 mm. The pressure was set to 8 bar, while the applied temperature profile can be seen in figure 7.5. The temperature profile is contracted which is typical for lamps that presumably emit optically thin radiation The model includes a mixture of 12 species and four elements (Xe, In, I, e). At the symmetry axis, homogeneous Neumann conditions are used for all the elements. At the lamp wall, the elemental mass fractions are set to 0.30, 0.44, 0.26 and 0.00 for In, I, Xe and e, respectively.

In Figures 7.6,7.7 and 7.8, the results of this calculation can be seen.

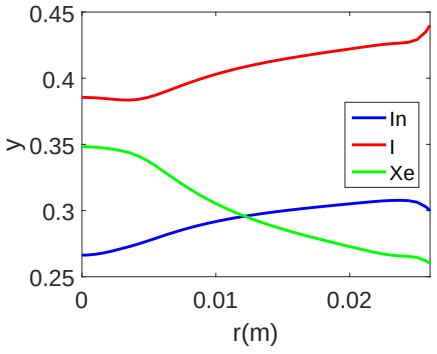

Figure 7.6: Elemental mass fractions in the lamp of Xe, In and I.

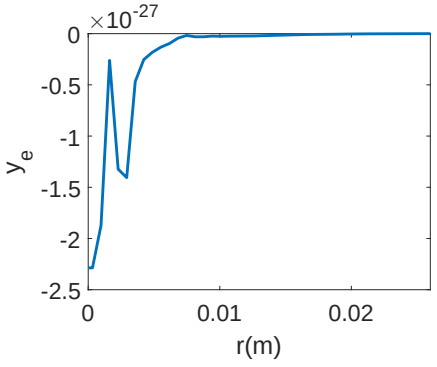

Figure 7.7: Elemental mass fractions of the electrons. This represents charge conservation.

[4]See Supplemental Material at [133] for the source code of this demixing case study (inputfile XeInI.txt).

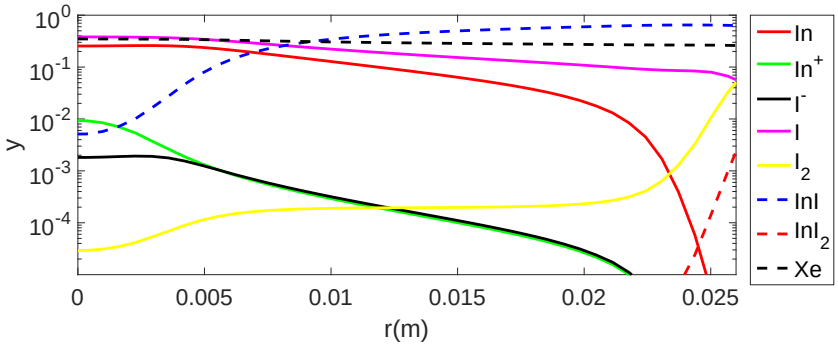

Figure 7.8: Species mass fractions.

We can see that the elemental electron mass fraction vanishes as should be the case according to the derivation in section 7.4.2. Furthermore, the demixing of Xe, In and I under the influence of the applied temperature gradient can clearly be seen. It can be seen that In and I are expelled from the center, while Xe shows the opposite behavior. The reason is that Xe is primarily present as atoms, while In and I are present in the form of molecules which diffuse more difficultly due to their larger size. This effect can also be seen from the thermal demixing coefficient which is depicted in figure 7.9. Xenon has a negative thermal demixing coefficient, pushing it toward the hotter center of the discharge. In and I have positive thermal demixing coefficients. In the thermal demixing coefficients, three transitions can be identified. The first one around 0.5 mm is caused by the ionization of In. The second one in the middle of the domain is due to the dissociation of InI into In and I. The third transition near the wall is caused by the fact that I_2, InI_2 and InI_3 are formed at low temperatures. Gradients in the elemental fractions are largest when the temperature gradient is largest. The reason is as follows. The elemental fluxes should be divergence free. This conditions translates to a zero flux for a 1D simulation. Looking at equation (7.31), it can thus be seen that a temperature gradient should be balanced by a gradient in the elemental mass fractions.

The elemental mass fractions are constraints to the local composition, which is temperature dependent. At the wall of the lamp, In and I are mostly present in the form of InI. These molecules dissociate towards the center of the lamp. Even further towards the center of the lamp some of the atoms ionize, although the ionization degree remains quite low.

A recent description of a mercury free metal-halide lamp [152] concerns a lamp with the salt InI and the start gas Xe. This 1D-model calculates the temperature profile self-consistently by accounting for radiation transfer, ohmic heating and thermal conductivity. However, constant elemental mass fractions were used because an algorithm that solves the Stefan-Maxwell equations was not available at that time. The modeled spectrum contains a large contribution from molecular radiation. This radiation is predominantly attributed to recombination (or free-bound) radiation between the molecular levels A and X. However, not all of

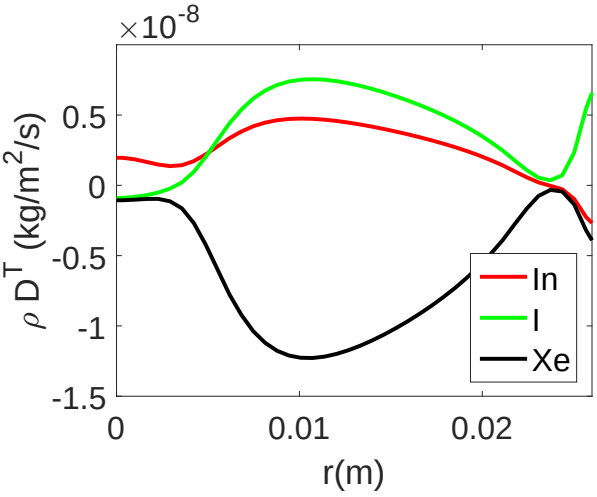

Figure 7.9: Elemental thermal demixing coefficient.

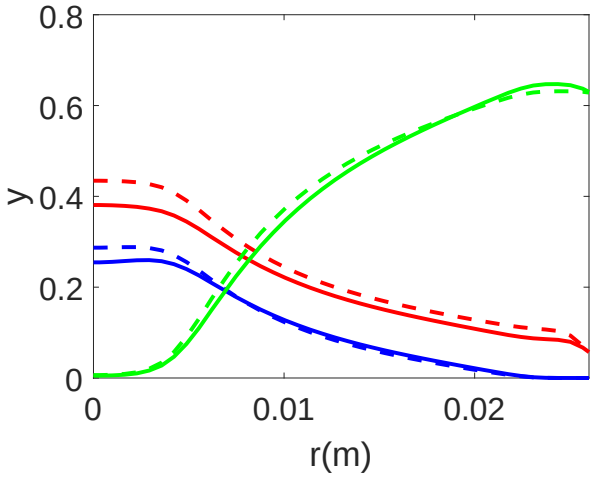

Figure 7.10: The species mass fractions (In, —; I, —; InI, —) calculated with constant elemental mass fractions (dashed lines) are compared with a calculation where demixing is accounted for (full lines). Near the wall an increase of InI can be observed.

the molecular features could be reproduced. For example the absorption in the spectral interval up to 450 nm could not be reproduced. Additionally, the molecular emission between 450 and 1500 nm was slightly overestimated. The effect of demixing on the mass fractions of the species In, I and InI is shown in figure 7.10. The figure shows that in the hot part of the lamp ($r < 0.75$ mm) the mass fraction of the species In and I decreases. Thus the excess molecular radiation is at least partly accounted for. Additionally, the amount of InI in the coolest part of the lamp ($r > 2$ mm) is increased. This is the area where the absorption of radiation is most effective. Thus the increased density of InI will aid in explaining the missing absorption up to 450 nm.

7.7 Discussion and conclusions

In this article, we introduced a method to discretize the elemental continuity equations in closed form. In the discretization scheme the effects of cross-diffusion are taken into account by introduction of the concept of a Péclet matrix. It was shown analytically and numerically that by this definition of the discretization scheme mass and charge constraints are fulfilled exactly. The test case and the case study from sections 7.5 and 7.6 show that indeed the mass and charge constraints are satisfied numerically. It was shown that the coupled scheme shows second order convergence in cases where no flow is present.

The results of the case study of the metal-halide lamp show that the proposed algorithm is capable of describing elemental demixing in real simulations. We hope that our results are useful to actually solve the equations of the closed formulation of LTE diffusion.

7.7.1 Acknowledgements

This work was supported by the IWT-SCHELP project from the Belgian agency for Innovation by Science and Technology (Project number 110003), the CATRENE SEEL project (CA502) and the combined STW-Draka project (10744).

7.A Derivation of the discrete mass end charge conservation equations

To derive the discrete equations for σ^m and σ^c, we start with the discretized equation for the mass fraction vector $\mathbf{y}$. When we apply the coupled exponential scheme from section 7.4.1 to equation (7.18), the following expression is obtained:

$$\mathbf{A}_C\mathbf{y}_C = \mathbf{A}_E\mathbf{y}_E + \mathbf{A}_W\mathbf{y}_W + \mathbf{s}_C\Delta x. \tag{7.52}$$

To derive the discrete equations for σ^m and σ^c, we start with the discretized equation for the mass fraction vector $\mathbf{y}$. When we apply the coupled exponential scheme from section 7.4.1 to equation (7.18), the following expression is obtained:

$$\mathbf{A}_C\mathbf{y}_C = \mathbf{A}_E\mathbf{y}_E + \mathbf{A}_W\mathbf{y}_W + \mathbf{s}_C\Delta x. \tag{7.53}$$

Left multiplication with $\mathbf{u}^{\mathrm{T}} = (1, \ldots, 1)$ and $\mathbf{r}^{\mathrm{T}} = (q_1/m_1, \ldots, q_N/m_N)$, respectively, gives:

$$\begin{aligned} \mathbf{u}^{\mathrm{T}}\mathbf{A}_C\mathbf{y}_C &= \mathbf{u}^{\mathrm{T}}\mathbf{A}_E\mathbf{y}_E + \mathbf{u}^{\mathrm{T}}\mathbf{A}_W\mathbf{y}_W, \\ \mathbf{r}^{\mathrm{T}}\mathbf{A}_C\mathbf{y}_C &= \mathbf{r}^{\mathrm{T}}\mathbf{A}_E\mathbf{y}_E + \mathbf{r}^{\mathrm{T}}\mathbf{A}_W\mathbf{y}_W, \end{aligned} \tag{7.54}$$

since $\mathbf{u}^{\mathrm{T}}\mathbf{s}_C = 0$ and $\mathbf{r}^{\mathrm{T}}\mathbf{s}_C = 0$. If $\mathbf{u}^{\mathrm{T}}$ and $\mathbf{r}^{\mathrm{T}}$ are left eigenvectors of the discretization matrices $\mathbf{A}_E$, $\mathbf{A}_W$ and $\mathbf{A}_C$, this can be written as:

$$\begin{aligned} a_C^m\mathbf{u}^{\mathrm{T}}\mathbf{y}_C &= a_E^m\mathbf{u}^{\mathrm{T}}\mathbf{y}_E + a_W^m\mathbf{u}^{\mathrm{T}}\mathbf{y}_W, \\ a_C^c\mathbf{r}^{\mathrm{T}}\mathbf{y}_C &= a_E^c\mathbf{r}^{\mathrm{T}}\mathbf{y}_E + a_W^c\mathbf{r}^{\mathrm{T}}\mathbf{y}_W, \end{aligned} \tag{7.55}$$

where a_E^m, a_W^m, a_C^m, a_E^c, a_W^c and a_C^c are the corresponding eigenvalues. The above equation is equivalent to equation (7.50). We will now prove that $\mathbf{u}^{\mathrm{T}}$ and $\mathbf{r}^{\mathrm{T}}$ are indeed left eigenvectors of all the discretization matrices. In section 7.3.5, it was already shown that $\mathbf{u}^{\mathrm{T}}$ and $\mathbf{r}^{\mathrm{T}}$ are left eigenvectors of the flux diffusion matrix. Now, we will consider the product with the Péclet matrix $\mathbf{P} = \rho v \delta x \boldsymbol{\Gamma}^{-1}$:

$$\begin{aligned} \mathbf{u}^{\mathrm{T}}\mathbf{P} &= \mathbf{u}^{\mathrm{T}}\rho v\delta x\boldsymbol{\Gamma}^{-1} = \rho v\delta x/\mathcal{D}^m\mathbf{u}^{\mathrm{T}} = P^m\mathbf{u}^{\mathrm{T}}, \\ \mathbf{r}^{\mathrm{T}}\mathbf{P} &= \mathbf{r}^{\mathrm{T}}\rho v\delta x\boldsymbol{\Gamma}^{-1} = \rho v\delta x/\mathcal{D}^c\mathbf{r}^{\mathrm{T}} = P^c\mathbf{r}^{\mathrm{T}}, \end{aligned} \tag{7.56}$$

where we define the 'constraint' Péclet numbers as $P^m = \rho v\delta x/\mathcal{D}^m$ and $P^c = \rho v\delta x/\mathcal{D}^c$. Note that these forms of the 'constraint' Péclet numbers can be understood from equation (7.50). To prove that $\mathbf{u}^{\mathrm{T}}$ and $\mathbf{r}^{\mathrm{T}}$ are left eigenvectors of $B(\mathbf{P})$, we have to diagonalize to the left eigenvectors of the Péclet matrix:

$$\mathbf{P} = \mathbf{W}^{-1}\boldsymbol{\Lambda}\mathbf{W} = \mathbf{W}^{-1}\begin{pmatrix} \lambda_1 & & \\ & \ddots & \\ & & \lambda_N \end{pmatrix}\mathbf{W}, \tag{7.57}$$

$$B(\mathbf{P}) = \mathbf{W}^{-1}B(\boldsymbol{\Lambda})\mathbf{W} = \mathbf{W}^{-1}\begin{pmatrix} B(\lambda_1) & & \\ & \ddots & \\ & & B(\lambda_N) \end{pmatrix}\mathbf{W}, \tag{7.58}$$

where $\mathbf{W}$ contains the left eigenvectors as its rows. Multiplying with $\mathbf{W}$ gives:

$$\mathbf{W}B(\mathbf{P}) = B(\boldsymbol{\Lambda})\mathbf{W} = \begin{pmatrix} B(\lambda_1) & & \\ & \ddots & \\ & & B(\lambda_N) \end{pmatrix}\mathbf{W}, \tag{7.59}$$

Since $\mathbf{u}^{\mathrm{T}}$ and $\mathbf{r}^{\mathrm{T}}$ are rows of $\mathbf{W}$, we can conclude that applying the Bernoulli function to the Péclet matrix does not change the left eigenvectors, but only the corresponding eigenvalues:

$$\begin{aligned} \mathbf{u}^{\mathrm{T}}B(\mathbf{P}) &= B(P^m)\mathbf{u}^{\mathrm{T}}, \\ \mathbf{r}^{\mathrm{T}}B(\mathbf{P}) &= B(P^c)\mathbf{r}^{\mathrm{T}}. \end{aligned} \tag{7.60}$$

With this result the product of $\mathbf{u}^{\mathrm{T}}$ and $\mathbf{r}^{\mathrm{T}}$ with the discretization matrices becomes:

$$\begin{aligned}\mathbf{u}^{\mathrm{T}}\mathbf{A}_E &= 1/\delta x_e \mathcal{D}_e^m B(P_e^m)\mathbf{u}^{\mathrm{T}} = a_E^m \mathbf{u}^{\mathrm{T}},\\ \mathbf{r}^{\mathrm{T}}\mathbf{A}_E &= 1/\delta x_e \mathcal{D}_e^c B(P_e^c)\mathbf{r}^{\mathrm{T}} = a_E^c \mathbf{r}^{\mathrm{T}}.\end{aligned} \tag{7.61}$$

Similar expressions for the west and central discretization matrices can be derived, with which we arrive at (7.50). Note that the discrete equations for σ^m and σ^c have the form as if the scalar exponential scheme was applied to equation (7.39) and (7.40), respectively. Left multiplication with $\mathbf{u}^{\mathrm{T}} = (1, \ldots, 1)$ and $\mathbf{r}^{\mathrm{T}} = (q_1/m_1, \ldots, q_N/m_N)$, respectively, gives:

$$\begin{aligned}\mathbf{u}^{\mathrm{T}}\mathbf{A}_C\mathbf{y}_C &= \mathbf{u}^{\mathrm{T}}\mathbf{A}_E\mathbf{y}_E + \mathbf{u}^{\mathrm{T}}\mathbf{A}_W\mathbf{y}_W,\\ \mathbf{r}^{\mathrm{T}}\mathbf{A}_C\mathbf{y}_C &= \mathbf{r}^{\mathrm{T}}\mathbf{A}_E\mathbf{y}_E + \mathbf{r}^{\mathrm{T}}\mathbf{A}_W\mathbf{y}_W,\end{aligned} \tag{7.62}$$

since $\mathbf{u}^{\mathrm{T}}\mathbf{s}_C = 0$ and $\mathbf{r}^{\mathrm{T}}\mathbf{s}_C = 0$. If $\mathbf{u}^{\mathrm{T}}$ and $\mathbf{r}^{\mathrm{T}}$ are left eigenvectors of the discretization matrices $\mathbf{A}_E$, $\mathbf{A}_W$ and $\mathbf{A}_C$, this can be written as:

$$\begin{aligned}a_C^m\mathbf{u}^{\mathrm{T}}\mathbf{y}_C &= a_E^m\mathbf{u}^{\mathrm{T}}\mathbf{y}_E + a_W^m\mathbf{u}^{\mathrm{T}}\mathbf{y}_W,\\ a_C^c\mathbf{r}^{\mathrm{T}}\mathbf{y}_C &= a_E^c\mathbf{r}^{\mathrm{T}}\mathbf{y}_E + a_W^c\mathbf{r}^{\mathrm{T}}\mathbf{y}_W,\end{aligned} \tag{7.63}$$

where a_E^m, a_W^m, a_C^m, a_E^c, a_W^c and a_C^c are the corresponding eigenvalues. The above equation is equivalent to equation (7.50). We will now prove that $\mathbf{u}^{\mathrm{T}}$ and $\mathbf{r}^{\mathrm{T}}$ are indeed left eigenvectors of all the discretization matrices. In section 7.3.5, it was already shown that $\mathbf{u}^{\mathrm{T}}$ and $\mathbf{r}^{\mathrm{T}}$ are left eigenvectors of the flux diffusion matrix. Now, we will consider the product with the Péclet matrix $\mathbf{P} = \rho v \delta x \mathbf{\Gamma}^{-1}$:

$$\begin{aligned}\mathbf{u}^{\mathrm{T}}\mathbf{P} &= \mathbf{u}^{\mathrm{T}}\rho v\delta x\mathbf{\Gamma}^{-1} = \rho v\delta x/\mathcal{D}^m\mathbf{u}^{\mathrm{T}} = P^m\mathbf{u}^{\mathrm{T}},\\ \mathbf{r}^{\mathrm{T}}\mathbf{P} &= \mathbf{r}^{\mathrm{T}}\rho v\delta x\mathbf{\Gamma}^{-1} = \rho v\delta x/\mathcal{D}^c\mathbf{r}^{\mathrm{T}} = P^c\mathbf{r}^{\mathrm{T}},\end{aligned} \tag{7.64}$$

where we define the 'constraint' Péclet numbers as $P^m = \rho v\delta x/\mathcal{D}^m$ and $P^c = \rho v\delta x/\mathcal{D}^c$. Note that these forms of the 'constraint' Péclet numbers can be understood from equation (7.50). To prove that $\mathbf{u}^{\mathrm{T}}$ and $\mathbf{r}^{\mathrm{T}}$ are left eigenvectors of $B(\mathbf{P})$, we have to diagonalize to the left eigenvectors of the Péclet matrix:

$$\mathbf{P} = \mathbf{W}^{-1}\mathbf{\Lambda}\mathbf{W} = \mathbf{W}^{-1}\begin{pmatrix}\lambda_1 & & \\ & \ddots & \\ & & \lambda_N\end{pmatrix}\mathbf{W}, \tag{7.65}$$

$$B(\mathbf{P}) = \mathbf{W}^{-1}B(\mathbf{\Lambda})\mathbf{W} = \mathbf{W}^{-1}\begin{pmatrix}B(\lambda_1) & & \\ & \ddots & \\ & & B(\lambda_N)\end{pmatrix}\mathbf{W}, \tag{7.66}$$

where $\mathbf{W}$ contains the left eigenvectors as its rows. Multiplying with $\mathbf{W}$ gives:

$$\mathbf{W}B(\mathbf{P}) = B(\mathbf{\Lambda})\mathbf{W} = \begin{pmatrix}B(\lambda_1) & & \\ & \ddots & \\ & & B(\lambda_N)\end{pmatrix}\mathbf{W}, \tag{7.67}$$

Since $\mathbf{u}^{\mathrm{T}}$ and $\mathbf{r}^{\mathrm{T}}$ are rows of $\mathbf{W}$, we can conclude that applying the Bernoulli function to the Péclet matrix does not change the left eigenvectors, but only the corresponding eigenvalues:

$$\begin{aligned} \mathbf{u}^{\mathrm{T}} B(\mathbf{P}) &= B(P^m)\mathbf{u}^{\mathrm{T}}, \\ \mathbf{r}^{\mathrm{T}} B(\mathbf{P}) &= B(P^c)\mathbf{r}^{\mathrm{T}}. \end{aligned} \tag{7.68}$$

With this result the product of $\mathbf{u}^{\mathrm{T}}$ and $\mathbf{r}^{\mathrm{T}}$ with the discretization matrices becomes:

$$\begin{aligned} \mathbf{u}^{\mathrm{T}} \mathbf{A}_E &= 1/\delta x_e \mathcal{D}_e^m B(P_e^m)\mathbf{u}^{\mathrm{T}} = a_E^m \mathbf{u}^{\mathrm{T}}, \\ \mathbf{r}^{\mathrm{T}} \mathbf{A}_E &= 1/\delta x_e \mathcal{D}_e^c B(P_e^c)\mathbf{r}^{\mathrm{T}} = a_E^c \mathbf{r}^{\mathrm{T}}. \end{aligned} \tag{7.69}$$

Similar expressions for the west and central discretization matrices can be derived, with which we arrive at (7.50). Note that the discrete equations for σ^m and σ^c have the form as if the scalar exponential scheme was applied to equation (7.39) and (7.40), respectively.

Chapter 8

Radiation transport

In a plasma there are various processes that are responsible for the production of radiation. The most common process is the spontaneous decay of an excited state in an atom, molecule or an ion. Such a transition occurs at a distinct frequency. Due to Doppler, natural and/or pressure broadening, radiation is also observed in a range around this distinct frequency. In the first sections of this chapter, these broadening mechanisms are discussed in more detail. The remaining sections discuss the discretization of the energy transported as radiation.

Typically, the radiation that is absorbed in a given part of the plasma is not necessarily generated at the same location. The transport associated with this type of plasma is thus non-local. In this chapter, a method is discussed that determines the energy and species source terms related to radiation transport. This is achieved by following the emission and absorption along a few probe lines through the plasma. The theory is applied to an infinite cylinder and is based on the work of Harm van der Heijden [19]. The scheme developed by Van der Heijden is subject to discretization errors. The errors are most severe in the central areas of the cylinder. The discretization errors rapidly decrease for larger radii. In this chapter, the discretization is improved to make sure that the errors indeed vanish when more probe lines are used. The method is tested by calculating and comparing the spectra of a few Hg and Hg–Na discharges. A good agreement is obtained with measured spectra.

8.1 Radiative processes

In this section, the radiative processes are discussed that occur in chapter 10, 11 and 12. These processes include line radiation and continuum radiation. Depending on the initial and final conditions these processes can also be categorized as bound-bound, bound-free, free-bound and free-free transitions. Line radiation of atoms, ions or molecules is accompanied by a change in the state of the emitting particle and can therefore also be considered as bound-bound radiation. The energy difference between the initial and final states defines the frequency of the emitted photon via $E = h\nu$. The total emission j corresponding to line radiation

can then be written as

$$j = \frac{h\nu}{4\pi} A_{ul} n_u, \tag{8.1}$$

with A_{ul} the transition strength for spontaneous emission and n_u the excited state density. In reality a range of frequencies around ν is observed. This profile is called the line profile ϕ. The spectral emission can then be expressed as

$$j_\nu = \frac{h\nu}{4\pi} A_{ul} n_u \phi(\nu) = j\phi(\nu), \tag{8.2}$$

The line profile can be considered as a distribution function and should therefore be normalized

$$\int \phi \mathrm{d}\nu = 1. \tag{8.3}$$

Various mechanisms can be responsible for the line profile. For example, a velocity difference between the emitter and the observer can induce Doppler shifts. Another broadening mechanism is natural broadening, where the uncertainty principle introduces small energy variations of the upper and lower states of the emitting particle. Additionally, the energy levels of the upper and lower states can be perturbed due to interactions with the electric field of other particles. This type of broadening mechanism is called pressure broadening.

Most broadening processes in the remainder of this chapter can be either described by a Lorentzian or a Gaussian profile. For that reason, these line profiles are considered before the processes are discussed in more detail. The Lorentz profile is given by

$$\phi_L = \frac{\Delta\gamma}{\pi\left(\Delta\gamma^2 + (\nu - \nu_0)^2\right)}, \tag{8.4}$$

with γ the half width at half maximum (HWHM). The Gaussian profile can be written as

$$\phi_G = \frac{1}{\sigma\sqrt{2\pi}} \exp\left(-\frac{(\nu - \nu_0)^2}{2\sigma^2}\right), \tag{8.5}$$

with the full width at half maximum (FWHM) given by $\Delta\nu_{\mathrm{FWHM}} = \sigma\sqrt{8\ln 2}$, σ the standard deviation and ν_0 the unperturbed frequency. In the case of multiple broadening mechanisms, the final line profile can be calculated as the convolution of the individual profiles [153, p. 101,102]. This procedure is only correct if the two broadening mechanisms are statistically independent. The convolution of multiple Lorentzian profiles results in another Lorentzian profile with γ the sum of the individual HWHM.

A different process that has not been discussed so far is continuum radiation. Two processes will be considered. The first process is called free-free continuum radiation where electrons are scattered on a neutral or an ion. In this case, radiation is emitted by charged particles that are accelerated or decelerated in the plasma. This process is also called Bremsstrahlung. The second process is called free-bound continuum radiation or recombination radiation. In the recombination process, an electron is captured by an ion and a photon is released.

8.1.1 Doppler broadening

The Doppler effect explains the frequency shift that is induced by the motion of the emitter relative to the observer [154, p. 248]. If the distribution of velocities is described by a Maxwellian distribution, the corresponding line profile is a Gaussian profile (8.5). Its FWHM is given by $\Delta\nu_{\mathrm{FWHM}} = \sqrt{\frac{8k_B T \ln 2}{mc^2}}\nu_0$.

8.1.2 Natural broadening

The quantum mechanical uncertainty principle of time and energy $\Delta E \Delta t \geq \frac{\hbar}{2}$ indicates that the uncertainty in the energy of the upper and lower states can induce a distribution of possible frequencies [154, p. 232-236]. The induced profile is a Lorentzian profile (8.4). The HWHM of this distribution can be estimated with $\gamma = \frac{1}{2\pi}\sum_i A_{ki}$. In plasmas, this contribution is usually small in comparison to other contributions.

8.1.3 Pressure broadening

The interaction potential between an excited atom and a perturber can be approximated with [154, p. 236-248]

$$\Delta V(r) = \frac{C_n}{r^n}, \tag{8.6}$$

with C_n a constant dependent on the excited state and the perturbing species. The cases $n = 2, 3, 4 or 6$ are most often encountered. For $n = 2$, the process is called linear Stark broadening, since the perturbation is proportional to the electric field. It is applicable for hydrogen and hydrogenic ions. For $n = 3$, the process is called resonance broadening. This can occur when the excited state is perturbed by a species of the same type. The magnitude of the perturbation is linearly dependent on the dipole transition strength between the excited state and the perturbing state. The process is described using the dipole potential [155, eq. 3]. For $n = 4$, the process is called quadratic Stark broadening. The potential is proportional to the square of the electric field induced by charged particles. Stark broadening is an important broadening mechanism for plasmas with a high ionization degree. For $n = 6$, the process is called Van der Waals broadening. This weak long-range interaction is caused by the dipole-dipole interaction. In high pressure discharges the dominant broadening mechanisms are resonance and Van der Waals broadening. Broadening mechanisms due to short-range interactions are neglected in the remaining sections.

The interaction potential (8.6) is required to describe the movement of a perturber in the vicinity of an atom at a given impact parameter. In order to account for a range of possible perturbations, multiple impact parameters have to be considered. Analytical expressions can only be obtained in the quasi-static or the impact limit. One can distinguish between these limits by comparing the duration of one collision, t_c, with the average time between collisions, T_c. The duration of

a collision can be approximated by [154, p. 239]

$$t_c = \frac{r_0}{\langle v \rangle}, \tag{8.7}$$

where r_0 is the distance of closest approach during the straight line trajectory and $\langle v \rangle$ is the average velocity at r_0.

- The quasi-static approximation is valid when the duration of a collision is much larger than the time between collisions

$$t_c \gg \frac{1}{2\pi\Delta\nu} \approx T_c. \tag{8.8}$$

  The relatively large collision time is caused by the slow movement of the perturbers. For that reason, the motion of the perturbers can be neglected. In that case, the broadening is dependent on the difference between the potential curves

$$\Delta\nu_{ki} = \frac{\Delta V_k(r) - \Delta V_i(r)}{h}, \tag{8.9}$$

  with $\Delta V_i(r) = V_i(r) - V_i(\infty)$. Quasi-static broadening is relevant when the density of perturbers is high. Additionally, the velocity of the perturbing particles should be low to ensure a long collision time. This is the case at low temperatures.

- The impact approximation is valid when the duration of the collisions is short compared to the time between collisions

$$t_c \ll \frac{1}{2\pi\Delta\nu} \approx T_c. \tag{8.10}$$

  These conditions are met when the pressure is low and when the temperature is high.

In general, the line profile contains contributions of both theories. In that case the core of the line broadening is given by the impact limit and the wings of the profile by the quasi-static limit. For example, these line profiles are used in chapters 10 and 11.

Quasi-static broadening

The radiation emitted at frequency ν in a bandwidth $\mathrm{d}\nu$ induced by the presence of a perturber in a region $\mathrm{d}r$ around r from the excited atom is given by

$$\phi(\nu)\,\mathrm{d}\nu = \frac{4\pi r^2 \mathrm{d}r}{V}, \tag{8.11}$$

with V the volume under consideration. The shift from the line center is given by

$$\Delta\nu = \frac{C'}{r^n}, \tag{8.12}$$

with $C' = \frac{C_k - C_i}{h}$. Changing variables from r to ν gives

$$\phi(\nu)\,\mathrm{d}\nu = \frac{4\pi C'^{3/n}}{nV}\frac{1}{(\nu-\nu_0)^{(n+3)/3}}\mathrm{d}\nu. \tag{8.13}$$

A more accurate approximation accounts for the distribution of perturbing particles. In that case, it is assumed that the nearest neighbor is the only perturbing particle. For such a modification, the quasi-static line profile can be approximated by [30]

$$\phi(\Delta\lambda) = \begin{cases} \frac{\Delta\lambda_0}{2(\Delta\lambda)^{3/2}}\exp\left(-\frac{\pi\Delta\lambda_0}{4\Delta\lambda}\right) & \lambda > \lambda_0 \\ 0 & \lambda \leq \lambda_0 \end{cases}, \tag{8.14}$$

with $\Delta\lambda_0 = \frac{\lambda_0^2}{2\pi c}C_6\left(4/\left[3\pi n_p\right]\right)^2$. This type of approximation can only be made for potentials that decay sufficiently fast: $n \geq 6$. For Stark broadening with $n = 2$, or $n = 4$ the simultaneous effect of all perturbers must be included. The previously described line profiles use a potential energy difference of $\Delta V \propto -C_6/r^6$. Such an energy difference only provides a reasonable estimate at pressures where only large interatomic separations contribute significantly to the line profile. For higher pressures the potential energy difference at lower interatomic separations are more prominently contributing. The result is that the line profile should be calculated according to Hedges [156, eq. 7,12]

$$\phi(\nu)\,\mathrm{d}\nu \propto \frac{n_p 4\pi r^2(\nu) f(r)\,\mathrm{d}\nu}{|\mathrm{d}\nu/\mathrm{d}r|}, \tag{8.15}$$

with n_p the perturber density and $f(r)$ the distribution function of the radiators. The distribution of the radiators $f(r)$ is proportional to $\exp\left(-\frac{(V_u(r)-V(\infty))}{k_B T}\right)$. The distribution proposed by Hedges is accurate if the time averaged probability of an excited particle being perturbed in a volume of $\frac{4}{3}\pi R^3$ is small. The radius R can be considered as the interatomic separation between the radiator and the perturber where $V(r)$ deviates significantly from $V(\infty)$. If $n_p\frac{4}{3}\pi R^3 \ll 1$ is valid, only binary encounters are important. For example, $n_p = 10^{25}\,\mathrm{m}^{-3}$ and $R = 5\times10^{-10}\,\mathrm{m}$ give a result of about 0.005, which still satisfies the criterion.

Impact broadening

The first version of the impact theory was proposed by Lorentz [154, p. 241]. He assumed that a classical wave train was emitted at the moment of excitation[1] at $t = 0$.

At the moment of collision $t = T_c$, he assumed that the wave train was terminated. The spectral distribution is then dependent on the distribution of times between collisions. By averaging over this distribution he obtained a Lorentzian profile. However, the cross sections that were derived from his theory were one or two orders of magnitude larger than the gas kinetic cross sections.

[1] The classical electric field that was considered by Lorentz is given by $E(t) = E(0)\exp\left(-i\left[\omega_0 - i\gamma/2\right]t\right)$ where γ is the decay rate of the oscillating electron.

Weisskopf modified the theory by assuming that the wave train is not terminated but is subject to a phase change. The phase shift for a straight line trajectory is given by[2]

$$\eta(b) = \int_{-\infty}^{\infty} 2\pi\Delta\nu \mathrm{d}t = \int_{-\infty}^{\infty} \frac{2\pi C_n' \mathrm{d}t}{\left(b^2 + \langle v\rangle^2 t^2\right)^{n/2}} = \frac{2\pi C_n' a_n}{\langle v\rangle b^{n-1}}. \tag{8.16}$$

Weisskopf assumed that the wave train with a phase change larger than unity is incoherent with the wave train emitted before the collision. Thus, from $\eta(b_W) = 1$ an optical collision radius can be derived

$$b_W = \left(\frac{2\pi C_n' a_n}{\langle v\rangle}\right)^{1/(n-1)}. \tag{8.17}$$

The HWHM is obtained from

$$2\pi\gamma = n_p \pi b_W^2 \langle v\rangle = n_p \pi \left(\frac{2\pi C_n' a_n}{\langle v\rangle}\right)^{2/(n-1)} \langle v\rangle, \tag{8.18}$$

with n_p the number density of perturbing particles.

Lindholm and Foley [157, eq. 17,18] [158, p. 179] [154, p. 245] improved Weisskopf's theory by including the phase changes smaller than unity by using correlation functions. The resulting line profile is again a Lorentzian profile. The line width and the line shift are given by $nv\sigma_r$ and $nv\sigma_i$, respectively. The real part of the optical collision cross section σ_r is given by

$$\sigma_r = 2\pi \int_0^{\infty} [1 - \cos\eta(b)]\, b\mathrm{d}b, \tag{8.19}$$

and the imaginary part σ_i is given by

$$\sigma_i = 2\pi \int_0^{\infty} \sin\eta(b)\, b\mathrm{d}b. \tag{8.20}$$

For $b < b_W$, the integrand of σ_i is an oscillating function. Its contribution to the integral vanishes. However, a significant contribution to σ_r originates from $b > b_W$.

In chapters 10, 11 and 12, the theory of Lindholm and Foley is used. A summary of the estimates for the parameters C_3, C_4 and C_6 is given in [159] and chapter 9. For interaction potentials of the type $V = -C_n/r^n$, the results for the theories of Weisskopf and Lindholm and Foley differ only by a numerical factor. These factors are given by Foley [157, p. 621] and Sobelman [158, p. 181]. When an interaction potential is available, (8.19) and (8.20) can be integrated numerically to obtain more accurate expressions for the line width according to impact theory. The phase shift can then be related to the interaction potential using the JWKB approximation [83, eq. 6].

[2] The last step uses the following substitution $\langle v\rangle t = b\tan\theta$ and $a_n = \int_{-\pi/2}^{\pi/2} \cos^{n-2}\theta \mathrm{d}\theta$.

Combined broadening processes

A broadening profile that is often encountered in plasma physics is the Voigt profile. It is the result of a convolution between a Gaussian and a Lorentzian profile. The Voigt profile can be calculated from [160–162]

$$\phi_V(z) = \sqrt{2}\frac{\mathcal{R}[w(z)]}{\sqrt{\pi}\sigma_G}, \tag{8.21}$$

with $z = \sqrt{\ln 2}(\nu - \nu_0 + i\gamma_L)/\sigma_G$ and σ_G and γ_L the Gaussian standard deviation and the Lorentzian HWHM, respectively.

At sufficiently high pressures, the line profile contains contributions from the theories of impact and quasi-static broadening. For the quasi-static profile given by (8.14), the convolution with a Lorentzian profile is given by [159, eq. 51]

$$\phi(\Delta\lambda) = \frac{4}{\pi^2\Delta\lambda_0}\left(\frac{b}{a}\right)^{3/2}\left[\frac{\sqrt{\pi}}{2}\left(w\left(\sqrt{b/a}\right) + w\left(-\sqrt{b/a}\right)\right)\right], \tag{8.22}$$

with $a = \Delta\lambda/\gamma_L$, $b = \pi\Delta\lambda_0/(4\gamma_L)$ and $w(x)$ the Faddeeva function. An analytical expression for the convolution of the quasi-static line profile given by (8.15) with a Lorentzian profile is not obtained. Instead the convolution integral is approximated by cutting off the quasi-static profile at interatomic separations larger than $r = R$. For $r > R$, the potential difference is given by $V = V_u(\infty) - V_l(\infty)$ and the modified quasi-static contribution can be written as

$$\phi_{QS,m}(\nu(r)) = F_1\phi_{QS,n}(\nu(r)) + F_2\delta(\nu - \nu_0), \tag{8.23}$$

with $\phi_{QS,n}$ given by (8.15) and normalized on $0 \leq r \leq R$. The remaining parameters are given by

$$F_1 = \int_0^R f(r)\,\mathrm{d}r/N, \tag{8.24}$$

$$F_2 = \exp\left(-\left(\frac{V(\infty)}{k_BT}\right)\right)\left(1 - \frac{4}{3}\pi R^3 n_p\right)/N, \tag{8.25}$$

$$f(r) = 4\pi r^2 n_p \exp\left(-\frac{V(r) - V(\infty)}{k_BT}\right), \tag{8.26}$$

$$N = 1/(F_1 + F_2). \tag{8.27}$$

The convolution can than be written as

$$\begin{aligned}(\phi_L * \phi_{QS,m}) &= F_1(\phi_L * \phi_{QS,n}(\nu(r))) + F_2(\phi_L * \delta(\nu - \nu_0)) \\ &\approx F_1\phi_{QS,n}(\nu) + F_2\phi_L,\end{aligned} \tag{8.28}$$

The first term on the RHS has been derived by considering the Lorentzian profile as a delta peak. Such an approximation is valid if the quasi-static profile is much broader then the Lorentzian profile.

8.1.4 Continuum radiation

Three types of continuum radiation are discussed: electron-atom, electron-ion free-free and electron-ion free-bound (recombination radiation). The electron-atom emission (Bremsstrahlung) is given by [163] [164, eq. 16,21]

$$j_\nu = C_{ea} \frac{n_e n_a}{c} \left(k_B T_e\right)^{3/2} Q^{(1)} \left[\left(1 + \frac{h\nu}{k_B T_e}\right)^2 + 1\right] \exp\left(-\frac{h\nu}{kT_e}\right), \tag{8.29}$$

with C_{ea} =2.000 $\mathrm{Wm^2J^{-3/2}sr^{-1}}$. Burm [164] notes that there are different possibilities to relate the Bremsstrahlung cross section to the momentum transfer cross section. The methods differ slightly in the factor before the exponent [164, eq. 19-21]. The free-free continuum radiation (Bremsstrahlung) emitted in an electron-ion encounter can be approximated with

$$j_\nu = C_{ei} \frac{n_e n_i}{\sqrt{k_B T_e}} \xi_{ff}^{ei} \exp\left(-\frac{h\nu}{k_B T_e}\right), \tag{8.30}$$

with C_{ei}=2.023 $\times$ 10^{-63} $\mathrm{WJ^{1/2}m^3Hz^{-1}sr^{-1}}$ and ξ_{ff}^{ei} the Biberman factor. The free-bound Bremsstrahlung for electron-ion collisions is given by

$$j_\nu = C_{ei} \frac{n_e n_i}{\sqrt{k_B T_e}} \left[1 - \exp\left(-\frac{h\nu}{k_B T_e}\right)\right] \xi_{fb}^{ei}. \tag{8.31}$$

The Biberman factors account for the non-hydrogenic behavior of the radiation levels of gases [164, p. 391]. Burm states that in practice the factors are approximately 1 for $\lambda > 800\,\mathrm{nm}$. For lower wavelengths a process specific Biberman factor is required for accurate calculations. In this wavelength range the Biberman factors also depend on the temperature.

8.2 Radiation theory

The power transported by radiation can be expressed as a function of the radiative flux. The radiative flux is a function of the radiance[3]. The radiance is determined by the local properties of the plasma and can be calculated with the equation of radiative transport. This equation is given by

$$\frac{\mathrm{d}I_\nu}{\mathrm{d}s} = j_\nu - \kappa_\nu I_\nu, \tag{8.32}$$

with j_ν the emission in $\mathrm{Wm^{-3}sr^{-1}Hz^{-1}}$, κ_ν the absorption in $\mathrm{m^{-1}}$, I_ν the spectral radiance in $\mathrm{Wm^{-2}sr^{-1}Hz^{-1}}$ and s the path traversed by the radiation. A subscript ν is used to indicate that a variable depends on the frequency. The emission, absorption and the spectral radiance all depend on the local composition of the plasma.

[3]Note that the radiance is also called intensity in the field of astrophysics [165, p. 1].

In case of local thermodynamic equilibrium (LTE) Kirchhoff's law [165, p. 8] can be used to determine the spectral radiance from

$$I_\nu = \frac{j_\nu}{\kappa_\nu} = \frac{2h\nu^3}{c^2}\frac{1}{\exp\left(\frac{h\nu}{k_B T_e}\right) - 1} = B_\nu, \tag{8.33}$$

with B_ν the thermal radiation or blackbody radiation. The spectral emission is given by [166, p. 8-13, p. 30-32] [19, p. 44-47]

$$j_\nu = \frac{h\nu}{4\pi} A_{ul} n_u \phi, \tag{8.34}$$

with ϕ the line profile, A_{ul} the transition strength and n_u the excited state density. The absorption can be written as

$$\kappa_\nu = \sigma_{\text{abs}} n_l - \sigma_{\text{stim}} n_u, \tag{8.35}$$

with n_l the density of the state where the species decays towards. The cross sections can be calculated by inserting (8.34) and (8.35) in (8.33). The cross sections for stimulated emission and absorption are thus given by

$$\sigma_{\text{stim}} = \frac{c^2}{8\pi\nu^2} A_{ul}\phi = \frac{h\nu}{4\pi} B_{ul}\phi, \tag{8.36}$$

$$\begin{aligned} \sigma_{\text{abs}} &= \frac{c^2}{8\pi\nu^2} A_{ul}\frac{g_u}{g_l}\exp\left(\frac{h\left(\nu-\nu_0\right)}{k_B T_e}\right)\phi \\ &\approx \frac{c^2}{8\pi\nu^2} A_{ul}\frac{g_u}{g_l}\phi = \frac{h\nu}{4\pi} B_{lu}\phi, \end{aligned} \tag{8.37}$$

with ν_0 the unperturbed frequency. In order to derive these equations the Boltzmann relation was used to relate the lower state density to the upper state density.

The derived cross sections are valid regardless of the state of the plasma. In general the plasma is not thermal. The local radiative equilibrium is then defined by

$$I_\nu = \frac{j_\nu}{\kappa_\nu} = \frac{2h\nu^3}{c^2}\frac{1}{\frac{n_l g_u}{n_u g_l}\exp\left(\frac{h(\nu-\nu_0)}{k_B T_e}\right) - 1}. \tag{8.38}$$

The cross section for stimulated emission can be simplified by neglecting the variation in $\nu - \nu_0$. However, this approximation induces deviations in cases where the emitting particle is subject to severe pressure broadening and $h\left(\nu-\nu_0\right) \gg k_B T_e$. For low pressure plasmas the absorption can be approximated with

$$\kappa_\nu = \frac{h\nu}{4\pi} n_l B_{lu}\left(1 - \frac{g_l n_u}{g_u n_l}\right)\phi, \tag{8.39}$$

from which it is apparent that stimulated emission can be neglected if $g_u n_l \gg g_l n_u$. Note that the Einstein relations have been used to rewrite the equations. These

relations are given by [166, p. 30][4]

$$g_l B_{lu} = g_u B_{ul}, \tag{8.40}$$

$$A_{ul} = \frac{2h\nu^3}{c^2} B_{ul}. \tag{8.41}$$

The radiative flux $\mathrm{d}^2\Phi_\nu$ that passes through a surface area $\mathrm{d}A$ in the direction $\vec{s}$, covering a solid angle $\mathrm{d}\Omega$ is given by

$$\mathrm{d}^2\Phi_\nu = I_\nu \vec{s} \cdot \mathrm{d}\vec{A}\mathrm{d}\Omega. \tag{8.42}$$

The spectral power density passing through that surface can then be calculated by integrating over the solid angle and the area

$$Q_{\nu,\mathrm{rad}} = \iint \frac{\mathrm{d}^2\Phi_\nu}{V}, \tag{8.43}$$

with V the local volume of the considered gas. In order to demonstrate that radiation transport is a non-local phenomenon it is useful to consider the radiation losses in a cylinder for a few constant values of j_ν and κ_ν. In figure 8.1 these losses are shown for $j_\nu = 10^{-10}\,\mathrm{Wm^{-3}Hz^{-1}sr^{-1}}$. The figure shows that for $\kappa = 0.01\,\mathrm{m}^{-1}$ the radiation losses per unit volume are practically constant. This is expected for radiation that is not reabsorbed. However, for plasmas with higher absorption coefficients the radiation losses are larger in the outer volume of the plasma. The reason is that for higher absorption coefficients the radiation approaches equilibrium faster. In that situation the net energy transferred approaches zero since the energy emitted as radiation is balanced by the energy absorbed.

8.3 Change of spectral radiance

The calculation of the radiative energy transport can in general not be evaluated analytically. Computer models are required for these calculations. These models require a discretization of the radiative energy transport. In this section an expression for the change of the radiance is given for an arbitrary direction through an arbitrary volume. This section also discusses the optically thick and thin limits.

The solution of (8.32) for a ray originating at s_0 can be written down in integral form as

$$I_\nu(s) = \int_{s_0}^{s_1} j_\nu(s') \exp\left(-\int_{s'}^{s_1} \kappa_\nu(s")\,\mathrm{d}s"\right)\mathrm{d}s'. \tag{8.44}$$

This equation can be simplified to

$$I_\nu(s) = \int_{s_0}^{s_1} j_\nu(s') \exp(-\tau_\nu)\,\mathrm{d}s', \tag{8.45}$$

[4] Note that the derivation in the cited work uses the mean spectral radiance $J_\nu = \frac{1}{4\pi}\int I_\nu \mathrm{d}\Omega$. By using the total radiation density for the derivation $u_\nu = \frac{4\pi}{c} J_\nu$ the relation between A_{ul} and B_{ul} changes with the factor $\frac{4\pi}{c}$ due to the different definition.

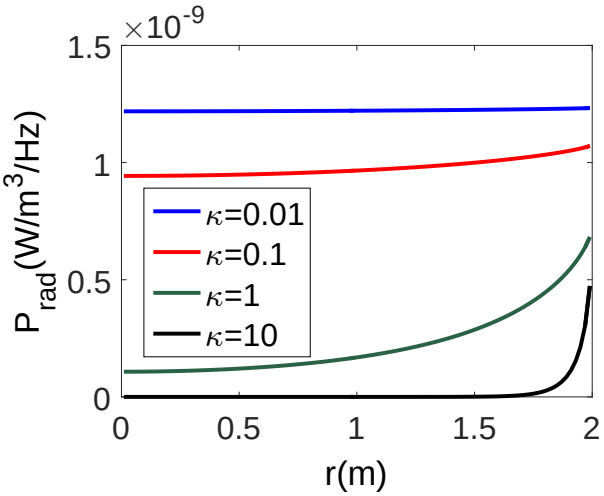

Figure 8.1: The radiation losses per unit volume are shown for $j_\nu = 10^{-10}\,\mathrm{Wm^{-3}Hz^{-1}sr^{-1}}$ and a few different values of the absorption coefficient.

by introducing the optical depth, τ_ν, defined as

$$\tau_\nu = \int_{s'}^{s_1} \kappa_\nu\left(s"\right) \mathrm{d}s". \tag{8.46}$$

For an arbitrary distance Δs through a small piece of plasma with constant j_ν and κ_ν it is possible to integrate (8.45) analytically. The result of this integration is given by

$$\begin{aligned} & j_\nu \int_s^{s+\Delta s} \exp\left(-\int_{s'}^{s+\Delta s} \kappa_\nu s'' \mathrm{d}s''\right) \mathrm{d}s' \\ = \;& j_\nu \exp\left(-\kappa_\nu\left(s+\Delta s\right)\right) \int_s^{s+\Delta s} \exp\left(\kappa_\nu s'\right) \mathrm{d}s' \\ = \;& \frac{j_\nu}{\kappa_\nu}\left[1-\exp\left(-\kappa_\nu \Delta s\right)\right]. \end{aligned} \tag{8.47}$$

By also considering the spectral radiance which entered this piece of plasma and is traveling in the same direction, $I_\nu\left(s\right)$, the radiation leaving the plasma at, $I_\nu\left(s+\Delta s\right)$ is given by

$$\begin{aligned} I_\nu\left(s+\Delta s\right) &= I_\nu\left(s\right)\exp\left(-\kappa_\nu \Delta s\right) + \frac{j_\nu}{\kappa_\nu}\left[1-\exp\left(-\kappa_\nu \Delta s\right)\right] \\ &= I_\nu \exp\left(-\tau_\nu\right) + \frac{j_\nu}{\kappa_\nu}\left[1-\exp\left(-\tau_\nu\right)\right]. \end{aligned} \tag{8.48}$$

The change of the radiance along this path, ΔI_ν, can then be expressed as

$$\Delta I_\nu = I_\nu\left(s+\Delta s\right) - I_\nu\left(s\right) = \left(\frac{j_\nu}{\kappa_\nu} - I_\nu\left(s\right)\right)\left[1-\exp\left(-\tau_\nu\right)\right]. \tag{8.49}$$

This equation shows that the plasma reduces the difference between the local source $S_\nu = \frac{j_\nu}{\kappa_\nu}$ and the ingoing radiance $I_\nu(s)$ by a factor $[1 - \exp(-\tau_\nu)]$. In the special case of LTE this result can be rewritten as

$$\Delta I_\nu = (B_\nu - I_\nu)\left[1 - \exp(-\tau_\nu)\right], \tag{8.50}$$

with B_ν the thermal radiance. The plasma thus tries to reduce the difference between the radiance and the local thermal radiance.

Two limits can be distinguished. In the optical thick limit $\tau \gg 1$ the outgoing radiance, $I_\nu(s + \Delta s)$, is always equal to the local source, S_ν. In this limit the radiation achieved a local equilibrium. The spectral power emitted as radiation can be calculated locally as

$$Q_{\nu,\mathrm{rad}} = \iint (B_\nu - B_{\nu,\mathrm{ext}})\, \vec{s} \cdot \mathrm{d}\vec{A}\mathrm{d}\Omega, \tag{8.51}$$

with $B_{\nu,\mathrm{ext}}$ the ingoing thermal radiation from the environment. In the optically thin limit $\tau \ll 1$ (8.49) can be approximated with

$$\begin{aligned} \Delta I_\nu &\approx \left(\frac{j_\nu}{\kappa_\nu} - I_\nu(s)\right)\kappa_\nu \Delta s \\ &\approx j_\nu \Delta s - I_\nu \kappa_\nu \Delta s \\ &\approx j_\nu \Delta s. \end{aligned} \tag{8.52}$$

The power emitted as thin radiation can be calculated locally as

$$Q_{\nu,\mathrm{rad}} = \int j_\nu 4\pi \mathrm{d}V. \tag{8.53}$$

In general a local calculation of the radiation losses is not possible. The energy transferred should then be evaluated numerically.

Besides the energy source term the radiation module should also calculate the source term for the species. The species source term can be written as [19, p. 105]

$$\frac{\partial n_i}{\partial t} = \int \frac{4\pi}{h\nu}\left(\kappa_{\nu,i} J_\nu - j_{\nu,i}\right)\mathrm{d}\nu, \tag{8.54}$$

with J_ν the angle averaged radiance. This averaged radiance is given by [165, p. 4]

$$J_\nu = \frac{1}{4\pi}\int I_\nu \mathrm{d}\Omega. \tag{8.55}$$

In the next section a grid-based numerical method is discussed that can evaluate the energy and species source terms for arbitrary optical depths.

8.4 Cylindrical geometry

Section 8.3 showed how the spectral radiance of a ray with an arbitrary direction vector changes due to interaction with the gas in a given volume. In this section

a numerical method is described which is used to calculate the radiative energy transport in an infinite cylinder. The method is called ray tracing and is based on the description given by van der Heijden [19, p. 109-114] [20]. In section 8.7 is shown that the algorithm developed by van der Heijden contains discretization errors and an improved algorithm is presented. This section describes the original implementation. The radiative losses are estimated by considering the evolution of the radiance along a set of rays in multiple directions.

In section 8.2 it was shown that the spectral radiative flux can be calculated as

$$\mathrm{d}^2\Phi_\nu = I_\nu \vec{s} \cdot \mathrm{d}\vec{A}\mathrm{d}\Omega. \tag{8.56}$$

The spectral radiative flux passing through the area $\mathrm{d}\vec{A}$ on the surface of a cylindrical shell can be discretized by following the evolution of the radiance along a few rays. Later in this section it is shown that the spectral radiative flux transported along ray segment k, i, t can be discretized as

$$\Delta\vec{\Phi}_{k,i,t,\nu} = \mp 4\pi\Delta z \Delta I_{k,i,t,\nu}\left(\Delta s_{k,i,t}\right)\sin^2\theta_t \Delta r_k \Delta\theta. \tag{8.57}$$

The radiative energy source term can then be derived from (8.43) as

$$Q_{\nu,\mathrm{rad}} = \iint \frac{\mathrm{d}^2\Phi_\nu}{V} \approx \sum_t \sum_{k=1}^{k=i} \frac{\Delta\Phi_{k,i,t,\nu}}{V_k}. \tag{8.58}$$

The local change of the spectral radiance $I_{k,i,t,\nu}\left(\Delta s_{k,i,t}\right)$ is taken from (8.49).

The probe lines that are used in the discretization procedure are characterized by their direction vector $\vec{s}$. These are chosen in a way that all rays originate on a boundary point and form a tangent line to a different nodal point. These tangent lines are only drawn for nodal points with a smaller radius than the radius of the boundary point. The first and last nodal points are not included since they represent no volume. The discretization of the radiative flux through $\mathrm{d}\vec{A}$ for the two boundary points with the largest radii is shown in figure 8.2. For both cases the rays can be rearranged by making use of azimuthal symmetry. The result is shown in figure 8.3. This figure shows that rays originating on the outer boundary point follow the same path as rays originating on other boundary points. The number of rays required to sample the radiance is thus reduced to the number of control volumes. The distance through a control volume $\Delta s_{k,i}$, shown in figure 8.5 for rays in a horizontal plane, is given by

$$\begin{cases} \Delta s_{k,i} = \sqrt{R_i^2 - r_k^2} - \sqrt{R_{i-1}^2 - r_k^2} & i > k \\ \Delta s_{k,i} = 2\sqrt{R_k^2 - r_k^2} & i = k, \end{cases} \tag{8.59}$$

with k the nodal point number with the smallest radius the ray passes through, and i the nodal point number indicating in what control volume this distance is calculated. R is the radius of the boundary points and r is the radius of the nodal points. Note that due to azimuthal symmetry only half of the azimuthal angle is considered: $\int_{-\pi/2}^{\pi/2}\mathrm{d}\alpha = 2\int_0^{\pi/2}\mathrm{d}\alpha$.

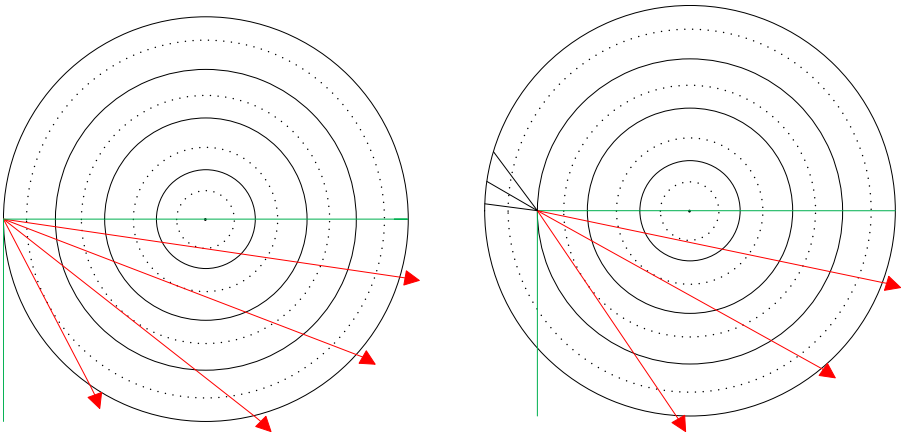

Figure 8.2: Discretization of the radiative flux at a point on the largest (left) and second largest (right) boundary point. The nodal points are shown in dotted lines and the boundary points are shown in solid lines. A red line shows the direction vector. The direction vectors of the rays are chosen in such a way that every ray is a tangent line to a different nodal point. The black lines preceeding the red lines in the figure on the right hand side show where the lines used for the sampling of the second shell originated. The green lines show the sampled angle in the cylindrical plane.

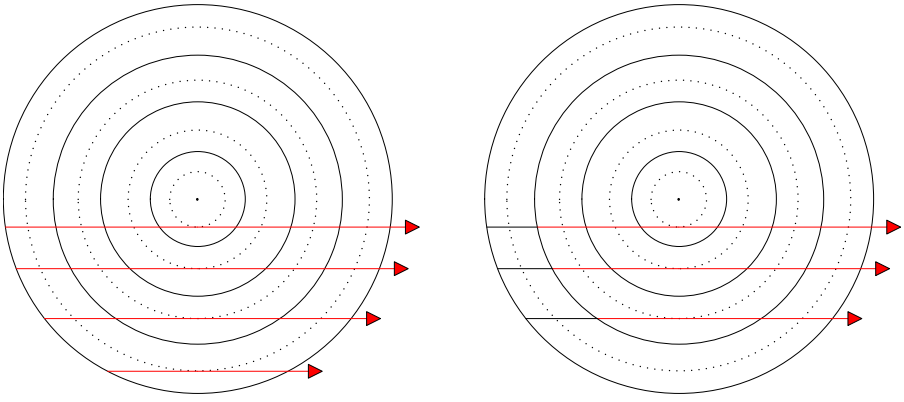

Figure 8.3: Rays emerging at different boundary points can all be rearranged to the same set of parallel rays. In the left figure the rays emerging at the outer shell are shown and in the right figure the rays that emerge at the second largest shell are shown. The rays in the left and right figures follow the same path. This procedure significantly reduces the number of rays required to sample the radiance.

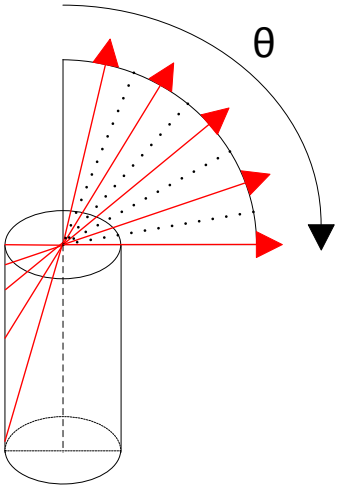

Figure 8.4: The red arrows indicate how the zenith angle has been discretized. The black dots indicate the section of the zenith angle that is represented by the red arrows. The ray at $\theta = \pi/2$ covers a part of the zenith angle that is half above and half below the symmetry plane.

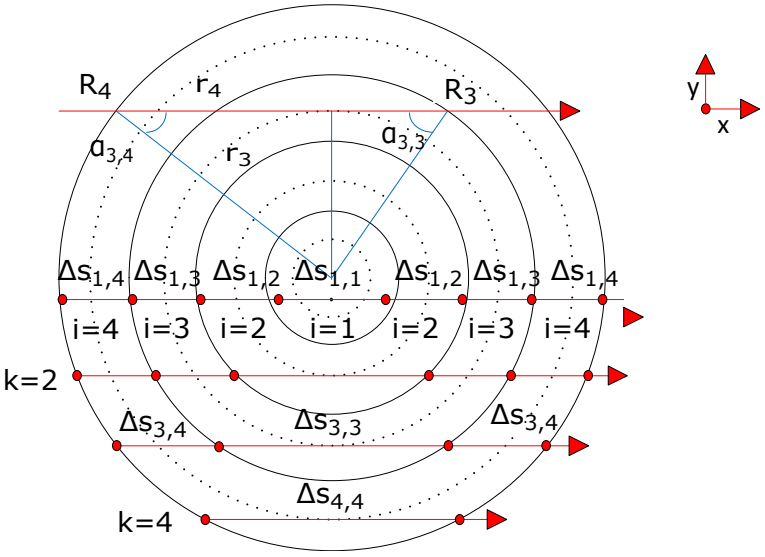

Figure 8.5: The distance a ray travels between control volumes is given by the line segments between the red dots.

In order to account for the full solid angle a discretization of the zenith angle θ_t should also be considered. This angle is discretized as

$$\theta_t = \frac{\pi}{2}\left(1 - \frac{t}{t_m - \frac{1}{2}}\right), \tag{8.60}$$

with $0 \leq t < t_m$ and t_m the total number of points used for the discretization of θ. Only the upper half of the zenith angle is considered due to the symmetry with respect to $\theta = \pi/2$. The integration is thus written as $Q_{\nu,\mathrm{rad}} = \iint_0^{\pi} \frac{\mathrm{d}^2\Phi_\nu}{V} = 2\iint_0^{\pi/2} \frac{\mathrm{d}^2\Phi_\nu}{V}$. The discretization was made in such a way that no ray has a zenith angle of zero. The first ray has a zenith angle with a value of $\theta = \pi/2$ and covers a part of the zenith angle which lies half above and half below the symmetry plane. An image of the zenith angle points is shown in figure 8.4. The distance through a control volume $\Delta s_{k,i,t}$ can now be expressed as

$$\begin{cases} \Delta s_{k,i,t} = \frac{\sqrt{R_i^2 - r_k^2} - \sqrt{R_{i-1}^2 - r_k^2}}{\sin\theta} & i > k \\ \Delta s_{k,i,t} = \frac{2\sqrt{R_k^2 - r_k^2}}{\sin\theta} & i = k. \end{cases} \tag{8.61}$$

The calculation of the radiative flux also requires the calculation of the inner product between the normal of the area of the control volume and the ray. The angle in the plane $\alpha_{k,i}$ can be expressed as

$$\sin\alpha_{k,i} = \frac{r_k}{R_i}, \tag{8.62}$$

with the indices k and i defined similarly as the indices in $\Delta s_{k,i,t}$. In figure 8.5 the calculations of $\alpha_{k,i}$ and $\Delta s_{k,i,t}$ are clarified.

The radiative flux going through area $\vec{n}\mathrm{d}A$ can be written as

$$\mathrm{d}^2\Phi_\nu = I_\nu\left(\vec{n}\cdot\vec{s}\right)\mathrm{d}A\mathrm{d}\Omega. \tag{8.63}$$

The normal vector $\vec{n}$ and the ray's direction vector $\vec{s}$ can be expressed in Cartesian coordinates as

$$\begin{aligned} \vec{n}_{\mathrm{out}} &= \cos\alpha\hat{x} + \sin\alpha\hat{y}, \\ \vec{n}_{\mathrm{in}} &= \cos\left(\pi - \alpha\right)\hat{x} + \sin\left(\pi - \alpha\right)\hat{y} = -\cos\alpha\hat{x} + \sin\alpha\hat{y}, \\ \vec{s} &= \sin\theta\hat{x} + \cos\theta\hat{z}. \end{aligned} \tag{8.64}$$

The dot product is thus given by $\mp\sin\theta\cos\alpha$ with the sign indicating a ray entering or leaving the volume, respectively. The solid angle can be written as $\mathrm{d}\Omega = \sin\theta\mathrm{d}\theta\mathrm{d}\alpha$. The change of the radiative flux induced by passing through $\mathrm{d}A$ can now be rewritten as

$$\mathrm{d}^2\Phi_{k,i,t,\nu} = \mp 4\pi R_i \mathrm{d}z\mathrm{d}I_{k,i,t,\nu}\sin^2\theta_t\cos\alpha_{k,i}\mathrm{d}\alpha_{k,i}\mathrm{d}\theta_t. \tag{8.65}$$

Note that a factor of 2 has been included due to azimuthal symmetry. The expression can be rewritten by taking the derivative of (8.62) with respect to the nodal point coordinate

$$\cos\alpha_{k,i}\mathrm{d}\alpha_{k,i} = \frac{\mathrm{d}r_k}{R_i}. \tag{8.66}$$

The substitution gives

$$\mathrm{d}^2\Phi_{k,i,t,\nu} = \mp 4\pi \mathrm{d}z \mathrm{d}I_{k,i,t,\nu} \sin^2\theta_t \mathrm{d}r_k \mathrm{d}\theta_t. \tag{8.67}$$

The contribution of ray segment i belonging to ray k can be calculated by integrating from one boundary point to the next boundary point. The contribution to the power density is given by

$$\begin{aligned} \mathrm{d}Q_{k,i,t,\nu} &= \frac{1}{V}\iint_{R_{i-1}}^{R_i} \frac{\mathrm{d}^2\Phi_{k,i,t,\nu}}{\mathrm{d}r_k}\mathrm{d}r_k \\ &\approx \frac{4\pi\Delta z \Delta I_{k,i,t,\nu} \sin^2\theta_t \left(R_i - R_{i-1}\right)\mathrm{d}\theta_t}{\pi\left(R_i^2 - R_{i-1}^2\right)\Delta z}. \end{aligned} \tag{8.68}$$

The value of $\Delta I_{k,i,t,\nu}$ is calculated with (8.49) using the distance from (8.61). The contribution to the control volume with nodal point number i is given by summing all contributions from all rays that reach this control volume. These contributions are given by

$$\mathrm{d}Q_{i,t,\nu} = \frac{4\pi \sin^2\theta \left(R_i - R_{i-1}\right)\sum_{k=1}^{k=i}\left(\Delta I^{(1)}_{k,i,t,\nu} + \Delta I^{(2)}_{k,i,t,\nu}\right)\mathrm{d}\theta_t}{\pi\left(R_i^2 - R_{i-1}^2\right)}, \tag{8.69}$$

with $\Delta I^{(1)}_{k,i,t,\nu}$ the contribution from the first time that ray k passes through control volume i and $\Delta I^{(2)}_{k,i,t,\nu}$ the contribution from the second passage. The total contribution is given by integrating over the frequency and the zenith angle. The integral over the zenith angle uses the symmetry with respect to $\theta = \pi/2$ to write $\int_0^\pi \mathrm{d}Q_i$ as $2\int_0^{\pi/2}\mathrm{d}Q_i$. The total contribution can then be expressed as

$$\begin{aligned} Q_{\nu,\mathrm{rad}} &= \int \frac{\mathrm{d}Q_{i,t,\nu}}{\mathrm{d}\theta_t}\mathrm{d}\theta_t \\ &= \frac{\int_0^{\pi/2} 8\pi \sin^2\theta_t \left(R_i - R_{i-1}\right)\sum_{k=1}^{k=i}\left(\Delta I^{(1)}_{k,i,t,\nu} + \Delta I^{(2)}_{k,i,t,\nu}\right)\mathrm{d}\theta_t}{\pi\left(R_i^2 - R_{i-1}^2\right)} \\ &\approx \frac{\sum_t 8\sin^2\theta_t \sum_{k=1}^{k=i}\left(\Delta I^{(1)}_{k,i,t,\nu,t} + \Delta I^{(2)}_{k,i,t,\nu,t}\right)\Delta\theta_t}{R_i + R_{i-1}}. \end{aligned} \tag{8.70}$$

8.5 Optically thin radiation

In this section the discretization for optically thin radiation is discussed. This section also describes the discretization error that occurs in the method of van der Heijden. For optically thin radiation the results obtained from that method do not reduce to the correct limit.

The radiation losses in control volume i can be expressed as (8.70)

$$Q_{i,t,\nu} = \frac{\sum_t 8\sin^2\theta_t \sum_{k=1}^{k=i}\left(\Delta I^{(1)}_{k,i,t,\nu} + \Delta I^{(2)}_{k,i,t,\nu}\right)\Delta\theta_t}{R_i + R_{i-1}}. \tag{8.71}$$

The central volume is poorly discretized since it is only visited by a single ray. For optically thin radiation $\Delta I_{k,i,t,\nu} \approx j_\nu \Delta s_{k,i,t}$ is an accurate approximation. For the central volume the distance through the entire volume is given by

$$\Delta s_{k,i,t} = 2\frac{\sqrt{R_i^2 - r_k^2}}{\sin\theta_t} = \frac{\sqrt{3}R_i}{\sin\theta_t}. \tag{8.72}$$

By substituting $R_{i-1} = 0$ in (8.71) an expression for the radiated energy in the central volume can be derived as

$$Q_{i,t,\nu} = 8\sqrt{3}\sum_t \sin\theta_t j_{i,\nu}\Delta\theta_t. \tag{8.73}$$

The analytical expression for optically thin radiation is given by $Q_{i,\nu} = j_{i,\nu}4\pi$. The ratio of these expressions is given by

$$\frac{Q_{i,t,\nu}}{j_{i,\nu}4\pi} = \frac{8\sqrt{3}\sum_t \sin\theta_t\Delta\theta_t}{4\pi} = \frac{2\sqrt{3}}{\pi} \approx 1.10. \tag{8.74}$$

This ratio shows that the error is approximately 10%. The current radiative description is thus subject to errors in the optically thin case. The errors are largest for the central grid cell. Cells that are visited by multiple rays are subject to a smaller discretization error. The relative error for the nodal point approach is given in figure 8.6 in red. The figure shows that the relative error for optically thin radiation is already reduced to values below 1 % for the volume corresponding to the third smallest nodal point. In cylindrically symmetric plasmas the core region is the region where most radiation originates from. In that case a large grid is required to minimize the discretization error of the radiation in the central volumes. A correct discretization can prevent the need for such large grids. Such a discretization is provided in section 8.7.

8.6 Optically thick radiation

Optically thick plasmas are characterized by $\tau \gg 1$. The equation of radiative transfer can then be reduced to

$$\Delta I_{k,i,t,\nu} = I_{k,i,t,\nu} - I_{k,i\pm1,t,\nu} = \frac{j_{i,\nu}}{\kappa_{i,\nu}} - \frac{j_{i\pm1,\nu}}{\kappa_{i\pm1,\nu}}, \tag{8.75}$$

with the $\pm$ sign indicating whether the ray is moving inwards or outwards. The energy source term can be calculated analytically as

$$\begin{aligned} Q_{i,t,\nu} &= \frac{1}{V}2\pi L\left[R_i\left(\frac{j_{i,\nu}}{\kappa_{i,\nu}} - \frac{j_{i+1,\nu}}{\kappa_{i+1,\nu}}\right) + R_{i-1}\left(\frac{j_{i,\nu}}{\kappa_{i,\nu}} - \frac{j_{i-1,\nu}}{\kappa_{i-1,\nu}}\right)\right] \times \\ &\quad \int_0^\pi \sin^2\theta \mathrm{d}\theta \int_0^\pi \cos\alpha \mathrm{d}\alpha \\ &= \frac{2\pi^2 L}{V}\left(R_i\left[\frac{j_{i,\nu}}{\kappa_{i,\nu}} - \frac{j_{i+1,\nu}}{\kappa_{i+1,\nu}}\right] + R_{i-1}\left[\frac{j_{i,\nu}}{\kappa_{i,\nu}} - \frac{j_{i-1,\nu}}{\kappa_{i-1,\nu}}\right]\right), \end{aligned} \tag{8.76}$$

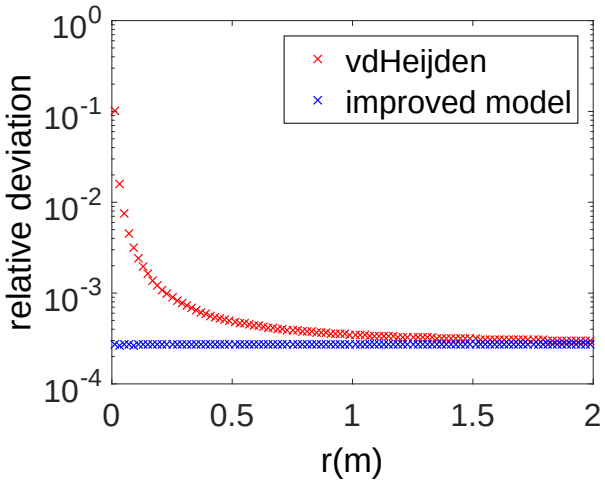

Figure 8.6: The relative error between the analytical power density and the numerical approximation in an optically thin plasma. There are 100 nodal grid points and 20 zenith angles. The discretization error using van der Heijden's method is largest in the center. The remaining errors in the improved discretization scheme are related to the discretization of θ. These errors vanish when more zenith angles are used.

with L the length of the plasma in axial direction and $V = \pi \left(R_i^2 - R_{i-1}^2\right) L$. In the special case of constant $j_{i,\nu}$ and $\kappa_{i,\nu}$ these losses cancel in every control volume, since there is no difference between the inward and the outward radiance. The only exception is the outer control volume which is responsible for the difference between the radiance at the wall and the local equilibrium value. In that case the radiation losses can be expressed as

$$Q_{n,\nu} = \frac{2\pi R_n}{R_n^2 - R_{n-1}^2} \left[\frac{j_{n,\nu}}{\kappa_{n,\nu}} - I_{w,\nu} \right], \tag{8.77}$$

with $I_{w,\nu}$ the radiance emitted by the wall. A more interesting case is given by a quadratic emission

$$j_\nu(r) = j_{0,\nu} \left(1 - \left(\frac{r}{R}\right)^2\right), \tag{8.78}$$

and a constant absorption $\kappa_\nu(r) = \kappa_{0,\nu}$. The source function $S_{i,\nu} = \frac{j_{i,\nu}}{\kappa_{i,\nu}}$ is now a quadratic function as well. The radiation losses can then be calculated from

(8.76) and are given by

$$\begin{aligned} Q_{i,\nu} &= \frac{2\pi}{R_i^2 - R_{i-1}^2}\frac{j_{0,\nu}}{\kappa_{0,\nu}}\left(R_i\left(\left[\frac{r_{i+1}}{R}\right]^2 - \left[\frac{r_i}{R}\right]^2\right)\right. \\ &\quad \left. + R_{i-1}\left(\left[\frac{r_{i-1}}{R}\right]^2 - \left[\frac{r_i}{R}\right]^2\right)\right), \\ &= \frac{2\pi}{2\Delta R R_i - \Delta R^2}\frac{j_{0,\nu}}{\kappa_{0,\nu}}\left(R_i\left(\left[\frac{r_{i+1}}{R}\right]^2 - 2\left[\frac{r_i}{R}\right]^2 + \left[\frac{r_{i-1}}{R}\right]^2\right)\right. \\ &\quad \left. - \Delta R\left(\left[\frac{r_{i-1}}{R}\right]^2 - \left[\frac{r_i}{R}\right]^2\right)\right), \\ &= \frac{4\pi\Delta R}{R^2}\frac{j_{0,\nu}}{\kappa_{0,\nu}}. \end{aligned} \tag{8.79}$$

The energy source term is thus constant for these conditions. The expression for the outer control volume is slightly different because there is no plasma emission entering via the outer boundary. The radiation losses for the cases of constant and quadratic emission constants are both in agreement with the analytical results up to 10^{-14}. The discretization scheme proposed by van der Heijden thus produces the largest errors for optically thin radiation. For larger optical depths the errors vanish.

8.7 Improved discretization

In section 8.5 it was shown that the discretization procedure from van der Heijden does not reduce to the correct limit for optically thin radiation. In this section an improved scheme is presented that provides results that reduce to the correct limits in both the optically thin and thick limits.

In section 8.4 the indices k and i are used to describe the individual line segments. Previously the index k referred to a position halfway between the inner and outer radius of the control volumes. The correct way of placing the rays is by taking a proper average using $\langle f(x)\rangle = \frac{\int_a^b f(x)\mathrm{d}x}{\int_a^b \mathrm{d}x}$. The rays should thus pass through the point $\langle r_k\rangle$ that satisfies

$$\langle \Delta s_{k,k}\rangle (R_k - R_{k-1}) = 2\sqrt{R_k^2 - \langle r_k\rangle^2}\,(R_k - R_{k-1}) = \int_{R_{k-1}}^{R_k} 2\sqrt{R_k^2 - r^2}\mathrm{d}r. \tag{8.80}$$

Due to the non-linearity of this integral it is not correct by simply placing the points $\langle r_k\rangle$ halfway between the boundary points. In this case the path length is chosen to ensure that the total area in the discretized chord segments is the same as the analytical result for the optically thin case. This choice does not affect the result for the optically thick calculation, since that result is independent of the path length. This is illustrated in figure 8.7. The integral for the line segment

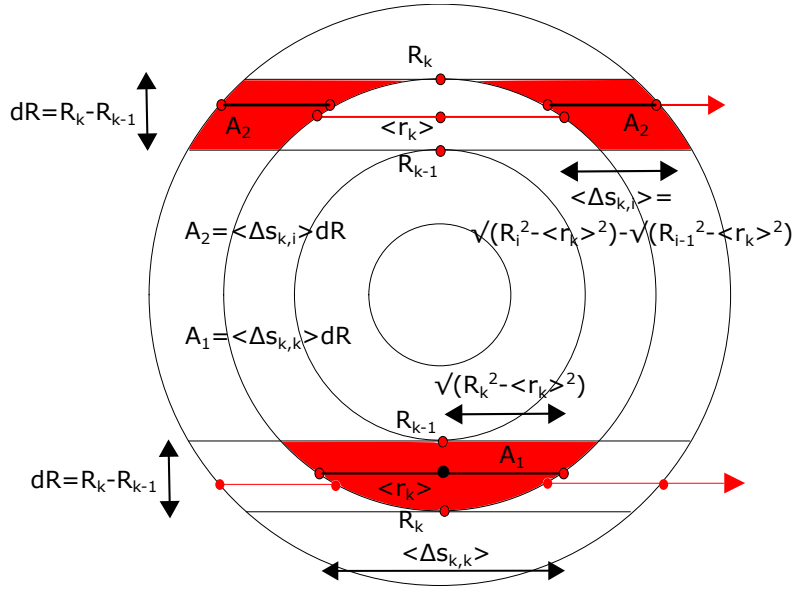

Figure 8.7: The discretization error in van der Heijden's algorithm can be removed by placing $\langle r_k \rangle$ in such a way that the length through the segment multiplied by the width is equal to the area of the segment. A consequence of this procedure is that the lines through the segments are no longer continuous.

that is closest to the cylindrical axis can be solved as[5]

$$\begin{aligned}\langle \Delta s_{k,k} \rangle &= \frac{2\int_{R_{k-1}}^{R_k} \sqrt{R_k^2 - r^2}\mathrm{d}r}{\int_{R_{k-1}}^{R_k} \mathrm{d}r} \\ &= \frac{2R_k^2 \int_{\alpha_{k-1}}^{\alpha_k} \sqrt{1-\sin^2\alpha}\cos\alpha \mathrm{d}\alpha}{R_k - R_{k-1}} = \frac{2R_k^2 \left[\frac{\alpha}{2} + \frac{\sin(\alpha/2)}{4}\right]_{\alpha_{k-1}}^{\alpha_k}}{R_k - R_{k-1}} \\ &= \frac{2R_k^2}{R_k - R_{k-1}} \left(\frac{1}{2}\left(\frac{\pi}{2} - \arcsin\frac{R_{k-1}}{R_k}\right) - \frac{R_{k-1}}{2R_k}\sqrt{1 - \left(\frac{R_{k-1}}{R_k}\right)^2} \right). \end{aligned} \quad (8.81)$$

The new positions can be obtained from (8.80) and are thus defined as

$$r_k = \sqrt{R_k^2 - \left(\frac{\langle \Delta s_{k,k} \rangle}{2}\right)^2}. \quad (8.82)$$

[5] Note that the relation $\sin\alpha_{k,i} = \frac{r_k}{R_i}$ is used. Additionally, $0 \leq \alpha \leq \pi/2$ is valid which ensures that $\cos\alpha \geq 0$.

The distance through a control volume for $k \neq i$ is given by

$$\begin{aligned}
\langle \Delta s_{k,i} \rangle &= \frac{\int_{R_{k-1}}^{R_k} \left(\sqrt{R_i^2 - r^2} - \sqrt{R_{i-1}^2 - r^2} \right) \mathrm{d}r}{\int_{R_{k-1}}^{R_k} \mathrm{d}r} \\
&= \frac{R_i^2}{R_k - R_{k-1}} \left[\frac{1}{2} \left(\arcsin \frac{R_k}{R_i} - \arcsin \frac{R_{k-1}}{R_i} \right) \right. \\
&\left. + \frac{1}{2} \left(\frac{R_k}{R_i} \sqrt{1 - \left(\frac{R_k}{R_i} \right)^2} - \frac{R_{k-1}}{R_i} \sqrt{1 - \left(\frac{R_{k-1}}{R_i} \right)^2} \right) \right] \\
&- \frac{R_{i-1}^2}{R_k - R_{k-1}} \left[\frac{1}{2} \left(\arcsin \frac{R_k}{R_{i-1}} - \arcsin \frac{R_{k-1}}{R_{i-1}} \right) \right. \\
&\left. + \frac{1}{2} \left(\frac{R_k}{R_{i-1}} \sqrt{1 - \left(\frac{R_k}{R_{i-1}} \right)^2} - \frac{R_{k-1}}{R_{i-1}} \sqrt{1 - \left(\frac{R_{k-1}}{R_{i-1}} \right)^2} \right) \right] . \qquad (8.83)
\end{aligned}$$

Using the new discretization of the chord segments the errors in the optically thin case are much smaller in comparison to the previous discretization method. The remaining errors shown in figure 8.6 are related to the discretization of the zenith angle.

8.8 Model verification

A few HID lamps are used to verify the accuracy of the ray tracing model. For this purpose lamp mixtures involving Hg and Hg and Na are considered. The calculation procedure is described in detail in chapter 10 and Gnybida et al. [152]. The energy balance that is considered is the Elenbaas-Heller equation and is given by

$$\nabla \cdot (-\lambda \nabla T) = \sigma E^2 - q_{\mathrm{rad}}, \qquad (8.84)$$

with the thermal and electrical conductivity calculated as indicated in chapter 5. The calculation of the radiation losses are discussed in section 8.4. The electric field is assumed to be uniform in the axial direction. In that case it can be obtained from

$$Q_{\mathrm{in}} - Q_{\mathrm{elec}} = \int_0^R \sigma\,(r)\, E^2 \mathrm{d}V = 2\pi L E^2 \int_0^R r\sigma\,(r)\, \mathrm{d}r, \qquad (8.85)$$

with Q_{in} the input power and Q_{elec} the power dissipated in the electrodes. Additionally, constant elemental pressures are assumed.

8.8.1 Hg

The lamp described by Stormberg [167, p. 4341,4345] is modeled. The pressure is 5 bar. The dimensions of the burner vessel are $R = 7\,8$ mm and $L = 42$ mm. The input power for the lamp is $Q_{\mathrm{in}} = 259$ W, the electrode losses are $Q_{\mathrm{elec}} = 17\,5$ W and the wall temperature is $T_w = 900$ K. The broadening constants of Hartel [168,

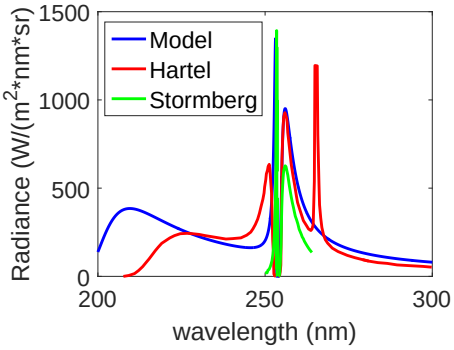

Figure 8.8: Calculations of the side-on radiance for a Hg discharge.

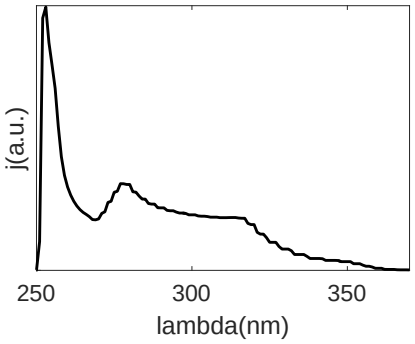

Figure 8.9: Emission from the $\Omega = 2u, \#1 - X$ transition at 5000 K.

p. 7082] are used. The simulated 253.7 nm line is shown in figure 8.8 and is compared to the simulations of Stormberg and Hartel. Hartel suggests to adjust Stormberg's broadening constant for the 253.7 nm line. For that reason the model deviates slightly from Stormberg's line profile. Additionally, Hartel uses a Hg pressure of 6 bar which explains why the self-reversal peak of the 184.95 nm line is located at a different position. Hartel et al. also use a shorter distance between the electrodes ($L = 2.59$ cm).

At higher pressures the validity of the Van der Waals profile is questionable. In that case the quasi-static line profile must be calculated based on the true potential curves. The total line profile can then be approximated with (8.28). The potential curves listed in section 8.A.1 are used. These curves predict a continuum that covers the spectral band from 250 nm up to 380 nm. In the minimum of the $\Omega = 2u, \#1$ potential a transition of 316 nm can occur. The transition at this interatomic separation is also called a satellite peak. Such a peak cannot be obtained using Stormberg's line shape. For a temperature of 5000 K the emission from the $\Omega = 2u, \#1 - X$ transition is shown in figure 8.9. The emission indeed reveals a peak at 316 nm. Another peak can be observed at 277 nm. This peak is related to a peak in the calculated transition strength. For a temperature of about 3000 K the peak at 316 nm reaches approximately the same height as the peak at 277 nm. At lower temperatures the satellite peak dominates the continuum.

8.8.2 Na and NaI additives

The spectrum of a high pressure sodium (HPS) lamp operated at 70 W is measured in an integrating sphere setup [21]. In the numerical model it is assumed that about 10 % of the energy is dissipated in the electrodes or plasma sheath. The broadening constants of the sodium D-lines are taken from de Groot and van Vliet [169, p. 85] as $C_3 = 1.56 \times 10^{-14}\,\mathrm{m^3 s^{-1}}$ for D_1 and $C_3 = 2.39 \times 10^{-14}\,\mathrm{m^3 s^{-1}}$ for D_2[6]. Using

[6]Note that the book uses a different definition of the broadening constant.

these broadening constants the sodium pressure was adjusted to obtain the correct self-reversal width. The obtained pressure is $p_{\mathrm{Na}} = 10^4\,\mathrm{Pa}$. The mercury pressure was set to $9 \times 10^4\,\mathrm{Pa}$ to match the lamp voltage of 75 V. Using these settings the Van der Waals broadening constant was set to $C_6 = 5 \times 10^{-42}\,\mathrm{m^6 s^{-1}}$ to represent the wing of the resonant lines correctly. This value is more than ten times the value reported by de Groot and van Vliet [169, p. 145]. The simulated spectrum is compared with a measured spectrum in figure 8.11. The spectrum shows that the resonant line has the correct shape, but the total amount of emitted radiation is too large. The simulated luminous efficacy of $119\,\mathrm{lumW^{-1}}$ and measured luminous efficacy of $86\,\mathrm{lumW^{-1}}$ confirm this statement. The reason for the large emission is shown in figure 8.10. A typical HPS lamp reaches a maximum temperature of about 4000 K while the simulation calculated a profile with a peak of 4500 kK. Possibly the wall temperature is overestimated. The experiment used a lamp with a removed outer bulb. This removal will increase the radiative losses, since the outer wall can not heat the burner vessel with reflected radiation. Additionally, the Van der Waals broadening constant could be fixed to the literature value. The mercury pressure should then be adjusted again to get the correct lamp voltage. The temperature can also be too high, because the self-reversal of other emission lines is not correctly taken into account. In spite of these limitations the overall agreement is satisfactory.

The formation of a self-reversal maximum is explained in figure 8.12. The figure shows the evolution of the spectral radiance traversing a path from $r = -R$ through the center of the discharge towards the opposite wall at $r = R$. For the central wavelength the optical depth reaches a maximum. For the NaD lines this optical depth is sufficiently high to be in perfect radiative equilibrium. When the wavelength is decreased the optical depth also decreases. The lag of the local spectral radiance with respect to the local thermal radiance is increasing. Eventually there is hardly any absorption which means the radiation becomes optically thin. In this scala of spectra the dashed black line reaches the optimal optical depth to obtain the largest radiant output at $r = R$.

For larger pressures the exact structure of the $\mathrm{Na} - \mathrm{Hg}$ interaction becomes important. Ab initio results for $\mathrm{Na} - \mathrm{Hg}$ are displayed in section 8.A.2. An emission spectrum for a temperature of 5000 K is shown in figure 8.13. A satellite peak at 671 nm can be observed. This peak slightly deviates from the value that is predicted based on the minimum of the potential (675 nm) due to the shape of the transition probability. Woerdman [170] also reported an experimental value of 671 nm for the satellite peak. Additionally, he showed an undulation structure on the blue side of the satellite peak which appears when a correction for the classical singularity ($\frac{\mathrm{d}r}{\mathrm{d}\nu} = 0$) is made. In the current calculation this undulation structure appears on the red side of the satellite peak. This correction is dependent on the second derivative of the potential with respect to the position. The fact that this undulation structure is slightly misplaced indicates that the potential curves are not fully resolved yet.

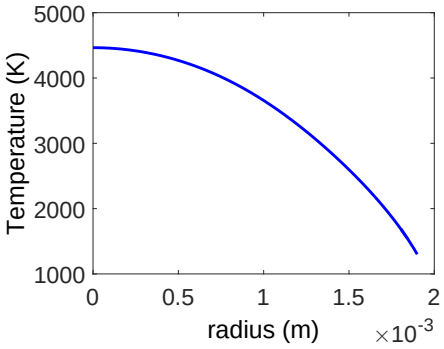

Figure 8.10: The simulated temperature profile in the HPS lamp.

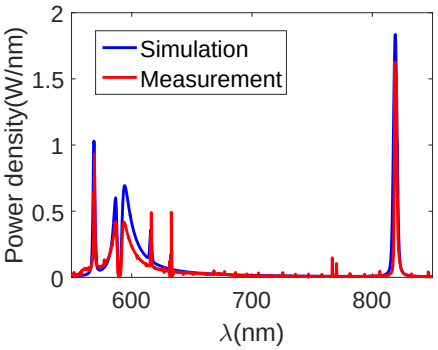

Figure 8.11: The simulated HPS spectrum is compared to a measured spectrum.

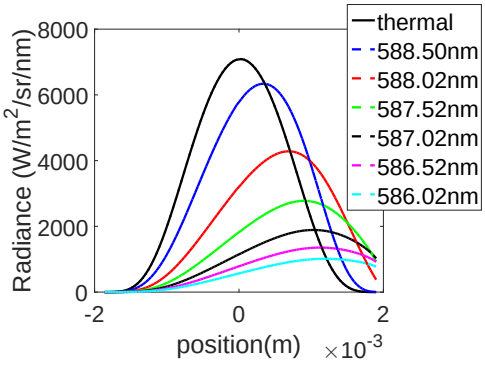

Figure 8.12: For a ray passing through the center of the discharge the evolution of the spectral radiance for multiple wavelengths is shown.

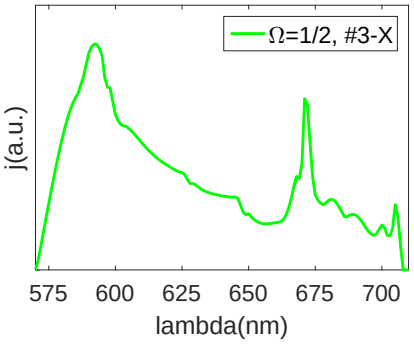

Figure 8.13: The emission from the $\Omega = 1/2, \#3 - \mathrm{X}$ transition at a temperature of 5000 K.

8.A Ab initio potential curves

In this section the calculation of the potential curves for the Hg–Hg and Hg–Na interactions are discussed. The potential curves are used to calculate the Van der Waals broadening. The emitted wavelength is proportional to the inverse of the potential difference of both states involved in the transition. The ab initio package DIRAC [107] has been used to calculate the interaction potential and the transition dipole moments as a function of the interatomic separation.

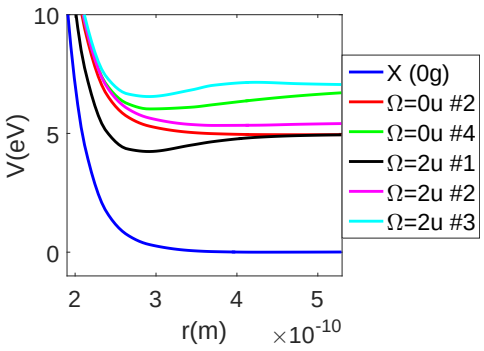

Figure 8.14: The Hg – Hg potential curves.

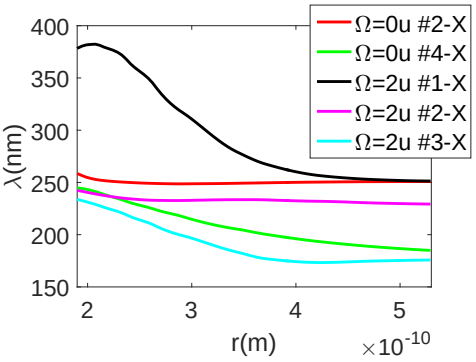

Figure 8.15: The wavelength as a function of interatomic separation.

8.A.1 Hg–Hg

The potential curve and the corresponding emitted wavelength for Hg–Hg that are included in the model are shown in figure 8.14 and 8.15. The asymptotic limits of the curves are 4.94 eV, 5.41 eV and 6.70 eV, respectively. Within approximately 0.05 eV, this corresponds to the atomic levels reported by NIST [53]. A comparison with the molecular states calculated by Kullie [171] is difficult, since Kullie only provides the absolute energy of the excited states. This information is not directly comparable to our result, since the methods MCSCF and TDDFT using CAMB3LYP produce a different energy offset.

8.A.2 Na–Hg

The potential curve and the corresponding emitted wavelength for Na–Hg that are included in the model are shown in figures 8.16 and 8.17. The asymptotic limits of the curves correspond to 0.07 eV and 2.23 eV, respectively. The atomic excitation energy is thus 2.16 eV, which shows an error of 0.06 eV with the atomic levels reported by NIST. According to measurements by Woerdman [170] satellite peaks are visible around 671 nm. The current calculations show that the wavelength corresponding to a transition from the minimum of the $\Omega = 1/2, \#3$ potential to the ground state is 675 nm. The error in the difference potential is then 0.01 eV. For smaller interatomic separations the potential curves are thus more accurate.

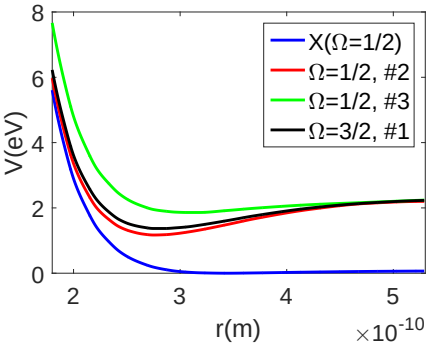

Figure 8.16: The Na–Hg potential curves.

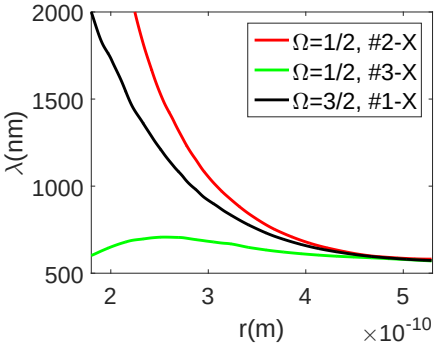

Figure 8.17: The wavelength as a function of interatomic separation.

Chapter 9

On the atomic line profiles in high pressure plasmas

9.1 Abstract

Stormberg (J. Appl. Phys. 51 (4), p. 1963) presented an analytical expression for the convolution of Lorentz and Levy line profiles; the resulting line profile describes atomic radiative transitions in high pressure plasmas. Unfortunately, the derivations are flawed with errors and the final expression, while correct, is accompanied by misguiding comments about the meaning of the symbols used therein, in particular the 'complex error function'. In this chapter, we discuss the broadening mechanisms that give rise to Stormberg's model and present a correct derivation of his final result. We will also provide an alternative expression, based on the Faddeeva function, which has decisive computational advantages and emphasizes the real-valuedness of the result. The MATLAB/Octave scripts of our implementation have been made available on the publisher's website for future reference.

9.2 Introduction

Modeling and numerical simulation have been widely used to aid the understanding and guide the development of High-Intensity Discharge (HID) lamps. An important aspect of such models is the transport of energy via radiation, which depends critically on broadening mechanisms. When multiple statistically independent broadening mechanisms are present, the resulting line profile is obtained as the convolution product of the individual line profiles (see Ref. [172, p. 56]). A well-known example is the Voigt profile, which is obtained by convolving the Gaussian and Lorentzian profiles that result from Doppler and resonance or Stark

Published as: J. F. J. Janssen, M. Gnybida, J. L. G. Suijker, A. J. Rijke and J. van Dijk; *On the atomic line profiles in high pressure plasmas* in Journal of Applied Physics: Vol 114, number 18

broadening, respectively. The Voigt profile [160–162] can be expressed as

$$P_V(z) = \frac{\mathcal{R}[w(z)]}{\sigma_G\sqrt{2\pi}}, \tag{9.1}$$

where $z = \frac{\nu-\nu_0+i\gamma_L}{\sigma_G\sqrt{2}}$, σ_G and γ_L represent the Gaussian and Lorentzian half widths at half maxima (HWHM), ν is the frequency, ν_0 is the unperturbed frequency, and the Faddeeva function $w(z)$ is given by

$$w(z) = \exp\left(-z^2\right)\mathrm{Erfc}\left(-iz\right). \tag{9.2}$$

The function Erfc is the complementary error function, which is given by

$$\mathrm{Erfc}(z) = \frac{2}{\sqrt{\pi}}\int_z^\infty e^{-t^2}\mathrm{d}t = 1 - \mathrm{Erf}(z), \tag{9.3}$$

where the error function is given by

$$\mathrm{Erf}(z) = \frac{2}{\sqrt{\pi}}\int_0^z e^{-t^2}\mathrm{d}t. \tag{9.4}$$

Stormberg [30] derived an analytical expression for the case that the center of the spectral line can be described by a Lorentzian profile and the red wing by a van der Waals profile. This case is particularly relevant for atomic transitions in high-pressure plasmas. He showed that the resulting line profile is given by

$$\begin{aligned} P(\Delta\lambda) = &\frac{1}{\pi\Delta\lambda_{1/2}(1+a^2)} - \frac{ic\pi}{2}\left[Z_1^{1.5}\exp(Z_1 b)\,\mathrm{Erfc}\left(\sqrt{Z_1 b}\right)\right. \\ &\left. - Z_2^{1.5}\exp(Z_2 b)\,\mathrm{Erfc}\left(\sqrt{Z_2 b}\right)\right], \end{aligned} \tag{9.5}$$

where $\Delta\lambda_{1/2}$ represents the full width at half maximum (FWHM) of the Lorentzian profile and $\Delta\lambda_0$ the characteristic width of the van der Waals (also called Levy) profile. The auxiliary parameters a, b, c and $Z_{1,2}$ are given by

$$a = \frac{\Delta\lambda}{\Delta\lambda_{1/2}}, \tag{9.6}$$

$$b = \frac{\pi\Delta\lambda_0}{4\Delta\lambda_{1/2}}, \tag{9.7}$$

$$c = \frac{\sqrt{\Delta\lambda_0}}{2\pi\left(\Delta\lambda_{1/2}\right)^{3/2}} = \frac{\sqrt{b}}{\pi^{3/2}\Delta\lambda_{1/2}}, \tag{9.8}$$

$$Z_{1,2} = \frac{-a \mp i}{1+a^2}. \tag{9.9}$$

Stormberg creates some confusion about the meaning of Erfc by mentioning a method for calculating the *complex error function* in the accompanying text, probably referring the evaluation of the error function for complex *arguments*

instead [173, 174]. But more commonly, the term 'complex error function' refers to the Faddeeva function [160, 162, 174].

Most authors who cite Stormberg's article [30] merely indicate that they used his expression, without any further remarks on the mistakes in Stormberg's paper or the meaning of Erfc. Only two articles known to the authors discuss Stormberg's expression any further. Weiß et al. [175] mention that they calculate a Faddeeva function, but do not even provide an expression in which that function occurs. Hartel et al. [168] present an interesting alternative form of Stormberg's expression that avoids the need to subtract two terms involving the complementary error function, the result is

$$P(\Delta\lambda) = \frac{1}{\pi\Delta\lambda_{1/2}(1+a^2)} + \pi c \exp\left(\frac{-ab}{1+a^2}\right) \times \mathcal{I}\left[Z^{3/2}\exp\left(\frac{-ib}{1+a^2}\right)\operatorname{Erfc}\left(\sqrt{Zb}\right)\right], \tag{9.10}$$

with $Z = Z_1$ and $\mathcal{I}$ denoting the imaginary part. Unfortunately, they also use the confusing term 'complex error function' to refer to the complementary error function and do not provide a derivation of their result, or discuss its advantages.

In this paper we will first provide a short introduction to the theory of line broadening that is relevant for the present discussion. We continue the text with a complete and corrected derivation of Stormberg's and Hartel's result, which shows that indeed Erfc represents the complementary error function in all expressions. We will then derive a novel expression for Stormberg's result that employs the Faddeeva function. This expression has decisive analytical and computational advantages: it highlights the real-valuedness of the result and avoids the subtraction of two possibly (nearly-)equal terms. The MATLAB/Octave source code that has been used in our tests has been made available on the publisher's website for future reference.

9.3 Line broadening

The most important broadening mechanisms in high pressure plasmas are resonance, van der Waals and Stark broadening. Resonance, Stark and van der Waals broadening can be calculated in the impact approximation, which is valid when the collision time is much shorter than the time between collisions [158, 176], or $\lambda - \lambda_0 = \Delta\lambda < \Delta\lambda_L$, with

$$\Delta\lambda_L = \frac{\langle v\rangle \lambda^2}{2\pi c \rho_W}. \tag{9.11}$$

Here λ_0 is the wavelength of the unperturbed transition and $\langle v\rangle$ the average thermal velocity of the interacting particles. The potential of the perturbation is assumed to be of the form

$$V = h\frac{C_n}{r^n}, \tag{9.12}$$

where h is Planck's constant and C_n is the broadening constant with dimensions $\mathrm{m}^n\mathrm{s}^{-1}$. For such a potential the Weißkopf radius is given by

$$\rho_W = \left(\frac{\alpha_n C_n}{\langle v \rangle}\right)^{\frac{1}{n-1}}, \tag{9.13}$$

with

$$\alpha_n = \sqrt{\pi}\frac{\Gamma\left(\frac{n-1}{2}\right)}{\Gamma\left(\frac{n}{2}\right)}, \tag{9.14}$$

where Γ is the gamma function. This results in a Lorentzian line profile,

$$P_{\mathrm{Lorentz}}\left(\Delta\lambda\right) = \frac{\Delta\lambda_{1/2}}{\pi\left(\Delta\lambda_{1/2}^2 + \Delta\lambda^2\right)}, \tag{9.15}$$

with $\Delta\lambda_{1/2}$ the Lorentzian HWHM. The convolution of two Lorentzian profiles is again a Lorentzian profile with a HWHM that is equal to the sum of the HWHM of the individual profiles. In other words, the HWHM's are additive for all statistically independent mechanisms that result in a Lorentzian profile.

For resonance broadening in the impact approximation the HWHM is given by

$$\Delta\lambda_{\mathrm{res}} = \sum_i \sum_j C_{R,ji} n_i = \sum_i \sum_j \frac{\lambda^2}{2c_0}\pi C_{3,ji} n_i, \tag{9.16}$$

where $C_{R,ji}$ and $C_{3,ji}$ are resonance broadening constants for exchange of excitation energy (see Ref. [172, p. 101-103]) between states j and i, n_i is the density of the radiating particle in state i and c_0 is the speed of light in vacuum. Laux et al. [177] note that the following perturbations in general are sufficient

$$\Delta\lambda_{\mathrm{res}} = \frac{\lambda_{ul}^2\pi}{2c_0}\left(C_{3,lg} n_g + C_{3,ug} n_g + C_{3,ul} n_l\right), \tag{9.17}$$

where the indices l, u and g refer to the lower state, upper state and ground state of the radiating particle. The resonance broadening constant is given by

$$C_{3,ji} = k_{J_j,J_i}\frac{1}{64\pi^3}\left(\frac{g_j}{g_i}\right)A_{ji}\lambda_{ji}^3, \tag{9.18}$$

with k_{J_j,J_i} a constant which depends on the total angular momentum quantum numbers J_j and J_i. Corney [154, p. 263] reports the value $k_{1,0} = 1.53$ for the case $J_j = 1$, $J_i = 0$. This value is in good agreement with experiments in helium where the transition probability is accurately known for the $^1\mathrm{P}_1$–$^1\mathrm{S}_0$ resonance line. An expression often used for the resonance broadening constant is the value from Griem [172, 175, 178, 179] which is given by

$$C_{3,ji} = \frac{1}{8\pi^4}\sqrt{\frac{g_j}{g_i}}A_{ji}\lambda_{ji}^3. \tag{9.19}$$

Although this expression is not as accurate as Corney's expression it has the advantage that it does not rely on the constant k_{J_j,J_i}. In case of resonance broadening by a $^1P_1$–$^1S_0$ line the ratio of Griem's expression to Corney's expression is only 0.961. It is also interesting to note that Lawler [180] states that the linear relation between density and resonance line width in Hg is valid at least up to $4 \cdot 10^{25}\,\mathrm{m}^{-3}$. This density is outside the validity of the impact approximation. Additionally, Lawler claims that the Lorentzian line profile may also be valid to line offsets that are significantly larger than suggested by the validity of the impact theory.

In the impact approximation the HWHM due to Stark broadening is calculated with various degrees of sophistication. Stormberg [167] uses a HWHM given by

$$\Delta\lambda_{\mathrm{Stark}} = C_S n_e, \tag{9.20}$$

while Refs. [175, 178, 179] use the model

$$\Delta\lambda_{\mathrm{Stark}} = \frac{\lambda^2}{4\pi c_0} 11.37 C_4^{2/3} v_e^{1/3} n_e, \tag{9.21}$$

with C_S and C_4 the Stark broadening constants, v_e the thermal velocity of the electrons and n_e the electron density. The second relation features a weak temperature dependency which is not present in the first relation. Another expression for the HWHM of Stark broadening is found in Griem [153, p. 91] [176],

$$\Delta\lambda_{\mathrm{Stark}} = \left[1 + 1.75\alpha\left(1 - 0.75r\right)\right]\omega, \tag{9.22}$$

with r the ratio of the mean distance between ions ρ_m and the Debye length ρ_D

$$r = \frac{\rho_m}{\rho_D} = \frac{\left(\frac{4\pi n_e}{3}\right)^{-1/3}}{\left(\frac{\epsilon_0 k_B T}{e^2 n_e}\right)^{1/2}} = 6^{1/3}\pi^{1/6}\left(\frac{e^2}{4\pi\epsilon_0 k_B T}\right)^{1/2} n_e^{1/6}, \tag{9.23}$$

where α and ω are tabulated [1] Stark broadening parameters by Griem [153, p. 454-527].

The contribution of van der Waals broadening in the impact approximation [175, 178, 179] is given by

$$\Delta\lambda_{\mathrm{vdW}} = \frac{\lambda^2}{2\pi c_0} 4.04 \left(\frac{8 k_B T}{\pi}\right)^{3/10} \sum_i C_{6,i}^{2/5} \frac{n_i}{\mu_i^{3/10}}, \tag{9.24}$$

with C_6 the van der Waals broadening constant, n_i the density of the perturbing particle and μ the reduced mass calculated for the radiating and the perturbing particle. The van der Waals broadening constant can be estimated based on a hydrogen like approximation as [178]

$$C_6 = \frac{1}{2h\epsilon_0} e^2 \alpha_{\mathrm{pert}} \left|\left\langle r_u^2\right\rangle - \left\langle r_l^2\right\rangle\right|, \tag{9.25}$$

[1] Note that the values of ω are tabulated in Åfor $n_e^* = 10^{19}\mathrm{m}^{-3}$. The real value of ω can be obtained by multiplying with n_e/n_e^*. Similarly the values for α should be multiplied by $(n_e/n_e^*)^{1/4}$ [153, p. 454].

with α_{pert} the polarizability of the perturbing particle and $\left\langle r_i^2 \right\rangle$ the mean square radius of the atoms in state i, which is given by

$$\left\langle r_i^2 \right\rangle = a_0^2 \frac{\left(n_i^*\right)^2}{2} \left\langle 5\left(n_i^*\right)^2 + 1 - 3l_i\left(l_i+1\right) \right\rangle . \tag{9.26}$$

Here a_0 is the Bohr radius, l_i is the orbital quantum number of state i and $\left\langle n_i^* \right\rangle^2$ is the effective quantum number,

$$\left\langle n_i^* \right\rangle^2 = \frac{E_H}{E_{\text{ion}} - E_i}, \tag{9.27}$$

with E_H the ionization energy of hydrogen, E_{ion} the ionization energy of the radiating species and E_i the energy of state i.

The van der Waals interaction can also be calculated in the quasi-static approximation. This approximation assumes that the radiating particles are perturbed by a slowly varying potential field which can be considered quasi-static. This approximation results in a Levy profile [176, 178],

$$P\left(\Delta\lambda\right) = \begin{cases} \dfrac{\sqrt{\Delta\lambda_0}}{2\left(\Delta\lambda\right)^{3/2}} \exp\left(-\dfrac{\pi\Delta\lambda_0}{4\Delta\lambda}\right) & \Delta\lambda > 0 \\ 0 & \Delta\lambda \leq 0 \end{cases}, \tag{9.28}$$

with $\Delta\lambda_0$ given by

$$\Delta\lambda_0 = \sum_{\text{pert}} C_{W,\text{pert}} n_{\text{pert}}^2 \tag{9.29}$$

$$= \sum_{\text{pert}} \frac{\lambda^2}{2\pi c_0} C_{6,\text{pert}} \left(\frac{4}{3}\pi n_{\text{pert}}\right)^2, \tag{9.30}$$

with C_W and C_6 van der Waals broadening constants and n_{pert} the perturber density.

9.4 Stormberg's expression

A comparison with experiments shows that the Lorentz profile describes the center of the line profile accurately while the Levy profile is an accurate estimate of the red wing. Stormberg determines the total line profile by taking the convolution of the Lorentz and the Levy profile. In this section we present a corrected derivation of Stormberg's expression, derive Hartel's result, and provide a numerically superior expression, based on the Faddeeva function. The starting point is the convolution integral

$$P\left(\Delta\lambda\right) = \int_{-\infty}^{\infty} P_{\text{Levy}}\left(\Delta\lambda\right) P_{\text{Lorentz}}\left(\epsilon - \Delta\lambda\right) \mathrm{d}\epsilon. \tag{9.31}$$

Substitution of (9.15) and (9.28) yields

$$P(\Delta\lambda) = \frac{\sqrt{\Delta\lambda_0}}{2\pi(\Delta\lambda_{1/2})^{3/2}}\sqrt{\Delta\lambda_{1/2}} \quad \times \\ \int_0^\infty \frac{1}{(\epsilon)^{1.5}} \exp(-\frac{\pi\Delta\lambda_0}{4\Delta\lambda_{1/2}}\frac{\Delta\lambda_{1/2}}{\epsilon}) \frac{1}{1+\left(\frac{\Delta\lambda-\epsilon}{\Delta\lambda_{1/2}}\right)^2} \mathrm{d}\epsilon, \tag{9.32}$$

and by changing to the integration variable

$$y = \frac{\Delta\lambda_{1/2}}{\epsilon}, \tag{9.33}$$

and using the definitions (9.6) and (9.7) one obtains

$$P\left(\Delta\lambda\right) = c\int_0^\infty \sqrt{y}\frac{y}{y^2+(ya-1)^2}\exp(-by)\mathrm{d}y. \tag{9.34}$$

Using definition (9.9), one gets

$$\frac{y}{y^2+(ya-1)^2} = \frac{-i}{2\left(1+a^2\right)}\left(\frac{a+i}{y+Z_1}+\frac{-a+i}{y+Z_2}\right), \tag{9.35}$$

which allows us to write equation (9.34) as

$$P\left(\Delta\lambda\right) = \frac{ic}{2\left(1+a^2\right)}\int_0^\infty \left[\frac{(-a-i)\sqrt{y}}{y+Z_1}\exp(-by) \right. \\ \left. -\frac{(-a+i)\sqrt{y}}{y+Z_2}\exp(-by)\right]\mathrm{d}y. \tag{9.36}$$

This equation has the form of a (unilateral) Laplace transform,

$$\mathcal{L}\left\{f\left(t\right)\right\} = \int_0^\infty f\left(t\right)\exp\left(-st\right)\mathrm{d}t, \tag{9.37}$$

and in a book of Laplace tables like Ref. [181] one finds that

$$\int_0^\infty \frac{\sqrt{y}}{y+Z}\exp\left(-by\right)\mathrm{d}y = \sqrt{\frac{\pi}{b}} - \pi\sqrt{Z}\exp\left(Zb\right)\mathrm{Erfc}\left(\sqrt{Zb}\right), \tag{9.38}$$

where Erfc is the *complementary* error function. This result is valid under the conditions that

$$\mathcal{R}(b) = \mathcal{R}\left(\frac{\pi\Delta\lambda_0}{4\Delta\lambda_{1/2}}\right) > 0, \tag{9.39}$$

$$\left|\arg\left(Z\right)\right| = \left|\arg\left(\frac{-a\mp i}{1+a^2}\right)\right| < \pi, \tag{9.40}$$

which are always met because of the definitions of b and $Z_{1,2}$. Note that $\mathcal{R}$ is used to refer to the real part of an expression. By substituting (9.38) in (9.36)

Stormberg's original expression (9.5) can be obtained, with the observation that Erfc is the *complementary* error function.

In the remaining part of this section an alternative expression will be derived that is based on the Faddeeva function. We start by rearranging the Laplace transform as

$$\sqrt{\frac{\pi}{b}} - \pi\sqrt{Z}\exp\left(Zb\right)\operatorname{Erfc}\left(\sqrt{Zb}\right) = \sqrt{\frac{\pi}{b}}\left(1 - \sqrt{\pi}\sqrt{Zb}\exp\left(Zb\right)\operatorname{Erfc}\left(\sqrt{Zb}\right)\right). \tag{9.41}$$

Using

$$\sqrt{Zb} = -i^2\sqrt{Zb} = -id, \tag{9.42}$$

with $d = i\sqrt{Zb}$, the Laplace transform can be expressed in terms of d as

$$\sqrt{\frac{\pi}{b}}\left(1 + i\sqrt{\pi}d\exp\left(-d^2\right)\operatorname{Erfc}\left(-id\right)\right) = \sqrt{\frac{\pi}{b}}\left(1 + i\sqrt{\pi}dw\left(d\right)\right), \tag{9.43}$$

where we have introduced the Faddeeva function (9.2). The final line profile can then be rewritten as

$$\begin{aligned}\frac{P\left(\Delta\lambda\right)}{P_{\mathrm{Lor}}\left(\Delta\lambda\right)} =& \frac{-i\left(+a+i\right)}{2}\left(1 + i\sqrt{\pi}d_1w\left(d_1\right)\right) + \frac{-i\left(-a+i\right)}{2}\left(1 + i\sqrt{\pi}d_2w\left(d_2\right)\right)\\ =& 1 - \frac{i\left(1+a^2\right)d_1^2}{2b}i\sqrt{\pi}d_1w\left(d_1\right) + \frac{i\left(1+a^2\right)d_2^2}{2b}i\sqrt{\pi}d_2w\left(d_2\right)\\ =& 1 + \frac{\left(1+a^2\right)\sqrt{\pi}}{2b}\left\{d_1^3w\left(d_1\right) - d_2^3w\left(d_2\right)\right\}.\end{aligned} \tag{9.44}$$

The term $d_1^3w\left(d_1\right)$ can be related to $d_2^3w\left(d_2\right)$ by noting that

$$\overline{d_1} = \overline{i\sqrt{Z_1b}} = -i\sqrt{\overline{Z_1}b} = -i\sqrt{Z_2b} = -d_2, \tag{9.45}$$

as a result of which

$$\overline{d_1^3w\left(d_1\right)} = \overline{d_1^3}\,\overline{w\left(d_1\right)} = \overline{d_1}^3w\left(\overline{-d_1}\right) = -d_2^3w\left(d_2\right). \tag{9.46}$$

In the last step we have used $w\left(\overline{z}\right) = \overline{w\left(-z\right)}$ (see Ref. [182, eq. 7.1.12]). Then the final expression can be simplified to

$$\frac{P\left(\Delta\lambda\right)}{P_{\mathrm{Lor}}\left(\Delta\lambda\right)} = \left[1 + \frac{\left(1+a^2\right)\sqrt{\pi}}{b}\mathcal{R}\left\{d_1^3w\left(d_1\right)\right\}\right]. \tag{9.47}$$

When the Faddeeva function is expressed in terms of the complementary error function this yields Hartel's expression.

Equation (9.47) has decisive analytical and computational advantages, compared with Stormberg's and Hartel's expressions. It is more compact, emphasizes that the line profile is real-valued, and avoids the subtraction of possibly (nearly-)equal terms. Moreover, there is no need to evaluate the product of a complex

exponent and an error function, since specialized algorithms exist for the numerically stable evaluation of the Faddeeva function itself [183].

Before discussing the numerical stability further, it is instructive to explore the limiting cases in which one of the broadening mechanisms is absent. The Lorentzian profile can be retrieved trivially by using

$$\lim_{\Delta\lambda_0 \downarrow 0} b = \frac{\pi \Delta\lambda_0}{4\Delta\lambda_{1/2}} = 0, \tag{9.48}$$

which implies that

$$\lim_{\Delta\lambda_0 \downarrow 0} \frac{d_{1,2}^3}{b} = \lim_{\Delta\lambda_0 \downarrow 0} \frac{\left[i\left(-a \mp i\right) b\right]^3}{\left(1+a^2\right)^{3/2} b} = 0. \tag{9.49}$$

Recovering the Levy profile is more tricky, since $\lim_{\Delta\lambda_{1/2} \downarrow 0} a = \infty$, $\lim_{\Delta\lambda_{1/2} \downarrow 0} b = \infty$ and $\lim_{\Delta\lambda_{1/2} \downarrow 0} c = \infty$. But since

$$\lim_{\Delta\lambda_{1/2} \downarrow 0} \frac{a}{b} = \frac{4\Delta\lambda}{\pi\Delta\lambda_0} \tag{9.50}$$

is constant, for $\lim_{\Delta\lambda_{1/2} \downarrow 0}$ we can easily derive that

$$P\left(\Delta\lambda\right) = \frac{4}{\pi^2 \Delta\lambda_0} \left(\frac{b}{a}\right)^{1.5} \left[\frac{\sqrt{\pi}}{2} \left\{ w\left(\sqrt{\frac{b}{a}}\right) + w\left(-\sqrt{\frac{b}{a}}\right) \right\}\right]. \tag{9.51}$$

Using $w\left(z\right) + w\left(-z\right) = 2\exp\left(-z^2\right)$ (see Ref. [182, eq. 7.1.11]) and the definitions of a and b, we arrive at the expression for the Levy profile.

9.5 Numerical stability

The line profile calculated with (9.5) shows oscillations for large values of b. First an example is given of a physical situation where these high values of b can occur. After that an implementation of (9.47) in MATLAB and its numerical stability are discussed.

The line profile can be characterized with the variables $\Delta\lambda_{1/2}$ and $\Delta\lambda_0$. A more insightful description is given by the parameter b which contains the ratio of the impact and quasi-static linewidths. By only taking into account resonance broadening in the impact limit and van der Waals broadening in the quasi-static limit, this ratio can be expressed in terms of the broadening constants as

$$b = \frac{\pi}{4} \frac{16 C_6 n_p^2}{9 C_3 n_r}, \tag{9.52}$$

with n_r the density of radiating species and n_p the density of perturbing species. In a situation where the radiating particles are not the same as the perturbing particles a high value of b can occur. For example in a high pressure mercury

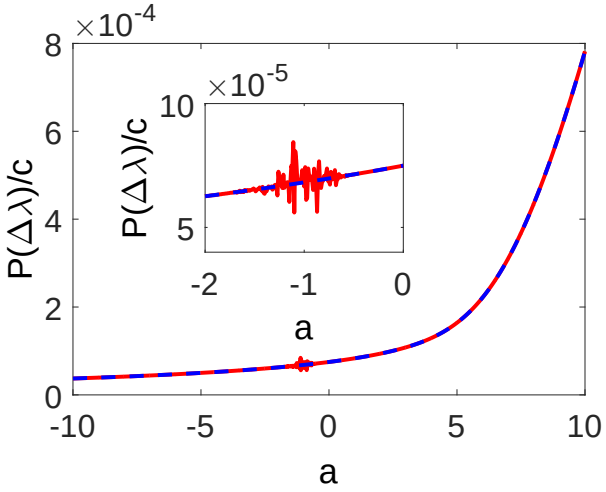

Figure 9.1: For $b = 50$ the line profile can become numerically unstable when Stormberg's original expression (9.5) is used (solid line). The new expression (9.47) is stable for all b values (dashed line).

discharge containing sodium iodide the ratio can become large at lower temperatures where the sodium is bound in molecules. In methods like ray tracing [184] a correct calculation of the line profile at lower temperatures is also required to account for the absorption accurately.

The calculation of the line profile [185] according to (9.5) in MATLAB requires an implementation of the error function. Since this is not a built-in function, we used the implementation from Leutenegger [186] for our tests. For $b > 50$ these revealed numerical artifacts in the line shape that can be attributed to inaccuracies in Leutenegger's implementation. Our new expression (9.47), that was tested with the implemented Faddeeva function of Ikuma [183] did not have such problems.

These results are shown in figure 9.1. Since the line profiles are proportional to c, we have plotted $P(\Delta\lambda)/c$ in these graphs. The figure clearly shows the oscillations for $b = 50$ when Stormberg's original expression is used with Leutenegger's algorithm for calculating the error function; the noise rapidly increases in magnitude and width when b is increased further.

For a few values of b the resulting line profiles are shown in figures 9.2-9.5. These figures show that the oscillations which start to occur around $b = 50$ arise when the line profile is dominated by the Levy contribution. Wharmby [187] already mentioned that impact and quasi-static theory have their limitations and that for high densities the Levy profile can cause unrealistically large red wings. He was still able to obtain accurate results by convolving again with a Gaussian profile to artificially limit these wings. A correct calculation of the line profile requires to take into account accurate potential curves of the interacting species. Such curves are not always available and in some cases a more simple calculation

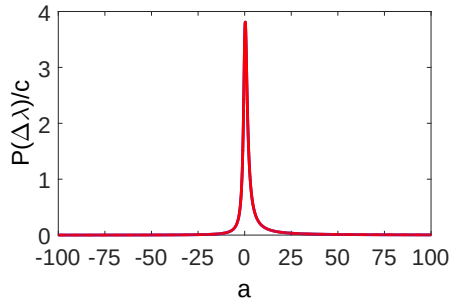

Figure 9.2: $P(\Delta\lambda)/c$ for $b = 0.1$

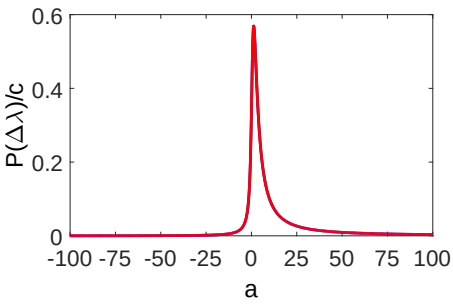

Figure 9.3: $P(\Delta\lambda)/c$ for $b = 1$

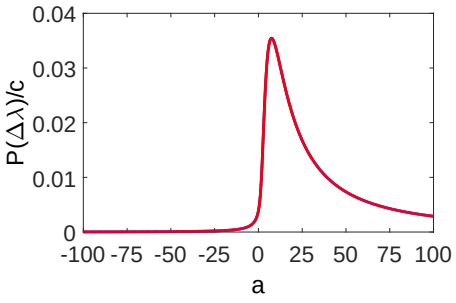

Figure 9.4: $P(\Delta\lambda)/c$ for $b = 10$

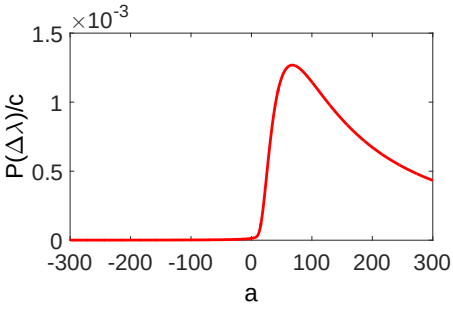

Figure 9.5: $P(\Delta\lambda)/c$ for $b = 100$

of the line profile is preferred. For these cases Stormberg's line profile can be used as a first order approximation.

9.6 Conclusion

We have evaluated the dominant broadening mechanisms of atomic lines in high pressure plasma. We have shown that when Stormberg's original expression is used in conjunction with a popular implementation of the error function in MATLAB/Octave, intolerable numerical errors are observed when the broadening is dominated by the Levy contribution. We have presented a novel expression that is based on the Faddeeva function, which is more elegant, computationally efficient and accurate under all circumstances. The MATLAB/Octave scripts of our implementation have been made available on the publisher's website for future reference [183, 185, 186].

Chapter 10

Numerical investigation on the replacement of mercury by indium iodide in HID lamps

Abstract

Mercury-free high-pressure discharge lamps have been studied by means of a radial-dependent model. Xenon and indium iodide are chosen as start gas and buffer, respectively. Local thermodynamic equilibrium (LTE) is assumed with a single temperature for all species. The model consists of the coupled description of the balance equation for the plasma temperature with the radiation transport equation. The plasma composition is calculated according to the Guldberg-Waage, Boltzmann and Saha laws. These laws were supplemented by additional equations specifying the total pressure, constant element ratios and quasi-neutrality. The model takes into account atomic, molecular as well as continuum radiation. The broadening of the optically thick lines is approximated by Stormberg's approach. In order to predict the continuum radiation we performed ab initio calculations to obtain the potential curves and the transition dipole moments. The predicted spectrum is compared with a measured spectrum. The comparison shows that the model is able to reproduce the continuum radiation. The conclusion from this comparison is that the largest part of the continuum radiation is produced by free-free and free-bound transitions in InI. The free-bound A-X transition is the dominant process.

Published as: M. Gnybida, J.F.J. Janssen, J. van Dijk, J.L.G. Suijker, K.S.C. Peerenboom, A.J. Rijke, M. Gendre and G.M.W. Kroesen, *Numerical investigation on the replacement of mercury by indium iodide in high-intensity discharge lamps* in Journal of Physics D: Applied Physics, 47, p. 125201

10.1 Introduction

High-intensity discharge (HID) lamps have been used for general lighting applications for almost a century. There are three principal types of HID lamps [8,169,188]: high-pressure mercury, high-pressure sodium and metal-halide lamps, which differ by the nature of their radiating species. In all cases mercury is used as buffer gas. Mercury provides a high vapor pressure and a large momentum transfer cross section which generates the necessary ohmic heating at low currents. Mercury has an impact on the discharge temperature profile due to radiation transport, which leads to a broad temperature profile. The high mass of mercury results in a low thermal conductivity. Mercury has high excitation/ionization levels, which leads to a small contribution to the net radiative output and a small contribution to electron production in a metal-halide lamp.

However, mercury compounds are extremely toxic and should therefore be replaced by environmental-friendly elements without decreasing the lamp efficacy. Replacement of mercury by metallic zinc is suggested by Born [16]. However, this causes corrosion of the wall material due to the high temperature. A sulfur lamp operating with a microwave discharge shows high luminous efficacy [189]. However, the lifetime and efficacy of sulfur lamps is limited by the magnetron used to generate the microwaves. Despite these and other attempts, mercury remains the main component of most commercial HID lamps.

K$\acute{}$aning [17] suggest to replace mercury with strong molecular radiators. The discharge voltage of these mercury-free lamps is then increased by shrinking the arc cross section. Such a contraction is caused by molecular radiation emitted in the colder mantle region of the discharge. A possible candidate to replace mercury is indium iodide, which delivers a large amount of continuum radiation in the visible and infrared (IR) ranges [190, 191]. Grabner et al. [190] claim that the IR continuum is caused by recombination radiation and the visible continuum by a combination of strong broadening of the indium resonance lines and molecular radiation.

The goal of this investigation is to understand the effects of replacing mercury in HID lamps with a mixture of xenon and indium iodide. These effects are investigated by numerical simulations. The focus lies on the calculation of the plasma temperature profile and the spatially integrated spectrum (spectral power density). Furthermore, the calculated spectral power density is compared with a measurement obtained from an integrating sphere setup. This comparison demonstrates that the process responsible for the broadband continuum radiation is understood.

10.2 Modeling

10.2.1 Assumptions

The plasma simulation platform PLASIMO [25] is used to model the replacement of mercury in high-pressure discharge lamps. A 1D cylindrically symmetric plasma is considered with a radius $R = 3\,\mathrm{mm}$. The distance between the electrodes is $L_{\mathrm{el}} =$

7.1 mm. Based on simulation results of an electrode model [192], the electrode losses are estimated to be 10 % of the lamp power. Thus 90 % of the power is dissipated in the discharge as ohmic heating. The plasma temperature at the tube wall is assumed to be 1400 K which is based on wall temperature measurements of similar mercury-containing lamps. Additionally, LTE [172, p. 187] is assumed.

A correct description of demixing in a mercury-free lamp requires solving the Stefan-Maxwell diffusion equations. In our xenon indium iodide discharge there is no species that is dominant over the entire temperature range since the elemental fractions of xenon, indium and iodide are of the same order of magnitude. Because of the replacement of the dominant buffer gas mercury by a mixture, standard demixing algorithms that are based on Fick's law are no longer valid. Constant elemental pressures will be assumed, since a correct description based on the Stefan-Maxwell equations is not available. This approximation is equivalent to the convection limit given by Fischer [193]. The usage of the convection limit is not optimal considering the pressure and the radius of the lamp. However, the model will be accurate enough to reveal what process in the discharge is causing the continuum radiation.

10.2.2 Governing equations

The model couples the energy balance with the radiation transport equation self-consistently. A fixed power is applied to the gas in the energy equation. This is achieved by adjusting the electric field after every calculation of the temperature profile. The total power dissipated in the discharge column is given by

$$P_{\mathrm{in}} - P_{\mathrm{el}} = \int \sigma\,(r)\, E^2 \mathrm{d}V = E^2 L_{\mathrm{el}} \int_0^R 2\pi r \sigma(r) \mathrm{d}r, \tag{10.1}$$

with $\mathrm{d}V$ a volume element, r the radius, P_{in} the total input power, P_{el} the power lost in the electrodes, E the axial electric field and $\sigma(r)$ the electrical conductivity. The electric field is thus calculated as

$$E = \sqrt{\frac{P_{\mathrm{in}} - P_{\mathrm{el}}}{L_{\mathrm{el}} \int_0^R 2\pi r \sigma(r) \mathrm{d}r}}. \tag{10.2}$$

The energy equation is given by [16]

$$-\frac{1}{r}\frac{\partial}{\partial r}\left(r\lambda \frac{\partial T}{\partial r}\right) = \sigma E^2 - P_{\mathrm{rad}}, \tag{10.3}$$

where λ is an effective thermal conductivity that includes contributions from reactions, P_{rad} the net radiative power and T the temperature. The term P_{rad} is the power density that is derived from the evolution of the spectral radiance along multiple probe lines. The local change in spectral radiance is given by [20]

$$\frac{\mathrm{d}I_\nu}{\mathrm{d}s} = j_\nu - \kappa_\nu I_\nu, \tag{10.4}$$

with j_ν the local emission coefficient, κ_ν the local absorption coefficient, I_ν the spectral radiance and s the path traversed by the radiation. The radiative flux $\mathrm{d}^2\Phi_\nu$ passing through a surface area $\mathrm{d}A$ in the direction $\vec{s}$ and covering a solid angle $\mathrm{d}\Omega$ is given by

$$\mathrm{d}^2\Phi_\nu = I\vec{s}\cdot\mathrm{d}\vec{A}\mathrm{d}\Omega. \tag{10.5}$$

The net radiative power passing through that surface can then be calculated by integration over the frequency. The local power density can then be calculated as

$$P_{\mathrm{rad}} = \iiint \frac{\mathrm{d}^2\Phi_\nu}{V}\mathrm{d}\nu = \iiint \frac{I_\nu\vec{s}\cdot\mathrm{d}\vec{A}\mathrm{d}\Omega\mathrm{d}\nu}{V}, \tag{10.6}$$

with V the local volume under consideration. The probe lines that make a zenith angle of 90 ° lay in the horizontal plane and are taken into account from one side of the wall at $-R$ to the other side of the wall at R. Probe lines at a different zenith angle could start from the bottom or top cover of the cylinder. According to the infinitely long cylinder approximation, these lines are extended to the walls and are therefore also taken into account from $-R$ to R. This means that radiation transfer is also taken into account for sections of probe lines that are in fact partly outside the lamp. Using this method the radiative losses are slightly underestimated in the center of the plasma.The absorption in the mantle is slightly overestimated. These effects are small in our plasma since the molecular radiation is mostly optically thin and for a qualitative comparison of the spectra such an approximation is sufficiently accurate. Additionally, we do not include absorption or reflection from the wall of the discharge vessel[1].

The plasma composition used for the model was calculated by solving a system of Guldberg-Waage equations

$$\frac{\Pi_i\left[n_{X_i}\right]^{a_i}}{\Pi_j\left[n_{Y_j}\right]^{b_j}} = \frac{\Pi_i\left(Z_{X_i}\right)^{a_i}}{\Pi_j\left(Z_{Y_j}\right)^{b_j}}\left(\frac{2\pi k_B T}{h^2}\right)^{\frac{3}{2}\left(\sum_i a_i-\sum_j b_j\right)} \times \left(\frac{\Pi_i\left(m_{X_i}\right)^{a_i}}{\Pi_j\left(m_{Y_j}\right)^{b_j}}\right)^{\frac{3}{2}} \exp\left(-\frac{\sum_i a_i E_{X_i}-\sum_j b_j E_{Y_j}}{k_B T}\right), \tag{10.7}$$

with Π denoting the product of a sequence, k_B the Boltzmann constant and h Planck's constant; the following properties correspond to the reactants X_i and the products Y_j: m_{X_i} the mass, n_{X_i} the number density, E_{X_i} the energy and Z_{X_i} the internal partition sum (electronic and rovibrational states); the quantities X_i,a_i, Y_j and b_j are specified by the reaction

$$a_1X_1 + a_2X_2 + \cdots + a_iX_i \leftrightarrow b_1Y_1 + b_2Y_2 + \cdots + b_jY_j. \tag{10.8}$$

These laws were supplemented by additional equations specifying the total pressure p, uniform elemental fractions and quasi-neutrality. The elemental pressure

[1]The reflection can be included in a 1D radial symmetrical model according to Haverlag et al. [194]. In order to account for reflection the spectral radiance can be multiplied with $T/\left(1-R\exp\left(-\tau\right)\right)$ where T is the transmission and R the reflection.

for indium and iodine is kept constant as a function of the radius. The elemental pressure is defined as

$$p_\alpha = \sum_i R_{\alpha i} p_i, \tag{10.9}$$

with p_i the partial pressure of particle i and $R_{\alpha i}$ the stoichiometric coefficient [113], which states how often element α occurs in particle i. The quasi-neutrality constraint is given by

$$\sum_i q_i n_i = 0, \tag{10.10}$$

with q_i the charge of the particle. The elemental fraction of Xe is adjusted in order to obtain a constant pressure as a function of the radius. Thermodynamic data is taken from [195–199]. The composition contains the following species: e, Xe, Xe^+, In, In^+, I, I^+, I_2, I^-, InI, InI_2 and InI_3.

10.2.3 Transport coefficients

The model requires knowledge of the transport coefficients i.e. thermal and electrical conductivity. The Chapman-Enskog expansion [34, p464-491] is used to calculate the transport coefficients. A set of collision integrals, which describes the interaction of one species with every other species, is required to compute the transport properties.

The collision integral for collisions between species of type i and type j is given by

$$\Omega_{ij}^{(l,s)} = \left(\frac{k_B T^*}{2\pi\mu_{ij}}\right)^{1/2} \int_0^\infty \gamma^{2s+3} e^{-\gamma^2} Q_{ij}^{(l)} \mathrm{d}\gamma, \tag{10.11}$$

where l and s are two parameters defining the order of the collision integrals, $\gamma^2 = (\mu_{ij}/2k_B T^*)g^2$ is a reduced energy where $\mu_{ij} = m_i m_j/(m_i + m_j)$ is the reduced mass, g is the relative velocity and T^* is an effective collision temperature [200], which is equal to the temperature T in LTE. Q_{ij}^l is the lth moment collision cross section which is given by

$$Q_{ij}^l = 2\pi \int_0^\infty (1 - \cos^l(\chi)) b \mathrm{d}b, \tag{10.12}$$

where b is the impact parameter and χ the scattering angle given by

$$\chi = \pi - 2b \int_{r_m}^\infty \frac{\mathrm{d}r}{r^2[1 - (b^2/r^2) - (2\phi(r)/\mu g^2)]^{1/2}}, \tag{10.13}$$

where r_m is the distance of closest approach and $\phi(r)$ the interaction potential.

Each type of collision is described by a different interaction potential. For neutral-neutral and neutral-ion cases the modified Lennard-Jones potential has been used according to Laricchiuta et al. [5]. The approach requires knowledge of the polarizability of the interacting particles. Patil [104] published a list containing the polarizability for a large number of atoms and ions. Molecular polarizabilities have been computed according to Thole's approach [105]. Resonant charge

transfer is included according to Rapp and Francis [74]. For charged-charged cases the screened-Coulomb potential has been used. Highly accurate tabulations for the collision integrals are available from Mason et al. for the repulsive as well as attractive collisions [87]. There is no straightforward way to treat electron-neutral collisions, because the energy at which it occurs and the magnitude of the Ramsauer minimum strongly varies for different collisions. Specific momentum transfer cross sections were used to describe $e - Xe$, $e - I$, $e - In$ interactions [201–205]. For In, there are two data sets. These sets describe different energy ranges and therefore the intermediate energy range is interpolated. The polarizability model of Langevin [64, p. 15] has been used to treat other electron-neutral collisions. This model uses a relative polarizability α_r that is calculated as

$$\alpha_r = \frac{(R_1 + R_2)^3}{8a_0^3}, \tag{10.14}$$

with R_i the radius of particle i and a_0 the Bohr radius. A rigid sphere interaction is used if no interaction type is specified.

The total thermal conductivity of the plasma is given by

$$\lambda = \lambda_t + \lambda_e + \lambda_r + \lambda_i, \tag{10.15}$$

where λ_t is the translational thermal conductivity of the heavy particles, λ_e is the translational thermal conductivity of the electrons, λ_r is the reactive thermal conductivity and λ_i is the internal thermal conductivity. The second-order translational thermal conductivity is given by Muckenfuss and Curtis [111]. The Devoto's third-order approximation is used to calculate the electronic thermal conductivity [108]. To describe the reactive thermal conductivity we use the relations of Butler and Brokaw [50, 112]. The internal contribution is calculated using the Eucken-like expression from Gupta [206]. Devoto's second-order approximation is used to compute the electrical conductivity [108].

10.2.4 Local radiation properties

The model takes into account atomic and molecular radiation as well as radiation emitted as Bremsstrahlung. The local emission coefficient [172, p. 226] for an atomic transition between state u and state l is given by

$$j_\nu = \frac{h\nu}{4\pi} n_u A_{ul} \phi_\nu, \tag{10.16}$$

where h is Planck's constant, n_u is the density of the upper level, A_{ul} is the transition probability, ν is the frequency and ϕ_ν is the spectral line profile. Subscripts ν indicate that the quantity is dependent on the frequency. The density of the upper level is calculated using the Boltzmann distribution which is given by

$$n_u = n \frac{g_u}{Z(T)} \exp\left(-\frac{E_u}{k_B T}\right), \tag{10.17}$$

where n is the total particle density, g_u is the statistical weight of the upper level, $Z(T)$ is the partition function and E_u is the energy of the upper level.

The local emission coefficient for a molecular transition is given by [207]

$$j_{\nu,r} = \frac{4\pi\sigma_{\text{sym}}}{V_{st}} \frac{r^2}{4\pi} A_{ul} \left| \frac{\partial\nu}{\partial r} \right|^{-1} h\nu \left[\frac{n_u}{Z_u} \exp\left(-\frac{V_u(r)}{k_B T} \right) \right], \tag{10.18}$$

with σ_{sym} a statistical factor which is 1 for heterogeneous molecules and $\frac{1}{2}$ for homogeneous molecules. The state volume V_{st} is calculated as

$$V_{st} = \left(\frac{h^2}{2\pi\mu_{ij} k_B T} \right)^{3/2}. \tag{10.19}$$

The emitted frequency is given by

$$\nu(r) = \frac{\Delta E + V_u(r) - V_l(r)}{h}, \tag{10.20}$$

where ΔE is the potential difference between the two states, $V_u(r)$ and $V_l(r)$ are the potential energies of respectively the upper and the lower states relative to their minimum potential energies. The transition probability [154, p. 103] is given by

$$A_{ul} = \frac{16\pi^3 D^2(r)\, \nu^3}{3h g_u \varepsilon_0 c^3}, \tag{10.21}$$

where $D(r)$ is the transition dipole moment, ϵ_0 is the electric permittivity of vacuum and c is the speed of light. We calculated this variable using the program DIRAC [208–211]. The total partition sum of the molecular state is [207]

$$Z = \frac{\sigma_{\text{sym}}}{V_{st}} \int_{r_{\min}}^{r_{\max}} 4\pi r^2 \exp\left(-\frac{V(r)}{k_B T} \right) \mathrm{d}r, \tag{10.22}$$

where $r_{\min}$ and $r_{\max}$ represent the minimum and the maximum interatomic separations that are included in the calculation. The local absorption coefficient is

$$\kappa_{\nu,r} = \frac{4\pi\sigma_{\text{sym}}}{V_{st}} \frac{c^2}{8\pi} A_{ul} \frac{r^2}{\nu^2} \left| \frac{\partial\nu}{\partial r} \right|^{-1} \left[\frac{g_u}{g_l} \frac{n_l}{Z_l} \exp\left(-\frac{V_l(r)}{k_B T} \right) - \frac{n_u}{Z_u} \exp\left(-\frac{V_u(r)}{k_B T} \right) \right]. \tag{10.23}$$

We used the relativistic ab initio calculation program DIRAC [211] to calculate the potential curves and the transition dipole moments. The excited states were approximated by Kramers restricted configuration interaction calculations according to the generalized active space concept [211]. The active space is formed by the 5s and the 5p electrons with one excitation allowed[2]. Virtual states up to 1 Hartree above the ground state energy were taken into account. We used the Triple-Zeta Basis Set from K.G. Dyall that is built in into Dirac12 [208–210].

[2]Note that the paper [152] incorrectly mentions that the 4d electrons are included. Additionally, only one excitation is taken into account instead of two excitations.

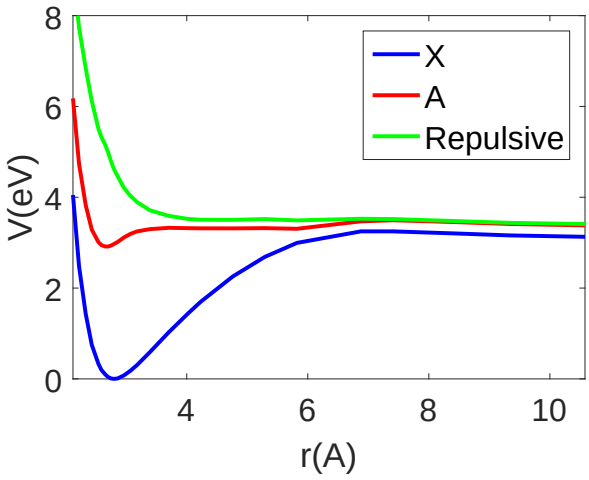

Figure 10.1: Calculated ab initio energy curves for the InI molecule using DIRAC [208–211].

According to measured spectra, lamps containing InI have a broad continuum [190]. The main source of that continuum is claimed to be molecular radiation and strongly broadened atomic radiation. In this model two radiative transitions between ground and excited states of InI will be considered: InI[A] $\rightarrow$ InI[X] and InI[rep] $\rightarrow$ InI[X]. Potential curves of the ground state and two excited states of InI are plotted in figure 10.1. The transition dipole moments are shown in figure 10.2. The potential curves other than the ground state show a shallow or a completely repulsive interaction potential. These curves show that the phase-space population of the excited states predominantly are free states ($V(r) > V(\infty)$) rather than molecular/bound states ($V(r) < V(\infty)$). A large part of the continuum is thus free-bound or free-free radiation. We will call this radiation quasi-molecular radiation. The increasing transition dipole moment in the range of 4-5 Å for the transition from InI[A] to InI[X] is responsible for most of the IR radiation.

The continuum radiation consists of electron-atom Bremsstrahlung j_ν^{eab}. The continuum is approximated with the expression given by De Regt [163]

$$j_\nu^{eab} = 2n_e n_a (k_B T)^{3/2} Q_m(T) \left[\left(1 + \frac{h\nu}{k_B T} \right)^2 + 1 \right] \exp\left(-\frac{h\nu}{k_B T} \right), \qquad (10.24)$$

where n_e, n_a and $Q_m(T)$ are the electron density, the atom density and the mean cross section for momentum transfer [201–205] for electrons with atoms, respectively.

Under LTE conditions the absorption coefficient can be deduced from Kirch-

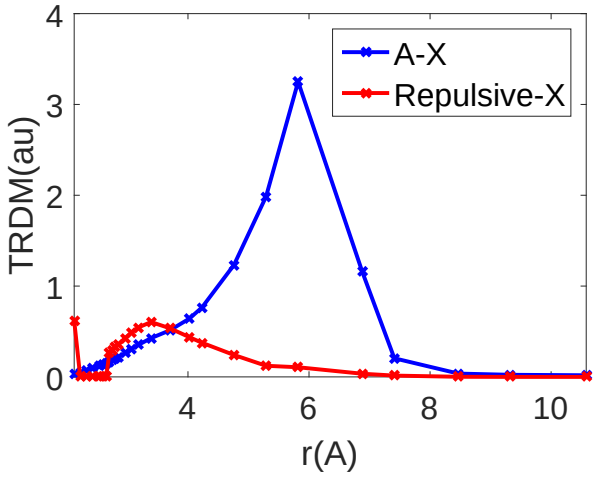

Figure 10.2: Calculated ab initio transition dipole moments for the InI molecule using DIRAC [208–211].

hoff's law as [207]

$$\kappa_\nu = \frac{j_\nu}{B_\nu}, \tag{10.25}$$

where B_ν is the spectral radiance of an object in thermal equilibrium. This radiance is given by

$$B_\nu = \frac{2h\nu^3}{c^2}\left[\exp\left(\frac{h\nu}{k_B T}\right) - 1\right]^{-1}. \tag{10.26}$$

10.2.5 Spectral line broadening

It is assumed that atomic transitions from xenon and iodine atoms can be neglected because of the high energy levels of the excited states. Therefore only contributions from indium atoms are included into the model. A list of the included energy levels, transitions and broadening constants of the indium atom is displayed in table 10.1. The only atomic line in the UV or visible spectrum that is not completely absorbed by the plasma is the 451 nm line. The broadening constants for this line were adjusted to ensure a correct shape in the simulation. The constants for the other lines are assumed to be equal to the constants for the 451 nm line. The broadening of the optically thick atomic lines of Indium is approximated by Stormberg's approach [30, 159]

$$\phi_\lambda = \frac{\lambda_{\text{res}}}{\pi((\lambda - \lambda_0)^2 + (\lambda_{\text{res}})^2)}\mathbf{R}\left(1 + \frac{1+a^2}{b}\sqrt{\pi}d_1^3 w(d_1)\right), \tag{10.27}$$

with $\mathbf{R}(s)$ the real part of s , λ_{res} the half width at half maximum (HWHM) of the resonance line profile, λ_0 the wavelength of the unperturbed line and the scaling

parameters a, b and $d_{1,2}$ given by

$$\lambda_{\text{res}} = \frac{\lambda_0^2 \pi}{2c} C_3 n_0, \tag{10.28}$$

$$\lambda_{\text{vdw}} = \frac{C_6 \lambda_0^2}{2\pi c} \left(\frac{4}{3}\pi n_{\text{p}}\right)^2, \tag{10.29}$$

$$d_1 = i\sqrt{b\frac{(-a-i)}{1+a^2}}, \tag{10.30}$$

$$a = \frac{(\lambda - \lambda_0)}{\lambda_{\text{res}}}, \tag{10.31}$$

$$b = \frac{\pi \lambda_{\text{vdw}}}{4\lambda_{\text{res}}}, \tag{10.32}$$

where C_3 is the resonance broadening constant, λ_{vdw} the characteristic wavelength of the Van der Waals profile n_0 is the ground state of the radiating particle, C_6 is the Van der Waals broadening constant and n_p is the ground state of the perturber. The expression of the line profile depends on the Faddeeva function

$$w(d) = \exp(-d^2)\text{Erfc}(-id). \tag{10.33}$$

More details about the correct analytical expression for the line profile calculated as the convolution of Lorentzian and Van der Waals profiles can be found in [159].

Table 10.1: Spectral line data of indium atom [53]

λ (nm)	E_l (eV)	E_u (eV)	g_l	g_u	A_{ul} (s^{-1})	C_3 ($m^3 s^{-1}$)	C_6 ($m^6 s^{-1}$)
303.936	0.00000	4.08099	2	4	1.30×10^{8}	1.00×10^{-15}	1.9×10^{-44}
325.609	0.27432	4.08099	4	6	1.30×10^{8}	1.00×10^{-15}	1.9×10^{-44}
325.856	0.27432	4.07910	4	4	3.77×10^{7}	1.00×10^{-15}	1.9×10^{-44}
410.176	0.00000	3.02185	2	2	5.60×10^{7}	1.00×10^{-15}	1.9×10^{-44}
451.131	0.27432	3.02185	4	2	1.02×10^{8}	1.00×10^{-15}	1.9×10^{-44}

10.3 Results and discussion

In this section simulation results for power loads $P = 70\,\text{W}$ are reported as well as the most important plasma properties in the relevant temperature range. The numerical results have been obtained by solving a discrete representation of the coupled set of equations (10.3), (10.4) on an equidistant grid in space and frequency. The spatial and frequency domains have been discretized using 98 and 2600 intervals, respectively. In order to reach a converged solution an iterative scheme has been applied. The computations were performed on a 2.5 GHz CPU. It took around 8 hours to reach a residue for the temperature lower than 1×10^{-8}. The calculation of the radiation losses is responsible for the largest amount of the total calculation time. The results have been obtained for a discharge containing Xe and InI.

10.3.1 Plasma composition

Figure 10.3 shows the number densities as a function of temperature for a XeInI discharge. Due to the high pressure of xenon and iodine their number densities dominate over the complete temperature range. Additionally, the low temperature region from 1 kK to 3 kK contains high molecular densities. With increasing temperature, molecules start to dissociate. In particular, diatomic iodine dissociates into two iodine atoms around 1.5 kK and indium iodide dissociates into indium and iodine atoms around 3 kK. Xenon and iodine have higher ionization energies than indium. Therefore, the population of electrons is almost equal to the population of indium ions in the high temperature region.

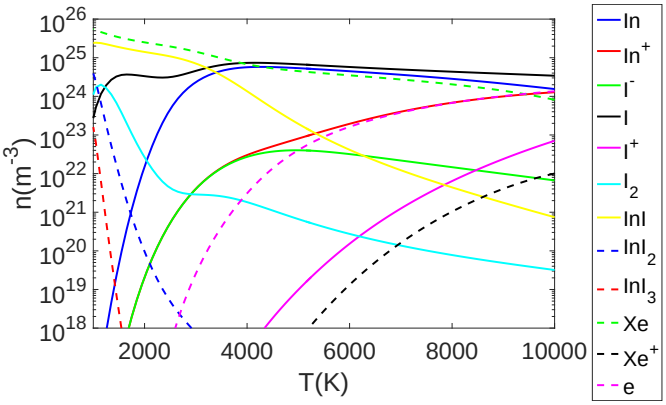

Figure 10.3: Calculated number densities of indicated species of the XeInI discharge. The elemental pressures are $p_{\{\mathrm{In}\}} = 3.9\,\mathrm{bar}$ and $p_{\{\mathrm{I}\}} = 4.83\,\mathrm{bar}$. The total pressure is kept constant at 11.73 bar.

10.3.2 Transport coefficients

The temperature dependence of the total thermal conductivity and its components, for the XeInI discharge lamp are plotted in figure 10.4. The internal thermal conductivity is not displayed in this plot, because its values are of the order of $1 \times 10^{-3}\,\mathrm{Wm^{-1}K^{-1}}$ which is significantly lower than the other contributions. The reactive contribution to the total thermal conductivity reaches local maxima in the temperature range where dissociation and ionization reactions occur. In particular, the I_2 and InI molecules dissociate around 1.5 kK and 3 kK, respectively. The heavy particle translational thermal conductivity dominates in the medium temperature range from 2 kK to 6 kK. Due to the high relative ionization at high temperatures, the electron translational thermal conductivity is the major contribution to the total thermal conductivity in this temperature range.

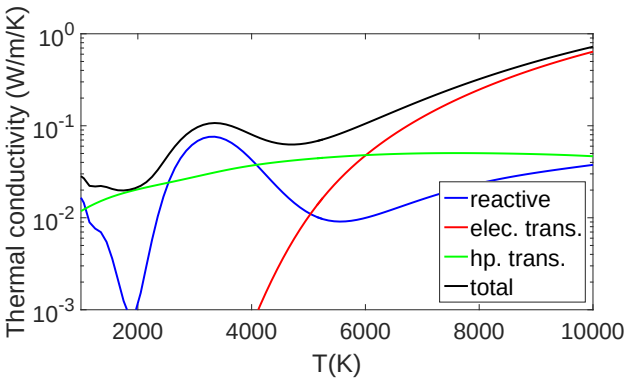

Figure 10.4: Calculated components of the thermal conductivity of the XeInI discharge. The elemental pressures are $p_{\{\mathrm{In}\}} = 3.9\,\mathrm{bar}$ and $p_{\{\mathrm{I}\}} = 4.83\,\mathrm{bar}$. The total pressure is kept constant at 11.73 bar.

The temperature dependence of the electrical conductivity for the XeInI discharge lamp is plotted in figure 10.5. The electrical conductivity strongly depends on the electron density. Therefore, the evolution of the electrical conductivity and the electron density as a function of the temperature is very similar.

10.3.3 Comparison with measured spectrum

The spectrum obtained from simulations has been compared with measurement results determined by means of an integrating sphere [21]. The discharge vessel is dosed with 6.48 mg of InI, 0.25 mg of AlI_3 and is filled with 0.35 bar of Xe at room temperature. The measured lamp is operated at a 120 Hz square wave current with a total power of 70 W. The model assumes a DC current. The indium and iodine pressures are estimated as 3.9 and 4.83 bar, respectively. These pressures were determined by assuming constant elemental pressures and a cold spot temperature of 1.2 kK [212]. The cold spot temperature is set equal to the cold spot temperature of mercury-containing lamps. Due to this assumption the pressure in the lamp may deviate from the pressure used in the simulation.

The simulated and measured spectra of the XeInI discharge are displayed in figure 10.6. The measured IR and visible contributions are 44.1 and 23.7 W. The amount of energy lost via thermal conduction through the electrodes is estimated to be 2.2 W. In the simulation the IR, visible and UV contributions are 25.4, 26.0 and 1.8 W, respectively. Since the simulated spectrum does not account for thermal radiation from the wall, a correction to the IR radiation must be made. It is assumed that the conduction through the electrodes is also 2.2 W in the model. The remaining energy lost in the electrodes and the energy lost via thermal conduction to the wall of 14.6 W is expected to be lost as thermal radiation. The

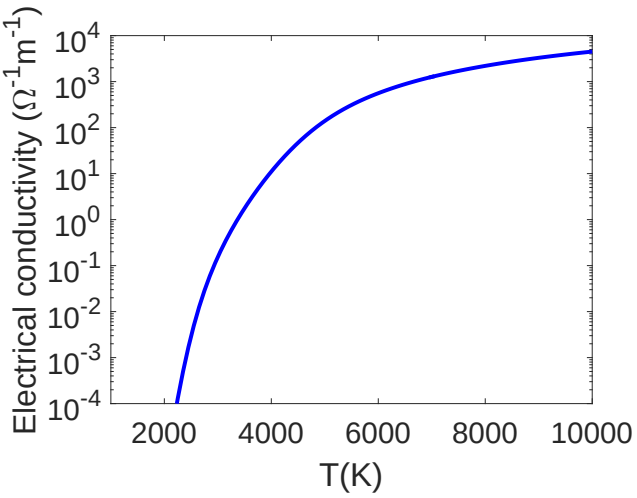

Figure 10.5: Calculated electrical conductivity of the XeInI discharge. The elemental pressures are $p_{\{\mathrm{In}\}} = 3.9\,\mathrm{bar}$ and $p_{\{\mathrm{I}\}} = 4.83\,\mathrm{bar}$ and the total pressure is 11.73 bar.

IR losses are thus 40.1 W. The agreement between the energy balances is thus good.

The spectrum calculated by the model also agrees well with the experiments. In particular, the model reproduces the experimentally observed broad molecular band from 410 nm to the far IR. The main origin of this broad band continuum are transitions from the free A state to the X state of InI. The five atomic indium lines[3] between 1250 and 1500 nm are not included in the model because of unknown transition probabilities of those lines. The integral with respect to wavelength which determines the power in these 5 lines is small compared to the power in the continuum. The impact on the energy balance is thus expected to be small when these IR lines are included. All other experimentally observed peaks are mainly caused by contamination in the salt dosage and from lamp materials entering the discharge. The UV spectrum is completely absorbed in the experiments in contrast to the modeled spectrum, where atomic as well as a part of the molecular radiation is still present. Such difference can be caused by not accounting for all of the molecular transitions; a deviation from LTE in the molecular population; a deviating cold spot temperature; and neglecting demixing.

The simulated temperature profile is shown in figure 10.7. The arc contraction caused by molecular radiation can be clearly observed in the simulated temperature profile. In spite of the contraction, the measured electrical potential of the

[3] There are actually 6 lines visible between 1250 nm and 1500 nm. The second peak at 1312 nm is from aluminum

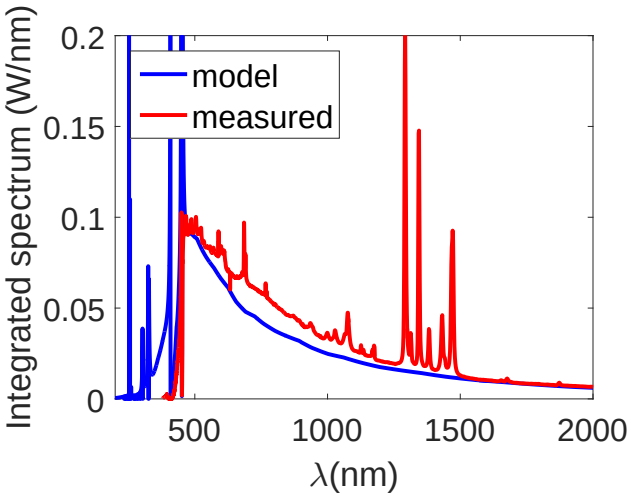

Figure 10.6: Calculated and measured spectra of the XeInI discharge. The power is 70 W, the elemental pressures are $p_{\{\mathrm{In}\}} = 3.9$ bar and $p_{\{\mathrm{I}\}} = 4.83$ bar and the total pressure is 11.73 bar. The electrode distance is 7.1 mm and the power is 70 W.

lamp was only 40.7 V. The calculated potential for this lamp is 26.6 V. The lower voltage indicates that the temperature profile is too high. This is expected since a 1D model does not account for end losses. Additionally, the observed IR radiation from the model was a bit too low. Possibly the contraction of the temperature profile is underestimated by underestimating the molecular IR losses. The reasons for these deviations have been discussed in the previous paragraph. In order to built a practical lamp, the lamp voltage should be increased further. This can be achieved by adding more InI. When more InI is added the temperature profile will be more constricted and the voltage will increase. However, the InI pressure can not be increased indefinitely. At much higher pressures the contribution of the UV and parts of the visible radiation will become optically thick. As a result a relative increase of optically thin IR radiation is expected.

The cumulative energy flows of power dissipated as ohmic heating, thermal conduction and radiation are shown in figure 10.8. Due to the strong contraction in the temperature profile most input power is dissipated in the cylindrical volume enclosed by a radius of 0.75 mm. Initially, the power transported via thermal conduction increases because the power dissipated as ohmic heating exceeds the radiation losses. For $r \geq 0.75$ mm the thermal conduction losses decrease because the local radiation losses exceed the local input power from ohmic heating. Near the wall the thermal conduction losses increase again because of absorption of radiation.

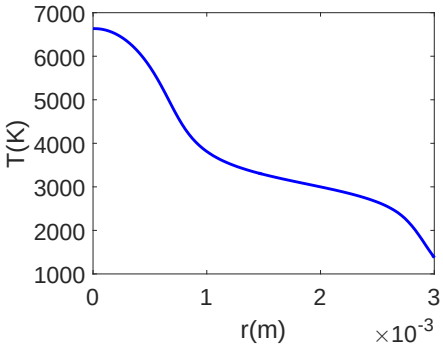

Figure 10.7: The calculated temperature profile of the XeInI discharge with an input power of 70 W, a radius of 3 mm and an electrode distance of 7.1 mm. The elemental pressures are $p_{\{\mathrm{In}\}} = 3.9\,\mathrm{bar}$ and $p_{\{\mathrm{I}\}} = 4.83\,\mathrm{bar}$ and the total pressure is 11.73 bar.

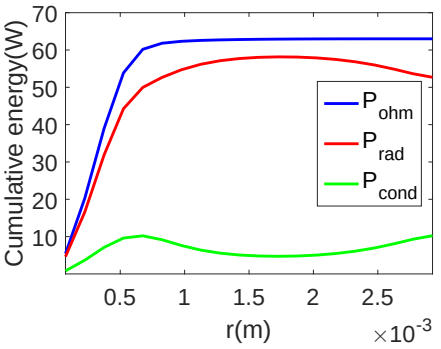

Figure 10.8: The cumulative energy flows of power of the XeInI discharge. The power is 70 W, the elemental pressures are $p_{\{\mathrm{In}\}} = 3.9\,\mathrm{bar}$ and $p_{\{\mathrm{I}\}} = 4.83\,\mathrm{bar}$ and the total pressure is 11.73 bar. The electrode distance is 7.1 mm and the power is 70 W.

10.4 Summary

The replacement of mercury in high-intensity discharge lamps by a mixture of xenon and indium iodide has been investigated by means of a 1D radial dependent fluid model. The main features of the self-consistent model of the cylindrical, axially homogeneous plasma are presented involving the plasma temperature, the radiation transport as well as transport coefficients. The model has been qualitatively validated by comparison of a predicted spectrum with a measured one, which shows relatively good agreement. However, not all spectral features could be reproduced. This is partly caused by neglecting the five atomic indium transitions in the IR. Their combined impact on the energy balance is small since the power radiated via these lines is limited. Other possible causes are the limited number of molecular transitions that have been considered; neglecting demixing; and an incorrect prediction of the cold spot temperature.

The main conclusions are as follows:

- The largest contributions to the continuum radiation arise from molecular transitions from the free state A towards the ground state in InI.
- In spite of the contraction, of the temperature profile the simulated voltage is only 26 V. The voltage can be increased with higher InI pressures. However, at very high pressures a relative increase of IR losses is expected, because of the shape of the potential curves. As a result there must be an optimum InI pressure.

Chapter 11

Modeling of Diffusive LTE Plasmas with Integral Constraints: Application to mercury-free lamp mixtures.

The mercury free lamp model previously discussed in Gnybida et al. (J. Phys. D: Applied Physics, 47, 125201) or chapter 10 of this thesis did not account for self-consistent diffusion and included only two molecular transitions. In this chapter we apply, for the first time, an algorithm that features 1) species/mass conservation up to machine accuracy and 2) an arbitrary mix of integral (total mass) and local (cold spot) constraints on the composition. Another advantage of the self-consistent diffusion model is that the model determines the total pressure of the gas instead of using a predetermined gas pressure.

Additionally, the number of association processes has been increased from 2 to 6. The population as a function of interatomic separation determines the spectrum of the emitted continuum radiation. Previously, this population was calculated using the limit of low densities. In this work an expression is used that removes this limitation. The result of these improvements is that the agreement between the simulated and measured spectra has improved considerably.

11.1 Introduction

Standard HID lamps contain the toxic component mercury. Several attempts have been made to partially or completely replace it by a more environmentally friendly species. A few of these options were also discussed by Gnybida et al. [152]. A short summary is given here: Born [16] tried to replace mercury with zinc. Sulfur lamps

Submitted as: J.F.J. Janssen, J.L.G. Suijker, K.S.C. Peerenboom, J. van Dijk, *Modeling of Diffusive LTE Plasmas with Integral Constraints: Application to mercury-free lamp mixtures.* to Journal of Physics D: Applied Physics

[18] operated with a microwave discharge showed a promising luminous efficacy. Although promising results were obtained the lamp performance of the lamps using zinc or sulfur never reached the level of a comparable mercury containing lamp. Recently Käning [17] tried to remove mercury completely by using molecular species. The voltage that was previously generated by the high pressure of mercury is in these lamps produced by arc contraction. The molecular radiation in the colder mantle decreases the temperature of the discharge. As a result the core temperature must increase in order to transport a given amount of current.

In this work the molecular species that is responsible for arc contraction is InI. This species is known for its large amount of continuum radiation in both the visible and infrared (IR) ranges. Previously, in chapter 10 a simulation model for such a discharge has been presented. In that model radial diffusion was neglected. In this work the method for describing diffusive fluxes proposed by Peerenboom et al. [133] or described in chapter 10 is applied and extended with conservation rules. These conservation rules can be used to impose two types of constraints. The first constraint corresponding to unsaturated species can be used to fix the amount of mass of a particular element in the entire discharge. The second constraint models saturated species in the cold spot by adjusting the elemental pressure on the boundary. Additionally, more molecular transitions have been taken into account as radiative association processes and the number of associated molecules is calculated in a different way. As a result, the strong absorption of ultraviolet (UV) radiation can now be reproduced in the model. The number of atomic transitions of indium in the IR has also been increased.

11.2 Model

The plasma simulation model PLASIMO [25] is used to model the lamp. The lamp is considered to be radially symmetric and uniform in the axial direction. A cylindrical geometry with a radius of R=2.6 mm and an electrode separation of L_{el}=14 mm is used. Based on an electrode simulation program [192] the power dissipated in the electrodes is in the order of 10 % for an input power of 70 W. Additionally, LTE [172, p. 187] is assumed. A wall temperature of 1.4 kK is assumed based on wall temperature measurements of similar Hg lamps. The composition is calculated based on a solution of the Stefan-Maxwell equations for the elements as described in section 11.3. By using the Guldberg-Waage equations the composition in terms of the elemental species can be calculated. A plasma mixture containing the following 12 species has been considered: In, $\mathrm{In^+}$, $\mathrm{I^-}$, I, $\mathrm{I^+}$, $\mathrm{I_2}$, InI, $\mathrm{InI_2}$, $\mathrm{InI_3}$, Xe, $\mathrm{Xe^+}$, e. The energy balance that is considered in this work is given by

$$-\frac{1}{r}\frac{\partial}{\partial r}\left(r\lambda\frac{\partial T}{\partial r}\right) = \sigma E^2 - q_{\mathrm{rad}}, \tag{11.1}$$

with λ the thermal conductivity, σ the electrical conductivity, E the electric field and q_{rad} the radiated power. The electric field is calculated from the total dissi-

pated power in the plasma. The dissipated power is

$$P_{\text{in}} - P_{\text{el}} = \int \sigma(r) E^2 \mathrm{d}V = 2\pi E^2 L_{\text{el}} \int_0^R \sigma(r) r \mathrm{d}r, \tag{11.2}$$

with P_{in} the total input power, P_{el} the power dissipated in the electrodes. The electric field is assumed to be uniform in axial direction. The radiative energy is calculated from

$$q_{\text{rad}} = \iiint \frac{I_\nu \vec{s} \cdot \vec{n} \mathrm{d}A \mathrm{d}\Omega}{V} \mathrm{d}\nu, \tag{11.3}$$

with I_ν the spectral radiance, $\vec{s}$ the direction vector for the radiation, $\vec{n}$ the normal vector to the surface area $\mathrm{d}A$, V the volume corresponding to the local cylindrical shell and ν representing the frequency of the emitted radiation. For more details related to the calculation procedure of the transport coefficients, the energy balance or the calculation of q_{rad} the reader is referred to [152] or chapter 10.

11.2.1 Radiation

The model accounts for atomic, molecular and Bremsstrahlung radiation. The atomic emission can be calculated from [172, p. 226]

$$j_\nu = \frac{h\nu}{4\pi} n_u A_{ul} \phi_\nu, \tag{11.4}$$

with n_u the density of the upper level, A_{ul} the transition probability between states u and l and ϕ_ν represents the line profile. The atomic line profile is calculated using the convolution of the Lorentz and van der Waals profiles according to Stormberg [30, 159]. The broadening constants were adjusted to approximate the red and blue self-reversal widths of the resonant lines. The consequence is that the large C_6 parameter produces an unrealistically large red wing. This red wing is damped by multiplying the line profile with $\exp\left(-\left[\nu-\nu_0\right]^2/C^2\right)$ with C corresponding to a 6 nm offset from the line center. Such a strategy is similar to the method described by Wharmby [187]. The broadening constants for these processes are given in Table 11.1. The absorption is calculated using the cross sections for absorption and stimulated emission

$$\kappa = \sigma_{\text{abs}} n_l - \sigma_{\text{stim}} n_u. \tag{11.5}$$

These cross sections are given by

$$\sigma_{\text{abs}} = \frac{c^2}{8\pi\nu^2} A_{ul} \frac{g_u}{g_l} \frac{Z_u}{Z_l} \exp\left(\frac{h(\nu-\nu_0)}{k_B T}\right) \phi_\nu, \tag{11.6}$$

$$\sigma_{\text{stim}} = \frac{c^2}{8\pi\nu^2} A_{ul} \phi_\nu, \tag{11.7}$$

with Z_i the internal partition sum of state i and ν_0 the unperturbed frequency. The molecular emission is calculated using

$$j_\nu = \frac{h\nu(r)}{4\pi} A_{ul}(r) \left|\frac{\mathrm{d}r}{\mathrm{d}\nu}\right| n_u f_u, \tag{11.8}$$

with n_u the total amount of radiators and f_u the spatial distribution is derived from (11.50). Absorption and stimulated emission due to molecules is taken into account with

$$\sigma_{\text{abs}} = \frac{c^2}{8\pi\nu\left(r\right)^2} A_{ul} \frac{g_u}{g_l} \left|\frac{\mathrm{d}r}{\mathrm{d}\nu}\right| f_l, \tag{11.9}$$

$$\sigma_{\text{stim}} = \frac{c^2}{8\pi\nu\left(r\right)^2} A_{ul} \left|\frac{\mathrm{d}r}{\mathrm{d}\nu}\right| f_u. \tag{11.10}$$

Numerical instabilities can occur when these classical expressions are used, since $\left|\frac{\mathrm{d}r}{\mathrm{d}\nu}\right| = \infty$ is possible. Szudy and Bayliss [213] solved this problem by noting that the semiclassical Franck-Condon points interfere. This interference amounts to a multiplication of the line profile with

$$\left|36\pi z_c\right|^{1/2} L\left(z_c\right), \tag{11.11}$$

where

$$z_c = \frac{1}{2}\left(\frac{\mu}{k_B T}\right)^{1/3}\left(\frac{2\pi}{\hbar}\right)^{2/3}\left[\frac{\mathrm{d}\nu}{\mathrm{d}r}\right]^2\left|\frac{\mathrm{d}^2\nu}{\mathrm{d}r^2}\right|^{-4/3}, \tag{11.12}$$

$$L\left(z_c\right) = \int_0^\infty \xi^{-2}\left|\mathrm{Ai}\left(-z_c\xi\right)\right|^2 \exp\left(-\xi^{-3}\right)\mathrm{d}\xi. \tag{11.13}$$

This multiplication ensures that close to the singularity the line profile drops to zero. Further away this term can be approximated with 1.

Additionally, electron-atom Bremsstrahlung is accounted for with [163, 164]

$$j_\nu = C_{ea} c n_e n_a \left(k_B T\right)^{3/2} Q_{m,ea}\left(T\right)\left[\left(\frac{h\nu}{k_B T}+1\right)^2+1\right]\exp\left(-\frac{h\nu}{k_B T}\right), \tag{11.14}$$

with $C_{ea} = \frac{2}{3}\sqrt{2}\frac{e^2}{\epsilon_0 c^2 m_e^{3/2}\pi^{5/2}}$ W m^2 J$^{-3/2}$ sr^{-1}, n_e is the electron density, n_a the neutral density and $Q_{m,ea}\left(T\right)$ is the momentum transfer cross section. The momentum transfer cross sections for e-InI, e-Xe, e-I and e-In are obtained from [201–205, 214].

11.3 Diffusion

In previous work by Gnybida et al. [152] (or chapter 10 in this chapter) the elemental mass fractions were kept constant. Now the elemental mass fractions are calculated self-consistently using the method developed by Peerenboom et al. [133] (or chapter 7 in this thesis). In this section the method is extended by using integral boundary conditions. These integral conditions can be used to impose a cold spot (vapor) pressure for saturated species or the total mass in the discharge for unsaturated species. First a short introduction to the solution procedure for the system of equations is given. After that the boundary conditions will be discussed.

Table 11.1: The properties of the atomic lines included in the simulation. The data for the lines in the UV and visible has been taken from the NIST database and the data for the IR lines was taken from Safronova et al. [215]

$\lambda\,(\mathrm{nm})$	$E_l\,(\mathrm{eV})$	$E_u\,(\mathrm{eV})$	$A_{ul}\,(\mathrm{s}^{-1})$	$C_3\,(\mathrm{m}^3\mathrm{s}^{-1})$	$C_6\,(\mathrm{m}^6\mathrm{s}^{-1})$
256.02	0.00000	4.84139	$4.00\cdot10^{7}$	$1.00\cdot10^{-15}$	$6.00\cdot10^{-42}$
271.03	0.27432	4.84758	$4.00\cdot10^{7}$	$1.00\cdot10^{-15}$	$6.00\cdot10^{-42}$
303.94	0.00000	4.08099	$1.30\cdot10^{8}$	$1.00\cdot10^{-15}$	$6.00\cdot10^{-42}$
325.61	0.27432	4.08099	$1.30\cdot10^{8}$	$1.00\cdot10^{-15}$	$6.00\cdot10^{-42}$
325.86	0.27432	4.07810	$3.77\cdot10^{7}$	$1.00\cdot10^{-15}$	$6.00\cdot10^{-42}$
410.18	0.00000	3.02185	$5.60\cdot10^{7}$	$1.00\cdot10^{-13}$	$6.00\cdot10^{-42}$
451.13	0.27432	3.02185	$1.02\cdot10^{8}$	$1.00\cdot10^{-13}$	$6.00\cdot10^{-42}$
1291.61	3.02183	3.98174	$1.57\cdot10^{7}$	$1.00\cdot10^{-13}$	0
1343.36	3.02183	3.94476	$1.43\cdot10^{7}$	$1.00\cdot10^{-13}$	0
1382.83	3.94476	4.84135	$7.35\cdot10^{6}$	$1.00\cdot10^{-13}$	0
1432.02	3.98174	4.84753	$9.12\cdot10^{6}$	$1.00\cdot10^{-13}$	0
1442.32	4.98174	4.84135	$1.54\cdot10^{6}$	$1.00\cdot10^{-13}$	0
1467.27	4.07808	4.92306	$1.32\cdot10^{7}$	$1.00\cdot10^{-13}$	0
1472.31	4.08097	4.92306	$9.46\cdot10^{5}$	$1.00\cdot10^{-13}$	0
1472.31	3.08097	4.92306	$1.42\cdot10^{7}$	$1.00\cdot10^{-13}$	0
2229.71	3.94476	4.50081	$3.48\cdot10^{6}$	$1.00\cdot10^{-13}$	0
2388.57	3.98174	4.50081	$6.36\cdot10^{6}$	$1.00\cdot10^{-13}$	0

11.3.1 System of equations

The Stefan-Maxwell equations can be written in species form or in elemental form. In this work the elemental form is used. The elemental form can be derived from the species formulation. Therefore the species formulation is discussed first.

Species form

The continuity equations for the species are given by

$$\frac{\partial \rho y_i}{\partial t} + \nabla \cdot \left(\rho \vec{v} y_i + \vec{J_i} \right) = m_i \omega_i, \tag{11.15}$$

with ρ the mass density, y_i the mass fraction of species i, $\vec{v}$ the flow velocity, $\vec{J_i}$ the diffusive mass flux of species i, m_i the mass of species i and ω_i the volume production processes. The diffusive mass fluxes can be obtained by solving the Stefan-Maxwell equations [128, 143–146]. This set of equations is given by

$$\sum_j H_{ij} \vec{J_j} = -\vec{d_i} \quad \Leftrightarrow \quad \mathbf{HJ} = -\mathbf{d}, \tag{11.16}$$

with $\mathbf{H} = (H_{ij})$ the mass flux based friction matrix, $\mathbf{J} = \left(\vec{J_i}\right)$ the vector of diffusive mass fluxes and $\mathbf{d} = \left(\vec{d_i}\right)$ the driving forces for species i. The diffusive

mass fluxes can be obtained as

$$\vec{J_i} = -\sum_j L_{ij}\vec{d_j} \quad \Leftrightarrow \quad \mathbf{J} = -\mathbf{L}\mathbf{d}, \tag{11.17}$$

with $\mathbf{L}$ the multicomponent flux diffusion matrix. The elements H_{ij} are obtained from

$$H_{ij} = \begin{cases} \frac{1}{\rho}\frac{\sigma m}{m_j}\sum_{l\neq j}\frac{x_l}{D_{ij}} & \text{if } i = j \\ -\frac{1}{\rho}\frac{\sigma m}{m_j}\frac{x_i}{D_{ij}} & \text{if } i \neq j \end{cases}, \tag{11.18}$$

with $\sigma = \sum_i y_i$, x_i the mole fraction of species i and D_{ij} the binary diffusion coefficient. The driving forces can be written as

$$\vec{d_i} = \nabla x_i - z_i\vec{E}/p \quad \Leftrightarrow \mathbf{d} = \partial\mathbf{x} - \mathbf{z}\vec{E}/p, \tag{11.19}$$

with $\mathbf{x}\,(x_i)$ the vector of mole fractions and $\mathbf{z} = (z_i)$ the vector of charge densities, $\vec{E}$ the ambipolar electric field and p the pressure. There are two constraints that apply to the diffusive mass fluxes. There should be no net mass transport

$$\sum_i \vec{J_i} = 0, \tag{11.20}$$

and the diffusive fluxes should not transport any net current:

$$\sum_i r_i y_i = 0, \tag{11.21}$$

with $r_i = q_i/m_i$ the ratio of the charge over the mass of species i. Under influence of ambipolar fields, the calculation of the diffusive fluxes (11.17) is modified to

$$\mathbf{J} = -\left(\mathbf{L} - \frac{\mathbf{L}\mathbf{z}\mathbf{r}^{\mathrm{T}}\mathbf{L}}{\mathbf{r}^{\mathrm{T}}\mathbf{L}\mathbf{z}}\right)\partial\mathbf{x} = -\hat{\mathbf{L}}\partial\mathbf{x}. \tag{11.22}$$

The second term in this equation represents the diffusive flux induced by the ambipolar field. Since $\mathbf{L}$ is singular it must be regularized as

$$\mathbf{L} = (\mathbf{H} + \alpha\mathbf{y}\otimes\mathbf{u})^{-1} - \alpha^{-1}\mathbf{y}\otimes\mathbf{u}, \tag{11.23}$$

with $u_i = 1$.

Elemental form

The elemental mass fraction can be expressed in terms of the species mass fractions as

$$\sum_i \phi_{i\alpha} y_i m_{\{\alpha\}}/m_i = y_{\{\alpha\}}, \tag{11.24}$$

with $\phi_{i\alpha}$ the stoichiometric coefficient, which indicates the number of particles of element α are used to 'construct' species i. The elemental continuity equation can be obtained by multiplying (11.15) with $\phi_{i\alpha}m_{\{\alpha\}}/m_i$ and summing over all

species. The elemental diffusive mass flux can be obtained by writing the driving forces in elemental form as

$$\partial \mathbf{x} = \left.\frac{\partial \mathbf{x}}{\partial T}\right|_{p,\{\mathbf{y}\}} \partial T + \left.\frac{\partial \mathbf{x}}{\partial \{\mathbf{y}\}}\right|_{p,T} \partial \{\mathbf{y}\}. \tag{11.25}$$

The first term can be obtained from the N_r independent reactions. The second term ensures elemental conservation. It is now possible to rewrite the driving forces as

$$\partial \mathbf{x} = \mathbf{A}^{-1} \begin{pmatrix} \partial \boldsymbol{\theta} \\ \partial \{\mathbf{y}\} \end{pmatrix}, \tag{11.26}$$

with $\partial \theta_r = \frac{\Delta h_r}{R_u T^2} \partial T$, Δh_r the molar enthalpy of reaction r and R_u the universal gas constant. The elemental mass fluxes are thus given by

$$\{\mathbf{J}\} = -\operatorname{diag}(\{\mathbf{m}\})\, \boldsymbol{\phi}\, \operatorname{diag}^{-1}(\mathbf{m})\, \hat{\mathbf{L}} \mathbf{A}^{-1} \begin{pmatrix} \partial \boldsymbol{\theta} \\ \partial \{\mathbf{y}\} \end{pmatrix} = \begin{pmatrix} \boldsymbol{\Gamma}^{\theta} & \boldsymbol{\Gamma} \end{pmatrix} \begin{pmatrix} \partial \boldsymbol{\theta} \\ \partial \{\mathbf{y}\} \end{pmatrix}. \tag{11.27}$$

Regularization of the elemental flux diffusion matrix $\boldsymbol{\Gamma}$ gives

$$\tilde{\boldsymbol{\Gamma}} = \boldsymbol{\Gamma} + \alpha \{\mathbf{y}\} \otimes \{\mathbf{u}\} + \beta \{\mathbf{z}\} \otimes \{\mathbf{r}\}. \tag{11.28}$$

A possible choice for the regularization constants is $\alpha = \max(\boldsymbol{\Gamma}) / \langle \mathbf{y}, \mathbf{u} \rangle$ and $\beta = \max(\boldsymbol{\Gamma}) / \langle \mathbf{z}, \mathbf{r} \rangle$. For more details related to the diffusive algorithm the reader is referred to [133] or chapter 7.

11.3.2 Integral boundary conditions

In closed vessels there are no natural boundary conditions for the pressure or for the elemental mass fractions. In at least one point these values should be fixed in order to have a unique solution. In the case of the elemental mass fractions these boundary values must be chosen such that the constraint $\sum_\alpha y_\alpha = 1$ is respected.

These boundary conditions come from *integral constraints* on the amount of building blocks of type α, say, in the system (for unsaturated species) and from *local constraints* on the pressures of species β at the 'cold spot' of the system (for saturated species). For given pressure and elemental mass fraction fields, the idea is to calculate a set of offset values δp and δy_α in such a way that these constraints are satisfied. These corrections must be chosen such that $\sum_\alpha \delta y_\alpha = 0$, so the constraint on the sum of the mass fractions continues to be satisfied. Once the adjustments have been satisfied, these can be applied in the entire system, or only at the cold spot boundary point. This algorithm seems similar to what is called a 'naive' algorithm in [216], where the convergence of the algorithm is proven.

The elemental mass density of element α can be expressed in terms of the pressure, temperature and elemental mass fractions as

$$\rho_\alpha(p, T, \{\boldsymbol{y}\}) = \rho(p, T, \{\boldsymbol{y}\}) y_\alpha = n(p, T) m(\boldsymbol{y}(p, T, \{\boldsymbol{y}\})) y_\alpha = \frac{p}{kT} m(\boldsymbol{y}(p, T, \{\boldsymbol{y}\})) y_\alpha, \tag{11.29}$$

where $n(p,T)$ is the particle density and $m(\boldsymbol{y})$ is the *mixture mass*, representing the local average mass of a particle. In the derivations below we investigate the change of the elemental mass density as a result of applying a uniform pressure offset δp and elemental mass fraction offsets δy_α. To that end the effects of such changes on the mixture mass should also be taken into account, since $m = m(\boldsymbol{y})$ and the composition itself depend on the elemental mass fractions and pressure. From experience we have learned that the variations of m can be disregarded in the formulation of the corrections. Since iterations are needed anyway, and the mixture mass is updated every cycle, this does not influence the final results.

Unsaturated elements

For unsaturated elements the total amount of mass, M_α, is fixed. This quantity can be calculated from

$$M_\alpha = \int n_\alpha m_\alpha \mathrm{d}V = \int \frac{pm}{k_B T} y_\alpha \mathrm{d}V, \tag{11.30}$$

with $m = \frac{1}{\sum_j y_j/m_j}$ the average mass. Possible causes for an incorrect total mass are an incorrect pressure or incorrect elemental mass fractions. The total elemental mass can be corrected with

$$\delta M_\alpha = M_\alpha^f - M_\alpha = \int \frac{(p+\delta p)\, m}{k_B T} \left(y_\alpha + \delta y_\alpha\right) \mathrm{d}V - M_\alpha, \tag{11.31}$$

where M_α^f is the desired elemental mass. Expanding this equation and neglecting quadratic corrections gives

$$\begin{aligned} \delta M_\alpha &= \int \frac{pm}{k_B T} \delta y_\alpha \mathrm{d}V + \int \frac{\delta p m}{k_B T} y_\alpha \mathrm{d}V \\ &= M \delta y_\alpha + M_\alpha \delta p / p, \end{aligned} \tag{11.32}$$

with M the current total mass in the system. This equation can be rewritten as

$$\delta p P_\alpha + \delta y_\alpha Y_\alpha + C_\alpha = 0, \tag{11.33}$$

with

$$\begin{aligned} P_\alpha &= \int \frac{m}{k_B T} y_\alpha \mathrm{d}V = M_\alpha / p \\ Y_\alpha &= \int \frac{pm}{k_B T} \mathrm{d}V = M \\ C_\alpha &= M_\alpha - M_\alpha^f \\ M_\alpha &= \int \frac{pm}{k_B T} y_\alpha \mathrm{d}V. \end{aligned} \tag{11.34}$$

In order to ensure that the mass fractions still sum up to one after applying the corrections there is an additional constraint given by

$$\sum_\alpha \delta y_\alpha = 0. \tag{11.35}$$

The pressure correction can be used to modify the constant total pressure and the boundary conditions for the mass fractions can be calculated from

$$y^{BC}_{\text{new},\alpha} = y^{BC}_{\alpha} + \delta y_{\alpha}. \tag{11.36}$$

Such a solution procedure is similar to the first algorithm described in [216].

Saturated elements

For saturated elements the pressure on the cold spot is fixed. It is given by

$$p_{\alpha} = \frac{pmy_{\alpha}}{m_{\alpha}}. \tag{11.37}$$

The elemental pressure can again be written in terms of the current value and a correction. Ignoring the quadratic corrections gives

$$y_{\alpha}p + y_{\alpha}\delta p + \delta y_{\alpha}p = \frac{m_{\alpha}p^{f}_{\alpha}}{m}, \tag{11.38}$$

with y_{α} and p evaluated on the cold spot and p^{f}_{α} the desired elemental pressure. Multiplying (11.38) with $\frac{M}{p}$, the constants P_{α}, Y_{α} and C_{α} are now given by

$$\begin{aligned} 0 &= \delta p P_{\alpha} + \delta y Y_{\alpha} + C_{\alpha} \\ P_{\alpha} &= y_{\alpha}\frac{M}{p} \\ Y_{\alpha} &= M \\ C_{\alpha} &= M\left(y_{\alpha} - \frac{m_{\alpha}p^{f}_{\alpha}}{mp}\right). \end{aligned} \tag{11.39}$$

Solution procedure

The elemental correction equations can be solved for the pressure correction by summing over all elements

$$\begin{aligned} \delta p\sum_{\alpha} P_{\alpha} + \sum_{\alpha}\delta y_{\alpha}Y_{\alpha} + \sum_{\alpha} C_{\alpha} &= 0 \\ \delta p\sum_{\alpha} P_{\alpha} + M\sum_{\alpha}\delta y_{\alpha} + \sum_{\alpha} C_{\alpha} &= 0 \\ \delta p\sum_{\alpha} P_{\alpha} + \sum_{\alpha} C_{\alpha} &= 0. \end{aligned} \tag{11.40}$$

The pressure correction is then given by

$$\delta p = \frac{-\sum_{\alpha} C_{\alpha}}{\sum_{\alpha} P_{\alpha}}. \tag{11.41}$$

Thus the correction for the elemental mass fraction can be expressed as

$$\delta y_{\alpha} = \frac{-C_{\alpha} - \delta p P_{\alpha}}{Y_{\alpha}} \tag{11.42}$$

11.4 An improved model for the calculation of the population of molecular states

The calculation of the molecular continuum is improved with respect to [152] (chapter 10 of this thesis) by including more molecular transitions. A meaningful calculation of the continuum radiation also requires an accurate spatial distribution of the perturbers relative to the emitters. Such a distribution is obtained from thermodynamics [156, eq. A.10]

$$n_{\mathrm{mol},j} = n_{\mathrm{rad}} n_{\mathrm{pert}} \frac{Z_{t,\mathrm{mol}}}{Z_{t,\mathrm{rad}} Z_{t,\mathrm{pert}}} \frac{Z_{\mathrm{int,mol},j}}{Z_{\mathrm{int,rad}} Z_{\mathrm{int,pert}}} = n_{\mathrm{mol}} \frac{Z_{\mathrm{int,mol},j}}{Z_{\mathrm{int,mol}}}, \tag{11.43}$$

with $n_{\mathrm{mol},j}$ referring to both the bound and free energy levels of state j, $Z_{t,x} = \left(\frac{2\pi m_x k_B T}{h^2}\right)^{3/2}$ the translational partition sum and Z_x the internal partition sum. Classically the internal partition sum of the combined bound and free states is given by [156, p. 1541]

$$Z_{\mathrm{int,mol},j} = \left(\frac{2\pi\mu k_B T}{h^2}\right)^{3/2} \int_0^R 4\pi r^2 \exp\left(-\frac{V_j(r) - V_j(\infty)}{k_B T}\right) \mathrm{d}r, \tag{11.44}$$

with R the interatomic separation corresponding to the transition to the atomic system and μ the reduced mass. This expression is valid for low perturber densities, $\frac{4}{3}\pi R^3 n_{\mathrm{pert}} \ll 1$. For larger densities the excluded volume of the perturbed atoms becomes significant in comparison to the total volume. In the next section an expression is derived that accounts for this excluded volume.

11.4.1 Distribution function

The probability of finding an In particle somewhere in the volume, V_r, is proportional to [156, p. 1520]

$$P(r) = \tilde{n} \exp\left(-\beta V(r)\right), \tag{11.45}$$

with $\beta = 1/(k_B T)$, $V(r)$ the potential and $\tilde{n}$ a normalization constant. The probability of finding such a radiating particle within a radius R of a perturbing particle is given by

$$P_{\mathrm{inside}} = \tilde{n} N_{\mathrm{pert}} \int_0^R 4\pi r^2 \exp\left(-\beta V(r)\right) \mathrm{d}r, \tag{11.46}$$

with N_{pert} the number of perturbing particles (iodine in this case). The probability of a radiating particle not being inside a sphere of radius R is given by

$$P_{\mathrm{outside}} = \tilde{n} \exp\left(-\beta V(\infty)\right) \left[V_r - \frac{4}{3} N_{\mathrm{pert}} \pi R^3\right], \tag{11.47}$$

where it is assumed that the radius R is large enough to make sure that $V(R) \approx V(\infty)$. The normalization constant can be obtained from

$$P_{\mathrm{inside}} + P_{\mathrm{outside}} = 1, \tag{11.48}$$

which gives

$$\tilde{n} = \frac{1}{N_{\text{pert}} \int_0^R 4\pi r^2 \exp\left(-\beta V\left(r\right)\right) \mathrm{d}r + \exp\left(-\beta V\left(\infty\right)\right) \left[V_r - \frac{4}{3}\pi N_{\text{pert}} R^3\right]}. \tag{11.49}$$

By dividing $\tilde{n}$, P_{inside} and P_{outside} by the volume, expressions in terms of the number densities can be obtained. The perturber density is taken as the atomic perturber density corresponding to a given atomic limit. Similarly the radiator density is taken as the atomic radiator density. For $r \leq R$ the potential curves belonging to atomic limit k are summed to get the total probability as

$$\begin{aligned} P_{\text{inside},k} &= \tilde{n} \sum_j n_{\text{pert},a_j} \delta_{a_j,a_k} \int_0^R 4\pi r^2 \exp\left(-\beta V_j\left(r\right)\right) \mathrm{d}r \\ P_{\text{outside},k} &= \tilde{n} g_{\text{rad},a_k} g_{\text{pert},a_k} \exp\left(-\beta V_k\left(\infty\right)\right) \left[1 - \frac{4}{3} n_{\text{pert},a_k} \pi R^3\right] \\ 1 &= P_{\text{inside,k}} + P_{\text{outside,k}}, \end{aligned} \tag{11.50}$$

with a_j describing the atomic limit of molecular state j.

11.4.2 Molecular properties

The molecular potential curves and transition dipole moments are recalculated with the relativistic ab-initio calculation program DIRAC [107]. The excited states are approximated by Kramers Restricted configuration interaction calculations according to the generalized active space concept. The 5s and 5p electrons form the active space with up to two excitations. Note that Gnybida et al. [152] incorrectly state that the 4d electrons are included in the active space. Another error in that paper is the fact that only one excitation is taken into account instead of two excitations. The current calculation includes transitions to states up to 1 Hartree. The Quadruple-Zeta Basis set from K.G. Dyall that is built in into Dirac14 [210] has been used for the calculations.

The calculated potential curves that are involved in a transition that is used in the model are shown in figure 11.1. The ground state of InI has a dissociation energy of 3.68 eV. The ground state reaches this maximum at $r = 7.4$ Å. After this maximum the potential energy decreases to $V = 3.50$ eV. Barrow obtained a dissociation energy of 3.50 eV [217] using thermodynamic data. Allowing two excitations instead of one excitation thus increases the dissociation energy from 3.25 eV to 3.68 eV. These energies are not achieved at $r = \infty$, but at $r \approx 7$ Å. It is therefore expected that for 6 Å$\leq r \leq$ 11 Å the ground state is not fully relaxed to the lowest energy. If the dissociation energy is measured between the potential minimum and $r = \infty$ the values are 3.13 eV and 3.50 eV for the previous and the current simulation, respectively. Thus, in comparison to the calculations presented in [152] and [218] the calculated dissociation energy of the ground state has improved considerably.

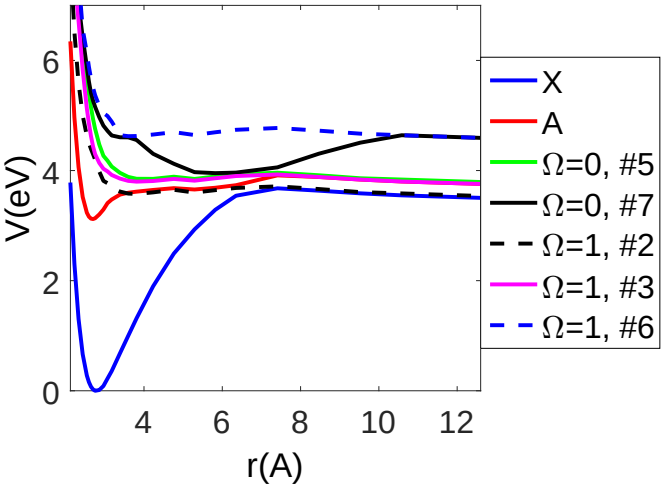

Figure 11.1: The molecular states that are included in the model. Only the ground state is a strongly bound state. The legend contains # signs followed by a number. This number indicates the energy ordering for a given Ω with 1 representing the potential curve with the lowest energy

The model only includes molecular transitions towards the ground state. The optical depth measured along a ray through the center is displayed in figure 11.2. The figure shows that for $\lambda > 440\,\text{nm}$ the transition that contributes most to the IR radiation is $\Omega = 0$ #7 − X. For $387 \leq \lambda \leq 440\,\text{nm}$ the A − X transition dominates. Below 380 nm the optical depth increases rapidly due to the overlap of various transitions. At 220 nm the optical depth decreases again because other transitions have been neglected.

11.4.3 Results

A cylindrical discharge vessel with a radius of 2.6 mm and an electrode separation of 14 mm has been considered. The total power dissipated in the lamp is 70 W. Three different dosages of In and I are considered. The dosages are listed in table 11.2. The masses of the species are conserved due to an unsaturated boundary condition in the diffusion algorithm. In and I are assumed to be fully evaporated. This is confirmed by calculations using Gibbs free energy minimization with a cold spot temperature of 1.2 kK. The program used for the Gibbs energy minimization is based on Schnedler's methods [212]. The calculated temperature profile is shown for multiple dosages of InI in figure 11.3. The figure shows that for increasing InI dosage the temperature profile is more contracted. Close to the wall the impact on the temperature profile is very small. One of the advantages of using the self-consistent diffusion method is that the total pressure is automatically adjusted. For low, medium and high dosages of InI the calculated total

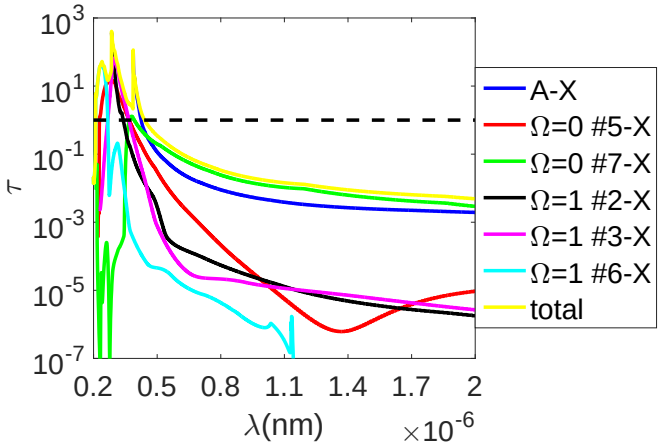

Figure 11.2: The optical depth of all included molecular transitions is shown. The simulated lamp contained 1.11 mg of In and 1.46 mg of I.

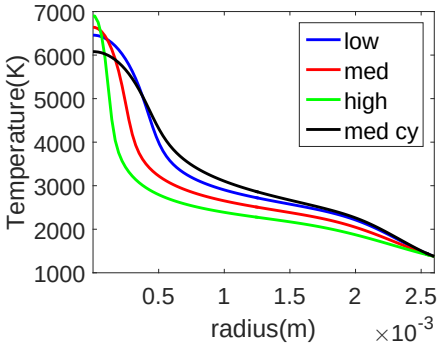

Figure 11.3: The gas temperature of the lamp for various InI dosages. The results using constant mass fractions are indicated with 'med cy'.

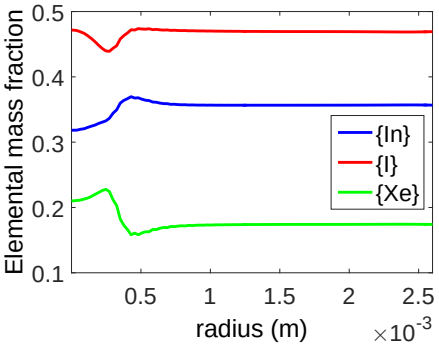

Figure 11.4: The elemental mass fractions for the medium InI dosage.

pressures are 6.7 bar, 9.1 bar and 17.2 bar, respectively. For a pressure of 9.1 bar the calculation is repeated using fixed elemental mass fractions ($y_{\{\mathrm{Xe}\}} = 0.1739$, $y_{\{\mathrm{In}\}} = 0.3569$ and $y_{\{\mathrm{I}\}} = 0.4692$); (11.44) for the population of molecular states; the broadening constants as given in this paper and the two association transitions from [152]. The results of that calculation are indicated with 'med cy' in 11.3. This comparison shows that the temperature profile is more contracted in the case of the new calculation.

The impact on the elemental mass fractions of demixing are shown in figure 11.4. The build up of {In} and {I} at $r = 0.5$ mm is caused by the smaller

Table 11.2: Composition of the three considered lamps.

Dosage	m_{In}(mg)	m_{I}(mg)	m_{Xe}(mg)
low	0.513	0.801	0.542
med	1.11	1.46	0.542
high	2.39	2.88	0.542

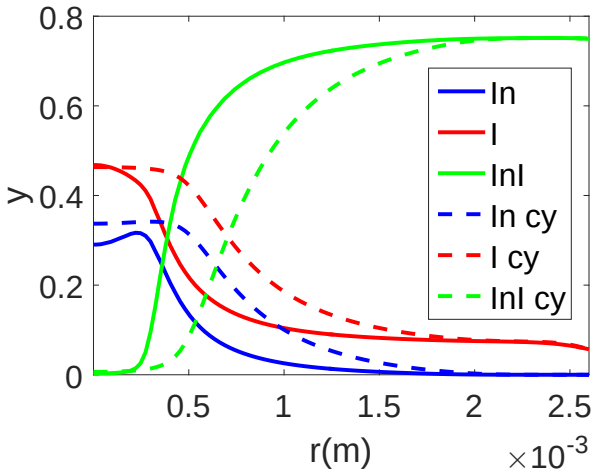

Figure 11.5: Comparison of the densities of radiating species by including demixing and 6 association transitions using (11.50) with the calculation that uses the two transitions from [152] with (11.43) and constant elemental mass fractions (indicated with cy). In both cases the medium InI dosage is considered.

diffusive flux of InI that is moving inwards in comparison to the outward flux of In and I. This accumulation continues until a balance is achieved. The larger density of In and I is responsible for the removal of Xe. For $r > 0.5\,\mathrm{mm}$ the decreasing temperature flattens the gradients of In and I until the inward flux of InI is balanced. For $0 \leq r \leq 0.5\,\mathrm{mm}$ the {In} mass fraction decreases. This is caused by the ambipolar flux of In^+. In the center this ion reaches a mass fraction of $y \approx 0.02$. In the same area a small inward flux of {I} occurs due to I^- which reaches $y \approx 0.0025$ at $r \approx 0.2\,\mathrm{mm}$. The void created by {In} is compensated by {Xe} and {I}. The resulting species densities are compared with the results from the 'med cy' calculation in figure 11.5. In comparison to the 'med cy' calculation the amount of InI has increased considerably between $0.2 \leq r \leq 1.5\,\mathrm{mm}$. Additionally, using 'med cy' the fractions of In and I are equal or larger in comparison to the calculation proposed in this paper.

Another cause for the more contracted temperature profile are the additional transitions that have been included in the model. Similarly to the transitions that

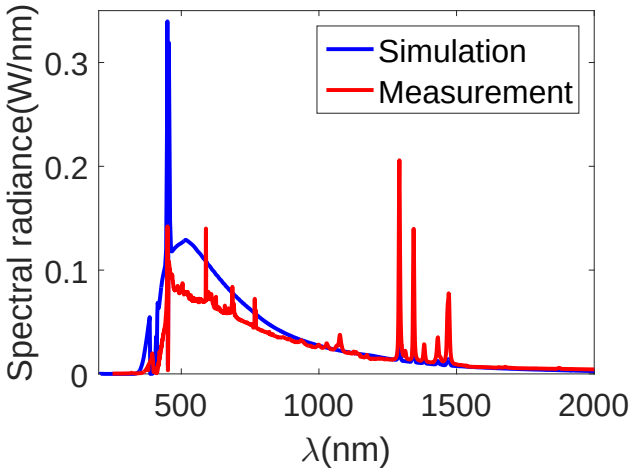

Figure 11.6: The calculated integrated spectrum is compared to a measured spectrum. The calculation procedure uses the medium InI dosage.

were already included by Gnybida [152] these transitions also are predominantly emitting radiation via radiative association. A comparison with a measured spectrum of a lamp operated at a 120 Hz square wave current is shown in figure 11.6. The continuum radiation is well reproduced. The experimental spectrum shows a self reversal gap at 399.6 nm which is related to the A − X transition. In the simulation this gap occurs at 387 nm. This offset provides an indication of the accuracy of the difference potential by the ab initio calculations.

The emission of the resonant atomic lines and the IR peaks suggest that the peak temperature has been underestimated. The broadening constants of the resonant lines were adjusted to obtain the same self-reversal width as in in the experiment. It is therefore expected that the radiative thermal conduction is comparable. Using these broadening constants the predicted self-reversal peaks are about twice as high compared to the measured spectrum indicating that the optically thin losses related to this atomic line are overestimated. The losses related to the IR lines are underestimated. Additionally, the width of the resonant lines is significantly larger than the validity of the impact regime [159, eq. 11]. Empirically Lawler [180] showed that a linear relation between HWHM and pressure was to be expected up to $2 \times 10^{26}\,\mathrm{m}^{-3}$ of Hg. It is not clear whether this can also be expected for In. Other possible errors can be caused by the assumption of LTE. In a large part of the lamp the gas temperature and thus the electron density is quite low. The momentum transfer collision frequency between electrons and heavy particles may not be able to compensate for all of the radiative losses at every location in the discharge. The reaction rates for In are largely unavailable. A solution could be the usage of empirical formulas as was done by Ögun [219].

An error in the temperature profile is also possible for other reasons. Since a 1D model has been used end-losses and convection are neglected. Additionally, the accuracy of the transition rate for the radiative association processes can not be checked. The transition dipole moments have been compared to the results of Banerjee et al. [218] for A − X and show a good agreement. However, Banerjee et al. only calculated the transition dipole moment for a small number of transitions in a limited range of interatomic separations. The transition probability is dependent on the square of the transition dipole moments which demonstrates that a small error in the transition dipole moments can have an appreciable effect on the emission via the radiative association process.

Another possible improvement can be obtained from a more accurate calculation of the rate of association. Gustafson [220] [221] suggests a calculation based on

$$\epsilon = g \int A\,(r)\,\mathrm{d}t, \tag{11.51}$$

which is proportional to the time spent of In and I at a given interatomic separation. The excess radiation around 400-500 nm may disappear when accounting for the lower amount of time spent in the attractive potential well.

In figure 11.7 the calculated spectra are for the three dosages are compared to the 'med cy' calculation. The difference in the continuum radiation is mainly caused by the self-consistent calculation of the diffusive mass fluxes. The 'med cy' calculation strongly underestimates the InI population. A result of the demixing is that a larger amount of continuum radiation is emitted and that the arc is more contracted. The consequence is that the path length of the UV radiation through InI and therefore the optical depth is now sufficiently large to absorb the UV radiation. In figure 11.8 the evolution of the spectrum through the plasma is shown for a ray passing through the center of the discharge ($-R \leq s \leq R$). The figure shows that the association radiation is produced in the center of the discharge (most visible at $\lambda \approx 400\,\mathrm{nm}$) and is absorbed on the way out of the plasma. The association continuum is optically thin starting from $\lambda \approx 550\,\mathrm{nm}$. For molecules like SnI and TlI a similar process occurs. Calculations for these molecules are shown in appendix 11.A.

11.5 Conclusions

The lamp model described by Gnybida [152] has been improved considerably by including self-consistent diffusion with conservation equations Additionally, an improved calculation for the population of associating atoms is used. One of the major advantages of the self-consistent diffusion is that the pressure is adapted via the boundary conditions. The boundary conditions are a specification of the total amount of mass for {Xe}, {In} and {I}. Alternatively it is possible to specify an elemental pressure which represents the cold spot. Additionally, due to the improved calculation of the associative continuum and including more association transitions the contraction in the temperature profile is more pronounced. The agreement of the shape of the continuum radiation with the measured continuum

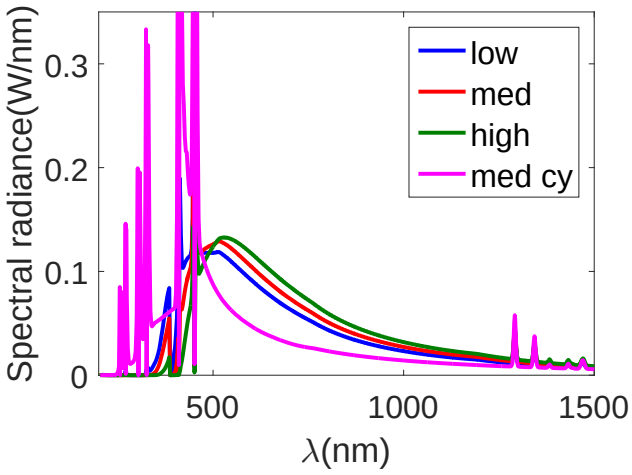

Figure 11.7: Comparison of the calculated spectra for all dosages. Additionally, the calculation using thermal populations for the association continuum and fixed elemental pressures is shown with 'med cy'.

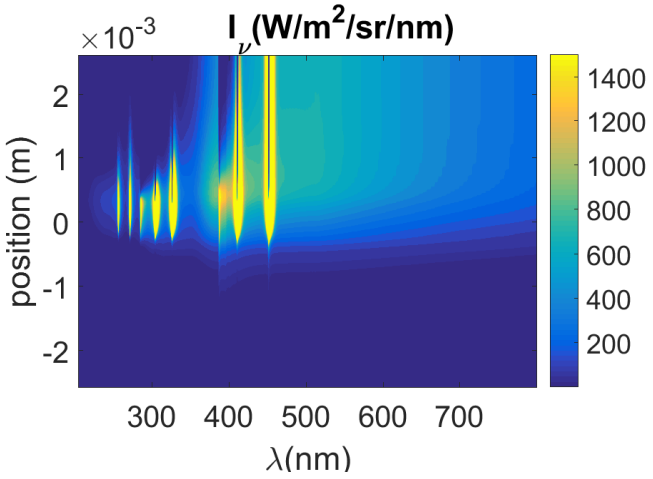

Figure 11.8: For the medium InI dosage the evolution of the spectrum is shown for a ray passing through the center of the discharge (bottom to top).

has therefore improved. It has been observed that due to the enhanced contraction the optical depth for the UV radiation has been increased considerably. As a result the absorption of the UV radiation is now correctly modeled.

Acknowledgements

Peter Bobbert is acknowledged for discussions that led to the development of (11.50). This work was supported by the IWT-SCHELP project from the Belgian agency for Innovation by Science and Technology (Project number 110003), the CATRENE SEEL project (CA502) and the combined STW-Draka project (10744).

11.A Ab initio curves

The recombination continuum observed for InI is not unique. A similar continuum is observed for TlI and SnI. The potential curves for these interactions are discussed in this section.

For TlI the potential curves are shown in figure 11.9 and the emitted wavelengths are shown in figure 11.10. The asymptotic limits for these curves are 0.92 eV, 0.96 eV and 1.88 eV. These values are the result of the first excited states of I and Tl. In the last limit both atoms are in the first excited state. These limits correspond to the values reported by NIST [53] within 0.03 eV. The predicted dissociation energy for the molecule in the ground state is 3.08 eV. Schlie [222] reports two experimental values of 2.7 eV and 2.83 eV. This indicates that the accuracy of the potential curves as a function of the interatomic separation is not constant. The included transitions cover the spectral band from 200 nm till 1500 nm. The transition $\Omega = 0, \#3$ even reaches 7 µm near the avoided crossing.

The simulated spectrum of a lamp containing TlI and Hg is shown in figure 11.13. The elemental pressures are set to 7 bar for Tl and I. Such a pressure corresponds to a cold spot of 1.2 kK. The elemental Hg is set to 20 bar. The atomic transitions with a known transition probability from NIST [53] are included. These transitions cover mainly the UV part of the spectrum. The only visible transition included is the 535.05 nm line. Several other lines are not included. Despite the missing atomic lines a relatively good agreement is obtained. Again the spectrum is dominated by continuum radiation. The optical depth is correctly modeled for wavelengths up to approximately 550 nm. In this spectral band the large optical depth ensures a thermal spectrum. For wavelengths larger than 550 nm the decay of the optical depth is too slow. For that reason the simulated spectrum still resembles the shape of a thermal radiator for these wavelengths. The overestimated optical depth for those wavelengths is the consequence of small errors in the potential curve. This can be understood based on the fact that the absorption is proportional to the transition probability. The transition probability scales as $A \propto |D|^2 / \lambda^3$ with D the dipole transition strength and λ the wavelength emitted at the local interatomic separation.

The SnI potential curves are shown in figure 11.11 and the wavelengths of the included transitions are shown in figure 11.12. The asymptotic limits of these

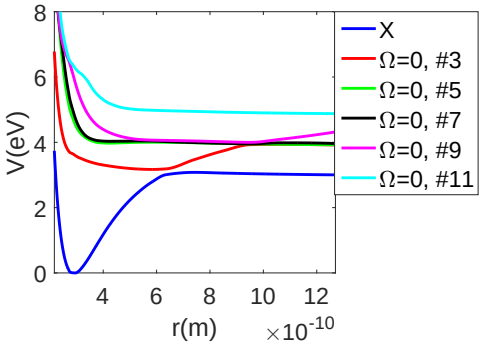

Figure 11.9: The included TlI potential curves.

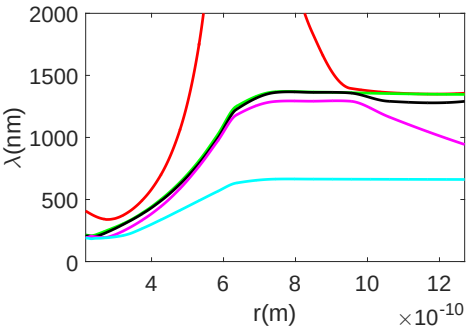

Figure 11.10: The wavelength as a function of interatomic separation. The colors correspond to states from figure 11.9. Only transitions towards the ground state are included.

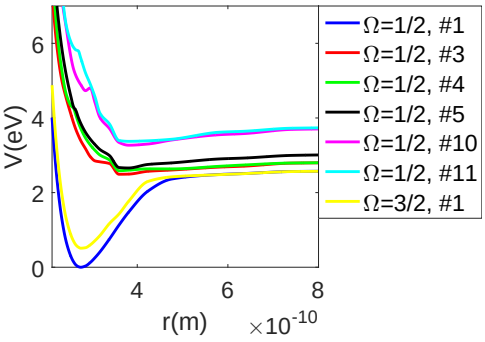

Figure 11.11: The included SnI potential curves.

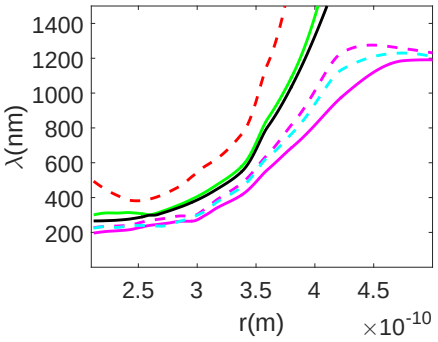

Figure 11.12: The wavelength as a function of interatomic separation. The colors correspond to states in figure 11.11. Full lines are transitions towards $\Omega = 1/2$, #1 and dashed lines are transitions towards $\Omega = 3/2$, #1.

potential curves correspond to 0.23 eV, 0.46 eV and 1.17 eV. According to NIST [53] these levels have an energy of 0.21 eV, 0.42 eV and 1.15 eV. The atomic limit of the highest energy is a combination of the excited states $I^2\,P_{1/2}$ and $Sn\,^3P_1$. The predicted dissociation energy of SnI is 2.57 eV. NASA's thermodynamic database [223] suggests a dissociation energy of 2.41 eV. The calculated potential curves thus contain an error in the order of 0.1-0.2 eV at small interatomic distances.

The simulated spectrum of a lamp containing SnI and Xe is shown in figure 11.14. The lamp contains 340 μg of Sn, 720 μg of I and 542 μg of Xe. All of these

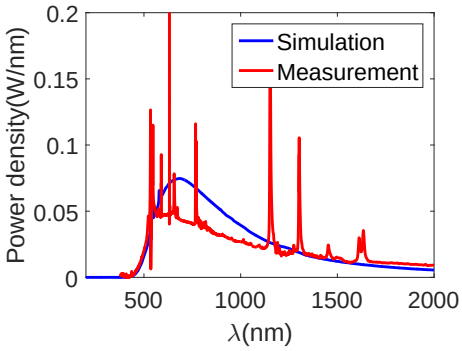

Figure 11.13: The calculated spectrum for a lamp containing TlI and Hg.

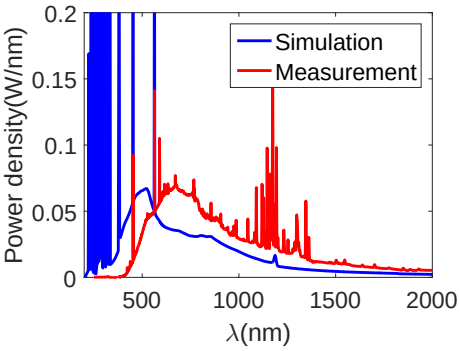

Figure 11.14: The calculated spectrum for a lamp containing SnI and Xe.

species are assumed to be completely evaporated. Again the atomic transitions with a known transition probability from NIST [53] are included. The dataset for the Sn transitions is also not complete, since many transitions in the IR are missing. However, also for this lamp the continuum radiation remains the dominant radiative loss process. In this spectrum the absorption of the UV radiation is not modeled correctly. The reason is that only a limited amount of transitions are included that are capable of absorbing this radiation. Additionally, the number of molecules that can absorb the UV radiation is too low due to the relatively broad temperature peak which reaches 7 kK. The consequence is a low optical depth in the UV. The broad temperature peak is a result of the underestimated contraction. A stronger contraction can be obtained by including more transitions that emit in the visible or IR spectral bands. The larger optical depth in this spectral area will increase the emission. Additionally, the wavelength for which $\tau = 1$ is reached will shift from 375 nm to larger wavelengths. As a consequence the same will happen for the peak of the continuum emission. Currently it is located at 525 nm in the simulations and at 680 nm in the measurement.

Chapter 12

The effect of resonant Ar-lines on metastable densities

Global models are very popular to describe the chemistry of various discharges. Their advantage is that they are relatively simple which allows them to provide results quickly. However, the simplification often means that some physical processes are not fully captured. One of those processes is the absorption of radiation. In a global model, optically thick radiative transitions are modeled with an escape factor. The escape factor describes the net amount of radiation that is emitted from the plasma. Since global models only describe average densities the effect of non-local absorption cannot be accounted for. In real plasmas the emitted radiation can be absorbed both locally and non-locally. The amount of radiation that is absorbed non-locally depends on the species and temperature profiles.

In this work an argon plasma containing seven species is studied. This system is suggested to the author by Emile Carbone and Nader Sadeghi after reading Golubovskii's paper [224]. They propose an effective transport of metastable species directly from the center to the outer parts of the plasma. This scheme includes the production of a resonant state in the center of the discharge from a metastable state. The resonant state produces a photon that is eventually reabsorbed in the outer parts of the plasma. Thus in that area another resonant state is created. Via collisional coupling a new metastable state can be produced. The effect of this effective transport mechanism on the metastable 4s densities is investigated using a 1D model. Two cases are investigated: in the first case the non-local absorption is included and in the second case only escape factors are used.

12.1 Introduction

Holstein [31, 225] investigated the effect of resonant radiation quantitatively. He derived analytical expressions for the escape factors for an infinite slab and an infinitely long cylinder. Additionally, the line profiles corresponding to Doppler, impact and statistical broadening were considered [31, p. 1166]. The final expressions are derived by assuming that stimulated emission can be neglected and

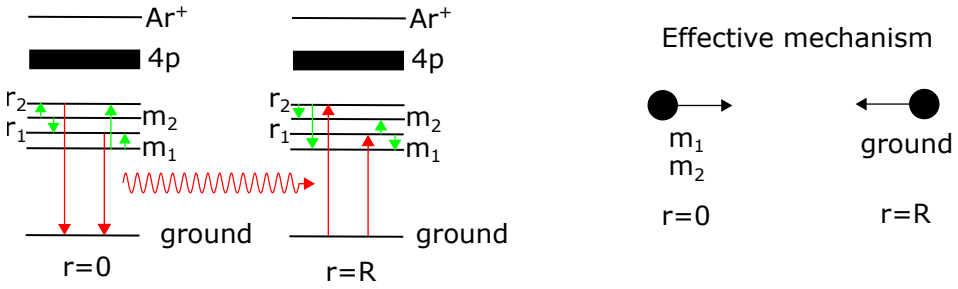

Figure 12.1: The considered energy levels and the proposed transport mechanism for the metastable species.

by assuming a parabolic profile for the radiating species. Additionally, only the asymptotic forms of the line profiles are included and the absorption is considered to be constant in space.

Golubovskii et al. [224] also looked into radiation transport by considering a low pressure (0.5-7 Pa) discharge in Ar generated by RF (radio-frequency) pulses for power densities between 3.8×10^4 and 5.8×10^5 W/m^3. The assumptions related to the usage of a parabolic profile for the radiating species (an asymptotic line profile and a constant absorption) are removed. They consider species variations in the axial direction between the two disks that generate the RF pulses. Comparisons with experiments showed that the model that accounts for radiative transport self-consistently, agreed better with experiments than the model that used an escape factor. For the displayed results, the differences between the densities of the resonant Ar species is in the order of a factor 1-80 while the impact on the metastable species is much smaller with factors ranging between 1-1.5. The large differences for the resonant states are mainly reached near the wall where absorption strongly influences the plasma. Due to the low pressure the coupling between the resonant and the metastable species is limited.

In this work the effect of resonance radiation is investigated for an Ar discharge with pressures ranging from 40 to 4000 Pa. The considered Ar system consists of 7 species, i.e., the ground state, the four 4s-states, the lumped 4p-states and the ion level. A 1D cylindrically symmetric model is used to investigate whether resonant radiation emitted in the center of the plasma can contribute to an increased density of Ar metastable species. In order to contribute to an enhanced metastable density the radiation must be absorbed in the outer regions of the cylinder by resonantly coupled levels. These resonant levels can create metastable species via collisions. In figure 12.1 the considered energy levels and the proposed mechanism are displayed schematically.

Due to the higher pressure the effect of the radiation on the metastable densities is expected to be larger in comparison to Golubovskii's observations. Additionally, using this simplified chemistry a comparison is made between the self-consistent calculation of the radiation transfer and the simplified approach that approximates the radiation as optically thin by using escape factors. The result of the self-

consistent calculation is used to calculate the escape factor. This escape factor is compared with the one that is obtained from Holstein's result for an infinitely long cylinder.

12.2 Model

The considered discharge vessel is cylindrically symmetric. Only variations in the radial dimension are taken into account. This makes the model 1D. In the next sections the transport equations are discussed. These equations are the mass balances, the coupled system of equations for diffusion and the equations for the electron and heavy particle temperatures. Subsequently, Holstein's analytical expressions for the escape factor are considered. The used rate constants for the chemical reactions are given in the last section.

12.2.1 Transport balances

In this section the mass balances, diffusion and the temperature balances for the electrons and the heavy particles are discussed. The mass balance is given by (3.17)

$$\nabla \cdot (\rho y_i \vec{u}_i) = m_i \omega_i,$$

with ρ the mass density, y_i the species mass fraction, $\vec{v}_{d,i}$ the diffusive velocity and ω_i the species production rate. The species production rate is calculated from

$$\omega_i = \sum_j \nu_{ji} R_j, \tag{12.1}$$

with ν_{ji} the stoichiometry coefficient and R_j the chemical rate. The chemical rate of reaction j can be calculated from

$$R_j = k_j \prod_{i,LHS} n_i^{\nu_{ji}}, \tag{12.2}$$

with k_j the rate coefficient given by (3.42). The indices i only include species on the left hand side of the reaction.

The velocities $\vec{v}_{d,i}$ introduced in the mass balance are obtained from a reduced set of coupled momentum balances. This system of equations for the diffusive velocities can be written as (6.11)

$$\mathbf{F}\mathbf{v} = -\mathbf{d},$$

with the elements of $\mathbf{F}$ given by $f_{ij} = z_i z_j / D_{ij}$, z_i the pressure fractions, D_{ij} the diffusion coefficient, $\mathbf{v}$ a vector containing the diffusive velocities and $\mathbf{d}$ the driving forces. The included driving forces are given by (6.36)

$$\mathbf{d} = \partial \mathbf{z} - \frac{\boldsymbol{\rho}_\mathbf{c} E_{\text{amb}}}{p},$$

with ρ_c the charge density, p the pressure and E_{amb} the ambipolar field. The solution procedure is discussed in more detail in chapter 6. The final expression for the diffusive flux is given in (6.41).

The heavy particle temperature is calculated from (3.22)

$$\nabla \cdot \left(\sum_i n_i E_i v_{d,i} \right) - \nabla \cdot \lambda_h \nabla T_h = Q_{eh} - Q_{\text{rad}} + Q_{\text{inel},e}, \tag{12.3}$$

with λ_h the thermal conductivity of the heavy particles, Q_{eh} the energy transferred from the electrons to the heavy particles via elastic collisions, Q_{rad} the energy emitted as radiation and $Q_{\text{inel},e}$ the energy gained from chemical reactions involving the electron as a reactant. The electron temperature is calculated from (3.23)

$$-\nabla \cdot \lambda_e \nabla T_e = \sigma E^2 - Q_{eh} - Q_{\text{inel},eh}, \tag{12.4}$$

with λ_e the thermal conductivity of the electrons, σ the electrical conductivity, E the electric field and $Q_{\text{chem},eh}$ the energy transferred from the electrons to the heavy particles via inelastic collisions. The calculation of the thermal and electrical conductivity is discussed in more detail in section 5.2. A constant electric field is assumed. It is obtained from

$$P_{\text{in}} = \int \sigma(r) E^2 \mathrm{d}V = E^2 L \int_0^R 2\pi r \sigma(r) \mathrm{d}r, \tag{12.5}$$

with P_{in} the input power, L the length of the plasma column and R the radius of the cylinder. The energy transfer from the electrons to the heavy particles is calculated from (3.43) [54, p. 34,45,51]

$$Q_{eh} = \sum_{h \neq e} \frac{3}{2} k_B (T_e - T_h) 2 \frac{m_e}{m_h} n_e \nu_{eh},$$

with n_i the number density of particle i, ν_{eh} the elastic collision frequency given by (3.44) [54, p. 45]. Contributions from chemical reactions to the energy balance can be calculated from

$$Q_{\text{inel},e} = \sum_j \Delta h_j R_j, \tag{12.6}$$

with j the reaction index (summed over all reactions with the electrons as a reactant) and Δh_j the reaction enthalpy. The radiation losses are calculated using

$$Q_{\text{rad}} = \iiint \frac{\mathrm{d}^2 \Phi_\nu}{V} \mathrm{d}\nu, \tag{12.7}$$

with $\mathrm{d}^2\Phi$ the spectral radiative flux that passes through the local volume V. The radiative flux can be calculated from

$$\mathrm{d}^2 \Phi_\nu = I_\nu \vec{s} \cdot \mathrm{d}\vec{A} \mathrm{d}\Omega, \tag{12.8}$$

with I_ν the spectral radiance probed in the direction $\vec{s}$. By using a set of probe lines the radiation losses can be estimated. More details can be found in section 8.4.

12.2.2 Escape factor

Holstein [31,225] derived the following expression for the escape factor corresponding to an infinitely long cylinder[1]

$$\Lambda = \frac{1.115}{\sqrt{\pi \kappa_p R}}, \tag{12.9}$$

with κ_p the absorption (integrated over the line profile). Note that this expression is derived by assuming a parabolic profile for the densities of the radiating particle. The two coefficients that describe the species profile are chosen in such a way that the escape factor reaches a minimum. The absorption κ_p is given by [31, eq. 3.4]

$$\kappa_p = \frac{\lambda^2 n_l}{2\pi} \frac{g_u}{g_l} \frac{A_{ul}}{\gamma_p}, \tag{12.10}$$

with g_u and g_l the degeneracies of the upper and lower states, A_{ul} the transition coefficient and $\gamma_p = \frac{\gamma_L}{4\pi}$ where γ_L is the Lorentzian half-width at half-maximum (HWHM). The escape factor derived by Holstein can be compared to the result of the 1D model. The escape factor for line x that describes the net radiative emission for the entire plasma volume can be defined as

$$\Lambda_x = \frac{P_{s,x}}{P_{t,x}}, \tag{12.11}$$

with $P_{s,x}$ the total power emitted as radiation in spectral line x obtained from the self-consistent model. It is given by $P_{s,x} = \iiint Q_{\text{rad}} \mathrm{d}V$. $P_{t,x}$ is the total power emitted if an optically thin plasma is considered. In that case the emitted power is calculated from $P_{t,x} = \int h\nu n_u A_{ul} \mathrm{d}V$.

The escape factor can also be calculated locally using [19, p. 50]

$$\Lambda = \frac{\int (j_\nu - J_\nu \kappa_\nu) \, \mathrm{d}\nu}{\int j_\nu \mathrm{d}\nu}, \tag{12.12}$$

with j_ν the local emission, κ_ν the local absorption and the local mean radiance is given by [166, p. 6]

$$J_\nu = \frac{1}{4\pi} \int I_\nu \mathrm{d}\Omega. \tag{12.13}$$

The local escape factor can be calculated from a self-consistent solution of the radiation losses. Such a method is described in chapter 8.

12.2.3 Chemistry

A 7 species Ar system is considered. The included species are given in table 12.1. The list of reactions along with the rate coefficient is given in table 12.2. Ionization

[1] Note that the escape factor for an infinite slab rather than an infinite cylinder is obtained using [31, eq. 5.32, 5.33]. By using $m = 1/2$ a prefactor of 1.125 can be found. This value is close to the value for an infinite cylinder. Additionally, the radius must be replaced by the thickness of the slab.

Table 12.1: The included species and their properties.

Name	Full name	g	E(eV)
Ar	Ar^1S_0	1	0
Ar[m_1]	4s[3/2]2	5	11.5484
Ar[r_1]	4s[3/2]1	3	11.6236
Ar[m_2]	4s′[1/2]0	1	11.7232
Ar[r_2]	4s′[1/2]1	3	11.8281
Ar[4p]	Ar[4p]	36	13.170535
Ar^+	Ar^+	6	15.759
e	electron	2	0

reactions starting from a 4s or 4p level are taken from Vlček [226]. The reverse reactions are included according to Carbone [227]. Carbone determined the total recombination rate. In this work the assumption is made that the recombination products are 4s states. The total rate is distributed according to the statistical weight over the 4s states. In [227] Carbone determined the reaction coefficients for four of the six 4s–4s transitions via the accurate laser pump-probe technique. The remaining two transitions are taken from the ab initio calculations of Zatsarinny and Bartschat [32]. The rates of Carbone are preferred over the theoretical results from Zatsarinny, since Carbone notices that the theoretical results are at least a factor two smaller in comparison to his experimental results. At the wall all species follow the reaction $Ar^x + e \leftrightarrow Ar + e$, with x representing an excited or an ionic state. The reaction rate is calculated from the thermal flux to the wall. It is given by $\Gamma_W = \frac{1}{4} n_x \sqrt{\frac{8 k_B T_h}{\pi m_x}}$. Note that the flux for the ions is calculated with T_e instead of T_h.

12.3 Spectral lines

The radiative flux is calculated based on 31 atomic transitions. These transitions are listed in table 12.3. The 10 4p-states are included via a lumped state. The result is that transitions involving this state are multiplied with the fractional statistical weight $g_j / \sum_j g_j$ to ensure that the correct amount of energy is emitted. Additionally, an energy offset is taken into account to correct for the energy difference between the energy level of the lumped state and the individual state.

Line broadening is discussed in sections 8.1 and 9.3 of this thesis. The non-resonant transitions are included in the ray tracing calculation with a Doppler profile. This profile is given by

$$\phi_G = \frac{1}{\sigma_{\mathrm{Dop}} \sqrt{2\pi}} \exp\left(-\frac{(\nu - \nu_0)^2}{2\sigma_{\mathrm{Dop}}^2} \right), \tag{12.14}$$

with the full width at half maximum (FWHM) given by $\Delta\nu_{\mathrm{FWHM}} = \sigma_{\mathrm{Dop}} \sqrt{8 \ln 2} = \nu_0 \left(8 k_B T \ln 2 / mc^2\right)^{1/2}$ and ν_0 the unperturbed frequency. The resonant lines are

Table 12.2: The list of reactions along with their rates for the 7 species Ar system. Using a σ in the column 'Rate' indicates that the cross section is taken from a tabulation. The column 'DB' indicates whether the reverse reaction is also included via detailed balancing. Note that T_e is specified in eV.

Reaction	Rate(m^3/s)	Reference	DB
$Ar + e \leftrightarrow Ar[m_1] + e$	σ	[228]	Yes
$Ar + e \leftrightarrow Ar[r_1] + e$	σ	[228]	Yes
$Ar + e \leftrightarrow Ar[m_2] + e$	σ	[228]	Yes
$Ar + e \leftrightarrow Ar[r_2] + e$	σ	[228]	Yes
$Ar + e \leftrightarrow Ar[4p] + e$	σ	[228]	Yes
$Ar[m_1] + e \leftrightarrow Ar[4p] + e$	σ	[32, 229]	Yes
$Ar[r_1] + e \leftrightarrow Ar[4p] + e$	σ	[32, 229]	Yes
$Ar[m_2] + e \leftrightarrow Ar[4p] + e$	σ	[32, 229]	Yes
$Ar[r_2] + e \leftrightarrow Ar[4p] + e$	σ	[32, 229]	Yes
$Ar + e \leftrightarrow Ar^+ + 2e$	σ	[228]	Yes
$Ar[m_1] + e \leftrightarrow Ar^+ + 2e$	σ	[226]	No
$Ar^+ + 2e \leftrightarrow Ar[m_1] + e$	$\frac{5}{12} 1.29 \times 10^{-38} n_e T_e^{-4.5}$	[230]	No
$Ar[r_1] + e \leftrightarrow Ar^+ + 2e$	σ	[226]	No
$Ar^+ + 2e \leftrightarrow Ar[r_1] + e$	$\frac{3}{12} 1.29 \times 10^{-38} n_e T_e^{-4.5}$	[230]	No
$Ar[m_2] + e \leftrightarrow Ar^+ + 2e$	σ	[226]	No
$Ar^+ + 2e \leftrightarrow Ar[m_2] + e$	$\frac{1}{12} 1.29 \times 10^{-38} n_e T_e^{-4.5}$	[230]	No
$Ar[r_2] + e \leftrightarrow Ar^+ + 2e$	σ	[226]	No
$Ar^+ + 2e \leftrightarrow Ar[r_2] + e$	$\frac{3}{12} 1.29 \times 10^{-38} n_e T_e^{-4.5}$	[230]	No
$Ar[4p] + e \leftrightarrow Ar^+ + 2e$	σ	[226]	No
$Ar[m_1] + e \leftrightarrow Ar[r_1] + e$	1.9×10^{-13}	[227]	Yes
$Ar[m_1] + e \leftrightarrow Ar[m_2] + e$	σ	[32, 229]	Yes
$Ar[m_1] + e \leftrightarrow Ar[r_2] + e$	σ	[32, 229]	Yes
$Ar[r_1] + e \leftrightarrow Ar[m_2] + e$	σ	[32, 229]	Yes
$Ar[m_2] + e \leftrightarrow Ar[r_2] + e$	9×10^{-13}	[227]	Yes
$Ar[r_1] + e \leftrightarrow Ar[r_2] + e$	2.1×10^{-13}	[227]	Yes

calculated using a Voigt profile. This profile is obtained as the convolution of a Lorentzian and a Gaussian profile. It is given by [160–162]

$$\phi_V(z) = \sqrt{2} \frac{\mathcal{R}[w(z)]}{\sqrt{\pi}\gamma_G}, \tag{12.15}$$

with $w(z)$ the Faddeeva function, $z = \sqrt{\ln 2}(\nu - \nu_0 + i\gamma_L)/\sigma_{\text{Dop}}$ and σ_{Dop} and γ_L the Gaussian standard deviation and the Lorentzian HWHM, respectively. The Lorentzian HWHM is calculated by including resonance broadening only as

$$\gamma_L = \frac{\pi}{2} C_3 n_{\text{Ar}}. \tag{12.16}$$

The broadening constants are given by $C_3 = 1.95 \times 10^{-15}\,\text{Hz}\,\text{m}^3$ for the transition from $Ar[r_2]$ and $C_3 = 4.84 \times 10^{-16}\,\text{Hz}\,\text{m}^3$ for the transition from $Ar[r_1]$ [231, eq. 1].

Table 12.3: The included transitions are listed with the wavelength, transition probability and the fraction of the upper state that is participating in the transition. The data are taken from NIST [53].

Initial state	Final state	λ(nm)	$A(\mathrm{s}^{-1})$	g_u
Ar[r_2]	Ar	104.8	5.1×10^8	1
Ar[r_1]	Ar	106.7	1.19×10^8	1
Ar[4p]	Ar[r1]	667.7	2.36×10^5	1/36
Ar[4p]	Ar[m1]	696.5	6.39×10^6	1/12
Ar[4p]	Ar[m1]	706.9	3.8×10^6	5/36
Ar[4p]	Ar[m1]	714.7	6.25×10^5	1/12
Ar[4p]	Ar[r1]	727.3	1.83×10^6	1/12
Ar[4p]	Ar[r1]	738.4	8.47×10^6	5/36
Ar[4p]	Ar[r1]	747.1	2.2×10^4	1/12
Ar[4p]	Ar[r2]	750.4	4.45×10^7	1/36
Ar[4p]	Ar[r1]	751.5	4.02×10^7	1/36
Ar[4p]	Ar[m1]	763.5	2.45×10^7	5/36
Ar[4p]	Ar[m1]	772.4	5.18×10^6	1/12
Ar[4p]	Ar[m2]	772.4	1.17×10^7	1/12
Ar[4p]	Ar[m2]	794.8	1.86×10^7	1/12
Ar[4p]	Ar[r1]	800.6	4.9×10^6	5/36
Ar[4p]	Ar[m1]	801.5	9.28×10^6	5/36
Ar[4p]	Ar[r1]	810.4	2.5×10^7	1/12
Ar[4p]	Ar[m1]	811.5	3.31×10^7	7/36
Ar[4p]	Ar[r2]	826.5	1.53×10^7	1/12
Ar[4p]	Ar[r2]	840.8	2.23×10^7	5/36
Ar[4p]	Ar[r1]	842.5	2.15×10^7	5/36
Ar[4p]	Ar[r2]	852.1	1.39×10^7	1/12
Ar[4p]	Ar[m2]	866.8	2.43×10^6	1/12
Ar[4p]	Ar[m1]	912.3	1.89×10^7	1/12
Ar[4p]	Ar[r2]	922.4	5.03×10^6	5/36
Ar[4p]	Ar[r2]	935.4	1.06×10^6	1/12
Ar[4p]	Ar[r1]	965.8	5.43×10^6	1/12
Ar[4p]	Ar[r2]	978.5	1.47×10^6	5/36
Ar[4p]	Ar[m2]	1047.8	9.8×10^5	1/12
Ar[4p]	Ar[r2]	1148.8	1.9×10^5	1/12

By only including resonance broadening in (12.10) the escape factor can be written as

$$\Lambda = \frac{1.115}{\sqrt{4\lambda^2 \frac{g_u}{g_l} \frac{A_{ul}}{C_3} R}}. \tag{12.17}$$

12.4 Results

In order to investigate the effect of the self consistent calculation of the radiation losses, multiple Ar plasmas are simulated with and without ray tracing. The investigated cases are

- **case 1: self-consistently**. The radiation is included using the ray tracing procedure described in chapter 8. The results can be converted to a local escape factor using (12.12).
- **case 2: Holstein**. A global escape factor is obtained from (12.17). An effective transition probability is introduced as $A'_{ul} = \Lambda A_{ul}$.
- **case 3: Adjusted escape factor**. A global escape factor is obtained from (12.11). An effective transition probability is introduced as $A'_{ul} = \Lambda A_{ul}$.

The next sections evaluate the spatial dependency of the escape factor for case 1, the shape of the resonant lines and the impact on the species profiles. A reference model is considered with a radius of 2.5 cm, a power density of $2.0 \times 10^4\,\mathrm{W/m^3}$ and a pressure of 400 Pa. The impact of the power density and pressure are investigated. Additionally, the effect of the radius of the cylinder is considered. The radius and pressure can be varied in such a way that the optical depth remains constant.

12.4.1 Escape factor and resonant lines

A comparison of the escape factors for case 2 and case 3 is given in table 12.4. In all cases the escape factor for case 3 is about a factor 10 larger in comparison to the escape factor for case 2. The main reason for the discrepancy is caused by the specific parabolic profile that is assumed by Holstein [31, p. 1165]. He assumes the following profile for the radiating species $n(r) = a_0 + a_1\left(1 - r^2/R^2\right)$ with $a_0/a_1 = 0.31$. This profile is not in agreement with the profile that follows from the self-consistent simulation. Due to the presence of wall reactions the ratio between $n(0)/n(R) = 1 + a_1/a_0 \approx 4.2$ is significantly larger in the self-consistent model.

One of the reasons for the differences between the species densities is the spatial variation of the escape factor for case 1. For the reference model the escape factors of the resonant lines are displayed in figure 12.2. The profiles typically have a peak in the center and decay towards the wall. This is related to the species profiles as shown in figure 12.3. Due to wall reactions the species profiles also decay towards the wall. The result is that I_ν from (8.38) also decreases for larger r. In places where a strong gradient of I_ν occurs, J_ν is dominated by the contribution from the center. A value of J_ν that is larger than the local equilibrium value decreases the escape factor. Since all rays are initialized with $I_\nu = 0$ at the wall, the average over the solid angle J_ν decreases significantly. For that reason, the escape factor increases near the wall. For transitions other than the resonant transitions the radial evolution of the escape factor depends on the evolution of the ratio of the resonant and metastable densities over the 4p densities.

Table 12.4: The escape factor for various models using the self-consistent approach from ray tracing (sc) or an escape factor from Holstein(12.17).

				λ=104.8 (nm)	
Model	P(W/m^3)	R(mm)	p(Pa)	Λ (12.17)	Λ_{sc}
Model 1	2.0×10^4	25	400	3.77×10^{-5}	4.41×10^{-4}
Model 2	2.0×10^5	25	400	3.77×10^{-5}	4.28×10^{-4}
Model 3	2.0×10^4	25	40	3.77×10^{-5}	4.78×10^{-4}
Model 4	2.0×10^4	2.5	400	1.19×10^{-4}	1.51×10^{-3}
Model 5	2.0×10^4	2.5	4000	1.19×10^{-4}	1.48×10^{-3}
Model 6	2.0×10^6	25	400	3.77×10^{-5}	5.08×10^{-4}
Model 7	2.0×10^6	2.5	400	1.19×10^{-4}	1.52×10^{-3}
Model 8	2.0×10^6	2.5	4000	1.19×10^{-4}	1.43×10^{-3}
				λ=106.7 (nm)	
Model	P(W/m^3)	R(mm)	p(Pa)	Λ (12.17)	Λ_{sc}
Model 1	2.0×10^4	25	400	3.85×10^{-5}	4.63×10^{-4}
Model 2	2.0×10^5	25	400	3.85×10^{-5}	4.47×10^{-4}
Model 3	2.0×10^4	25	40	3.85×10^{-5}	4.23×10^{-4}
Model 4	2.0×10^4	2.5	400	1.22×10^{-4}	1.49×10^{-3}
Model 5	2.0×10^4	2.5	4000	1.22×10^{-4}	1.49×10^{-3}
Model 6	2.0×10^6	25	400	3.85×10^{-5}	5.46×10^{-4}
Model 7	2.0×10^6	2.5	400	1.22×10^{-4}	1.53×10^{-3}
Model 8	2.0×10^6	2.5	4000	1.22×10^{-4}	1.45×10^{-3}

In Fig 12.4 the resonant lines are shown for the Ar model. The central part of the lines is solely determined by $n_l(R)/n_u(R)$. It can be calculated from (8.38). The ratio is then given by

$$\frac{n_l(R)}{n_u(R)} = \left(\frac{2h\nu_0^3}{c^2 I(\nu_0)} - 1\right)\frac{g_l}{g_u}. \tag{12.18}$$

The positions of the self-reversal maxima for both resonant lines for these conditions occur roughly at $\tau = 2.6$. For larger optical depths the net emitted radiation decreases due to absorption and for lower optical depths the spectral radiance is below its maximum value.

12.4.2 Species profiles

The models using ray tracing (case 1) are compared to two different models that use escape factors for the resonant lines. The escape factors for the remaining transitions are set to 1. The determination of the escape factors is described in the beginning of section 12.4 with case 2 and case 3. The escape factors are listed in table 12.4. The relative species profiles for models 1–5 are shown in figure 12.5.

The results from model 1 show that using the escape factor from Holstein produces species densities for the excited states that are in the order of 2–4 times larger than the results for case 1. The ion density is only moderately affected by

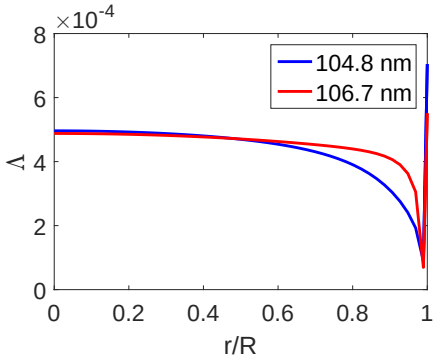

Figure 12.2: The spatial dependency of the escape factors determined using the self-consistent radiation calculation in model 1.

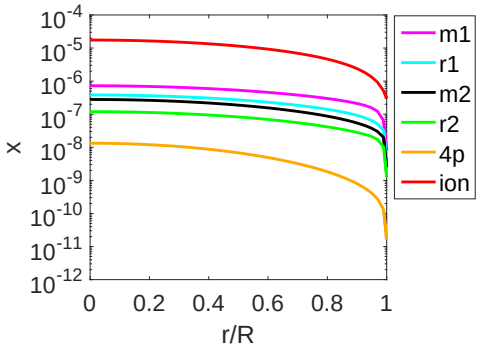

Figure 12.3: The excited and ionic state densities in model 1 using a self-consistent calculation of radiation.

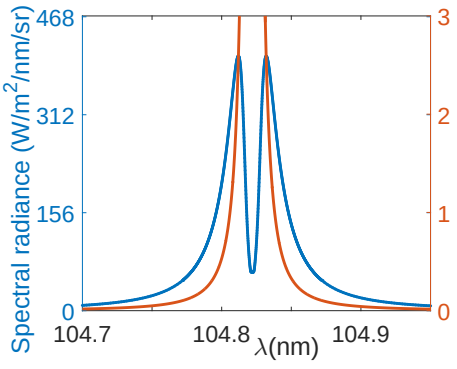

(a) Transition: Ar [r2] − Ar.

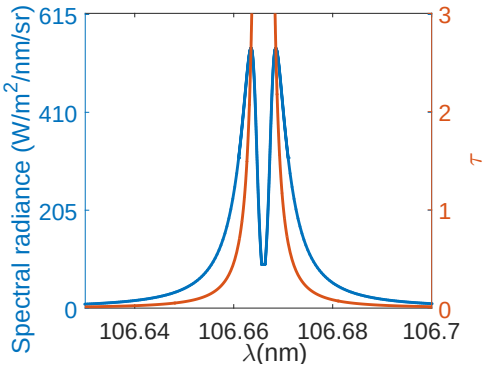

(b) Transition: Ar [r1] − Ar.

Figure 12.4: The spectral radiance and the optical depth for a ray passing through the center of the discharge using the density profiles from model 1.

the larger excited state densities. Its density is only increased by a factor of about 1.3. As a result the energy transferred from the electrons to the heavy particles is also affected and T_e is reduced by about 1.2 kK to 10.9 kK. Closer to the wall the importance of radiation transport increases. The escape factors in the ray tracing model decrease as indicated in figure 12.2. The relative densities are approaching one for $r = R$, since the escape factor is getting closer to the value predicted by Holstein. The 4p state is an exception, since this density reaches a ratio of 0.35 relative to model 1. The reason for the larger density in the ray tracing model is the absorption of radiation from the 811.5 nm line. Interestingly, Holstein's expression for a Gaussian line profile[2] produces an escape factor larger than 1 for this transition. For this reason, all non-resonant transitions have an escape factor of 1 for all simulations using the conditions described in case 2. Between $r/R =$ 0.6–0.9 the species ratios for the resonant and metastable species increase briefly. This is related to the wall reactions and the lower escape factors for case 2. The species with the lowest escape factor require a shorter distance measured from the wall to reach the chemical equilibrium in the bulk.

Using a global escape factor (case 3) deduced from the ray tracing model, produces relative densities in the center between 0.84 and 1.15 for the excited species. The reason for these discrepancies is partially caused by the fact that the global escape factor is smaller than the local escape factor at $r = R$. Other causes are the not-fully optically thin non-resonant transitions. The Ar[r2] state is significantly more affected by the radiation than the Ar[r1] state. This is caused by the escape factor for the 104.8 nm transition that is already changing at smaller radii than the escape factor for the 106.7 nm transition. The result is that the Ar[r2] state density increases in case 1 and that the metastable densities are following this trend. Due to the smaller volume where the escape factor for the 104.8 nm transition significantly deviates from the value at $r = 0$ the impact on the species profile is also smaller for the Ar[r1] state. The decaying species ratios confirm the metastable transport mechanism.

In model 2 the power input is 10 times larger. The profiles of the escape factors are similar to model 1. However, due to the larger power input the electron density is more than a factor 10 larger in comparison to model 1. The result is that in the center the relative deviations between cases 1, 2 and 3 are smaller due to the fact that the plasma is more collisionally dominated. Near the wall a peak can be observed in the relative species profiles for case 2. This is also related to the wall reactions. Due to the larger electron density it occurs closer to the wall. For the case 2 the relative densities for the metastable and resonant states are between 1.28 and 1.55 near the wall. At the same location the species ratios for case 3 are between 0.62 and 0.90. The decreasing trend near the wall again confirms that the metastable species are affected by the resonant radiation. The species ratios for the 4p states in the center deviate from 1 due to absorption from non-resonant lines. This is not included in cases 2 or 3.

The model 3 results are more in line with model 1. The escape factors are com-

[2] For a cylinder it is given by $\Lambda = 1.60/\left(\kappa_0 R\sqrt{\pi \ln(\kappa_0 R)}\right)$ with $\kappa_0 = \frac{\lambda_0^3 n_l}{8\pi}\frac{g_u}{g_l}\frac{A}{\sqrt{\frac{2\pi k_B T_h}{m}}}$.

parable to model 1. This is in agreement with Holstein's expression which states that the escape factors do not depend on the density for resonant broadening. The small differences are caused by the higher T_e and the lower T_h which affect the species profiles. The resonant and metastable species reach relative ratios between 1.69 and 3.10 near the wall for case 2. In the center the ratios are between 3.08 and 3.67. For case 3 the species ratios near the wall for the metastable and resonant states increase. In the center they range from 0.90 to 1.143 while the ratios reach 1.01 to 1.25 close to the wall. This increase is related to the fact that the escape factors for case 1 slowly increase for larger r. Near the wall the net escape factor for case 1 is therefore larger than the average value. The decrease of the species ratio near the wall for case 2 can not be explained using the spatial variation of the escape factor. In this case, the wall reactions are determining the local species densities near the wall for case 2. The fact that the wall reactions can cause such a profile suggests that it is difficult to distinguish the effects from the wall chemistry from the effects induced by radiation in the comparison between case 1 and case 2.

The simulations for model 4 use a radius that is decreased by a factor ten in comparison to model 1 while the same power density is used. The escape factors in case 1 slowly decay towards the wall. The consequence is that the species ratios for case 2 also decay towards the wall. In the center the metastable and resonant densities reach a ratio of 1.90 to 14.3 while this decreases near the wall to 1.41 to 6.10. For the same reason the simulation for case 3 shows a decrease from 0.98 to 1.10 in the center to 0.80 to 1.055 close to the wall. In this case the impact on the ratio of the Ar[r1] state is again smaller than the impact on the Ar[r2] level. Under these circumstances the Ar[m2] ratio remains approximately constant while the Ar[m1] ratio is most strongly affected with a decrease from 1.06 to 0.80. The metastable transport mechanism is not as visible as was the case in the previous models. This is related to the larger impact of the wall reactions on the bulk chemistry caused by the smaller radius.

In addition to decreasing the radius and keeping the power density constant, the simulations for model 5 also maintain the same optical depth in comparison to model 1. The results for this model for case 2 are similar to model 4. For case 3, the species ratios of the metastable and resonant densities are close to one. Most species ratios remain within the range given by 0.93 to 1.10. Exceptions are the ratio for Ar[r2] and Ar[m1] which decrease near the wall due to a strongly decreasing escape factor for Ar[r2]. Another species that is strongly affected is Ar[4p]. In the center the ratio is smaller than 1 because in the ray tracing calculation an escape factor smaller than 1 is obtained for the 811.8 nm line. Near the wall the escape factor for this line decreases even further which should result in a decreasing species ratio. However, due to the chemical coupling to the species Ar[r2] and Ar[m1] and the wall reactions the opposite trend occurs. In comparison to model 4 the higher optical depth increases the impact of the metastable transport mechanism.

The effect of a self-consistent calculation of the radiation is also investigated for the same conditions at a higher power density. The results for these models are shown in figure 12.6. The power density in model 6 is 100 times larger in com-

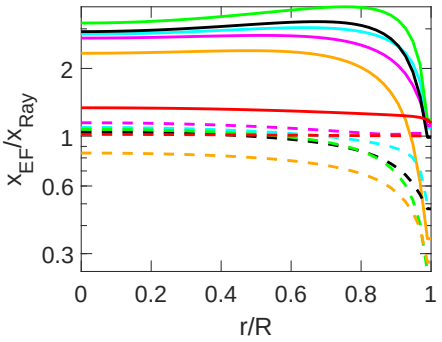

(a) Model 1.

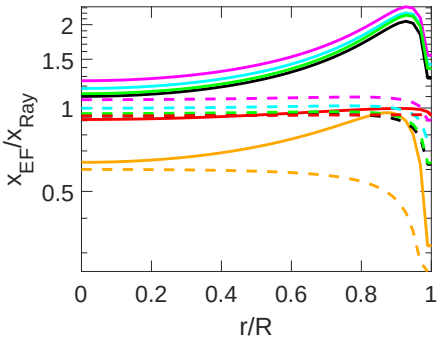

(b) Model 2.

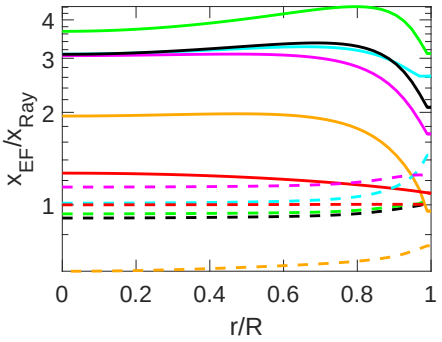

(c) Model 3.

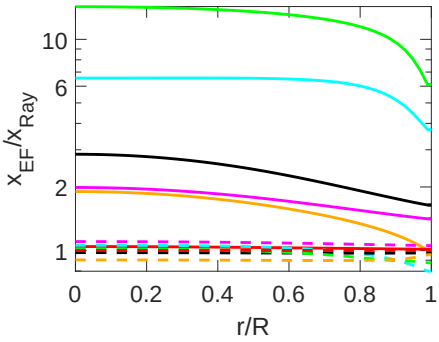

(d) Model 4.

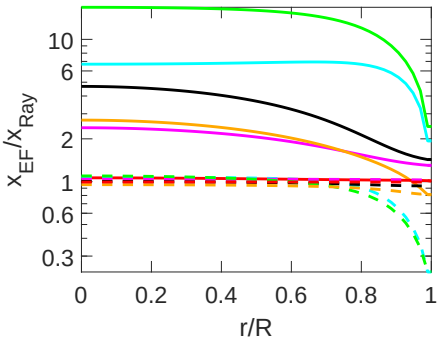

(e) Model 5.

Figure 12.5: Relative species ratios of the density profiles normalized to the densities of the self-consistent calculation of radiation transport (case 1). Dashed lines use the escape factor from the self-consistent calculation (case 3) and the full line represents the escape factor obtained from Holstein, (12.17) (case 2). Legend: m_1 ; r_1 ; m_2 ; r_2 ; 4p ; Ar^+ .

parison to the power density in model 1. The consequence is that T_h increased from 0.43 kK to 3 kK and that T_e increased from 12.1 kK to 13.1 kK. In spite of the large variation of the temperature and species profiles the escape factor for the resonant lines only increased by 15-20 %. This result is close to Holstein's prediction which states that the escape factors are independent of the power density and the species and temperature profiles. The species ratios for the metastable and resonant species for case 2 and 3 cover the range from 0.91 to 1.02 at the axis. This indicates that the plasma composition is mostly determined by collisions with electrons. Near the wall these ratios are between 1.22 and 1.34 for case 3 and between 1.67 and 1.82 for case 2. The curves for the species ratios increase near the wall, because the escape factors monotonically increase for larger r. The effective metastable transport is thus still visible, but its impact is reduced. The main reason for this effect is the increased impact of the chemistry due to the increased electron densities in comparison to model 1.

The power density in model 7 is 100 times larger than in model 4. Since this model uses a smaller radius, the gas heating is limited to about 330 K for the heavy particle temperature and the electron temperature reaches 15.6 kK. Due to the smaller impact of the wall reactions, a peak is visible again in the species ratios for case 2. For the metastable and resonant species these ratios are in the range of 1.86 to 2.15 in the center and 1.48 to 1.65 near the wall. The species ratios for case 3 exhibit smaller spatial variations, because the escape factors obtained from the self-consistent approach also show small variations. The resonant and metastable species ratios still vary between 0.93 and 1.25. In this particular case the metastable transport mechanism thus cannot occur.

Similarly, the power density in model 8 is 100 times larger than in model 5. Due to the higher pressure, the heavy particle temperature reaches 440 K while the electrons reach a temperature of 11.5 kK. The increased importance of the chemistry also limits the species ratios of the metastable and resonant species for this model. For case 2 the species ratios for the metastable and resonant species are between 0.87 and 2.50. Case 3 gives species ratios between 0.24 and 1.03. The lower species ratios are reached near the wall where the escape factor in the self consistent calculation is decreasing due to the higher optical depth. In comparison to model 5, the metastable transport mechanism for m_2 is now also visible.

12.5 Conclusion

We confirmed that Nader Sadeghi and Emile Carbone indeed proposed an effective transport mechanism for the metastable species. The strong impact of radiation transport thus not only impacts the resonant levels, but is also passed on to the metastable species via collisional coupling. The mechanism is more important for cylinders with small radii, while the effect of the pressure is limited. Additionally, the usage of Holstein's expression for the escape factor for an infinite cylinder has been investigated. In all simulations the global escape factor that can be derived from a self-consistent treatment of radiation (ray tracing) is about a factor 10 larger in comparison to Holstein's estimate.

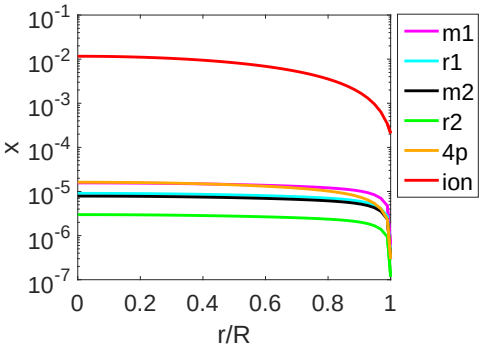

(a) Molar fractions for model 6 obtained using a self-consistent calculation of the radiation.

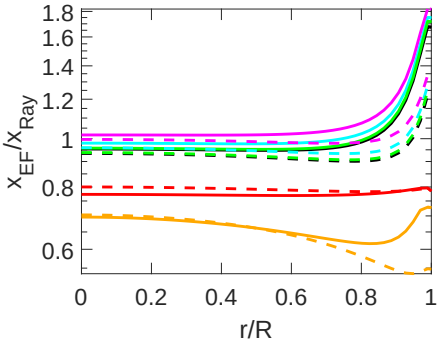

(b) Model 6.

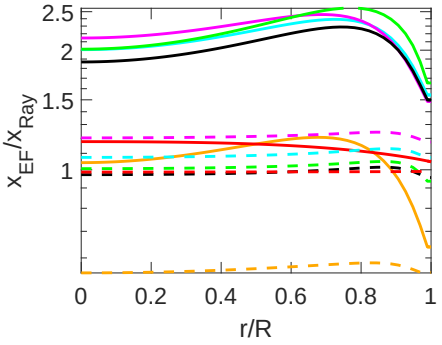

(c) Model 7.

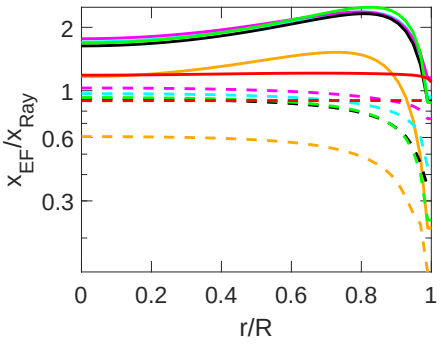

(d) Model 8.

Figure 12.6: Relative species ratios for the density profiles normalized to the densities from the self-consistent calculation of radiation transport (case 1) for a power density of $2 \times 10^6\,\mathrm{W/m^3}$. Dashed lines use the escape factor from the self-consistent calculation (case 3) and the full line represents the escape factor obtained from Holstein (12.17) (case 2). In figure 12.6a the effects of the increased power density on the excited and ionic molar fractions is shown. Legend: m_1 ; r_1 ; m_2 ; r_2 ; 4p ; Ar^+ .

The ratios of the metastable and resonant species relative to the densities predicted by the self-consistent radiation transport model are compared. For escape factors predicted by Holstein these ratios vary in the order of 1-4 for cylinders that have a radius of 2.5 cm. The species ratios can increase up to 16 for cylinders with a radius of 2.5 mm. Near the wall these ratios decay as a result of wall reactions and the radiative transport of resonant and indirectly the metastable species. Simulations using a self consistent calculation of the radiation transport are necessary to reduce the error in the predicted species profiles.

More accurate escape factors are obtained by using a global average of the escape factor predicted by the self consistent model. In that case the species ratios reach approximately 1 on the axis. However, near the wall, absorption is not included in the global escape factor. In that area the ratio of species densities ranges between 0.2 and 1.4. When the power density is increased from 2×10^4 to $2 \times 10^6\,\mathrm{W/m^3}$ the species ratios show smaller variations on the axis due to the larger impact of electron collisions. However, the impact of absorption near the wall is still significant. Thus, even when a correct global escape factor is known the local errors in the species densities can be considerable. For accurate results, self-consistent radiation transport is therefore recommended.

Chapter 13

Surfatron plasmas in mixtures containing $SiCl_4$

Microwave discharges are used for the production of glass fibers [3, 4, 232]. A schematic representation of such a setup is shown in figure 13.1. These setups consist of a dielectric tube with a surfatron launcher placed around it. The launcher can move back and forth in the direction of the tube. A mixture of O_2 and $SiCl_4$ is introduced in the tube at the inlet side. The absorption of microwaves induces the formation of a plasma in the launcher. One of the reactions that will take place is the formation of quartz according to $SiCl_4 + O_2 \leftrightarrow SiO_2 + 2Cl_2$. The SiO_2 is deposited on the wall. The moving launcher guarantees a homogeneous deposition of quartz across the entire tube. After sufficient deposition of quartz the diameter of the tube has shrunk considerably. In order to produce an optical fiber two successive production steps are required: collapsing and drawing.

13.1 Introduction

The setup that is used for deposition of SiO_2 is not suitable for an experimental study, since the presence of the furnace makes the reactor difficult to access for diagnostic purposes. For that reason a surfatron reactor is built that is more easily studied [232]. In this work a computer model of that setup is discussed. An image of this surfatron is shown in figure 13.2. The surfatron launcher's position is fixed and the chemistry is reduced by using an inlet mixture of $Ar + SiCl_4$. Additionally, the design of the launcher is simplified since there are no chokes to confine the electromagnetic waves to the launcher. In section 13.2 the surfatron model is discussed in more detail.

This setup has been studied before by Jiménez [3] for a mixture containing only Ar. Recently, Kemaneci [4, ch. 5] studied the $SiCl_4 + O_2$ chemistry in a global model. That model contained 37 species and 175 volume reactions. A part of this chemistry is validated with experiments. These are the O_2 and Cl_2 reaction subsets. In this study the reaction subsets [4, Table. 5.A.5,5.A.8] related to reactions involving Cl_x and $SiCl_x$ species are studied for the first time in a 2D

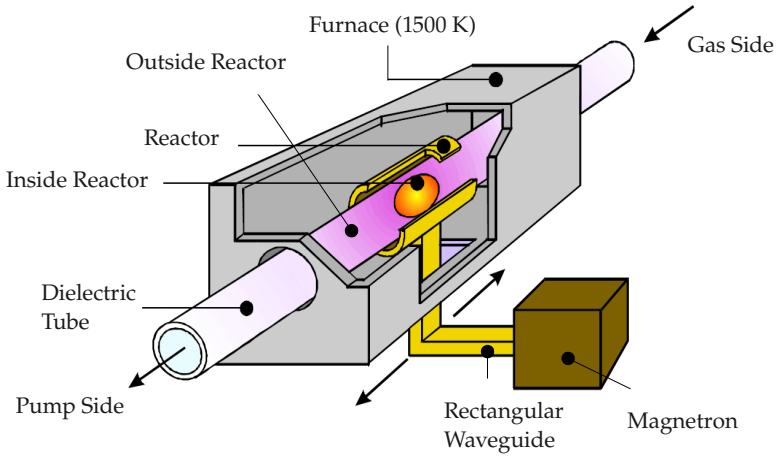

Figure 13.1: A schematic representation of the setup that is used for the production of glass fibers. The image is taken from Jiménez [3, p. 17].

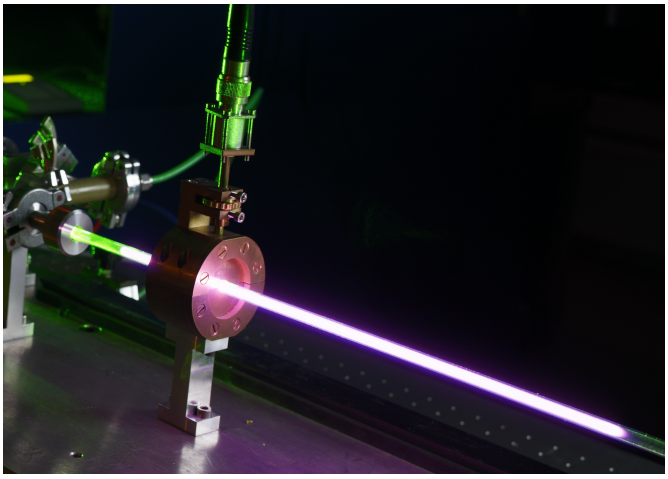

Figure 13.2: A picture of the surfatron setup built at the TU/e that is studied in this chapter. The image is taken from the PLASIMO website [233] and is originally produced by Bart van Overbeeke.

model. A comparison is made between simulation results of mixtures containing pure Ar and mixtures that also contain $SiCl_4$ to evaluate the impact of $SiCl_4$.

Experiments on this surfatron provided an absolutely calibrated spectrum of the molecular emission of the B–X transition in SiCl. The modeling results can be used to predict a spectrum. Since the considered set of reactions does not contain any excited states of SiCl an additional model is required to estimate the population of the B state. The excited state is assumed to be coupled to the ground state via electron collisions. It is assumed that the rate is given by an Arrhenius's law. The proportionality factor of this rate is adjusted to obtain agreement with the measured spectrum.

13.2 Model

In the following sections the numerical representation of the surfatron geometry and the most important physical aspects are considered. The physical modules that are considered are the electromagnetic, chemistry and transport modules. These modules are briefly discussed.

13.2.1 Geometry

The modeled surfatron is depicted in figure 13.3. It is the same setup that Jiménez [3, p. 167-169] used to model the Ar surfatron plasmas. The metal walls of the surfatron launcher form a concentric cylindrical cavity. Electromagnetic waves are fed to this cavity via a waveguide. A gap is created in the cavity on the pump side. The dimensions of the surfatron are chosen to maximize the electric field in the gap. The electric field is used to excite the transversal magnetic surface waves [4, p. 32-33].

13.2.2 Electromagnetic module

The electromagnetic waves that are produced by the launcher are partially absorbed by the plasma. The energy obtained from the field sustains the plasma. In order to describe the power absorption, the electromagnetic waves must be calculated first. These waves are described by Maxwell's equations. A few approximations are made to simplify this system of equations:

- **Harmonic fields**: By assuming harmonic fields the field intensities $\vec{\mathcal{F}}$ can be written as a complex amplitude $\vec{F}$ multiplied by a common time dependent term as $\vec{\mathcal{F}} = \mathcal{R}\left(\vec{F}\exp\left(i\omega t\right)\right)$.
- **Non-magnetic media**: In this work only non-magnetic media are considered. The consequence is that the relative magnetic permeability has a uniform value of $\mu_r = 1$.
- **Steady-state**: The temporal variations of the plasma are neglected. The species densities and therefore parameters like the electric relative permittivity ϵ_r are assumed to be independent of time.

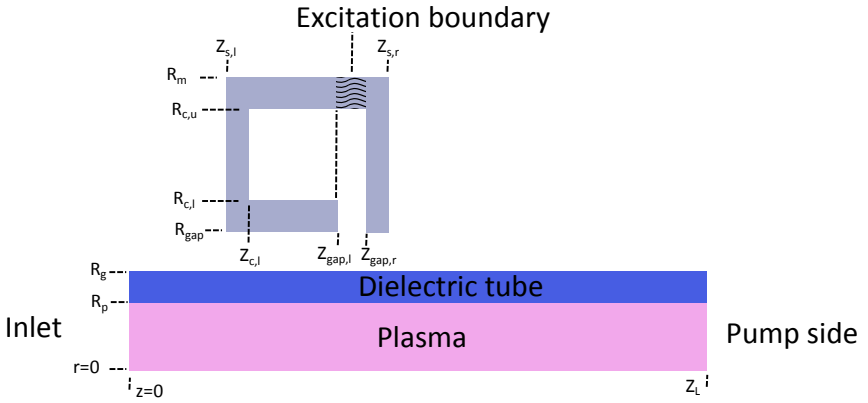

Figure 13.3: The numerical representation of the surfatron is similar to the surfatron considered by Jiménez [3, p. 169]. The variables are defined as: $R_p = 3.1\,\text{mm}$; $R_g = 4.4\,\text{mm}$; $R_{\text{gap}} = 5.7\,\text{mm}$; $R_{c,l} = 13\,\text{mm}$; $R_{c,u} = 52\,\text{mm}$; $R_m = 66\,\text{mm}$; $Z_{s,l} = 72\,\text{mm}$; $Z_{c,l} = 87\,\text{mm}$; $Z_{\text{gap},l} = 105\,\text{mm}$; $Z_{\text{gap},r} = 108\,\text{mm}$; $Z_{s,r} = 111\,\text{mm}$

Maxwell's equations can then be expressed as [4, p. 29]

$$\nabla \cdot \left(\epsilon_0 \epsilon_r \vec{E}\right) = \rho_c \tag{13.1}$$

$$\nabla \cdot \vec{H} = 0 \tag{13.2}$$

$$\nabla \times \vec{E} = -i\omega\mu_0 \vec{H} \tag{13.3}$$

$$\nabla \times \vec{H} = \vec{J} + i\omega\epsilon_0\epsilon_r \vec{E}, \tag{13.4}$$

with the electric field $\vec{E}$, magnetic field intensity $\vec{H}$ and the current density $\vec{J}$ the complex amplitudes of $\vec{\mathcal{E}}$, $\vec{\mathcal{H}}$ and $\vec{\mathcal{J}}$, respectively. Additionally, μ_0 is the magnetic permeability of vacuum, ϵ_0 the electric permittivity of vacuum and ϵ_r the relative permittivity of the local medium. Ohm's law $\vec{J} = \hat{\sigma}\vec{E}$ with a complex electrical conductivity $\hat{\sigma}$ can be used to rewrite (13.4) as

$$\nabla \times \vec{H} = i\omega\epsilon_0 \hat{\epsilon}_r \vec{E}, \tag{13.5}$$

with $\hat{\epsilon}_r$ the complex relative permittivity given by

$$\hat{\epsilon}_r = \epsilon_r + \frac{\hat{\sigma}}{i\omega\epsilon_0}. \tag{13.6}$$

The wave that is considered is a TM wave that propagates in the axial direction. Near the surfatron the wave can also propagate in the radial direction. The non-zero components of the electric and magnetic field are thus E_r, E_z and H_ϕ. The coupled system of equations is solved using the Yee algorithm [4, p. 31] [3, p. 48-54]. In the cylindrical grid defined in figure 13.3 the component H_ϕ is solved on the nodal points using a coupled system of (13.5) and (13.3). The E_r and E_z components are evaluated on the cell interfaces. The electric flux is thus

guaranteed to be continuous on interfaces that contain no charge. Additionally, the staggered grid is ideal for dealing with the gradients that occur in the described system.

The boundary conditions for the electromagnetic waves are described in detail by Jiménez [3, p. 52-54,123-125]. At the metal interfaces a homogeneous Dirichlet condition is applied, since metal is considered as a perfect electrical conductor. At the axis, homogeneous Neumann conditions are applied. The electric field at the excitation boundary is scaled to obtain the correct power dissipation in the entire numerical domain. The boundary conditions at $z = 0$ and $z = L_z$ are propagation conditions determined from $\frac{\partial E_r}{\partial z} = -ikE_r$ with $k = \omega\sqrt{\mu_0\epsilon_0\epsilon_r}$. Similarly at $r = R_m$ the propagation condition is derived from $\frac{\partial E_z}{\partial r} = -k\frac{H_1^{\{2\}}(kr)}{H_0^{\{2\}}(kr)}E_z$ with $H_x^{\{2\}}$ a Hankel function.

13.2.3 Transport equations

The various transport balances are discussed in this section. These are the species particle balance, the bulk momentum balance and the energy balances of the electrons and the heavy particles. The model is based on the previous work of Kemaneci [4, p. 90-93] and Jiménez [3, p. 166-171]. Due to the instabilities that occur in the current self-consistent diffusion algorithm (see chapter 6) the diffusion is included using Fick's law[1]. Note that in comparison to the work of Kemaneci the particle balances are solved in terms of fractions rather than densities. The consequence of using this diffusion model is that a change in the temperature profile does not initiate diffusion if the species fractions remain constant[2].

In PLASIMO's implementation of Fick's law one particle is considered as the background particle. For all other species the following stationary species balance, deduced from (3.17), is solved[3]

$$\nabla \cdot \left(\rho y_i \vec{u} - \rho \frac{y_i}{z_i} D_i \nabla z_i \right) = m_i \omega_i, \tag{13.7}$$

[1] In the surfatron plasma Ar is the dominant species. In that case the coupled system presented in (6.11) reduces to a diagonally dominant system if $\frac{z_i z_{\mathrm{Ar}}}{D_{i\mathrm{Ar}}} \gg \sum_{j\neq i} \frac{z_i z_j}{D_{ij}}$ for every i. This can be rewritten as $\frac{z_{\mathrm{Ar}}}{z_j} \gg \frac{D_{i\mathrm{Ar}}}{D_{ij}}$. For neutral-neutral and neutral-ion interactions the ratio of the diffusion coefficients is expected to be close to one. Having a dominant background gas is therefore sufficient to use Fick's law. If i and j correspond to charged-charged interactions D_{ij} can become very small due to the large Coulomb collision integrals (see figure 4.2). The inequality may be violated for a few charged species. However, Fick's law remains a good approximation. As shown by Rahimi [234, p. 101-106] the deviations between results for Fick's diffusion model and the self-consistent model remain small when the mole fraction of the negatively charged species is smaller than the mole fraction of positively charged species.

[2] In Kemaneci's case [4, eq. 2.14] the second term in $D\nabla x_i = \frac{1}{n}D\nabla n_i - \frac{n_i}{n^2}D\nabla n$ is not included. Additionally, he uses ∇x_i rather than ∇z_i which neglects the contribution from the temperature.

[3] Note that the diffusive mass flux has been substituted with $\rho y_i \vec{v}_{d,i} = -\rho\frac{y_i}{z_i}D_i\nabla z_i = -\rho\frac{m_i T}{mT_i}D_i\nabla z_i$. The only driving force that is included is ordinary diffusion (6.9). This expression is derived from [234, p. 99] by approximating the fractions of the dominant background gas with one. Ambipolar diffusion is included by changing the coefficients D_i.

with y_i the species mass fraction, z_i the species pressure fraction, $\vec{u}$ the bulk velocity, D_i the effective diffusion coefficient, m_i the species mass and ω_i the production rate per unit volume due to chemical reactions. The effective diffusion coefficient is given by [4, p. 91]

$$D_i = p \left(\sum_{j \neq i} \frac{p_j}{D_{ij}} \right)^{-1}, \tag{13.8}$$

note that in the case of a dominant background gas this expression reduces to $D_i \approx D_{ib}$ with b the index of the dominant background gas. In that case the diffusion model is equivalent to Fick's limit. For positively charged species a correction factor is applied to account for the ambipolar electric field. In that case the effective diffusion coefficient is given by [4, p. 91]

$$D_i = p \left(\sum_{j \neq i} \frac{p_j}{D_{ij}} \right)^{-1} \left(1 + \frac{q_i}{q_e} \frac{T_e}{T_h} \right), \tag{13.9}$$

with q_i the charge of particle i and T_i and T_e the heavy particle and electron temperatures. The correction term follows from the solution of a system containing an atom, an ion and an electron [6, p. 51,52]. The approximation is valid when the neutral particle is dominant. In plasmas with multiple ions such an expression can not be derived. The approximation can still be used if the additional requirement for the species densities $\nabla n_i / n_i \approx \nabla n_e / n_e$ is satisfied [235, p. 420]. Equations of the type (13.7) are not used for the electrons and the background species. The electron mass fraction is calculated from quasi-neutrality

$$y_e = \frac{m_e}{q_e} \sum_{i \neq e} \frac{q_i}{m_i} y_i. \tag{13.10}$$

The density of the background species is calculated from

$$n_b = p - \sum_{i \neq b} n_i k_B T_i, \tag{13.11}$$

to ensure that the correct pressure is obtained. Homogeneous Neumann (HN) boundary conditions are applied for all species at the inlet, outlet, quartz wall and at the axis. Kemaneci and Jiménez used a flux condition. A flux boundary condition can be derived from

$$- \frac{n_i}{z_i} D_i \nabla z_i = \gamma_i \frac{n_i}{4} \sqrt{\frac{8 k_B T}{\pi m_i}}, \tag{13.12}$$

with γ_i the reaction probability. The usage of this condition introduced large gradients directly near the wall. In order to improve the stability of the model this condition is replaced by a HN condition.

The sum of all species mass balances (13.7) gives the continuity equation (3.18)

$$\nabla \cdot (\rho \vec{u}) = 0.$$

The bulk velocity is solved from the stationary Navier-Stokes equations (3.20)

$$\nabla \cdot (\rho \vec{u}\vec{u}) = -\nabla p + \nabla \cdot \bar{\bar{\tau}},$$

with p the pressure and $\bar{\bar{\tau}}$ the viscous stress tensor. The gravitational forces are neglected. The SIMPLE algorithm is used to solve for the bulk velocity. It is described in more detail by Peerenboom [6, p. 69-73]. HN boundary conditions are also used for the pressure and the axial and radial velocity components. Exceptions are the no slip condition $u_z(R_p) = 0$ at the wall and $u_r(0) = u_r(R_p) = u_r(r)|_{z=0} = 0$. Other deviating conditions are the inlet and outlet pressure which are $p_{\text{in}} = 40.02\,\text{mbar}$ and $p_{\text{out}} = 40\,\text{mbar}$. The pressure difference approximately compensates the viscous losses[4].

A two temperature plasma is considered. The temperature of the electrons is calculated from (3.23)

$$\nabla \cdot \left(\frac{5}{2} n_e k_B T_e \vec{u}\right) + \nabla \cdot \vec{q}_e - \vec{u} \cdot \nabla p_e = Q_{\text{ohm}} - Q_{\text{elas},eh} - Q_{\text{inel},e},$$

with $\vec{q}_e = -\lambda_e \nabla T_e$ the conductive heat flux of the electrons, λ_e the electronic thermal conduction coefficient, Q_{ohm} the ohmic dissipation, $Q_{\text{elas},eh}$ the elastic energy transfer and $Q_{\text{inel},eh}$ the inelastic energy transfer to the heavy particles. The ohmic dissipation is calculated from

$$Q_{\text{ohm}} = \frac{1}{2}\text{Re}(\hat{\sigma})|\mathbf{E}|^2, \tag{13.13}$$

with $\mathbf{E}$ the electric field and $\hat{\sigma}$ the complex electrical conductivity. This complex conductivity is derived in appendix 13.A and is given by

$$\hat{\sigma} = \frac{\epsilon_0 \omega_p^2}{\nu_{eh} + i\omega}, \tag{13.14}$$

with $\omega_p = \frac{n_e q_e^2}{m_e \epsilon_0}$ the plasma frequency, $\nu_{eh} = \sum_{j \neq e} \nu_{ej}$ the elastic collision frequency between electrons and heavy particles, $\nu_{ij} = \frac{16}{3} n_j \Omega_{ij}^{(1,1)}$ is taken from (3.44) and ω the microwave frequency. The elastic energy transfer is given by (3.43) [54, p. 34,45,51]

$$Q_{\text{elas},eh} = \sum_{i \neq e} \frac{3}{2} n_e \nu_{ei} \frac{m_e}{m_j} k_B (T_e - T_h). \tag{13.15}$$

[4]The momentum balance is simplified by assuming that the velocity most important component is $u_z(r)$ which gives $\frac{\partial p}{\partial z} = \eta \frac{\partial^2 u_z}{\partial r^2}$. The solution of the Hagen-Poiseuille equation is $u_z = \frac{1}{4}\eta \frac{\partial p}{\partial z}(R^2 - r^2)$. The mass flow rate is obtained from $Q = \int_0^{R_p} \rho u_z 2\pi r \text{d}r$. Solving for the pressure gradient gives $\frac{\partial p}{\partial z} = 8\eta Q/(\rho \pi R^4)$. Using $\eta_{\text{Ar}} = 2 \times 10^{-5}\,\text{kg/m/s}$, $Q = \rho C_{\text{slm}}\,\text{kg/s}$ with $C_{\text{slm}} = 2 \times 10^{-4}\,\text{m}^{-3}/(60\,\text{s})$ and $\rho = \frac{p}{k_B T_h} m_{\text{Ar}}$ with $T_h = 300\,\text{K}$ produces the value for the pressure gradient.

The inelastic energy transfer is obtained from

$$Q_{\text{inel},e} = \sum_i R_i \Delta h_i, \tag{13.16}$$

with R_i the reaction rate and Δh_i the reaction enthalpy. This term only includes the reactions that involve electrons as a reactant. The energy balance for the heavy particles is obtained from (3.22)

$$\nabla \cdot \left(\sum_{i \neq e} \frac{5}{2} n_i k_B T_h \vec{u} + n_i E_i \vec{u}_i \right) + \nabla \cdot \vec{q}_h - \vec{u} \cdot \nabla \sum_{i \neq e} n_i k_B T_h - \tau : \nabla \vec{u} = Q_{\text{elas},eh} + Q_{\text{inel},e} + Q_{\text{rad}},$$

with the heat flux given by $\vec{q}_h = -\lambda_h \nabla T_h$ and λ_h the thermal conductivity of the heavy particles. The contributions to the energy balance from viscous dissipation and expansion work are small. At the inlet, outlet and axis of the surfatron HN conditions are used for the heavy particle temperature. At the quartz boundary the heat flux is assumed to be continuous[5]. For the electron temperature HN boundary conditions are applied at the inlet, outlet, axis and the quartz wall.

13.2.4 Chemistry

A total of 20 species is included in the model. An overview of the included species and their energy level is given in table 13.1. The energy levels of the $SiCl_x$ and $SiCl_x^+$ species deviate significantly from the values that are reported in [4, p. 79]. For example, the energy of $SiCl_4$ is listed as 6.17 eV while analysis of thermodynamic data [223] suggests a value of -11.45 eV. A discrepancy of several eV has also been observed for other species. The consequence is that the reaction energy for dissociation and ionization of $SiCl_x$ is also strongly affected. These reactions impact T_e and T_h via the inelastic energy transfer. In comparison to the chemistry described by Kemaneci, Cl_2^+ and vibrational excitation of Cl_2 are neglected. The reaction kinetics are taken from Kemaneci [4, p. 83,85] for the Cl_2 and $SiCl_4$ related reactions. Reaction number 175 in that work for $SiCl_4 \leftrightarrow SiCl_3 + Cl$ contains a reaction rate of $k = 1.7 \times 10^{14} \exp\left(-3.5764 \times 10^{-4}\,\text{K}/T_h\right)/\text{s}$. This rate is not in agreement with the indicated reference and is therefore corrected to $k = 1.7 \times 10^{14} \exp\left(-48\,229\,\text{K}/T_h\right)/\text{s}$. Additionally, a typing mistake occurred in the documentation of reaction number 152 where the prefactor had an exponent of 10^{-3} which should be 10^{-13} (the input file contained the correct value). The Cl_2 chemistry is modified by adding $Cl + 2e \leftrightarrow Cl^- + e$ with an assumed rate of 1×10^{-60}. The Ar chemistry is taken from Gudmundsson [236]. This chemistry is modified by adding detailed balancing to the reactions $2Ar\,[4p] \leftrightarrow Ar + Ar^+ + e$

[5] By using $\nabla \cdot q_h = \frac{\lambda_w}{r} \frac{\partial}{\partial r} \left(r \frac{\partial T}{\partial r} \right) = 0$ and $-\lambda_h \frac{\partial T_h}{\partial r}|_{r=R_p} = -\lambda_w \frac{\partial T}{\partial r}|_{r=R_p}$ the heat flux through the wall is given by $-\lambda_w \frac{\partial T}{\partial r}|_{r=R_p} = -\frac{\lambda_w (T_0 - T_h(R_p))}{R_p \ln \frac{R_q}{R_p}}$. Note that λ_w is assumed to be constant and T_0 is the temperature of the environment.

Table 13.1: The list of included species. The data for the atomic ions and neutrals is derived from NIST [53]. The neutral molecular data is obtained from NASA [223] and the data for the molecular ions is taken from Kothari [237].

Species	Energy(eV)	Species	Energy(eV)
Ar	0	Ar [m]	11.57
Ar [r]	11.73	Ar [4p]	13.17
Ar^+	15.76	Cl_2	0
Cl	1.24	Cl^-	-2.44
Cl^+	14.27	Si	0
Si^+	8.15	SiCl	-3.16
$SiCl^+$	7.77	$SiCl_2$	-6.31
$SiCl_2^+$	4.04	$SiCl_3$	-8.09
$SiCl_3^+$	4.21	$SiCl_4$	-11.45
$SiCl_4^+$	0.33	e	0

and $Ar\,[4p] + e \leftrightarrow Ar^+ + 2e$. The purpose of these modifications is to prevent the depletion of Cl^- and Ar [4p] in specific locations of the plasma. For Cl^- this modification is required because of reactions of the type $SiCl_x^+ + Cl^- \leftrightarrow SiCl_x + Cl$ which are included with a constant rate coefficient. Due to the stable density of the $SiCl_x^+$ species exponential decay[6] occurs for Cl^-. The modification for Ar [4p] is required since at low T_e the production is severely limited by terms like $\exp(-C/T_e)$. These terms are absent in the most important destructive reactions. This is related to range of validity for the Gudmundsson rates. These fitted rates are valid in the range between 1–7 eV.

13.3 Results

In the following sections a comparison is made between an Ar plasma and an $Ar + SiCl_4$ plasma. Additionally the simulated densities are used to predict an absolutely calibrated spectrum. This spectrum is compared to a measured spectrum for the purpose of verifying the $SiCl_4$ chemistry. Experiments using the surfatron depicted in figure 13.3 used a mass flow rate of 210 sccm of Ar and 10 sccm of $SiCl_4$. A pressure of 40 mbar and an input power of 100 W were used. Due to instabilities in the 2D model the simulated input power is reduced to 10 W. The flow rate has also been decreased in order to improve the stability. The elemental flow rates used in the model correspond to an influx of 0.5 sccm of $SiCl_4$.

13.3.1 Influence of $SiCl_4$ chemistry

In this section simulations are compared for an Ar and a $Ar + SiCl_4$ chemistry. The impact on the temperature profile and the species densities is shown.

[6] The decay rate can be derived from $\frac{\partial n_{Cl^-}}{\partial t} = -n_{SiCl_x^+} n_{Cl^-} k$,where k is the rate coefficient.

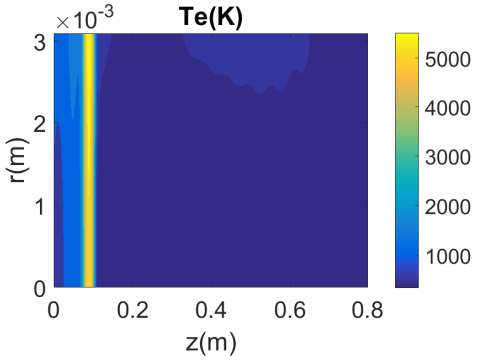

(a) T_e for the $Ar + SiCl_4$ mixture.

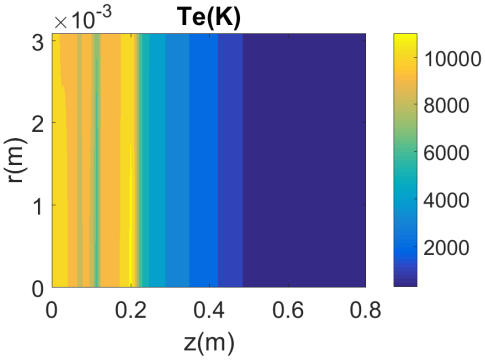

(b) T_e for the Ar mixture.

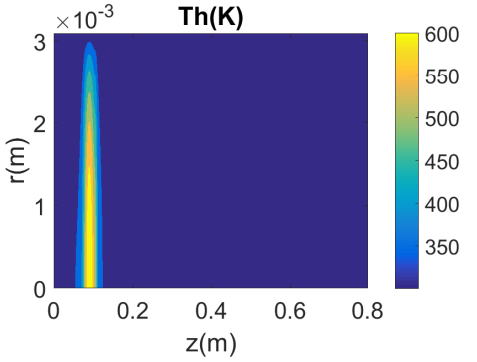

(c) T_h for the $Ar + SiCl_4$ mixture.

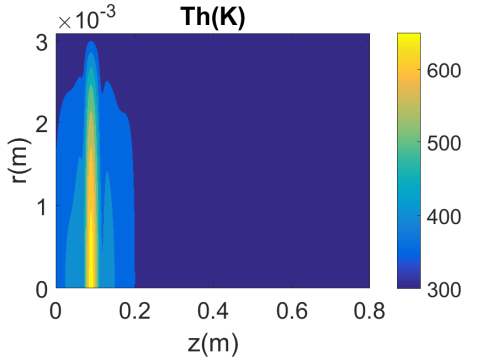

(d) T_h for the Ar mixture.

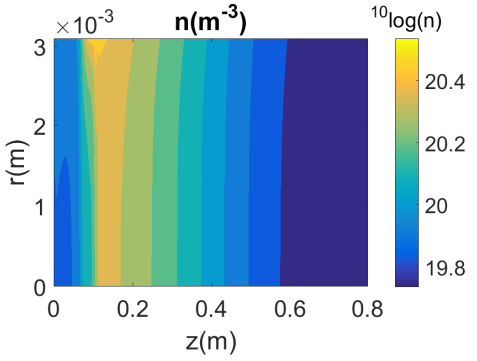

(e) n_e for the $Ar + SiCl_4$ mixture.

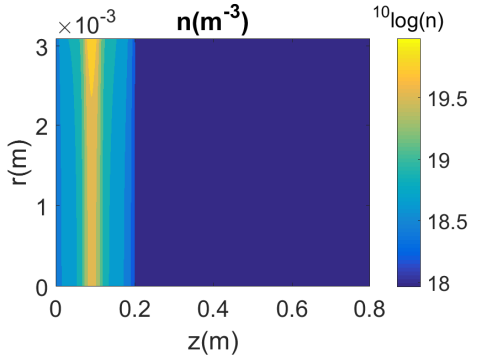

(f) n_e for the Ar mixture.

Figure 13.4: The electron density and the electron and heavy particle temperatures for the $Ar + SiCl_4$ and Ar mixtures.

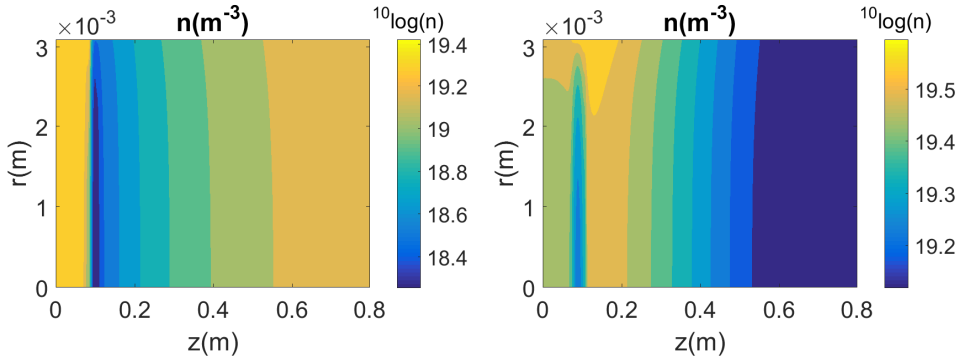

(a) SiCl. (b) $SiCl_4^+$.

Figure 13.5: Species densities in the $Ar + SiCl_4$ mixture.

The electron density, T_e and T_h for both simulations are shown in figure 13.4. The electron temperature in the Ar plasma reaches a maximum value of 11.5 kK. A stable plateau of about 10 kK is maintained for about 20 cm in axial direction. After that it decays towards the pump side via elastic collisions with the heavy particles. The electron temperature in the $Ar + SiCl_4$ plasma reaches an equilibrium that is in the range of 4-5.9 kK. In this case the elastic collisions are also the dominant loss process. The electron temperature is lower in the mixture with $Ar + SiCl_4$ due to the higher electron density. The electron density in the $Ar + SiCl_4$ mixture reaches a peak value right below the gap of the surfatron where the power coupling is largest. The heavy particle temperature in the Ar mixture is larger in comparison to the $Ar + SiCl_4$ mixture in spite of the lower peak value of $n_e\,(T_e - T_h)$. This is related to the very narrow peak in the $Ar + SiCl_4$ plasma.

One of the most interesting results of the $SiCl_4$ chemistry is the small variation of $SiCl_x$ and $SiCl_x^+$ in terms of species densities. The species densities of SiCl and $SiCl_3$ vary in the order of $10^{18.2}$–$10^{19.4}\,m^{-3}$ and $10^{16.4}$–$10^{20.1}\,m^{-3}$, respectively. The neutral species $SiCl_2$ and $SiCl_4$ are larger and vary in the range of $10^{19.2}$–$10^{20.5}\,m^{-3}$ and $10^{18.5}$–$10^{20.4}\,m^{-3}$. The ion densities show an even smaller variation. Again the species containing one or three Cl atoms have the lowest densities. These densities vary in the range of $10^{18.4}$–$10^{19.1}\,m^{-3}$ and $10^{18.7}$–$10^{19.3}\,m^{-3}$, respectively. The species $SiCl_2^+$ and $SiCl_4^+$ are the most important ions in the discharge. They cover the ranges $10^{19.4}$–$10^{20.3}\,m^{-3}$ and $10^{19.1}$–$10^{19.6}\,m^{-3}$, respectively. The species profiles for SiCl and $SiCl_4^+$ are shown in figure 13.5. The validation of the $SiCl_x$ species densities is difficult due to the limited amount of data available. Most reactions for the $SiCl_x$ chemistry are taken from Lee [238] who based the reaction rates on cross sections of SiF_x species. The pressure that was used in those models is a factor 10^4 smaller. In spite of the large differences in pressure, the observation that the molecules are more important than atomic Si species is also made in Lee's model. Additionally, the resulting $SiCl_x$ neutral species densities differ by only one order of magnitude. Lee does not mention the

species densities of the $SiCl_x^+$ species.

One of the current limitations of the model is that all species are assumed to bounce back from the quartz wall into the plasma. This assumption is currently required to ensure the stability of the $Ar + SiCl_4$ model. In reality the wall reactions have a strong impact on the concentration profiles near the wall. In order to test the influence of the wall reactions the Ar chemistry is extended with a flux condition given by (13.12). The reaction probability is set to $\gamma_i = 1$ for all reactions. The results are shown in figure 13.6. Recombination reactions at the wall do not modify the electron density in the core of the plasma. Near the wall the density decreases about two orders of magnitude in comparison to the bulk value. Due to the wall reactions also a lower peak value is reached at $z = 9\,\mathrm{cm}$. The modified profile of the electron density ensures that the largest power density due to ohmic heating is now reached on the axis rather than near the wall. The overall lower number of electrons decreases the elastic energy losses to the heavy particles and therefore increases the electron temperature by about 4 kK. When wall reactions are included in the $Ar + SiCl_4$ mixture the electron density is also expected to decrease several orders of magnitude near the wall. Its value on the axis is expected to be slightly lower as well. The decreased electron density will cause a similar increase in the electron temperature.

Currently, the wall chemistry is only dependent on the fluxes towards the wall. The model can further be improved by allowing species to be deposited on the quartz wall. Similarly to Lee [238] the wall chemistry is then dependent on the fractional coverage of the surface.

One of the main reasons for the instabilities in the model is the implementation of the current diffusion model. Since the background and electron species are not explicitly treated one of these quantities can reach negative values due to chemical reactions of other species. A self-consistent-diffusion model (see [6] or chapter 6) can prevent the occurrence of negative densities and will conserve mass.

Additionally, the model requires many iterations to converge. This is partially unavoidable due to the coupled nature of the modules for the chemistry, flow, electromagnetics and the energy balances. However, a decrease in calculation time can be obtained by making the code parallel or by using an adaptive grid. Also the chemistry can be simplified further using chemical reduction techniques. Two of the possible methods are ILDM (intrinsic low dimensional manifold, [4, ch. 7]) or PCA (principal component analysis [239]).

13.3.2 Spectral comparison

In order to obtain an estimate of the population of SiCl [B] an absolutely calibrated spectrum can be used. The vibrational spectrum measured in the experiment is integrated to obtain

$$L = \int_{\nu_a}^{\nu_b} I_\nu \mathrm{d}\nu. \tag{13.17}$$

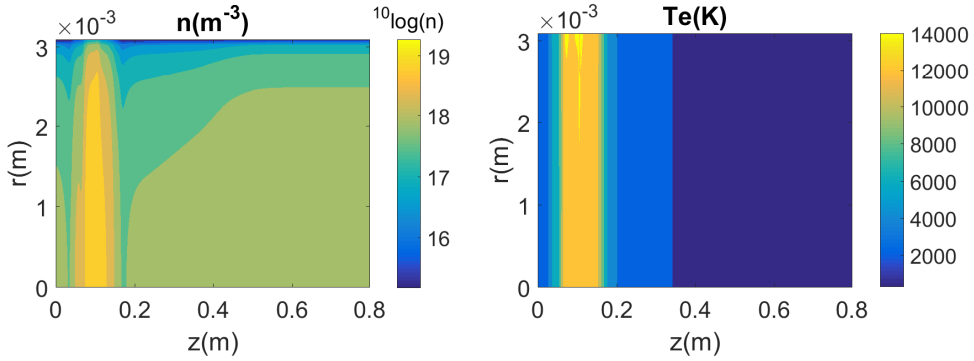

(a) Electron density. (b) Electron temperature.

Figure 13.6: Ar mixture with wall reactions.

The radiance from the vibrational spectrum is calculated using the optically thin limit

$$\begin{aligned} L &= \sum_{v'}\sum_{v''}\sum_{s} j_{\nu,v',v''}\Delta s \\ &= \sum_{v'}\sum_{v''}\sum_{s} \frac{h\nu_{v',v''}}{4\pi} n_{\mathrm{B},s,v'} q_{v',v''} A_{\mathrm{BX}} \Delta s, \end{aligned} \tag{13.18}$$

with v' the upper vibrational level, v'' the lower vibrational level and $q_{v',v''}$ the Franck-Condon factor[7]. In order to simplify the calculation, Kogelschatz is followed considering a single electro-vibrational transition and by neglecting the spatial variation of the species profile [241]. The transition probability is taken from Kogelschatz [241, p. 1959] as $A_{\mathrm{BX}} = 10^8\,\mathrm{s}^{-1}$. Based on the emission of visible light Δs is about 10 cm. The population of the first three vibrational states is then in the range of 1.0×10^{14}–$2.5 \times 10^{14}\,\mathrm{m}^{-3}$. The measured radiance is $2.7 \times 10^4\,\mathrm{W/m^2/sr}$.

In principle the simulation results from the 2D model can be used to predict a spectrum. Since wall reactions have been neglected the 2D results have a weak dependency on the radial coordinate. Therefore a simpler 1D model is considered by averaging the 2D profiles in radial direction. The species density is now only dependent on the axial coordinate. The following particle balance is considered

$$n_e n_{\mathrm{X}} K_{\mathrm{XB}} - n_e n_{\mathrm{B}} K_{\mathrm{BX}} - n_{\mathrm{B}} A_{\mathrm{BX}} + n_{\mathrm{e}}^2 n_{\mathrm{SiCl^+}} K_1 = 0, \tag{13.19}$$

with X referring to the ground state and B referring to the excited state. The rate

[7] In this case the Franck-Condon factors are calculated for the harmonic oscillator potential, see Chang [240].

coefficient for excitation is assumed to be given by the Arrhenius law

$$K_{\mathrm{XB}} = C \exp\left(-\frac{E_{\mathrm{BX}}}{k_B T_e}\right) \mathrm{m}^3/\mathrm{s} \tag{13.20}$$

$$K_{\mathrm{BX}} = C \frac{Z_{\mathrm{X}}}{Z_{\mathrm{B}}} \mathrm{m}^3/\mathrm{s} \tag{13.21}$$

$$K_1 = 7.54 \times 10^{-14} \frac{Z_{\mathrm{B}}}{2 Z_{\mathrm{SiCl}^+}} \left(\frac{h^2}{2\pi m_e k_B T_e}\right)^{3/2}, \tag{13.22}$$

with C an adjustable constant and K_{BX} the de-excitation rate calculated using detailed balancing. The partition sums are calculated by assuming that the vibrational temperature is equal to the heavy particle temperature.The rate coefficient K_1 is based on Lee's rate [238, table. 4] with an adjusted energy threshold. The rate is calculated by applying detailed balancing. In the current chemistry the most important production mechanism of SiCl is the reaction of electrons with $SiCl_2$. For SiCl [B] the increased threshold energy makes this reaction less important.

The calculated density profile of SiCl [B] is shown in figure 13.7. The most important production reactions are the direct excitation from SiCl and the recombination from $SiCl^+$. The dominant production reaction is dependent on the chosen value for C. For small values of C the recombination determines the equilibrium density while for large values of C the LTE value is approached. Neither of these limits is capable of reaching the spectral radiance measured in the experiment. This is related to the limitations of the 2D model where the influx of $SiCl_4$ and the input power where reduced to obtain a stable model. When the stability of the model is improved such a procedure can be used to gain more insight in the internal chemistry of $SiCl_x$ species. For now the density profile corresponding to $C = 1\,\mathrm{m}^3/\mathrm{s}$ is scaled to match the measured spectrum. The results are shown in figure 13.8. When more accurate modeling results are available such a procedure can be used to verify the predicted species and temperature profiles.

13.4 Conclusion

A 2D model of a surfatron plasma with an $\mathrm{Ar} + SiCl_4$ chemistry is made. The chemistry is compared to a pure Ar plasma. The presence of $SiCl_x$ increases the electron density with a factor 10 due to the lower ionization potential. In both plasmas it is observed that the dominant energy loss process for electrons is elastic energy transfer. The increased electron density decreases the maximum value for the electron temperature from 11.5 kK in pure Ar to 5.9 kK in $\mathrm{Ar} + SiCl_4$. The effect on the heavy particle temperature is smaller since the larger electron density is accompanied by a smaller volume with a significant difference between T_e and T_h. Additionally, it is observed that $SiCl_x$ and $SiCl_x^+$ with $x = 2$ and $x = 4$ are the most important species. They reach densities in the order of 10^{19}-$10^{20}\,\mathrm{m}^{-3}$.

The experimental conditions could not be modeled and therefore a simplified system was considered. These simplifications are necessary since the current diffusion algorithm (Fick's law) does not conserve mass. For that reason negative

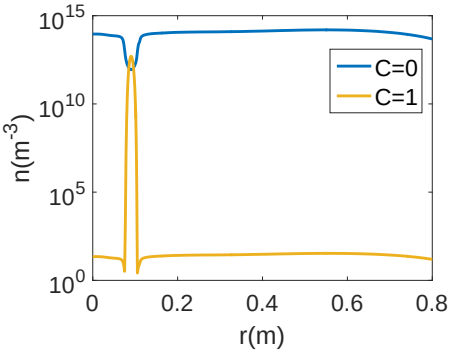

Figure 13.7: The estimated density profile of SiCl [B] in the two limits for C. For $C = 0\,\mathrm{m}^3/\mathrm{s}$ the recombination from $SiCl^+$ determines the equilibrium. For $C = 1\,\mathrm{m}^3/\mathrm{s}$ the excitation from the ground state of SiCl determines the equilibrium density.

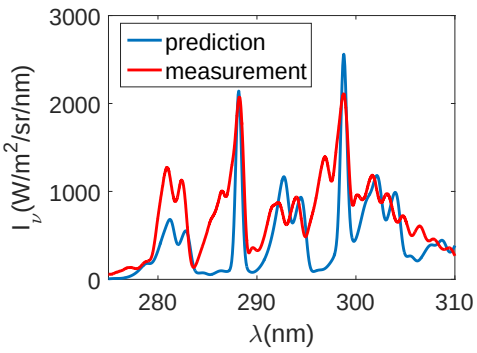

Figure 13.8: The density profile corresponding to $C = 1\,\mathrm{m}^3/\mathrm{s}$ (see figure 13.7) is scaled to match the measured spectrum.

densities are not strictly forbidden for the background gas or the electron density. It is expected that the self-consistent diffusion algorithm described in chapter 6 will improve the stability. Other improvements are related to a reduction of the calculation time. This could be achieved by parallelizing the code or using an adaptive grid. Chemistry reduction techniques can also be used to improve the convergence rate of the model.

In the future the model can be used as a diagnostic tool for the interpretation of spectra. An automatic routine should be developed that adjusts the predicted species densities in such a way that the simulated spectrum matches with the experimental spectrum. Such a routine uses integral quantities like the optical depth or $\int j_\nu ds$ to optimize the species densities. In order to approach a unique solution the spectrum should be measured and compared to the modeling results for multiple different viewing angles.

13.A Complex electrical conductivity

The derivation of the complex electrical conductivity is based on the work of Jiménez [3, p. 71,72]. In this section the vector nature is indicated with a bold font rather than the $\vec{x}$ notation. In the first step the momentum balance for the electrons is written as

$$m_e n_e \frac{\partial \tilde{\mathbf{u}}_e}{\partial t} = -\nabla \tilde{p}_e - e n_e \tilde{\mathbf{E}} + \tilde{\mathbf{R}}_e, \tag{13.23}$$

with a tilde indicating that the parameter is time dependent. The time dependency of the electron density during one pulse is neglected. Additionally the inertial term

and the viscosity are neglected. The friction of the electrons can be described with

$$\tilde{\mathbf{R}}_e = -m_e n_e \nu_{eh} \tilde{\mathbf{u}}_e, \tag{13.24}$$

with ν_{eh} the total collision frequency for electrons with heavy particles. In the cold plasma approximation the assumption is made that $\tilde{p_e} = 0$. By additionally assuming a harmonic time dependency the momentum balance is rewritten as

$$i\omega \mathbf{u}_e + \nu_{eh} \mathbf{u}_e = -\frac{e}{m_e} \mathbf{E}, \tag{13.25}$$

which gives

$$\mathbf{u}_e = \frac{-q_e \mathbf{E}}{m_e \left(\nu_{eh} + i\omega\right)}. \tag{13.26}$$

By introducing the current density $\mathbf{J} = q_e n_e \mathbf{u}_e = \tilde{\sigma} \mathbf{E}$ the conductivity can be derived as

$$\tilde{\sigma} = \frac{e^2 n_e}{m_e \left(\nu_{eh} + i\omega\right)} = \frac{\epsilon_0 \omega_p^2}{\nu_{eh} + i\omega}, \tag{13.27}$$

with ω_p the plasma frequency.

Chapter 14

Evaluation of angular scattering models for electron-neutral collisions in Monte Carlo simulations

In Monte Carlo simulations of electron transport through a neutral background gas, simplifying assumptions related to the shape of the angular distribution of electron-neutral scattering cross sections are usually made. This is mainly because full sets of differential scattering cross sections are rarely available. In this work simple models for angular scattering are compared to results from the recent quantum calculations of Zatsarinny and Bartschat for differential scattering cross sections (DCSs) from zero to 200 eV in argon. These simple models represent in various ways an approach to forward scattering with increasing electron energy. The simple models are then used in Monte Carlo simulations of range, straggling, and backscatter of electrons emitted from a surface into a volume filled with a neutral gas. It is shown that the assumptions of isotropic elastic scattering and of forward scattering for the inelastic collision process yield results within a few percent of those calculated using the DCSs of Zatsarinny and Bartschat. The quantities which were held constant in these comparisons are the elastic momentum transfer and total inelastic cross sections.

14.1 Introduction

In Monte Carlo simulations of electron transport in low temperature plasmas, it is commonly assumed that the elastic momentum transfer cross section and the total cross sections for the inelastic scattering processes and for ionization provide sufficient information about electron interactions with the neutral background gas.

Published as: J.F.J. Janssen, L.C. Pitchford, G.J.M. Hagelaar, J. van Dijk, *Evaluation of angular scattering models for electron-neutral collisions in Monte Carlo simulations* in PSST

The approach to forward scattering with increasing energy in electron-neutral collisions is usually not taken into account although some authors have done so by using simplified models for the angular scattering based on classical theory using a screened Coulomb potential or purely empirical formulae (see, for example, Boeuf & Marode [85]; Kushner [242]; Surendra et al. [243]; Belenguer & Pitchford [84]). The absence of detailed knowledge about the differential scattering cross sections (DCS) for electron-neutral collisions generally precludes more precise calculations.

Previous work suggests that the additional information about the DCS's is not very important in electron swarm conditions (low degree of excitation and ionization, uniform field [244]) except for high values of reduced electric field strength, E/N, the ratio of the electric field strength to the neutral density or when high precision is required. See for example, discussions in Haddad et al. [245]; Phelps and Pitchford [246]; Thomas & Thomas [247]; Reid [248]; Kunhardt & Tseng [249], Stojanovic and Petrovic [86]; among others. The conclusion from this literature is that the elastic momentum transfer cross section and total cross sections for excitation and ionization provide sufficient information for calculations of reasonably accurate swarm parameters up to E/N values of some 1000 Td. Note that assumptions related to the exact treatment of ionization processes are also important at high values of E/N. For example, assumptions related to growth renormalization [250, p. 724,725,729] and energy sharing in ionization can impact the swarm parameters significantly [246,251]. In this work we are mainly interested in effects of anisotropy on parameters that are more sensitive to the shape of the DCS at small scattering angles. For that purpose a special test case is developed where the impact on the range and straggling of an electron beam is considered.

Recently Zatsarinny and Bartschat (ZB) calculated the DCSs for elastic and a number of inelastic processes in argon for electron energies ranging from threshold to 200 eV [32]. These results are available through the LXCat website [252]. These calculated cross sections are in excellent agreement with recent high-precision measurements (Allan et al. [33]) Thus, these calculations provide an opportunity to benchmark assumptions commonly made about the influence of anisotropic scattering in Monte Carlo simulations in conditions where the electron energy distribution function is not in equilibrium with the local value of E/N. The work presented in this paper is a step towards this objective.

In section 14.2 of the following, several models for angular scattering are described, and the extent to which these models accurately represent the approach to forward scattering with increasing incident electron energy is evaluated by comparing with the DCSs from Zatsarinny and Bartschat for elastic scattering and for excitation of the upper resonance level, $4s[1/2]_1$, with a threshold at 11.828 eV. The DCS for this process is representative of most of the other allowed transitions. The accuracy of simple fitting formulas is evaluated in section 14.3. In Section 14.4, we present results using the different models for anisotropy in Monte Carlo simulations of range, straggling and backscatter of electrons injected from a surface with a given energy into a background gas. An electron beam with an initial energy of 500-1000 eV is considered in section 14.5 by extrapolating the cross sections beyond 200 eV. In section 14.6, conclusions and a discussion about the relevance of this work to more general discharge situations are presented.

14.2 Differential scattering cross sections

The total cross section, $Q_t(\epsilon)$, is defined by integrating the DCS over all scattering directions Ω. By assuming azimuthal symmetry the scattering directions can be calculated from $\mathrm{d}\Omega = 2\pi \sin\chi \mathrm{d}\chi$. The relation between the cross section and the DCS, $\frac{\mathrm{d}\sigma(\epsilon,\chi)}{\mathrm{d}\Omega}$, is then given by

$$Q_t(\epsilon) = 2\pi \int \frac{\mathrm{d}\sigma(\epsilon,\chi)}{\mathrm{d}\Omega} \sin\chi \mathrm{d}\chi, \tag{14.1}$$

with ϵ the energy and χ the angle between the velocity vectors of the incident particle before and after the collision. The angular distribution, $I(\epsilon,\chi)$, can be obtained by normalizing the DCS with the total cross section

$$I(\epsilon,\chi) = \frac{1}{Q_t(\epsilon)} \frac{\mathrm{d}\sigma(\epsilon,\chi)}{\mathrm{d}\Omega} \quad \leftrightarrow \quad \frac{\mathrm{d}\sigma(\epsilon,\chi)}{\mathrm{d}\Omega} = Q_t(\epsilon) I(\epsilon,\chi). \tag{14.2}$$

A consequence of this definition is that the angular distribution has the property

$$2\pi \int I(\epsilon,\chi) \sin\chi \mathrm{d}\chi = 1. \tag{14.3}$$

Equation 14.2 is a convenient formulation for our purposes because the shape of the cross section can be changed while keeping the total cross section, Q_t, constant. This is an important consideration when comparing results using different scattering models for the inelastic cross sections. For elastic collisions the constant quantity should be the elastic momentum transfer cross section so as to maintain the same momentum and energy loss in elastic scattering. This is easily accomplished in Monte Carlo simulations by setting the total elastic cross section equal to the momentum transfer cross section and thereafter assuming isotropic elastic scattering. The momentum transfer cross section Q_m can be calculated from

$$Q_m(\epsilon) = Q_t(\epsilon) 2\pi \int I(\epsilon,\chi)(1-\cos\chi)\sin\chi \mathrm{d}\chi. \tag{14.4}$$

Three types of analytical models for the angular distribution $I(\epsilon,\chi)$ will now be discussed. The first is derived from classical theory screened Coulomb scattering, and the second is from the Born approximation for inelastic scattering. These are all dependent on a single parameter. Thirdly, purely empirical formulae have also been proposed to describe the approach to forward scattering and these will also be briefly discussed.

In all cases, for numerical convenience in Monte Carlo simulations these analytical models are kept simple. In that case it is possible to obtain an analytical expression for the scattering angle in terms of a random number R by inverting

$$R = \frac{2\pi \int_0^{\chi} I(\epsilon,\chi') \sin\chi' \mathrm{d}\chi'}{2\pi \int_0^{\pi} I(\epsilon,\chi) \sin\chi \mathrm{d}\chi}. \tag{14.5}$$

The denominator in this expression is equal to one.

14.2.1 Elastic screened Coulomb scattering

Expressions for the angular distribution for elastic scattering have been derived for screened Coulomb scattering and presented previously in the low temperature plasma literature as discussed in references [84, 253, 254].

Belenguer & Pitchford [84] based their work on the screened Rutherford formula for differential scattering cross section given by Strickland et al. [255] who express the angular distribution as,

$$I(\epsilon, \chi) = \frac{\eta(\eta+1)}{\pi(2\eta+1-\cos\chi)^2}, \tag{14.6}$$

where η is the Coulomb screening parameter. According to Mott, the screening parameter can be calculated theoretically as [256, p. 463] [1]

$$\eta = \frac{1.89\text{eV}Z^{2/3}}{\epsilon}, \tag{14.7}$$

with Z the atomic number of the colliding particle and ϵ the energy. Strickland et al. refer to Jacob [257] for the screening parameter, who gives an expression similar to eq. 14.7 but with a prefactor of 10.9. The differences in the prefactor are not critical for the discussion here. Let us simply point out that several previous works have used the larger prefactor (references [258, p. 70] [259, p. 34] [121, p. 610]). Note that a higher prefactor causes the DCS to change from an isotropic to a forward directed distribution at a much higher energy.

The ratio of elastic momentum transfer to total elastic cross section, Q_m/Q_t, from the data compiled by Hayashi [260] in argon for energies up to 10 keV is not consistent with screened Coulomb scattering with a screening parameter depending on $1/\epsilon$. In an attempt to improve the accuracy of the angular distribution in eq. 14.6, Belenguer and Pitchford let η be a fitting function determined by matching to the Hayashi data for Q_m/Q_t. Although there is no reason to suppose that an angular distribution yielding a good representation of Q_m/Q_t will also represent well the forward peak. Nevertheless, we use this ratio to fix η because these data are sometimes available for elastic scattering of electrons and atoms or simple molecules whereas there are very few other data related to the angular distributions.

A similar approach was taken by Okhrimovskyy [253] et al. who proposed a generalized expression for the angular distribution for screened Coulomb scattering:

$$I(\epsilon, \chi) = \frac{1}{4\pi}\frac{1-\xi^2(\epsilon)}{(1-\xi(\epsilon)\cos\chi)^2}, \tag{14.8}$$

[1] Mott uses $\eta = \alpha^2 = \left(0.565 Z^{1/3} s \frac{2\pi e^2}{hv}\right)^2 = 0.565^2 Z^{2/3} s^2 \frac{2\pi^2 e^4 m_\epsilon}{h^2 \epsilon}$ with s dimensionless. Note that a factor $\frac{1}{(4\pi\epsilon_0)^2}$ is required to convert to SI units. Mott uses $s = 0.66$ to get agreement with the high energy limit of the Thomas-Fermi function. Additionally, Mott mentions that in order to get agreement with the DCS from Hartree-Fock calculations for $Z > 10$ the values cover the interval between $0.46 \leq s \leq 0.68$

where $\xi(\epsilon)$ is a fitting function. Equation 14.8 reduces to the angular distribution for conventional screened Coulomb scattering when [253, 254]

$$\xi = \frac{4\epsilon/\mathrm{E_H}}{1 + 4\epsilon/\mathrm{E_H}}, \tag{14.9}$$

with E_H representing one Hartree. Equations 14.6 and 14.8 are identical for $\xi = 1/(2\eta + 1)$ and so the screening length in eq. 14.6 can be formally identified as

$$\eta = \frac{\mathrm{E_H}}{8\epsilon} \approx \frac{3.4\mathrm{eV}}{\epsilon} \tag{14.10}$$

This expression differs again from eq. 14.7 in the prefactor but also by the lack of dependence on Z. Note that this relation is purely formal because η can no longer be identified with the physical concept of a screening length for the Coulomb potential. We will henceforth not use the term screening length, but will retain the symbol η and allow it to depend more generally on energy. As mentioned above, an alternate approach for estimating the energy dependence of the angular distribution is to choose η or ξ so that the ratio Q_m/Q_t is well represented by eq. 14.6 or eq. 14.8, respectively. However, in order to use this method, both Q_m and Q_t must be known. The ratio can be calculated analytically from

$$\frac{Q_m}{Q_t(\epsilon)} = 2\eta(\eta + 1)\ln\left(1 + \frac{1}{\eta}\right) - 2\eta, \tag{14.11}$$

where $-\infty < \eta < -1$ for $\frac{Q_m}{Q_t(\epsilon)} > 1$ and $0 < \eta < \infty$ for $\frac{Q_m}{Q_t(\epsilon)} < 1$.

Okhrimovskyy et al. provide estimates of $\xi(\epsilon)$ (and hence η) for Ar, N_2 and CH_4 based on the data compiled by Hayashi for the ratio Q_m/Q_t. As noted by Okhrimovskyy, a form for the angular dependence based on a screened Coulomb potential is not expected to be valid for polar molecules or other systems without spherical symmetry. Note, too, that many people use the formula for the scattering angle derived by Okhrimovskyy from the theory of screened Coulomb scattering for both elastic and inelastic scattering whereas inelastic scattering tends to be more peaked in the forward direction for a given energy (see for example, [256, p. 483] or the data from Zatsarinny and Bartschat on LXCat [252]).

Scattering angles can be related to a random number via

$$\cos\chi = \frac{\eta + 1 - R(1 + 2\eta)}{\eta + 1 - R}. \tag{14.12}$$

14.2.2 Inelastic scattering

An expression for the angular distribution of inelastic scattering can be derived from Mott et al. [256] and Massey et al. [261]. Interestingly this formula appears to be identical to an empirical formula suggested by Surendra. Surendra [243] used this formula for the elastic and inelastic scattering cross section of electrons and atoms. Surendra's expression is given by

$$I(\epsilon, \chi) = \frac{\epsilon/\mathrm{eV}}{4\pi\left[1 + \epsilon/\mathrm{eV}\sin^2\left(\frac{\chi}{2}\right)\right]\ln(1 + \epsilon/\mathrm{eV})}, \tag{14.13}$$

with eV used to obtain a dimensionless expression. Okhrimovskyy [253] and Khrabrov [254] note that this expression does not reduce to the correct limit for screened Coulomb interactions at high energies. Additionally, Okhrimovskyy observed that the energy normalization is arbitrary (for example 1 eV or 1 Hartree) and has no scientific background.

Based on the work of Mott et al. [256, p. 477,493] and Massey et al [261, p. 437] an expression for excitation can be obtained from

$$I(K)\,K\mathrm{d}K \propto \frac{1}{K^2}, \tag{14.14}$$

with

$$K^2 = k_0^2 + k_n^2 - 2k_0k_n\cos\chi, \tag{14.15}$$

representing the momentum change of the scattered electron [256, p. 476]. The relation between momentum and energy is given by

$$\epsilon_k = \frac{\hbar^2k^2}{2m}. \tag{14.16}$$

This approximation uses the expansion $\exp(iKz) \doteq 1 + iKz$ and is therefore not valid when the momentum exchange is large. Note that the momentum exchange is largest for backscattering. The formula is therefore most accurate for small angles. Additionally, the assumption is made that the relative energy transfer in collisions is small. Substituting this result in the DCS and changing variables from K to χ gives

$$I(\epsilon,\chi)\sin\chi\mathrm{d}\chi \propto \frac{\sin\chi\mathrm{d}\chi}{K^2}. \tag{14.17}$$

After normalization the DCS is given by [262] [2]

$$I(\epsilon,\chi) = \frac{\beta}{2\pi\ln\left(\frac{1+\beta}{1-\beta}\right)(1+\beta^2-2\beta\cos\chi)}, \tag{14.18}$$

with

$$\beta = \sqrt{1-\frac{\epsilon_{n0}}{\epsilon_n}}, \tag{14.19}$$

where ϵ_{n0} is the atomic transition energy and ϵ_n the initial energy of the electron. By applying the substitution $\epsilon/\mathrm{eV} = \frac{4\beta}{(\beta-1)^2}$ it can be shown that the inelastic formula is identical to Surendra's formula.

Alternatively, the parameter β can be determined from Q_t and Q_m as was done by Surendra [243]. In terms of the inelastic formula this ratio can be expressed as

$$\frac{Q_m}{Q_t(\epsilon)} = 1 - \frac{1+\beta^2}{2\beta} - \frac{1}{\ln\left(\frac{1+\beta}{1-\beta}\right)}. \tag{14.20}$$

[2] Based on the theory of the generalized oscillator strength [256, p. 478] [263] the same angular distribution is obtained.

The momentum transfer cross section for inelastic processes are rarely available and so this approach is of limited utility. For this DCS the scattering angle is related to a random number via

$$\cos\chi = \frac{1+\beta^2-(1+\beta)^2\exp(R)}{2\beta}. \tag{14.21}$$

14.2.3 Empirical formulae

In this section various empirical formulae and the corresponding relations between scattering angle and random number are discussed. The considered DCS are isotropic scattering, forward scattering and empirical formulae given by Kushner, Longo et al. and Belenguer et al.

Isotropic scattering is often used to describe the angular behavior of elastic collisions. The angular distribution is constant

$$I(\epsilon,\chi) = \frac{1}{4\pi}, \quad \cos\chi = 1-2R. \tag{14.22}$$

The ratio of the momentum transfer cross section and the total cross section reveals that for an isotropic DCS the momentum transfer cross section is equal to the total cross section ($Q_t = Q_m$). Inelastic processes are sometimes modeled with forward scattering. In that case the electron continues in the same direction without being scattered

$$I(\epsilon,\chi) = \frac{\delta(\chi)}{2\pi\sin\chi}, \quad \cos\chi = 1. \tag{14.23}$$

Longo and Capitelli [264] propose another way of using Q_t and Q_m for elastic scattering, when both are available, in Monte Carlo codes. Their idea is to model the DCS as the sum of two terms one representing isotropic scattering in the forward direction ($\chi \leq \pi/2$) and the other isotropic scattering in the backward direction ($\chi \geq \pi/2$). The magnitudes of each of the two terms are adjusted for consistency with known values of Q_t and Q_m. Kushner [242] introduced an empirical expression for forward scattering which is given by

$$I(\epsilon,\chi) = \frac{n+2}{8\pi}\cos^n\left(\frac{\chi}{2}\right), \tag{14.24}$$

with n an energy dependent fitting parameter. Kushner suggests to set $n = 3$ when no experimental data are available. This parameterization contains no dependence on the initial kinetic energy and thus will not be able to reproduce the DCS for a large spectrum of energies. In this case the connection between the scattering angle and a random number is given by

$$\cos\chi = 2(1-R)^{2/(n+2)} - 1. \tag{14.25}$$

Another empirical formula has been suggested by Belenguer and Pitchford [84] and is given by

$$I(\epsilon,\chi) = I_0(\epsilon) + I_1(\epsilon)\cos\chi + I_2(\epsilon)\cos^2\chi. \tag{14.26}$$

Table 14.1: Definition of the labels that have been used in the figures 14.1a-14.2b.

Label	Explanation
ZB	Quantum mechanical calculation of DCS data from Zatsarinny and Bartschat
Mott	Elastic screened Coulomb (14.6) with η from (14.7) for the screening parameter
SC	Elastic screened Coulomb (14.6) with η from (14.10)
SC Q_m/Q_t	Elastic screened Coulomb (14.6) with η from the ratio Q_m/Q_t (14.11) using the data from ZB for elastic scattering
SCI	Inelastic screened Coulomb (14.18) with β from (14.19)
SCI Q_m/Q_t	Inelastic screened Coulomb (14.18) with β from the ratio Q_m/Q_t (14.20) using the data from ZB for inelastic scattering
Surendra	Empirical formula proposed by Surendra (14.13) for elastic and inelastic processes.
Kushner	Empirical formula (14.24) suggested by Kushner with $n = 3$.
CUS	Direct fit using (14.28) for optically allowed inelastic transitions with C given by (14.29) and η given by (14.30).

This method requires $Q_t(\epsilon)$, $Q_m(\epsilon)$ and $Q_v(\epsilon)$ (the viscosity cross section, obtained by multiplying the DCS by $\left(1-\cos^2\chi\right)$ and integrating over all angles) to obtain the values of $I_0(\epsilon)$, $I_1(\epsilon)$ and $I_2(\epsilon)$. The calculations reported by Belenguer and Pitchford used data from Hayashi [260] for these quantities for elastic scattering.

14.2.4 Comparison to the ab initio DCS

This section contains an evaluation of the theoretical estimates of the DCS's given in the previous sections. Only the results for the excitation from the ground state to 4s'$[1/2]_1$ are shown since the results of the other optically allowed transitions are very similar. The results for incident energies of 25, 80 and 200 eV for the inelastic process and the 200 eV for the elastic process are shown in figures 14.1a-14.1d. The half-width-at-half-maximum (HWHM) for the angular distribution of both processes is shown in figures 14.2a and 14.2b. The labels in the figures are explained in table 14.1.

The excitation process is not well described by any of the generalized models. The best results are obtained by using the ratio $\frac{Q_m}{Q_t(\epsilon)}$ to estimate η in the elastic screened Coulomb formula. This approach roughly describes the increased probability at small angles and the subsequent decay for larger angles. The HWHM of the angular distribution is also roughly described accurately by this approach. However, the oscillations at larger angles found by Zatsarinny and Bartschat are of course not reproduced. Especially the probability for backscattering is underes-

timated. The inelastic formula with the analytical parameterization gives the best agreement with the HWHM derived from the data of Zatsarinny and Bartschat. However, the angular distribution does not describe the peak well and significantly overestimates the probability for large angle scattering. Similarly a fit of Q_m/Q_t using the inelastic formula underestimates the peak and its width while it describes the large angle scattering relatively well. The remaining methods describe neither the peak nor the width accurately.

For elastic collisions the theoretical expressions perform better. The model SC which uses the parameterization given by Okhrimovskyy performs well for the probability at small angles. The HWHM of the angular distribution approaches the correct value for energies above 60 eV. The decreasing trend for the probability at larger angles is also reproduced. However, the oscillations in the angular distribution which lead to a considerably larger backscattering probability are not captured by the model. Interestingly the model proposed by Surendra and the SCI fit of Q_m/Q_t also produces a reasonable agreement with the scattering probability at small angles. The backscattering probability is slightly underestimated. Additionally, the width of the angular distribution follows a similar behavior as the SC model for energies above 100 eV. In comparison to the SC model the decaying trend for the probability of scattering is much smaller. This trend is more in agreement with the large angle behavior of Zatsarinny and Bartschat, but still cannot capture the various oscillations.

In summary, the simple models aim only to capture the approach to forward scattering with increasing energy. They are not intended to reproduce the structure at low energy or the backscatter at intermediate energies. The inelastic processes are approximated most accurately with the SC Q_m/Q_t model where "accuracy" is evaluated by comparing the probability at small angles and the HWHM of the forward peak in the calculations. This approximation still underestimates the scattering probability at small angles by a factor in the order of 2 at 200 eV. Additionally, the width of the angular distribution is overestimated by this formula. The inelastic processes are therefore not accurately represented with the theoretical formulae. The elastic cross sections are most accurately represented by the SC model. Both the probability for small angles and the width of the distribution are described accurately. However, the large angle scattering is underestimated.

14.3 Direct fits

The analytical formulas for representing the DCS are not easily modified to account for the quantum mechanical oscillations that are significant at low energies. Additionally, the DCS at low scattering angles for multiple processes may not be captured by a single parameterization. In order to avoid these difficulties a fit is used for individual collision processes. Two fit functions are considered. The first

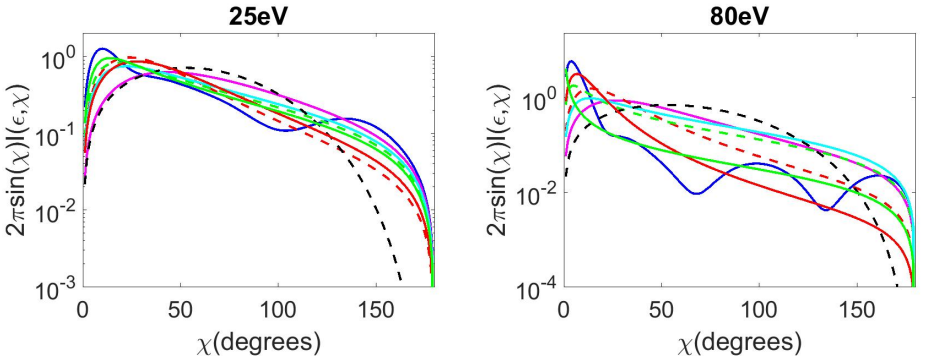

(a) Inelastic DCS at 25 eV.

(b) Inelastic DCS at 80 eV.

(c) Inelastic DCS at 200 eV.

(d) Elastic DCS at 200 eV.

Figure 14.1: The DCS for various angular distributions and initial kinetic energies. The inelastic process refers to excitations towards 4s'$[1/2]_1$. The labels are explained in table 14.1. Legend: ZB ; Mott ; SC ; SCI ; Surendra ; Kushner ; SC Q_m/Q_t ; SCI Q_m/Q_t .

fit function is given by

$$2\pi I(\epsilon,\chi)\sin\chi = \left(\frac{C}{2} + (1-C)\frac{\beta}{\ln\left(\frac{1+\beta}{1-\beta}\right)(1+\beta^2-2\beta\cos\chi)}\right)\sin\chi. \quad (14.27)$$

and the second fit function is given by

$$2\pi I(\epsilon,\chi)\sin\chi = \left(\frac{C}{2} + 2(1-C)\frac{\eta(\eta+1)}{(2\eta+1-\cos\chi)^2}\right)\sin\chi. \quad (14.28)$$

The DCS thus consists of two contributions. The first function is responsible for the large angle scattering. All structure that is present in the quantum mechanical calculations is approximated with an isotropic scattering function. The

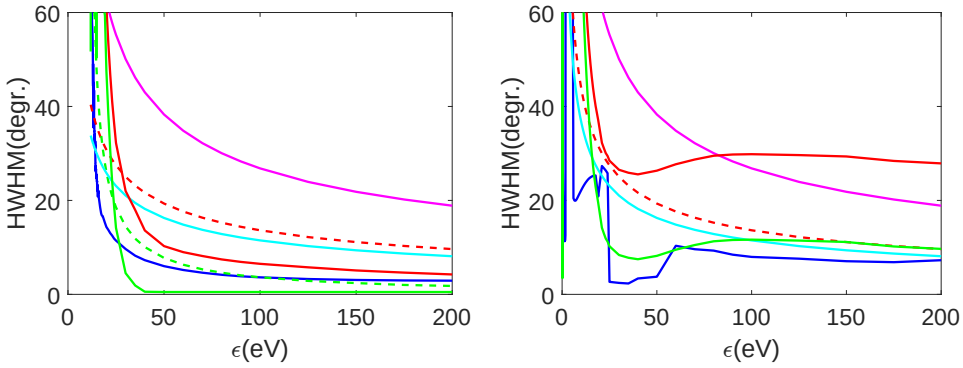

(a) Excitation from the ground state to 4s'$[1/2]_1$.

(b) Elastic collisions.

Figure 14.2: The HWHM for various angular distributions. The labels are explained in table 14.1. Legend: ZB (—), Mott (—), SC (- - -), SCI (- - -), Surendra (—), SC Q_m/Q_t (—) and SCI Q_m/Q_t (—).

second function is included for fitting the angular distribution for small scattering angles at high energies. The parameter C should be considered as the probability of a collision with an isotropic angular distribution. In this case the quantity $2\pi I(\epsilon,\chi)\sin\chi$ rather than $I(\epsilon,\chi)$ was fitted, because the former quantity is directly proportional to the angular distribution that is used in Monte Carlo simulations. The fit results using both quantities deviate in the order of a few percent.

In principle it is possible to determine the parameters analytically by using (14.3) and an additional criterion. These criteria can for example be the value at $I(\epsilon,\chi_x)$, the width at $r = \frac{I(\epsilon,\chi_r)}{I(\epsilon,0)}$, the ratio $\frac{Q_m}{Q_t(\epsilon)}$ [84, 253, 254] or the ratio of forward over backward scattering [265] $\frac{f}{b} = \frac{2\pi\int_0^{\pi/2} I(\epsilon,\chi)\sin(\chi)d\chi}{2\pi\int_{\pi/2}^{\pi} I(\epsilon,\chi)\sin(\chi)d\chi}$. The drawback of most of these methods is that knowledge of the DCS is required in order to use these methods. However, when such data are available a direct fit is superior. The method that uses the ratio of the momentum transfer cross section and the total cross section can be used without knowing the DCS. However, the previous sections have shown that the results are not very accurate for the inelastic processes.

The fitted DCS and the ab initio results are compared in figures 14.3 and 14.4 for the inelastic transition from the ground state to 4s'$[1/2]_1$. The images show that the overall agreement between (14.28) and the ab initio results is better than the overall agreement with (14.27). This behavior is similar for different energies and different excitation processes. For this reason only fit function (14.28) is considered in the remainder of this section. Surendra already noted that the inelastic DCS is approximately similar to the elastic DCS when the energy of the electron after the inelastic process is used to calculate the DCS [243, p. 1118]. He based his conclusion on data provided by Massey and Burhop. The similarity is

	a_1(1/eV)	a_2
p_1	-24(±30)	2.5×10^2 (±400)
p_2	-0.22(±0.3)	3.9 (±4)
d_1	0.37(±0.4)	-3.1 (±5)
d_2	0.053(±0.08)	0.77 (±1)

Table 14.2: Fit parameters for the parameters p_i and d_i that are used to calculate C and η. The values indicated in brackets define a 95% confidence interval.

confirmed by the fact that the fitted elastic screened Coulomb formula gives the best description of the calculated DCS. However, the inelastic optically allowed processes seem to converge to $\lim_{\epsilon\to\infty}\eta = 0$ while the data up to 200 eV suggests an asymptote for η corresponding to the elastic process.

The usage of the parameters C and η as a function of ϵ is a simplification of the original large lookup table obtained from LXCat. Another simplification is possible by using a fit function for these parameters. These formulas are given by

$$C(\epsilon) = \frac{\epsilon}{p_1} + p_2, \tag{14.29}$$

and

$$\eta(\epsilon) = \left(\frac{d_1}{\epsilon}\right)^{d_2}, \tag{14.30}$$

with p_i and d_i fit parameters. Note that C is should not exceed the range $0 \leq C \leq 1$. In figure 14.5 the fit for C is shown. This figure shows that for low energies the DCS reduces to an isotropic angular distribution. In figure 14.6 the fit for η is shown. When η approaches 0 at high energies the angular distribution is strongly peaked at small angles. For lower energies the quality of the fit decreases. Since the DCS becomes isotropic at these energies a decreased accuracy in the fit for η is less of a concern in this energy range.

Another generalization is possible by writing the parameters d_i and p_i as

$$x_i = a_1\Delta\epsilon + a_2, \tag{14.31}$$

with a_i a fit parameter and $\Delta\epsilon$ the excitation energy obtained from the ab initio calculations. The values obtained by including the excitations from the ground state to $4s[3/2]_1$, $4s'[1/2]_1$, $5s[3/2]_1$, $3d[3/2]_1$, $5s'[1/2]_1$ and $3d'[3/2]_1$ are shown in Table 14.2. The fit parameters have a 95% confidence interval. The confidence interval is of the order of magnitude of the magnitude of the fit parameters. Such an error can be expected since the data points at $\Delta\epsilon \approx 14$ eV cover a wide range of values as is shown in figures 14.7-14.8. Since the confidence intervals are significant the fit is not able to reproduce the DCS of all the included excitation processes accurately. Due to the limited applicability of the general fit from now on only the specific fits are considered for the excitation processes.

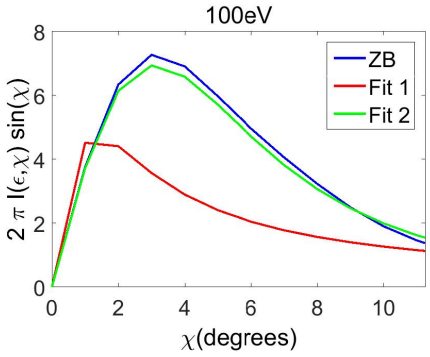

Figure 14.3: For the excitation from the ground state to 4s'$[1/2]_1$ and an incident energy of 100 eV the fit functions (14.27), Fit 1, and (14.28), Fit 2, are compared with the ab initio results of Zatsarinny and Bartschat.

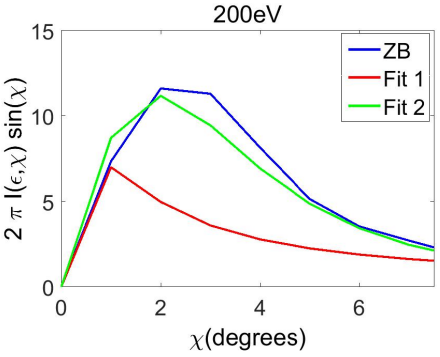

Figure 14.4: For the excitation from the ground state to 4s'$[1/2]_1$ and an incident energy of 200 eV the fit functions (14.27), Fit 1, and (14.28), Fit 2, are compared with the ab initio results of Zatsarinny and Bartschat.

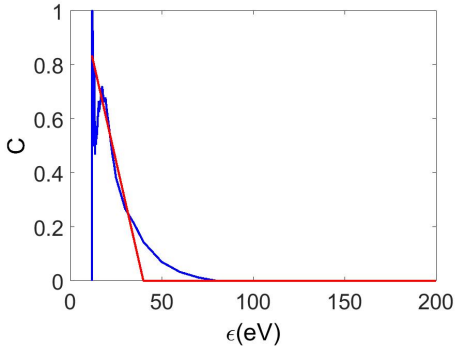

Figure 14.5: For the excitation from the ground state to 4s'$[1/2]_1$ the results of the fit using (14.28) for parameter C are shown in blue. These results are fitted with (14.29) as shown in red.

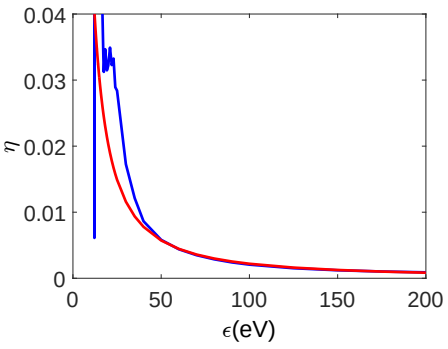

Figure 14.6: For the excitation from the ground state to 4s'$[1/2]_1$ the results of the fit using (14.28) for parameter η are shown in blue. These results are fitted with (14.30) as shown in red.

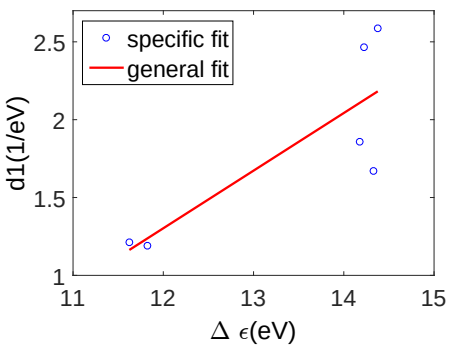

Figure 14.7: Fit of the coefficients d_1.

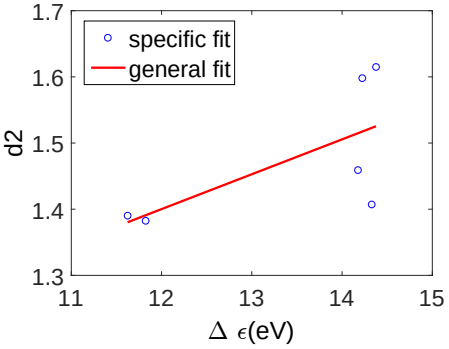

Figure 14.8: Fit of the coefficients d_2.

14.4 Quantification of anisotropy using Monte Carlo

The effects of the different scattering models are investigated for Monte Carlo simulations of a very simple model system using the modeling platform PLASIMO [25, 259]: a 50-200 eV electron beam injected into a background gas of simplified argon atoms. Electrons in this energy range occur in negative glows near the cathode in DC gas discharges and constitute perhaps the most basic system in which effects of anisotropic scattering are expected to show up. The simplified argon atoms that are considered can interact with an electron according to the following processes:

- An elastic process.
- An excitation process. The angular distribution is taken from the excitation from the ground state towards 4s'$[1/2]_1$. The cross section of the inelastic process is scaled to vary the importance of the inelastic collisions.

This two-level system is sufficient for the purpose of comparing quantities calculated with different models for the angular scattering for both processes individually[3]. The scattering of the elastic process is approximated with two different models. These are isotropic scattering and the DCS calculated by Zatsarinny and Bartschat. Different scattering models are considered for the inelastic process.

The scale factors that are considered are based on the sum of all cross sections. These cross sections are given in figure 14.9. The data for the excitation processes are obtained by integrating the DCS provided by Zatsarinny and Bartschat. The DCS for the ionization process was not calculated so the total scattering from other calculations of Zatsarinny and Bartschat is considered here in calculating the sum

[3]The data set provided by Zatsarinny and Bartschat does not contain the ionization process. An improved model can be made if the DCS for the ionization process is more accurately known. Additionally, when ionization processes are included other choices impact the model as well. One of these choices is the energy sharing ratio. In this work only the impact of the DCS on the range and straggling is evaluated.

of the total cross sections [32, 33, 229]. The strongest excitation process is the transition towards 4s'$[1/2]_1$. However, the ionization process has an even larger cross section. In order to represent approximately the sum of all inelastic and ionization processes, the transition towards 4s'$[1/2]_1$ should be scaled by a factor of about 10 as indicated in figure 14.10. An overestimate of the importance of the inelastic DCS can be obtained by scaling the inelastic process with a factor of 100. Both cases are investigated. The total cross sections and momentum transfer cross section for the elastic and inelastic processes considered are displayed in figure 14.11. For $\epsilon > 50\,\mathrm{eV}$ the elastic and the inelastic processes have approximately equal probabilities when isotropic scattering is used with $Q_t = Q_m$ for elastic scattering.

The simulated geometry consists of an infinite half-space ($z \leq 0$). This plane represents a cathode. Electrons are emitted with a given energy from the center of the cathode at $r = 0$ with a velocity directed normal to the surface. Electrons backscattered to the cathode are removed from the simulation. In this test the focus lies on the distribution of the inelastic scattering events. Electrons that do not have enough energy left for another excitation process are therefore removed. Two statistics related to this position are collected

- Range: It is defined as the average position in space where electrons are removed from the simulation, i.e., where their energy drops below the excitation threshold. These electrons will be referred to as 'stopped' electrons. The range can thus be calculated from

$$R_z = \langle z \rangle = \int_0^\infty z P\left(r, z\right) \mathrm{d}V, \tag{14.32}$$

  with $P\left(r, z\right)$ the probability density function of stopped electrons per volume V.

- Straggling: It is a measure of the spread in the range. It is defined as the standard deviation of the range and can be calculated from

$$S_z = \left\langle \left(z - R_z\right)^2 \right\rangle = \int_0^\infty z^2 P\left(r, z\right) \mathrm{d}V - R_z^2. \tag{14.33}$$

Analogous expressions can be derived for the radial direction. A total number of 1×10^8 electrons is considered. The Monte Carlo code used for these simulations is described by Brok [259] The standard deviation of the mean (range) is then given by [266]

$$S_R = \frac{S}{\sqrt{n}} = \frac{S}{10^4}, \tag{14.34}$$

with R representing the range and S the straggling. Similarly the standard deviation of the straggling is approximated with

$$S_S = \frac{S}{\sqrt{2\left(n-1\right)}} \approx 7 \times 10^{-5} S. \tag{14.35}$$

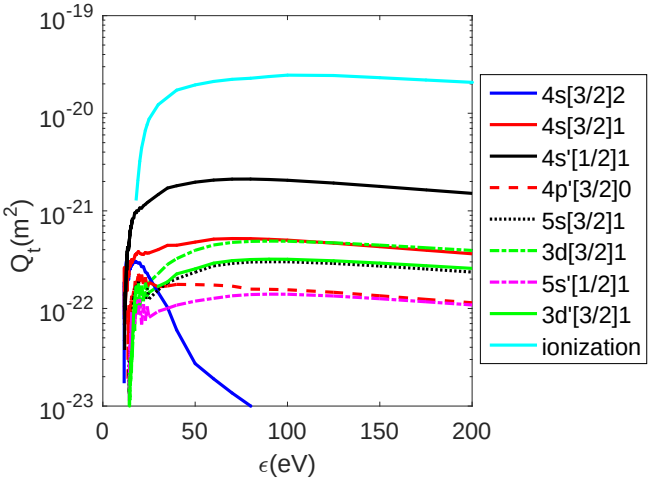

Figure 14.9: Cross sections obtained by integrating the DCS from [252]. The ionization cross section is taken from [32, 33, 229]. The excitation cross sections deviate slightly between both datasets.

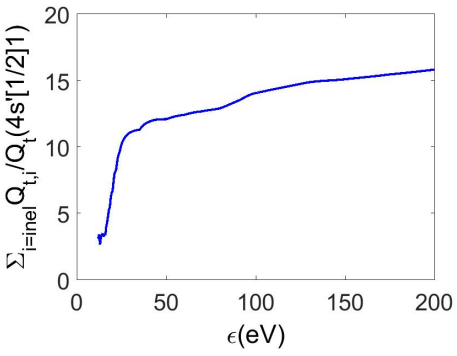

Figure 14.10: The ratio of the sum of all inelastic processes (including ionization) relative to the excitation process towards $4s'[1/2]_1$.

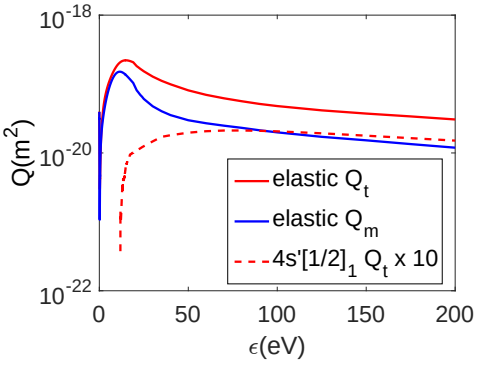

Figure 14.11: The total and momentum transfer cross section for the elastic and the inelastic $4s'[1/2]_1$ transition are shown. The inelastic cross sections are scaled by a factor of 10.

Since the straggling is of the same order of magnitude as the range the relative accuracy of both quantities is in the order of 10^{-4}.

For an initial energy of 200 eV and a scale factor of 10 the distribution of stopped electrons is shown for different elastic and inelastic scattering models in figures 14.14a, 14.14e and 14.14e. The spatial profile of stopped electrons using the data from Zatsarinny and Bartschat is similar to the profile obtained using forward scattering (FOR). The calculated range using isotropic scattering (ISO) is significantly reduced in comparison to the other models. These differences can be explained by noting that the probabilities for an inelastic collision are in the order of 50 % for $\epsilon > 100$ eV. For isotropic inelastic collisions all collisions are isotropic while for forward scattering only half of the collisions are isotropic. The differences between FOR and the ab initio results are much smaller since for $\epsilon > 100$ eV the ab initio results converge to the FOR model. The differences between FOR and the data from Zatsarinny and Bartschat are more pronounced on the axis since the probability of forward scattering decreases for lower energies in the ab initio results. Further away from the axis the discrepancies between the two sets are smaller, since electrons that can reach these positions encountered at least one (random) large angle collision.

The data for all considered models is shown in Table 14.3. The table shows that the CUS model, given by eq. 14.28, and the elastic screened Coulomb fit using SC $\frac{Q_m}{Q_t}$ provide an accurate description of the range and straggling. In comparison with the ab initio data the relative errors for the axial range are in the order of 1 %. The elastic screened Coulomb model (SC) and the inelastic screened Coulomb model (SCI) are less accurate with relative errors ranging from 5 to 10 %. In the absence of any DCS or Q_m data the CUS and SC $\frac{Q_m}{Q_t}$ models cannot be used. The best approximation in such a situation is the FOR model with a relative error of 2.4 % in comparison to the ab initio data. The backscattering for most models is predicted correctly within 2 % of the data from Zatsarinny and Bartschat. The exceptions are the isotropic and SCI models which differ more from the baseline case (ZB) than the other models do. Similar conclusions can be made when the DCS calculated by Zatsarinny and Bartschat is used for elastic collisions. In fact the results only differ up to 2 % in comparison to the simulation that uses isotropic scattering for elastic collisions with the same momentum transfer cross section. The results confirm that the elastic collisions are approximated well with isotropic scattering. This is expected since figure 14.1d shows a DCS at 200 eV that decays slowly as a function of scattering angle.

The influence of use of different models for anisotropic scattering can be emphasized by using a scaling factor of 100 for the inelastic process. These results are shown in figures 14.14b, 14.14d and 14.14f. The spatial profile of stopped electrons using the FOR model is still quite similar to the results of the ab initio calculations. The main differences are visible on the axis. Due to the increased cross section of the inelastic collision the probability of an inelastic collision is larger than two times the probability of an elastic collision for $\epsilon > 20$ eV. As a result many electrons in the FOR model did not have a single elastic encounter. These electrons are still on the axis when their energy drops below the threshold energy. Another effect of the increased probability of the inelastic process is that

Table 14.3: Results for a scale factor of 10 and an input energy of 200 eV. 'R' represents the range, 'S' the straggling and 'B' the electrons backscattered to the cathode. The top section shows the results by assuming an isotropic DCS for the electrons with the elastic Q_m from ZB. The bottom section shows the results by using the elastic DCS calculated by ZB. The labels are defined in Table 14.1.

Simulation	R_z(m)	error(%)	S_z(m)	error (%)	S_x(m)	B(%)
Isotropic elastic scattering with Q_m from ZB						
ZB	1.98e-02	0.0	1.16e-02	0.0	1.50e-02	51.6
CUS	2.00e-02	1.3	1.18e-02	1.1	1.53e-02	51.1
FOR	2.03e-02	2.4	1.19e-02	2.3	1.53e-02	51.0
ISO	1.45e-02	-26.7	8.74e-03	-25.0	1.19e-02	65.1
SC Q_m/Q_t	1.97e-02	-0.5	1.16e-02	-0.7	1.51e-02	51.4
SC	1.87e-02	-5.3	1.10e-02	-5.2	1.48e-02	52.6
SCI	1.79e-02	-9.6	1.06e-02	-8.9	1.43e-02	55.2
Anisotropic elastic scattering from ZB						
ZB	2.01e-02	0.0	1.18e-02	0.0	1.51e-02	50.8
CUS	2.03e-02	1.3	1.19e-02	1.1	1.53e-02	50.4
FOR	2.06e-02	2.5	1.20e-02	2.3	1.54e-02	50.3
ISO	1.45e-02	-27.5	8.77e-03	-25.4	1.20e-02	64.7
SC Q_m/Q_t	1.99e-02	-0.6	1.17e-02	-0.7	1.52e-02	50.6
SC	1.89e-02	-5.8	1.11e-02	-5.3	1.49e-02	51.9
SCI	1.80e-02	-10.3	1.07e-02	-9.1	1.43e-02	54.6

the differences between the ab initio results and the ISO model are much more pronounced in the spatial profile of stopped electrons.

The data for all considered models is shown in Table 14.4. Again the CUS and SC Q_m/Q_t model give the best reproduction of the axial range. The relative errors are 7.1 % and 4.1 % respectively. Even for these extreme conditions the FOR model produces a relative error of only 15.6 %. These errors are mainly caused by the fact that the ab initio data contain a small probability for large angle scattering. This effect is more pronounced for a DCS at lower energies. The predictions for the axial range by the SC and SCI models are off by 24.7 % and 36.1 %, respectively. Thus for an initial kinetic energy of 200 eV the FOR model also requires no additional input and performs better. The backscattering is not well predicted with such large cross sections. Most models make an error in the order of 14-22 %. Larger errors are made for the ISO and the SCI models. The impact on the results induced by changing the elastic cross section to the calculated cross section by Zatsarinny and Bartschat now is a bit stronger. However, the impact is restricted to about 5 % and is therefore still relatively small.

Similar tests have been made for input energies of 50 eV. The results of these tests are shown in Table 14.5. For a scale factor of 10 the results are similar to the ab initio results, since the probability for an inelastic process is low. The ISO model produces the largest relative error with 9 %. The errors for the FOR model is in the order of 2-3 %. The usage of forward scattering as an approximation for

Table 14.4: Results for a scale factor of 100 and an input energy of 200 eV. 'R' represents the range, 'S' the straggling and 'B' the electrons backscattered to the cathode. The top section shows the results by assuming an isotropic DCS for the electrons with the elastic Q_m from ZB. The bottom section shows the results by using the elastic DCS calculated by ZB. The labels are defined in 14.1.

Simulation	R_z(m)	error(%)	S_z(m)	error (%)	S_x(m)	B(%)
Isotropic elastic scattering with Q_m from ZB						
ZB	5.01e-03	0.0	2.59e-03	0.0	2.27e-03	18.6
CUS	5.37e-03	7.1	2.59e-03	0.0	2.35e-03	14.9
FOR	5.79e-03	15.6	2.79e-03	7.8	2.18e-03	14.6
ISO	1.98e-03	-60.5	1.26e-03	-51.5	1.64e-03	58.6
SC Q_m/Q_t	4.80e-03	-4.1	2.41e-03	-6.9	2.51e-03	16.0
SC	3.77e-03	-24.7	2.11e-03	-18.4	2.54e-03	22.0
SCI	3.20e-03	-36.1	1.93e-03	-25.4	2.34e-03	33.3
Anisotropic elastic scattering from ZB						
ZB	5.13e-03	0.0	2.54e-03	0.0	2.25e-03	19.1
CUS	5.51e-03	7.3	2.52e-03	-0.9	2.33e-03	15.4
FOR	5.99e-03	16.8	2.67e-03	4.8	2.14e-03	15.5
ISO	1.98e-03	-61.4	1.26e-03	-50.6	1.64e-03	58.6
SC Q_m/Q_t	4.88e-03	-4.8	2.39e-03	-6.1	2.50e-03	16.1
SC	3.80e-03	-26.0	2.12e-03	-16.7	2.54e-03	21.8
SCI	3.21e-03	-37.4	1.94e-03	-23.8	2.35e-03	33.1

Table 14.5: Results for a scale factor of 10 and 100 and an input energy of 50 eV. 'R' represents the range and 'S' the straggling for a specific coordinate. The definitions of the abbreviations for the simulations are given in the text.

Simulation	R_z(m)	error(%)	S_z(m)	error (%)	R_x(m)	S_x(m)
scale factor 10						
ZB	6.62e-03	0.0	4.26e-03	0.0	-1.47e-07	5.04e-03
FOR	6.78e-03	2.5	4.33e-03	1.5	-3.77e-07	5.08e-03
ISO	6.02e-03	-9.0	4.04e-03	-5.3	-8.88e-07	4.90e-03
scale factor 100						
ZB	1.62e-03	0.0	1.04e-03	0.0	1.46e-07	9.61e-04
FOR	1.87e-03	15.5	1.12e-03	7.6	-1.44e-07	8.89e-04
ISO	1.11e-03	-31.4	8.40e-04	-19.6	-1.15e-07	9.71e-04

inelastic processes thus appears to be very accurate. For a scale factor of 100 the differences in results from the various models are more pronounced. Again the ISO model has the largest relative error with 31.4 %. The FOR model reaches a relative error of 15.5 %. The relative errors for predicting the range for a beam of 50 eV are similar to the errors for the 200 eV beam. The relative error of the predicted straggling is about 5 % larger for the 50 eV beam for a scale factor of 10. The differences between the predictions for the beams are thus relatively small.

14.5 Extrapolating the cross sections

Predictions of the range, straggling and backscattering for energies above 200 eV are possible if the cross sections are extrapolated. The elastic cross section and the inelastic total cross section are extrapolated with

$$Q_t(\epsilon) = c_1 \frac{\ln \epsilon + c_2}{\epsilon}, \tag{14.36}$$

which is based on a simplified Bethe formula for excitation cross sections [267, eq. 10]. The high energy part of the momentum transfer cross section was fitted with [246, eq. A.2]

$$Q_m = \frac{s_1}{(\epsilon - s_2)^2}, \tag{14.37}$$

with c_i and s_i fit parameters. The results using the extrapolated cross section for a beam with an initial energy of 500 eV are given in table 14.6. Due to the absence of a calculated DCS for $\epsilon \geq 200$ eV the accuracy of the individual models cannot be evaluated. The reference for the calculations is therefore the FOR model which would be used if no data are available. By using an isotropic elastic DCS the results using CUS and SC Q_m/Q_t agree well with forward scattering with differences below 1 %. These models gave the best reproduction of the ab initio data below 200 eV. This is an indication that the FOR model results are a good approximation for the real DCS. When the SC and SCI models are used the errors increase up to 13 %. Using an isotropic model for the inelastic DCS results in large errors again. The same calculations with the elastic cross section replaced by the ab initio results show similar differences relative to the FOR case. The differences between both sets are in the order of 1 %. Since the ab initio results above 200 eV use the DCS at 200 eV the results may change when the correct DCS is used. However, a fit using (14.28) shows that the parameters C and η seem to approach an asymptote. This is an indication that the chosen extrapolation method could be accurate. The results of this fit are displayed in 14.12 and 14.13.

The results for a beam with an initial energy of 1000 eV are given in table 14.7. The table shows similar relative differences from the FOR model as the 500 eV beam. This time the differences between both elastic cross section sets are in the order of 2-3 %. A calculation of the elastic DCS for energies above 200 eV is desirable to evaluate the accuracy of the used extrapolations. In that case it is also possible to verify the trend suggested in 14.12 and 14.13.

14.6 Conclusions

Analytical formulae for the DCS have been compared with the DCS calculated by Zatsarinny and Bartschat who used the B-spline R-matrix method for elastic and inelastic collisions for electrons with argon. The forward scattering of the elastic DCS can be approximated accurately by the screened Coulomb model that uses the parameterization given in eq. 14.10. However, the large angle behavior is not taken into account which makes the overall agreement rather poor. The

Table 14.6: Results for a scale factor of 10 and an input energy of 500 eV. 'R' represents the range, 'S' the straggling and 'B' the electrons backscattered to the cathode. The top section shows the results by assuming an isotropic DCS for the electrons and using Q_m. The bottom section uses the ZB DCS. Energies above 200 eV use the DCS at 200 eV. The labels are defined in 14.1. In this case the errors are measured relative to forward scattering.

Simulation	R_z(m)	error(%)	S_z(m)	error (%)	S_x(m)	B(%)
Isotropic elastic scattering with Q_m from ZB						
CUS	5.64e-02	-0.5	3.21e-02	-0.5	4.48e-02	60.6
FOR	5.67e-02	0.0	3.23e-02	0.0	4.50e-02	60.6
ISO	3.76e-02	-33.6	2.14e-02	-33.6	3.11e-02	73.7
SC Q_m/Q_t	5.58e-02	-1.5	3.17e-02	-1.6	4.45e-02	60.7
SC	5.37e-02	-5.2	3.05e-02	-5.6	4.34e-02	61.4
SCI	4.98e-02	-12.1	2.83e-02	-12.2	4.07e-02	64.3
Anisotropic elastic scattering from ZB						
CUS	5.61e-02	-0.5	3.20e-02	-0.5	4.48e-02	60.7
FOR	5.64e-02	0.0	3.21e-02	0.0	4.50e-02	60.7
SC Q_m/Q_t	5.55e-02	-1.5	3.16e-02	-1.6	4.45e-02	60.8

Table 14.7: Results for a scale factor of 10 and an input energy of 1000 eV. 'R' represents the range, 'S' the straggling and 'B' the electrons backscattered to the cathode. The top section shows the results by assuming an isotropic DCS for the electrons and using Q_m. The bottom section uses the ZB DCS. Energies above 200 eV use the DCS at 200 eV. The labels are defined in 14.1. In this case the errors are measured relative to forward scattering.

Simulation	R_z(m)	error(%)	S_z(m)	error (%)	S_x(m)	B(%)
Isotropic elastic scattering with Q_m from ZB						
CUS	1.33e-01	-0.2	7.43e-02	-0.3	1.08e-01	68.5
FOR	1.33e-01	0.0	7.45e-02	0.0	1.08e-01	68.5
ISO	8.50e-02	-36.1	4.72e-02	-36.6	7.03e-02	79.7
SC Q_m/Q_t	1.32e-01	-0.8	7.38e-02	-0.9	1.08e-01	68.5
SC	1.28e-01	-3.5	7.16e-02	-3.8	1.05e-01	68.9
SCI	1.17e-01	-11.7	6.55e-02	-12.0	9.70e-02	71.5
Anisotropic elastic scattering from ZB						
CUS	1.29e-01	-0.2	7.26e-02	-0.2	1.06e-01	69.0
FOR	1.30e-01	0.0	7.28e-02	0.0	1.06e-01	69.0
SC Q_m/Q_t	1.29e-01	-0.7	7.22e-02	-0.8	1.06e-01	69.0

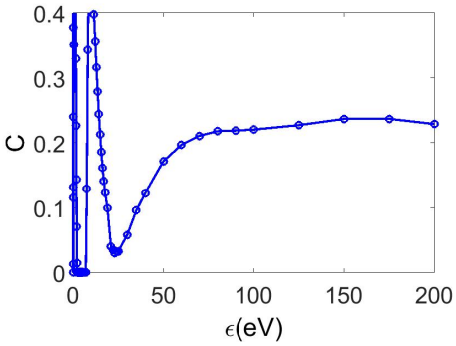

Figure 14.12: For the elastic DCS the results of the fit using (14.28) for parameter C are shown.

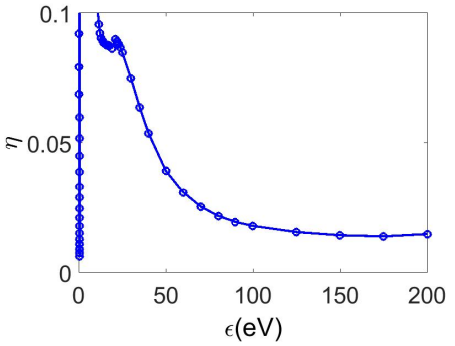

Figure 14.13: For the elastic DCS the results of the fit using (14.28) for parameter η are shown.

inelastic DCS can not be accurately captured by any of the formulae that have been considered. Due to the lack of good analytical formulae direct fits of the DCS using eq. 14.28 have been considered as well.

The degree of anisotropy has been quantified by comparing the range, straggling and backscattering of the various DCS models in a Monte Carlo simulation. An imaginary atom has been considered were only one elastic and one inelastic process is possible. The excitation process towards $4s'[1/2]_1$ is scaled by a factor 10 to approximately represent the total inelastic cross section of Ar. The simulations indicate that the DCS from the calculations of Zatsarinny and Bartschat can be approximated accurately. Errors in the order of one percent are obtained by using a direct fit of the DCS or an analytical fit using the ratio of $\frac{Q_m}{Q_t}$. For a scale factor of 10 for the inelastic cross section the errors using pure forward scattering are in the order of a 2-3 % which makes the forward model almost as accurate as a direct fit. Additionally, replacing the isotropic elastic scattering by the DCS calculated by Zatsarinny and Bartschat only modifies the results up to 2 %. This confirms that elastic scattering is accurately represented by the momentum transfer cross section from Zatsarinny and Bartschat and assuming isotropic scattering. It should be emphasized that the total elastic cross section and the elastic momentum transfer cross section are different, as shown in figure 14.11. By using scale factors for the inelastic process of 100 the total inelastic cross section is overestimated by a factor 10 approximately. The relative errors for the direct fit and the $\frac{Q_m}{Q_t}$-method are in the order of 0-7%. The forward model gives relative errors of 7-15%. Based on the considered tests the following recommendations are given

- For inelastic collisions, assume forward scattering (i.e. do not change the velocity angle)
- For elastic collisions, use the momentum-transfer cross section Q_m (rather than the total cross section) for the collision probability, combined with an

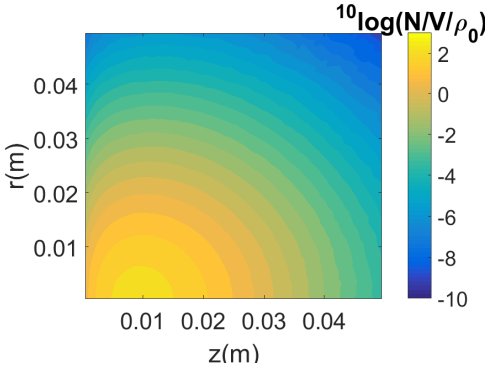

(a) Elastic and inelastic scattering: isotropic; scale factor: 10.

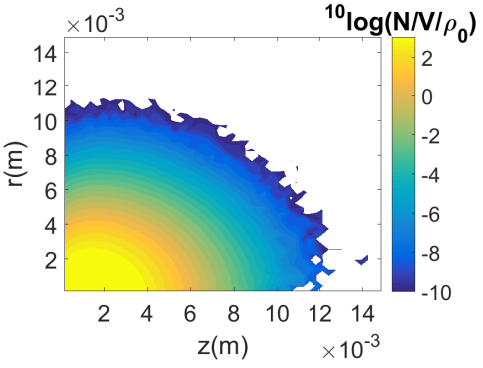

(b) Elastic and inelastic scattering: isotropic; scale factor: 100.

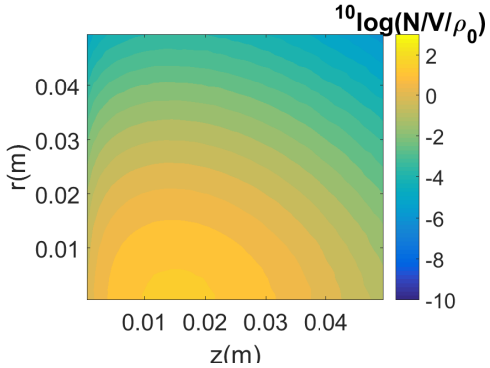

(c) Elastic scattering: isotropic; Inelastic scattering: forward; scale factor: 10.

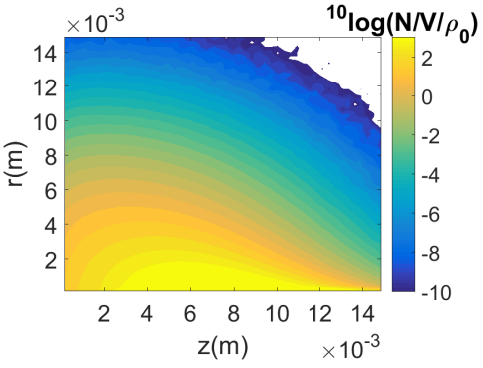

(d) Elastic scattering: isotropic; Inelastic scattering: forward; scale factor: 100.

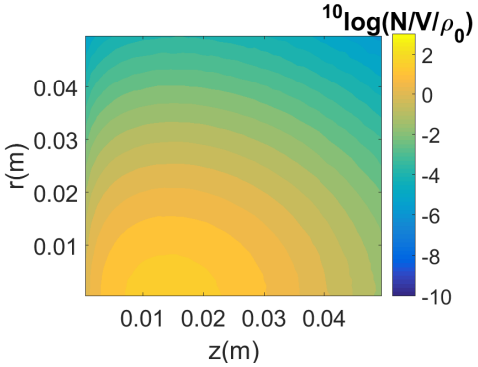

(e) Elastic and inelastic scattering: ZB; scale factor: 10.

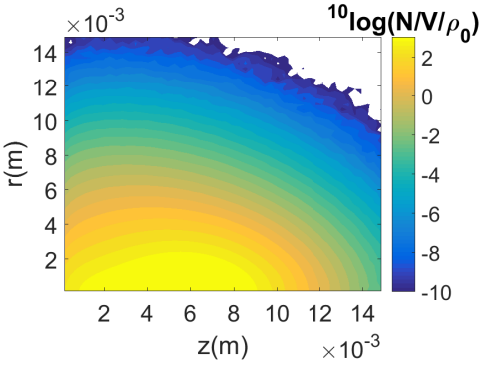

(f) Elastic and inelastic scattering: ZB; scale factor: 100.

Figure 14.14: Spatial profile of stopped electrons expressed as a density by dividing the number of electrons removed by the local volume. The results are normalized by ρ_0 which is calculated as the total number of electrons divided by the displayed volume. An input energy of 200 eV has been used in all cases. The scale factor for the inelastic transition is varied and the DCS of the elastic and inelastic DCS are varied.

isotropic scattering angle from equation 14.22.

- This simple treatment performs better than any of the other theoretical/empirical analytical formulae for the range of conditions considered in our analysis, and we expect it to perform at least as well for general low-temperature plasma modeling purposes. The only way to obtain more accurate results is to use the full DCS, provided this is available.

There are a few caveats concerning these recommendations. The first is that our analysis did not take into account ionization because the data set from Zatsarinny and Bartschat does not include the ionization DCS. Ionization involves the additional question of how energy and momentum are shared between the primary and secondary electrons, a question that is not directly related to the anisotropy issue but can be equally important [251]. Secondly, in some molecular gases, unlike the argon-like gas in our analysis, angular velocity scattering by low-threshold rotational and vibrational processes can contribute significantly to the overall electron momentum losses. We could imagine that treating such low-threshold inelastic processes with forward scattering has consequences for the electron swarm parameters [268].

Previous works [245, 246] suggest that anisotropic scattering effects on swarm parameters are generally small. Calculations by Hagelaar of swarm parameters in Ar using cross sections from Zatsarinny and Bartschat [229] have been made for two types of scattering models (forward and isotropic) and two types of energy sharing models for ionization (50/50, the energy is split evenly between the electrons; 100/0 the secondary electron gets no energy). A more realistic description of the energy redistribution [269] yields results intermediate between the two limiting cases 50/50 and 100/0.

The calculations show that changing the DCS for the inelastic processes from isotropic to forward scattering results in relative differences larger than 1 % for E/N values above 100 Td for the mobility, average energy and the ionization rate. For the transverse and longitudinal diffusion coefficients differences of the order of 1 % are already observed for 10 Td. At 1000 Td the relative differences increased up to 29-32 % for the mobility μN. The impact of the energy sharing models is shown to be of the order of 1-9 %. For the ionization rate coefficient the impact of the anisotropy at 1000 Td appeared to be 21-24 % while the effect of the energy sharing model was smaller with 1-10 %. For the mean energy at 1000 Td the effect of both models is smaller with the inelastic scattering models changing the results in the range of 13-15 % and the energy sharing models changing the results only with 1-2 %. The longitudinal diffusion coefficient shows relative differences up to 100 % at 1000 Td induced by the anisotropy. The energy sharing model induces differences up to 35 % at 250 Td. These results confirm that anisotropy is also important for swarm parameters and that over the E/N range considered (10-1000 Td) its impact is comparable to the impact of the energy sharing models.

A more detailed study, that includes low-energy threshold processes, is required to evaluate the effect of anisotropy on swarm parameters relative to other assumptions in swarm calculations related to how electron number changing processes are taken into account.

Chapter 15

Conclusions

The work discussed in this thesis has resulted in a more accurate description of collision integrals and transport coefficients. The more accurate transport models have been applied in simulations of mercury-free HID lamps with the PLASIMO platform. Simulations of these lamps have also been improved by using a self-consistent diffusion algorithm and a corrected radiation transport module. Ab initio calculations have been used successfully to predict the shape of the continuum radiation of the considered mercury replacement candidates. Three other topics are discussed in this thesis. The first topic is radiation transport as an effective particle transport mechanism in argon. Secondly, a comparison between an argon mixture and an argon-silicon-tetrachloride mixture in a surfatron is made. Thirdly, the impact of the particular choice of the angular distribution function of the differential cross section for electron-argon collisions on the evolution of a high energy electron beam is evaluated. The results and recommendations for all of these topics are briefly summarized in the following sections.

Transport coefficients

- An improved method for estimating collision integrals is implemented in PLASIMO and discussed in chapter 4. This new approach replaces the inaccurate rigid sphere and Coulomb approximations. It now automatically chooses the most accurate method available without requiring any specifications in the input file.

- More accurate expressions for the calculation of the transport coefficients are used as discussed in chapter 5. These expressions are derived from the Chapman-Enskog expansion. The improved estimates for the collision integrals also improve the accuracy of the calculated transport coefficients.

- New methods for acquiring potential parameters are developed. The new approach for calculating collision integrals requires knowledge of the polarizability of the species involved in the collision. Nowadays, the polarizability of most atoms is well known. For ions and molecules this type of data is more

scarce. Quantum mechanical software packages are used to obtain estimates of the polarizability for the cases where it is not available. A small step further is the direct calculation of the potential curves. Collision integrals can be obtained directly from these calculated interaction potentials.

Currently, PLASIMO uses the collision integral for the ground state of a given species also for all excited states. However, the potential curves for interactions with the excited state can deviate significantly from the potential curves for interactions with the ground state. By making polarizabilities or potential curves available for excited species, more accurate estimates of these interactions can be made.

Self-consistent diffusion

- The usage of more accurate collision integrals greatly improved the stability of the self-consistent diffusion model. However, the self-consistent model appeared to be unstable for certain conditions. In spite of the improved stability, the model is still not stable for all conditions. It is observed that the model is more stable for higher pressures and larger amounts of nodal points as discussed in chapter 6. The exact origins of the numerical instabilities are not yet understood. The self-consistent algorithm for the calculation of the diffusive velocities was previously developed by Peerenboom. This model is an improvement of Fick's model which only takes interactions with the background species into account while the self consistent model includes interactions with all particles.

- When LTE conditions are valid, the system of equations is solved for the elemental species and supplemented with elemental constraints. Solving the species system in terms of elemental species, as described in chapter 7, reduces the number of coupled equations. Elemental constraints are used that either guarantee a given amount of mass in the gas phase or specify a given elemental pressure on one of the boundaries. The last condition resembles the liquid-gas interface for species that are saturated. The instabilities that can occur in the species system have not been observed in the elemental system that is used in LTE.

Radiation transport

- A discretization error is found in the ray tracing algorithm developed by Van der Heijden. In the central parts of cylindrical or spherical grids, the radiation losses were calculated inconsistently. In chapter 8, an improved discretization scheme is presented.

- The required time for the evaluation of the radiation losses is reduced by parallelizing the code.

A drawback of the current method is that the spectral grid has to be defined prior to the simulation. The consequence is that the spectral grid in practice contains more points than necessary due to the fact that this grid is used for every ray. An adaptive grid may reduce the calculation time. The calculation time can be reduced even further by only using ray tracing for the spectral points that have an optical depth in a given range. This range should be chosen in such a way that the error introduced by using a simpler calculation, using either the optically thin or the optically thick calculation, is below a predefined tolerance.

One of the required inputs for the ray tracing model is the selection of a line profile. Expressions for various line profiles are provided in chapter 8. A commonly used model for the line profile that is obtained as the convolution of a van der Waals and a Lorentzian profile is discussed in chapter 9.

- The expression given by Stormberg is numerically unstable and should therefore be replaced by the alternative expression presented in chapter 9.

In the ideal case the van der Waals profile is avoided since it only includes the attractive part of the potential. Whenever possible the pressure broadening should be calculated using a complete potential curve.

Mercury-free HID lamps

- Numerical models of mercury-free lamps are developed and discussed in chapters 10 and 11. In both models, InI is considered as a replacement candidate for mercury.

- The emitted continuum radiation is derived from the potential curves that have been calculated using a quantum mechanical software package. These data reveal that the broad continuum originates from recombining In and I atoms. The model is able to describe the shape of the continuum quite well. Specific features, like the absorption of the ultraviolet and the absorption related to the $A - X$ transition, are reproduced. A similar recombination continuum is demonstrated in SnI and TlI mixtures.

- The models are able to explain that arc contraction is responsible for the generation of the lamp voltage. The usage of InI as a buffer gas is not feasible, since the pressure required to generate the lamp voltage by arc contraction is accompanied by a strong infrared continuum. Such a continuum limits the lamp's efficiency.

Currently, the potential curves have an estimated error in the order of one or two tenths of an electronvolt. This accuracy limits the precision of the reproduction of spectral features. Another improvement can be realized by describing the plasma as a non-thermal plasma. The arc contraction limits the temperature and therefore the electron density in the mantle. It is not clear whether in that area the number of electron collisions is sufficient to enforce species densities that satisfy LTE. The current simulations have been performed using a one-dimensional

grid. The consequence is that the convective flow could not be modeled. In a two-dimensional grid the convective flow, can be included.

Effect of resonant levels on the metastable levels in an argon plasma

- The necessity of ray tracing is demonstrated for a low pressure argon plasma. This is done by comparing results from models that use ray tracing with models that use a uniform escape factor. The comparison shows that using Holstein's expression for the escape factors provides relative errors for the species that can reach up to a factor 20. The relative errors can be reduced by using an escape factor that is derived from the ray tracing result. However, those simulations still show that the spatial dependency of the escape factor is important. Near the wall, the relative errors of the species can still amount to 80% of the results obtained in the model that uses ray tracing.

- The model demonstrates that the effects of including ray tracing are not limited to the species that are directly involved in the transition. Due to chemical reactions, the impact of adjusted resonant levels is also passed on to the metastable species. The result is that metastable species in the center of the discharge are effectively transported directly to the wall via chemical and radiative coupling.

Surfatron plasmas

- For the first time, a mixture of argon and $SiCl_4$ has been considered spatially resolved in a surfatron plasma using a 2D cylindrically symmetric grid with a self-consistent electromagnetic module.

In chapter 13, a comparison is made between a plasma in pure argon and a mixture of argon and $SiCl_4$. A few approximations were made to improve the stability of the code. Firstly, Fick's diffusion module rather than the self-consistent diffusion module was used. Secondly, the input power and the flow rate of $SiCl_4$ were reduced in comparison to experimental conditions. By using the same conditions, a comparison of a mixture containing $Ar + SiCl_4$ and a mixture of pure argon confirms that the electron temperature decreases significantly in the $Ar + SiCl_4$ mixture. The effect on the heavy particle temperature is small. Additionally, the electron density is about an order of magnitude larger in the mixture containing $Ar + SiCl_4$.

In order to make a comparison possible with experimental results, the stability of the model must improve. It is expected that an improved self-consistent diffusion module will provide the necessary stability. Currently, the convergence rate is rather low. The usage of an adaptive grid may reduce the calculation time. Chemistry reduction techniques can also reduce the calculation time.

Differential cross sections

In chapter 14, the ab initio quantum mechanical calculations from Zatsarinny and Bartschat for the differential cross section (DCS) for electron-argon collisions are considered. The angular distribution function derived from these DCS is compared to various analytical angular distribution functions.

- The agreement between analytical functions for the angular distribution function and the distribution derived from ab initio results is rather poor.

In Monte Carlo simulations the range, straggling and backscattering are compared for these distributions. The best reproduction of the angular distribution predicted by Zatsarinny and Bartschat were obtained using the following DCS:

- isotropic scattering for elastic processes.
- forward scattering for inelastic processes.

Effects of ionization are neglected and should be included in a future study.

Ab initio calculations

- Two ab initio quantum mechanical software packages have been considered in this work: DIRAC and DALTON. The main difference between the packages is the fact that DIRAC accounts for relativistic effects while DALTON does not. DALTON has the advantage that it contains a potential energy minimization routine.
- The minimization routine can be used to calculate polarizabilities of molecules in their equilibrium positions. It is recommended that a database of this type of data is built to ensure that the collision integrals are estimated with the best available data.
- For species that are frequently considered in simulations, it is recommended to calculate the potential curves and obtain the collision integrals from a direct integration. Having access to the potential curves also opens up the possibility to use more accurate collision integrals for excited species.
- The packages DIRAC and DALTON can also be used to calculate transition dipole moments which are required to calculate the Einstein coefficients for a specific transition.

In many cases, a theoretical estimate is becoming an accurate and affordable addition to data obtained from experiments. In specific cases, such calculations are already accurate enough to provide an alternative for experiments.

Bibliography

[1] J.A. Bittencourt. *Fundamentals of plasma physics*. Springer, 2004.

[2] R. Fitzpatrick, editor. *Plasma Physics: An introduction*. CRC Press, Taylor & Francis Group, 2014.

[3] Manuel Jiménez Díaz. *Modelling of microwaves induced plasmas*. PhD thesis, Eindhoven University of Technology, The Netherlands, 2011.

[4] Efe Hasan Kemaneci. *Modelling of Plasmas with Complex Chemistry: Application to Microwave Deposition Reactors*. PhD thesis, Eindhoven University of Technology, The Netherlands, 2014.

[5] A. Laricchiuta, G. Colonna, D. Bruno, R.Celiberto, C. Gorse, F. Pirani, and M. Capitelli. Classical transport collision integrals for a Lennard-Jones like phenomenological model potential. *Chem. Phys. Let.*, 445:133–139, 2007.

[6] K.S.C. Peerenboom. PhD thesis, Eindhoven University of Technology, The Netherlands, 2012.

[7] Glow discharge laboratory. Website consulted at February 5 2016. url: http://www.glow-discharge.com/?Physical_background:Glow_Discharges:Discharge_Regimes.

[8] M.F. Gendre. Two centuries of electric light source innovations. url: http://www.einlightred.tue.nl/lightsources/history/light_history.pdf.

[9] Preparatory study on light sources for ecodesign and/or energy labelling requirements ('Lot 8/9/10'). Final report, Task 4. Technologies. Prepared by VITO. Ordered by the European Commission, Directorate-General for Energy. url:http://ecodesign-lightsources.eu/documents.

[10] Preparatory study on light sources for ecodesign and/or energy labelling requirements ('Lot 8/9/10'). Final report, Task 5. Environment & Economics. Prepared by VITO. Ordered by the European Commission, Directorate-General for Energy. url:http://ecodesign-lightsources.eu/documents.

[11] CIE Proceedings (1964). Vienna Session. 1963. Vol. B. p 209-220. Bureau Central de la CIE, Paris.

[12] Colour & Vision Research Laboratory. University college London. url: http://cvrl.ioo.ucl.ac.uk/, section: CMFs, subsection: CIE 1964 10-deg XYZ CMFs.

[13] C.S. McCamy. Correlated color temperature as an explicit function of chromaticity coordinates. *Color Research & Application*, 17(2):142–144, 1992.

[14] Erratum. *Color Research & Application*, 18(2):150–150, 1993.

[15] Dorothy Nickerson. Light Sources and Color Rendering. *J. Opt. Soc. Am.*, 50(1):57–69, Jan 1960.

[16] M. Born. Investigation on the replacement of mercury in high-pressure discharge lamps by metallic zinc. *J. Phys. D: Appl. Phys.*, 34:909–924, 2001.

[17] M. Käning, L. Hitzschke, B. Schalk, M. Berger, St. Franke, and R. Methling. Mercury-free high pressure discharge lamps dominated by molecular radiation. *J. Phys. D: Appl. Phys.*, 44:224005, 2011.

[18] C.W. Johnston, H.W.P. van der Heijden, A. Hartgers, K. Garloff, J. van Dijk, and J.J.A.M. van der Mullen. An improved LTE model of a high pressure sulfur discharge. *Journal of Physics D: Applied Physics*, 37(2):211, 2004.

[19] H.W.P. van der Heijden, editor. *Modelling of radiative transfer in light sources*. 2003.

[20] Harm van der Heijden and Joost van der Mullen. General treatment of the interplay between fluid and radiative transport phenomena in symmetric plasmas: the sulphur lamp as a case study. *Journal of Physics D: Applied Physics*, 35(17):2112, 2002.

[21] A.J. Rijke, S. Nijdam, M. Haverlag, J.F.J. Janssen, J.J.A.M. van der Mullen, and G.M.W. Kroesen. A calibrated integrating sphere setup to determine the infrared spectral radiant flux of high-intensity discharge lamps. *J. Phys. D: Appl. Phys.*, 44:224007, 2011.

[22] A.J. Rijke. PhD thesis, Eindhoven University of Technology, The Netherlands, 2013.

[23] T.L. Lemmens, 2013. MSc thesis. Eindhoven University of Technology. The Netherlands.

[24] D. Küppers, J. Koenings, and H. Wilson. Deposition of Fluorine-Doped silica layers from a $SiCl_4/SiF_4/O_2$ Gas Mixture by the Plasma-CVD Method. *Journal electrochemical society*, 125:1298, 1978.

[25] Jan van Dijk, Kim Peerenboom, Manuel Jimenez, Diana Mihailova, and Joost van der Mullen. The plasma modelling toolkit PLASIMO. *Journal of Physics D: Applied Physics*, 42(19):194012, 2009.

[26] C.W. Johnston. *Transport and equilibrium in molecular plasmas - the sulfur lamp*. PhD thesis, Eindhoven University of Technology, The Netherlands, 2003.

[27] M. Capitelli, D. Bruno, and A. Laricchiuta. *Fundamental aspects of plasma chemical physics. Transport*. Springer, 2013.

[28] K.S.C. Peerenboom, J. van Dijk, J.H.M. ten Thije Boonkkamp, L. Liu, W.J. Goedheer, and J.J.A.M. van der Mullen. Mass conservative finite volume discretization of the continuity equations in multi-component mixtures. *Journal of Computational Physics*, 230(9):3525 – 3537, 2011.

[29] K.S.C. Peerenboom, J. van Dijk, W.J. Goedheer, and J.J.A.M. van der Mullen. On the ambipolar constraint in multi-component diffusion problems. *Journal of Computational Physics*, 230(10):3651 – 3655, 2011.

[30] H.P. Stormberg. Line broadening and radiative transport in high-pressure mercury discharges with NaI and TlI as additives. *J. Appl. Phys.*, 51:1963–1969, 1980.

[31] T. Holstein. Imprisonment of Resonance Radiation in Gases. II. *Phys. Rev.*, 83:1159–1168, Sep 1951.

[32] O. Zatsarinny and K. Bartschat. B -spline BreitPauli R -matrix calculations for electron collisions with argon atoms. *Journal of Physics B: Atomic, Molecular and Optical Physics*, 37(23):4693, 2004.

[33] M. Allan, O. Zatsarinny, and K. Bartschat. Near-threshold absolute angle-differential cross sections for electron-impact excitation of argon and xenon. *Phys. Rev. A*, 74:030701, Sep 2006.

[34] J.O. Hirschfelder, C.F. Curtiss, and R.B. Bird, editors. *Molecular Theory of Gases and Liquids*. (New York: Wiley & Sons), 1964.

[35] M. Capitelli and A. D'Angola G. Colonna, editors. *Fundamental aspects of plasma chemical physics. Thermodynamics*. Springer, 2012.

[36] G. Herzberg. *Molecular Spectra and Molecular Structure I: Spectra of Diatomic Molecules*. D. Van Nostrand Company, Inc., Princeton, New Jersey, 1963.

[37] Peter Atkins and Julio de Paula, editors. *Physical Chemistry*. (Oxford University Press), 2006.

[38] G.H. Fuller. Nuclear spins and moments. *J. Phys. Chem. Ref. Data*, 5:835, 1976.

[39] P.M. Morse. Diatomic Molecules According to the Wave Mechanics. II. Vibrational Levels. *Phys. Rev.*, 34:57–64, Jul 1929.

[40] Hugh M. Hulburt and Joseph O. Hirschfelder. Potential Energy Functions for Diatomic Molecules. *The Journal of Chemical Physics*, 9(1):61–69, 1941.

[41] Hugh M. Hulburt and Joseph O. Hirschfelder. Erratum: Potential Energy Functions for Diatomic Molecules. *The Journal of Chemical Physics*, 35(5):1901–1901, 1961.

[42] D. Pagano, A. Casavola, L.D. Pietanza, M. Capitelli, G. Colonna, D. Giordano, and L. Maraffa. *ESA Scientific Technical Review*, 257, 2009.

[43] M.W. Chase, editor. *NIST-JANAF Thermochemical tables fourth edition.* NIST, Gaithersburg, Maryland, 1998.

[44] M. Capitelli, G. Colonna, D. Giordano, L. Marraffa, A. Casavola, P. Minelli, D. Pagano, L. D. Pietanza, F. Taccogna, and B. Warmbein. Tables of internal partition functions and thermodynamic properties of high-temperature Mars-atmosphere species from 50K to 50000K. *ESA Scientific Technical Review*, 246, October 2005.

[45] G. Herzberg. *Molecular Spectra and Molecular Structure III: Spectra and Electronic Structure of Polyatomic Molecules.* D. Van Nostrand Company, Inc., Princeton, New Jersey, 1966.

[46] G. Herzberg. *Molecular Spectra and Molecular Structure II: Infrared and Raman Spectra of Polyatomic Molecules.* D. Van Nostrand Company, Inc., Princeton, New Jersey, 1960.

[47] H.W. Woolley. Calculation of Thermodynamic Functions for Polyatomic Molecules'. *Journal of Research of the National Bureau of Standards*, 56(2):105, 1956.

[48] NIST ASD Team. NIST Chemistry webbook. `http://webbook.nist.gov/chemistry/name-ser.html`.

[49] S. Ghorui, J.V.R. Heberlein, and E. Pfender. Thermodynamic and Transport Properties of Two-Temperature Nitrogen-Oxygen Plasma. *Plasma Chemistry and Plasma Processing*, 28(4):553–582, 2008.

[50] J.N. Butler and R.S. Brokaw. Thermal conductivity of gas mixtures in chemical equilibrium. *J. Chem. Phys.*, 26:1636, 1957.

[51] J.M.L. Martin, J.P. François, and R. Gijbels. Ab initio spectroscopy and thermochemistry of the BN molecule. *Z. Phys. D -Atoms, Molecules and Clusters*, 21:47–55, 1991.

[52] J.M.L. Martin, J.P. François, and R. Gijbels. First principles computation of thermochemical properties beyond the harmonic approximation. I. Method and application to the water molecule and its isotopomers. *Journal of chemical physics*, 96:7633, 1992.

[53] NIST ASD Team. NIST Atomic spectra database levels data. `http://physics.nist.gov/PhysRefData/ASD/levels_form.html`.

[54] M. Mitchner and C.H. Kruger. *Partially ionized gases*. Wiley series in plasma physics. Wiley, 1973.

[55] E.H. Holt and R.E. Haskell, editors. *Foundations of Plasma Dynamics*. (New York: The Macmillan Company), 1965.

[56] H.W. Drawin. Validity conditions for local thermodynamic equilibrium. *Zeitschrift fr Physik*, 228(2):99–119, 1969.

[57] S. Whitaker. Derivation and application of the stefan-maxwell equations. *Revista Mexicana de Ingeniería Química*, 8(3):213–243, 2009.

[58] M.A. Lieberman and A.J. Lichtenberg. *Principles of plasma and materials processing*. Wiley-Interscience, 2005.

[59] J.D. Ramshaw. Hydrodynamic Theory of Multicomponent Diffusion and Thermal Diffusion in Multitemperature Gas Mixtures. *Journal of Non-Equilibrium Thermodynamics*, 18:121–134, 1993.

[60] J.C. Slater. Atomic Radii in Crystals. *The Journal of Chemical Physics*, 41(10):3199–3204, 1964.

[61] E. Clementi, D.L. Raimondi, and W.P. Reinhardt. Atomic Screening Constants from SCF Functions. II. Atoms with 37 to 86 Electrons. *The Journal of Chemical Physics*, 47(4):1300–1307, 1967.

[62] Joseph O. Hirschfelder and Morton A. Eliason. The estimation of the transport properties for electronically excited atoms and molecules. *Annals of the New York Academy of Sciences*, 67(9):451–461, 1957.

[63] R.A. Svehla. Estimated Viscosities and Thermal Conductivities of Gases at High Temperatures. Technical Report R-132, Glenn Research Center, January 1962.

[64] Gerhard Franz, editor. *Low pressure plasmas and microstructuring technology*. (Springer-Verlag Berlin Heidelberg), 2009.

[65] Steve H. Kang and Joseph A. Kunc. Viscosity of high-temperature iodine. *Phys. Rev. A*, 44:3596–3605, Sep 1991.

[66] K.T. Tang and J. Peter Toennies. An improved simple model for the van der Waals potential based on universal damping functions for the dispersion coefficients. *The Journal of Chemical Physics*, 80(8):3726–3741, 1984.

[67] K.T. Tang and J.Peter Toennies. New combining rules for well parameters and shapes of the van der Waals potential of mixed rare gas systems. *Zeitschrift für Physik D Atoms, Molecules and Clusters*, 1(1):91–101, 1986.

[68] Louis Monchick. Collision Integrals for the Exponential Repulsive Potential. *Physics of Fluids (1958-1988)*, 2(6):695–700, 1959.

[69] M. Klein and F.J. Smith. Tables of Collision Integrals for the (m,6) Potential Function for 10 Values of m. *Journal of research of the National Bureau of Standards-A. Physics and Chemistry*, 72A:359–423, 1968.

[70] E.A. Mason, J.T. Vanderslice, and J.M. Yos. Transport properties of high temperature multicomponent gas mixtures. *Phys. Fluids*, 2:688, 1959.

[71] T. Holstein. Mobilities of positive ions in their parent gases. *J. Phys. Chem.*, 56:832, 1952.

[72] A.B. Murphy and C.J. Arundell. *Plasma Chemistry and Plasma Processing*, 14(4):451, 1994.

[73] A.B. Murphy. *Plas. Chem. and Plas. Proc.*, 15(2):279, 1995.

[74] D. Rapp and W.E. Francis. Charge exchange between gaseous ions and atoms. *J. Chem. Phys.*, 37:2631, 1962.

[75] A. Dalgarno. *Phil. Trans. Roy. Soc. London*, A250:426, 1958.

[76] R.S. Devoto. Transport coefficients of partially ionized argon. *Phys. of Fluids*, 10(2):354, 1967.

[77] Jan van Dijk. *Modelling of Plasma Light Sources — an object-oriented approach*. PhD thesis, Eindhoven University of Technology, The Netherlands, 2001.

[78] B.M. Smirnov. Atomic structure and the resonant charge exchange process. *Physics-Uspekhi*, 44:221, 2001.

[79] A.V. Kosarim and B.M. Smirnov. Electron terms and resonant charge exchange involving oxygen atoms and ions. *Journal of Experimental and Theoretical Physics*, 101:611–627, 2005.

[80] A.V. Kosarim, B.M. Smirnov, M. Capitelli, R. Celiberto, and A. Laricchiuta. Resonant charge exchange involving electronically excited states of nitrogen atoms and ions. *Physical Review A*, 74:062707, 2006.

[81] A. Messiah. *Quantum Mechanics*, volume 2. Amsterdam: North Holland, 1962.

[82] D. Terr. MATLAB implementation of Wigner 3j symbol, 2004. http://www.mathworks.com/matlabcentral/fileexchange/5275-wigner3j-m/content/Wigner3j.m.

[83] Larry A. Viehland and Martin Hesche. Transport properties for systems with resonant charge transfer. *Chemical Physics*, 110(1):41 – 54, 1986.

[84] Ph. Belenguer and L.C. Pitchford. Effect of anisotropy in the elastic scattering cross sections on the ionization source terms in glow discharges in argon. *Journal of Applied Physics*, 86(9):4780–4785, 1999.

[85] J.P. Boeuf and E. Marode. A Monte Carlo analysis of an electron swarm in a nonuniform field: the cathode region of a glow discharge in helium. *Journal of Physics D: Applied Physics*, 15(11):2169, 1982.

[86] V.D. Stojanović and Z. Lj. Petrović. Comparison of the results of Monte Carlo simulations with experimental data for electron swarms in from moderate to very high electric field to gas density ratios. *Journal of Physics D: Applied Physics*, 31(7):834, 1998.

[87] E.A. Mason, R.J. Munn, and F.J. Smith. Transport coefficients of ionized gases. *Phys. Fluids*, 10:1827–1832, 1967.

[88] R.S. Devoto. Transport coefficients of ionized argon. *Phys. of Fluids*, 16:616, 1973.

[89] L.A. Viehland and Y. Chang. Transport cross sections for collisions between particles. *Computer Physics Communications*, 181:1687–1696, 2010.

[90] G. Colonna and A. Laricchiuta. General numerical algorithm for classical collision integral calculation. *Computer Physics Communications*, 178:809–816, 2008.

[91] H. O'Hara and F.J. Smith. The efficient calculation of the transport properties of a dilute gas to a prescribed accuracy. *Journal of computational physics*, 5:328, 1970.

[92] G. von Winckel. Fast Clenshaw-Curtiss quadrature, 2005. http://www.mathworks.com/matlabcentral/fileexchange/6911-fast-clenshaw-curtis-quadrature.

[93] Philip D. Neufeld, A.R. Janzen, and R.A. Aziz. Empirical Equations to Calculate 16 of the Transport Collision Integrals $\Omega^{(l,s)*}$ for the Lennard-Jones (12-6) Potential. *The Journal of Chemical Physics*, 57(3):1100–1102, 1972.

[94] Francis J. Smith and R.J. Munn. Automatic Calculation of the Transport Collision Integrals with Tables for the Morse Potential. *The Journal of Chemical Physics*, 41(11):3560–3568, 1964.

[95] E.A. Mason and H.W. Jr. Schamp. Mobility of gaseous ions in weak electric fields. *Annals of physics*, 4:233–270, 1958.

[96] Eugene Levin, David W. Schwenke, James R. Stallcop, and Harry Partridge. Comparison of semi-classical and quantum-mechanical methods for the determination of transport cross sections. *Chemical Physics Letters*, 227(6):669 – 675, 1994.

[97] R.S. Devoto. *Phys. of Fluids*, 10(10):2105, 1967.

[98] R. Cambi, G. Liutti D. Cappelletti, and F. Pirani. *J. Chem. Phys.*, 95:1852, 1991.

[99] G. Liuti and F. Pirani. Regularities in van der Waals forces: correlation between the potential parameters and polarizability. *Chemical Physics Letters*, 122(3):245 – 250, 1985.

[100] A.D. Koutselos and E.A. Mason. Correlation and prediction of dispersion coefficients for isoelectronic systems. *The Journal of Chemical Physics*, 85(4):2154–2160, 1986.

[101] J. Norton Wilson. On the London Potential Between Pairs of RareGas Atoms. *The Journal of Chemical Physics*, 43(7):2564–2565, 1965.

[102] D. Cappelletti, G. Liuti, and F. Pirani. Generalization to ion-neutral systems of the polarizability correlations for interaction potential parameters. *Chem. Phys. Let.*, 183:297–303, 1991.

[103] Vincenzo Aquilanti, David Cappelletti, and Fernando Pirani. Range and strength of interatomic forces: dispersion and induction contributions to the bonds of dications and of ionic molecules. *Chemical Physics*, 209(2-3):299 – 311, 1996. Structure and Reactivity of Molecular Ions.

[104] S.H. Patil. Thomas-Fermi model electron density with correct boundary conditions: applications to atoms and ions. *Atomic data and nuclear data tables*, 71:41–68, 1999.

[105] B.T. Thole. Molecular polarizabilities calculated with a modified dipole interaction. *Chem. Phys*, 59:341–350, 1981.

[106] P.T. van Duijnen and M. Swart. Molecular and atomic polarizabilities: Thole's Model revisited. *The journal of physical chemistry A*, 102:2399, 1998.

[107] DIRAC, a relativistic ab initio electronic structure program, Release DIRAC14 (2014), written by H.J. Aa. Jensen, R. Bast, T. Saue, and L. Visscher, with contributions from V. Bakken, K.G. Dyall, S. Dubillard, U. Ekström, E. Eliav, T. Enevoldsen, T. Fleig, O. Fossgaard, A.S.P. Gomes, T. Helgaker, J.K. Lærdahl, J. Henriksson, M. Iliaš, Ch.R. Jacob, S. Knecht, S. Komorovský, O. Kullie, C.V. Larsen, H.S. Nataraj, P. Norman, G. Olejniczak, J. Olsen, Y.S. Park, J.K. Pedersen, M. Pernpointner, K. Ruud, P. Sałek, B. Schimmelpfennig, J. Sikkema, A.J. Thorvaldsen, J. Thyssen, J. van Stralen, S. Villaume, O. Visser, T. Winther, and S. Yamamoto (see http://www.diracprogram.org).

[108] R.S. Devoto. *Phys. of Fluids*, 9(6):1230, 1966.

[109] C.R. Wilke. A Viscosity Equation for Gas Mixtures. *The Journal of Chemical Physics*, 18(4):517–519, 1950.

[110] Jörg Liesen and Volker Mehrmann. *Linear algebra*. Springer, 2015.

[111] C. Muckenfuss and C.F. Curtiss. Thermal conductivity of multicomponent gas mixtures. *J. Chem. Phys.*, 29:1273, 1958.

[112] R.S. Brokaw. Thermal conductivity of gas mixtures in chemical equilibrium II. *J. Chem. Phys.*, 32:1005, 1960.

[113] P. Rini, D. Vanden Abeele, and G. Degrez. Closed form for the equations of chemically reacting flows under local thermodynamic equilibrium. *Physical Review E*, 72(1, 1), 2005.

[114] Jerrold M. Yos. Transport properties of nitrogen, hydrogen, oxygen and air to 30,000 K. Technical report, AVCO Corporation, March 1963. RAD-TM-63-7, reprinted 8. August.

[115] S. Ghorui and A.K. Das. Collision integrals for charged-charged interaction in two-temperature non-equilibrium plasma. *Physics of Plasmas*, 20(9):093504, 2013.

[116] R.H. Williams and H.E. DeWitt. QuantumMechanical Plasma Transport Theory. *Physics of Fluids*, 12(11):2326–2342, 1969.

[117] H. Hahn, E.A. Mason, and F.J. Smith. Quantum transport cross sections for ionized gases. *Physics of fluids*, 14:278, 1971.

[118] Wei Zong Wang, Ming Zhe Rong, J.D. Yan, A.B. Murphy, and Joseph W. Spencer. Thermophysical properties of nitrogen plasmas under thermal equilibrium and non-equilibrium conditions. *Physics of Plasmas*, 18(11), 2011.

[119] A.B. Murphy. Transport coefficients of hydrogen and argon-hydrogen plasmas. *Plasma Chemistry and Plasma Processing*, 20, 2000.

[120] P. André, W. Bussière, and D. Rochette. Transport coefficients of Ag-SiO2 plasmas. *Plasma Chem. Plasma Process*, 27:381–403, 2007.

[121] A. Laricchiuta, D. Bruno, M. Capitelli, C. Catalfamo, R. Celiberto, G. Colonna, P. Diomede, D. Giordano, C. Gorse, S. Longo, D. Pagano, and F. Pirani. High temperature Mars atmosphere. Part I: transport cross sections. *Eur. Phys. J. D*, 54:607–612, 2009.

[122] D. Bruno, C. Catalfamo, M. Capitelli, G. Colonna, O. De Pascale, P. Diomede, C. Gorse, A. Laricchiuta, S. Longo, D. Giordano, and F. Pirani. Transport properties of high-temperature Jupiter atmosphere components. *Physics of Plasmas*, 17:112315, 2010.

[123] Data is part of the package SAHprog which has been obtained from Marco Haverlag.

[124] R.D. Johnson III. NIST Computational Chemistry Comparison and Benchmark Database. url:http://cccbcb.nist.gov/.

[125] K. Aidas, C. Angeli, K.L. Bak, V. Bakken, R. Bast, L. Boman, O. Christiansen, R. Cimiraglia, S. Coriani, P. Dahle, E.K. Dalskov, U. Ekstrm, T. Enevoldsen, J.J. Eriksen, P. Ettenhuber, B. Fernndez, L. Ferrighi, H. Fliegl, L. Frediani, K. Hald, A. Halkier, C. Httig, H. Heiberg, T. Helgaker, A.C. Hennum, H. Hettema, E. Hjertens, S. Hst, I.-M. Hyvik, M.F. Iozzi, B. Jansik, H.J. Aa. Jensen, D. Jonsson, P. Jrgensen, J. Kauczor, S. Kirpekar, T. Kjrgaard, W. Klopper, S. Knecht, R. Kobayashi, H. Koch, J. Kongsted, A. Krapp, K. Kristensen, A. Ligabue, O.B. Lutns, J.I. Melo, K.V. Mikkelsen, R.H. Myhre, C. Neiss, C.B. Nielsen, P. Norman, J. Olsen, J.M.H. Olsen, A. Osted, M.J. Packer, F. Pawlowski, T.B. Pedersen, P.F. Provasi, S. Reine, Z. Rinkevicius, T.A. Ruden, K. Ruud, V. Rybkin, P. Salek, C.C.M. Samson, A. Snchez de Mers, T. Saue, S.P.A. Sauer, B. Schimmelpfennig, K. Sneskov, A.H. Steindal, K.O. Sylvester-Hvid, P.R. Taylor, A.M. Teale, E.I. Tellgren, D.P. Tew, A.J. Thorvaldsen, L. Thgersen, O. Vahtras, M.A. Watson, D.J.D. Wilson, M. Ziolkowski, and H. gren, "The Dalton quantum chemistry program system", WIREs Comput. Mol. Sci. 2014, 4:269284 (doi: 10.1002/wcms.1172).

[126] Dalton, a molecular electronic structure program, Release Dalton2013 (2013), see http://daltonprogram.org.

[127] Richard L. Martin, Ernest R. Davidson, and David F. Eggers. Ab initio theory of the polarizability and polarizability derivatives in H2S. *Chemical Physics*, 38(3):341 – 348, 1979.

[128] Vincent Giovangigli. Mass conservation and singular multicomponent diffusion algorithms. *IMPACT of Computing in Science and Engineering*, 2(1):73 – 97, 1990.

[129] Vincent Giovangigli. Convergent iterative methods for multicomponent diffusion. *IMPACT of Computing in Science and Engineering*, 3(3):244 – 276, 1991.

[130] G.M. Janssen. *Design of a General Plasma Simulation Model, Fundamental Aspects and Applications*. PhD thesis, Eindhoven University of Technology, The Netherlands, 2000.

[131] A. Hartgers. *Modelling of a Fluorescent Lamp Plasma*. PhD thesis, Eindhoven University of Technology, The Netherlands, 2003.

[132] Khalid Alhumaizi. Flux-limiting solution techniques for simulation of reactiondiffusionconvection system. *Communications in Nonlinear Science and Numerical Simulation*, 12(6):953 – 965, 2007.

[133] Kim Peerenboom, Jochem van Boxtel, Jesper Janssen, and Jan van Dijk. A conservative multicomponent diffusion algorithm for ambipolar plasma flows

in local thermodynamic equilibrium. *Journal of Physics D: Applied Physics*, 47(42):425202, 2014.

[134] A. Hartgers, H.W.P. van der Heijden, M.L. Beks, J. van Dijk, and J.A.M. van der Mullen. An elemental diffusion description for LTE plasma models. *Journal of Physics D: Applied Physics*, 38(18):3422, 2005.

[135] M.L. Beks, A.J. Flikweert, T. Nimalasuriya, W.W. Stoffels, and J.J.A.M. van der Mullen. Competition between convection and diffusion in a metal halide lamp, investigated by numerical simulations and imaging laser absorption spectroscopy. *Journal of Physics D: Applied Physics*, 41(14):144025, 2008.

[136] Anthony B. Murphy. The effects of metal vapour in arc welding. *Journal of Physics D: Applied Physics*, 43(43):434001, 2010.

[137] P. Rini, D. Vanden Abeele, and G. Degrez. Analysis of Diffusion Phenomena in Reacting Mixtures Under LTE with Application to CO_2/N_2 Stagnation Line Flows. *Proceedings of the 9th AIAA/ASME Joint Thermophysics and Heat Transfer Conference*, 2006.

[138] G. Colonna, A. DAngola, A. Laricchiuta, D. Bruno, and M. Capitelli. Analytical Expressions of Thermodynamic and Transport Properties of the Martian Atmosphere in a Wide Temperature and Pressure Range. *Plasma Chemistry and Plasma Processing*, 33(1):401–431, 2013.

[139] O.N. Suslov, G.A. Tirsky, and V.V. Shchennikov. Flows of Multicomponent Ionized Mixtures in Chemical Equilibrium. Description within the Framework of the Navier-Stokes and Prandtl Equations. *Prikl. Mekh. and Tekhn. Fiz*, 1971.

[140] A.B. Murphy. Demixing in free-burning arcs. *Phys. Rev. E*, 55:7473–7494, Jun 1997.

[141] Alexandre Ern and Vincent Giovangigli. The kinetic chemical equilibrium regime. *Physica A: Statistical Mechanics and its Applications*, 260(12):49 – 72, 1998.

[142] M.L. Beks, A. Hartgers, and J.J.A.M. van der Mullen. Demixing in a metal halide lamp, results from modelling. *Journal of Physics D: Applied Physics*, 39(20):4407, 2006.

[143] S. Chapman and T. Cowling. *The Mathematical Theory of Non-uniform Gases*. Cambridge University Press, Cambridge, 1960.

[144] J. Ferziger and H. Kaper. *Mathematical Theory of Transport Processes in Gases*. North Holland, Amsterdam, 1972.

[145] F.A. Williams. Elementary derivation of the multicomponent diffusion equation. *Am. J. Phys.*, 26:467–469, 1958.

[146] D. Burnett. The Distribution of Molecular Velocities and the Mean Motion in a Non-Uniform Gas. *Proceedings of the London Mathematical Society*, s2-40(1):382–435, 1936.

[147] Adi Ben-Israel and Thomas N.E. Greville. *Generalized Inverses — Theory and Applications*. John Wiley and Sons, New York, 1973.

[148] D.L. Scharfetter and H.K. Gummel. Large-signal analysis of a silicon Read diode oscillator. *IEEE Transactions on Electron Devices*, 16(1):64–77, 1969.

[149] S. Patankar. *Numerical heat transfer and fluid flow*. Taylor and Francis, Levittown, 1980.

[150] J.H.M. ten Thije Boonkkamp, J. van Dijk, L. Liu, and K.S.C. Peerenboom. Extension of the Complete Flux Scheme to Systems of Conservation Laws. *Journal of Scientific Computing*, 53(3):552–568, 2012.

[151] H.T. Cullinan. Analysis of Flux Equations of Multicomponent Diffusion. *Industrial & Engineering Chemistry Fundamentals*, 4(2):133–139, 1965.

[152] M. Gnybida, J.F.J. Janssen, J. van Dijk, J.L.G. Suijker, K.S.C. Peerenboom, A.J. Rijke, M. Gendre, and G.M.W. Kroesen. Numerical investigation on the replacement of mercury by indium iodide in high-intensity discharge lamps. *Journal of Physics D: Applied Physics*, 47(12):125201, 2014.

[153] H.R. Griem. *Plasma spectroscopy*. New York: McGraw-Hill, 1964.

[154] A. Corney, editor. *Atomic and laser spectroscopy*. Oxford University press, 1977.

[155] A.W. Ali and H.R. Griem. Theory of Resonance Broadening of Spectral Lines by Atom-Atom Impacts. *Phys. Rev.*, 140:A1044–A1049, Nov 1965.

[156] R.E.M. Hedges, D.L. Drummond, and Alan Gallagher. Extreme-Wing Line Broadening and Cs-Inert-Gas Potentials. *Phys. Rev. A*, 6:1519–1544, Oct 1972.

[157] H.M. Foley. The Pressure Broadening of Spectral Lines. *Phys. Rev.*, 69:616–628, 1946.

[158] I.I. Sobelman. Uber die Theorie der Linienbreite von Atomen. *Fortschritte der Physik*, 5:175–210, 1957.

[159] J.F.J. Janssen, M. Gnybida, J.L.G. Suijker, A.J. Rijke, and J. van Dijk. f. *Journal of Applied Physics*, 114(18), 2013.

[160] F. Schreier. The Voigt and complex error function: a comparison of computational methods. *J. Quant. Spectrosc. Radiat. Trans.*, 48:743–762, 1992.

[161] J. Humlíček. Optimized computation of the voigt and complex probability functions. *Journal of Quantitative Spectroscopy and Radiative Transfer*, 27(4):437 – 444, 1982.

[162] A.K. Hui, B.H. Armstrong, and A.A. Wrays. Rapid computation of the voigt and complex error functions. *J. Quant. Spectrosc. Radiat. Trans.*, 19:509–516, 1978.

[163] J.M. de Regt, J. van Dijk, J.A.M. van der Mullen, and D.C. Schram. Components of continuum radiation in an inductively coupled plasma. *Journal of Physics D: Applied Physics*, 28(1):40, 1995.

[164] K.T.A.L. Burm. Continuum radiation in a high pressure argonmercury lamp. *Plasma Sources Science and Technology*, 13(3):387, 2004.

[165] S. Chandrasekhar. *Radiative transfer.* Dover publications, Inc. New York, 1960.

[166] G.B. Rybicki and A.P. Lightman. *Radiative processes in astrophysics.* Wiley-VCH, 1979.

[167] H.P. Stormberg and R. Schäfer. Time-dependent behavior of high-pressure mercury discharges. *J. Appl. Phys.*, 54:4338–4347, 1983.

[168] G. Hartel, H. Schöpp, H. Hess, and L. Hitzschke. Radiation from an alternating current high-pressure mercury discharge: A comparison between experiments and model calculations. *J. Phys. D: Appl. Phys.*, 85:7076–7088, 1999.

[169] J. de Groot and J. van Vliet. *The high-pressure sodium lamp.* Kluwer Technische boeken, 1985.

[170] J.P. Woerdman, J. Schlejen, J. Korving, M.C. van Hemert, J.J. de Groot, and R.P.M. van Hal. Analysis of satellite and undulation structure in the spectrum of Na+Hg continuum emission. *Journal of Physics B: Atomic and Molecular Physics*, 18(21):4205, 1985.

[171] Ossama Kullie. A relativistic time-dependent density functional study of the excited states of the mercury dimer. *The Journal of Chemical Physics*, 140(2), 2014.

[172] H.R. Griem. *Principles of Plasma Spectroscopy.* Cambridge University Pressl, 1997.

[173] J.M. Luque, M.D. Calzada, and M. Saez. A new procedure for obtaining the Voigt function dependent upon the complex error function. *J. Quant. Spectrosc. Radiat. Trans.*, 94:151–161, 2005.

[174] J.A.C. Weideman. Computation of the complex error function. *SIAM Journal on Numerical Analysis*, 31:1497–1518, 1994.

[175] M. Weiß, H. Schubert, S. Meier, M. Born, D. Reiter, and M. Strösser. Determination of line broadening constants in high pressure discharge lamps. *J. Phys. D: Appl. Phys.*, 38:3170–3174, 2005.

[176] J.H. Tortai, A. Bonifaci, N. Denat, and C. Trassy. Diagnostic of the self-healing of metallized polypropylene film by modeling of the broadening emission lines of aluminum emitted by plasma discharge. *J. Appl. Phys.*, 97:053304, 2005.

[177] C.O. Laux, T.G. Spence, C.H. Kruger, and R.N. Zare. Optical diagnostics of atmospheric pressure air plasmas. *Plasma Sources Sci. Technol.*, 12:125–138, 2003.

[178] H. Skenderovic and V. Vujnovic. A study of the line broadening constants obtained in a high-pressure mercury discharge. *J. Quant. Spectrosc. Radiat. Trans.*, 55:155–162, 1996.

[179] M. Born. Line broadening measurements and determination of the contribution of radiation diffusion to thermal conductivity in a high-pressure zinc discharge. *J. Phys. D: Appl. Phys.*, 32:2492, 1999.

[180] J.E. Lawler. Resonance broadening of Hg lines as a density diagnostic in high intensity discharge lamps. *Plasma Sources Sci. Technol.*, 13:321–328, 2004.

[181] H. Bateman. *Tables of Integral Transforms.* New York: McGraw-Hill, 1954.

[182] M. Abramowitz and I.A. Stegun. *Handbook of mathematical functions with formulas, graphs, and mathematical tables.* Dover publications, New York, 1970.

[183] See supplementary material as for a MATLAB/Octave implementation of the Faddeeva function written by Ikuma, K. (mathworks fileexchange 22207-faddeeva-function-fft-based).

[184] C.W. Johnston, H.W.P. van der Heijden, G.M. Janssen, J. van Dijk, and J.J.A.M. van der Mullen. A self-consistent LTE model of a microwave-driven, high-pressure sulfur lamp. *J. Phys. D: Appl. Phys.*, 35:342–351, 2002.

[185] See supplementary material as for a MATLAB/Octave implementation of a numerical comparison between Stormberg's original expression and the new expression presented in this article.

[186] See supplementary material as for a MATLAB/Octave implementation of the error function for complex numbers written by Leutenegger, M. (mathworks fileexchange 18312-error-function-of-complex-numbers).

[187] D.O. Wharmby. Estimates of molecular absorption cross-sections in mercury plasmas at very high pressures using self-reversed line diagnostics. *J. Phys. D: Appl. Phys*, 41:144017, 2008.

[188] W. Elenbaas. *The high pressure mercury vapour discharge.* North-Holland Pub. Co., 1951.

[189] J.T. Dolan, M.G. Ury, and C.H. Wood. Lamp including sulfur. *US Patent 5404076*, 1966.

[190] H. Grabner and M. Zauter. Indiumjodid-Hochdrucklampen fuer Projektionszwecke. *Technische-wissenschaftliche Abhandlungen der Osram-Gesellschaft*, 9:29–38, 1967.

[191] Ch. Kaiser, C.M. Ögün, R. Kling, and W. Heering. Electrodeless Mercury-Free Microwave-Driven Indium-Iodine-Based High-Intensity Discharges with High Color Rendering Index. *IEEE Trans. Plasma Sci.*, 41:77–81, 2013.

[192] G.M.J.F. Luijks, S. Nijdam, and H. v Esveld. Electrode diagnostics and modelling for ceramic metal halide lamps. *J. Phys. D: Appl. Phys.*, 38:3163–3169, 2005.

[193] E. Fischer. Axial segregation of additives in mecury-metal-halide arcs. *J.Appl. Phys.*, 47:2954, 1976.

[194] M. Haverlag, editor. *An energy balance model for hid lamps including radiation transport; model update begin 2003; CDL 03/xx.* HID-Physics, Philips, 2003.

[195] L.V. Gurvich, I.V. Veyts, and C.B. Alcock. *Thermodynamic properties of individual substances.* Hemisphere Publishing Corp., New York, 1989.

[196] L.V. Gurvich, I.V. Veyts, and C.B. Alcock. *Thermodynamic properties of individual substances.* Hemisphere Publishing Corp., New York, 1994.

[197] D.R. Stull and H. Prophet. *JANAF thermochemical tables second edition.* NIST, Washington, 1971. NSRDS-NBS 37.

[198] M.W. Chase, J.L. Curnutt, H. Prophet, R.A. McDonald, and A.N. Syverud. *JANAF thermochemical tables 1975 supplement*, volume 4. 1975.

[199] M.W. Chase, C.A. Davies, J.R. Downey Jr, D.J. Frurip, R.A. McDonald, and A.N. Syverud. JANAF thermochemical tables third edition. *J. Phys. Chem. Ref. Data*, 14:1, 1985.

[200] V. Rat, P. André, J. Aubreton, M.F. Elchinger, P. Fauchais, and A. Lefort. Transport properties in a two-temperature plasma: Theory and application. *Phys. Rev. E*, 64:026409, 2001.

[201] S.R. Hunter, J.G. Carter, and L.G. Christophorou. Low-energy electron drift and scattering in krypton and xenon. *Phys. Rev. A*, 38:5539–5551, 1988.

[202] M. Hayashi. Determination of electron-xenon total excitation cross sections, from experimental values of townsend's alpha. *J. Phys. D:Appl. Phys.*, 16:581, 1983.

[203] O. Zatsarinny, K. Bartschat, G. Garcia, F. Blanco, L.R. Hargreaves, D.B. Jones, R. Murrie, J.R. Brunton, M.J. Brunger, M. Hoshino, , and Buckman S.J. Electron-collision cross sections for iodine. *Phys. Rev. A*, 83:042702, 2011.

[204] Z. Felfli, A.Z. Msezane, and D. Sokolovski. Slow electron elastic scattering cross sections for In, Tl, Ga and At atoms. *J. Phys. B: At. Mol. Opt. Phys.*, 45:189501, 2012.

[205] M.S. Rabasović, V.I. Kelemen, S.D. Tošić, D Šević, M.M. Dovhanych, V. Pejčev, D.M. Filipović, E.Yu. Remeta, and B.P. Marinković. Experimental and theoretical study of the elastic-electronindium-atom scattering in the intermediate energy range. *Phys. Rev. A*, 77:062713, 2008.

[206] R.N. Gupta, J.M. Yos, R.A. Thompson, and K.P. Lee. A review of reaction rates and thermodynamic and transport properties for an 11-species air model for chemical and thermal nonequilibrium calculations to 30000 K. *NASA Rept.*, page 1232, 1990.

[207] H van der Heijden and J. van der Mullen. Semiclassical and quantum-mechanical descriptions of S_2 molecular radiation. *J. Phys. B: At. Mol. Opt. Phys.*, 34:4183–4201, 2001.

[208] K.G. Dyall. Relativistic and nonrelativistic finite nucleus optimized triple-zeta basis sets for the 4p, 5p and 6p elements. *Theor. Chem. Acc.*, 108:335–340, 2002.

[209] K.G. Dyall. Relativistic and nonrelativistic finite nucleus optimized triple zeta basis sets for the 4p, 5p and 6p elements (vol 108, pg 335, 2002). *Theor. Chem. Acc.*, 109:284, 2003.

[210] K.G. Dyall. Relativistic quadruple-zeta and revised triple-zeta and double-zeta basis sets for the 4p, 5p, and 6p elements. *Theor. Chem. Acc.*, 115:441–447, 2006.

[211] DIRAC, a relativistic ab initio electronic structure program, Release DIRAC12 (2012), (see http://www.diracprogram.org).

[212] E. Schnedler. The calculation of complex chemical equilibria. *Calphad*, 8:265–279, 1984.

[213] J. Szudy and W.E. Baylis. Unified Franck-Condon treatment of pressure broadening of spectral lines. *Journal of Quantitative Spectroscopy and Radiative Transfer*, 15(78):641 – 668, 1975.

[214] Ab initio calculation for e-InI performed by Quantemol. Results can be obtained from j.v.dijk@tue.nl.

[215] U. Safronova, M. Safronova, and M. Kozlov. Relativistic all-order calculations of In I and Sn II atomic properties. *Phys. Rev. A*, 76:022501, Aug 2007.

[216] A. Brandt, M. Israeli, I. Yavneh, and A. Siegel. Multigrid Solution of an Elliptic Boundary-Value Problem with Integral Constraints. *SIAM Journal on Scientific Computing*, 21(4):1357–1369, 1999.

[217] R.F. Barrow. Dissociation energies of the gaseous mono-halides of boron, aluminium, gallium, indium and thallium. *Trans. Faraday Soc.*, 56:952–958, 1960.

[218] Amartya Banerjee and Kalyan Kumar Das. Theoretical spectroscopic studies of InI and InI+. *International Journal of Quantum Chemistry*, 112(2):453–469, 2012.

[219] C.M. Ögün, W. Truong, C. Kaiser, R. Kling, and W. Heering. Modelling of indium(I) iodide-argon low pressure plasma. *Journal of Physics D: Applied Physics*, 47(28):285202, 2014.

[220] Magnus Gustafsson, Sergey V. Antipov, Jan Franz, and Gunnar Nyman. Refined theoretical study of radiative association: Cross sections and rate constants for the formation of SiN. *The Journal of Chemical Physics*, 137(10), 2012.

[221] D.R. Bates. Rate of formation of molecules by radiative association. *Royal astronomical society*, 111:303, 1951.

[222] L.A. Schlie, L.E. Jusinski, R.D. Rathge, R.A. Hamil, and D.L. Drummond. Strong TlXe excimer band emission via electron beam initiated discharges in TlI and Xe mixtures. *The Journal of Chemical Physics*, 72(8):4529–4548, 1980.

[223] CEA NASA. Thermo Build. `http://cearun.grc.nasa.gov/cea/index_ds.html`.

[224] Yu. Golubovskii, S. Gorchakov, D. Loffhagen, and D. Uhrlandt. Influence of the resonance radiation transport on plasma parameters. *The European Physical Journal - Applied Physics*, 37:101–104, 1 2007.

[225] T. Holstein. Imprisonment of Resonance Radiation in Gases. *Phys. Rev.*, 72:1212–1233, Dec 1947.

[226] J. Vlcek. A collisional-radiative model applicable to argon discharges over a wide range of conditions. I. Formulation and basic data. *Journal of Physics D: Applied Physics*, 22(5):623, 1989.

[227] Emile Carbone, Eddie van Veldhuizen, Gerrit Kroesen, and Nader Sadeghi. Electron impact transfer rates between metastable and resonant states of argon investigated by laser pumpprobe technique. *Journal of Physics D: Applied Physics*, 48(42):425201, 2015.

[228] Ángel Yanguas-Gil, Jos Cotrino, and Lus L. Alves. An update of argon inelastic cross sections for plasma discharges. *Journal of Physics D: Applied Physics*, 38(10):1588, 2005.

[229] BSR database, Data type: scattering cross sections, www.lxcat.net, retrieved november 2013.

[230] Emile Carbone, Nader Sadeghi, Erik Vos, Simon Hübner, Eddie van Veldhuizen, Jan van Dijk, Sander Nijdam, and Gerrit Kroesen. Spatio-temporal dynamics of a pulsed microwave argon plasma: ignition and afterglow. *Plasma Sources Science and Technology*, 24(1):015015, 2015.

[231] G.H. Copley and D.M. Camm. Pressure broadening and shift of argon emission lines. *Journal of Quantitative Spectroscopy and Radiative Transfer*, 14(9):899 – 907, 1974.

[232] Emile Carbone. *Laser diagnostics and modelling of microwave plasmas.* PhD thesis, TUE, 2013.

[233] Overview of applications that have been modelled with the software package PLASIMO. Website consulted at June 16 2016. URL : https://plasimo.phys.tue.nl/applications/index.html.

[234] Sara Rahimi. *Modelling of microwave induced deposition plasmas.* PhD thesis, TUE, 2014.

[235] A.V. Phelps. The diffusion of charged particles in collisional plasmas: Free and ambipolar diffusion at low and moderate pressures. *J. Res. NIST*, 95:407, 1990.

[236] J.T. Gudmundsson and E.G. Thorsteinsson. Oxygen discharges diluted with argon: dissociation processes. *Plasma Sources Science and Technology*, 16(2):399, 2007.

[237] Harshit N. Kothari, Siddharth H. Pandya, and K.N. Joshipura. Electron impact ionization of plasma important SiCl X (X = 14) molecules: theoretical cross sections. *Journal of Physics B: Atomic, Molecular and Optical Physics*, 44(12):125202, 2011.

[238] C. Lee, D.B. Graves, and M.A. Lieberman. Role of etch products in polysilicon etching in a high-density chlorine discharge. *Plasma Chemistry and Plasma Processing*, 16(1):99–120, 1996.

[239] Kim Peerenboom, Alessandro Parente, Tomáš Kozák, Annemie Bogaerts, and Gérard Degrez. Dimension reduction of non-equilibrium plasma kinetic models using principal component analysis. *Plasma Sources Science and Technology*, 24(2):025004, 2015.

[240] Jia-Lin Chang. A new formula to calculate FranckCondon factors for displaced and distorted harmonic oscillators. *Journal of Molecular Spectroscopy*, 232(1):102 – 104, 2005.

[241] Martin Kogelschatz, Gilles Cunge, and Nader Sadeghi. Identification of halogen containing radicals in silicon etching plasmas and density measurement by UV broad band absorption spectroscopy. *Journal of Physics D: Applied Physics*, 37(14):1954, 2004.

[242] Mark J. Kushner. Application of a particle simulation to modeling commutation in a linear thyratron. *Journal of Applied Physics*, 61(8):2784–2794, 1987.

[243] M. Surendra, D.B. Graves, and G.M. Jellum. Self-consistent model of a direct-current glow discharge: Treatment of fast electrons. *Phys. Rev. A*, 41:1112–1125, Jan 1990.

[244] Z. Lj. Petrović, S. Dujko, D. Marić, G. Malović, Ž. Nikitović, O. Šašić, J. Jovanović, V. Stojanović, and M. Radmilović-Radenović. Measurement and interpretation of swarm parameters and their application in plasma modelling. *Journal of Physics D: Applied Physics*, 42(19):194002, 2009.

[245] G.N. Haddad, S.L. Lin, and R.E. Robson. The effects of anisotropic scattering on electron transport. *Australian Journal of Physics*, 34:243, 1981.

[246] A.V. Phelps and L.C. Pitchford. Anisotropic scattering of electrons by N_2 and its effect on electron transport. *Phys. Rev. A*, 31:2932–2949, May 1985.

[247] R.W.L. Thomas and W.R.L. Thomas. Monte Carlo simulation of electrical discharges in gases. *Journal of Physics B: Atomic and Molecular Physics*, 2(5):562, 1969.

[248] Ivan D. Reid and Scott R. Hunter. Comparison between the Boltzmann and Monte Carlo Simulation Methods for the Determination of Electron Swarm Transport Coefficients in Molecular Hydrogen. *Australian Journal of Physics*, 32:255–260, 1979.

[249] E.E. Kunhardt and Y. Tzeng. Role of electron-molecule angular scattering in shaping the electron-velocity distribution. *Phys. Rev. A*, 34:2158–2166, Sep 1986.

[250] G.J.M. Hagelaar and L.C. Pitchford. Solving the Boltzmann equation to obtain electron transport coefficients and rate coefficients for fluid models. *Plasma Sources Science and Technology*, 14(4):722, 2005.

[251] S. Yoshida, A.V. Phelps, and L.C. Pitchford. Effect of electrons produced by ionization on calculated electron-energy distributions. *Phys. Rev. A*, 27:2858–2867, Jun 1983.

[252] BSR database, Data type: differential scattering cross sections, www.lxcat.net, retrieved november 2013.

[253] A. Okhrimovskyy, A. Bogaerts, and R. Gijbels. Electron anisotropic scattering in gases: A formula for Monte Carlo simulations. *Phys. Rev. E*, 65:037402, Feb 2002.

[254] Alexander V. Khrabrov and Igor D. Kaganovich. Electron scattering in helium for Monte Carlo simulations. *Physics of Plasmas (1994-present)*, 19(9):093511, 2012.

[255] D.J. Strickland, D.L. Book, T.P. Coffey, and J.A. Fedder. Transport equation techniques for the deposition of auroral electrons. *Journal of Geophysical Research*, 81(16):2755–2764, 1976.

[256] N.F. Mott and H.S.W. Massey. *The Theory of Atomic Collisions*. Oxford University Press, 1965.

[257] J.H. Jacob. Multiple Electron Scattering through a Slab. *Phys. Rev. A*, 8:226–235, Jul 1973.

[258] G.J.M. Hagelaar. *Modeling of Microdischarges for Display Technology*. PhD thesis, Eindhoven University of Technology, The Netherlands, 2000.

[259] W.J.M. Brok. *Modelling of Transient Phenomena in Gas Discharges*. PhD thesis, Eindhoven University of Technology, The Netherlands, 2005. ISBN 90-386-2291-0.

[260] M. Hayashi. Report No. IPPJ-AM-19. Technical report, Institute of Plasma Physics, Nagoya University, 1981.

[261] H.S.W. Massey and E.H.S. Burhop. *Electronic and ionic impact phenomena*. Oxford University Press, 1969.

[262] G.J.M. Hagelaar and G.M.W. Kroesen. A Monte Carlo modelling study of the electrons in the microdischarges in plasma addressed liquid crystal displays. *Plasma Sources Science and Technology*, 9(4):605, 2000.

[263] M.D. White, K.J. Ross, and H. Bolouri. Differential cross section and generalised oscillator strength for the 1s to (2s+2p) transition in atomic hydrogen for incident electron kinetic energies 136, 200 and 300 eV and scattering up to 20 degrees. *Journal of Physics B: Atomic and Molecular Physics*, 12(5):811, 1979.

[264] S. Longo and M. Capitelli. A simple approach to treat anisotropic elastic collisions in Monte Carlo calculations of the electron energy distribution function in cold plasmas. *Plasma Chemistry and Plasma Processing*, 14(1):1–13, 1994.

[265] R. Browning, T.Z. Li, B. Chui, Jun Ye, R.F.W. Pease, Z. Czyewski, and D.C. Joy. Empirical forms for the electron/atom elastic scattering cross sections from 0.1 to 30 keV. *Journal of Applied Physics*, 76(4):2016–2022, 1994.

[266] S. Ahn and J.A. Fessler. Standard errors of mean, variance, and standard deviation estimators, 2003. EECS Department, The University of Michigan, url: http://web.eecs.umich.edu/ fessler/papers/files/tr/stderr.pdf.

[267] L. Vriens and A.H.M. Smeets. Cross-section and rate formulas for electron-impact ionization, excitation, deexcitation, and total depopulation of excited atoms. *Phys. Rev. A*, 22:940–951, Sep 1980.

[268] M.C. Bordage, P. Ségur, and A. Chouki. Determination of a set of electron impact cross sections in tetrafluoromethane consistent with experimental determination of swarm parameters. *Journal of Applied Physics*, 80(3):1325–1336, 1996.

[269] C.B. Opal, W.K. Peterson, and E.C. Beaty. Measurements of Secondary-Electron Spectra Produced by Electron Impact Ionization of a Number of Simple Gases. *The Journal of Chemical Physics*, 55(8):4100–4106, 1971.

Acknowledgements

After finishing my master thesis I was not sure whether I should stay at the university and obtain a PhD or work in the industry. An ideal opportunity was presented to me via the Schelp and Seel projects where I could work at the university on a subject that was highly relevant for the industry. For about one year I worked as *researcher* at the university. Since I truly enjoyed this work I decided to turn this project into a PhD thesis.

I was already involved in the Schelp project via the work for my master thesis. Originally, I started as an experimentalist where I worked with Arij Rijke, Sander Nijdam and Marco Haverlag on an integrating sphere setup that was designed to measure absolutely calibrated lamp spectra from the ultraviolet up to the infrared. During this work I became more and more interested in the possibility of predicting the measured spectra based on their input power and salt filling. This interest brought me in contact with Jan van Dijk who helped me setup numerical models of these lamps. The work in my master thesis focused on mercury containing lamps, while in this project the focus changed to developing a model for mercury-free lamps. In order to complete this challenging task I am very grateful for the useful discussions and experimental and numerical support from Arij, Sander, Marco, Jan, Mykhaylo, Kim, Thomas, Jos, Maxime and Gerrit.

From these people I especially want to thank my supervisor Jan van Dijk. You have been a very enthusiastic and supporting supervisor. In many cases your profound knowledge of physics, mathematics and computers was able to give a boost to my research. Additionally, I would like to thank Jos Suijker for always making some time available for me on the Friday afternoon. Your contribution was essential to become familiar with the quantum mechanical ab initio software packages. I enjoyed working with the two of you.

Unfortunately, Philips decided that a mercury free lamp was not feasible and therefore the Schelp and Seel projects came to an end. Via the STW-DRAKA project I got the opportunity to learn about other types of plasmas. I would like to thank Jan, Jos, Efe, Sander, Emile, Sven and Mathé for valuable discussions that made me familiar with microwave plasmas. Also I want to thank Mathé van Stralen for showing the impressive production process of glass fibers.

During my brief stay in Toulouse, I met Gerjan Hagelaar and Leanne Pitchford. I remember your warm welcome on the day of my arrival, that apparently was a French holiday. I want to thank you for all the interesting discussions we had, that each time led to an improved understanding of kinetic modeling.

I also want to express my gratitude to all committee members: Mark Kushner, Leanne Pitchford, Federico Toschi, Philip de Goey, Jos Suijker, Jan van Dijk, Gerrit Kroesen and Ton van Leeuwen. Thank you for taking the time to read my thesis and to participate in my defense committee.

Additionally, I want to thank all members of EPG for the pleasant atmosphere and the organization of many activities. I especially want to thank the people I shared an office with for our discussions that were both useful and fun. Due to multiple relocations those are quite a lot of people: Wouter, Niels, Simon, Arij, Dirk, Sara, Efe, Tafizur, Peter, Samaneh, Kim, Danka and Manon. I also want to thank the members of the PLASIMO team that have not been mentioned yet (in particular Diana) and my intern Stef Bardoel for their valuable contributions. During the thesis reading session the remaining errors and spelling mistakes were found and fixed. I want to thank Jan, Ferdi, Wouter, Diana, Sander, Marc, Peter, Bart, Samaneh, Susana and Luuk for the valuable suggestions and improvements. Our secretaries, Rina and Anita, have been very good at minimizing the bureaucratic work that I had to do myself. I am grateful for your efforts on my behalf!

Finally, I want to thank my friends for providing many fun opportunities to spend our time together. In particular I want to thank Buddy for designing the cover of this thesis. I would also like to thank my parents. You supported me throughout the last few years and took a lot of work off my hands: Thank you!

Curriculum vitæ

11 March 1988

Born in Roermond, the Netherlands.

2000–2006

Pre-university education (VWO), B.C. Broekhin, Roermond, the Netherlands.

2006–2009

Bachelor of Science in Applied Physics at Eindhoven University of Technology, the Netherlands.

2009–2012

Master of Science in Applied Physics at Eindhoven University of Technology, the Netherlands.

- Traineeship at ASML, Veldhoven, the Netherlands, *Experimental analysis of impinging plane micro jets*, supervised by dr.ir. L.J.A. van Bokhoven and prof.dr.ir. G.J.F. van Heijst, Turbulence and Vortex Dynamics
- Master thesis, *The energy balance of HID lamps*, supervised by dr.ir. A.J. Rijke, dr.ir. S. Nijdam, prof.dr.ir. M. Haverlag and prof.dr.ir. G.M.W. Kroesen, Elementary Processes in Gas discharges

2012–2016

Ph.D. candidate in the Elementary Processes in Gas discharges group, department of Applied Physics at Eindhoven University of Technology, the Netherlands. Results presented in this thesis. Supervised by dr.ir. J. van Dijk, dr.ir. J.L.G. Suijker and prof.dr.ir. G.M.W. Kroesen.